



Production and Application of Textile Materials

Edited by

Fernando B.N. Ferreira

Ana Maria Rocha

Andrea Zille

António Dinis Marques

Raul Fangueiro



TRANS TECH PUBLICATIONS

Production and Application of Textile Materials

Edited by
Fernando B.N. Ferreira
Ana Maria Rocha, Andrea Zille
António Dinis Marques
Raul Figueiro

Production and Application of Textile Materials

Special topic volume with invited peer-reviewed papers only

Edited by

**Fernando B.N. Ferreira, Ana Maria Rocha, Andrea Zille,
António Dinis Marques and Raul Fanguero**

Copyright © 2022 Trans Tech Publications Ltd, Switzerland

All rights reserved. No part of the contents of this publication may be reproduced or transmitted in any form or by any means without the written permission of the publisher.

Trans Tech Publications Ltd
Kapellweg 8
CH-8806 Baech
Switzerland
<https://www.scientific.net>

Volume 1063 of
Materials Science Forum
ISSN print 0255-5476
ISSN web 1662-9752

Full text available online at <https://www.scientific.net>

Distributed worldwide by

Trans Tech Publications Ltd
Kapellweg 8
CH-8806 Baech
Switzerland

Phone: +41 (44) 922 10 22
e-mail: sales@scientific.net

Preface

This specialized publication is dedicated to technical and technological solutions in textile production. Engineering solutions in the production of fibers and fabrics for both technical and domestic use are considered.

Particular attention in the book is given to the study of textile products for biomedical applications. Modern medical fabrics and fibers are used as dressing and suture material and significantly accelerate the recovery processes after surgical operations and burn injuries.

Fibers and fabrics are currently often used as a reinforcing element in the production of various composite materials, which are often used in mechanical engineering and in the construction sector. A separate chapter is devoted to textile reinforcing materials.

Environmental problems in textile production are mainly related to the dyeing process and the chemical treatment of fabrics and fibers. Some aspects of textile dyeing and wastewater treatment processes are also discussed in this publication.

The book will be useful to specialists involved in textile production and related industries.

Table of Contents

Preface

Chapter 1: Materials and Technologies for Fibers and Fabrics Fabrication

Orange Waste Films as a Raw Material for Designing Bio-Based Textiles: A Hybrid Research Method

D. Dumitrescu, M. Kooroshnia, S. Syed and A. Zamani 3

Evaluation of Denim Fabric Performances from Sustainable Yarn

O. Babaarslan, A. Shahid and S. Dilek 15

Influence of Fabric Structure on the Adhesion and Functional Properties of 3D Printed Polymers on the Woven Fabric

M. Čuk, K. Gramc, D. Muck and M. Bizjak 25

A Preliminary Study of Analising Weft Cover Factor of Woven Fabrics by Image Treatment

I. Montava, P. Díaz-García, A. Carbonell, J. Gisbert-Payá and E. Bou-Belda 35

Chapter 2: Fabrics and Fibers for Biomedical Application

Exploring Nanofibers and Hydrogels as Collagenase Carriers for the Development of Advanced Wound Dressings

J. Antunes, A. Ribeiro, D. Lemos, T. Miranda, J. Santos and G. Soares 43

Preliminary Studies on Antimicrobial Properties for Nanofiber Air Filters

F.A.P. Scacchetti, D.S. de Almeida, R. Santos, M.H.S. Santana, F.M. Bezerra, M. Lopes Aguiar and L.D. Martins 57

Antibacterial Nonwoven with Propolis for Use in Surgical Masks

N. Aral and I. Yigit 63

Electrospinning of Poly(Caprolactone)/Gelatin/Clindamycin Nanocomposites as an Antibacterial Wound Dressing

P. Mohamadi, G. Mirmoeini, H. Bahrami, E. Mohsenzadeh, C. Cochrane and V. Koncar 71

Development of Antimicrobial Polyester Fabric by a Green *In Situ* Synthesis of Copper Nanoparticles Mediated from Chitosan and Ascorbic Acid

B. Mehravani, A.I. Ribeiro, M. Montazer and A. Zille 83

Enhancing the Antimicrobial Efficacy of Polyester Fabric Impregnated with Silver Nanoparticles Using DBD Plasma Treatment

A.I. Ribeiro, B. Mehravani, C. Magalhães, T. Nicolau, L. Melro, R. Fernandes, V. Shvalya, U. Cvelbar, J. Padrão and A. Zille 91

Chapter 3: Fabrics and Fibers for Reinforcing of Composite Materials

Biologically Inspired Load Adapted 3D Textile Reinforcement Structures

D. Friese, L. Hahn and C. Cherif 101

Textile-Based 3D Truss Reinforcement for Cement-Based Composites Subjected to Impact Loading - Part II: *In Situ* Stress Analysis under Quasistatic and Dynamic Tensile Loading

H.L. Xuan, D.M.P. Vo, A. Nocke, C. Sennewald, G. Hoffmann and C. Cherif 111

Textile-Based 3D Truss Reinforcement for Cement-Based Composites Subjected to Impact Loading Part I: Development of Reinforcing Structure and Composite Characterization

D.M.P. Vo, C. Sennewald, A. Golla, M. Vorhof, G. Hoffmann, H.L. Xuan, A. Nocke and C. Cherif 121

Uni-Directional Tape Structures Consisting of Recycled Carbon Fibres and Polyamide 6 Fibers for High-Performance Thermoplastic Composites

M.F. Khurshid, M.M.B. Hasan, S. Hoebel, A. Abdkader and C. Cherif 133

From Grave to Cradle - Development of Weft Knitted Fabrics Based on Hybrid Yarns from Recycled Carbon Fibre Reclaimed by Solvolytic Process from of EOL-Components	
D. Rabe, M.M.B. Hasan, E. Häntzsche, C. Cherif, Y. Murakami, L.M. Bao and K. Kajiwara	139
Low Twist Hybrid Yarns from Long Recycled Carbon Fibres for High Performance Thermoplastic Composites	
M.M.B. Hasan, S. Bachor, A. Abdkader and C. Cherif	147

Chapter 4: Dyeing, Surface and Fibers Treatment

Thermochromic Properties of Textile Fabrics	
D. Matsouka, S. Vassiliadis, S. Galata, D. Gkoutzeli and A. Çay	157
New Method for Prediction of Photochromic Textiles Fatigue Behavior	
U. Solanki, M. Viková and M. Vik	163
Polyester-Polyvinylalcohol Hydrophilization Strategies	
T. Miranda, C. Pinto, J. Santos and G. Soares	173
Investigation of the Dyeability Behaviors of Cotton Surfaces with Natural Dyes Extracted from Rubia Tinctorum and Reseda Luteola L. Plants	
G. Caliskan, P. Sezgin, E.D. Kocak, S. Altindere and O. Kosemek	181
Pre, Post and Meta Mordanting Recycled Cotton with Chitosan	
S. Uysal, E. Bou-Belda, M. Bonet-Aracil and J. Gisbert-Payá	189
Substrate Color Prediction through Active Monitoring of the Exhaustion Dyeing Process	
B. Alves, L. Silva, G. Soares and J. Santos	195
Durable Moisture/Thermal Management Self-Adhesive Coating for Polyester Fabric	
G. Xia and J.H. Xin	203
Extraction Optimization of <i>Sorghum vulgare</i> for Natural Wool Dyeing Applications	
N. Belino, E. Alves, E. Almeida, C. Gameiro, T. Rosado, L. Passarinha, E. Gallardo, M. Pinto and J. Rodilla	209

Chapter 5: Environmental Engineering in Textile Production

Secondary Raw Plastic Materials in Applied Design	
J. Frajová and A. Opálková Šišková	227
Direct and Reactive Dyes Recovery in Textile Wastewater Using Calcinated Hydrotalcite	
E. Bou-Belda, D. López-Rodríguez, B. Micó-Vicent and M. Bonet-Aracil	233
Polyamide 6.6 Degradation through Photo-Fenton Process	
E. Marcelino-Perez, M. Bonet-Aracil, E. Bou-Belda, A. Amat Payá, A. Arques Sanz and R. Vicente	243

CHAPTER 1:

Materials and Technologies for Fibers and Fabrics Fabrication

Orange Waste Films as a Raw Material for Designing Bio-Based Textiles: A Hybrid Research Method

Delia Dumitrescu^{1,a}, Marjan Kooroshnia^{2,b*}, Samira Syed^{3,c}, Akram Zamani^{4,d}

^{1&2}The Swedish School of Textiles, University of Borås, 501 90 Borås, Sweden

^{3&4}Swedish Centre for Resource Recovery, University of Borås, 501 90 Borås, Sweden

Email: delia.dumitrescu@hb.se, marjan.kooroshnia@hb.se, syed.samiira@gmail.com
akram.zamani@hb.se

Keywords: Bio-based textiles, orange waste, textile and fashion design, subtractive textures, ultrafine friction grinding, hybrid research method.

Abstract. Bio-based textiles are an emerging area of cross-disciplinary research, involving material science and design and contributing to textile sustainability. An example of a bio-based textile is an orange-waste film, which is plant-based and biodegradable and possesses mechanical properties which are comparable to some commodity plastics. The research project presented in this article aimed to explore orange-waste film as a new material for textile and fashion design and highlights how experimental co-design processes and innovation involving orange waste film as a textile material adds a new layer of material understanding to both textile design and technology-driven material research. Material-development methods were used to develop the orange-waste film, as were textile design methods with a focus on surface design. The results show that material variables such as tensile strength and elongation are dependent on the grinding process and drying temperature used for the raw material, as these determined the quality and durability of the orange-waste film and its applicability to the field of textile design. The use of orange waste in the creation of textiles opens up for more ways of thinking about and working with materials, and orange waste could become a desirable raw material for textile design on the basis that it introduces certain aesthetic and functional possibilities through its visual and tactile expression and material behaviour, in addition to defining methods of producing textiles.

Introduction

Current sustainability challenges within textile practice are creating a demand for the field to develop sustainable textiles with the future in mind. With regard to this, new models of circularity and material-driven design processes could be used to address different parts of the textile design and production process, from material science and textile engineering to industry, consumption, and design [19, 21, 25]. Consequently, sustainability research in relation to bio-based textiles involves a complexity of thinking from material to product that cannot only be approached using the limited methodology of one discipline and instead requires a cross-disciplinary approach that merges advanced science and design methodologies.

Textile design takes material expressiveness as its central notion. The quest for novelty and solutions to complex material-research problems motivates the expansion of research beyond current methodological limitations and the adoption of different methods of conducting cross-disciplinary research. Bio-based textiles are an emerging area of cross-disciplinary research, involving material science and design and contributing to textile sustainability [11]. Research in the field of biotextile design tackles diverse strategies using unique methods to expand the array of raw materials and methods for use with textiles, providing a sustainable perspective on textile production and consumption which contrasts with the highly technological practices of textile mass-production [23] and establishes new models for cross-disciplinary collaborations between science and art [16]. Consequently, a change in the raw materials used to make textiles could lead to a shift in the methods used to produce textiles and create new material definitions.

Working with biomaterials in scientific laboratories offers new possibilities for designers, and crucially allows them to become involved during the material development stage in order to influence the development of new textile products. As [22, p.31] argues: “The renewability, climate-friendliness and bio-degradability of cellulose-based materials are not the only properties that make these materials attractive when compared to the finite materials that they are substituting for. The organic nature of biomaterials also involves unique properties and allows for previously unimaginable applications”.

One of the key biomaterials that designers have recently explored to create sustainable products is fruit and vegetable waste, which has attracted the interest of experimental design practitioners and researchers due to the fact that designers can be involved in the development of the materials they use when designing products, allowing them to create design proposals with sustainability as a focus [15, 4, 10, 29]. The ‘SONNET155’ project [4] involved the design of translucent bags made of “fruit leather”, which dissolve in water and can be used to fertilise plants when the bags are no longer needed. The material is fully biodegradable in water or soil as it is made from a composite of two raw materials: cellulosic production waste from the textile industry and pectin, a plant-based polysaccharide and by-product of juice production. The goal of the project was to develop sustainable design strategies in order to create beauty and pleasure throughout the life-cycle of a product. Thus, the bag can be worn, used, and loved until it has dissolved. While these and other research and design projects use fruit and vegetable waste to provide designers with alternative materials for products, this leaves space for further research in the textile and fashion design area with regard to exploring fruit and vegetable waste as a functional raw material for design by expanding not only its visual but mechanical properties.

Annually, several million tonnes of orange waste (OW) are generated as by-products of juice-production processes, representing 50–60% of the total mass of mass of the fruit before processing. Due to its acidic nature OW is not suitable for animal feed, and the landfilling of this waste involves environmental concerns [1]. However, OW contains valuable biopolymers such as cellulose, hemicellulose, and pectin, which can be used for the development of bioplastic materials. Batori et al. [2] developed biocomposite materials using OW, reinforcing a matrix of pectin and hemicelluloses with cellulose; further, the hypothesis in this study was that ultrafine friction grinding of OW would result in homogenisation and cellulose fibrillation, improving the material’s mechanical strength. A similar technique was reported with regard to the development of cellulose nanofibres using carrot residue [7].

Biomaterials developed using fruit and vegetable waste have shown good potential for a wide variety of applications, such as packaging, wastewater treatment, and biomedical uses [3, 5, 6, 7]. To investigate the potential of fruit and vegetable waste, and OW specifically, for textile products, a hybrid research approach involving both material science and design is required. Thus, the research project presented in this article focused on combining an experimental research methodology, technology-driven material processes, and textile design methods to develop OW films with competitive mechanical properties and explore them as an alternative material for textile and fashion design.

Experimental Setup

Development of OW film

The OW was obtained from a local juice company called Brämhults Juice AB, located in Borås, Sweden. Before any processing, the OW was stored in a freezer at -18°C. Citric acid (anhydrous >99.5%, Sigma-Aldrich) and glycerol (>99%, VWR Chemicals) were used as solvents for pectin and plasticisers, respectively. To create the OW films, the OW was defrosted and soaked in tap water overnight to remove the sugars and other water-soluble fractions (3.2 kg water/Kg wet OW). The insoluble fraction was then recovered using a kitchen sieve. A suspension of washed OW (2 wt%) in water was prepared and subjected to mechanical grinding using a supermasscolloider disc-mill grinder (MKCA6-5J, Masuko Sangyo, Kawaguchi, Japan) with MKE #46 grinding stones (fine silicon carbide, standard grinding stones for soft materials) to homogenise the OW suspension.

This was passed through the grinder once with an opening of +50 μm and up to 30 times in contact mode, with an opening of -70 μm , at 1500 rpm. Samples of 1000 ml were taken during different grinding cycles to study the effect of grinding on the mechanical properties of the OW films. The viscosity of the ground OW was measured using a Vibro viscometer SV-10.

The intention was to make a bio-composite film without the use of chemicals; when it was found that this would not be successful, a small quantity of glycerol was added to augment the already present citric acid. Preliminary experiments indicated that a mixture of 100 ml of ground OW, 0.5 g of glycerol, and 0.4 g of citric acid resulted in films with acceptable qualities for designing of biobased textiles. The obtained suspension was mixed in a water bath shaker at 110 rpm for 10 min. The effects of mixing temperatures of 20 and 60°C were investigated with regard to the properties of the OW films, which were produced by casting the OW suspension in plastic moulds after the mixing (which took place in a water bath); the resulting casts were dried at 35°C in an oven.

The mechanical properties were measured according to ISO 527-2 (Plastics – Determination of tensile properties) using a tensile testing machine (H10KT, Tinius Olsen, USA). The antibacterial properties of the OW films were investigated using *E. coli*. A single colony of the bacterium was transferred to 20 ml of fresh medium containing tryptone (1%), yeast extract (0.5%), and NaCl (1%). The bacteria was grown overnight at 37°C; 50 μl of the obtained bacterial suspension was transferred to a flask containing 5 mg of OW film, which was then incubated for 24 h. Finally, 10 ml of fresh liquid medium was added to each flask and the growth was followed for 10 hrs. The automated timelapse microscopy pictures were recorded every two hours using FluidScope™ scanning technology to follow the bacterial growth.

Textile and surface design methods

Textile design materials are built on the fundamental variables of fibers, yarns, and structure; together these elements define a fabric's qualities, properties, and structure [18]. However, another central element of fabric that is often neglected in design is the interstitial space left unoccupied by yarns and fibres. This void space, which occurs at the interplay between the fundamental variables, is outlined by the solid space occupied by the actual textile structure. The attributes of the void space in the textile structure are shaped by the technique used in the construction process: weaving, knitting, or lacing. Thus, the techniques used for fabric construction create variations in the form and properties of the fabric's voids. The interplay of the interstitial spaces and voids left unoccupied by the textile structure, together with the properties of the structural design, define the behaviour and comfort attributes, such as elasticity, handle, breathability, pliability, and drape ability, of the resulting fabric.

The OW films had a solid surface (contrasting with those of textiles), which led to an investigation of subtractive processes and methods for achieving textile-like attributes and enhancing the visual and tactile qualities of the films produced. The purpose of this exploration was to combine the visual elements of the surface with fundamental textile behaviours such as elasticity, breathability, handle, and draping. Diverse geometric tessellations and patterns were cut into the film's surface while it was in a flat position. The use of this method was motivated not just by the variations in the visual expression of the film achieved by the different designs but by the changes that this created in terms of the mechanical properties of the surface, facilitating textile-like behaviours such as stretchability, handle, and draping. Thus, the experimental investigations looked at the proportion of negative and positive space in the surface which influenced the fabric's handle and pliability, as well as the form of the structural pattern applied and the size and orientation of the cutting lines, which varied according to the direction of stretch. This in turn determined the elasticity of the surface and openness of the textile-like structure.

A method of straight-knife cutting was chosen for further investigation of the design possibilities afforded by OW films. Similar to laser-cutting technology, straight-knife cutting allows the creation of surface designs with complex geometries, which can be defined by high-resolution lines which can be straight or curved. This process also enables the designer to combine digital

tools for generating complex pattern designs based on vector drawing with directly cutting the material to create intricate motifs, patterns, and textures. The method is a useful way to work in cross-disciplinary creative processes between pattern design and construction, allowing the merging of textile and fashion design methods. Moreover, the fabrication process uses a sustainable approach to materials and fabric-cutting. As compared to related technologies for cutting, such as laser-cutting machines, straight-knife cutting machines produce less fumes during the fabrication process, and the cutting lines are clearer due to the mechanical action, as compared to a thermal process that burns the surface and influences the visual qualities of the end design. This is particularly marked with OW film, in that laser-cutting produces a severe change in the colouration of the material and burns the edges due to the cellulosic composition of the material.

The OW films were cast on fabricated moulds made using thin acrylic plastic sheets with high surface smoothness. The smoothness, glossiness, and grain of the surface of the mould were important in ensuring the high quality of the films, with smooth faces that were possible to cut and etch. The resulting films had two distinct faces: one was highly smooth and even, and the result of the properties of the surface of the mould, and one had a fine texture that was influenced by the material grain and the decisions made during the grinding process. The smooth-face had good adhesion to the cutting mattress that was required in order to be able to cut high-quality lines 0.5–1 mm from each other. The thickness of the resulting films varied between 0.5 and 1 mm, which is similar to a plain weave in polyester or cotton. This property allowed the films to be cut through with a depth of protrusion of 4 of protrusion and with pressure 1. For etching, the depth of protrusion was 3 and no pressure was applied.

To create a wider array of options in terms of design possibilities, the OW films were coloured with edible colour agents to increase the complexity of the colour palette. Different shades of green, red, or brown; 10 variants of each colour were produced of varying levels of saturation, increasing from 0 to 100% saturation in even increments. The colour palette was made using 100 ml of ground OW, 0.5 g of glycerol, 0.4 g of citric acid, and mixing each colour in different proportions until the desired number of intermediate colours was obtained produced a gradation of colour, progressing from one orange to another.

From a design perspective, it was essential to understand whether the OW films possessed textile behaviours such as bending and folding, and to ascertain whether they were able to withstand mechanical surface-treatment methods such as etching and knife-cutting. Thus, different textile methods focusing on surface design were used. The surface designs were influenced by traditional Japanese method of paper such as the krigami technique, as well as artworks such as Iris Van Herpen [30], Kieran Flaherty [14], and Matt Shlian [28].

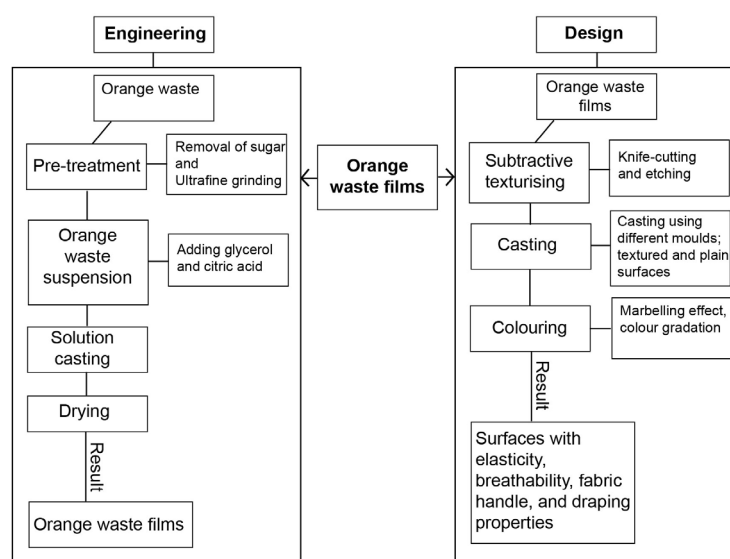


Figure 1: The different methods used, which were borrowed from the fields of engineering and design.

Result

Production of films from OW

Ultrafine grinding of the OW resulted in a homogenous suspension with no visible particles. The viscosity of the OW suspension after five grinding cycles was 120 mPa·S. The viscosity generally increased with number of grinding cycles (Fig. 2c). An increase in viscosity during ultrafine grinding is an indication of cellulose fibrillation [8]. Direct casting of the OW suspension was not successful, and therefore citric acid and glycerol were incorporated into the suspension prior to casting. Citric acid is known to be an effective solvent for pectin [2]. Dissolution of pectin facilitated the film formation, and glycerol improved the flexibility of the OW films. The OW films can be considered to be biocomposite materials, in which a matrix of pectin and hemicelluloses are reinforced with cellulose fibres [2].

The effects of mixing temperatures of 20 and 60°C were investigated with regard to the properties of the OW films. Previous research found that a higher temperature resulted in better dissolution of pectin [2, 3]. Figure 2a and b show the tensile strength and elongation at break, respectively, of OW films. After five grinding cycles, the OW films mixed at 20°C had significantly higher tensile strength than those mixed at 60°C. However, treatment of cellulose nanofibres at high temperatures with citric acid was found to result in the crosslinking of cellulose [6]. The crosslinking of the cellulose fibres in the films during the five cycles of grinding likely resulted in partial coagulation of the cellulose fibres, causing a reduction in the reinforcing effect of the cellulose fibres. Increasing the number of grinding cycles generally improved the tensile strength of the OW films. This was a result of the higher degree of fibrillation of the cellulose fibres, and better reinforcement of the OW films. Furthermore, mixing at the higher temperature (60°C) resulted in lower tensile strength due to the higher degree of cellulose crosslinking for all grinding cycles. The films mixed at the lower temperature (20°C) generally showed higher flexibility. This was also due to the lower crosslinking degree of the cellulose, which facilitated the movement of the cellulose fibres and thereby increased the elongation at break. The highest tensile strength obtained for OW films in this study was 31.6 MPa, which is significantly higher than the best tensile strength reported in the literature, which was 21.7 MPa [2, 3]. The higher tensile strength achieved in this study was the consequence of the ultrafine friction-grinding of OW, which effectively fibrillated the cellulose fibres and improved the properties of the OW film.

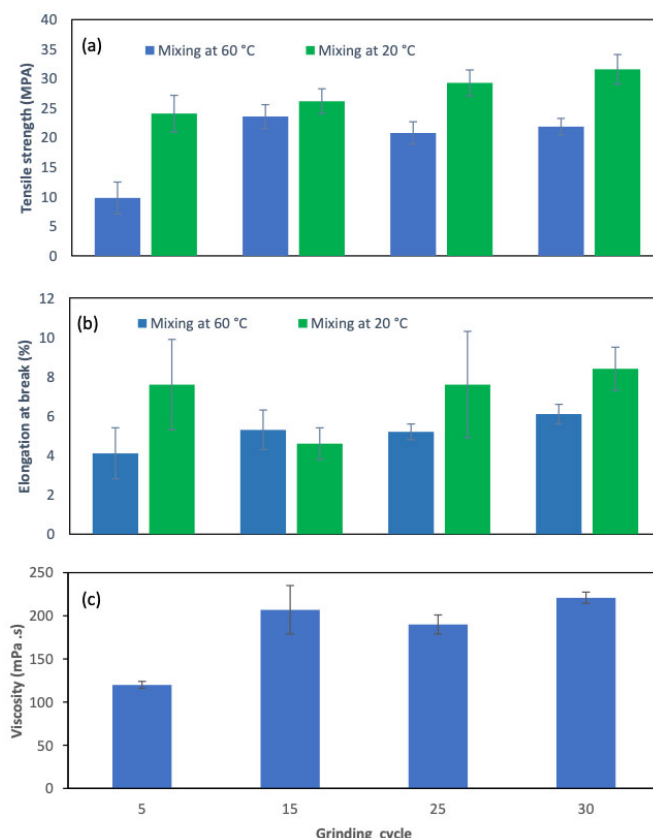


Figure 2: The effect of the number of grinding cycles and mixing temperature on (a) tensile strength and (b) elongation at break of the OW bioplastics. (c) shows how the viscosity was affected by increasing the number of fibrillation cycles.

As shown in Figure 3, the bacterial cells (*E. coli*) which were in contact with the OW films lost their ability for reproduction compared to the control experiment. The bacterial growth was followed online by taking microscopic images every 2 hour. Therefore, the OW films demonstrate some antimicrobial potentiality possibly due to the presence of limonene, which is a major component of the oil of citrus peels and a well-known antibacterial [17]. Furthermore, citric acid, which was used in the formulation of the OW films, has strong antimicrobial properties and can be used as a sanitiser and preservation agent [12], and has been suggested as an antimicrobial finishing agent for use with textile materials [9]. The antimicrobial properties are beneficial for applications such as packaging and medical textiles.

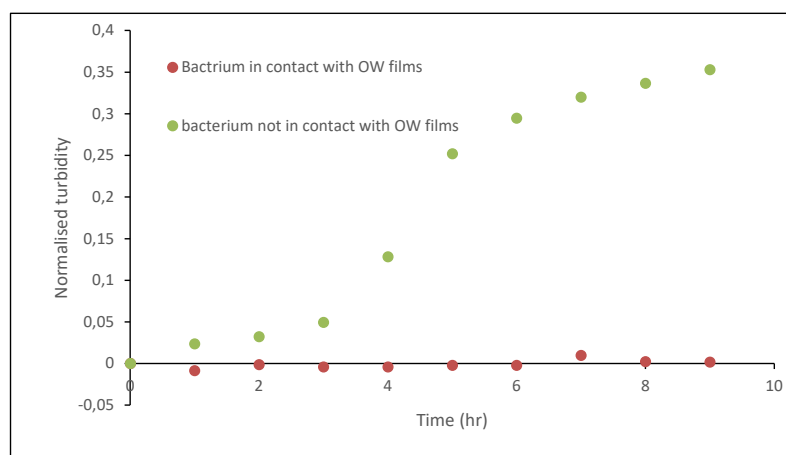


Figure 3: The antimicrobial properties of the OW films, measured in terms of effect against *E. coli*.

Textile design methods: surface design

The first explorations were conducted from a design perspective, and involved cutting tessellated patterns using parallel lines and varied cutting depths, from partially to entirely penetrating. A textured pattern was designed using diagonal lines, and was similar to a woven twill pattern. The cutting lines were discontinuous dashed lines, with 5 mm dashes spaced 3 mm apart. The grain of the OW surface was relatively large, such that its scale was similar to that of the cutting lines, creating a delicate and textured visual expression, similar to that of woven twill. Although the surface featured many cut lines, it remained robust and highly pliable. The fine cuts changed the initial behaviour of OW film by making it more bendable, softer, and more drapeable (Fig. 4).

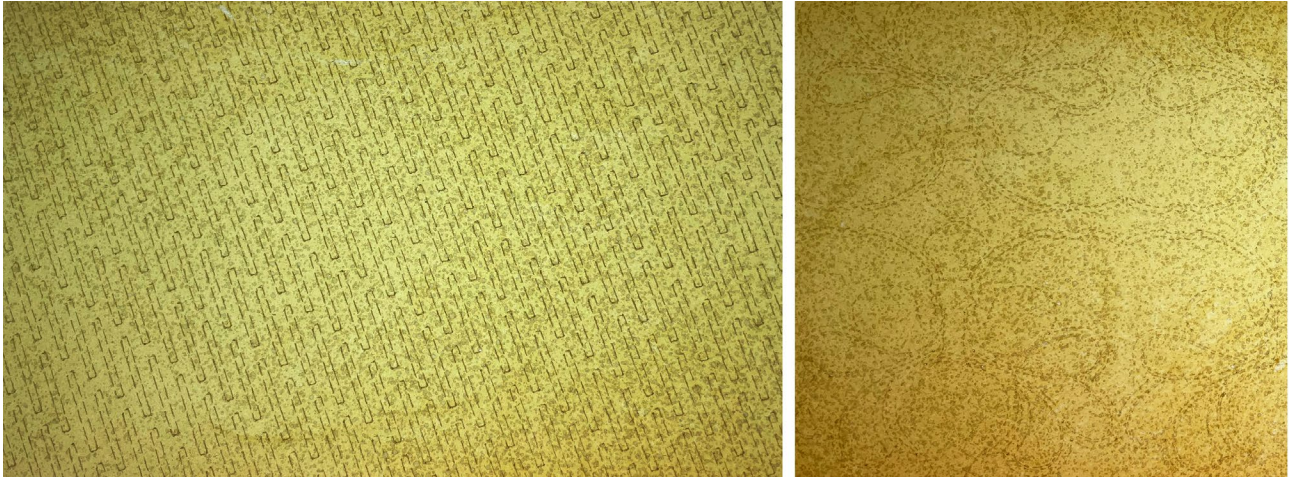


Figure 4: Close-ups of the surface of the textile.

Next, a structural pattern was applied to the surface of the OW film. The lines were 2.5 mm wide and 25 mm long. The pattern of the mesh was made using the principle of positive and negative spaces with different proportions. The cut areas constituted 65% of the surface. The initial surface was cast using a marbling technique using analogous colour scheme. The many cuts influenced the behaviour of the end design, making the mesh highly breathable and drapeable. Stretch occurred horizontally and diagonally, perpendicular to the lines of the mesh, allowing the surface to be increased in size by 50%. The colours visible on the surface of the material created a delicate expression when the material was not being stretched; when stretched, the gradation of the colours was evident in the expression of the mesh (Fig. 5).

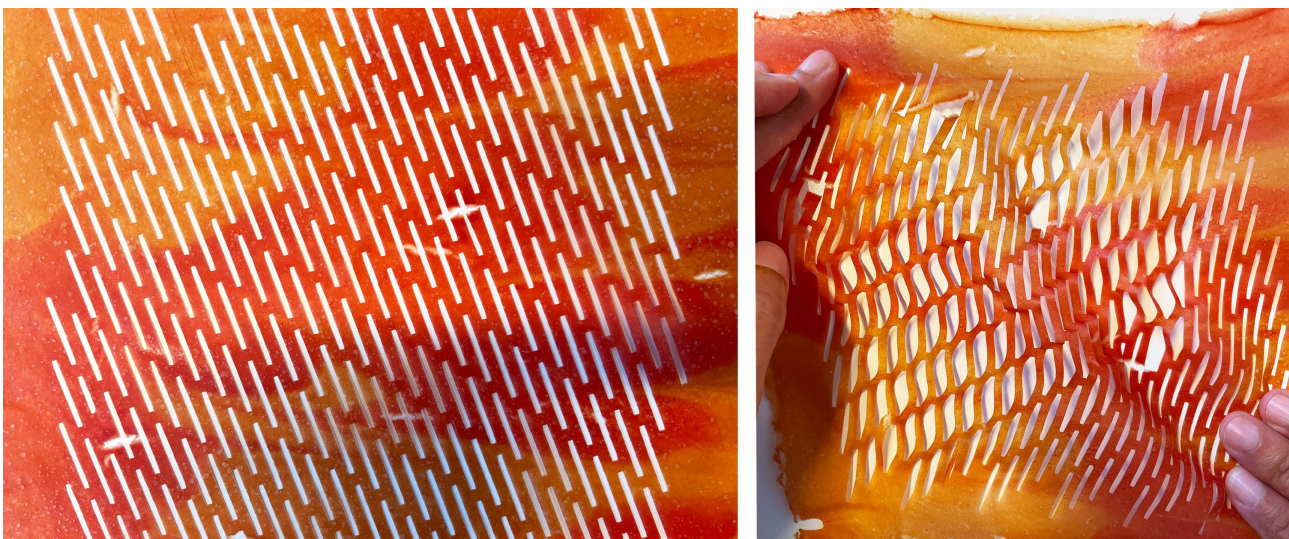


Figure 5: The surface was highly elastic and pliable. The auxetic property caused the surface marbling effect to be visible in the parts of the fabric that were not being stretched.

Next, extended elasticity was explored. Parallel rows of cuts were made in the surface in a half-drop repeated pattern. The initial surface was cast using a marbling technique to create analogue colour scheme and a textured expression. Stretch in the surface occurred horizontally, perpendicular to the mesh lines, and increased the area of the surface by more than 100%. The surface was highly elastic and pliable. This allowed OW films to be manipulated and stretched. Due to its auxetic properties, the surface marbling effect was visible in the parts of the fabric that were not being stretched (Fig.6).

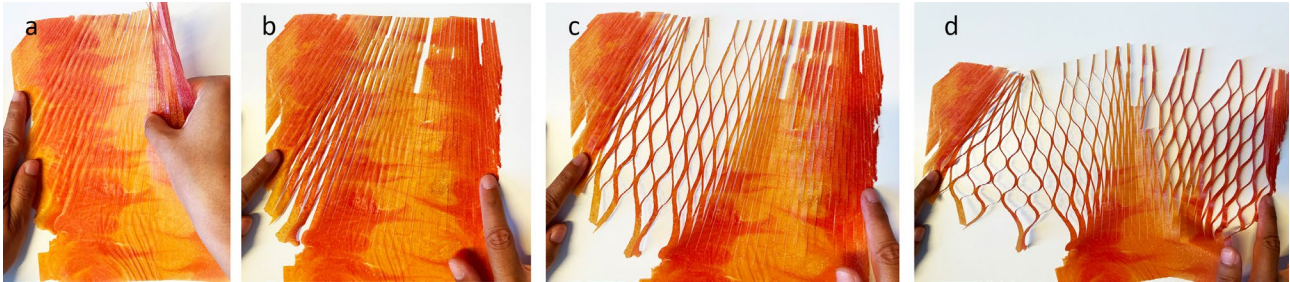


Figure 6: 6a to 6d show the OW film stretched horizontally perpendicular to the mesh lines.

The effect of etching was achieved when the cutting depth was less than the thickness of the film. The films were cast using adjacent shades of dark and light green. The surface was etched with delicate zig-zag lines, which were partially cut into the surface in a houndstooth pattern. To obtain a better visual effect, the etched pattern was applied to the more rigorous face of the film. The resulting surface was pliable, but not elastic or drapeable. The subtraction of material in the etching process left the parts of the material that had been etched partially transparent and patterned (Fig. 7).

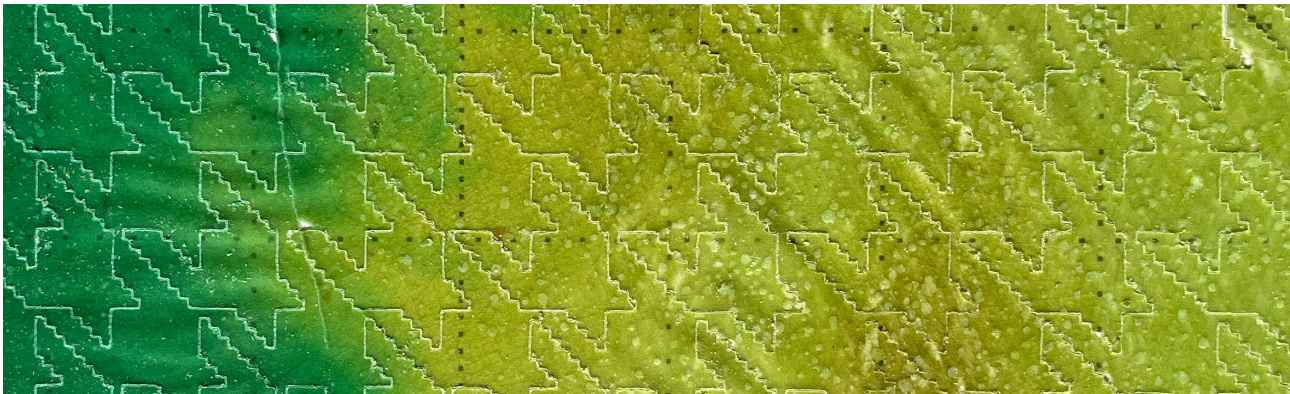


Figure 7: The fine lines of the regular geometry of the houndstooth pattern, which had the appearance of sewing thread applied to quilted leather.

In order to create floats, regular and irregular arrangements of floats were explored. To explore the latter, the surface of OW film was cut using two intersecting sets of lines at a distance varying between 1 and 3 mm from one another. The lines were organised around two ellipses, and formed round paths. In contrast to the rectangular angles of a woven textile, the cut floats in the OW film were round, and intersected in various ways. By being round paths rather than arranged in perpendicular grids, the floats expanded the surface in different directions, emphasising the changes in direction in the manner of a garment on a body and creating an overall sense of a three-dimensional form (Figure 8a). Another sample explored regular arrangements of floats; here, the structure was inspired by woven herringbone patterns, and consisted of rows of angled lines measuring 7 cm, which were mirrored and cut parallel at a distance of 1.5 mm. This made the surface elastic, allowing it to stretch horizontally. Due to the open structure, the surface was draped on three-dimensional objects. When tension was applied horizontally, the fabric had a high degree

of expansion, facilitating a three-dimensional form. The elastic behaviour of the surface depended on the length of the cut lines: shorter lines resulted in behaviour that was less elastic in nature (Figure 8b).

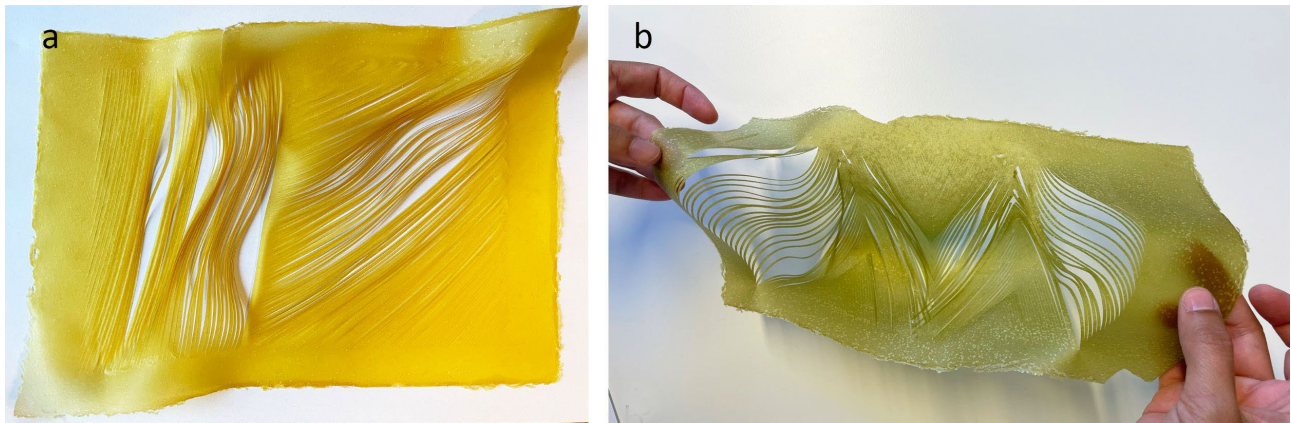


Figure 8: Creating floats made the surface elastic and possible to stretch horizontally.

Later, fringes were cut in parallel lines of different widths, varying from 1 to 4 mm. The shapes were organised in ellipses. As compared to conventional fringes, which are generally cut in straight, uniform lines, these rounded fringes were softer and appeared more voluminous due to being pre-shaped (Fig. 9).



Figure 9: Fringes enhanced the material behaviour in terms of adapting to the lines of the body and underlining the intersection of the shapes of the garment.

The final pattern was a development of the herringbone pattern, with a design based on sinuous parallel lines of two different lengths which enhanced the expression of the three-dimensional surface. The pattern was less elastic than the herringbone design due to the sinuous lines, which limited the extension of the surface. This pattern made the film drapeable (Fig.10).

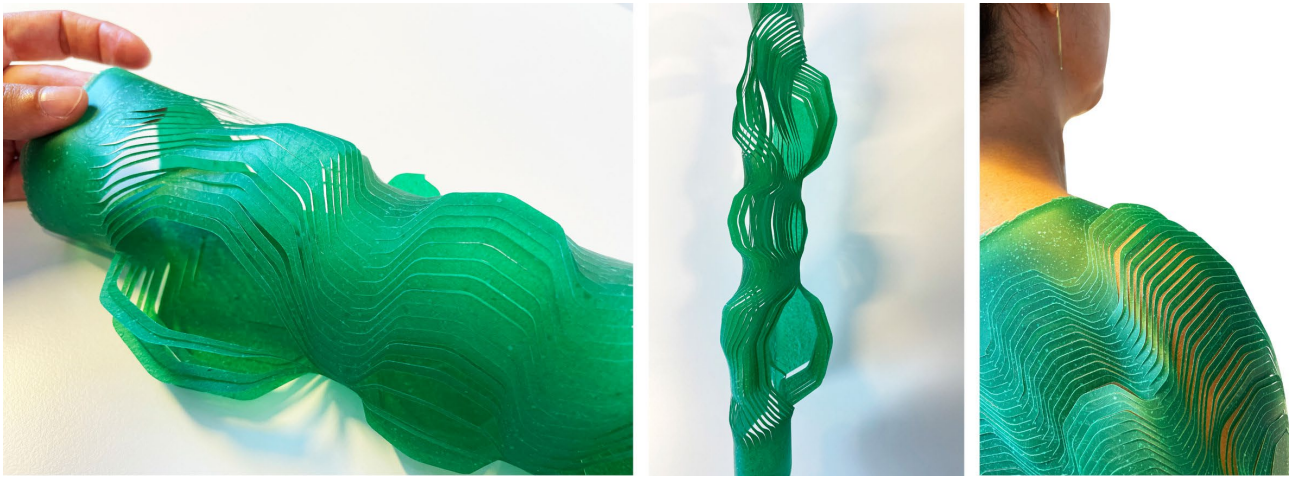


Figure 10: The final experiment produced a drapeable film that delicately followed [the contours of] the body.

Discussion

The results of the experiments show that for the studied material, mechanical properties such as tensile strength and elongation at break are dependent on the number of grinding cycles and the mixing temperature; these determined the quality and durability of the OW films and their applicability to the textile design field. OW films opens up for more ways of thinking about and working with materials; by changing their mechanical qualities through cutting and grinding, the films can embed textile-like qualities and become a desirable material for use in textile and fashion design. The different patterns and methods of cutting show how the visual and mechanical properties of a surface can interact with each other during a design process, improving the textile-like qualities of bioplastics. In addition to these qualities and properties, the resulting samples have antibacterial properties, a gentle orange scent, and a wide range of visual expressions. The process described in this article introduces certain aesthetic and functional possibilities through the visual and tactile expressions and behaviour of the material, in addition to defining complex bottom-up methods for material design and development. These materials present an alternative with a gentle footprint, facilitating recycling, upcycling, and circularity and ensuring a sustainable future. This collaboration between design and science opened up for a wider range of material design and functional possibilities, as well as more circular value chains for materials.

The processing of fruits and vegetables generates several million tonnes of residue annually, resulting in the wasting of valuable bio-based resources [27]. Bioconversion of fruit waste to biogas or ethanol are among the suggested sustainable treatments [26, 24], however, these wastes have a greater potential if used in the development of bio-based products [13] before they are used to produce e.g. biogas. These waste-derived biomaterials have the potential to be further processed into alternative functional materials to replace non-renewable and non-biodegradable fossil-derived products, which could be used to create textiles. Biodegradation into e.g. biogas is a sustainable approach which could complete the circular life-cycle of such biobased textiles at the end of their lifetimes.

The hydrophilic nature of natural biopolymers is often a drawback for newly developed bio-based textiles. Therefore, post-treatment strategies such as crosslinking and coating with a hydrophobic layer are required to improve the durability of bio-based textiles.

Another approach is exemplified by the ‘AuREUS’ project [15], which involved using ultraviolet rays from the sun to generate electrical energy, and combining this with fruit and vegetable waste to create a new material. The project shows there is a great deal of potential in using fruit and vegetable waste more than to create bioplastics such as OW films [4, 20] or pigments with which to dye fabrics [29]. In the ‘AuREUS’ project, fruit and vegetables are crushed, filtered, and distilled in order to extract bioluminescent dyes from them. These are mixed with resin

and poured into moulds to create colourful cladding panels, which can be placed on walls or sandwiched between the two panes of a double-glazed window. Unlike traditional solar panels, which must face the sun – which in turn must not be covered by clouds – in order to generate electricity due to their reliance on visible light, the translucent AuREUS material is able to generate power using the ultraviolet rays that pass through clouds up to 50% of the time.

In order to push the boundaries and further explore fruit and vegetable waste as a new material for design, future explorations could investigate them in weaving, knitting, and 3D printing techniques, and propose new products that allow consumers to change their perception of consumption.

Conclusion

In order to move our material world in the direction of sustainability, new and more sustainable materials and production processes need to be designed and developed. The findings of the study presented in this article indicate that OW films may offer one such solution. In the future, vegan materials could replace ones originating from animals or complex chemical processes, providing environmentally friendly and ethical alternatives to existing textile products. Although a wide array of methods for producing vegan leather exist in the textile and fashion field, combining the rigour of material science with design methodology could be more convincing in moving materials away from basic research and towards industrial applications to demonstrate their functional properties of materials. This process will require foundational knowledge of new materials from a cross-disciplinary perspective, combined with a strong understanding of their design potential and applications.

References

- [1] ANGEL SILES LÓPEZ, J., LI, Q. & THOMPSON, I. P. 2010. Biorefinery of waste orange peel. *Crit Rev Biotechnol*, 30, 63-9.
- [2] BÁTORI, V., JABBARI, M., ÅKESSON, D., LENNARTSSON, P. R., TAHERZADEH, M. J. & ZAMANI, A. 2017. Production of Pectin-Cellulose Biofilms: A New Approach for Citrus Waste Recycling. *International Journal of Polymer Science*, 2017, 9732329.
- [3] BÁTORI, V., LUNDIN, M., ÅKESSON, D., LENNARTSSON, P. R., TAHERZADEH, M. J. & ZAMANI, A. 2019. The Effect of Glycerol, Sugar, and Maleic Anhydride on Pectin-Cellulose Thin Films Prepared from Orange Waste. *Polymers*, 11, 392.
- [4] BECKFELD AND HEHEMEYER-CÜRTEN. 2020. *SONNET155* [Online]. Available: <https://www.thisispaper.com/mag/sonnet155-lobke-beckfeld-and-johanna-hehemeyer-curten> [Accessed Oct.13th 2021].
- [5] BERGLUND, L. 2019. *From bio-based residues to nanofibers using mechanical fibrillation for functional biomaterials*. Doctoral Thesis, Luleå University of Technology.
- [6] BERGLUND, L., FORSBERG, F., JONOBI, M. & OKSMAN, K. 2018. Promoted hydrogel formation of lignin-containing arabinoxylan aerogel using cellulose nanofibers as a functional biomaterial. *RSC Advances*, 8, 38219-38228.
- [7] BERGLUND, L., NOËL, M., AITOMÄKI, Y., ÖMAN, T. & OKSMAN, K. 2016a. Production potential of cellulose nanofibers from industrial residues: Efficiency and nanofiber characteristics. *Ind Crop Prod*, 92, 84-92.
- [8] BERGLUND, L., NOËL, M., AITOMÄKI, Y., ÖMAN, T. & OKSMAN, K. 2016b. Production potential of cellulose nanofibers from industrial residues: Efficiency and nanofiber characteristics. *Industrial Crops and Products*, 92, 84-92.
- [9] BISCHOF, S., FLINČEC GRGAC, S., KATOVIC, D. & GORSKI, D. 2009. Antibacterial Properties of Citric Acid Used as Easy-Care Finishing Agent. *AATCC Review*, 9, 37-41.
- [10] CARLORATTI ASSOCIATI. 2019. Available: <https://carloratti.com/project/feel-the-peel/> [Accessed Oct.13th, 2021].

-
- [11] COLLET, C. Biotextiles: Evolving Textile Design Practices for the Bioeconomy and the Emerging Organism Industry. In: NIMKULRAT, N., RAEBILD, U., PIPER, A., ed. Soft Landing, 2018 Helsinki, Finland. Cumulus International Association of Universities and Colleges in Art, Design, Media, 87-99.
 - [12] EL BAABOUA, A., EL MAADOUDI, M., BOUYAHYA, A., BELMEHDI, O., KOUNNOUN, A., ZAHILI, R. & ABRINI, J. 2018. Evaluation of Antimicrobial Activity of Four Organic Acids Used in Chicks Feed to Control *Salmonella typhimurium*: Suggestion of Amendment in the Search Standard. *International Journal of Microbiology*, 2018, 7352593.
 - [13] FAO 2019. Global production of wood products posts highest growth in 70 years. Food and Agriculture Organization of the United Nations (FAO).
 - [14] FLAHERTY, K. (n.d), Available: <https://2020.gsapostgradshowcase.net/2020/07/14/kierran-flaherty/> [Accessed Oct.13th, 2021].
 - [15] GANDHI, S. & LIU, A. 2021. Living Energy: A Novel Approach to Using Biofluorescent Bacteria in Solar Concentrators. *Consilience*.
 - [16] GROTH, C., PEVERE, M., NIINIMÄKI, K. & KÄÄRIÄINEN, P. 2020. Conditions for experiential knowledge exchange in collaborative research across the sciences and creative practice. *CoDesign*, 16, 328-344.
 - [17] HAN, Y., SUN, Z. & CHEN, W. 2019. Antimicrobial Susceptibility and Antibacterial Mechanism of Limonene against *Listeria monocytogenes*. *Molecules (Basel, Switzerland)*, 25, 33.
 - [18] HATCH, K. L. 1993. *Textile science*, Minneapolis/St. Paul, West Publishing Company.
 - [19] HILDEBRANDT, J., THRÄN, D. & BEZAMA, A. 2021. The circularity of potential biotextile production routes: Comparing life cycle impacts of bio-based materials used within the manufacturing of selected leather substitutes. *Journal of Cleaner Production*, 287, 125470.
 - [20] KANIGEL, R. 2010. Faux real: Genuine leather and 200 years of inspired fakes. *Faux Real: Genuine Leather and 200 Years of Inspired Fakes*, 1-288.
 - [21] KARANA, E., BLAUWHOFF, D., HULTINK, E. J., & CAMERE, S. 2018. When the material grows: A case study on designing (with) mycelium-based materials. *International Journal of Design*, 12.
 - [22] KÄÄRIÄINEN, P. T., L (ed.) 2017. *Lost in the Wood(s): The New Biomateriality in Finland*, Finland: Aalto
 - [23] LEE, S. 2012. Biocouture. In: MYERS, W. (ed.) *Biodesign*. New Youk: Museum of Modern Art.
 - [24] MORALES-POLO, C., CLEDERA-CASTRO, M. D. M. & MORATILLA SORIA, B. Y. 2019. Biogas Production from Vegetable and Fruit Markets Waste—Compositional and Batch Characterizations. *Sustainability*, 11, 6790.
 - [25] NIINIMÄKI, K. & HASSI, L. 2011. Emerging design strategies in sustainable production and consumption of textiles and clothing. *Journal of Cleaner Production*, 19, 1876-1883.
 - [26] PATSALOU, M., SAMANIDES, C. G., PROTOPAPA, E., STAVRINOU, S., VYRIDES, I. & KOUTINAS, M. 2019. A Citrus Peel Waste Biorefinery for Ethanol and Methane Production. *Molecules*, 24.
 - [27] SAGAR, N. A., PAREEK, S., SHARMA, S., YAHIA, E. M. & LOBO, M. G. 2018. Fruit and Vegetable Waste: Bioactive Compounds, Their Extraction, and Possible Utilization. *Compr. Rev. Food Sci. Food Saf.*, 17, 512-531.
 - [28] SHLIAN, M. (n.d), Available: <https://www.mattshlian.com/research> [Accessed Oct.13th, 2021].
 - [29] STJERNSWÄRD, (n.d), Available: <https://www.stjernsward.co/kaiku-living-color> [Accessed Oct.13th 2021].
 - [30] THYS, M., CONNELLAN, L. 2012. Iris van Harpen, transforming fashion. Atlanta: High Museum Of Art inAtlanta and De Groeniger Museum.

Evaluation of Denim Fabric Performances from Sustainable Yarn

Osman Babaarslan^{1,a}, Md Abul Shahid^{2,b*} and Dilek Sarapnal^{3, c}

^{1,2}Engineering Faculty, Textile Engineering Department, Cukurova University, Adana, Turkey

³Çalık Denim Tekstil AŞ. R&D Department, Yeşilyurt/Malatya, Turkey

^ateksob@cu.edu.tr , ^{b*}shahidbutex@gmail.com, ^cdilek.sarapnal@calikdenim.com

Keywords: Lyocell, cellulosic acetate fiber, blended yarn, sustainable regenerative yarn, denim fabric performance.

Abstract. Denim fabric is well accepted, and still, now it has appeal for its variation and technological improvement. Denim is mostly produced from cotton, which is concerned with the sustainability issue. In this article, a new generation of sustainable yarn has been developed from lyocell and cellulosic acetate fiber, blended with cotton fiber having the object to alternate and minimize the cotton fiber amount in the denim production. In this study, denim fabric was produced from Lyocell (Tencel®)/Cotton blended warp yarn, and Cellulosic acetate (CA(Naia®))/Cotton blended dual core-spun weft yarn then fabric performances have been analyzed. From the analysis, 100% CO fabric weight changes more than other samples due to higher shrinkage than others. Regenerated yarn samples have lower growth percentages with high elasticity than 100% cotton. Regenerated blended yarn fabric samples have lower tear strength on the weft side than 100% CO sample, but they have more tear and tensile strength on the warp side. Denim fabric from sustainable yarns is also wear comfortable.

Introduction

From the beginning, all ages have accepted denim fabric due to its fashionable look and durability. Cotton is the key raw material for the denim industry as it has supreme properties and unique characteristics but raises sustainable issues. Cotton is the king of textile fiber and one of the highest-produced natural fibers, but it uses many insecticides or pesticides and chemicals for its cultivation [1]. 1/3 of the total agricultural chemical is used for cotton cultivation. 1/4 of total insecticide and 1/10 of total pesticide are used for cotton cultivation.[2]

Furthermore, for cultivating cotton fiber, a lot amount of water is required. For example, 1kg of fiber cotton accounts for 9788-9958L water, which is higher than others [2-3]. Therefore cotton cultivation has a negative effect on human health as well as contamination of wildlife and land degradation. Due to having a bad impact on the environment and sustainability issues, alternative sustainable resources for denim production are required. Nowadays, new generation sustainable fibers from different sources are used as the alternative to cotton. Regenerated cellulosic fiber from wood pulp has a good prospect to alternate cotton fiber as well as in the denim industry to make the textiles more comfortable, soft, durable, and sustainable[1]. Lyocell and CA are good potential regenerated cellulosic sustainable fiber produced by the closed-loop process[2]. Lyocell (Tencel®) fiber has good strength and less hairiness than cotton fiber and good comfort properties on denim fabric [4]. Tencel blended with viscose, modal and bamboo showed good mechanical and comfort properties on plain-woven fabric[6-7].

On the other hand, cellulosic acetate fiber is attributed with good hand feel properties, good drapability, and comfort to wear. Furthermore, having good textile processing performance broadens its wide range of applications, including woven products [8]. This study produced warp yarn by lyocell fiber and cotton fiber blending, and weft yarn was produced by cellulosic acetate fiber and cotton fiber blending. Later on, denim fabric was produced and evaluated to understand the denim fabric performances from this sustainable yarn.

Materials and Methods

For this study, the fabric was produced from Tencel/Cotton warp and CA/Cotton weft dual core-spun yarn along with 100% Cotton stretched denim fabric. For dual core-spun yarn, 5.5 tex PET/PTT (T400®) filament and 7.8 tex elastane (Lycra®) were used. A modified ring spinning method is used to produce these yarns, and Fig. 1 shows the schematic view of the modified ring spinning method, which is commercially more accepted[9]. For producing yarn, PET/PTT filament draft was 1, and elastane draft was 3.5. Table 1 shows the yarn properties used in this study, and table 2 represents the fabric construction and the design of the experiment. Fabric performances were analyzed after three home laundering at 60⁰ Celsius and conditioned according to ASTM D1776.

In this study, denim fabric's weight, elasticity, and growth properties, stiffness, tear strength, tensile strength, and shrinkage were investigated according to ASTM D3776, ASTM D3107, ASTM D4032, ASTM D1424, ASTM 5034 - GRAB METHOD, and AATCC 135 standard methods respectively. To measure the fabrics pilling properties, abrasion resistance, and color fastness to crocking ISO 12945-2, TS EN ISO 12947-2, and AATCC 8 is used sequentially. Fabrics comfort properties: air permeability and water vapor permeability were evaluated according to T391 EN ISO 9237:1999 and TS257 EN20811:1996 standard method.

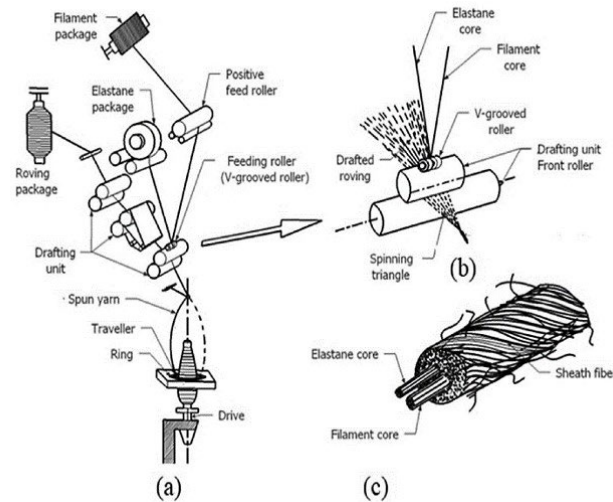


Fig. 1: Schematic illustration of modified ring spinning method for dual core-spun yarn; (a) modified ring-spinning arrangement, (b) combination of materials, (c) cross-sectional view of dual core-spun yarn[9]

Table 1: Yarns properties used in this study

		Strength [cN/Tex]	Elongation [%]	Unevenness [U%]	Hairiness [H]
Warp yarn	55.55 tex (Ne 18/1, 100% Cotton)	15.23	6.17	11.2	7.63
	50 tex (Ne 20/1, 60% Tencel+ 40% Cotton)	19.52	5.9	11.9	6
	71.43 tex (Ne 14/1 60% Tencel+ 40% Cotton)	21.47	8.72	14.1	5.74
	83.33 tex (Ne 12/1, 60% Tencel+ 40% Cotton)	20.23	8.43	14.07	7.71
Weft yarn	55.55 tex (Ne 18/1, Sheath fiber- 100% Cotton) dual core	12.6	10.47	11.08	7.77
	55.55 tex (Ne 18/1, Sheath fiber- 60% CA + 40% Cotton) dual core	13.03	11.81	8.34	6.92

Table 2: Fabric construction and experimental design

Sample	Warp yarn	Weft yarn	Weave	Reed number	Reed width [cm]	Weft density [Ends/cm]
100% CO	55.55 tex (Ne 18/1, 100% Cotton)	55.55 tex (Ne 18/1, Sheath fiber-100% Cotton) dual core	3/1 Z twill	70/4	215	20
S1	50 tex (Ne 20/1, 60% Tencel+ 40% Cotton)	55.55 tex (Ne 18/1, Sheath fiber- 60% CA + 40% Cotton) dual core	3/1 Z twill	160/2	215	21
S2	71.43 tex (Ne 14/1, 60% Tencel+ 40% Cotton)	55.55 tex (Ne 18/1, Sheath fiber -60% CA + 40% Cotton) dual core	3/1 Z twill	70/4	210	22.5
S3	83.33 tex (Ne 12/1, 60% Tencel+ 40% Cotton)	55.55 tex (Ne 18/1, Sheath fiber -60% CA + 40% Cotton) dual core	3/1 Z twill	70/4	210	24

Results and Discussion

Weight of Fabric and Dimensional Stability

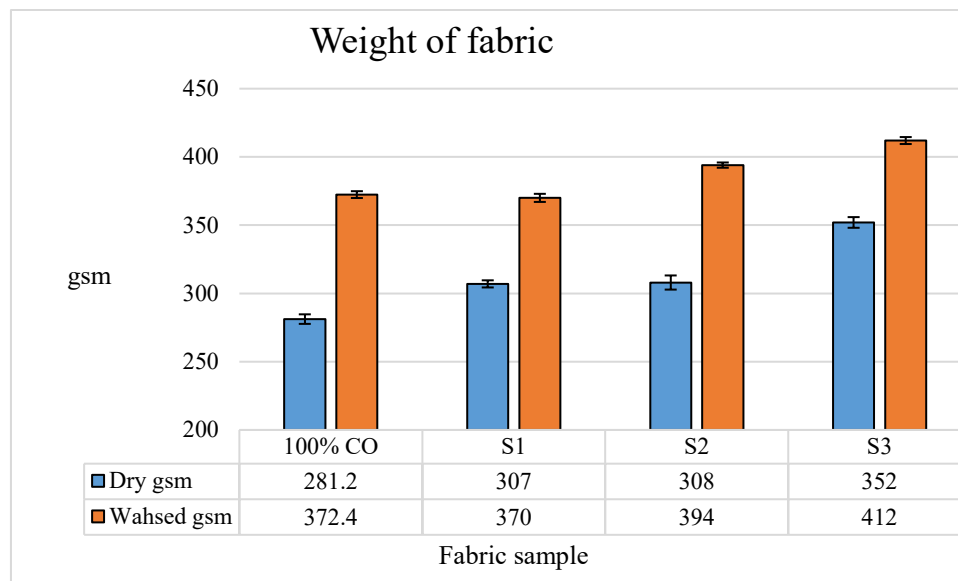


Fig. 2: Dry and washed weight (gsm) of fabrics studied in this study

The areal density of a woven fabric depends on the warp and weft yarn count, as well as the weave type and the washing treatment done on the sample. Fig. 2 depicts the fabric weight changes after three home washing. Results found from the experiment show that 100% CO fabric gsm changes a lot than other samples. 100% CO is increased more than 32% weight while regenerative fabric samples S1, S2, and S3 is increased almost 20%, 27%, and 17% of weight after normal wash, respectively. Due to having elastic material in the weft yarn structures, fabric samples gained weight. 100% CO fabric is gained more weight due to having more shrinkage. Fig. 3 illustrates the fabric's dimensional stability or shrinkage values in the warp and weft direction. After washing, regenerated yarn fabric samples have shown lower shrinkage than 100% CO fabric. Increasing the fabric's warp yarn linear density decreases the shrinkage in the weft direction of the fabric. The analysis shows that

the weft side shrinkage of fabric is higher as weft yarns were incorporated with elastic filament. Increasing the fabric's warp yarn linear density decreases the shrinkage in the weft direction of the fabric.

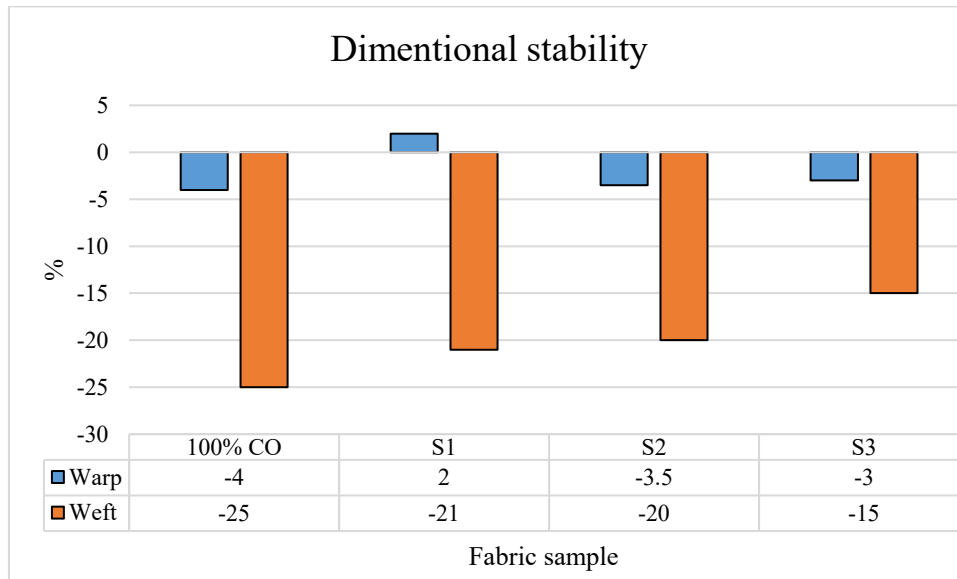


Fig. 3: Dimensional stability of the fabrics

Elasticity and Growth Properties

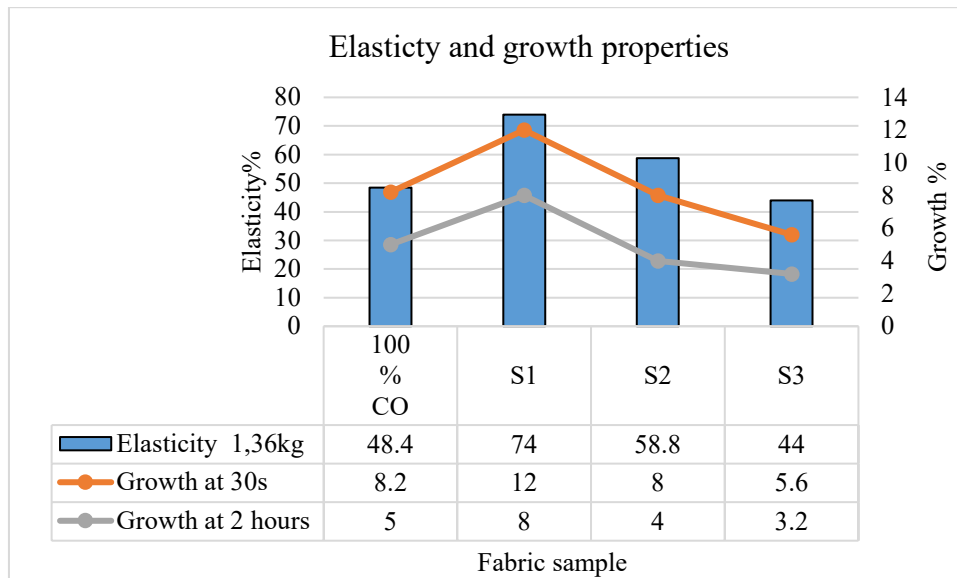


Fig. 4: Elasticity and growth properties of the fabrics

Fabric elasticity and growth properties depend on the fiber properties inside yarns. The amount of deformation under a specific tension depends on the raw material properties. Nowadays, Elastane fiber is being used widely for its comfort behavior and becoming popular also. Using elastic material as core components in denim fabric is a common phenomenon. Fig. 4 shows the elasticity and growth% at 30 seconds and 2 hours of the fabric. From the figure, it can be seen that the S1 sample has higher growth% and higher elasticity properties than other samples. S1 and S2 fabric samples have approximately 52% and 21% more elasticity than 100% CO samples. Having high elasticity and less growth% is required for more comfortable and economic denim production, and in these terms, regenerative fabric samples are quite acceptable.

Fabric Stiffness

Stiffness denotes the resistance to bending that directly influences fabric's drapability, handle, and indirect influence on fabric deformation. Fabric stiffness is dominated by fiber and yarn stiffness which is controlled by the fiber-forming materials. In this study, fabrics stiffness is measured, which

is shown in Fig. 5. The analysis found that 100% CO and S2 samples have similar low stiffness, whereas the S3 sample has higher stiffness. The stiffness of the S3 sample is higher due to having coarser yarn in its weft direction.

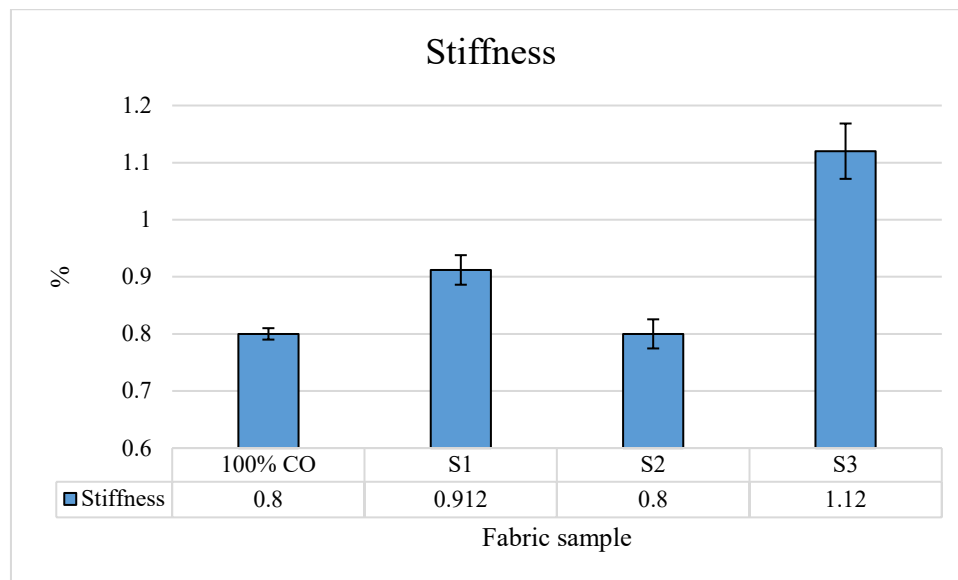


Fig. 5: Stiffness of the fabrics

Strength Analysis

In this study, the tearing and tensile strength of fabrics were evaluated according to the standard method, and Fig. 6 and 7 denote the fabric tearing strength and tensile strength simultaneously. The workable power needed to begin, proceed, or then again spread a tear in a texture under indicated conditions is defined as tear strength, while before breaking, the behavior of a sample under axial loading is denoted by tensile strength, and its amount depends on the fabric geometry, raw material property, and fiber arrangement. From the analysis, it is found that having regenerative tencel fiber in the warp direction tearing strength of the fabric's warp direction is increased. However, a lower tearing strength is observed in the weft direction of the fabric. From Fig. 7, for tensile strength, it is also found that in the warp direction, regenerative fabric samples have higher tensile strength and lower tensile strength except for the S3 sample. Increasing the warp yarn linear density increases the fabric's tensile strength in the warp direction for the sustainable blended yarn.

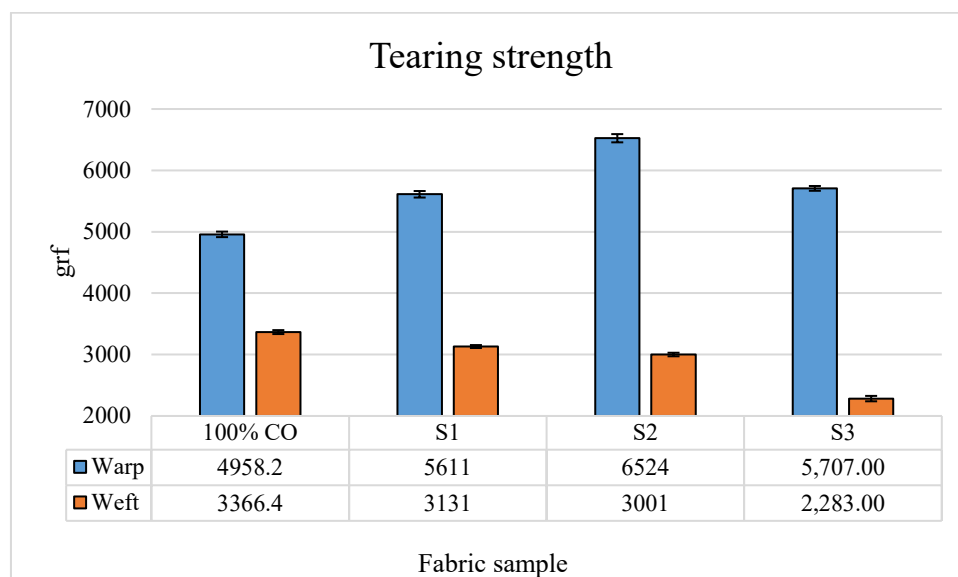


Fig. 6: Tearing strength of the fabrics

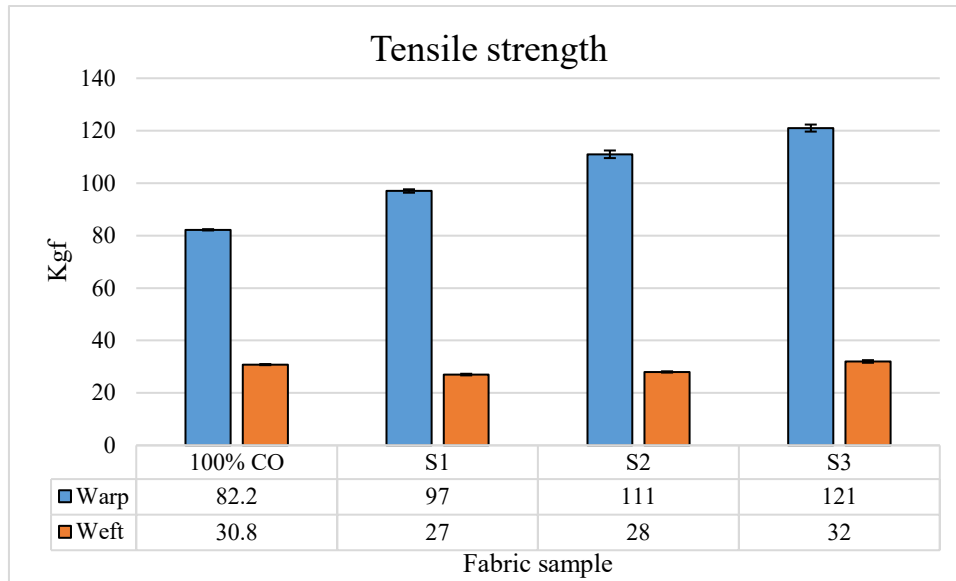


Fig. 7: Tensile strength of the fabrics

Pilling, abrasion resistance and color fastness properties

Pilling is a fault of the fabric surface which is formed during wear and washing. During wear, frictional or abrasive force affects pilling formation. Abrasion resistance defines the ability to withstand wear from repeated rubbing. During the washing and rubbing, the color of the denim fabric may be changed, and color fastness determines the amount of color that will fade or resist the material to change its color properties. From Fig. 8, it is observed that regenerative sustainable yarn sample fabrics have good abrasion resistance. Pilling and color fastness to crocking is also quite good, and the obtained results are shown in Table 3.

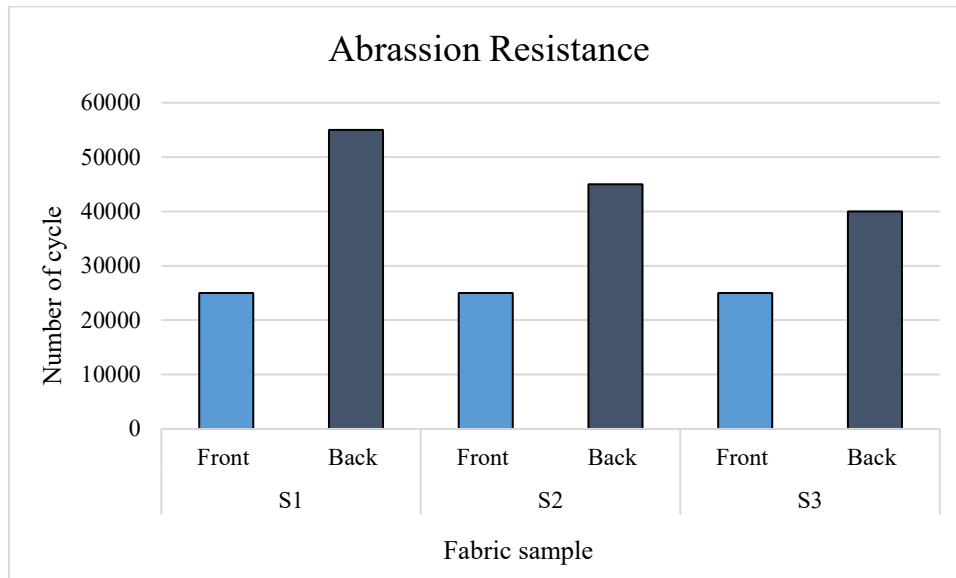


Fig. 8: Abrasion resistance of the fabrics

Table 3: Pilling points and color fastness grade to crocking of the fabric samples

Samples	S1		S2		S3	
Pilling points	Front	back	Front	back	Front	back
	3-4	2	1-2	1-2	2-3	1-2
Color fastness grade	Dry	Wet	Dry	Wet	Dry	Wet
	4	1-2	3-4	1-2	4	1-2

Comfort Properties

To understand the comfort properties of the investigated denim fabrics, air permeability and water vapor permeability have been measured. The cotton version of the studied samples has been produced to compare the comfort properties properly where the warp is similar as before, and instead of CA/CO blended sheath fiber, 100% CO fiber is used for weft yarn. The following table shows the warp and weft yarn structure of the studied fabric sample's comfort properties. Moreover, Fig. 8 describes the comfort properties of the denim samples. From Fig., it can be depicted that increasing the warp yarn linear density water vapor and air permeability are decreased as both have close relationships with each other. When yarn's linear density increases, the inter-space between the yarn decreases, and due to the high resistance of air and water vapor flow, it is hard to pass into the environment. For comfort wearers, it is desired to have high water vapor and air permeability. The obtained results show that fabric from CA/CO blended weft yarns have similar comfort properties compared with cotton-covered weft yarn samples fabric, which shows studied samples are promising for alternating the cotton fiber-based denim fabric.

Table 4: Fabric construction for comfort properties evaluation

		warp yarn	weft yarn
S1	CA/CO	50 tex (Ne 20/1, 60% Tencel+ 40% Cotton)	55.55 tex (Ne 18/1, Sheath fiber- 60% CA + 40% Cotton) + 5.5 tex PET/PTT + 7.8 tex elastane
	CO	50 tex (Ne 20/1, 60% Tencel+ 40% Cotton)	55.55 tex (Ne 18/1, Sheath fiber- 100% Cotton) + 5.5 tex PET/PTT + 7.8 tex elastane
S2	CA/CO	71.43 tex (Ne 14/1, 60% Tencel+ 40% Cotton)	55.55 tex (Ne 18/1, Sheath fiber- 60% CA + 40% Cotton) + 5.5 tex PET/PTT + 7.8 tex elastane
	CO	71.43 tex (Ne 14/1, 60% Tencel+ 40% Cotton)	55.55 tex (Ne 18/1, Sheath fiber- 100% Cotton) + 5.5 tex PET/PTT + 7.8 tex elastane
S3	CA/CO	83.33 tex (Ne 12/1, 60% Tencel+ 40% Cotton)	55.55 tex (Ne 18/1, Sheath fiber- 60% CA + 40% Cotton) + 5.5 tex PET/PTT + 7.8 tex elastane
	CO	83.33 tex (Ne 12/1, 60% Tencel+ 40% Cotton)	55.55 tex (Ne 18/1, Sheath fiber- 100% Cotton) + 5.5 tex PET/PTT + 7.8 tex elastane

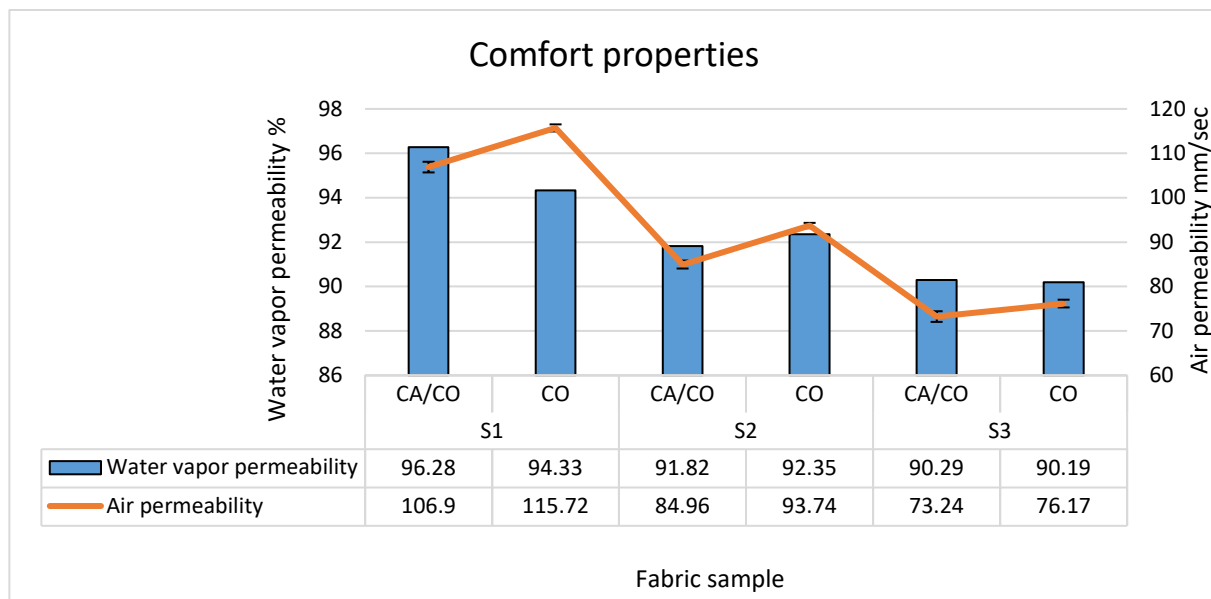


Fig. 9: Water vapor permeability and air permeability of the fabric samples.

Conclusion

For producing sustainable denim fabric, it is high time to look forward to alternative sustainable raw materials. Regenerative cellulosic fiber from wood pulp like lyocell and cellulosic acetate has good potential for sustainable denim production. The impact of denim performance from the sustainable fiber was highlighted in this study. Blending with cotton gives the denim fabric cotton characteristic along with minimizing the sustainable issues. According to the results, fabric from regenerated cellulosic and cotton blended fiber shows fewer weight changes and more dimensional stability than cotton samples after washing. With regenerated fiber and cotton blended yarn, fabric provides good tear and tensile strength than 100% CO fabric and low shrinkage and considerable stiffness properties. Based on water vapor permeability and air permeability, studied denim fabrics are quite comfortable to wear. It is also noticeable that denim fabrics from sustainable fiber have good pilling and abrasion resistance. So, the fabric that is made from cotton can be replaced by regenerated cellulosic and cotton blended fabric, which will be beneficial for the environment and reduce the dependency on cotton fiber.

Acknowledgment

The authors are grateful to the *Çalık Denim Tekstil AŞ* for their cooperation and support.

References

- [1] M. A. Franco, "Circular economy at the micro level: A dynamic view of incumbents' struggles and challenges in the textile industry," *J. Clean. Prod.*, vol. 168, pp. 833–845, 2017, doi: 10.1016/j.jclepro.2017.09.056.
- [2] G. Gedik and O. Avinc, "Hemp Fiber as a Sustainable Raw Material Source for Textile Industry: Can We Use Its Potential for More Eco-Friendly Production?," pp. 87–109, 2020, doi: 10.1007/978-3-030-38541-5_4.
- [3] N. J. B. A. C. M. C. M. J. C. Cherrett, "Ecological footprint and water analysis of cotton, hemp and polyester," *Vasa*, p. 39, 2005, [Online]. Available: <https://www.sei-international.org/mediamanager/documents/Publications/SEI-Report-EcologicalFootprintAndWaterAnalysisOfCottonHempAndPolyester-2005.pdf>.

-
- [4] A. Kumari and K. Khurana, “Regenerated Cellulose-Based Denim Fabric for Tropical Regions: An Analytical Study on Making Denim Comfortable,” *J. Text.*, vol. 2016, pp. 1–10, 2016, doi: 10.1155/2016/4614168.
 - [5] S. Radhakrishnan, *Roadmap to Sustainable Textiles and Clothing*, no. June. Singapore: Springer Singapore, 2014.
 - [6] A. Basit *et al.*, “Comparison of mechanical and thermal comfort properties of tencel blended with regenerated fibers and cotton woven fabrics,” *Autex Res. J.*, vol. 19, no. 1, pp. 80–85, 2019, doi: 10.1515/aut-2018-0035.
 - [7] W. Latif, A. Basit, Z. Ali, and S. Ahmad Baig, “The mechanical and comfort properties of cotton and regenerated fibers blended woven fabrics,” *Int. J. Cloth. Sci. Technol.*, vol. 30, no. 1, pp. 112–121, 2018, doi: 10.1108/IJCST-07-2017-0101.
 - [8] R. C. Law, “Cellulose acetate in textile application,” *Macromol. Symp.*, vol. 208, pp. 255–266, 2004, doi: 10.1002/masy.200450410.
 - [9] E. Sarloğlu, O. Babaarslan, and M. E. Avci, “Effect of Filament Fineness on Composite Yarn Residual Torque,” *Autex Res. J.*, vol. 18, no. 1, pp. 7–12, 2018, doi: 10.1515/aut-2016-0036.

Influence of Fabric Structure on the Adhesion and Functional Properties of 3D Printed Polymers on the Woven Fabric

ČUK Marjeta^{1,a*}, GRAMC Kristina^{1,b}, MUCK Deja^{1,c} and BIZJAK Matejka^{1,d}

¹University of Ljubljana, Faculty of Natural Sciences and Engineering, Department of Textiles, Graphic Arts and Design, Snežniška 5, 1000 Ljubljana, Slovenia

^{a*}marjeta.cuk@ntf.uni-lj.si, ^bgkristina.gramc@gmail.com, ^cdeja.muck@ntf.uni-lj.si, ^dmatejka.bizjak@ntf.uni-lj.si

Keywords: 3D printing, woven structure, adhesion, protective textiles

Abstract. In the textile industry, various 3D printing technologies are used in fashion design and functional clothing (protective, military, and sportswear, including wearable electronics), where the textile substrate is functionalized using additive technology. 3D printing enables the personalization of the product, which in the apparel industry translates into the customized production of garments with additional functions at a more rational cost. In our research, we developed and investigated textiles with enhanced protective properties produced by direct 3D polymer printing on fabrics. Twelve woven fabrics were produced in sateen, twill and hopsack with two different weft yarns and in two weft densities. A preliminary T-peel test was used to determine the optimal fabric structure that would ensure maximum adhesion for direct 3D printing of thermoplastic materials onto fabric. The 3D objects were printed on textile substrates using fused deposition modeling (FDM) technology and thermoplastic acrylonitrile butadiene styrene (ABS) and polylactic acid (PLA) filaments. The main objective was to develop functional textiles with improved protective properties. The results of the physical-mechanical and permeability properties of the functional textiles indicate a promising increase in abrasion resistance by at least 70%, although some other properties deteriorate.

Introduction

3D printing technology has developed very rapidly in the last decade and is used in various industries, including textiles and fashion. It is an additive manufacturing (AM) technology based on the principle of building objects by adding layers of materials and is used for production in the field of fashion design [1], in the production of sports equipment [2], and in the production of functional clothing [3, 4] including wearable electronics [5] and smart textiles [6, 7].

Creating multi material objects with 3D printing on textile substrate, which is currently the most widely used process, it is used to endow textiles with various features and functions that can result in a personalized and optionally customized product. Much research has been conducted on the adhesion of 3D-printed material to textile substrates, with various parameters being investigated. The main challenge has been to achieve sufficient adhesion between the textile surface and the printed polymer while maintaining all the required physical and mechanical properties, comfort, and ease of maintenance [7, 8, 9]. Until recently, only Fused Deposition Modeling (FDM) technology was used for 3D printing on textiles [7, 8, 11-17], using low-cost desktop 3D printers.

FDM technology is best suited for printing on existing substrates [15], and thus is commonly used to fabricate multi-material objects with textiles. FDM is the AM technology based on material extrusion, in which a preheating station raises the temperature of the thermoplastic material so that it can flow in semi-fluid form through a feed system. The material is fed to the system in the form of a filament [18].

Thermoplastic materials commonly used for 3D printing with FDM technology are polylactic acid (PLA), the most commonly used material, acrylonitrile butadiene styrene (ABS), and some other materials such as polycarbonate (PC), a mixture of PC and ABS, and others [19].

Some studies have been conducted to evaluate the effects of pre- and after-treatment of textile substrates for 3D printed textiles on adhesion strength. Some pretreatment processes, such as chemical pretreatment [15], polymer coating on textiles [14], and ironing [15], improved the adhesion

between the printed polymer and the textile substrate. Washing the textile substrate prior to the 3D printing process has negative effects on adhesion in some cases [20]. We hypothesise that the sizing of warp threads, which is necessary for high-speed weaving machines, should also have some effect on the adhesion of 3D-printed objects, so unsized warps were used in our study.

The most important property of multi-material objects fabricated from 3D printed layers on textile substrates is good adhesion, while maintaining the flexibility of the fabric. In particular, good adhesion is a very important factor, as it affects the quality and durability of the final product.

3D printing on textiles opens up a whole new field with the possibility of partial 3D printing on garments or only on parts of garments, which allows customization of the product. For garment manufacturing, this means more user-centric production and increased functionality of the garment for specific purposes. This type of functionalization is particularly important in the field of sports and protective clothing, as 3D printing of protective and support elements allows the production of functional clothing that perfectly adapts to the body [10]. Maintaining the flexibility of textile products while achieving protective properties is achieved by carefully designed and placed 3D printed geometric shapes on textiles [3, 10].

This research was conducted as a preliminary investigation [8] to determine the most suitable shapes of 3D-printed polymers on textiles that provide adequate protection against impact without significantly affecting the useful properties of textiles, such as excessive weight, compromised flexibility, and deterioration of permeability properties.

The main objective of our research was to develop and investigate textiles for protective equipment with improved resistance to impact/abrasion, produced by direct 3D printing of thermoplastic materials on woven fabrics with different structures, namely weave, thread type and thread density, which have the greatest influence on the fabric surface. In addition to the fabric surface, which is crucial for adhesion in 3D printing on textiles, the shape and distribution of the 3D printed geometric objects are also important to achieve satisfactory protective properties.

The objective of this research was to determine the optimal fabric construction for the best adhesion and flexibility of various 3D-printed thermoplastic materials using FDM technology, ensuring optimal functional properties of the protective fabric. Additional protective properties, e.g. against abrasion and injury, could be achieved by 3D printing thermoplastic materials directly onto fabric. Small 3D-printed elements would provide additional protection for the skin by preventing damage to the fabric surface and increasing tear resistance due to abrasion and external forces, e.g., in case of work accidents or falls.

Materials and Methods

Twelve woven fabrics were produced in sateen, twill and hopsack, with two different weft yarns (100% polyester and 100% cotton) and two weft densities, namely 25 and 30 threads/cm, Table 1. The warp (100% cotton, 16 tex, unsized) was the same for all fabrics, with on-loom density of 40 threads/cm. All samples were woven on Minifaber sample looms with electronic Jacquard T.I.S., with the same production settings.

3D models were created in Blender software and exported as stl files. The stl files were imported into the slicing software Simplify3D, where the parameters for 3D printing were set. The samples were printed with two thermoplastic materials: ABS and PLA, Table 2. Wanhao Duplicator 4S was used for printing, which is based on FDM technology.

Table 1. Properties of the fabric samples with their designations (weave: S - sateen, T - twill, H - hopsack; weft density: 25 for 25 threads/cm, 30 for 30 threads/cm; weft composition: CO - cotton, PES - polyester).

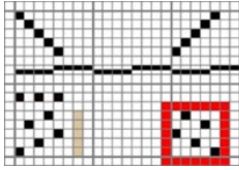
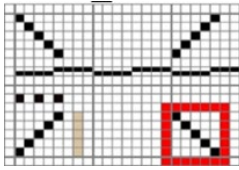
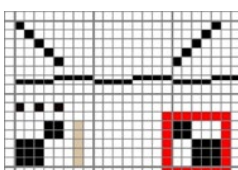
Weave	 sateen $\frac{1}{4}Z_2$	 twill $\frac{1}{4}Z$	 hopsack 5/5
Sample designation	S25 CO	T25 CO	H25 CO
	S25 PES	T25 PES	H25 PES
	S30 CO	T30 CO	H30 CO
	S30 PES	T30 PES	H30 PES

Table 2. 3D printing conditions used for each thermoplastic material.

Thermoplastic filaments	PLA (Plastika Trček) Filament Diameter: 1,75 mm; red and blue	ABS (Plastika Trček) Filament Diameter: 1,75 mm; black
Printing conditions	Temperature: 210 °C Nozzle Diameter: 0,40 mm Extrusion Multiplier: 0,9 Printing speed: 40 mm/s	Temperature: 260 °C, Nozzle Diameter: 0,40 mm Extrusion Multiplier: 1,0 Printing speed: 40 mm/s

The 3D-printed samples for the adhesion test were rectangular, 150 mm × 25 mm in size, and 0,4 mm thick, according to the standard DIN 53530. The corresponding thickness was obtained by printing two layers, each 0,2 mm in size, at the angle of 45°. Based on the measured adhesion properties (DIN 53530) of all samples, the most optimal fabric constructions were selected, on which geometric forms were 3D printed for further investigation.

3D-printed objects on the fabric would allow good mechanical properties while keeping the fabric flexible and comfortable to wear. The functionalization of the fabric depends on the shape and density of the printed objects. Three geometric shapes were printed on the fabric: square (4 mm × 4 mm), semisphere (diameter 4 mm), and ellipse (max diameter 4 mm), with a distance of 2 mm between them. The adhesion of the printed shapes was tested manually by bending the test specimens. Only the semisphere shape adhered well to the fabric after bending. After selecting the shape, different sizes and arrangements of the printed semispheres were tested on the fabric. For the final fabric functionalization, semispheres with a diameter of 3 mm were selected, arranged diagonally and 1.5 mm apart. Fig. 1 shows the arrangement of the 3D printed objects on the woven fabric.

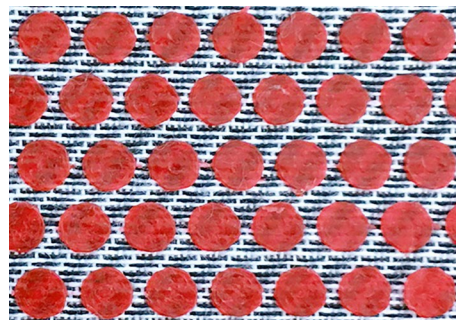


Fig. 1. The 3D printed hemispheres on the fabric in diagonal arrangement.

The analysed properties of the 3D printed fabrics were compared with the properties of the non-printed fabrics: mass per unit area (SIST EN 12107), thickness SIST EN ISO 5084), burst strength (ASTM D 3787), air permeability (SIST EN ISO 9237) and abrasion resistance (Martindale).

Results and Discussion

T - Peel adhesion tests were performed according to the standard DIN 53530 using an Instron 5567 dynamometer, the separation rate was 100 mm/min. The results showed relatively low adhesion forces (max measured force: 11.5 N), which is due to the fact that we did not optimize the printing parameters and embedding of the samples in the preliminary study. The highest adhesion force was obtained at the lowest weft density (25 threads/cm) for both weaves, sateen and twill. The adhesion forces of the hopsack samples were similar, but were considered unsuitable for further investigation in the field of protective fabrics due to their too loose structure. The samples with the highest measured separation forces were selected to continue the experimental work: five-end sateen and five-end twill, both with polyester in the weft and a density of 25 threads/cm, printed with PLA. The sateen and twill samples with cotton in the weft and a weft density of 25 threads/cm printed with both PLA and ABS were also selected to ensure better comparability of results.

Physical mechanical properties such as thickness, mass per square meter, warp and weft density, air permeability and bursting strength, and abrasion resistance were measured according to the standards.

Table 3 and Table 4 show the measured values of the physical mechanical properties of selected woven fabrics used as substrates for 3D printing.

Table 3. Thread density [threads/cm], thickness [mm] and mass per unit area [g/m²] of selected woven fabrics used as substrates for 3D printing.

Sample	Warp density	Weft density	Thickness			Mass		
	[threads/cm]		<i>d</i> [mm]	SD [mm]	CV [%]	<i>m</i> [g/m ²]	SD [g/m ²]	CV [%]
S25 CO	49	29	0,434	0,007	1,646	122,83	0,46	0,38
S25 PES	50	30	0,407	0,006	1,446	120,80	0,95	0,79
T25 CO	50	30	0,438	0,011	2,228	125,57	1,59	1,27
T25 PES	50	30	0,408	0,009	2,206	121,87	2,73	2,24

Table 4. Bursting strength [N], air permeability [l/h] and air permeability [m³/(m²min)] of selected woven fabrics used as substrates for 3D printing

Sample	Bursting strength			Air permeability			Air permeability [m ³ /(m ² min)]
	F [N]	SD [N]	CV [%]	[l/h]**	SD [l/h]	CV [%]	
S25 CO	508,25	3,30	0,65	2185	3,61	0,17	7,28
S25 PES	344,67	26,71	7,75	2328	140,30	6,03	7,76
T25 CO	405,51	29,79	7,35	1854	113,50	6,12	6,18
T25 PES	601,48	99,99	16,62	2234	66,65	2,98	7,45

**50 cm²/50 Pa

Table 5 shows the measured values of mass per unit area and thickness of the 3D-printed samples, as well as the percentage increase in values compared to unprinted fabrics.

Table 5. Mass per unit area and thickness of 3D printed samples and increase in values compared to unprinted fabrics (the sample label also contains the designation for the 3D printed thermoplastic material: A – ABS and P – PLA).

Sample	Mass			Increase in mass* [%]	Thickness			Increase in thickness* [%]
	m [g/m ²]	SD [g/m ²]	CV [%]		d [mm]	SD [mm]	CV [%]	
S25 CO-A	297,77	1,365	0,46	+ 142,24	0,755	0,018	2,45	+ 73,96
S25 CO-P	313,97	1,650	0,53	+ 155,61	0,807	0,031	3,85	+ 85,94
S25 PES-P	316,30	1,300	0,41	+ 161,83	0,692	0,026	3,81	+ 70,02
T25 CO-A	303,53	0,850	0,28	+ 141,72	0,842	0,031	3,70	+ 92,24
T25 CO-P	321,23	0,586	0,18	+ 155,81	0,766	0,008	1,04	+ 74,86
T25 PES-P	315,20	2,081	0,66	+ 158,63	0,706	0,014	1,99	+ 73,04

* compared to unprinted fabric

As expected, 3D printing increased the mass per unit area for all samples, from 142% to 162% on average. The twill sample with polyester weft printed with PLA filament has the highest mass per unit area. The differences in the mass of the printed samples result from the use of different thermoplastic materials for 3D printing, as the differences in the masses of the unprinted fabrics are very small. However, the mass per unit area of the samples printed with PLA is 13% to 14% higher than that of the samples printed with ABS.

The values for the thickness of the samples show an analogy with the mass (Table 5), since the construction parameters are interdependent. The thickness of the 3D- printed samples increases by more than 70% on average. The differences in thickness between samples with different thermoplastic materials are noticeable but very small (between 3% and 9%), making it difficult to attribute the differences to different materials, but rather to unequal printing conditions.

A large increase in the mass per square meter and thickness of the printed samples indicates that only partial 3D printing on the fabrics is useful to improve the protective properties of the fabric.

Table 6 shows the measured values of bursting strength and Table 7 shows the air permeability of the 3D printed samples and the percentage increase in values compared to unprinted fabrics.

Table 6. Bursting strength and changes in values compared to unprinted samples.

Sample	Bursting strength [N]			Increase in bursting strength* [%]
	F [N]	SD [N]	CV [%]	
S25 CO-A	443,89	117,66	26,65	+ 0,5
S25 CO-P	454,02	25,32	5,58	+ 2,7
S25 PES-P	656,08	106,15	16,18	+ 90,0
T25 CO-A	506,39	76,93	15,19	+ 24,9
T25 CO-P	466,64	6,07	1,30	+ 15,1
T25 PES-P	635,85	59,65	9,38	+ 5,7

* compared to unprinted fabric

In the bursting strength measurements, the samples were loaded spherically until bursting, so the equality of the 3D-printed samples and the same clamping position are also important in this test. Large variations occurred in the bursting strength measurements, which were reflected in high coefficients of variation. Samples S25 PES -P and T25 PES -P, with different weave but both with polyester in the weft, showed the highest bursting forces, namely 656,1 N and 635,9 N, respectively (Table 6). The sateen samples printed with ABS show lower bursting force than the samples printed with PLA. For the twill samples, the results are just the opposite. The bursting strength is highest for the twill samples with polyester weft, indicating a large influence of the weft strength and, to some extent, the adhesion strength between the 3D printed polymer and the fabric.

Table 7. Air permeability of 3D printed samples and changes in values compared to unprinted samples.

Sample	Air permeability			Air permeability [m ³ /(m ² min)]	Decrease in air permeab. * [%]
	[l/h]**	SD [l/h]	CV [%]		
S25 CO-A	904	4,36	0,48	3,01	- 65,8
S25 CO-P	1113	98,44	8,84	3,71	- 49,0
S25 PES-P	1149	46,32	4,03	3,83	- 50,6
T25 CO-A	1038	70,59	6,80	3,46	- 44,0
T25 CO-P	1038	70,59	6,80	3,49	- 43,5
T25 PES-P	1071	94,33	8,81	3,57	- 52,1

* compared to unprinted fabric

**50 cm²/50 Pa

Comparing the air permeability values of the unprinted samples (Table 4), we find that the differences are very small, although the highest value is obtained for the S25 PES - sateen sample with 25 threads/cm and polyester weft. A slightly lower air permeability is shown by the T25 CO - twill sample with 25 wefts/cm and cotton weft, which is due to the more compact weave structure with more interlacing points and a hairier cotton weft.

Samples with 3D printed and partially closed surface have poorer air permeability compared to unprinted fabrics (Table 7). The air permeability properties of sample S25 CO -A deteriorate the most, by 65%. Comparing the values of air permeability of 3D-printed samples in different weaves, in general, a smaller decrease in air permeability is observed for satin samples. On average, air permeability decreases by 50% to 65% for sateen samples and 44% to 52% for twill samples (Table 7).

Fig. 2 shows the surfaces of the tested samples as a result of the Martindale abrasion test.

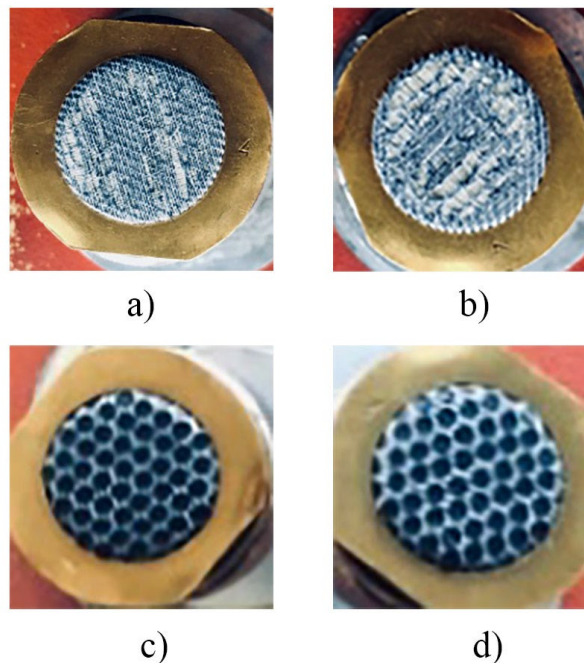


Fig. 2. Abrasion resistance (Martindale): a) sample S25 CO at 16,000 revolutions, b) sample S25 CO at 20,000 revolutions, c) sample S25 CO-A at 16,000 revolutions and d) sample T25 CO-A at 16,000 revolutions.

When testing the abrasion resistance (Martindale) of woven fabrics, no changes were found on the surface of all satin and twill fabrics up to 3,000 revolutions. At 4,000 revolutions, small knots appeared on the surface of the samples with cotton weft, and at 6,000 revolutions, the first pilling appeared. At 12,000 revolutions, severe peeling appeared, and at 14,000 revolutions, the first thread broke. At 16,000 revolutions, a larger number of threads broke, and at 20,000 revolutions the samples with cotton weft were destroyed (Fig. 2a and Fig. 2b).

For fabric samples S25 PES and T25 PES with polyester weft, the process of changing the surface during abrasion was similar, except that the first damage of the surface occurred at 8,000 revolutions due to the more abrasion-resistant polyester weft. At 16,000 revolutions, the first thread broke, and at 25,000 revolutions, the surface of the sample was destroyed.

When the abrasion resistance of the 3D printed samples was tested, no changes were observed on the sample surface up to 16,000 revolutions (Fig. 2c and Fig. 2d). The abrasion resistance results show that the 3D printed thermoplastic material on the fabric significantly increases the abrasion resistance of the fabric, as the samples remained undamaged even after 35,000 revolutions. The test procedure was performed on all samples with 3D printed semispheres with both PLA and ABS polymer only up to 35,000 revolutions, when slight color changes of the printed polymer were observed. However, it can be assumed that the abrasion resistance is increased by at least 70% by applying the polymer to the fabric with 3D printing.

Conclusion

The effectiveness of functionalizing fabrics with 3D printing depends largely on the adhesion between the fabric and the polymer. The adhesion of 3D printed objects to textiles is influenced by many factors, of which the structure of the fabric is one of the most important.

As expected, 3D printing increased the mass per unit area for all samples, on average by about 150%. The differences in mass between samples resulted from the use of different thermoplastic materials for 3D printing. For the samples printed with PLA, the mass is more than 10% higher than for the samples printed with ABS. The increase in thickness of the samples shows an analogy to the mass, with the thickness of the 3D printed samples increasing by more than 70% on average. A large increase in mass per square meter and thickness of the printed samples indicates that only partial 3D printing on the fabrics is useful to improve the protective properties of the fabric.

Bursting strength measurements show resistance to spherical loading, which is very important in impacts. Despite the large variations that occurred in bursting strength measurements, the tendency is evident that the resistance depends more on the fabric's construction parameters, such as the strength of the weft threads and the weave, than on the adhesion strength between the 3D-printed polymer and the fabric.

The air permeability of 3D-printed fabrics is reduced by about half compared to unprinted fabrics due to the partially closed surface, but a smaller decrease in air permeability is observed for sateen samples.

The abrasion resistance results show that the 3D-printed thermoplastic shapes on the fabric significantly increase the abrasion resistance of the fabric, by at least 70%, as the samples remained undamaged even after 35,000 revolutions.

The measured physical-mechanical properties and permeability of the functional fabrics showed that 3D printing of thermoplastic polymers on the fabric increased abrasion resistance, but compromised some other fabric properties. Compared with unprinted fabrics, the mass per unit area and thickness of 3D-printed fabrics increased, while their air permeability decreased. The results of our preliminary research show that this method of functionalization is only suitable for partial reinforcement of protective clothing.

References

- [1] T. Penko, Technology of 3D printing garments in fashion design, *Tekstilec*. 60 (2017) 50-58. DOI: 10.14502/Tekstilec2017.60.00-00.
- [2] L. Gregurić, Adidas 3D Printed Shoes: The Latest Advancements. All3DP, Information on <https://all3dp.com/2/adidas-3d-printed-shoes/>
- [3] J. H. Park, J. R. Lee, Developing Fall-Impact Protection Pad with 3D Mesh Curved Surface Structure Using 3D Printing Technology, *Polymers*. 11 (2019). DOI: 10.3390/polym11111800.
- [4] N. Grimmelsmann, Y. Martens, P. Schael, H. Meissner and A. Ehrmann, Mechanical and electrical contacting of electronic components on textiles by 3D printing, *Procedia Technology*. 26 (2016) 66-71. DOI: 10.1016/j.protcy.2016.08.010.
- [5] M. Zhang et al., Printable Smart Pattern for Multifunctional Energy-Management E-Textile. *Matter*. 1 (2019) 168-179. DOI: 10.1016/j.matt.2019.02.003.
- [6] K. Mondal, Recent Advances in Soft E-Textiles. *Inventions*. 3/23 (2018). DOI: 10.3390/inventions3020023.
- [7] N. Grimmelsmann, M. Kreuziger, M. Korger, H. Meissner and A. Ehrmann, Adhesion of 3D printed material on textile substrates. *Rapid Prototyping Journal*. 24/1 (2018) 166-170. DOI: 10.1108/RPJ-05-2016-0086
- [8] M. Čuk, M. Bizjak, D. Muck, T.N. Kočevr, 3D printing and functionalization of textiles, in S. Dedijer (Ed.), *Proceedings of 10th International Symposium on Graphic Engineering and Design GRID 2020*, Novi Sad, 2020, p.p. 499-506. DOI: 10.24867/GRID-2020-p56.
- [9] D. Rant, Development of multifunctional 3D knitted structures with auxetic potential. Ph. D. Thesis, *Oddelek za tekstilstvo, NTF, Univerza v Ljubljani, Ljubljana*, 2018.
- [10] M. Korger, A. Glogowsky, S. Sanduloff, C. Steinem, S. Huysman, B. Horn, M. Ernst, M. Rabe, Testing thermoplastic elastomers selected as flexible three-dimensional printing materials for functional garment and technical textile applications, *Journal of Engineered Fibers and Fabrics*. 15 (2020) 1-10. DOI: 10.1177/1558925020924599.
- [11] T. Spahiu, M. Al-Arabiyyat, Y. Martens, A. Ehrmann, E. Piperi, E. Shehi, Adhesion of 3D printing polymers on textile fabrics for garment production. In *IOP Conference Series: Materials Science and Engineering*, 459 (2018). DOI: 10.1088/1757-899X/459/1/012065
- [12] M. ten Bhömer, D. Tate, S. Wang, F. Campanile and Y. Chen, Application of robust design techniques for 3D printing on textiles, in M. Di Nicolantonio, E. Rossi, T. Alexander (Eds.), *Advances in Additive Manufacturing, Modeling Systems and 3D Prototyping*. Springer, Cham. AG, 2020, Vol. 975, 2020, 153-165. DOI: 10.1007/978-3-030-20216-3_15.
- [13] T. Spahiu, N. Grimmelsmann, A. Ehrmann, E. Piperi and E. Shehi, Effect of 3D printing on textile fabric. In *Proceedings of the 1st International Conference: Engineering and Entrepreneurship*, Tirana, Albania, 2017.
- [14] L. Unger, M. Scheideler, P. Meyer, J. Harland, A. Goerzen, M. Wortmann, A. Dreyer, A. Ehrmann, Increasing Adhesion of 3D Printing on Textile Fabrics by Polymer Coating, *Tekstilec*. 61/4 (2018) 265-271. DOI:10.14502/Tekstilec2018.61.265-271.
- [15] T. Kozior, C. Döpke, N. Grimmelsmann, I. Juhász Junger, A. Ehrmann, Influence of fabric pretreatment on adhesion of three-dimensional printed material on textile substrates, *Advances in Mechanical Engineering*. 10/8 (2018) 1-8. DOI:10.1177/1687814018792316.

-
- [16] R.H. Sanatgar, C. Campagne, V. Nierstrasz, Investigation of the adhesion properties of direct 3D printing of polymers and nanocomposites on textiles: Effect of FDM printing process, *Applied Surface Science*. 403 (2017) 551-563. DOI: 10.1016/j.apsusc.2017.01.112.
- [17] N. S. Mpofu, J.I. Mwasiagi, L. C. Nkiwane, D. Njuguna, Use of regression to study the effect of fabric parameters on the adhesion of 3D printed PLA polymer onto woven fabrics, *Fashion and Textiles*. 6/1 (2019). DOI: 10.1186/s40691-019-0180-6.
- [18] I. Gibson, D. Rosen, D., B. Stucker, Introduction and Basic Principles. In *Additive Manufacturing Technologies: 3D Printing, Rapid Prototyping, and Direct Digital Manufacturing*, Springer New York, New York, 201, pp. 1–18.
- [19] D. Muck, I. Križanovskij, 3D tisk. Pasadena, Ljubljana, 2015, 80-82.
- [20] A. Narula, C.M. Pastore, D. Schmelzeisen, S. El Basri, J. Schenk, S. Shajoo, Effect of knit and print parameters on peel strength of hybrid 3-D printed textiles. *Journal of Textiles and Fibrous Materials*, 2018. DOI:10.1177/2515221117749251.

A Preliminary Study of Analising Weft Cover Factor of Woven Fabrics by Image Treatment

Ignacio Montava^{1,a}, Pablo Díaz-García^{1,b}, Andrea Carbonell^{1,c},
 Jaime Gisbert-Payá^{1,d}, Eva Bou-Belda^{1,e*}

¹Departamento de Ingeniería Textil y Papelera, Universitat Politècnica de València, Plaza Ferrándiz y Carbonell s/n, Alcoy, Spain; imontava@txp.upv.es (I.M.);

^aimontava@txp.upv.es, ^bpdiazga@txp.upv.es; ^candrea@ateval.com, ^djagispa@txp.upv.es, ^{e*}evbobel@upv.es

*Email: evbobel@upv.es(E.B-B)

Keywords: fabric, weave, matlab, thickness, yarn, opacity.

Abstract: Cover factor is defined as the ratio of the area covered by yarns to the total area of the fabric. This fabric's characteristic is a basic construction parameter of woven cloth related to its end-use behaviour. Different authors are focused on studying the effect of the cover factor fabric on different properties of the fabric, like air permeability, ultraviolet protection, noise absorption and light transmission. However, the aim of this work is study the capacity of the weft to achieve a certain degree of coverage in the woven fabric, taking advantage of the warp's ability to allow light to pass through its own structure and the opacity of the weft.

Introduction

The structure of the weave fabrics, as well as threads properties used and the material which is composed, play an important role in the properties acquired by the textile. Their characteristics, such as grams per square metre, tensile strength, texture, smooth, cover factor, among others, are important to define the end-use or application of the textile. Cover factor is a fabric parameter defined as the ratio of the area covered by component yarns to the total area of the fabric [1, 2]. This gives a measure of how closely a cloth is set by indicating the fraction of available space in the cloth that is occupied by yarn [3, 4]. Review of published scientific literature defined the horizontal porosity as a complement to the woven fabric cover factor [5, 6].

The effect of cover factor of the fabric on different properties have been studied by some authors, like flammability [7,8], UPF protection [9, 10], air permeability [11-14], moisture transport [15, 16], shrinkage [17, 18], light transmittance [19, 20] or noise absorption [21].

For any woven fabric, there are two cover factors: a warp cover factor and a weft cover factor. It depends on thread density and thread count. The higher the thread density is the higher the cover factor but the higher the thread count is the lower the cover factor.

The fabric cover factor was also determined using equation (1) (FCF (%)) [22]:

$$FCF(\%) = \frac{([n1 \cdot d1] + [n2 \cdot d2] - [n1 \cdot d1 \cdot n2 \cdot d2])}{([n1 \cdot d1] + [n2 \cdot d2])} \times 100 \quad (1)$$

where $n1$ and $n2$ are the warp and weft density per cm, and $d1$ and $d2$ are the warp and weft yarn diameter (cm), respectively.

The aim of this work is to study the influence that the weight has on the coverage factor of the fabric. In order to carry out this work the characteristics of the polyester warp (density and count) have remained immovable and only the density of the weft and the weave have been modified. Taking advantage the fact that the structure of the warp thread used is multifilament without twisting, allows light to pass through its own structure. In this way, only the weft thread shows opacity, being able to

achieve the weft coverage factor value. This fabric data can be important in different applications, such as those in which fabric is functionalized by the type of thread used in the weft direction, conductive or shielding textiles for example.

Materials and Methods

In order to obtain the aim of this work, different fabrics were made using the same warp density (60 yarns/cm) and the same warp and weft yarn in all of them, which are described in Table 1.

Table 1. Yarn characteristics used in warp and weft direction

	TYPE	YARN COUNT
WARP YARN	Polyester multifilament yarn air texturized	167 dtex
WEFT YARN	Acrylic yarn spun	10/2c Nm

Shown in Table 2 are shown the main features of fabrics made, where maximum densities allowed by the loom were applied.

Table 2. Main features of woven fabrics performed

	DENSITY (PICKS/CM)	STRUCTURE
T-11	11	Plain weave
S/6-17	17	1/5 Z-twill
S/9-25	25	1/8 Z-twill
R/5-20	20	5-end sateen move 2
R/9-22	22	9-end sateen move 4

It can be observed that the greater size of the weaving repeat, the greater the ability to insert wefts. It could be possible to insert only 11 threads/cm in the plain weave (repeat of 2x2) and values greater than 20 threads/cm in structure of 9x9. Of course, all fabrics were weaved making use of same warp, the same weft and the same weaving machine.

To determine the weft cover factor of each fabric a magnifying glass was used to take the image of each fabric and afterwards the images were processed by Matlab software.

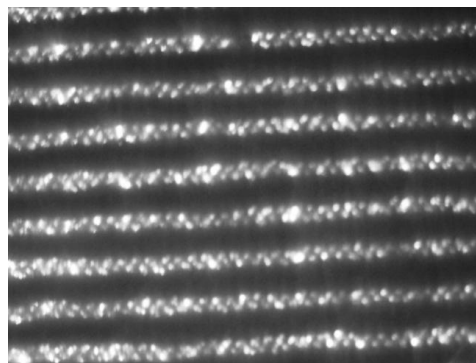
Results and Discussion

Images taken from the magnifying glass were binarised by Matlab, in Fig. 1 images of analyzed fabrics before and after binarised process are shown.

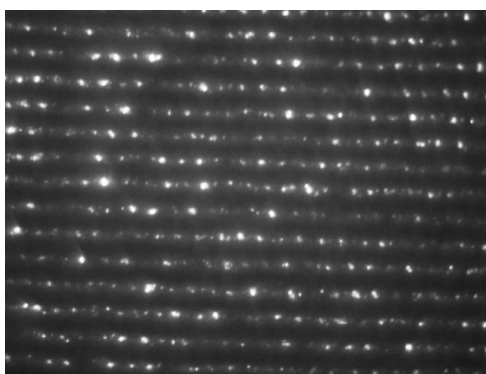
Images taken from the
magnifying glass

Binarized images by
Matlab software

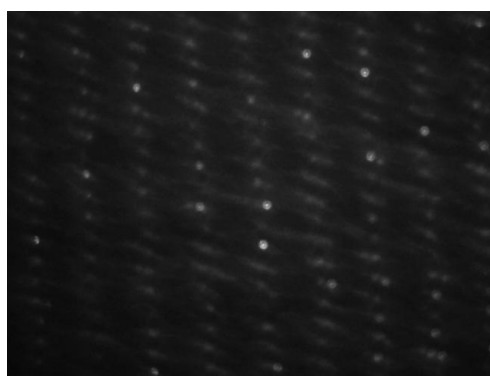
T-11



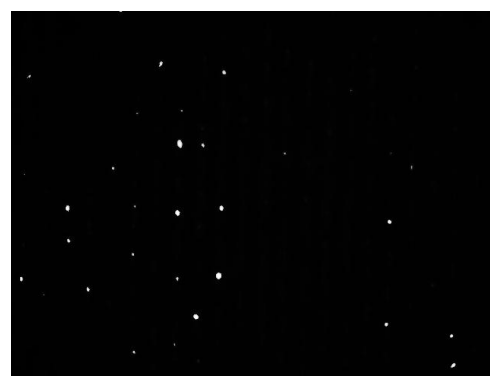
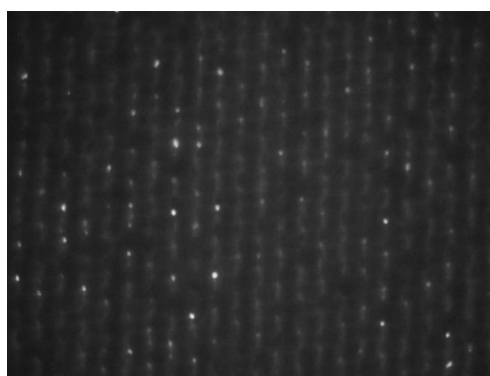
S/6-17



S9-25



R5-20



R9-22

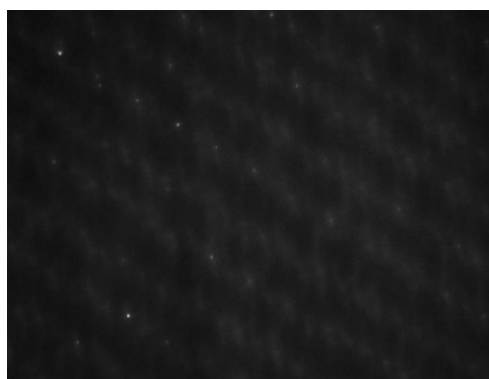


Figure 1. Images before and after binarized process by Matlab software

All the test pieces developed have the ability to transmit light through the profile of the warp yarn due to the fact that this section of yarns is made up of polyester multifilaments without twisting that allow the passage of light between their filaments. It can be seen in all images that the full opacity of the fabric is obtained thanks to the weft that completely obscures the area of the image that they cover.

The opacity of the weft thread and the translucency of the warp thread is observed. As weft cover factor is given by the % of black in the image.

Table 3. Degree of weft cover factor defined by image treatment

FABRIC	% OF BLACK
T-11	89,44
S/3-15	92,06
S/9-25	99,22
R/5-20	99,82
R/9-22	99,96

From the results obtained is observed that satin weave shows a greater covering capacity than that offered by the twill weave and much greater than the plain weave.

The increase in the weave unit also helps to achieve a gradual increase in the coverage capacity, achieving an almost full coverage value in the most favorable case: 9x9 weave unit.

It can be seen in the magnifying glass image of T11 that the weft yarns are separated from each other, not being able to offer full coverage. The juxtaposition that the plain weave generates by its way of evolving warp and weft threads causes an area of the image occupied by the warp, so it is not possible the contact between the adjoining weft yarns.

On the other hand, both the twill and the satin do allow that contact between adjacent threads, as the evolution of their threads allows the overlapping of the points of binding and therefore a greater proximity between the contiguous wefts.

The differences obtained between the coverage values of the twill fabrics, always somewhat lower, and those of the plain ones, slightly higher, correspond to the unic binding point of both structures present. In the case of twill, this binding point is arranged in staggered 1, preventing a total overlapping of the float which in turn prevents the total approach of the wefts yarns. On the other hand, the fact that the value of the step in the plain is different from 1 (of values 2 and 4 in the cases of the references R-5/20 and R-9/22) allows a total overlap of the generated floats in the weave unit and therefore that the weft has the ability to hide the point where the warp prevails.

Conclusions

The results show a different percentage of the coverage factor of the weft depending on the structure and density used. These fabric data can be important in different applications, such as those in which the fabric is functionalized by the type of yarn used in the weft direction.

In addition, from the work carried out, it can be concluded that multifilaments without twisting allow the passage of light through the interstices that are generated between their component filaments. To achieve total opacity, the threads used must be twisted.

Moreover, it has worked with totally light ligaments, in which the warp only makes one take point in each thread and in each pass, but instead the tightness results are very different depending on the type of structure applied.

References

- [1] Tàpias, M., Ralló, M., Escofet, J., Algaba, I., Riva, A. Objective measure of woven fabric's cover factor by image processing. *Textile research journal*, 80.1, (2010) 35-44.
- [2] Tàpias, Montserrat, Jaume Escofet, and Miquel Ralló. Cover factor determination by means of reflectance measurement in translucent textile webs. *AIP Conference Proceedings*. American Institute of Physics, 992(1) (2008).
- [3] Peirce, Frederick Thomas. 5—The geometry of cloth structure. *Journal of the Textile Institute Transactions*, 28.3, (1937) 45-96.
- [4] Hamilton, J. B. 7—A general system of woven-fabric geometry. *Journal of the Textile Institute Transactions*, 55.1, (1964) 66-82.
- [5] Havlová, Marie. Model of vertical porosity occurring in woven fabrics and its effect on air permeability. *Fibres & Textiles in Eastern Europe* (2014).
- [6] Zupin, Živa, Aleš Hladnik, and Krste Dimitrovski. Prediction of one-layer woven fabrics air permeability using porosity parameters. *Textile Research Journal* 82.2 (2012) 117-128.
- [7] Gotipamul, R. L., Dandgole, P. B., Dudagi, I. B., Prasad, J., Surwase, V. S., Yuvraj, T., & Deori, R. Effect of cover factor and weave factor on flammability characteristics of 100% cotton fabric. *Melliand International*, 20.1 (2014).
- [8] Baltušnikaitė, J., Šuminskienė, R., Milašius, R. Influence of Woven Fabrics Structure upon Flammability Properties. *Materials Science (MEDŽIAGOTYRA)*, 12, (2006) 167-70.
- [9] Kostajnshek, K., Dimitrovski, K. Use of Extended Cover Factor Theory in UV Protection of Woven Fabric. *Polymers*, 13(8), (2021) 1188.
- [10] Dubrovski, P. D., Golob, D. Effects of woven fabric construction and color on ultraviolet protection. *Textile Research Journal*, 79(4), (2009) 351-359.
- [11] Gabrijelčič, H., Urbas, R., Sluga, F., Dimitrovski, K. Influence of fabric constructional parameters and thread colour on UV radiation protection. *Fibres & Textiles in Eastern Europe*, 17.1, (2009) 46-54.
- [12] Epps, H. H., Leonas, K. K. The relationship between porosity and air permeability of woven textile fabrics. *Journal of testing and evaluation*, 25.1, (1997) 108-113.
- [13] Zupin, Ž., Hladnik, A., Dimitrovski, K. Prediction of one-layer woven fabrics air permeability using porosity parameters. *Textile Research Journal*, 82.2, (2012) 117-128.
- [14] Xu, G., Wang, F. Prediction of the permeability of woven fabrics. *Journal of Industrial Textiles*, 34.4, (2005) 243-254.
- [15] Wardiningsih, W., Troynikov, O. Influence of cover factor on liquid moisture transport performance of bamboo knitted fabrics. *Journal of the Textile Institute*, 103.1, (2012) 89-98.

- [16] Zhang, H., Liu, F., Wang, J., Zhu, C. Effects of fabric weave and cover factor on moisture transfer ability of moisture absorbent and fast drying fabric. *Journal of textile research*, 5 (2008).
- [17] Onal, L., Candan, C. Contribution of fabric characteristics and laundering to shrinkage of weft knitted fabrics. *Textile Research Journal*, 73.3, (2003)187-191.
- [18] Baird, K. Felting shrinkage and dimensional properties of hand-knitted wool fabrics. *Textile Research Journal*, 40.12, (1970) 1064-1069.
- [19] Szmyt, J., Mikolajczyk, Z. Light transmission through decorative knitted fabrics in correlation with their fabric cover. *AUTEX Research Journal*, 10.2, (2010) 44-48.
- [20] Militky, J., Travnickova, M., Bajzik, V. Air permeability and light transmission of weaves. *International journal of clothing science and technology* (1999).
- [21] Soltani, P., Zarrebini, M. Acoustic performance of woven fabrics in relation to structural parameters and air permeability. *Journal of the Textile Institute*, 104.9, (2013) 1011-1016.
- [22] Shanbeh, Mohsen, et al. Analysis of shear characteristics of woven fabrics and their interaction with fabric integrated structural factors. *Journal of Engineered Fibers and Fabrics* 14 (2019): 1558925019867520.

CHAPTER 2:

Fabrics and Fibers for Biomedical Application

Exploring Nanofibers and Hydrogels as Collagenase Carriers for the Development of Advanced Wound Dressings

JEROME Antunes^{1,a}, ARTUR Ribeiro^{2,b}, DANIELA Lemos^{2,c},
TERESA Miranda^{1,d}, JORGE Santos^{1,e} and GRAÇA Soares^{1,f,*}

¹Centre for Textile Science and Technology, University of Minho, Campus de Azurém, 4800-058
Guimarães, Portugal

²Centre of Biological Engineering, University of Minho, Campus de Gualtar, Braga, Portugal

^ajerome_a_@hotmail.com, ^barturibeiro@ceb.uminho.pt, ^ca88556@alunos.uminho.pt,
^dtmiranda@det.uminho.pt, ^ejsantos@det.uminho.pt, ^{f,*}gmb@det.uminho.pt

Keywords: Wound dressing, Collagenase, PCL nanofibers, Hydrogels

Abstract. Collagenase acts by promoting wound debridement, contributing to the tissue repair process. Several studies pointed collagenase as a substance involved in the elimination of devitalized tissue or any contaminated material found in the wound bed after the appearance of a lesion or skin burn. In the present work hydroxypropyl methylcellulose/cyclodextrins hydrogels and polycaprolactone nanofibers with the ability to transport collagenase for the treatment of skin lesions, were synthesized and characterized. The collagenase polymeric carriers showed good physicochemical properties and presented the ability to retain the enzyme in its structure. Moreover, the PCL carriers did not display cytotoxic effect on human skin fibroblasts. Controlled release and *in vitro* diffusion studies revealed a slow release of active collagenase confirming the ability of the new systems to be used as carriers' devices in the treatment of skin lesions.

Introduction

New approaches to develop wound dressings have been extensively studied to better contribute to the healing process. The improvement of these dressings has been focused on several aspects, such as polymeric materials with better properties, structures that are more suitable and bioactive additives that allow to predict or control the inflammation or infection at the wound. To address the increasing demand for new alternative wound repair dressings, different strategies have been pursued in the last years.

Degradable synthetic polymers are included in the materials often used in the construction of dressings for wound repair. Among these, polycaprolactone (PCL) is one of the most used due to its interesting characteristics, which contribute for the approval of PCL-based dressings by regulatory institutions like FDA. This semi-crystalline polyester is non-toxic, biocompatible, soluble in a wide variety of different solvents, and easy to combine with other polymers (PLA, PLGA, Chitosan, PEG), widening the range of potential applications [1]. Its low melting temperature and high viscoelastic properties makes easy to produce and to manipulate during the fabrication of PCL-based devices. Moreover, the slow degradation of PCL is particularly useful, and its use in long-term implants is advisable [2, 3].

Nanofibers have been a frequent option in the development of materials for therapeutic purposes, particularly for tissue engineering applications, as systems for controlled release and as wound healing dressings [4, 5]. Nanofibers can be obtained by self-assembly, structural moulding, phase separation and electrospinning, using various polymers and incorporating several bioactive compounds. Electrospinning is currently used for the production of nanofibers due to its simplicity and ability to generate materials with a high surface area and good mechanical stability. These requirements are essential for the use of nanofibers in biomedical applications [6, 7].

Most of the recent approaches for chronic wounds management are based on the topical application or on the release of active compounds, namely from polymeric structures such hydrogels and nanofibers. Hydrogels display unique characteristics, related to their moisture management properties

and their ability to release in a controlled manner different active agents. Nanofibers can also incorporate active agents in their structure, and the release of these compounds can be tuned according to different stimulus. These properties, makes hydrogels and nanofibers excellent candidates for the development of wound dressings. However, in both approaches, it is necessary to keep in mind the concern with potential side effects due to the accumulation of immunoreactive compounds at the wound site [7, 8].

Cyclodextrin-cellulose hydrogels have been identified as a viable options for the moist environment maintenance and as vehicles for the control delivery of bioactive molecules, pre-requisites mandatory for modern wound dressing [9- 12]. The ability to sustain the release of phenolic acids and thereby prevent the proliferation of bacteria has been proven. The integration in the polymeric structure of chitosan allows to have sensitivity to pH and to shape the release of medicines when the wounds become infected [13].

Collagenase is an enzyme that breaks down peptide bonds in collagen. This protease has been used in therapeutic formulations such as creams and ointments to remove cell debris and extracellular tissue necrosis. Its use in the treatment of wounds, ulcers and bedsores promotes the formation and reepithelization of new tissues without affecting healthy collagen and newly formed tissue. [14-20]

Collagenases can be obtained from animals or plants, however they are mostly obtained from microorganisms. This is due to the fact that they can be easily obtained, the process being reproducible and with high yield at a low cost. In addition, microbial collagenases have the advantage of being able to cleave the collagen triple helix in numerous locations, whereas mammalian collagenases cleaved in only one location. *Clostridium histolyticum* has been one of the most frequent sources for obtaining this type of enzymes [21- 24].

The permanent immobilisation of the active agents on the surface of the dressing would prevent overdoses in clinical application. Dressings for wounds with immobilized collagenase can be interesting and have therapeutic potential. However, as far as we know, no attempt has been made to incorporate collagenase in polymeric structures, such as hydrogels or nanofibers, for this purpose.

The objective of this work was to develop functional polymeric structures to incorporate collagenase, promoting the wound healing process. In this context, the present work describes the innovative development of Collagenase-Polycaprolactone nanofibers and Collagenase-Cyclodextrin/Cellulose hydrogels. The immobilization of the collagenase on these polymeric structures is seen as a promising strategy for the development of innovative dressings, with the potential to treat wound infections.

Materials and Methods

Materials. Polycaprolactone (PCL) (MW 45.000g/mol) was purchased from Primex-Iceland. Chloroform (analytical grade), Dimethylformamide (DMF) (analytical grade) and Dimethyl sulfoxide (DMSO) anhydrous $\geq 99.9\%$, Sodium chloride and Sodium Hydroxide and FALGPA were acquired from Sigma (Spain). Tricine was acquired from Acros Organics (Belgique) and Collagenase (from *Clostridium histolyticum*, Islet Isolation Grade, ~ 3500 units/g), was purchased from Fisher (USA). Hydroxypropyl methylcellulose (HPMC, $84.200 \text{ g mol}^{-1}$) was purchased from VWR Prolab Chemicals (Carnaxide, Portugal). 2-Hydroxypropyl- β -cyclodextrin (HP β CD, 1309 g mol^{-1}) was obtained from Appli-Chem (St Louis, Missouri, USA) and 1,4-butanediol diglycidyl ether (BDGE, 50-60% v/v in water) was purchased from Acros Organics (Geel, Belgium). L-histidine hydrochloride, di-Sodium hydrogen phosphate dihydrate, Sodium dihydrogen phosphate dihydrate were supplied by Panreac (Espanha). All solvents were used as received without further purification.

Production of Hydroxypropyl methylcellulose /Cyclodextrins Hydrogels. Hydrogels based on hydroxypropyl methylcellulose (HPMC) and cyclodextrins (β CD or HP β CD) were synthesized according to the previous described by our research group [9]. The collagenase was incorporated by adsorption in the hydrogels according to the described by Van Wart & Steinbrink [25].

Production of Polycaprolactone Nanofibers by Electrospinning. Stable and homogenous emulsions of polycaprolactone (PCL) (15%, 16%, 20% and 30% (w/v)) prepared in Chloroform/DMF (8:2) were electrospun in the NanonNF-103 (MECC, Japan) at room

temperature, using a 12 ml syringe with needles of 0.5 mm of inner diameter. An electric field of 24 kV was applied to all solutions and the feed rate was varied from 0.4 to 1 L.h⁻¹. The collection time was ~1.0 hour at 25 °C and relative humidity up to 35%. The PCL nanofibers were deposited on a collecting plate paced at 28 cm and were dried in the hood at room temperature until constant weight. The same electrospinning conditions were used to pure PCL with collagenase (5mL of 10mg/mL in buffer solution pH 7.5).

The nanofibers were washed several times and dried at room temperature.

Characterization of PCL nanofibers and HPMC/cyclodextrin hydrogels.

Attenuated total reflectance Fourier Transform Infrared Spectroscopy (ATR-FTIR). The chemical composition of the PCL nanofibers and HPMC/cyclodextrin hydrogels, with and without loaded collagenase, was analysed on a Shimadzu Irtaffinity-1S FT-IR spectrophotometer. Each spectrum was acquired over the range 400–4000cm⁻¹ in transmittance mode on a ZnSe ATR crystal cell by accumulation of 256 scans with a resolution of 4 cm⁻¹.

Surface Morphology. The surface morphology of the PCL nanofibers and hydrogels with and without loaded collagenase was investigated using an Ultra-high resolution Field Emission Gun Scanning Electron Microscopy (FEG-SEM), NOVA 200 Nano SEM, FEI Company. Secondary electron images were performed with an acceleration voltage at 5 kV. Backscattering Electron Images were realized with an acceleration voltage of 15 kV. Samples were covered with a film of Au–Pd (80–20 weight %) in a high-resolution sputter coater, 208HR Cressington Company, coupled to a MTM-20 Cressington High Resolution Thickness Controller. The fibre diameters were directly measured from SEM images using public domain software (Image J, National Institutes of Health, USA). After that, the fibres' average diameter were determined by applying SPSS Statistics 21.0 software (SPSS Inc. Chicago, USA).

Differential scanning calorimeter (DSC) and Thermal gravimetric analysis (TGA) analysis. The thermal properties of the hydrogels and PCL nanofibers were characterized by differential scanning calorimetry (DSC) and thermogravimetry. DSC measurements were carried in liquid nitrogen atmosphere using DSC-822e instrument (Mettler Toledo). The calibration was made with indium as standard. Samples were weighed (2.5 ± 0.2 mg) and sealed in aluminium pans. Then, they were heated from 0 °C to 500 °C, at a scanning rate of 10°C minute⁻¹. Data were treated using LAB Mettler Star SW 8.1 software (Mettler-Toledo International Inc., Swiss). Samples' thermal behaviour was also investigated employing the simultaneous thermogravimetry-differential scanning calorimetry (TGA) technique using a TA Instruments model Hitachi STA7200. The samples (10 mg) were heated (20 °C to 600 °C) in a standard alumina sample pan. All experiments were performed under dynamic nitrogen at a flow rate of 0.1 L minute⁻¹ using a heating rate of 10° C minute⁻¹ per run. Degradation onset temperature was assigned at the temperature at which 90% mass remained.

Swelling profile. The swelling profile of samples was assessed by immersing dry PCL nanofibers and HPMC/cyclodextrin hydrogels (50 ± 5 mg) in 5mL of synthetic sweat solution according to ISO 105-E04: 1994. The amount of buffer absorbed by the hydrogels and nanofibers was calculated based on the difference between the weight of fully swollen hydrogel (W) and the weight after the dry process (W₀). For that, samples weight was recorded in regular time periods, until the weight stabilized (fully swollen sample). For this measurement a Saitouris BL 1,205 (d = 0.1 mg) scale was used and the buffer from the sample surface was removed before weighing. The degree of swelling (Q) was calculated based on Eq. 1:

$$Q(\%) = \frac{W - W_0}{W_0} \times 100 \quad (1)$$

Loading of hydrogels with collagenase. Hydrogels samples (30 ± 5 mg) were immersed in 5 mL of a collagenase solution (10 mg/mL in buffer solution, pH 7.5) and maintained under constant rotation at a speed of 100 rpm for 24 h at 25 °C. At the end a sample of the solution was taken until

equilibrium and the concentration and activity of the collagenase was determined using a synthetic substrate FALGPA (described above). The tests were performed in triplicate.

In Vitro release of collagenase from HPMC/cyclodextrin hydrogels and PCL nanofibers. A continuous spectrophotometric assay for *Clostridium histolyticum* collagenase was used to analyse the *in vitro* release of collagenase from the hydrogels and PCL nanofibers. The test is based on the hydrolysis of 2-furanacryloyl-L-leucylglycyl-L-prolyl-L-alanine (FALGPA) that is hydrolysed by collagenase in appropriate buffer solution. Collagenase cleaves FALGPA at the leucyl-glycyl bond, and the rate of hydrolysis is monitored in terms of a decrease in absorbance at 345 nm as described by Van Wart & Steinbrink, 1981 [25].

Dry samples of PCL nanofibers or HPMC/cyclodextrin hydrogels loaded with collagenase (30 ± 5 mg) were immersed in 5 mL of acid and alkaline synthetic sweat solutions (pH 5.5 and 8) at 25 °C under constant rotation at 100 rpm. At predetermined timepoints (0, 5, 10, 15, 30, 45, 60, 120 min and 24 hours), samples were taken (100 µL) from release medium and an equal volume of the fresh synthetic sweat solution was added to maintain the volume constant. These samples were used to prepare the reaction mixtures for the enzymatic assay of collagenase. The mixtures were prepared in triplicate directly in a 96-well clear plate for immediate analysis on a multi-mode microplate reader (EZ Reader 200, BioTek). The angular coefficient of the linear region of the obtained curves (absorbance vs. time) was adopted to determine the enzyme activity (A) in U mL⁻¹ using Eq. 2:

$$A = \frac{[(-\text{SLOPE}_{\text{SAMPLE}}) - (-\text{SLOPE}_{\text{BKG}})] \times V}{V_0 \times 0.53} \quad (2)$$

Where, V is the total reaction volume in milliliters, V₀ is the volume of the enzyme aliquot in milliliters, and 0.53 is the millimolar extinction coefficient of FALGPA (as informed by the manufacturer in the Sigma product's technical bulletin)

In vitro Diffusion Studies. The *in vitro* diffusion of collagenase from PCL polymeric nanofibers was evaluated using Franz diffusion cells (V-Series Stirrers for Franz Cells; PermeGear, USA). Polysulfone membranes (Tuffryn® membrane filter with 0.45 µm pore size, PALL Life Sciences, USA) with a diffusion area of 0.64 cm² were fixed between the donor and the receptor compartment. 5 mL of a micellar-buffered medium (sodium lauryl sulfate 16mM, pH 5.5) was added to the receptor compartment. The membrane was acclimatized at 32 ± 2 °C for 0.5 h prior to the addition of the fibre mat samples. The receptor liquid was maintained at a constant temperature of 37 °C using a circulating water bath and was continually stirred for 24 h. The PCL nanofibers samples (100 mg) were fixed on the top of the acclimatized polysulfone membranes and were incubated. After 24 hours, the collagenase concentration in the receptor compartment was determined using the DC (detergent compatible) protein assay kit (Bio-Rad, Portugal). Each sample was assayed in triplicate.

Cytotoxic studies. The *in vitro* cytotoxicity of the PCL polymeric nanofibers to human BJ-5ta cell line (normal human skin fibroblasts immortalized by overexpression of telomerase) was assessed using the MTS metabolic viability assay. The methodology was adapted from ISO guidance on the biological evaluation of medical devices (ISO 10993-5:2009).

BJ-5ta cells were maintained according to ATCC recommendations (four parts of Dulbecco's modified Eagle's medium (DMEM) containing 4 mmol/l-glutamine, 4.5 g/L sodium bicarbonate and 1 part of Medium 199, supplemented with 10%(v/v) of fetal bovine serum (FBS), 1% (v/v) of penicillin/streptomycin solution and 10 µg/ml hygromycin B). The cells were maintained under routine conditions (37 °C, 5% CO₂, and 95% RH), while the culture medium was replaced every 2 days.

Extracts from disinfected fibres were obtained by incubation with cell culture medium (100 mg of fibre per mL of medium) at 37 °C for 24 hours. BJ-5ta cells were seeded at a density of 1×10^4 cells/well on 96-well tissue culture polystyrene (TCPS) plates (TPP, Trasadingen, Switzerland) the day before experiments and then were exposed to the conditioned medium and further incubated. A negative control (culture medium) and a positive control (30% DMSO) were also included. At the end of 24 and 48 h of contact, metabolic viability was assessed using the MTS assay. The reduction

in MTS by viable cells was measured with a 96-well plate reader at 490 nm in a microplate reader SpectraMax Plus (Molecular Devices). Samples were assayed in triplicate and the results were expressed as percentage of cell viability from negative control.

Results and Discussion

Characterization of PCL nanofibers and hydrogels. PCL nanofibers were produced by electrospinning (Fig. 1), using different conditions in terms of syringe diameter, magnetic field, distance from slider to fixed manifold, syringe outlet flow rate, syringe cleaning time, and fixed manifold deposition time (results not shown). To the best operation conditions, different concentrations of PCL (15%, 16%, 20% and 30% (w/v)) were analysed with and without collagenase incorporated. After inspection of the fibres we found that the more suitable polymer concentration was 20%. Samples with PCL concentrations below 20% showed a lack of uniformity while for concentrations higher than 20% the samples exhibited excessive density. These results are in agreement with those presented by Matos, 2016 [26], according to which the PCL samples produced from a solution with a concentration of 20% presented better morphological and structural characteristics, while samples of 30% PCL were very dense, with a film appearance and with little opacity.

The morphological properties of nanofibers were observed by SEM. The nanofibers presented a smooth morphology, without the formation of beads and with a high surface area, with medium diameters ranging between 195 – 200 nm and 110 – 137 nm, for the fibres with and without collagenase respectively (Fig. 1).

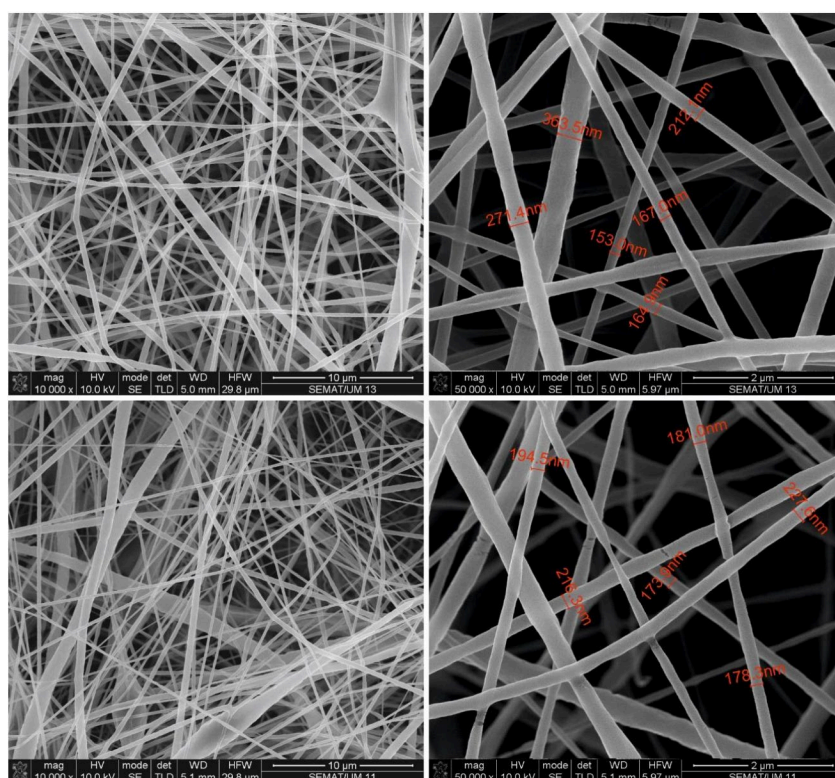


Figure1. SEM micrographs of PCL nanofibers without (top) and with collagenase (down)

Santos, et al., 2011 observed a relationship between the increase in polymer concentration and the increase in the mean diameter of PCL nanofibers [27]. The same effect could be observed in the developed PCL samples. It was also noted that the incorporation of collagenase resulted in more uniform and homogeneous nanofibers. The addition of another material to the polymer solution could result in the reduction of granules in the nanofibers. This process had already been described by Martins, et al. [28].

The hydrogels based on HPMC and cyclodextrins (β CD or HP β CD) presented a surface covered by a highly porous matrix, ideal for the capture and release of compounds (results not shown).

The properties of the PCL nanofibers and hydrogels were evaluated in terms of chemical structure, swelling behaviour, release profiles and biological activity. The Attenuated total reflectance-Fourier transform infrared spectroscopy (ATR-FTIR) spectra of PCL nanofibers showed the dominant absorption peaks at 2943, 2862 and 1724 cm^{-1} which were respectively attributed to the $\nu(\text{CH}_2)$ and $\nu(\text{C}=\text{O})$ in the ester groups [29-31]. The PCL nanofibers with collagenase exhibited in general the same peaks as those found in the PCL nanofibers. However, the absorption peaks related to stretching of the amide groups (1238 cm^{-1}) illustrated the successful entrapment of collagenase onto the nanofiber (Fig. 2). Hydrogels spectra had similar profiles and it was possible to confirm the formation of intermolecular boundaries between the monomers as described by Pinho et al. 2019 [13]. Moreover, it can be noted the characteristic bands of the enzyme, e.g., peaks corresponding to amide I at 1640 cm^{-1} (mainly from $\text{C}=\text{O}$ stretching) and amide III at 1238 cm^{-1} (Fig. 2). The stronger intensity peaks observed on the spectra of the HPMC-HP β CD hydrogels are: 3383 cm^{-1} (O – H stretch), 2866 cm^{-1} (C – H asymmetric vibrational stretch), 1647 cm^{-1} (hydrogen interactions), 1076 and 1026 cm^{-1} (ether bond). The spectrum of HPMC- β CD show bands at 3387 cm^{-1} (O – H stretch), 2866 cm^{-1} (C – H asymmetric vibrational stretch), 1647 cm^{-1} (hydrogen interactions) and 1056 cm^{-1} (carbonyl elongation) and 1033 cm^{-1} (C – O – C asymmetric vibrational stretch) [13,32].

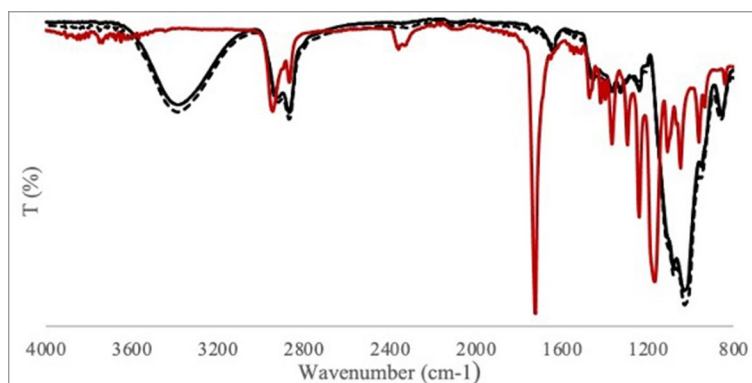


Figure 2. FTIR ATR of nanocarriers: Hydrogels with collagenase (HPMC- β CD cyclodextrin (black solid) and HPMC HP β CD (black) and PCL nanofibers with collagenase (red)

Thermal characterization. Fig. 3 shows the DSC thermograms of the produced PCL nanofibers. The area under the DSC endothermic peak was estimated as the heat of fusion value whereas the maximum point of the endothermic melting and decomposition peaks are recorded as the melting and decomposition temperatures. The crystallization of PCL nanofibers was considered via the heat of fusion. The thermograms of PCL nanofibers have two endothermic regions: (1) the first is at 63 °C, which is associated with the melting of the polymer and (2) the second is at 416 °C and is associated with the carbonization of the polymer [33-34], with enthalpy changes between 87 and 98 J / g. In the case of samples without collagenase n, the endothermic peaks are between 61.93 °C and 63.91 °C with enthalpies varying between 97.17 and 99.48 J / g. Thermograms for PCL samples with collagenase also show endothermic peaks between 59.44 °C and 64.81 °C and changes in enthalpy between 87.31 and 94.90 J / g. The enthalpy values are slightly lower for PCL nanofibers with collagenase, which means a slight decrease in the crystallinity of the nanofibers due to the incorporation of the enzyme in the polymeric structure. These results agree with those presented by Martins et al., who found similar behavior for PCL fibers with trypsin. [28] In general, it was noted that the addition of collagenase did not significantly modified the thermal decomposition pathway of PCL nanofibers.

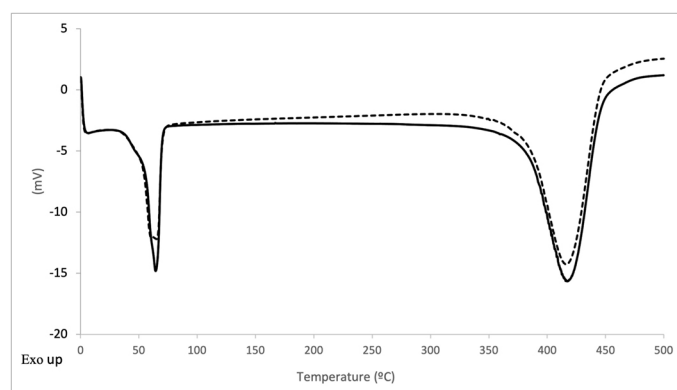


Figure 3. DSC spectra of PCL nanofibers: with collagenase (solid line) and without collagenase(dashed line)

The individual components of the hydrogel DSC thermal characterization were analysed. HPMC thermogram presents endothermic peaks at 64 °C ($\Delta H=137$ J/g), due to the water evaporation and at 328 °C ($\Delta H = 49$ J/g) and 361 °C ($\Delta H = 61$ J/g) as consequence of the thermal decomposition of cellulose. HP β CD thermogram showed a large endothermic peak at 80 °C due to water evaporation and another at 350 °C as consequence of their thermal decomposition. Similar transitions were noted at 100 °C and 350 °C for β CD [11]. The DSC of HPMC- β CD and HPMC-HP β CD hydrogels showed similar profiles with two endothermic regions: (1) 70-105 °C and 65-105 °C (water evaporation) and (2) 305 °C and 310 °C (thermal decomposition,) respectively [13,34].

The TGA results of PCL nanofibers (Table 1) reveals the existence of a single degradation stage between 290 and 420 °C, with a maximal degradation at 382 °C, with a mass loss of 92.10 %. Regarding the TGA curve in PCL fibers with collagenase, a single degradation region is visible in the temperature range 326 - 448 °C. For these samples a maximum degradation was observed at 411°C, with a mass loss of 96.55%. These results are in line with those presented in literature [29, 35].

Table 1. Values related to the initial (Ti) and final (Tf) temperatures associated with the degradation of the samples, as well as the percentage of loss of mass (TG) and the maximum temperature of degradation (DTG) of the hydrogels and components

Samples	Ti [°C]	Tf [°C]	TG [%]	DTG [°C]
HPMC	280	390	88.10	350
HP β CD	280	380	83.10	343
β CD	315	450	91.90	406
HPMC-HP β CD hydrogel with collagenase	315	450	91.90	406
HPMC- β CD hydrogel with collagenase	311	453	90.02	405
PCL	290	420	92.10	382
PCL Nanofibers with collagenase	318	444	95.39	404

The thermal profile of the nanofiber samples shows that there is a very slight decrease in the DTG, as well as in the Ti and Tf of the nanofibers with collagenase compared to those without collagenase. These results are in agreement with the results observed in the DSC.

The TGA curves of the individual components (HPMC and β CD) were described and analyzed by Monreal-Pérez, 2018 [36]. In the TGA curve for HPMC, a single degradation region is visible in the temperature range 280-400 °C and the maximum degradation was observed at 350 °C, with a mass loss of 88.10% in relation to the degradation of hydroxypropyl groups, constituents of HPMC [37, 38]. In the TGA curve of the β CD, there are two distinct stages of mass loss: (1) the first starts between 40-50 °C and ends at approximately 100 °C, and is attributed to the loss of water due to the dehydration of the OH groups that make up the β CD; and (2) the second starts at 320 °C and ends at 400 °C and corresponds to the thermal decomposition of DC. For this, the degradation is maximum at 340 °C with a percentage loss of mass of 81.00%. Regarding the HPMC- β CD hydrogel, a degradation stage between 311 and 453 °C is identified. The maximum degradation temperature for this sample occurred at 405 °C with a mass loss of 90.02% [36].

HPMC and HP β CD were also described and analyzed by Pinho et al. 2019 [13]. In the HP β CD curve, two distinct degradation phases are observed: (1) the first stage is visible between 50 and 100 °C, and corresponds to the loss of water by dehydrating of the HP β CD hydroxide groups; (2) the second stage presents a higher level of degradation of the CD located between the temperatures of 280 - 380 °C. There is maximum degradation at 343 °C with a loss of mass of 83.10% [39]. The TGA curve of the two synthesized hydrogels shows a very similar behavior. The TGA curve of the HPMC-HP β CD shows a decomposition region between 315 and 450 °C. The temperature where the decomposition was highest is 406 °C with a mass loss of 91.90%.

Table 1 shows the values referring to the initial (Ti) and final (Tf) temperatures related to the degradation of the samples, the percentage of loss of mass (TG) and the maximum temperature of degradation (DTG). The hydrogels have an average loss of mass of 90.96% in relation to the individual compounds, which reveal only 84.10% of mass loss. The thermal profile of the samples further demonstrates that the hydrogels degrade at a considerably higher temperature, which indicates greater thermal stability due to the chemical bonds that their constituents establish with each other [39].

Swelling. The swelling capacity of the developed nanofibers and hydrogels were analyzed under different environmental pH conditions. The HPMC-HP β CD hydrogel showed the highest water retention in all studied conditions. The results exhibited that the incorporation of collagenase into the hydrogels by adsorption resulted in an enzyme retention around 85.37% for the HPMC-HP β CD hydrogel and 84.15% for the HPMC- β CD hydrogel. The mechanism associated with the collagenase incorporation/retention in the hydrogel network was not exclusive of the hydrogels' swelling capacity. As reported before, HPMC-HP β CD hydrogel network has a large pore size to the presence of cyclodextrin hydroxypropyl group, increasing the flexibility of the network and the water molecule accommodation. [11]

In vitro Release of Collagenase. The release of collagenase from the polymeric structures was evaluated. The cumulative amount of activity detected over time, showed a slow release of the enzyme at the end of 24 hours. At this time point, only 0.5 % of the retained enzyme was released from the HPMC-HP β CD hydrogel, while for the HPMC- β CD hydrogel this value was around 0.18 %. Given that the HPMC-HP β CD hydrogel swelling was higher than the HPMC- β CD swelling, and due to the contribution of hydroxypropyl groups in the pore opening of the hydrogel, these results seem to be justified. In the case of the PCL nanofibers, only a residual amount of the enzyme (0.05 %) was released from the nanofibers at the end of 24h.

In vitro diffusion behaviour of collagenase. Besides analyzing the in vitro release of collagenase from the PCL nanofibers, it is important to assess whether the polymeric nanofibers maintain the collagenase diffusion capacity. For this purpose, Franz cell models using artificial polysulfone membranes have been described for the evaluation of the performance of products for topical administration [40]. Despite these artificial membranes do not completely mimic the complex diffusion phenomena observed *in vivo*; their stiffness, mechanical resistance, thermal stability, and oxidation resistance makes them widely used in diffusion studies [41] and their use is recognized by regulatory entities such as the FDA [42].

Regardless of the PCL polymeric nanofibers samples, only a residual amount of collagenase ($\sim 0.14\%$) was detected in the micellar-buffered medium present in the receptor compartment after 24h of diffusion/permeation (Fig. 4). Yet, the low amount of collagenase measured was slightly higher than the observed for the *in vitro* release studies (0.05%). These differences observed between the two assays might be related with the properties of the buffers used.

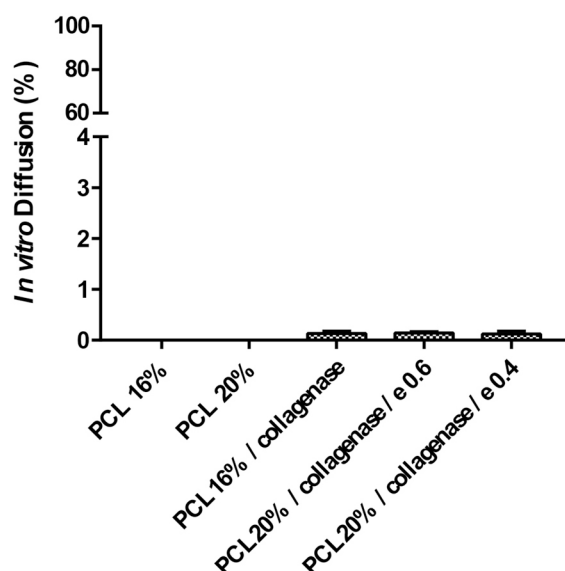


Figure 4. In vitro diffusion of collagenase after 24 hours of incubation with polycaprolactone (PCL) nanofibers obtained with two concentrations of polymer (16 and 20%), with two feed rate (0.4 and 0.6 L/h) and with and without collagenase. Results are the mean \pm SD of duplicates of three independent experiments.

***In vitro* evaluation of PCL nanofibers potential cytotoxicity.** During the development of a new product to be in direct contact with skin, is critical to evaluate the biocompatibility of the product and its constituents. Neither the substrate materials nor its degradation by-products should demonstrate cytotoxicity towards human cells [43]. To evaluate the cytotoxicity induced by constituents and leachables from the PCL nanofibers, BJ-5ta fibroblasts were exposed to undiluted culture medium pre-conditioned by contact with the polymeric nanofibers, with and without collagenase, for 24 hours. The cellular metabolic activity of human fibroblasts was evaluated by the MTS assay after 24 and 48 hours of contact.

The results of the indirect contact study after fibroblasts incubation for 24 and 48 hours with materials' leachables, depicted in Fig. 5, showed no signs of cell toxicity for any of the tested PCL nanofibers. The lowest viability was observed for the PCL nanofibers obtained with 16% of polymer and without collagenase after 24 hours of contact ($96.16 \pm 2.56\%$), which still was not significantly different from the life control.

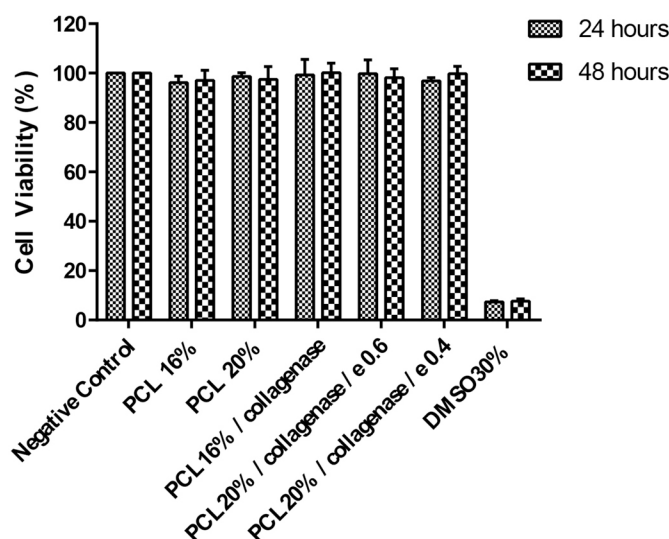


Figure 5. Relative viability of BJ-5ta human fibroblasts (evaluated by the MTS assay) after 24 and 48 h incubation with polycaprolactone (PCL) nanofibers obtained with two concentrations of polymer (16 and 20%), with two feed rate (0.4 and 0.6 L/h) and with and without collagenase. Cells incubated with culture medium only were used as life control (negative control) and cells incubated with 30% DMSO as death control. Data were calculated in relation to the life control (100%). Results are the mean \pm SD of triplicates of three independent experiments.

Conclusions

HPMC and CD hydrogels and PCL nanofibers with and without collagenase were developed and physicochemically characterized by FTIR, DSC, TGA and SEM techniques. The HPMC-HP β CD hydrogel showed the highest water retention for all the studied conditions, while the HPMC- β CD hydrogel was the least sensitive to pH variations. However, both hydrogels presented similar enzymatic adsorption.

Both polymeric structures presented higher retention of active collagenase and low enzyme release and diffusion. Particularly for the PCL nanofibers, the release of the enzyme in aqueous medium during 24h at room temperature was negligible, confirming that the collagenase is tightly bound within the polymeric matrix.

The PCL nanofibers also showed excellent biocompatibility as no cytotoxic effect was observed when human skin fibroblasts were exposed to nanofibers' degradation products and leachables.

The HPMC/CD hydrogels and PCL nanofibers developed in this work as systems for the entrapment and slow release of collagenase show great potential to be used as dressings in the management of wounds.

Acknowledgment

This study was supported by Programme - COMPETE and by national funds through FCT – Foundation for Science and Technology within the scope of the project POCI-01-0145-FEDER-007136; UIDB/ 04469/2020 unit, programme – COMPETE (POCI-01-0145-FEDER-007136) and BioTecNorte operation (NORTE-01-0145-FEDER- 000004) funded by the European Regional Development Fund under the scope of Norte 2020 - Programa Operacional Regional do Norte.

References

- [1] M.A. Woodruff, D.W. Hutmacher, The return of a forgotten polymer - Polycaprolactone in the 21st century, *Progress in Polymer Science (Oxford)*, 35 (10) (2010) 1217–1256.
- [2] D. Mondal, M. Griffith, S. Venkatraman, Polycaprolactone-based biomaterials for tissue engineering and drug delivery: Current scenario and challenges. *International Journal of Polymeric Materials and Polymeric Biomaterials*, 65 (5) (2016) 255-265.
- [3] J. Middleton, A. Tipton, Synthetic biodegradable polymers as orthopedic devices. *Biomaterials*, 21(23) (2000) 2335-2346.
- [4] N. Khan,. Applications of electrospun nanofibers in the biomedical field. *Undergraduate Researchers at Guelph*, 5 (2012) 63-73.
- [5] X. Zong, H. Bien , C.Y. Chung, L. Yin, D. Fang, B.S. Hsiao,B. Chu,E. Entcheva, Electrospun fine-textured scaffolds for heart tissue constructs. *Biomaterials*, 26 (26) (2005) 5330–5338.
- [6] M. Nasrollahzadeh, Z. Issaabadi, M. Sajjadi, S. M. Sajadi, M. Atarod, Types of Nanostructures., in: M. Nasrollahzadeh, Z. Issaabadi, M. Sajjadi, S. M. Sajadi, M. Atarod (Eds.), *Interface Science and Technology*. Elsevier, New York, 2019, pp. 29-80.
- [7] Y. Sun, S. Cheng, W. Lu, Y. Wang, P. Zhang, and Q. Yao, Electrospun fibers and their application in drug controlled release, biological dressings, tissue repair, and enzyme immobilization and enzyme immobilization, *RSC Advances* 9 (44) (2019) 25712-25729.
- [8] D. Balogh-Weiser, C. Németh, F. Ender, B. Gyarmati, A. Szilágyi and L. Poppe (September 12th 2018). Electrospun Nanofibers for Entrapment of Biomolecules, *Electrospinning Method Used to Create Functional Nanocomposites Films*, Tomasz Tański, Pawel Jarka and Wiktor Matysiak, IntechOpen, DOI: 10.5772/intechopen.76068. Available from: <https://www.intechopen.com/chapters/60633>
- [9] E. Pinho, M. Henriques, G. Soares, Cyclodextrin/cellulose hydrogel with gallic acid to prevent wound infection. *Cellulose*, 21(6) (2014) 4519-4530.
- [10] Pinho, M. Henriques, G. Soares, Cyclodextrins as encapsulation agents for plant bioactive compounds. *Carbohydr. Polym.* 101 (30) (2014) 121-135.
- [11] Pinho, M. Henriques, G. Soares, Caffeic acid loading wound dressing: physicochemical and biological characterization. *Ther. Deliv.* 5 (2014) 1063–1075.
- [12] E. Pinho, R. Calhelha, I. Ferreira, G. Soares, Cotton-hydrogel composite for improved wound healing: Antimicrobial activity and anti-inflammatory evaluation-Part 2. *Polymers for Advanced Technologies*, 30 (4) (2018) 863-871.
- [13] E. Pinho, S. Machado, G. Soares, Smart Hydrogel for the pH-Selective Drug Delivery of Antimicrobial Compounds. *Macromol. Symp.* 385 (1) (2019) 1800182.
- [14] H. Alipour, A. Raz, S. Zakeri, N. Djadid, Therapeutic applications of collagenase (metalloproteases): A review. *Asian Pacific Journal of Tropical Biomedicine*, 6 (11) (2016) 975- 981.
- [15] J. Boateng, O. Catanzano, Advanced Therapeutic Dressings for Effective Wound Healing. *Novembro. J Pharm Sci.* 104 (11) (2015) 3653-3680.
- [16] C. Martin, W.L. Low, M.C. Amin, I. Radecka, P. Raj, K. Kenward, Current trends in the development of wound dressings, biomaterials and devices. *Pharm Pat Anal.* 2(3) (2013) 341-59.

- [17] M. Shao, Z. Hussain, H.E. Thu, S. Khan, M. Matas, V. Silkstone, H.L. Qin, S.N.A. Bukhari, Emerging Trends in Therapeutic Algorithm of Chronic Wound Healers: Recent Advances in Drug Delivery Systems, Concepts-to-Clinical Application and Future Prospects. *Crit Rev Ther Drug Carrier Syst.* 34(5) (2017) 387-452.
- [18] A. Oliveira, S. Simões, A. Ascenso, C. P. Reis, Therapeutic advances in wound healing, *Journal of Dermatological Treatment*, *J Dermatolog Treat.* 26 (2020) 1-21.
- [19] D. Chouhan, N. Dey, N. Bhardwaj, B.B. Mandal, Emerging and innovative approaches for wound healing and skin regeneration: Current status and advances, *Biomaterials*, 216 (2019) 119267.
- [20] S. Domogatsky, Highly selective proteolytic enzymes preparation for debridement of necrotic tissue from burn wounds. S., 2010. [Online] Available at: Disponível em: <<http://www.crd.org/Events/bio2003-proteolityc-enzymes>> [Acedido em 28 8 2019].
- [21] H. Alipour, A. Raz, S. Zakeri, N. D. Djadid, Therapeutic applications of collagenase (metalloproteases): A review, *Asian Pacific Journal of Tropical Biomedicine*, 6 (11) (2016) 975-981.
- [22] G. Banerjee, A. Ray, Impact of microbial proteases on biotechnological industries. *Journal Biotechnology and Genetic Engineering Reviews*, 33 (2017) 119-143.
- [23] H. Hamdy, Extracellular collagenase from *Rhizoctonia solani*: Production, purification and characterization. *Indian Journal of Biotechnology*, 7 (2008) 333-340.
- [24] S. M. Daboor, S. M., Budge, A. E. Ghaly, S. Brooks, D. Dave, Extraction and Purification of Collagenase Enzymes: A Critical Review. *American Journal of Biochemistry and Biotechnology*, 6 (4) (2010) 239-263.
- [25] H. Van Wart, D. Steinbrink, A Continuous Spectrophotometric Assay for *Clostridium histolyticum* Collagenase. *Analytical Biochemistry*, 113 (1981) 356-365.
- [26] Matos (2016) Síntese e caracterização de nanofibras de policaprolactona com adição de progesterona utilizando o solvente ácido acético pelo método de eletrofiação, Universidade Federal de Minas Gerais, Brasil, 2016.
- [27] C. Santos, R. Bretas, M. Branciforti, T. Canova,, Preparação e Caracterização de Nanofibras de Nanocompósitos de Poliamida 6,6 e Argila Montmorilonita. *Polímeros*, Volume 21 (5) (2011) 398-408.
- [28] A. Martins, R. Reis, N. Neves, Electrospinning: processing technique for tissue engineering scaffolding. *International Materials Reviews*, 53 (5) (2008) 257-274.
- [29] C. Chen, F. Liu, X. Zhang, Z. Zhao, S. Liu, Fabrication, characterization and adsorption properties of cucurbit[7]uril- functionalized polycaprolactone electrospun nanofibrous membranes. *Beilstein J. Org. Chem*, 15 (2019) 992–999.
- [30] S. Saudi, S. Bhattarai, U. Adhikari, S. Khanal, J. Sankar, S. Aravamudhan, N. Bhattarai, Nanonet-nano fiber electrospun mesh of PCL-chitosan for controlled and extended release of diclofenac sodium. *Nanoscale* 2 (46) (2020) 23556-23569.
- [31] E. Ramírez-Cedillo, W. Ortega-Lara, M. R. Rocha-Pizaña, J. A. Gutierrez-Urbe, A. Elías-Zúñiga, C. A. Rodríguez., Electrospun Polycaprolactone Fibrous Membranes Containing Ag, TiO₂ and Na₂Ti₆O₁₃ Particles for Potential Use in Bone Regeneration. *Membranes (Basel)*, 9 (1) (2019) 2-14.
- [32] R. Sun, X. Sun, J. Tomkinson, Hemicelluloses and Their Derivatives. Em: In: Gatenholm P, Tenkanen M (Eds) *Hemicelluloses: Science and Technology*. Washington, DC: American Chemical Society, 2003, pp 2-22.

- [33] V- Speranza, A. Sorrentino, F. De Santis, R. Pantani, Characterization of the Polycaprolactone Melt Crystallization: Complementary Optical Microscopy, DSC, and AFM Studies. *The Scientific World Journal*, (2014) 1-9.
- [34] M. Raoov, S. Mohamad, M. Abas, Synthesis and Characterization of β -Cyclodextrin Functionalized Ionic Liquid Polymer as a Macroporous Material for the Removal of Phenols and As(V). *Int J Mol Sci*, 15 (2013) 100–119.
- [35] B. Massoumi, M. Ramezani, M. Jaymand, M. Ahmadinejad, Multi-walled carbon nanotubes-g-[poly(ethylene glycol)-b-poly(ϵ -caprolactone)]: synthesis, characterization, and properties. *Journal of Polymer Research*, 22 (2015) 1-10.
- [36] P. Monreal-Pérez, J.R. Isasi, J.González-Benito, D. Olmos, G. González-Gaitano, Cyclodextrin-Grafted TiO₂ Nanoparticles: Synthesis, Complexation Capacity, and Dispersion in Polymeric Matrices. *Nanomaterials*, 8 (9) (2018) 642.
- [37] S. Kwon, B. Kong, S. Park, Physicochemical properties of pH-sensitive hydrogels based on hydroxyethyl cellulose-hyaluronic acid and for applications as transdermal delivery systems for skin lesions. *Eur. J. Pharm. Biopharm. Off. J. Arbeitsgemeinschaft Pharm. Verfahrenstechnik EV*, 92 (2015)146–154.
- [38] L.O. Porfírio, A.A. Costa, R.R. Conceição, T.O. Matos, E.D. Almeida, V.H. Sarmento, A. Araújo, R.S. Nunes, A.M. Lira, Compatibility study of hydroxypropylmethylcellulose films containing zidovudine and lamivudine using thermal analysis and infrared spectroscopy. *J. Therm. Anal. Calorim*, 120 (2014) 817–828.
- [39] N. Malik, M. Ahmad, M. Minhas, Cross-linked β -cyclodextrin and carboxymethyl cellulose hydrogels for controlled drug delivery of acyclovir. (2017) *PloS One* 12. e0172727.
- [40] A.R. Caldas, J. Catita, R. Machado, A. Ribeiro, F. Cerqueira, B. Horta, R. Medeiros, M. Lúcio, C.M. Lopes, Omega-3- and resveratrol-loaded lipid nanosystems for potential use as topical formulations in autoimmune, inflammatory, and cancerous skin diseases, *Pharmaceutics*, 13 (2021) 1202.
- [41] N. Dhiman, R. Awasthi, B. Sharma, H. Kharkwal, G.T. Kulkarni, Lipid nanoparticles as carriers for bioactive delivery. *Front. Chem.*, 9 (2021) 580118.
- [42] M. Schmid, C. Wölk, J. Giselsbrecht, K.L.A. Chan, R.D. Harvey, A combined FTIR and DSC study on the bilayer-stabilizing effect of electrostatic interactions in ion paired lipids *Colloids Surf. B Biointerfaces*, 169 (2018) 298–304.
- [43] A. Ribeiro, V. Volkov, M.B. Oliveira, J. Padrão, J.F. Mano, A.C. Gomes, A. Cavaco-Paulo, BSA/HSA ratio modulates the properties of Ca²⁺-induced cold gelation scaffolds. *International Journal of Biological Macromolecules*, 89 (2016) 535–544.

Preliminary Studies on Antimicrobial Properties for Nanofiber Air Filters

Fabio A P Scacchetti^{1,a*}, Daniela S. de Almeida^{2,b}, Roberta Santos^{3,c},
Marcos H. S. Santana^{1,d}, Fabrício M. Bezerra^{1,e}, Mônica Lopes Aguiar^{2,f}
and Leila D. Martins^{3,g}

¹Federal University of Technology - Paraná, Rua Marcílio Dias, 635, Apucarana, PR, 86812-460, Brazil

²Federal University of São Carlos, Rod. Washington Luiz, km 235, SP 310, São Carlos, SP, 13565-905, Brazil

³Federal University of Technology - Parana, Av. dos Pioneiros, 3131, Londrina, PR, 86036-370, Brazil

^afabioscacchetti@utfpr.edu.br, ^bdannyutfpr@gmail.com, ^crobertasantos@alunos.utfpr.edu.br,

^dmarcossantana@alunos.utfpr.edu.br, ^efabriciom@utfpr.edu.br, ^fmlaguiar@ufscar.br,

^gleilamartins@utfpr.edu.br

*corresponding author

Keywords: nanofibers; electrospinning process; antimicrobial activity.

Abstract. The purpose of this study was to investigate a potential antimicrobial activity of biodegradable cellulose acetate (CA)/ cetylpyridinium bromide (CPB) nanofiber filters produced by electrospinning technique. Samples of these nanofibers were produced over a nonwoven substrate, using a polymeric solution in the electrospinning process. Wettability tests were performed by measuring the contact angle of droplets of water deposited on their surface. The evaluation of the antibacterial properties of the nanofibers was performed for *Escherichia coli* using quantitative methods. Regarding the contact angle measurement, it presented about 62.93°, showing that this material is hydrophilic. The antibacterial test results showed that the use of the surfactant provides antibacterial properties to the CA/CPB nanofibers, presenting 99.99% reduction for *Escherichia coli*. Further studies are necessary, however, these preliminary results showed that, based on these features, the nanofibers could be applied as a filter media for indoor air conditioning systems, mainly due to their biocidal properties.

Introduction

With the current scenario caused by the coronavirus-2019 pandemic, studies in search of materials with biocidal properties have increased rapidly. The control of indoor air quality with air filters and the employment in shades of high filtration efficiencies has been the new demand for the use of antibacterial additives. The electrospinning technique is quite versatile, because it is possible to produce polymeric nanofibers that are known to be excellent air filter media. Besides, different types of additives can be used to functionalize them.

As previously mentioned, when using the electrospinning technique to produce polymeric nanofibers, it is possible to use additives to attribute certain characteristics to the material produced. The main examples of additives are the incorporation of nanoparticles to improve the adsorption characteristics of the fiber [1,2], or also to assign biocidal action [3,4]. Surfactants are another group of additives commonly used in electrospinning to reduce the viscosity of the polymeric solution and, consequently, reduce the formation of beads [5].

When added to polymeric solutions, cationic surfactants showed that, even in small amounts, the ability to prevent the formation of beads [6,7]. On the other hand, using a nonionic surfactant no longer completely prevents the formation of granules. Therefore, it was hypothesized that charged surfactants increase the solution conductivity and net charge density, causing an increase in the instability, producing more uniform fibers [8]. In addition, compounds such as cetyltrimethylammonium bromide (CTAB), cetylpyridinium bromide (CPB), cetylpyridinium

chloride (CPC), and benzethonium chloride (benzethonium chloride – BztCl) are part of the group of quaternary ammonia surfactants. They are known to attribute antibacterial, antimycotic, antiprotozoal or antiproliferative action to various materials and are widely used as disinfectant agents in skin and oral care products [9–12]. Some of them are even used to attribute this characteristic to nanofibers obtained by electrospinning [11,12].

So, the main aim of this study is to investigate the antibacterial properties of cellulose acetate (CA) nanofibers and cationic surfactant cetylpyridinium bromide (CPB), which have been previously tested for use in air filters.

Materials and Methods

Nanofibers were made using cellulose acetate (CA) as polymer (MW 30 kDa) and cetylpyridinium bromide (CPB), both from Sigma-Aldrich, USA. Solvents of the polymeric solution were made by mixing with acetic acid (Synth, São Paulo, Brazil) and distilled water (3:1 v/v).

Preparation of CA/CPB nanofibers. Nanofibers were made by the electrospinning technique (home-made apparatus). Polymeric solutions of CA at 21 % (w/v) and CPB at 0.5 % (w/v) were used. The electrospinning conditions used were: 18 kV voltage and 10 cm distance from the collector, as described by Almeida et al., [13] and patent application [14]. Besides, a nonwoven textile was used as a substrate, in order to improve the breathability of the materials that were developed.

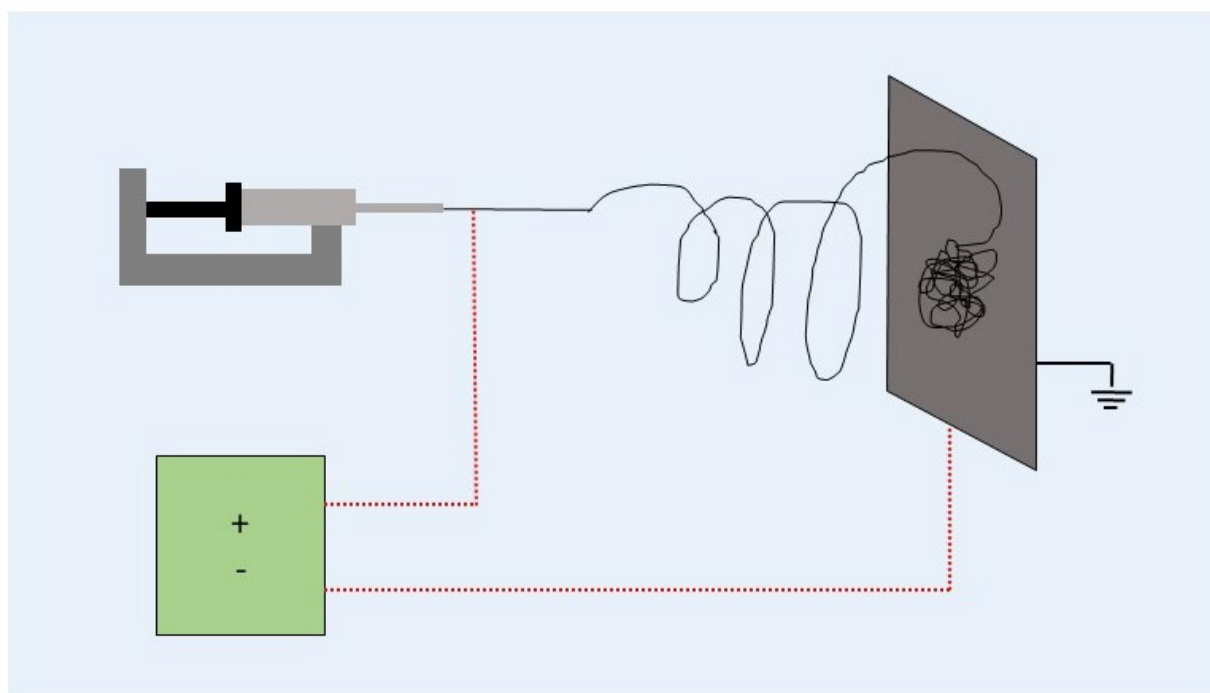


Figure 1. Scheme of Electrospinning (home-made) apparatus.

Nanofiber characterization. The CA/CPB nanofibers were characterized for mechanical and thermal tests, morphology analysis, water-solubility, Fourier transform infrared spectroscopy and texture data. This step is well described in de Almeida et al., [13]. In addition, water wettability tests were carried out on the nanofibers, which were evaluated by the contact angle test of a drop with its surface. The sample was glued with double-sided tape on a metallic exterior at a controlled temperature of 25 °C. A drop of distilled water of 9 μ L was deposited under the surface of the nanofiber, and the cell phone camera obtained its image. Thus, from the photograph of the drop on the surface of the nanofiber, it was possible to measure its contact angle using Image J© software.

Antibacterial Evaluation. The antibacterial activity of the samples for *Escherichia coli* ATCC® 25922™ (gram-negative) was tested according to a quantitative test method ASTM E2149-13:2020

(adapted), using selective/differential media by agar diffusion methods (MacConkey Agar). The growth of a fresh shake culture of bacterium in sterile Tryptic Soy Broth (TSB) at 35 ± 2 °C for 24 hours was necessary to perform the test. The culture was diluted in sterile solution ($0.3 \text{ mM KH}_2\text{PO}_4$) with a concentration ranging from 1.5×10^8 to 3.0×10^8 CFU (Colony Forming Units) mL^{-1} .

The samples (sterilized by ultraviolet radiation) were placed in a flask and inoculated with the suspension of microorganisms (50 mL) at a stroke for 1h and immediately serially diluted and plated. As a positive control, was used a flask with 50 mL of buffer and the same CFU mL^{-1} , but serial dilutions and standard plate count techniques from the “inoculum only” occurred at “0” time.

The results were expressed as average colony forming units CFU mL^{-1} , in accordance with the test method. The percentage of reduction and the log bacterial reduction of the microbial growth was determined according to the following equation:

$$\text{Log}_{10} \text{ bacterial reduction} = \text{Log}_{10}(\text{B}) - \text{Log}_{10}(\text{A}). \quad (1)$$

Where A indicates the number of CFU mL^{-1} for the flask containing the electrospun sample after the contact time and B represents the number of CFU mL^{-1} for the “inoculum only”.

Results and Discussion

Nanofiber characterization. As already mentioned, the complete characterization of the nanofibers was previously performed by Almeida et al. [13]. The solubility test showed that, in 10 days immersed in water, the specimen lost only 5% of its mass, indicating that it is quite resistant to water [13]. Additionally, a wettability test was performed by measuring the contact angle with the water, as shown in Figure 2.

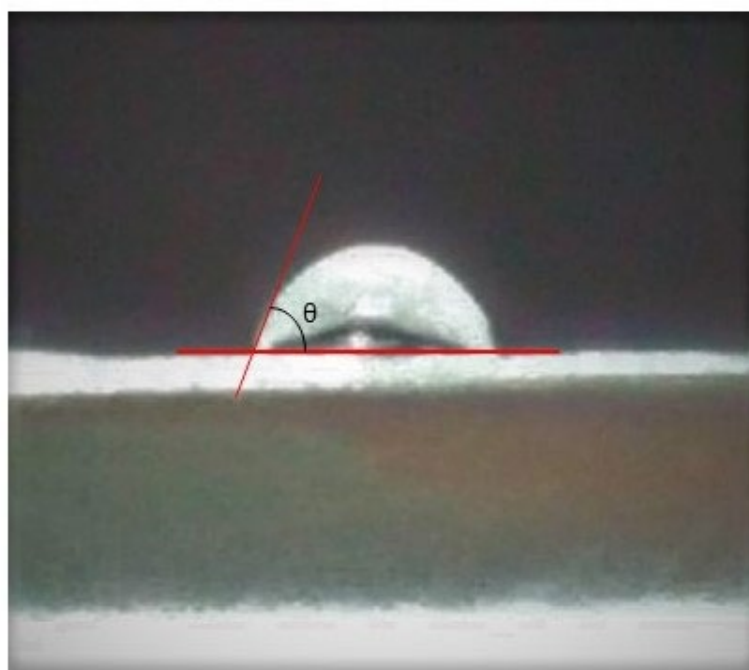


Figure 2. Contact angle formed between the nanofiber and the water drop.

The contact angle (θ) obtained was 62.93° . It is important to mention that contact angles less than 90° indicate that the solid is hydrophilic, and angles greater than 90° indicate a hydrophobic material. In comparison, 0° and 180° indicate complete wettability and complete non-wettability, respectively [15].

Antibacterial Evaluation. The antimicrobial activity of both the nanofiber and the positive control was evaluated. Table 1 presents the reduction percentage and log bacterial reduction of the microbial growth according to the equations described. It is known that CPB is a quaternary ammonium salt and has biocidal activity [16]. It is probable that CPB molecules tend to create cationic layers in the structure of the nonwoven and disrupt the normal functions of the membrane of the cell [17].

Table 1. Results of antibacterial activity for nanofibers (*E. coli*).

N. of bacterium (CFL/mL) at "0" time	N. of bacterium (CFL/mL) at "1h" contact	Log Reduction	Reduction (%)
0.41×10^5	0	4.61 ± 0.46	99.99%

The electrospun nanofiber presented a reduction of microorganisms in comparison with the positive control, which showed an expected growth of microorganisms. The results indicate the presence of CPB in the structure.

The possible mechanism of action occurs by adsorption on negatively charged bacterial cell surfaces, diffusion, attachment to the cytoplasmic membrane, release of electrolytes and, after that, release of nucleic materials and cell death [10]. Figure 3 shows the results of the antimicrobial activity.

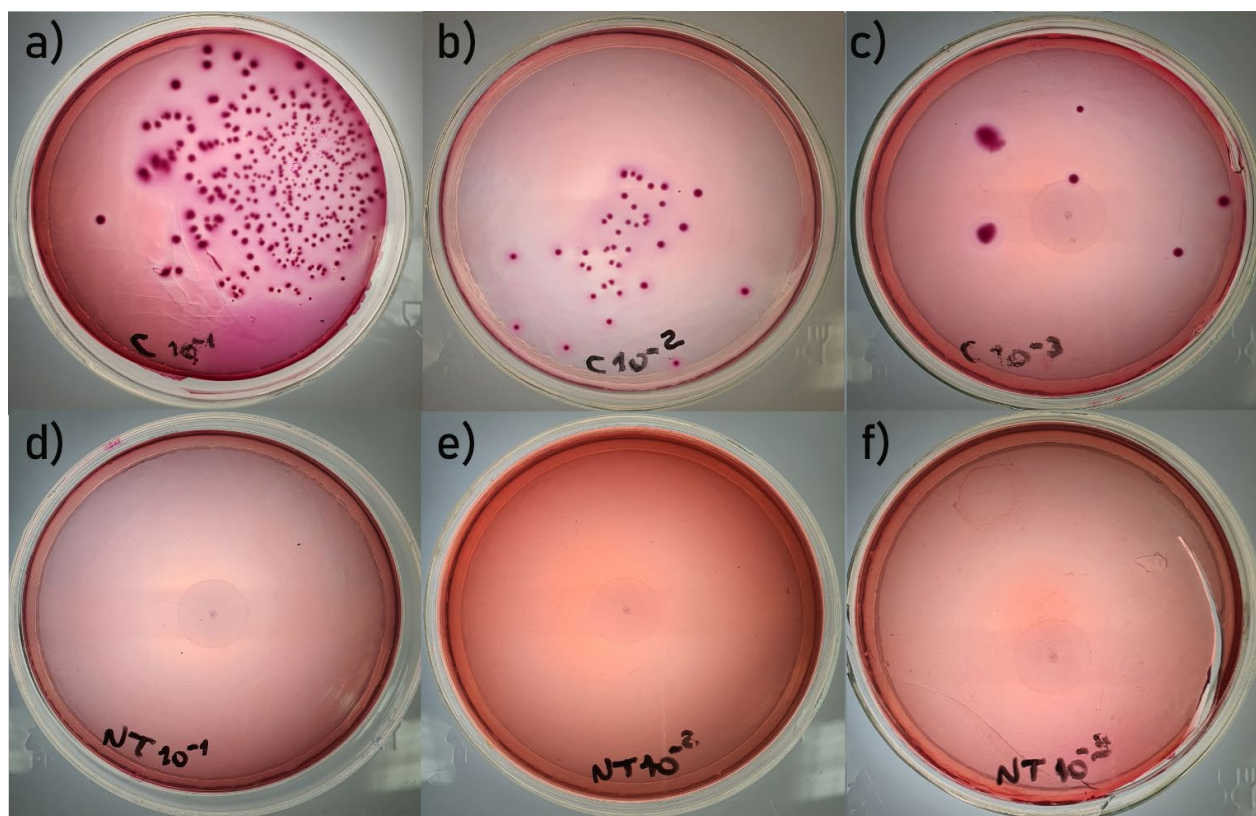


Figure 3. Antimicrobial activity of the sample, performed by serial dilution methods, for *E. coli*. Control serial dilution a) 10^{-1} , b) 10^{-2} , c) 10^{-3} . Sample serial dilution d) 10^{-1} , e) 10^{-2} , f) 10^{-3} .

Conclusion

In this preliminary study, the results were very promising. The biocidal properties of the CA/CPB electrospun nanofibers were investigated and this material presented biocidal characteristics and reduced 99.99% of *E. coli* presence in comparison with the positive control, which showed an

expected growth of microorganisms. The results obtained here demonstrate that the CA/CPB nanofibers obtained through the electrospinning technique can be a good alternative in the coating of commercial air filters. These nanofibers are eco-friendly, biodegradable, and a material of natural origin. In addition to their biocidal action, they can be useful to contain bioaerosols present in the air, especially in indoor environments. Therefore, this nanofiber can be used for this purpose with high efficiency.

Acknowledgment

The authors would like to acknowledge the National Council for Scientific and Technological Development (Conselho Nacional de Desenvolvimento Científico e Tecnológico - CNPq), process No. 306862/2018-2. This study was financed in part by the PROREC/PROPPG – UTFPR - Transferência tecnológica para o combate ao Covid-19 of UTFPR – Campus Londrina, UTFPR 02/2020 - DIREC-AP Apoio a projetos para o combate ao covid-19 of UTFPR – Campus Apucarana and UTFPR – DIRPPG-AP/DIRGE-AP 02/2021 Apoio à participação em eventos técnico-científicos.

References

- [1] U. Habiba, A.M. Afifi, A. Salleh, e B.C. Ang, “Chitosan/(polyvinyl alcohol)/zeolite electrospun composite nanofibrous membrane for adsorption of Cr^{6+} , Fe^{3+} and Ni^{2+} ”, *J. Hazard. Mater.*, vol. 322, p. 182–194, jan. 2017, doi: 10.1016/j.jhazmat.2016.06.028.
- [2] Q. Wang, D.-G. Yu, L.-L. Zhang, X.-K. Liu, Y.-C. Deng, e M. Zhao, “Electrospun hypromellose-based hydrophilic composites for rapid dissolution of poorly water-soluble drug”, *Carbohydr. Polym.*, vol. 174, p. 617–625, out. 2017, doi: 10.1016/j.carbpol.2017.06.075.
- [3] S. Kendouli *et al.*, “Modification of cellulose acetate nanofibers with PVP/Ag addition”, *Mater. Sci. Semicond. Process.*, vol. 28, p. 13–19, dez. 2014, doi: 10.1016/j.mssp.2014.03.010.
- [4] A. Ali *et al.*, “Antibacterial electrospun nanomat from nigella/PVA system embedded with silver”, *J. Text. Inst.*, vol. 112, n° 4, p. 561–567, abr. 2021, doi: 10.1080/00405000.2020.1768015.
- [5] C. Kriegel, K.M. Kit, D. J. McClements, e J. Weiss, “Influence of Surfactant Type and Concentration on Electrospinning of Chitosan–Poly(Ethylene Oxide) Blend Nanofibers”, *Food Biophys.*, vol. 4, n° 3, p. 213–228, set. 2009, doi: 10.1007/s11483-009-9119-6.
- [6] W. Zuo, M. Zhu, W. Yang, H. Yu, Y. Chen, e Y. Zhang, “Experimental study on relationship between jet instability and formation of beaded fibers during electrospinning”, *Polym. Eng. Sci.*, vol. 45, n° 5, p. 704–709, 2005, doi: 10.1002/pen.20304.
- [7] T. Lin, H. Wang, H. Wang, e X. Wang, “The charge effect of cationic surfactants on the elimination of fibre beads in the electrospinning of polystyrene”, *Nanotechnology*, vol. 15, n° 9, p. 1375–1381, ago. 2004, doi: 10.1088/0957-4484/15/9/044.
- [8] Q.P. Pham, U. Sharma, e A. G. Mikos, “Electrospinning of polymeric nanofibers for tissue engineering applications: a review”, *Tissue Eng.*, vol. 12, n° 5, p. 1197–1211, maio 2006, doi: 10.1089/ten.2006.12.1197.
- [9] S. Mohanan *et al.*, “Role of Quaternary Ammonium Compounds and ATMP on Biocidal Effect and Corrosion Inhibition of Mild Steel and Copper”, *Corros. Rev.*, vol. 23, n° 4-5-6, p. 425–444, dez. 2005, doi: 10.1515/CORRREV.2005.23.4-5-6.425.
- [10] M. Lukáč *et al.*, “Synthesis, self-aggregation and biological properties of alkylphosphocholine and alkylphosphohomocholine derivatives of cetyltrimethylammonium bromide, cetylpyridinium bromide, benzalkonium bromide (C16) and benzethonium chloride”, *Eur. J. Med. Chem.*, vol. 66, p. 46–55, ago. 2013, doi: 10.1016/j.ejmech.2013.05.033.

-
- [11] J.G. Lundin, P.N. Coneski, P.A. Fulmer, e J.H. Wynne, “Relationship between surface concentration of amphiphilic quaternary ammonium biocides in electrospun polymer fibers and biocidal activity”, *React. Funct. Polym.*, vol.77, p. 39-46, abr. 2014, doi:10.1016/j.reactfunctpolym.2014.02.004.
- [12] L.J. del Valle *et al.*, “Electrospun biodegradable polymers loaded with bactericide agents”, *AIMS Mol. Sci.*, vol. 3, nº 1, p. 52–87, 2016, doi: 10.3934/molsci.2016.1.52.
- [13] D. S. de Almeida *et al.*, “Development and characterization of electrospun cellulose acetate nanofibers modified by cationic surfactant”, *Polym. Test.*, vol. 81, p. 106206, jan. 2020, doi: 10.1016/j.polymertesting.2019.106206.
- [14] D. S. Almeida, E. H. Duarte, L. D. Martins, E. C. Muniz, e M. L. Gimenes, “Processo de Obtenção de Nanofibras a Base de Acetato de Celulose com Surfactante por Eletrofiação e Nanofibras Obtidas”, BR102019019386
- [15] B. J. Ryan e K. M. Poduska, “Roughness effects on contact angle measurements”, *Am. J. Phys.*, vol. 76, nº 11, p. 1074–1077, nov. 2008, doi: 10.1119/1.2952446.
- [16] S. Buffet-Bataillon, P. Tattevin, M. Bonnaure-Mallet, e A. Jolivet-Gougeon, “Emergence of resistance to antibacterial agents: the role of quaternary ammonium compounds—a critical review”, *Int. J. Antimicrob. Agents*, vol. 39, nº 5, p. 381–389, maio 2012, doi: 10.1016/j.ijantimicag.2012.01.011.
- [17] N.A.N.N. Malek e N.I. Ramli, “Characterization and antibacterial activity of cetylpyridinium bromide (CPB) immobilized on kaolinite with different CPB loadings”, *Appl. Clay Sci.*, vol. 109–110, p. 8–14, jun. 2015, doi: 10.1016/j.clay.2015.03.007.

Antibacterial Nonwoven with Propolis for Use in Surgical Masks

Nebahat Aral^{1,a*} and İdil Yiğit^{2,b}

¹Yeditepe University, Department of Materials Science and Nanotechnology Engineering,
Engineering Faculty, Istanbul, Turkey

²Bursa Uludag University, Department of Textile Engineering, Engineering Faculty, Bursa, Turkey

^anebahat.aral@yeditepe.edu.tr, ^bidilyigit@uludag.edu.tr

Keywords: Antibacterial, propolis, surgical mask, nonwoven

Abstract. Microorganisms that accumulate on the surfaces of protective mask surfaces increase the risk of the spread of infection. In the study, it is aimed to form antibacterial polypropylene (PP) nonwovens treated by propolis extracts for surgical masks. Propolis, which is biocompatible and known to be effective against many bacteria and other microorganisms, was preferred instead of metal compounds with toxic potential. In the study, two types of propolis extracts were used which were prepared in different solvent environment (50 % ethyl alcohol – 50 % pure water; 47 % propylene glycol – 53 % pure water). The amounts of phenolic compounds in the solutions obtained differently depending on the solvent and HPLC-DAD analysis of the extracts was performed. After the application of propolis extracts to PP nonwovens by immersion method, the change in their antibacterial activities were measured. According to the results, PP nonwovens with propolis show antibacterial activity against *Enterococcus hirae*, *Escherichia coli*, and *Staphylococcus aureus*. On the other hand, it was observed that the samples that were washed after drying (at 120 °C) lost their antibacterial effect. It is thought that the reason for this situation is that the phenolic compounds in propolis extracts, which are not fully adhered to PP fibers and soluble in water, are removed from the surface by washing.

Introduction

As stated by scientific studies, the use of protective masks reduces the rate of spread of respiratory diseases [1]. The facial masks are expected to act as a barrier and prevent the reaching of aerosols, which can carry viruses and bacteria, to the respiratory tract [2,3]. Microorganisms that can cause infection accumulation on the mask surfaces over time [3]. Therefore, prolonged and repeated use of masks can increase the risk of infection and it has been determined that masks with increased humidity during use lead to the formation of harmful microorganisms [4].

Although healthcare professionals need to change their masks periodically, it is known that they do not have the opportunity to change their masks as often as necessary during emergencies [2]. Viruses, bacteria, and other microorganisms accumulated on the outer surface of the mask during using and this accumulation pose a risk for infection [2, 5-8]. This situation can cause microorganisms to move into the inner layers of the mask with the effect of breathing and increase the risk of harmful agents reaching the respiratory tract [2].

There are various studies in the literature about the investigation of antibacterial and antimicrobial properties of masks [2,9-11]. It is seen that nano-sized silver nitrate (AgNO₃) and titanium dioxide (TiO₂) particles are used for antimicrobial properties in these studies [2,9]. In this study, using propolis extracts which are also safe to consume as food product, are preferred rather than the additives mentioned in the literature have possibility to cause toxic effects.

Propolis is a natural bee product that is used by bees for repairing and defending their habitats and creating protection against infections. Propolis contains various chemical compounds such as polyphenols (flavonoids, phenolic acid, and their esters), terpenoids, steroids, amino acids, and

inorganic compounds [12-13]. Although the composition of raw propolis varies according to its source, it generally consists of 50 % resin, 30 % wax, 10 % essential and aromatic oils, 5 % pollen, 5 % other organic compounds, and mineral substances [14-15]. Raw propolis can be extracted using solvents such as water, ethyl alcohol, and propylene glycol, on the other hand, the chemical compounds in propolis can dissolve at different rates in the extraction medium. Therefore, the chemical contents of propolis obtained from different extraction methods also differ [16-17] and should be determined and standardized by high performance liquid chromatography (HPLC-DAD) method.

There are many scientific studies on the effect of propolis on various bacteria, fungi, viruses, and other microorganisms. The studies examining the effect of propolis on selected target organisms are presented in Table 1 [18]. In recent years, propolis has also started to be used in studies about the development of antimicrobial materials [19-21]. There are also various studies about the usage of propolis in textile and fiber technology [22-28]. It is often emphasized that propolis provides antibacterial properties to fibers and fabrics and can be used for wound healing in textile and fiber applications [25,26,28-30]. Although there are many studies on obtaining propolis-doped fibre by using electrospinning and melt spinning methods using different polymers [24,25]. Also in studies [23, 28], propolis is used in finishing processes of textiles where the cotton and Tencel fabrics for use as wound dressing and bandage. The antibacterial tests were carried out according to AATTC standards after propolis finishing, and it was stated that textile materials containing propolis showed antibacterial effects [22,23,26-28].

Table 1: Examining studies on the effect of propolis on microorganisms and viruses [18].

Microorganism	Reference	Microorganism	Reference
Bacterial Effects		Fungicidal Effects	
<i>Bacillus larvas</i>	(Meresta and Meresta, 1988)	<i>Candida albicans</i>	(Petrie et al., 1988)
<i>B. subtilis and others</i>	(Meresta and Meresta, 1988)	<i>Aspergillus niger</i>	(Petrie et al., 1988)
<i>Staphylococcus types</i>	(Chernyak, 1973)	<i>Botrytis cinerea</i>	(La Torre et al., 1990)
<i>Staphylococcus aureus</i>	(Dimov et al., 1991)	<i>Ascospaera apis</i>	(Hofmann et al., 1989)
<i>Streptococcus</i>	(Rojas et al., 1990)	<i>Plasmopara viticola</i>	(Hofmann et al., 1989)
<i>Streptomyces</i>	(Simu'th et al., 1986)	Antiviral Effects	
<i>Saccharomyces cerevisiae</i>	(Petrie et al., 1988)	<i>Herpes</i>	(Popescu et al., 1985)
<i>Escherichia coli</i>	(Simu'th et al., 1986)	<i>Patates virus</i>	(Fahmy and Omar, 1989)
<i>Salmonella ve Shigella</i>	(Ghisalberti, 1979)	<i>Influenza</i>	(Serkedjieva, 1992)
<i>Salmonella</i>	(Okonenko, 1988)	Nematodisidal Effects	
<i>Klebsiella pneumoniae</i>	(Dimov vd., 1991)	<i>Ascaris suum</i>	(Bankova et al., 1989)

As mentioned before, bacteria accumulation and growth on surgical masks poses a health risk, and this study mainly focuses on the evaluation of antibacterial properties of liquid extracts obtained by different extraction methods of raw propolis by applying them to spunbond polypropylene (PP) nonwoven. In the literature review, no study was found in which the effect of different extracted propolis was observed by applying them to PP nonwoven that is suitable for being a layer of a surgical mask. Therefore, in this study, the phenolic compounds in propolis extracts obtained by two different extraction methods were analyzed and the efficacy of propolis applied fabrics against *Enterococcus hirae* (ATCC 10541), *Escherichia coli* (ATCC 11229), *Pseudomonas aeruginosa* (ATCC 15442) and *Staphylococcus aureus* (ATCC 6538) intended to be compared.

Materials and Methods

In the study, raw propolis from Sivas region of Turkey was used. Firstly, the extraction processes of the raw propolis were carried out, and the details of the process parameters were presented in Table 2. As it is given, the solvent of Extract 1 (E-1) is a mixture of ethyl alcohol and pure water, whereas propylene glycol and pure water were used as the solvent in Extract 2 (E-2). Propolis extracts were prepared with a 1:4 raw propolis: solvent ratio by weight. Thereafter, the HPLC-DAD analyses of the E-1 and E-2 after the extraction process were carried out and the phenolic compounds in extracts were determined and given in Table 3.

Table 2. The preparation parameters of the propolis extracts.

	Solvent	Duration	Temp.
E-1	50 % ethyl alcohol 50 % pure water	24 hours	40°C
E-2	47 % propylene glycol 53 % pure water	24 hours	30°C

Table 3. HPLC-DAD analysis results of propolies extracts, E-1 and E-2.

	E-1	E-2
	Amounts [$\mu\text{g/ml}$]	Amounts [$\mu\text{g/ml}$]
Gallic acid	6.83	18.9
Epigallocatechin Acid	51.5	39.1
Routine Trihydrate	13.2	-
Caffeic Acid	345.2	429.4
trans-Ferulic Acid	87.3	313.7
trans-Isopherulic Acid	254.5	276
3-4-Dimethoxycinnamic Acid	142.1	195.6
Quercetin	119.7	171
trans-Cinamic Acid	15.4	27.8
Naringenin	206.3	186
Apigenin	167.8	130.5
Kaempferol	133.8	119.4
Chrysin	401.8	359.8
Pinocembrin	1273.2	512.6
Galangin	924.4	587.2
Caffeic Acid Phenethyl Ester	2331.0	1157.5
Trans-chalcone	245.3	251.6

In the second stage, the analysed propolis extracts were applied on nonwovens which are used in the outer surface of surgical masks. PP spunbond nonwoven with a weight of 25 g/m² were used. In [28], Tencel fabrics were treated with propolis extract without using any additional chemicals for environmentally friendly production and it was stated that the application was successful to achieve antibacterial activity in fabrics. Based on this study, the applicability of propolis extracts on PP nonwoven surfaces has been tried without using additional binders or auxiliary chemicals as it is an environmentally friendly method.

The nonwoven samples were immersed into propolis extracts and were squeezed under 2.5 bar pressure in the foulard machine. For PP samples, drying was made at 120 °C for 2 minutes after processing to fix propolis on nonwoven surface. In order to observe the adhesion behaviour of propolis extracts after washing, a group of samples was washed and dried. In this second method, the samples were washed in 50 °C deionized and dried in the oven at 50 °C for 10 minutes. The extract E-1 was used in the immersion process of PN1 and PN1-W samples, and the extract E-2 was used for PN2 and PN2-W, and PN1-W and PN2-W are the samples that were washed and dried (Figure 1).

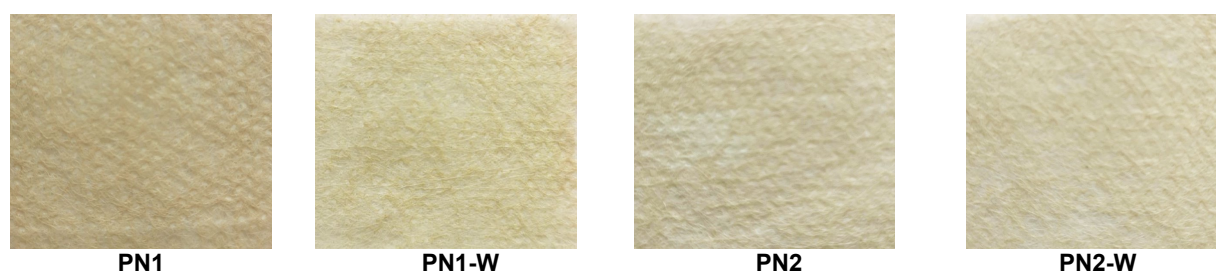


Figure 1. The image of the samples unwashed (PN1 and PN2) and washed samples (PN1-W and PN2-W) with propolis.

Antibacterial testing of the fabrics was carried out according to AATCC TM147-2011 standard [31]. As the control group, *Ofloxacin* 5 µg standard disc and untreated nonwoven were cut and placed in the same size. After placing the sample fabrics, *Enterococcus hirae* (ATCC 10541), *Escherichia coli* (ATCC 11229), *Pseudomonas aeruginosa* (ATCC 15442) and *Staphylococcus aureus* (ATCC 6538) plates were incubated at 35 ± 1 °C in a normal atmosphere for 16-20 hours. Mueller-Hinton Agar was used for *Enterococcus hirae* (AATCC 10541), *Staphylococcus aureus* (AATCC 6538), *Escherichia coli* (AATCC 11229), *Pseudomonas aeruginosa* (AATCC 15442). 25 mm diameter cut sample fabrics were placed on the agar so that the contact was tight and even. The diameter of the inhibition zone was measured and the efficiency of the sample fabrics was determined in mm.

Results and Discussion

The results obtained from the antibacterial activity test are given in Table 4 where PN1 indicated the samples prepared with E-1 extract and PN2 was prepared with E-2 extract (Table 2). PN1-W and PN2-W are samples that were washed and dried after fixation at 120°C. In agar diffusion test method, during the incubation period, if a clear inhibition zone of 5-10 mm is formed, it can be stated that the antibacterial agents leaching into the agar are effective against bacteria [32]. In the qualitative evaluation with the control sample, samples that form a clear zone of inhibition can be considered effective, and samples that do not form a clear zone of inhibition can be described as ineffective against bacteria. When the results were evaluated, it was seen that PN1 and PN2 samples have antibacterial effects against *S. aureus*, *E.coli* and *E. hirae* bacteria which showed 29-35 mm inhibition zone whereas the inhibition zone of control sample Ofloxacin is between 41-45 mm. Considering the effectiveness of the control sample, it can be said that nonwovens containing propolis show a slightly strong antibacterial activity.

Table 4. The results of antibacterial efficacy (Inhibition zone diameter in mm).

	<i>S. aureus</i> ATCC 6538	<i>P. aureginosa</i> ATCC 15442	<i>E. coli</i> ATCC 11229	<i>E. hirae</i> ATCC 10541
PN1	35 mm	-	33 mm	30 mm
PN1-W	-	-	-	-
PN2	33 mm	-	32 mm	29 mm
PN2-W	-	-	-	-
Untreated nonwoven	-	-	-	-
Ofloxacin	45 mm	40 mm	42 mm	41 mm

In the study, although the efficiencies of the samples formed with two different extracts were similar, it was observed that the PN1 sample formed relatively larger inhibition zones in the medium of *S. aereus*, *E.coli*, and *E. hirae* bacteria. As it is given in Table 3, the amount of phenolic compounds in propolis extracts were different due to the different extraction conditions (Table 2). Although the immersion of nonwovens was made under the same conditions, it is thought that the antibacterial activities of the fabrics are slightly different depending on the extraction conditions. As it may be seen, E-1 and E-2 contain many different phenolic compounds (Table 3) and the amount of caffeic acid phenethyl ester, pinocembrin, and galangin in the content of E-1 extract is significantly higher compared to E-2. Caffeic acid phenethyl ester, pinocembrin, and galangin are phenolic compounds

with known antibacterial activities, and it is thought that their higher amounts in E-1 may have been effective in forming a wider inhibition zone of PN1 samples (Table 4). On the other hand, since there are many compounds in the structure of propolis, more detailed analyzes are needed to evaluate the effect of the content.

As it is stated in the literature, the antibacterial activity of propolis is more pronounced on gram-positive bacteria (*Streptococcus*, *Staphylococcus aureus*, etc.) compared to gram-negative bacteria (*Salmonella*, *Escherichia coli*, *Pseudomonas*, etc.) [28,33]. In consistent with the literature, nonwovens with propolis showed a slightly higher inhibition zone against *Staphylococcus aureus*, which is gram-positive bacteria. On the other hand, it was determined that antibacterial activity could not be observed against *P. aures* bacteria.

Surgical masks are generally disposable, not washed and reused products. On the other hand, it was aimed to observe the propolis-applied nonwovens can maintain their effectiveness as a result of contact with water. By considering the washing effect, the results showed both PN1-W and PN2-W samples lost their antibacterial effects with washing (Table 4), where no clear inhibition zone was observed in agar diffusion test. Therefore, it is seen that PN1-W and PN2-W are ineffective against all bacteria used in tests such as the untreated nonwoven sample. In addition, it was observed that the samples still retained their yellowish color originating from propolis (Figure 1) whereas they lost their antibacterial properties. Consequently, it is thought that water soluble phenolic compounds, which play an important role in antibacterial activity, are removed from the surface after the washing process. Since chemical analysis was not performed on nonwovens, it was not determined that which phenolic compounds are removed from the surface of samples or remain in the nonwoven structure.

Conclusion

In the study, it has been observed that antibacterial activity can be achieved as a result of the application of propolis extracts to spunbond PP nonwoven surfaces without using an additional binder or chemical. It has been successfully achieved that PP nonwovens show antibacterial effect against *S. aureus*, *E. coli*, and *E. hirae* bacteria by using two different propolis extracts.

HPLC-DAD analyses showed that raw propolis extracted in ethyl alcohol-pure water and propylene glycol-pure water media have different phenolic components which lead to difference in antibacterial activity. Therefore, while it may be possible to obtain antibacterial textiles by using propolis extracts, it should be considered that extraction conditions of propolis change the chemical content in the extract. In future studies, the effects on textile surfaces can be observed in more detail by changing the parameters of the extraction media.

Although the study shows that spunbond nonwoven surfaces obtain antibacterial property, the organic solvent content of propolis extracts can reduce the static electricity of PP surfaces. Thus, the filtration effectiveness of nonwovens, which planned to be used in surgical masks, may be adversely affected. In this study, spunbond nonwovens, which are suitable for the outer layer of surgical masks, were used to form an antibacterial barrier. It can be assumed that filtration properties of the surgical masks can be preserved by using spunbond nonwoven with propolis, only in the outermost layer, and meltblown structures in the inner layers. In future studies, it can be observed how propolis extracts affect the filtration properties, and in addition, new methods can be developed on how to apply propolis without preventing the effect of static electricity. In addition, it has been observed that the materials that can be obtained by applying propolis to PP surfaces lose their antibacterial properties with contact with water. Therefore, in future studies, it would be appropriate to evaluate how long the propolis on nonwoven can maintain its effectiveness under respiratory humidity conditions.

Acknowledgment

We would also like to thank Umay Herbal for their support in propolis supply and technical assistance. Also, we would like to thank Yeditepe University, Faculty of Pharmacy for their support in conducting antibacterial activity tests.

References

- [1] Greenhalgh, T., Schmid, M. B., Czypionka, T., Bassler, D., & Gruer, L. Face masks for the public during the covid-19 crisis. *Bmj*, (2020) 369.
- [2] Li, Y., Leung, P., Yao, L., Song, Q. W., & Newton, E. Antimicrobial effect of surgical masks coated with nanoparticles. *Journal of Hospital Infection*, 62(1) (2006), 58-63.
- [3] Paxton, N. C., Forrestal, D. P., Desselle, M., Kirrane, M., Sullivan, C., Powell, S. K., & Woodruff, M. A. N95 Respiratory Masks for COVID-19: A Review of the Literature to Inform Local Responses to Global Shortages, (2020) Pre-Print.
- [4] Majchrzycka, K.; Okrasa, M.; Skóra, J.; Gutarowska, B. Evaluation of the survivability of microorganisms deposited on filtering respiratory protective devices under varying conditions of humidity. *Int. J. Environ. Res. Public Health*, 13, (2016), 98.
- [5] Lai, A.C.K.; Poon, C.K.M.; Cheung, A.C.T. Effectiveness of facemasks to reduce exposure hazard for airborne infections among general populations. *JRC Soc. Interface* 9, (2012), 938–948.
- [6] Makison Booth, C.; Clayton, M.; Crook, B.; Gawn, J.M. Effectiveness of surgical masks against influenza bioaerosol. *J. Hosp. Infect.*, 84, (2013) 22–26.
- [7] Sublett, J.L. Effectiveness of air filters and air cleaners in allergic respiratory diseases: A review of the recent literature. *Curr. Allergy Asthma Rep.* 11, (2011) 395–402.
- [8] Van Doremalen, N., Bushmaker, T., Morris, D. H., Holbrook, M. G., Gamble, A., Williamson, B. N., ... & Lloyd-Smith, J. O. Aerosol and surface stability of SARS-CoV-2 as compared with SARS-CoV-1. *New England Journal of Medicine*, 382(16), (2020) 1564-1567.
- [9] Aloufy, A. K., & El-Messiry, M. A. M. Nano-silver embeded nanofibrous face-mask for infection control. In *The 2013 World Congress on Advances in Nano, Biomechanics, Robotics and Energy Research (ANBRE13)*, Seoul, August (2013), 25-28.
- [10] Demir, B., Cerkez, I., Worley, S. D., Broughton, R. M., & Huang, T. S. N-halamine-modified antimicrobial polypropylene nonwoven fabrics for use against airborne bacteria. *ACS Applied Materials & Interfaces*, 7(3), (2015), 1752-1757.
- [11] Quan, F. S., Rubino, I., Lee, S. H., Koch, B., & Choi, H. J. Universal and reusable virus deactivation system for respiratory protection. *Scientific reports*, 7(1), (2017), 1-10.
- [12] Bankova, V. S., Popov, S. S., & Marekov, N. L. A study on flavonoids of propolis. *Journal of Natural Products*, 46(4), (1983), 471-474.
- [13] Moreno, M., Isla, M. I., Sampietro, A. R., & Vattuone, M. A. Comparison of the free radical-scavenging activity of propolis from several regions of Argentina. *Journal of ethnopharmacology*, 71(1-2), (2000), 109-114.
- [14] Sforcin, J. M. Propolis and the immune system: a review. *Journal of ethnopharmacology*, 113(1), (2007), 1-14.
- [15] Coneac, G., Gafițanu, E., Hădărugă, D. I., Hădărugă, N. G., Pînzaru, I. A., Bandur, G., ... & Gruia, A. Flavonoid contents of propolis from the west side of Romania and correlation with the antioxidant activity. *Chemical Bulletin "Politehnica" University Timisoara*, 53(67), (2008), 56-60.
- [16] Khacha-Ananda, S., Tragoolpua, K., Chantawannakul, P., & Tragoolpua, Y. Antioxidant and anti-cancer cell proliferation activity of propolis extracts from two extraction methods. *Asian Pacific Journal of Cancer Prevention*, 14(11), (2013), 6991-6995.
- [17] Pobiega, K., Kraśniewska, K., Derewiaka, D., & Gniewosz, M. Comparison of the antimicrobial activity of propolis extracts obtained by means of various extraction methods. *Journal of food science and technology*, 56(12), (2019), 5386-5395.

-
- [18] Doğan, N., & Hayoğlu, İ. Propolis ve Kullanım Alanları. *Harran Tarım ve Gıda Bilimleri Dergisi*, 16(3), (2012), 39-48.
- [19] Bankova, V., Popova, M., & Trusheva, B. New emerging fields of application of propolis. *Macedonian Journal of Chemistry and Chemical Engineering*, 35(1), (2016), 1-11.
- [20] Woo, C. G., Kang, J. S., Kim, H. J., Kim, Y. J., & Han, B. Treatment of air filters using the antimicrobial natural products propolis and grapefruit seed extract for deactivation of bioaerosols. *Aerosol Science and Technology*, 49(8), (2015), 611-619.
- [21] Jaganathan, S. K., Mani, M. P., Prabhakaran, P., Supriyanto, E., & Ismail, A. F. Production, blood compatibility and cytotoxicity evaluation of a single stage non-woven multicomponent electrospun scaffold mixed with sesame oil, honey and propolis for skin tissue engineering. *International Journal of Polymer Analysis and Characterization*, 24(5), (2019), 457-474.
- [22] Abramiuc, D., Ciobanu, L., Muresan, R., Chiosac, M., & Muresan, A. Antibacterial finishing of cotton fabrics using biologically active natural compounds. *Fibers and Polymers*, 14(11), (2013), 1826-1833.
- [23] Sharaf, S., Higazy, A., & Hebeish, A. Propolis induced antibacterial activity and other technical properties of cotton textiles. *International Journal of Biological Macromolecules*, 59, (2013), 408-416.
- [24] Kim, J. I., Pant, H. R., Sim, H. J., Lee, K. M., & Kim, C. S. Electrospun propolis/polyurethane composite nanofibers for biomedical applications. *Materials Science and Engineering: C*, 44, (2014), 52-57.
- [25] Stojko, M., Włodarczyk, J., Karpeta-Jarząbek, P., Sobota, M., Kasperczyk, J., Dobrzyński, P., ... & Olczyk, P. A. Electrospun, biodegradable, non-woven dressing with addition of propolis for difficult-to-heal wound treatment. *Engineering of Biomaterials*, 21, (2018).
- [26] Moradkhannejhad, L., Abdouss, M., Nikfarjam, N., Mazinani, S., & Heydari, V. Electrospinning of zein/propolis nanofibers; antimicrobial properties and morphology investigation. *Journal of Materials Science: Materials in Medicine*, 29(11), (2018), 165.
- [27] Ramasamy, F. A review on the investigation of biologically active natural compounds on cotton fabrics as an antibacterial textile finishing. *International Research Journal of Science and Technology*, 1(1), (2019), 49-55.
- [28] Rogina-Car, B., Rogina, J., Govorčin Bajsić, E., & Budimir, A. Propolis–Eco-friendly natural antibacterial finish for nonwoven fabrics for medical application. *Journal of Industrial Textiles*, 49(8), (2020), 1100-1119.
- [29] Sharaf, S., & El-Naggar, M. E. Wound dressing properties of cationized cotton fabric treated with carrageenan/cyclodextrin hydrogel loaded with honey bee propolis extract. *International journal of biological macromolecules*, 133, (2019), 583-591.
- [30] Adomavičiūtė, E., Baltušnikaitė-Guzaitienė, J., Juškaitė, V., Žilius, M., Briedis, V., & Stanys, S. Formation and characterization of melt-spun polypropylene fibers with propolis for medical applications. *The Journal of The Textile Institute*, 109(2), (2018), 278-284.
- [31] AATCC TM147-2011 (2016e), Test Method for Antibacterial Activity of Textile Materials: Parallel Streak
- [32] Gao, Y., Bach Truong, Y., Zhu, Y., & Louis Kyratzis, I. (2014). Electrospun antibacterial nanofibers: Production, activity, and in vivo applications. *Journal of Applied Polymer Science*, 131(18).
- [33] Silici, S., & Kutluca, S. Chemical composition and antibacterial activity of propolis collected by three different races of honeybees in the same region. *Journal of ethnopharmacology*, 99(1), (2005), 69-73.

Electrospinning of Poly(Caprolactone)/Gelatin/Clindamycin Nanocomposites as an Antibacterial Wound Dressing

Parian Mohamadi^{1,a*}, Ghazaal Mirmoeini^{2,b}, Hajir Bahrami^{2,c},
Elham Mohsenzadeh^{3,4,d}, Cedric Cochrane^{1,e}, and Vladan Koncar^{1,f}

¹Ecole Nationale Supérieure des Arts et Industries Textiles (ENSAIT), GEMTEX, 2 allée Louise et Victor Champier, 59056 Roubaix Cedex 1, France

²Department of Textile Engineering, Amirkabir University of Technology, Tehran, Iran

³Junia, F-59000 Lille, France

⁴Univ. Lille, F-59000 Lille, France

^{a*}parian-sadat.mohamm@ensait.fr, ^bghazal.mirmoeini@aut.ac.ir, ^chajirb@aut.ac.ir,
^delham.mohsenzadeh@junia.com, ^ecedric.cochrane@ensait.fr, ^fVladan.koncar@ensait.fr

Keywords: Electrospinning, Gelatin, Polycaprolactone, Clindamycin, Wound dressing.

Abstract. These days, nanofibers are used in the medical sector, such as drug delivery and wound dressing structures, because of their excellent characteristics, high permeability, and important surface area. Natural and synthetic polymers may be electrospun in the form of a blend. Besides, the antibiotics such as linezolid, enrofloxacin, and vancomycin are used in wound dressing due to their antibacterial properties. In this research, for the first time the blend nanofibrous made of polycaprolactone (PCL) and gelatin (Gel) with a 25:75 ratio were produced by adding Clindamycin HCL as an antibiotic for wound dressing applications. Surface morphology, functional groups, and hydrophilicity of nanofibers were examined using Scanning electron microscope (SEM), Fourier-transform infrared spectroscopy (FT-IR), and contact angle measurement, respectively. In addition, the antibacterial properties of nanofibers were evaluated quantitatively. The drug release mechanism of samples was investigated which the best-fitted model was recognized Korsmeyer-Peppas model. SEM images of scaffolds demonstrated uniform and bead-free morphology that, with incorporating the 6% of the drug, the diameters of mats were decreased from 398 nm to 303 nm. Moreover, the samples showed proper hydrophilicity and antibacterial properties against a gram-positive (89%) and a gram-negative (98%) bacterium. Finally, the nanofibers are capable of releasing the clindamycin gradually for 6 days.

1. Introduction

Skin is one of the most critical organs of the human body, which protects the body against external damages. Every day, thousands of people are prone to skin injuries by physical, chemical, or thermal damages through disease, chronic wounds, ultraviolet radiation, burning, and trauma. The damaged and or degenerated skin needs to be replaced or repaired. So far, several treatments and techniques such as harvesting autografts, allografts, and transplants were employed. However, each of these has significant problems [1, 2].

The tissue engineering field was developed in the 1980s to restore, replace or regenerate injured tissues. Tissue engineering consists of three parameters: scaffold, cells, and growth-stimulating signals. Scaffolds should include specific properties for tissue engineering applications such as biocompatibility, biodegradability, porosity, and proper mechanical properties. Porosity helps oxygen exchange between wound and environment to reduce healing time. The scaffolds, which are made of polymeric biomaterials, must retain surface moisture, and have the ability of cell adhesion and cell proliferation. They should also be able to bind to surrounding tissues and be non-cytotoxic. [3-5].

The scaffolds can be produced from natural (gelatin) or synthetic (PCL) polymers to use their good qualities. Gelatin is a protein heteropolymer. It contains 18 different amino acids with peptide bonds. Gelatin is a natural polymer known as a biocompatible, biodegradable, non-toxic, adhesiveness and

water-soluble material that leads to a wide application in food, medical, pharmaceutical, and military applications. Polycaprolactam (Nylon6) as a crystalline synthetic polymer is produced by the condensation method. It is molten at 68-69 °C and possesses advantages such as stiffness, brightness, excellent elasticity, and high tensile strength. In addition, it has good mechanical properties, high biocompatibility, low hydrophilicity, low degradation rate, and high melting point and crystallinity [6-8].

High surface area, filter properties, permeability, flexibility in surface functionalizing, remarkable mechanical properties such as toughness and tensile strength than typical fibers, controllable production process, and high porosity are some nanofibers bold features that make them good case to apply in essential fields such as tissue engineering scaffolds, biomedical applications, drug delivery carriers and wound dressing. These are candidates for nanofiber applications because of their high ability for drug loading, wound dressings, and excellent encapsulation ability. Methods for producing the nanofibers are melt blowing and phase separation [9-12].

Among these methods, electrospinning is a facile, cost-effective, and versatile technique used for tissue engineering applications. Electrospinning is a common way to obtain continuous nanofiber from natural or synthetic polymers. Recently, the production of nanofiber from composite materials has been developed. Nanofiber electrospinning is a simple and efficient technology that is based on electrostatic forces, and the main idea started 60 years ago. After 1980 the nanotechnology and nanofiber electrospinning attracted much attention so that more than 200 types of polymer in the form of a solution or molten have been successfully used to make nanofibers. Concepts of electrical spinning from solution had been presented firstly by Cooley and Morton in 1902. The technical faultiness of the first electrospinning was satisfied, and Formhals developed the equipment in 1934. Physical and mechanical properties of nanofibers can be influenced by fiber morphology depends on solution parameters (concentration, molecular weight, viscosity, temperature, etc.), process factors (exerted voltage, feeding rate, nozzles distant, needle features, etc.), and peripheral conditions (temperature and relative humidity) [13-15].

Clindamycin is an antibacterial agent that is a semisynthetic analog of Lincomycin. It has been used for diabetic wounds for many years. Diabetes can cause high blood sugar levels, poor circulation, nerve damage, immune system issues, and infections that can lead to foot ulcers. They take longer to heal, which may increase the risk of infections. Although, some literatures worked on Clindamycin for diabetic wounds healing but there is not enough research on incorporation of this drug into nanofibers and controlling drug delivery. Sangnim et al.[16] produced the nanofibers of PVA, tamarind seed gum by loading the clindamycin for wound dressing, and they reported the suitable properties as antibacterial with incorporating clindamycin. In the same study, Nadem et al.[17] used cross-linked poly(vinyl alcohol) (PVA) nanofibers as drug carriers for clindamycin. The in vitro drug release showed that cross-linked nanofibers had a lower drug release rate in a long time. Sadeghi et al.[18] offered an antibacterial wound dressing from carboxymethyl cellulose (CMC)-human hair keratin with topical clindamycin delivery. The in vitro release study indicated that clindamycin was released slower in samples containing higher keratin and the Fickian diffusion mechanism controlled their release profile. The fabricated dressing effectively inhibits *S. aureus* bacterial colonies growth after 24 h.

In Hivechi et al., studies, it is found that the presence of Gel in PCL structure can enhance some properties such as composite strength, drug release, and biodegradability [19, 20]. Kuppan et al. [21] fabricated nanofibrous scaffolds made of PCL and PCL-gelatin. The scaffolds could be explored as potential candidates for regeneration of the functional esophagus. The results showed that cell proliferation on PCL-gelatin nanofibrous scaffold was significantly higher than the PCL nanofibrous scaffold. Heidari et al.[22] evaluate the effect of graphene on the biological properties of PCL/gelatin nanofibrous mats. Drug release studies indicated that electrospun PCL/gelatin/graphene and PCL/gelatin nanofibrous scaffolds could release tetracycline HCl (TCH) properly. In this research, we fabricated PCL/gel/clindamycin blend nanofibers using the electrospinning method. FTIR, SEM, and antibacterial tests were carried out to characterize the nanofibers. As a result, it is shown that

porous blend mats can absorb wound exudates and gradually release the clindamycin exhibiting antibacterial properties, which makes them a great candidate for dermal injury treatment purposes.

2. Materials and Methods

2-1 Materials

All chemicals were of analytical grade. Gelatin and acetic acid were purchased from Merck(Germany) and used without further purification. Polycaprolactone (MW=70 kD) and glutaraldehyde were obtained from Sigma-Aldrich. Powder of Clindamycin HCL was provided from Sepidarj Company, And phosphate buffer saline (PBS 1x, pH= 7.4) was obtained from Roman Industrial Company Co. (USA).

2-2 Solution preparation and electrospinning

First, the Gel (15% w/v) and PCL (15% w/v) have been separately dissolved in 90% (v/v) acetic acid. The ratio of the polymers was chosen 75: 25 (v/v) of Gel and PCL to benefit the hydrophilicity, biodegradability, and biocompatibility of Gel as natural polymer and at the same time the proper mechanical properties of PCL as synthetic polymer. Their preparation followed by the addition of 2%, 4%, and 6% of clindamycin on the weight of total polymer content. All the solutions were stirred for 3 hours at ambient temperature. The electrospinning setup consisted of a stainless-steel blunt 19-gauge needle, a syringe pump, and a high voltage power supply (0-25 kV). Finally, electrospinning of the solutions as mentioned earlier into nanofibers was performed at voltage, feeding rate, and distance (between nozzle and collector) of 10 kV, 1 ml/h, and 15 cm, respectively. The composite scaffolds were fabricated by electrospinning of the Gel/ PCL and Gel/ PCL/CLIN solutions, and the electrospun fibers were deposited on the aluminum foil as a collector. The spinning time for each scaffold was set at 4 h. Then, the webs were cross-linked with the vapor of glutaraldehyde 25% for 24 hours.

2-3 Characterization

To investigate the morphology and diameter of nanofibers, a scanning electron microscope (SEM) (Philips XL30, Japan) was used at an accelerating voltage of 15 kV. After coating the samples with a thin layer of gold, the SEM images were recorded. Digimizer software was used to determine the average diameters of nanofibers. The average diameter of the nanofibers was measured and calculated by 50 random points chosen from the SEM images.

Fourier transform infrared spectroscopy (FTIR) was performed using a Thermo Nicolet NEXUS 670 at an applying spectra range of 400-4000 cm^{-1} using the KBr method to study the chemical structure PCL/Gel nanofibers and prove the presence of Clindamycin into webs.

2-4 Hydrophilicity

The wettability property of the fabricated scaffold was examined by a hydrophilicity test. The hydrophilicity of mats was measured by a video contact angle instrument (Sony model SSC-DC318P, Japan). All images were captured after 2 sec of falling the drop of water, and the test was repeated for three samples. Finally, the contact angle between the water drop and the mats' surface was scanned by Digimizer software.

2-5 Antibacterial activity

The antibacterial activity of the electrospun scaffolds against *Escherichia coli* (ATCC 25922) as Gram-negative bacteria and *Staphylococcus aureus* (ATCC 25923) as Gram-positive bacteria was evaluated using the broth dilution method. The antibacterial properties of nanofibers, including Clindamycin, were examined quantitatively according to the ASTM E2149-01 method with 3 times of repeat.

First, 21 g of Muller-Hinton-Bouillon powder was dissolved in 250 ml distilled water and placed in an autoclave for 20 min. The plates containing *Escherichia coli* as a Gram-negative bacteria and *Staphylococcus* as a Gram-positive bacteria and a control sample plate were situated in an incubator

at 37 °C and 120±2 rpm for 24 hours. The nanofibers were sterilized under UV radiation. Then, they were fixed in a 10 ml culture medium, and 10 µl of microbes (4.0×10^3 cfu/ml) and incubation process was carried out at 37 °C for 24 hours. Finally, the absorbance was observed in the range of 600 nm, and antibacterial activity using the number of colonies that grew on each plate was calculated by the following equation:

Antibacterial activity:

$$\frac{C-T}{C} \times 100 \quad (1)$$

Where T is the number of bacterial colonies of the test sample and C = control sample.

2-6 Drug release

To a better assessment of optimizing scaffold, its drug delivery behavior was investigated. For this purpose, Clindamycin HCL as a drug was loaded into the nanofibrous mats. To the preparation of CLINH-loaded nanofiber mats, CLINH powder (2, 4, and 6 % w/w based on the polymer used) was loaded to the polymer solution, and the electrospinning process was carried out. For evaluated clindamycin release, first, the calibration curve of clindamycin was specified and according to Fig 1, the characteristic peak of clindamycin was observed at $\lambda_{\max} = 210$ nm [23]. Then, the nanofibers were cut into 2×2 cm², placed in the bottles containing 4 ml phosphate buffer saline (pH 7.4), and held in the shaking incubator at 37 °C. At designated times, 4 ml of drug release medium was taken out, and the absorbance of released clindamycin in PBS was determined by using a UV-visible spectrophotometer. The concentration of drug released was calculated by the absorbance resulted from UV and standard curve for 120 hours with 3 times of repeat. The percentage of the cumulative clindamycin release was determined by equation 1:

$$\text{Cumulative drug release (\%)} = \frac{\sum_{t=0}^t M_t}{M_o} \times 100 \quad (2)$$

Where M_{total} denotes the total clindamycin content in nanofibers and M_i is the clindamycin concentration released at each time point.

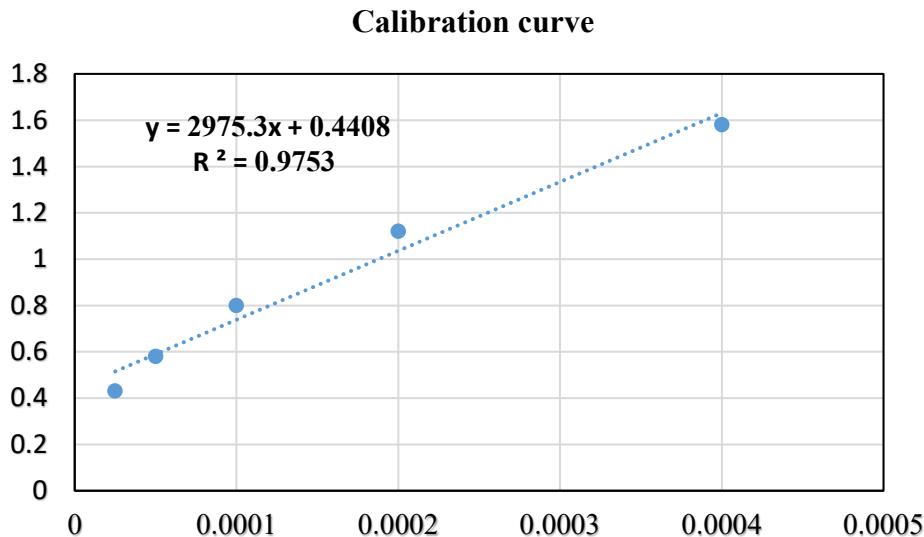


Fig 1. Standard curve of clindamycin

To analyze the kinetics and mechanism of a drug release, four models such as Zero-order, First-order, Higuchi, and Korsmeyer-Peppas were investigated, listed below (equation 2-5):

$$\text{Zero-order: } Q_t = Q_o + K_o t \quad (3)$$

$$\text{First-order: } L_n Q_t = L_n Q_o + K_1 t \quad (4)$$

$$\text{Higuchi: } Q_t = K_H \sqrt{t} \quad (5)$$

$$\text{Korsmeyer-Peppas: } \frac{M_t}{M_\infty} = K t^n, \frac{M_t}{M_\infty} \leq 0.6 \quad (6)$$

Where (M_t) and (M_∞) are the amounts of drug release at each time and initial weights of the clindamycin loaded in nanofibers, respectively. (K) is the constant characteristic of the polymer-drug system, and (n) is the diffusion system of nature release mechanism [12].

3. Result and Discussion

3-1 Scanning electron microscope

Scanning electron microscope (SEM) images were employed to indicate the morphology and average diameter of the PCL/Gel mats and the effect of clindamycin HCL (CLINH) concentration on the morphology of the PCL/Gel/CLINH nanofibers. The SEM images in Fig. 2 indicate that by increasing the drug concentration from 0% (fig. 2a) to 6% (fig. 2d), the average diameter of nanofibers decreased from 398 nm to 303 nm results. This might enhance the solution's conductivity. The gel will become negative by being in the ambient temperature and when CLIN is added the surface charge density increases and it will result in the formation of a thinner jet. When surface charge increases, the drop formed in the bevel of the syringe needs to overcome a lower electrostatic attraction force to reach the collector. Then, the electrostatic force can draw the fibers easily because It becomes more elongated in the electromagnetic field and narrower fibers are achieved [1]. The SEM imaged demonstrated bead-free and uniform nanofibers, as are shown in fig. 2. As incorporating the drug in fibrous composites decreased, the mean diameter of nanofibers decreased from 398 ± 22 to 377 ± 26 nm (a-b), 377 ± 26 to 354 ± 85 nm (b-c), 354 ± 85 to 303 ± 51 nm (c-d) ($n=50$ fibers). In addition, the beads were diminished with increasing the number of drugs. Rahimi et al. reported clindamycin to cause an increase in electrical conductivity and a decrease in diameters [24]. The same result was observed in Heidari et al paper.[22]. They observed that adding drugs into the solution of PCL/gelatin/graphene resulted in nanofibers with a slight decrease in the diameter of nanofibers. The obtained fiber diameter loaded with the drug was 135 ± 29 nm. They found that could be due to the higher polarity of the solution, which enhances the electrical conductivity of the solution, thereby reducing the nanofiber diameter. Sanguin et al.[16] reclaimed that with increasing drug concentration the conductivity of solution increases because the hydrochloride form of clindamycin was protonated in the aqueous solution. This resulted in a decrease in fiber diameter. Fig. 2 shows the morphology of the nanofibers.

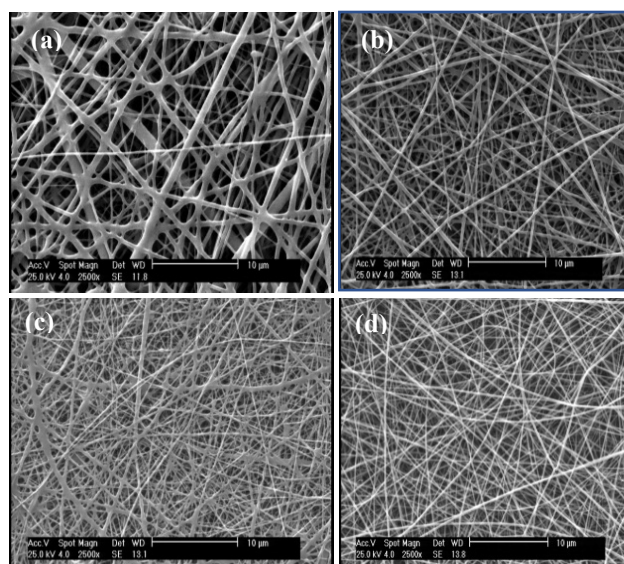


Fig.2 a) PCL/Gel, b) PCL/Gel/drug 2%, c) PCL/Gel/drug 4% and, d) PCL/Gel/drug 6%

3-2 Fourier-transform infrared spectroscopy (FT-IR)

To confirm the presence of the drug in nanofibers, the FT-IR spectrum of clindamycin, Gel/PCL, and Gel/PCL/clindamycin 6% nanofibrous scaffolds were compared, which are shown in Fig. 3. The FT-IR spectrum of clindamycin HCl showed characteristic peaks at 3375 cm^{-1} (OH stretching), 2959 and 2924 cm^{-1} (CH stretching), 1684 cm^{-1} (C=O stretching), 1553 cm^{-1} (N-H bending), 1455 cm^{-1} (C-N), 1311 cm^{-1} (SC-H), 1254 cm^{-1} (C-OH), 1080 cm^{-1} (C-O stretching) and 861 cm^{-1} (C-CL) [17, 24]. According to the FT-IR spectra, in the case of PCL the peaks appeared at 2945 , 2867 , 1731 , 1294 , 1240 , and 1173 cm^{-1} are attributed to asymmetric CH_2 stretching, symmetric CH_2 stretching, carbonyl (C=O) stretching, C-O, and C-C stretching, asymmetric C-O-C stretching, and symmetric C-O-C stretching, respectively. The FTIR spectrum of gelatin represented characteristic peaks at 3311 cm^{-1} (N-H stretching) which is overlapped by broad OH peak, 1652 cm^{-1} (C=O stretching of Amide I), and 1538 cm^{-1} (NH bending and C-N stretching of Amid II) [25]. As a result, FT-IR spectra cannot approve the presence of the drug in the structure of nanofibers since the peaks for both the clindamycin and PCL/Gel overlap in the spectrum.

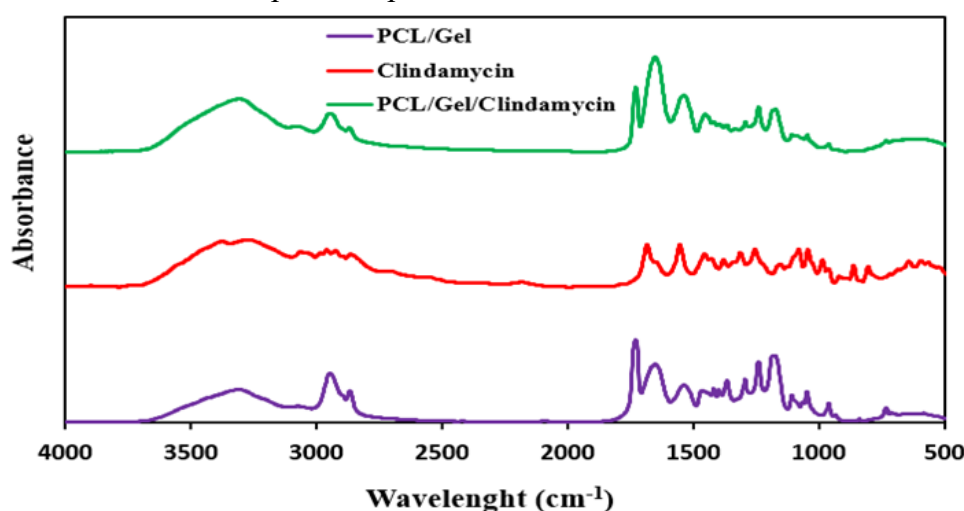


Fig 3. FTIR curves for the nanofibers and Clindamycin

3-3 Hydrophilicity

The hydrophilicity of nanofibers has an essential effect on cell attachment, biodegradability, and drug release. The contact angle between nanofibers and water droplets was measured to evaluate the hydrophilicity of the sample. The contact angles of $0-30^\circ$, $30-90^\circ$, and higher than 90° are attributed to hydrophilic, semi-hydrophilic, and hydrophobic properties, respectively [26]. Fig. 5 demonstrates the results obtain from contact angle measurement. As a result, natural gelatin polymer with 75% sample content can augment water absorption. However, after cross-linking, the hydrophilicity of gelatin was decreased because of the reaction between amine groups of gelatin and the aldehyde group of glutaraldehyde. However, the presence of clindamycin causes a decrease in contact angle, and hydrophilicity was increased with increasing the amounts of the drug. This phenomenon can be due to the presence of hydrophilic functional groups in the clindamycin structure (Fig. 4) that help the water solubility of the drug.

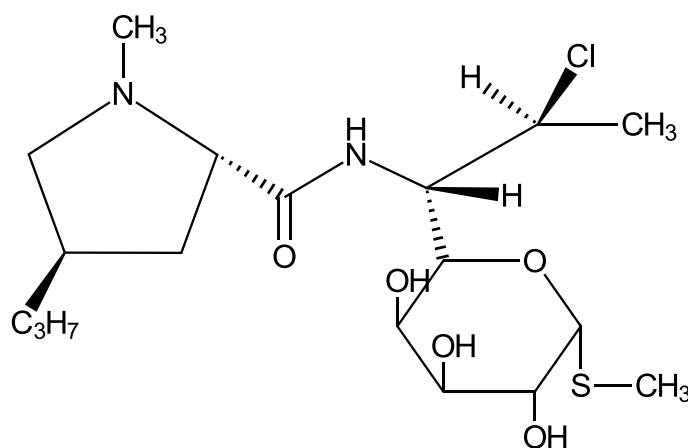


Fig 4. Structure of clindamycin

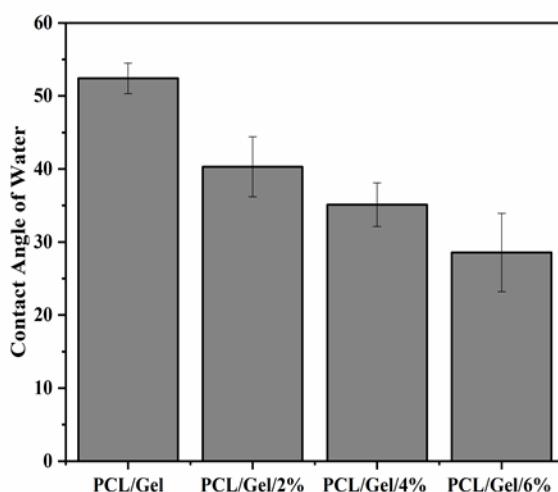


Fig 5. The hydrophilicity of nanofibers containing different percentages of clindamycin

3-4 Antibacterial activity

Antibacterial properties of nanofibers compared with the control sample were evaluated quantitatively, which is reported in Table 1. The nanofibers containing clindamycin had above 80%, and 90% antibacterial activity against Gram-negative and Gram-positive bacteria, respectively, and this property was augmented with increasing the amount of drug. Many studies claim that clindamycin disrupts bacterial cell membranes and has antibacterial properties [18]. However, the Gram-negative bacteria show more resistance against antibiotics and herbal extract because of their impenetrable wall, inner cell membrane, and hydrophobic property [6]. The same result is achieved in Sadeghi et al.[18] study. Clindamycin-loaded (6%) keratin:CMC (Carboxymethyl cellulose) (1:2) demonstrated the antibacterial activity of 97%. Sangnim et al.[16] observed that The nanofibers (consist of polyvinyl alcohol and tamarind seed gum) loaded with 1.0%–2.5% clindamycin HCl showed excellent bactericidal activity. As a result, as previously mentioned, clindamycin is a proper antibiotic for wound dressing application.

Table 1. The percentage of antibacterial activity of nanofibers

Sample	E.coli	S.aureus
PCL/Gel	47 ± 2.08	52 ± 2.54
PCL/Gel/Drug 2%	86 ± 1.80	92.5 ± 1.45
PCL/Gel/Drug 4%	88.5 ± 1.95	94 ± 2.09
PCL/Gel/Drug 6%	89 ± 2.01	97 ± 2.53

3-5 Release behaviors in vitro

To evaluate the clindamycin (CLIN) release with different concentrations from PCL/Gel/CLIN composite membranes, the release behaviors were measured in 4ml PBS buffers at PH=7 by ultraviolet-visible spectrophotometer at 207 nm.

Fig.6 displays the cumulative drug release of CLIN from various scaffolds for up to 6 days. The hydrophilic nature of Gel and CLIN caused a burst release in the first hours, while the presence of the hydrophobic nature of PCL and cross-linked membrane led to control drug release in 6 days. So, an initial burst release, about 30% within the first 8h observed (fig. 6), and by releasing about 65-80% for various scaffolds, drug release reached a plateau after 6 days. These results agree with the report of Sadeghi et al.[18] observed that the release profiles were started with burst release during first 4 h was 28.5 % for keratin: CMC (Carboxymethyl cellulose) (1:2). And the total amount of released clindamycin after 140 h (6 days) was 76.15%.

The burst release of CLIN with various amounts was similar, while nanofibers composite containing 6% CLIN showed higher burst release than other composites (80%). This can be related to the incompatibility of the drug-polymer system, the presence of drugs on the surface of nanofibers, and more hydrophilic behavior. Nadem et al, obtained 100% of CLIN release from poly(vinyl)alcohol nanofibers after 500 minutes and Ortega et al, reported 69% release of CLIN from poly(lactic)acid and gelatin nanofibers in 600 minutes. While, in this work, we controlled the drug release for 144 hours, which is recommended for wound healing applications [27] [28].

Data obtained from nanocomposite drug delivery were fitted to zero order, first order, Higuchi and Korsmeyer-Peppas models and compared with coefficient of determination (r^2), indicating a better fit with the kinetic model when the r^2 is higher (table 2). Also, the release exponent (n) parameter is presented in this table. Higuchi and Korsmeyer-Peppas equations can be used for describing models; it is written in Eq. 1 and 2:

$$Q_t = K_H t^{1/2} \quad (7)$$

$$\frac{M_t}{M_{inf}} = K t^n \quad (8)$$

Where, Q_t and K_H , respectively, are the amount of drug released over time and the release rate constant for the Higuchi model. In addition, M_t and M_{inf} are the cumulative drug release at the time “ t “ and Infinite time, K is the kinetic constant, and n is the diffusion exponent for Korsmeyer-Peppas, and “ t “ is time. Korsmeyer-Peppas allows to determined “n“ value by mean kinetic mode. When the value of “n” less than 0.45 indicates quasi Fickian and n=0.45 portend Fickian diffusion and diffusion-controlled drug release like that presented in Higuchi model. If the diffusion exponent is in the range of $0.45 < n < 0.89$ it shows non-Fickian diffusion or anomalous diffusion.

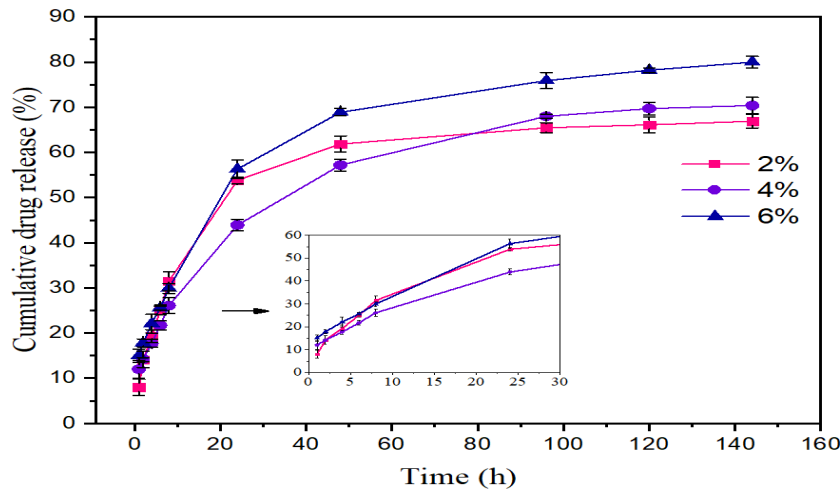


Fig. 6. Effect of drug concentration on drug release

Table 2. Shows comparison of regression and parameters of the mathematical models for CLIN released from gel-PCL nanofibers membrane with different drug concentrations.

Table 2. Regression and parameters of the mathematical models for CLIN release

Kinetic models/ drug concentration		2%	4%	6%
Zero-order	r^2	0.721	0.856	0.813
	n			
First-order	r^2	0.572	0.738	0.7124
	n			
Higuchi	r^2	0.870	0.960	0.9328
	n			
Korsmeyer-Peppas	r^2	0.934	0.987	0.977
	n	0.60 ± 0.02	0.41 ± 0.04	0.42 ± 0.03

As summarized in Table 2, for all concentrations of CLIN, r^2 values were found to be the highest value (correlation coefficient $r^2 > 0.91$) for Korsmeyer-Peppas model, and the lowest value r^2 was attained from the First Order. Thereupon, the best-fitted model was recognized Korsmeyer-Peppas model. Moreover, the “ n ” value of the system with 2% CLIN was in the range of 0.45-0.89 that showed a non-Fickian mechanism for drug release, but the system comprises 4% and 6% CLIN “ n ” value was close to 0.45 that indicated Fickian diffusion mechanism. As Sadeghi et al.[18] demonstrated, in the case of keratin: CMC (1:2) the R^2 value is 0.9803 which showed the best fit with the Peppas model. Based on the n -value results, Fickian diffusion is the main mechanism for clindamycin release from the studied nanocomposites.

4. Conclusion

In this study, PCL/Gel containing clindamycin as an antibacterial agent was fabricated. The wound dressing composite was produced by electrospinning. To investigate the morphology and mean diameters of nanofibers, a Scanning electron microscope (SEM) was employed. Digimizer software measured the average diameter of PCL/Gel nanofibers by 398 nm. The diameters of nanofibers decreased to 303 nm by adding clindamycin (6%). On the other hand, the presence of clindamycin provokes a decrease in contact angle, and hydrophilicity was increased with increasing the amounts of the drug. The samples showed adequate antibacterial properties (89% against E.coli and 98% against S.aureus), which could be conventional for wound dressing. The cumulative drug release of clindamycin indicated a burst release in the first hours because of the hydrophilic nature of Gel. In contrast, the presence of the hydrophobic nature of PCL and cross-linked membrane led to control

drug release in 6 days, and the best-fitted model for CLIN release was recognized Korsmeyer-Peppas model. Thus, the fabricated PCL/Gel/CLIN scaffold is proper for wound dressing, antibacterial, and drug delivery applications.

References

- [1] S. Najafi, A. Gholipour-Kanani, N. Eslahi, S.H. Bahrami, Study on release of cardamom extract as an antibacterial agent from electrospun scaffold based on sodium alginate, *The Journal of The Textile Institute* 112(9) (2021) 1482-1490.
- [2] S. Baghersad, S.H. Bahrami, M.R. Mohammadi, M.R.M. Mojtahedi, P.B. Milan, Development of biodegradable electrospun gelatin/aloe-vera/poly (ϵ -caprolactone) hybrid nanofibrous scaffold for application as skin substitutes, *Materials Science and Engineering: C* 93 (2018) 367-379.
- [3] M. Shokrollahi, S.H. Bahrami, M.H. Nazarpak, A. Solouk, Multilayer nanofibrous patch comprising chamomile loaded carboxyethyl chitosan/poly (vinyl alcohol) and polycaprolactone as a potential wound dressing, *International journal of biological macromolecules* 147 (2020) 547-559.
- [4] S. Saghebasl, S. Davaran, R. Rahbarghazi, A. Montaseri, R. Salehi, A. Ramazani, Synthesis and in vitro evaluation of thermosensitive hydrogel scaffolds based on (PNIPAAm-PCL-PEG-PCL-PNIPAAm)/Gelatin and (PCL-PEG-PCL)/Gelatin for use in cartilage tissue engineering, *Journal of Biomaterials science, Polymer edition* 29(10) (2018) 1185-1206.
- [5] Z.M. Goudarzi, T. Behzad, L. Ghasemi-Mobarakeh, M. Kharaziha, An investigation into influence of acetylated cellulose nanofibers on properties of PCL/Gelatin electrospun nanofibrous scaffold for soft tissue engineering, *Polymer* 213 (2021) 123313.
- [6] P.S. Mohamadi, A. Hivechi, H. Bahrami, N. Hemmatinegad, P.B. Milan, Antibacterial and biological properties of coconut oil loaded poly (ϵ -caprolactone)/gelatin electrospun membranes, *Journal of Industrial Textiles* (2021) 1528083721991595.
- [7] M. Rashtchian, A. Hivechi, S.H. Bahrami, P.B. Milan, S. Simorgh, Fabricating alginate/poly (caprolactone) nanofibers with enhanced bio-mechanical properties via cellulose nanocrystal incorporation, *Carbohydrate polymers* 233 (2020) 115873.
- [8] R. Yao, J. He, G. Meng, B. Jiang, F. Wu, Electrospun PCL/Gelatin composite fibrous scaffolds: mechanical properties and cellular responses, *Journal of Biomaterials science, Polymer edition* 27(9) (2016) 824-838.
- [9] O. Yördem, M. Papila, Y.Z. Menciloğlu, Effects of electrospinning parameters on polyacrylonitrile nanofiber diameter: An investigation by response surface methodology, *Materials & design* 29(1) (2008) 34-44.
- [10] A.G. Akerdi, S.H. Bahrami, Application of heterogeneous nano-semiconductors for photocatalytic advanced oxidation of organic compounds: a review, *Journal of Environmental Chemical Engineering* 7(5) (2019) 103283.
- [11] S.C. Coelho, B.N. Estevinho, F. Rocha, Encapsulation in food industry with emerging electrohydrodynamic techniques: Electrospinning and electrospraying—A review, *Food Chemistry* 339 (2021) 127850.
- [12] H. Souriyani-Reyhani pour, R. Khajavi, M.E. Yazdanshenas, P. Zahedi, M. Mirjalili, Cellulose acetate/poly (vinyl alcohol) hybrid fibrous mat containing tetracycline hydrochloride and phenytoin sodium: Morphology, drug release, antibacterial, and cell culture studies, *Journal of Bioactive and Compatible Polymers* 33(6) (2018) 597-611.
- [13] M. Shokrollahi, S.H. Bahrami, M.H. Nazarpak, A. Solouk, Biomimetic double-sided polypropylene mesh modified by DOPA and ofloxacin loaded carboxyethyl chitosan/polyvinyl alcohol-polycaprolactone nanofibers for potential hernia repair applications, *International Journal of Biological Macromolecules* 165 (2020) 902-917.

-
- [14] S. Ramakrishna, An introduction to electrospinning and nanofibers, World Scientific 2005.
- [15] Q.P. Pham, U. Sharma, A.G. Mikos, Electrospinning of polymeric nanofibers for tissue engineering applications: a review, *Tissue engineering* 12(5) (2006) 1197-1211.
- [16] T. Sangnim, S. Limmatvapirat, J. Nunthanid, P. Sriamornsak, W. Sittikijyothin, S. Wannachaiyasit, K. Huanbutta, Design and characterization of clindamycin-loaded nanofiber patches composed of polyvinyl alcohol and tamarind seed gum and fabricated by electrohydrodynamic atomization, *Asian Journal of Pharmaceutical Sciences* 13(5) (2018) 450-458.
- [17] S. Nadem, H. Ziyadi, M. Hekmati, M. Baghali, Cross-linked poly (vinyl alcohol) nanofibers as drug carrier of clindamycin, *Polymer Bulletin* 77(11) (2020) 5615-5629.
- [18] S. Sadeghi, J. Nourmohammadi, A. Ghatee, N. Soleimani, Carboxymethyl cellulose-human hair keratin hydrogel with controlled clindamycin release as antibacterial wound dressing, *International journal of biological macromolecules* 147 (2020) 1239-1247.
- [19] A. Hivechi, S.H. Bahrami, R.A. Siegel, Drug release and biodegradability of electrospun cellulose nanocrystal reinforced polycaprolactone, *Materials Science and Engineering: C* 94 (2019) 929-937.
- [20] A. Hivechi, S.H. Bahrami, R.A. Siegel, P.B. Milan, M. Amoupour, In vitro and in vivo studies of biaxially electrospun poly (caprolactone)/gelatin nanofibers, reinforced with cellulose nanocrystals, for wound healing applications, *Cellulose* 27(9) (2020) 5179-5196.
- [21] P. Kuppan, S. Sethuraman, U.M. Krishnan, PCL and PCL-gelatin nanofibers as esophageal tissue scaffolds: optimization, characterization and cell-matrix interactions, *J Biomed Nanotechnol* 9(9) (2013) 1540-55.
- [22] M. Heidari, S.H. Bahrami, M. Ranjbar-Mohammadi, P. Milan, Smart electrospun nanofibers containing PCL/gelatin/graphene oxide for application in nerve tissue engineering, *Materials Science and Engineering: C* 103 (2019) 109768.
- [23] M. Dedić, E. Bečić, B. Imamović, N. Žiga, Determination of clindamycin hydrochloride content in 1% clindamycin lotion, *Bull. Chem. Technol. Bosnia Herzeg* 50 (2018) 49-54.
- [24] N.R. Tanha, M. Nouri, Core-shell Nanofibers of Silk Fibroin/Polycaprolactone-Clindamycin: Study on Nanofibers Structure and Controlled Release Behavior, *Polymer Science, Series A* 61(1) (2019) 85-95.
- [25] F.R. Boroojen, S. Mashayekhan, H.-A. Abbaszadeh, The controlled release of dexamethasone sodium phosphate from bioactive electrospun PCL/gelatin nanofiber scaffold, *Iranian journal of pharmaceutical research: IJPR* 18(1) (2019) 111.
- [26] V. Leung, F. Ko, Biomedical applications of nanofibers, *Polymers for Advanced Technologies* 22(3) (2011) 350-365.
- [27] M. Castillo-Ortega, I. López-Peña, D. Rodríguez-Félix, T. Del Castillo-Castro, J. Encinas-Encinas, H. Santacruz-Ortega, J. Cauich-Rodríguez, J. Quiroz-Castillo, L. Chan-Chan, I. Lagarda-Diaz, Clindamycin-loaded nanofibers of polylactic acid, elastin and gelatin for use in tissue engineering, *Polymer Bulletin* (2021) 1-19.
- [28] S. Nadem, H. Ziyadi, M. Hekmati, M. Baghali, Cross-linked poly (vinyl alcohol) nanofibers as drug carrier of clindamycin, *Polymer Bulletin* (2019) 1-15.

Development of Antimicrobial Polyester Fabric by a Green *In-Situ* Synthesis of Copper Nanoparticles Mediated from Chitosan and Ascorbic Acid

Behnaz Mehravani^{1,a}, Ana Isabel Ribeiro^{1,b}, Majid Montazer^{2,c}
and Andrea Zille^{1,d*}

¹2C2T-Centro de Ciência e Tecnologia Têxtil, Campus de Azurém, Universidade do Minho 4800-058 Guimarães, Portugal

²Amirkabir University of Technology (Tehran Polytechnic), Hafez Avenue, Tehran, Iran

^abehnaz.mehravani@yahoo.com, ^bafr@2c2t.uminho.pt, ^ctex5mm@aut.ac.ir,
^dazille@2c2t.uminho.pt

Keywords: Copper nanoparticles, antimicrobial textiles, polyester, chitosan, ascorbic acid.

Abstract. The antimicrobial functionalization of polyester fabrics (PES) is useful to provide protection from pathogens and reducing odors. Copper nanoparticles (CuNPs) have been widely applied due to their antimicrobial properties and higher biocompatibility compared with other metal nanoparticles. However, the inherent instability of CuNPs under atmospheric conditions and the use of harmful chemicals during their synthesis limit their use. Thus, the development of efficient and safe methods for the CuNPs synthesis and their stabilization onto surfaces present high interest. In this work, PES was functionalized with CuNPs via *in situ* synthesis using cost-effective and safe chemicals in the presence and absence of chitosan. In sample without chitosan, the CuNPs showed a suitable stabilization onto PES due to the doubled stabilization of ascorbic acid (AA) and cetyl trimethyl ammonium bromide (CTAB). In sample with chitosan, less CuNPs were retained by the PES but also less CuNPs agglomeration was observed. Both samples presented excellent antibacterial effect against *Staphylococcus aureus* (*S. aureus*) and *Escherichia coli* (*E. coli*) as well as laundering durability.

Introduction

Recently, nanotechnology has been incorporated in textiles through various techniques such as coating and padding to induce some properties that are not inherent in textiles. Properties such as water repellency, antistatic, photocatalytic properties, electrical conductivity, thermal stability, flame retardancy and antibacterial can be improved by the surface functionalization of textiles [1,2]. Nanomaterials have attracted a lot of attention due to their unique physical, biological, and chemical properties. They display different properties at atomic levels due to the large surface area to volume ratio [3,4]. Nanotechnology has been used in many applications that include medicine, biotechnology, electronics, energy, and environment. Introducing nanoparticles in the fabric, called nano finishing, various properties will be provided such as UV blocking, antimicrobial, flame retardant, wrinkle resistant, antistatic, water repellent and self-cleaning properties [5,6]. Since the beginning of civilization, copper was considered a hygienic material and, during the last two decades, copper was proved to have good antibacterial properties in several research works [7]. Among metal nanoparticles, copper nanoparticles have been accepted in large due to their unique structure, good mechanical and thermal stability and ideal optical, magnetic, and catalytic properties [5]. However, oxidation is a noted demerit with the usage of copper and hence suitable stabilizing agents should be used while preparation of CuNPs [8]. Among several methods, the chemical reduction method is more often used because of cost effectiveness, high yields, and simplicity [9]. The main role of the reducing agent in the chemical reduction method is to reduce the precursor solution and avoid the oxidation of copper nanoparticles [10]. The most often used reductants that are used in the synthesis of CuNPs include hydrazine (N₂H₄), sodium borohydride (NaBH₄) and *L*-ascorbic acid (AA). However, those chemicals are expensive and quite toxic and hence it is essential to search for more

economical and safer reducing agents. Several works have been reported using sodium hypophosphite (SHP) or ascorbic acid (AA) as reducing agent in the preparation of CuNPs [9,11,12]. Most of the recent works are focusing on green synthesis to eliminate the usage of harmful chemical substances and as a part of this green synthesis, extracts from plants such as *Terminalia arjuna* bark, Magnolia leaf, *Datura metel* leaf and microorganisms like *Pseudomonas stutzeri*, *Morganella morganii* are used [13]. Besides the reducing agents, several capping agents have been used to control the NPs shape and protect them from agglomeration. In this group, cetyl trimethylammonium bromide (CTAB) and sodium dodecyl sulfate (SDS) have been widely used [14]. The addition of polymers can also be used for the stabilization of metal nanoparticles as the polymer functional groups may promote electronic interaction with the metal nanoparticles. After the reduction process, the larger protecting polymers cover or encapsulate the metal particles and there is a stabilization effect [15]. Various works discussed the usage of Chitosan, Starch ($C_6H_{10}O_5$), Polyacrylic acid (PAA), Poly methacrylic acid (PMAA) and Polyvinylpyrrolidone (PVP) as stabilizing agents [13,14]. Chitosan is a linear polysaccharide that is produced by the deacetylation of chitin. Its good biocompatibility, biodegradability, antimicrobial activity, wound healing property and antitumor effect has made it a candidate for having their application in various fields such as filtration, drug-delivery, wound dressing, cell culture, tissue engineering, cosmetic, ophthalmology, solid-state batteries and textiles [16]. In recent times, CuNPs have been gathering lot of attention owing to the ease of mixing with polymers [13]. It was reported in the literature that the presence of hydrophilic side chains in chitosan plays an important role in the stabilization of CuNPs and helps to reduce agglomeration [17]. Polyester is used in many applications due to its promising mechanical, chemical and thermal properties [18,19]. The fabrics produced by polyester are one of the most popular in the textile industry. However, problems such as low hydrophilicity, low dye-ability and the lack of functional groups in their polymeric chains make them difficult to induce any functionalities and hygienic problems emerge [20,21]. Therefore, inducing durable antibacterial properties in the polyester fabric presents high interest [22].

In this work, it was explored the functionalization of polyester fabric with CuNPs by an *in-situ* method using the naturally available chitosan as stabilizing agent. Here, SHP and ascorbic acid were used as reducing agents. Besides preventing oxidation, CTAB, it was also added to control the size of nanoparticles. Thereafter, the antibacterial and cytotoxicity of these fabrics were studied to investigate the potentiality of using them in biomedical applications.

Experimental

Materials

The chemical reagents were used without any purification. Copper (II) sulphate pentahydrate ($CuSO_4 \cdot 5H_2O$) and cetyl trimethyl ammonium bromide (CTAB) were purchased from Merck Co. (Germany); Ascorbic acid (AA, $C_6H_8O_6$) from BDH (England); Sodium hypophosphite (SHP, $NaPO_2H_2$) from Acros Co. (United States) and chitosan with a bulk density of 0.26 g.mL^{-1} and has a viscosity of 78 mPa.s. with a deacetylation degree of 90 % from Chitotech Co. (Iran). Commercial polyester fabric with weight per unit area of 105 g.m^{-2} was obtained from Broojerd Textile Co. (Iran).

Fabric Wash

The polyester fabric was primarily washed with 2 g.L^{-1} non-ionic detergent with liquor to ratio of L:G=50:1 at 80°C for 30 min to remove any impurities from the fabric surface. Then, the fabric was rinsed with distilled water and dried at room temperature.

Synthesis of Copper Nanoparticles

Two methods were used to synthesize CuNPs, one in the presence and another in absence of chitosan. In S1, the $CuSO_4 \cdot 5H_2O$ (1 g), AA (1 g) and SHP (0.6 g) were dissolved in 100 mL of distilled water at 50°C with magnetic stirring at 375 rpm. Next, PES was immersed in the solution. CTAB (0.5 g) was added when the solution reached 85°C . For S2, an initial solution of Cu salt (0.1 g) and AA(0.5

g) and SHP (0.6 g) was prepared in 80 mL of distilled water at 50°C with magnetic stirring. The PES was immersed in the solution. Chitosan (0.5 g) with AA (0.5 g) was dissolved in 20 mL of distilled water and the total volume was mixed with the initial solution at 70°C. The mixture was heated to 85 °C and CTAB (0.5 g) was added. Both solutions were kept at 85 °C under stirring for 1h. The procedure is shown graphically using Fig. 1.

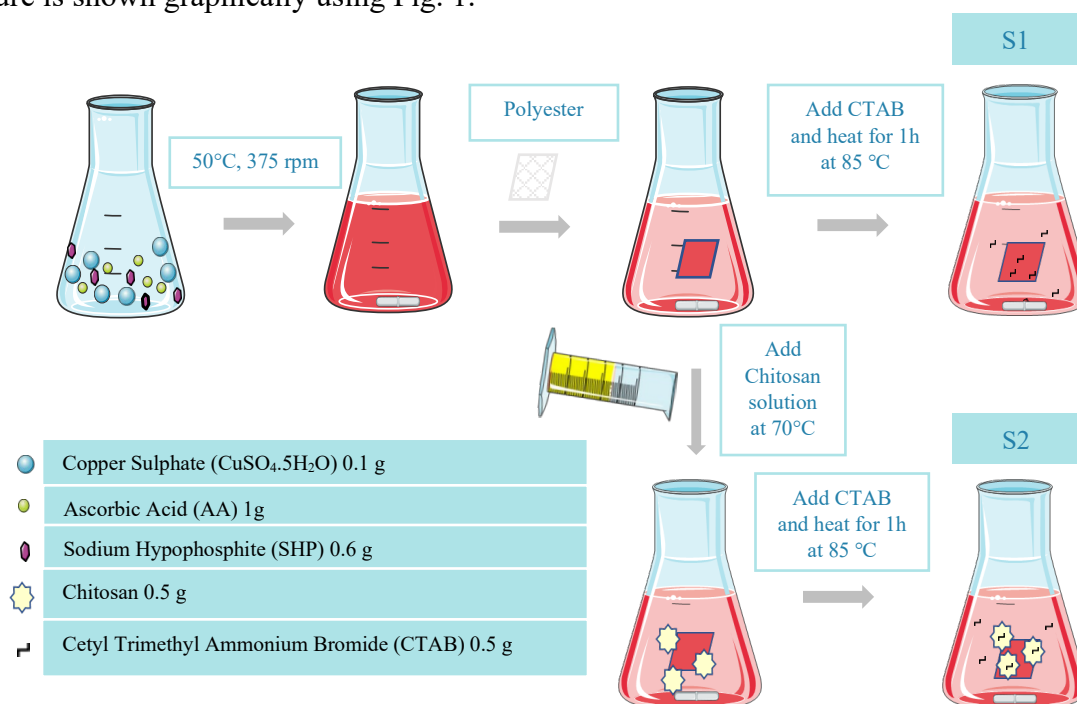


Fig. 1 Graphical Representation of Synthesis of CuNPs

UV-vis reflectance spectra

It is used to identify the confirmation of the formation of the copper nanoparticles on the fabric surface and the values are taken in the range of 200 to 800 nm. UV-Vis spectroscopy (Shimadzu UV-1800 spectrophotometer) was used to estimate the maximum absorbance of the copper nanoparticles.

X-Ray Diffraction (XRD)

X-ray diffraction patterns were obtained with an X-ray diffractometer using Cu K radiation ($\lambda=1.54$ nm) PW3040/60 from Panalitical Co. (Germany) to study the structure of the material. This equipment can analyse in the range of 5-150° with 0.001° resolution. The crystal size was calculated using the Debye-Scherrer equation according to Eq. 1.

$$D \text{ (crystal size)} = \frac{k\lambda}{\beta \cos \theta} \quad (1)$$

In this formula, K is a constant equal to 0.9 and λ is X-ray wavelength and β is the peak bandwidth at half maximum height [23].

Field Emission Scanning Electron Microscopy (SEM)

FESEM was carried out in the laboratory for materials characterization services of the University of Minho. Morphological analyses of polyester fabrics functionalised with copper nanoparticles were carried out with an ultra-high resolution field emission Scanning Electron Microscope (FEG-SEM), NOVA 200 Nano SEM, FEI Company with integrated microanalysis X-ray systems (EDS-energy dispersive spectrometer) and Electron Backscatter Diffraction (EBSD). Secondary electron images and Backscattering electron images were achieved with an acceleration voltage at 5 kV and 15 kV respectively. Samples were covered with a film of Au-Pd (80-20 weight %) in a high-resolution sputter coater, 208HR Cressington Company, coupled to a MTM-20 Cressington High Resolution

Thickness Controller. EDAX Si (Li) detector was used to observe atomic compositions of the samples with an acceleration voltage of 5 kV.

Antimicrobial Test

Suspension method was used to study the antibacterial properties of the samples according to the AATCC 100-2004 standard. This is a quantitative method, more time-consuming in comparison with the agar plate. 1 mL of bacteria was considered for the bacteria growth which will be absorbed by the textile, and then the textile was soaked in the inoculant substance cultured in the closed-door plates at 37 °C for 24 h and finally the number of the bacteria on the surface of the textile was evaluated by consecutive dilution. The antibacterial action can be calculated as a reduced percentage by using the formula given in Eq. 2. The control sample (blank) without finishing was used for comparing the bacteria growth with finished samples. Two bacteria including one Gram-positive bacteria, *Staphylococcus aureus* (*S. aureus*, ATCC 25923), and one Gram-negative bacteria, *Escherichia coli* (*E. coli*, ATCC 25922), were used. Washing cycles for 10 times has been performed on the samples for 30 mins at 40 °C according to the AATCC Test Method 61(2A)-1996.

$$R \% (\text{bacterial efficiency}) = \frac{B-A}{B} \times 100 \quad (2)$$

where A is the number of bacteria recovered after incubation for 24 hours and B is the number of bacteria recovered at the 0 contact time [16].

Results and Discussion

During the preparation of CuNPs it was observed that the color was changed from blue to red after the addition of ascorbic acid and SHP in both methods (S1 and S2) that indicated the emergence of CuNPs. This kind of observation has been reported as an indicator of the reduction of copper ions to metallic copper [24]. Then, the dispersion was further characterized by UV-Vis. UV-vis results were studied to confirm the presence of CuNPs on dispersion and it is known from the literature that the CuNPs used to present an absorbance peak between 500 and 600 nm [25]. The UV-vis spectra of the dispersions S1 and S2 showed the absorbance peak at 590 and 610 nm, respectively (Fig. 2). Hence, the presence of CuNPs was confirmed in both samples. The observations from the study were in coincidence with reports from the literature [25][26].

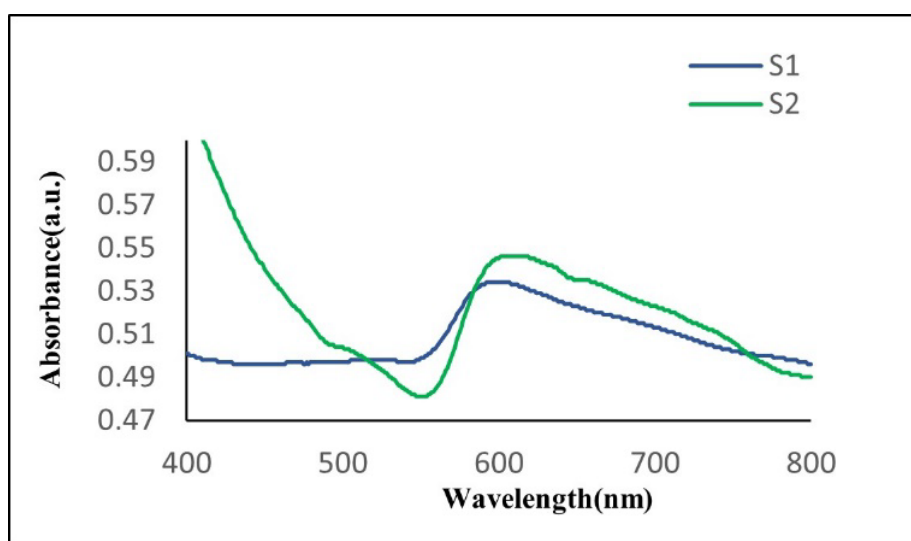


Fig. 2 UV-Vis spectra from S1 and S2 samples.

XRD analysis was used to analyse the crystal size of the CuNPs on the samples synthesized with and without the chitosan (S1 and S2). XRD patterns of the CuNPs were found in S1 and S2. The characteristic peaks are related to the plane index of (111) (200) (220), where in S1 the peaks appeared at $2\theta = 43.354^\circ$, 50.479° and 74.152° , and in S2 at $2\theta = 43.371^\circ$, 50.498° and 74.164° , respectively (Fig. 3). According to (JCPDS file no. 98-005-5321) the peaks of both samples are indexed to the pure copper. The average crystal size of the CuNPs was calculated by using the Debar Scherrer relation and was determined as 50.3 nm for S1 and 56.0 nm for S2. The crystal sizes of the CuNPs agreed with the values reported in the literature, where it was found that the crystal sizes of the copper nanoparticles are in the range of 35 to 75 nm [23]. It was observed from the XRD that the size of the copper nanoparticles with chitosan (56 nm) was larger than CuNPs in the absence of chitosan (50.33 nm). This draws to the conclusion that the presence of chitosan has resulted in the increment of the size of the CuNPs. This tendency can be due to the reason that chitosan covers the nanoparticles to avoid agglomeration during the synthesis process and hence improving their increase in size [27]. Another reason for the size enhancement with chitosan can be due to the coordination ability of the metallic ions towards the amino groups of the chitosan. They also reported that this could also make the polymer behave as a chelating agent. Hence these interactions will allow the metallic cations to act as templates and form chitosan nanoparticles [28].

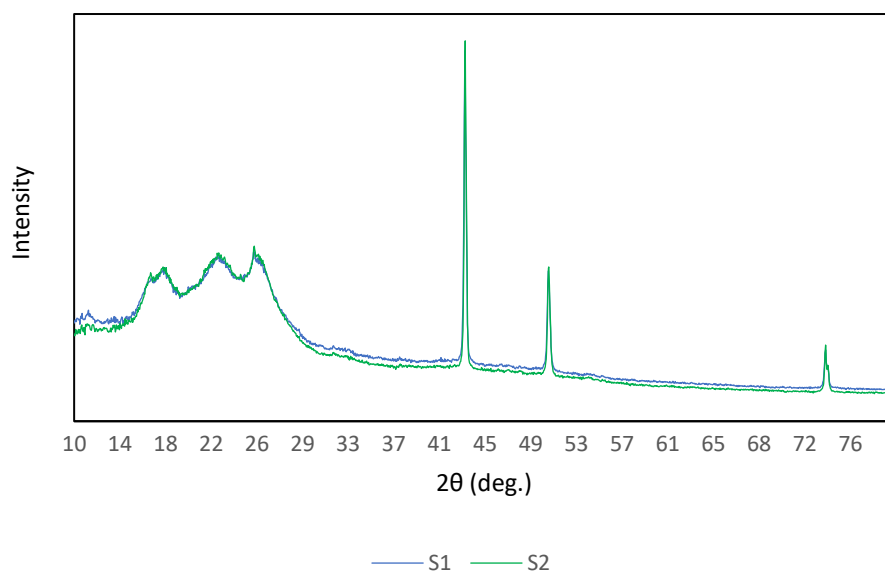


Fig. 3 XRD Pattern of Sample (Control Sample, S1 and S2)

SEM images were collected to analyse the morphology of CuNPs onto PES in the different conditions. First, it was possible to confirm the loading of CuNPs in both samples. Despite the S1 sample showed more CuNPs onto PES surface, also some agglomeration was observed. The CuNPs in S2 were less but they showed to be better distributed, with less agglomeration (Fig. 4). The presence of both CTAB and chitosan might have performed the role of capping agents and have prevented the agglomeration of CuNPs. The EDS analysis proved the superior adhesion of CuNPs in S1 (7.71%) than in S2 (1.71%) (Table 1).

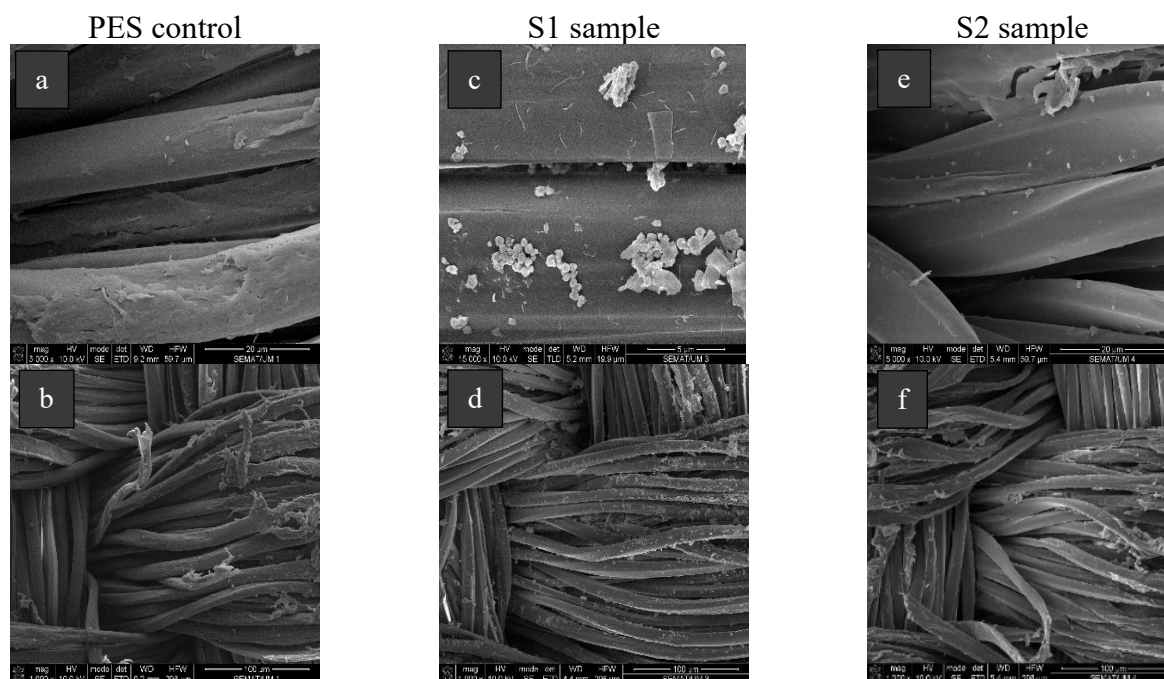


Fig. 4 SEM images of control sample (a and b), S1 (c and d) and S2 (e and f) at magnifications of 5000x and 1000x.

Table 1 EDS analysis of the PES (control), S1 and S2 samples.

Sample	C (W%)	O (W%)	Cu (W%)
Control	64.06	34.94	-
S1	66.77	25.25	7.71
S2	67.94	30.34	1.71

PES samples with CuNPs (S1 and S2) were tested against Gram-negative bacterial strain *E.coli* and Gram-positive strain *S. aureus*. In this test, the antimicrobial activities of S1 and S2 samples were compared with a blank sample, PES fabric without CuNPs (Table 2). The results showed a reduction percentage of 99.9% in both samples with CuNPs and any inhibition in the control sample. To understand the durability and the stability of the CuNPs onto the fabric, 10 washing cycles at 40°C for 30 minutes were performed. The antimicrobial efficacy after wash also showed 99.9% of bacterial reduction in both samples, with and without chitosan. Thus, it can be concluded that both samples have the potential to be used in medical applications. Despite the higher concentration of CuNPs in S1, proved on EDS results, the sample S2 also present equal antimicrobial efficacy. The stabilization of chitosan, ended with the same inhibitory activity towards Gram-negative and Gram-positive bacteria using a reduced concentration of CuNPs, which present several benefits namely in terms of the environmental contamination with metals, reduced cytotoxicity and economical aspects. The antimicrobial activity of CuNPs is commonly attributed to the ions released from the CuNPs. Interaction of the copper ions with the microbial membranes and production of radicals when the ions and nanoparticles are attached to the DNA molecules. It results in a disordering helical structure by cross-linking within and between the nucleic acid strands inducing the antimicrobial effect [29]. Chitosan may improve the antimicrobial effect due to its polycationic nature at pH under 6. It interacts with molecules with negatively charged components on the bacteria cell wall, forming an impermeable layer around the cell and changing the permeability of the cells which results in the blocking of transport into the cell [30].

Table 2. Antimicrobial activity of control, S1 and S2 samples before and after 10 washing cycles.

Sample	<i>S. aureus</i> (reduction %)	<i>E. coli</i> (reduction %)	<i>S. aureus</i> - washed (reduction %)	<i>E. coli</i> - washed (reduction %)
Control	0	0	0	0
1	99.9	99.9	99.9	99.9
2	99.9	99.9	99.9	99.9

Conclusion

The synthesis and deposition of CuNPs on PES were performed successfully using an *in-situ* method. Both samples demonstrated suitable antibacterial properties against Gram-positive and Gram-negative bacteria opening new opportunities for the development of efficient and safe-by-design antimicrobial PES fabrics.

References

- [1] A. Salman, F.A. Metwally, M. Elbisi, G.A.M. Emara, Applications of nanotechnology and advancements in smart wearable textiles: An overview, Egypt. J. Chem. 63 (2020) 2177–2184.
- [2] C.I. Idumah, Influence of nanotechnology in polymeric textiles, applications, and fight against COVID-19, J. Text. Inst. 0 (2020) 1–21.
- [3] S. Riaz, M. Ashraf, T. Hussain, M.T. Hussain, A. Rehman, A. Javid, K. Iqbal, A. Basit, H. Aziz, Functional finishing and coloration of textiles with nanomaterials, Color. Technol. 134 (2018) 327–346.
- [4] B. Mehravani, A.I. Ribeiro, A. Zille, Gold nanoparticles synthesis and antimicrobial effect on fibrous materials, Nanomaterials. 11 (2021) 1067.
- [5] P. Sharma, S. Pant, P. Poonia, S. Kumari, V. Dave, S. Sharma, Green Synthesis of Colloidal Copper Nanoparticles Capped with *Tinospora cordifolia* and Its Application in Catalytic Degradation in Textile Dye: An Ecologically Sound Approach, J. Inorg. Organomet. Polym. Mater. 28 (2018) 2463–2472.
- [6] A.I. Ribeiro, M. Modic, U. Cvelbar, G. Dinescu, B. Mitu, A. Nikiforov, C. Leys, I. Kuchakova, M. De Vrieze, H.P. Felgueiras, A.P. Souto, A. Zille, Effect of dispersion solvent on the deposition of PVP-silver nanoparticles onto DBD plasma-treated polyamide 6,6 fabric and its antimicrobial efficiency, Nanomaterials. 10 (2020) 607.
- [7] S. Anita, T. Ramachandran, R. Rajendran, cv Koushik, M. Mahalakshmi, A study of the antimicrobial property of encapsulated copper oxide nanoparticles on cotton fabric, Text. Res. J. 81 (2011) 1081–1088.
- [8] M.C. Sportelli, R.A. Picca, R. Ronco, E. Bonerba, G. Tantillo, M. Pollini, A. Sannino, A. Valentini, T.R.I. Cataldi, N. Cioffi, Investigation of industrial polyurethane foams modified with antimicrobial copper nanoparticles, Materials (Basel). 9 (2016) 1–13.
- [9] D. Lai, T. Liu, G. Jiang, W. Chen, Synthesis of highly stable dispersions of copper nanoparticles using sodium hypophosphite, J. Appl. Polym. Sci. 128 (2013) 1443–1449.
- [10] U. Kathad, h p Gajera, Synthesis of copper nanoparticles by two different methods and size comparison, Int. J. Pharma Bio Sci. 5 (2014) 533–540.
- [11] T.M.D. Dang, T.T.T. Le, E. Fribourg-Blanc, M.C. Dang, Synthesis and optical properties of copper nanoparticles prepared by a chemical reduction method, Adv. Nat. Sci. Nanosci. Nanotechnol. 2 (2011).
- [12] S. Jain, A. Jain, P. Kachhawah, V. Devra, Synthesis and size control of copper nanoparticles and their catalytic application, Trans. Nonferrous Met. Soc. China English Ed. 25 (2015) 3995–4000.
- [13] M.I. Din, R. Rehan, Synthesis, Characterization, and Applications of Copper Nanoparticles, Anal. Lett. 50 (2017) 50–62.

-
- [14] G. Granata, T. Yamaoka, F. Pagnanelli, A. Fuwa, Study of the synthesis of copper nanoparticles: the role of capping and kinetic towards control of particle size and stability, *J. Nanoparticle Res.* 18 (2016) 1–12.
 - [15] A. Travan, C. Pelillo, I. Donati, E. Marsich, M. Benincasa, T. Scarpa, S. Semeraro, G. Turco, R. Gennaro, S. Paoletti, Non-cytotoxic silver nanoparticle-polysaccharide nanocomposites with antimicrobial activity, *Biomacromolecules*. 10 (2009) 1429–1435.
 - [16] E. Hadipour-Goudarzi, M. Montazer, M. Latifi, A.A.G. Aghaji, Electrospinning of chitosan/sericin/PVA nanofibers incorporated with in situ synthesis of nano silver, *Carbohydr. Polym.* 113 (2014) 231–239.
 - [17] A.M. Muthukrishnan, Green Synthesis of Copper-Chitosan Nanoparticles and Study of its Antibacterial Activity, *J. Nanomed. Nanotechnol.* 06 (2015) 1–5.
 - [18] A. Bashiri, M. Montazer, One-step fabrication of fatty acids / nano copper / polyester shape-stable composite phase change material for thermal energy management and storage, *Appl. Energy*. 228 (2018) 1911–1920.
 - [19] A. Bashiri, M. Montazer, M. Mahmoudi, Photo and biocatalytic activities along with UV protection properties on polyester fabric through green in - situ synthesis of cauliflower-like CuO nanoparticles, *J. Photochem. Photobiol. B Biol.* 176 (2017) 100–111.
 - [20] A.B. Rezaie, M. Montazer, Amidohydroxylated polyester with biophotoactivity along with retarding alkali hydrolysis through in situ synthesis of Cu / Cu₂O nanoparticles using diethanolamine, *J. Appl. Polym. Sci.* 44856 (2017) 1–15.
 - [21] M.M. Abdul-Bari, R.H. McQueen, H. Nguyen, W. V. Wismer, A.P. de la Mata, J.J. Harynuk, Synthetic Clothing and the Problem With Odor: Comparison of Nylon and Polyester Fabrics, *Cloth. Text. Res. J.* 36 (2018) 251–266.
 - [22] A. Majumdar, B.S. Butola, S. Thakur, Development and performance optimization of knitted antibacterial materials using polyester-silver nanocomposite fibres, *Mater. Sci. Eng. C*. 54 (2015) 26–31.
 - [23] M.S. Usman, N.A. Ibrahim, K. Shameli, N. Zainuddin, W.M.Z.W. Yunus, Copper nanoparticles mediated by chitosan: Synthesis and characterization via chemical methods, *Molecules*. 17 (2012) 14928–14936.
 - [24] S. Pradhan, R. Shrestha, K. Bhandari, Effect of Various Parameters on Bio-Synthesis of Copper Nanoparticles Using Citrus Medica Linn (Lemon) Extract and Its Antibacterial Activity, *Amrit Resarch J.* 1 (2020) 51–58.
 - [25] M. Biçer, I. Şişman, Controlled synthesis of copper nano/microstructures using ascorbic acid in aqueous CTAB solution, *Powder Technol.* 198 (2010) 279–284.
 - [26] Y. Suresh, S. Annapurna, a K. Singh, G. Bhikshamaiah, Green Synthesis and Characterization of Tea Decoction Stabilized Copper Nanoparticles, *Int. J. Innov. Res. Sci. Eng. Technol.* 3 (2014) 11265–11270.
 - [27] E. Tabesh, H.R. Salimijazi, M. Kharaziha, M. Mahmoudi, M. Hejazi, Development of an in-situ chitosan-copper nanoparticle coating by electrophoretic deposition, *Surf. Coatings Technol.* 364 (2019) 239–247.
 - [28] G.R. Domínguez, M.C. Rodríguez-argüelles, N. Gonzalez Ballesteors, G. Rodriguez Dominguez, M. Campanini, L. Nasi, I. Vazquez, C. Sieiro, Broad-Spectrum Antimicrobial Activity of Silver Nanoparticles in Different Types of Chitosan Matrices, *Chem. J.* 1 (2015) 165–171.
 - [29] S.M. Dizaj, F. Lotfipour, M. Barzegar-Jalali, M.H. Zarrintan, K. Adibkia, Antimicrobial activity of the metals and metal oxide nanoparticles, *Mater. Sci. Eng. C*. 44 (2014) 278–284.
 - [30] C. keong Lim, A. sukari Halim, Biomedical-Grade Chitosan in Wound Management and Its Biocompatibility In Vitro, in: M.E. Magdy (Ed.), *Biopolymers, InTech*, 2010: pp. 19–33.

Enhancing the Antimicrobial Efficacy of Polyester Fabric Impregnated with Silver Nanoparticles Using DBD Plasma Treatment

Ana Isabel Ribeiro^{1,a}, Behnaz Mehravani^{1,b}, Cátia Magalhães^{1,c},
Talita Nicolau^{1,d}, Liliana Melro^{1,e}, Rui Fernandes^{1,f}, Vasyl Shvalya^{2,3,g},
Uroš Cvelbar^{2,h}, Jorge Padrao^{1,i} and Andrea Zille^{1,j*}

¹Centre for Textile Science and Technology (2C2T), Department of Textile Engineering, University of Minho, Campus of Azurém, 4800-058 Guimarães, Portugal

²Department of Gaseous Electronics (F6), Jožef Stefan Institute, Ljubljana SI-1000, Slovenia

³Faculty of Mathematics and Physics, University of Ljubljana, Ljubljana SI-1000, Slovenia

^aafr@2c2t.uminho.pt, ^bbehnaz.mehravani@yahoo.com, ^ccatiamagalhaes8@gmail.com,

^dtali_nicolau@hotmail.com, ^eliliana.melro@2c2t.uminho.pt, ^fruidvferndes@gmail.com,

^gvasyl.shvalya@ijs.si, ^huros.cvelbar@ijs.si, ⁱpadraoj@2c2t.uminho.pt, ^jazille@2c2t.uminho.pt

Keywords: Dielectric barrier discharge, antimicrobial textile, silver nanoparticles, exhaustion deposition

Abstract. The functionalization of polyester fabric (PES) with antimicrobial agents presents huge number of potential applications in advanced products. However, the lack of functional groups and the high PES hydrophobicity make the functionalization processes costly, prolonged and requires the use of polluting chemical compounds. In this work, dielectric barrier discharge (DBD) plasma treatment, an affordable and environmental-friendly method, was used to introduce new chemical groups, increase the surface energy and roughness of PES in order to improve the adhesion of silver nanoparticles (AgNPs) in its surface. The PES functionalization was evaluated by scanning electron microscopy (SEM), X-ray photoelectron spectroscopy (XPS) and antimicrobial efficacy against *Staphylococcus aureus* and *Escherichia coli*. Despite some additional oxidation, the DBD plasma-treated PES showed superior adhesion of AgNPs and excellent antimicrobial efficacy even after 10 washing cycles (WC).

Introduction

Polyester is one of the most applied synthetic fibers in the textile industry holding more than 50 % of the market share [1]. It has been preferred due to its good mechanical strength, processability, quick-drying, and dimensional stability [2]. This fiber strongly resists to the direct attack of microorganisms due to their molecular structure. However, it also induces higher perspiration, which commonly results in discomfort and microbial growth when it is used in direct contact with the skin [3]. In particular, textiles used in medical applications are in close contact to the human body for a long time, hence they are prone to increase the risk of infection [4]. Thus, it is essential to improve the antibacterial property of polyester for the production of advanced medical, protective and hygienic textiles [5]. New properties that are not intrinsic on textiles can be incorporated by chemical, physical or biological functionalization [6]. The incorporation of nanomaterials to generate nanocomposites has been a common strategy to introduce antimicrobial activity into textiles. Silver nanoparticles (AgNPs) has received huge attention due to the emergence of antibiotic-resistant strains and their low propensity to develop resistance. AgNPs exhibited a broad-spectrum antibacterial capability and demonstrated the potential to overcome some aspects of microbial resistance [7]. Nanoengineered textiles can be produced through several processes such as exhaustion, padding, dip coating, electroless, screen printing, dropwise, immersion, sonication and electrospinning [8, 9]. Some methods involve several steps and high temperature that are not cost-effective [10, 11]. Using the exhaustion method, the textiles are in constant contact with the nanoparticles-containing dispersion. The NPs are firstly moved from the dispersion to the fabric and then by adsorption and diffusion into the fiber interior. In this process, the temperature, time, NPs concentration, pH and auxiliary agents

are crucial parameters to control a suitable NPs deposition [12]. In addition, decreasing the difference between the surface energy of the particles and the material when they are incorporated may also improve their affinity [13].

Plasma treatments have been considered as promising tools to functionalize the surface of fabrics, whereby using a defined selection of plasma gas and treatment conditions can introduce novel properties and functionalities. It has been presented as an alternative to conventional wet-chemical treatments, since it does not require water and chemicals. Plasma consists of an ionized gas, where ions, electrons and radicals are created and may interact. The formed species react with the topmost atomic layers of the materials producing new reactive species [14]. Dielectric barrier discharge (DBD) plasma treatment has shown to enhance NPs adhesion. DBD plasma treatment activates the fabric surface, increasing the surface energy of the fabrics by the introduction of new functional groups according to the used gases. It also promotes the creation of micro-roughness that improves the NPs fixation [15, 16]. In previous works of our research group, the deposition of AgNPs onto polyamide was improved by the pre-functionalization of the fabrics with plasma treatments and using AgNPs dispersed in ethanol, allowing a deposition at low temperature [17]. In this work, the functionalization of PES fabric with AgNPs, also using the exhaustion process at low temperature, was tested by combining the DBD plasma treatment at atmospheric pressure in air to increase the surface energy and roughness of the polyester fabric using a low-cost and environmentally friendly method.

Materials and Methods

Materials. Commercial PES fabric with a weight per unit area of $100 \text{ g}\cdot\text{m}^{-2}$ was used in this work. First, the fabric was washed using a solution of $1.0 \text{ g}\cdot\text{L}^{-1}$ of a non-ionic detergent at 60°C for 60 minutes, rinsed with distilled water and dried. Commercial polyvinylpyrrolidone-coated (PVP) AgNPs (20-30 nm) were obtained from SkySpring Nanomaterials Inc, Houston, TX, USA. All the other reagents were purchased from Sigma-Aldrich without any purification.

Redispersion of AgNPs. AgNPs were dispersed in ethanol with a concentration of $1.0 \text{ mg}\cdot\text{mL}^{-1}$ using an ultrasonic bath for 30 minutes and ultrasound tip for more 30 minutes.

DBD Plasma treatment DBD plasma treatment was executed in a semi-industrial machine (Softal GmbH/University of Minho) that works at room temperature and atmospheric pressure in air. It uses a system of two metal electrodes coated with ceramic and counter electrodes coated with silicon with 50 cm of width, a gap distance of 3 mm and produces the discharge at high voltage 10 kV and low frequency 40 kHz. The machine was operated at 1 kW of power and velocity of $4 \text{ m}\cdot\text{min}^{-1}$. The plasma was applied 10 times in each side of the PES fabric that corresponds to a dosage of $5.0 \text{ kW}\cdot\text{min}\cdot\text{m}^{-2}$.

AgNPs deposition The AgNPs were applied onto PES fabric samples (sample non-treated and sample pre-treated with DBD plasma) by an exhaustion process at 30°C using a dispersion of NPs ($1 \text{ mg}\cdot\text{mL}^{-1}$), with a liquor ratio of 1:100. The process was carried out in a laboratory machine (Ibelus) that uses infra-red heating. The program started at room temperature and the temperature was increased to 30°C at a rate of $3^\circ\text{C}\cdot\text{min}^{-1}$. After remaining at this temperature for 60 min, the samples were dried at 40°C .

Scanning electron microscopy (SEM). The SEM analyses were carried out with an ultra-high resolution FEG-SEM, NOVA 200 Nano, FEI Company. Secondary electron images were carried out with an acceleration voltage at 5 kV. Backscattering electron images were performed with an acceleration voltage of 15 kV. Samples were covered with a film of Au-Pd (80-20 weight %) (208HR Cressington Company, coupled to a MTM-20 Cressington High Resolution Thickness Controller).

X-ray photoelectron spectroscopy (XPS). XPS analyses were carried out using a Kratos AXIS Ultra HAS. The VISION software was used for data acquisition and CASAXPS software for data analysis. The analysis was performed with a monochromatic Al K α X-ray source (1486.7 eV), operating at 15kV (150 W), in FAT mode (Fixed Analyser Transmission), with pass energy of 40 eV for regions ROI and 80 eV for the survey. Data acquisition was performed with a pressure lower than 1×10^{-6} Pa and it was used a charge neutralization system. Spectra have been charged corrected to give the adventitious C1s spectral component (C–C, C–H) binding energy of 285 eV. High-resolution spectra were collected using an analysis area of $\approx 1 \text{ mm}^2$. This process has an associated error of ± 0.3 eV. Deconvolution into sub-peaks was performed by least-squares peak analysis software, XPSPEAK version 4.1, using the Gaussian/Lorentzian sum function and Shirley-type background subtraction.

Antimicrobial test. The antibacterial efficacy of PES samples containing AgNPs and pristine PES fabric was determined following the standard ASTM-E2149. Bacteria pre-inoculums of *Staphylococcus aureus* (ATCC25923) and *Escherichia coli* (ATCC 25922) were prepared in tryptic soy broth (TSB) and, after 12 h of incubation at 37 °C and 120 rpm, the inoculum of each bacterium was centrifuged, the supernatant discarded and the bacteria washed with sterile phosphate buffer saline (PBS). Then, the initial concentration of each bacterium was adjusted to $1.5\text{--}3.0 \times 10^7$ CFUs·mL $^{-1}$ in PBS. The PES samples (2x1 cm) were inserted into falcon flasks of 10 mL and 5 mL of the diluted inoculum was transferred for each falcon. The samples were incubated for 24h at 37 °C and 120 rpm. Each of these dispersions was used to prepare 7-fold serial dilutions, which were plated out before (0 h) and after contact with the fabrics (24 h). The number of CFU was counted and the results were presented as log reduction. The antibacterial activity was performed in triplicates in two independent experiments.

Results and Discussion

PES samples impregnated with AgNPs presented in this work were developed using two distinctive particularities, being one of them related to the pre-functionalization of the textile with DBD plasma treatment. The applied DBD plasma treatment dosage was $5.0 \text{ kW min}\cdot\text{m}^{-2}$ with the goal to induce modifications onto PES fabric surface and improve the AgNPs adhesion. DBD plasma treatment has shown the ability to increase the fibre surface roughness and increase the availability of COOH chemical groups [18]. The second particularity of this work was the functionalization of PES using a low-temperature exhaustion method (30 °C), able to decrease the economic impact of high-temperature processes. Thus, PES samples with and without DBD plasma treatment were functionalized with AgNPs by exhaustion at 30 °C and characterized. SEM images were collected to understand the differences in the distribution, shape and quantity of AgNPs onto PES fabric surface (Fig. 1). The enlarged view of the SEM micrographs (magnification of 1000 x) showed the superior adhesion of AgNPs on DBD plasma-treated sample, with a more uniform and dense distribution. Using a higher magnification (5000 x) it was possible to perceive some agglomeration in both samples but even more in samples with DBD plasma treatment.

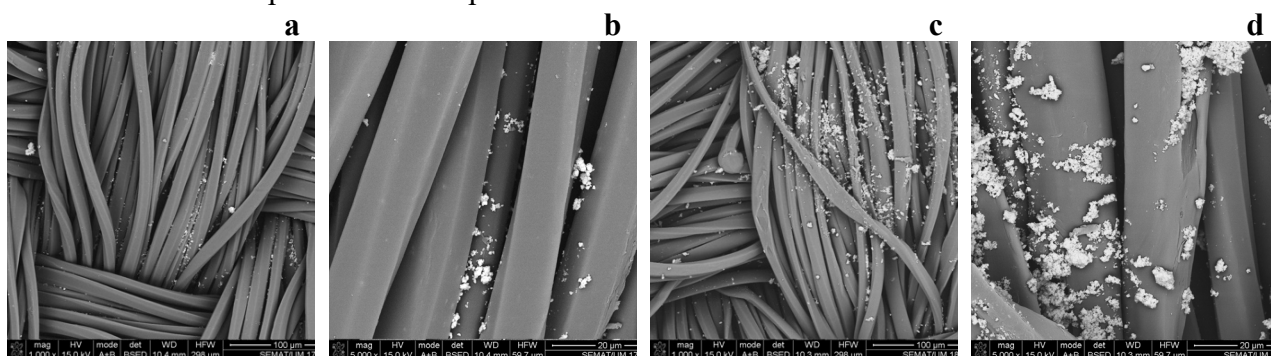


Fig. 1. SEM images of untreated (a and b) and DBD plasma-treated (c and d) PES samples with AgNPs with magnifications of 1000 x (a and c) and 5000 x (b and d).

The chemical modifications on the PES fabric surface induced by the functionalization with AgNPs and DBD plasma treatment, as well as the availability and oxidation state of Ag in the fabrics, was studied by XPS. DBD plasma treatment in air can create several species comprising atomic oxygen, nitrogen oxides, ozone, neutral and metastable molecules, radicals and ultraviolet radiation. The surface energy of materials treated with DBD increases by the introduction of oxygen polar group, due to the dissociation of oxygen molecules by electron impact. In addition, the excitation and dissociation of nitrogen molecules also can lead to other reaction paths able to produce extra atomic species [19]. In the deconvolution spectra of C 1s high-resolution spectra it was possible to observe three different peaks at 285.0 eV (C-C/C-H), 286.5 eV (C-O) and 288.9 eV (O=C) attributed to common chemical bonds in PES [20, 21]. The superior area in the O=C peak in DBD plasma-treated samples is in accordance with the reported increase in double bonded oxygen content (in the form of carboxylic groups) due to the plasma using air. This is also supported by the deconvolution's spectra of O 1s at 533.6 eV, where the C=O peak increased from 28.7 to 41.3 % (Fig. 2 and Table 1).

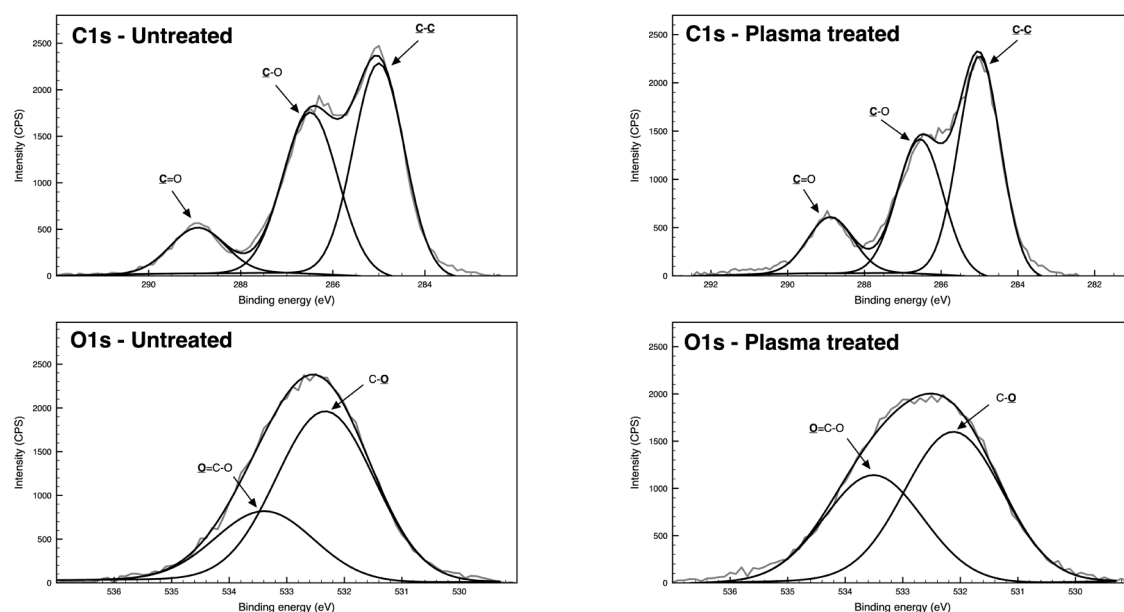


Fig. 2. Deconvolutions of the high-resolution XPS spectra of the C 1s and O 1s binding energy regions of PES fibers surface before and after DBD plasma treatment.

Lastly, the deconvolutions of the Ag 3d showed the presence of silver in untreated and DBD plasma-treated samples but a superior intensity in the treated sample. The deconvolution of the untreated PES sample showed the peaks with the binding energy of the Ag 3d_{5/2} and Ag 3d_{3/2} at 367.9 eV and 373.9 eV, respectively. These peaks were attributed to silver metals (Ag⁰) on polyester fabric [22, 23]. The Ag 3d deconvolution spectra of plasma-treated samples showed the same peaks as untreated samples with small deviations, where the peaks appeared at 368.2 eV and 374.3 eV. These peaks displayed an intensity 4 times higher in the DBD plasma-treated sample, proving a far superior content of AgNPs when DBD plasma treatment was applied. Moreover, in the DBD plasma-treated sample two different and lower peaks emerged at the binding energies of 369.4 eV and 375.5 eV (relative area of 6.2 and 4.0%, respectively) (Fig. 3 and Table 1). The new peaks demonstrated the presence of oxidated Ag species on the AgNPs surface when DBD was applied [24, 25].

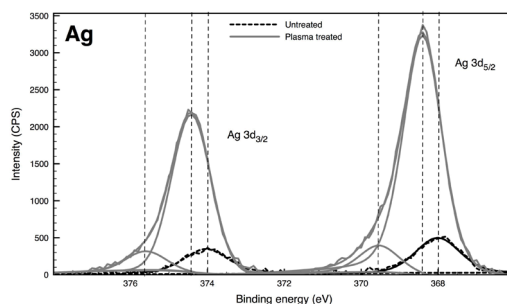


Fig. 3. Deconvolutions of the high-resolution XPS spectra of the Ag 3d binding energy region of PES fibers surface before and after plasma treatment.

Table 1. The relative percentage of chemical bonds in PES samples with and without DBD plasma treatment.

	Relative area of chemical bonds (%)								
	C1s			O1s		Ag3d			
	C-C/ C-H	C-O	C=O	C-O	O=C	Ag ⁰	Ag ⁺	Ag ⁰	Ag ⁺
	285.0 eV	286.5 eV	288.9 eV	532.6 eV	533.6 eV	367.9 - 368.2 eV	369.4 eV	373.9 - 374.3 eV	375.5 eV
Untreated PES	48.9	39.8	11.3	71.3	28.7	44.5	-	55.5	-
Plasma-treated PES	51.8	34.0	14.2	58.7	41.3	56.9	6.2	32.9	4.0

The antibacterial efficacy of the DBD plasma-treated and not treated PES fabric containing AgNPs was assessed using *S. aureus* and *E. coli* by shake flask method. The DBD plasma-treated samples showed superior antimicrobial activity when compared with the untreated sample against both tested bacteria (Fig. 4). The untreated sample showed a log reduction of 2.23 ± 0.06 and 3.40 ± 0.34 against *S. aureus* and *E. coli*, respectively, and the DBD plasma-treated sample showed a log reduction of 2.83 ± 0.08 in *S. aureus* and the complete reduction of *E. coli*. The superior action of DBD plasma-treated samples can be due to the higher concentration of AgNPs onto fabric surface observed in the SEM images and deduced by the superior intensity of the peaks in the XPS analysis. This can also be a result of the reactive oxygen species formed during the plasma process. Even after 5 and 10 washing cycles (WC) the antimicrobial activity showed to be similar or higher than the initial samples. During the washing processes, the AgNPs that were inside the fabric can be directed to the textile surface, being the availability of nanoparticles higher than the initial one onto the surface of the fabric. On the other hand, the oxidation state of nanoparticles could be changed during the washing steps, generating a different action against different bacteria. This may explain the different results in the antimicrobial results after the washing processes. Accordingly, the efficacy of PES samples against *S. aureus* increased using plasma-treated samples after 5 and 10 WC and decreased in the untreated samples. Nevertheless, against *E. coli*, the activity increased in both samples. In general, AgNPs are more effective against Gram-negative than Gram-positive bacteria due to their structural differences. The AgNPs bind to the thin layers of peptidoglycan in Gram-negative bacteria, changing the permeability and penetrating it. In this case, although the concentration of nanoparticles in the untreated samples was lower than the DBD plasma-treated one, the washing process provided enough AgNPs with the suitable oxidation state to the surface of the fabric to improve the antibacterial activity against *E. coli*.

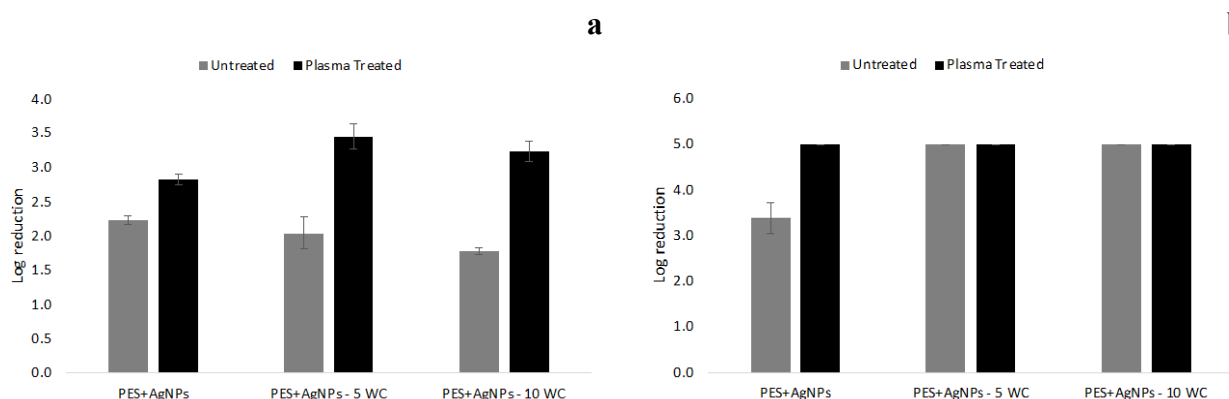


Fig. 4. Antimicrobial activity of PES samples against *S. aureus* (a) and *E. coli* (b) before and after 5 and 10 washing cycles (WC).

References

- [1] P. Gressier, D. De Smet, N. Behary, C. Campagne, M. Vanneste, Antibacterial polyester fabrics via diffusion process using active bio-based agents from essential oils, *Ind. Crops Prod.* 136 (2019) 11-20.
- [2] S. Chen, S. Zhang, M. Galluzzi, F. Li, X. Zhang, X. Yang, X. Liu, X. Cai, X. Zhu, B. Du, J. Li, P. Huang, Insight into multifunctional polyester fabrics finished by one-step eco-friendly strategy, *Chem. Eng. J.* 358 (2019) 634-642.
- [3] M. Orhan, Triclosan applications for biocidal functionalization of polyester and cotton surfaces, *J. Eng. Fibers Fabr.* 15 (2020).
- [4] C.M. Botelho, M.M. Fernandes, J.M. Souza, N. Dias, A.M. Sousa, J.A. Teixeira, R. Figueiro, A. Zille, New Textile for Personal Protective Equipment—Plasma Chitosan/Silver Nanoparticles Nylon Fabric, *Fibers* 9(1) (2021).
- [5] G.M. Malapit, R.Q. Baculi, Bactericidal efficiency of silver nanoparticles deposited on polyester fabric using atmospheric pressure plasma jet system, *J. Text. Inst.* (2021) 1-9.
- [6] E. Spielman-Sun, T. Zaikova, T. Dankovich, J. Yun, M. Ryan, J.E. Hutchison, G.V. Lowry, Effect of silver concentration and chemical transformations on release and antibacterial efficacy in silver-containing textiles, *NanoImpact* 11 (2018) 51-57.
- [7] F. Paladini, M. Pollini, Antimicrobial Silver Nanoparticles for Wound Healing Application: Progress and Future Trends, *Materials* 12(16) (2019).
- [8] B. Mehravani, A. Ribeiro, A. Zille, Gold Nanoparticles Synthesis and Antimicrobial Effect on Fibrous Materials, *Nanomaterials* 11(5) (2021).
- [9] A. Nadi, A. Boukhriess, A. Bentis, E. Jabrane, S. Gmouh, Evolution in the surface modification of textiles: a review, *Text. Prog.* 50(2) (2019) 67-108.
- [10] N.A. Ibrahim, E.M.R. El-Zairy, B.M. Eid, Eco-friendly modification and antibacterial functionalization of viscose fabric, *J. Text. Inst.* 108(8) (2016) 1406-1411.
- [11] S. Mowafi, M. Rehan, H.M. Mashaly, A. Abou El-Kheir, H.E. Emam, Influence of silver nanoparticles on the fabrics functions prepared by in-situ technique, *J. Text. Inst.* 108(10) (2017) 1828-1839.
- [12] C. Pereira, A.M. Pereira, C. Freire, T.V. Pinto, R.S. Costa, J.S. Teixeira, Nanoengineered textiles: from advanced functional nanomaterials to groundbreaking high-performance clothing, in C. M. Hussain (Eds.), *Handbook of Functionalized Nanomaterials for Industrial Applications*, 2020, pp. 611-714.
- [13] J. Pulit-Prociak, J. Chwastowski, A. Kucharski, M. Banach, Functionalization of textiles with silver and zinc oxide nanoparticles, *Appl. Surf. Sci.* 385 (2016) 543-553.
- [14] N. Krifa, W. Miled, N. Behary, C. Campagne, M. Cheikhrouhou, R. Zouari, Dyeing performance and antibacterial properties of air-atmospheric plasma treated polyester fabric using bio-based Haematoxylum campechianum L. dye, without mordants, *Sustain. Chem. Pharm.* 19 (2021).

-
- [15] A.I. Ribeiro, D. Senturk, K.S. Silva, M. Modic, U. Cvelbar, G. Dinescu, B. Mitu, A. Nikiforov, C. Leys, I. Kuchakova, M. Vanneste, P. Heyse, M. De Vrieze, A.P. Souto, A. Zille, Efficient silver nanoparticles deposition method on DBD plasma-treated polyamide 6,6 for antimicrobial textiles, *IOP Conf. Ser.: Mater. Sci. Eng.* 460 (2018).
- [16] V. Scholtz, J. Pazlarova, H. Souskova, J. Khun, J. Julak, Nonthermal plasma — A tool for decontamination and disinfection, *Biotechnol. Adv.* 33(6) (2015) 1108-1119.
- [17] A.I. Ribeiro, M. Modic, U. Cvelbar, G. Dinescu, B. Mitu, A. Nikiforov, C. Leys, I. Kuchakova, M. De Vrieze, H.P. Felgueiras, A.P. Souto, A. Zille, Effect of Dispersion Solvent on the Deposition of PVP-Silver Nanoparticles onto DBD Plasma-Treated Polyamide 6,6 Fabric and Its Antimicrobial Efficiency, *Nanomaterials* 10(4) (2020).
- [18] T.N.T. Kim, K. Vu Thi Hong, N. Vu Thi, H. Vu Manh, The Effect of DBD Plasma Activation Time on the Dyeability of Woven Polyester Fabric with Disperse Dye, *Polymers* 13(9) (2021).
- [19] N. De Geyter, R. Morent, C. Leys, Surface modification of a polyester non-woven with a dielectric barrier discharge in air at medium pressure, *Surf. Coat. Technol* 201(6) (2006) 2460-2466.
- [20] C.X. Wang, Y. Ren, Y.P. Qiu, Penetration depth of atmospheric pressure plasma surface modification into multiple layers of polyester fabrics, *Surf. Coat. Technol* 202(1) (2007) 77-83.
- [21] Z. Zhang, X. Zhang, Z. Xin, M. Deng, Y. Wen, Y. Song, Synthesis of monodisperse silver nanoparticles for ink-jet printed flexible electronics, *Nanotechnology* 22(42) (2011).
- [22] H.R. Hong, J. Kim, C.H. Park, Facile fabrication of multifunctional fabrics: use of copper and silver nanoparticles for antibacterial, superhydrophobic, conductive fabrics, *RSC Adv.* 8(73) (2018) 41782-41794.
- [23] A. Zille, M.M. Fernandes, A. Francesko, T. Tzanov, M. Fernandes, F.R. Oliveira, L. Almeida, T. Amorim, N. Carneiro, M.F. Esteves, A.P. Souto, Size and Aging Effects on Antimicrobial Efficiency of Silver Nanoparticles Coated on Polyamide Fabrics Activated by Atmospheric DBD Plasma, *ACS Appl. Mater. Interfaces* 7(25) (2015) 13731-13744.
- [24] S. Zanna, C. Saulou, M. Mercier-Bonin, B. Despax, P. Raynaud, A. Seyeux, P. Marcus, Ageing of plasma-mediated coatings with embedded silver nanoparticles on stainless steel: An XPS and ToF-SIMS investigation, *Appl. Surf. Sci.* 256(22) (2010) 6499-6505.
- [25] D.S. Im, B.M. Hong, M.H. Kim, W.H. Park, Formation of human hair-Ag nanoparticle composites via thermal and photo-reduction: A comparison study, *Colloids Surf. A Physicochem. Eng. Asp.* 600 (2020).

CHAPTER 3:

Fabrics and Fibers for Reinforcing of Composite Materials

Biologically Inspired Load Adapted 3D Textile Reinforcement Structures

Danny Frieese^{1,a*}, Lars Hahn^{1,b} and Chokri Cherif^{1,c}

¹Technische Universität Dresden, Institute of Textile Machinery and High Performance Material Technology (ITM), Hohe Straße 6, 01069 Dresden, Germany

^{a*}danny.frieese@tu-dresden.de, ^blars.hahn@tu-dresden.de, ^cchokri.cherif@tu-dresden.de

Keywords: Textile Reinforced Concrete, Textile Reinforcement Structures, Carbon Fiber, robot-supported, CAE-supported design, 3D-Roving Placement Rack.

Abstract. A significant strategy to reduce the demand for natural resources and the associated environmental impact is enhanced material efficiency in the design process for new building structures. Innovative concepts for designing, modelling, constructing, producing and utilising sustainable resource-efficient concrete-based building components will be the foundation for future-oriented constructions. For this reason, the ability to process biologically inspired 3D textile reinforcement structures is crucial to fully exploit the potential of carbon concrete. This research project provides a fundamentally realigned, CAE-supported approach so that optimization algorithms, numerical models for the generation of robot placement paths and bionically induced yarn positioning can be taken into account. The evolved intelligent and modular yarn placement system forms the basis to overcome current challenges involved in the placing and stabilizing of spatial and highly branched reinforcement topologies during the manufacturing process. Hence, the novel tool-independent, geometrically highly variable, robot-supported fibre placement technology is supposed to be capable of manufacturing biologically inspired load adapted 3D textile topologies with reinforcement in z-direction.

Introduction

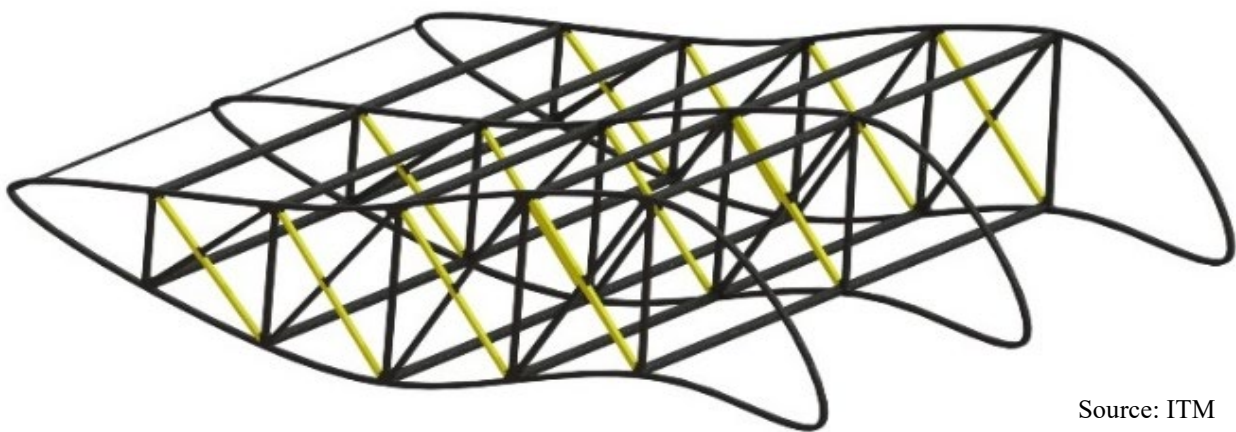
The consumption of natural resources and the accompanying environmental pollution are induced by the mass production of cement as a key component of concrete within the construction industry [1–3]. A significant strategy to reduce the demand for natural resources and the associated environmental impact is an enhanced material efficiency in the design process for new building structures [4]. The design graphic in Figure 1 shows the first carbon concrete house completely out of textile reinforced concrete (TRC) components in Dresden (Germany), which is currently under construction.



Figure 1: Final design draft of the CUBE-house in Dresden (Germany), which is currently under construction [5].

The application of textile reinforced concrete components will contribute to match the federal requirements of reducing CO₂-emissions until 2050 by 80 - 95 % regarding the reference year 1990[6], as the cement production is a main driver for the emission of greenhouse gases [4, 7]. Equally whether TRC-components with a one-dimensional or two-dimensional reinforcement structure or

complex and free-formed 3D topologies with three reinforcement directions, they all assist to achieve the significant reduction of CO₂-emissions in order to comply with the federal guidelines. Current manufacturing technologies for the production of rather simple shaped textile reinforcement show already high potential for a cost-effective and resource-efficient large scale production, such as the pultrusion process for one-dimensional reinforcement structures [8, 9] and the warp knitting technology for two-dimensional reinforcement structures [10–13]. Thus slightly curved and mesh reinforcements can be produced using this textile manufacturing technologies. New textile manufacturing technologies are needed in order to encounter the high wastage of expensive high-performance textile material during the manufacturing, to challenge the demand of fiber orientation according to the form-follows-force systematic or to reduce additional and redundant process steps. Along with innovative concepts for designing, modelling and constructing these new manufacturing technologies are able to establish construction methods for sophisticated and future-oriented buildings with a sustainable material-minimalism approach. These novel and comprehensive approaches towards a future-oriented building strategy is currently investigated in the Collaborative Research Center Transregio 280 (CRC/TRR280). This basic research project is a collaboration between two excellence universities in Germany, namely TU Dresden and RWTH Aachen. The motivation of this sophisticated project is to establish the constructing of future with the objective of a material minimized design based on carbon reinforced concrete. Novel and improved material compositions using interdisciplinary inspiration sources, such as the mathematic and biology, are supposed to attain load adapted fiber orientations of the high performance material carbon reinforced concrete. In order to bionically strengthen the concrete, the reinforcing carbon fiber structures needs to be arranged according the botanical role models and in a load adaptive way. Currently, there are not any appropriated material-efficient and cost-saving technologies aligning the fibers according the occurring courses of forces. Hence, the ability to process biologically inspired 3D textile reinforcement structures is crucial to fully utilize the potential of carbon concrete. This means, a new textile manufacturing technology must be developed to take advantage of the flexibility of textiles in dry condition to create complex, hierarchically structured and multiple branched textile topologies, such as in Figure 2. Various findings from the development of automated 3D coreless filament winding technology of Minsch et al. and from homologous robot-supported manufacturing technologies, such as the winding techniques by Michel et al. and Knippers et al., are taken into account [14–19].



Source: ITM

Figure 2: Exemplary presentation of a complex, multiple branched 3D textile structure on basis of carbon fibers for reinforcement purposes.

The subproject B01, as a substantial part of CRC/TRR280, will provide a fundamentally realigned, CAE-supported approach and a novel manufacturing technology to produce 3D textile reinforcements. Overall, the botanic-oriented fiber alignment, the finite element method (FEM) based designing and the optimizing algorithms used to generate the robot placement paths (machine control data) are taken into account in the development process.

Apart from the establishing of a design process to automatically create bionic and load adapted fiber reinforcement structures, the development of an intelligent 3D-roving placement rack (3D-RPR) is the key task towards the robot-supported fibre placement technology, which must take and safely fixate the carbon fibers strands (rovings) of the 3D textile topology. One specific feature of the developed 3D-RPR is the special capability taking rovings, which run out-of-plane (z-direction). This requirement enables the robot to flexible place the fibers in space with almost no limitation regarding fiber orientation or rather the potential risk of fiber slipping. However, the usage of the 3D-RPR is almost the last step on the value-added chain of manufacturing textile reinforcement structures for strengthening concrete components. The following section explains the methodological and constructive development process regarding the generic design procedure of the reinforcement structure and the novel 3D-RPR.

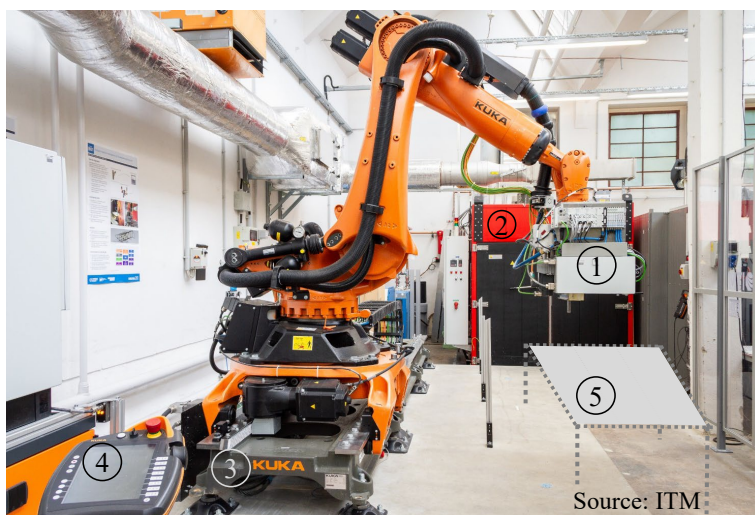
Materials and Methods

The carbon fiber multi-filament yarn used for preliminary investigations comply with the raw material of the approval textiles applied in the general type approval Z-31.10-182 [20]. The material specifications are shown in Table 1.

Table 1: Specification of material used for preliminary investigations.

Name of Material	Filament number [-]	Fineness [tex]	Tensile strength [MPa]	Tensile Modulus [GPa]
Tenax-J/E STS40	48,000	3200	4300	250

Figure 3 represents the current manufacturing technology on basis of an industrial 6-axis-robot with a range of 2100 mm [21]. The robot has the function to manipulate the fiber placement tool, where the drive technology benefits in general from its very high flexibility.



- ① Yarn placement tool for inline process:
 - Media storage
 - Impregnation media
 - Carbon Fiber
 - Roving impregnation
 - Deposition needle
- ② Convection furnace for consolidation and solidification
- ③ Linear unit for robot positioning
- ④ Robot control panel
- ⑤ Developed 3D-RPR

Figure 3: Current robot-supported technology for resource-saving and efficient yarn placement.

The generic process chain for the production of textile reinforcement structure (TRS) begins with the analysing and designing on basis of abstracted bionic structures (Figure 4). The biological groundwork as source of inspiration marks the starting point of the design process and the research activities. Here, special load transfer mechanism in fibrous plant structures must be identified, which are suitable to use the transfer load principles. For instance, peltate leaves, meaning leaves with the petiole more or less centrally attached to the underside of the lamina, serve as inspiration with its orientation of strengthening tissue in the transition area. Crucial scientific findings regarding the load transfer mechanisms could be done by analysing the plant zone from petiole to lamina is an important

junction, which provides the required stability and flexibility to resist a multitude of environmental, mechanical stresses.

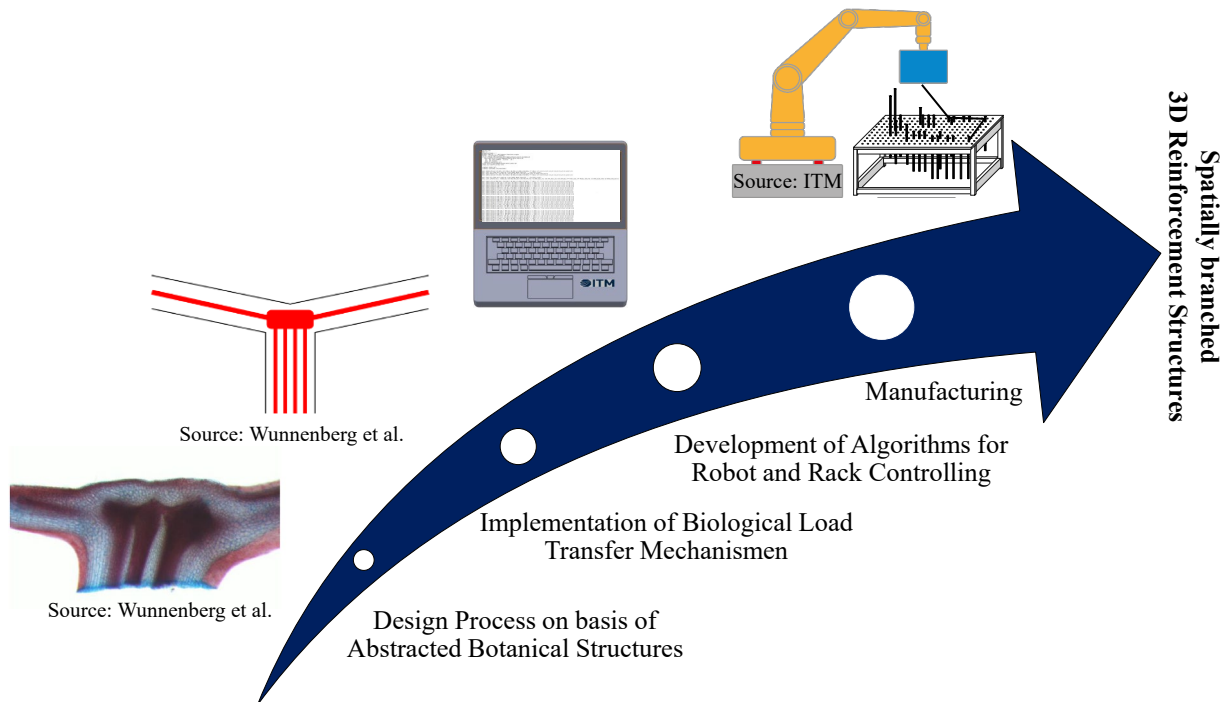


Figure 4: Generic process chain of design and manufacturing the textile reinforced structures according to provided load transfer mechanism from natural role model.

Development Process

The detailed investigation shows of Sacher et al.[22] and Wunnenberg et al.[23] several principles of how the strengthening tissue and thus the reinforcement fibers within the plant structure built. Figure 5 reveals the transition area of *Colocasia fallax* (C. fallax) and *Tropaeolum majus* (T. majus) as photographic and microscopic image. Subsequently, the generic process leads from the implementation of the biological load transfer mechanisms over the development of algorithms for the controlling of the yarn placement rack and the robot to the final manufacturing by means of an industrial 6-axis-robot.

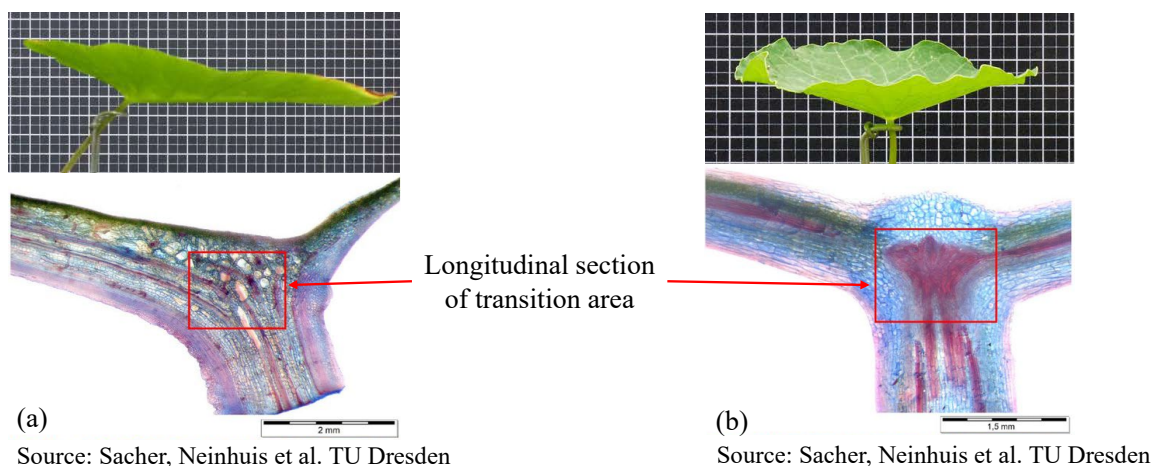


Figure 5: Comparison of peltate leaves of (a) C. fallax on the left and (b) T. majus on the right side. On top the individual leaves can be seen. The microscopic pictures of their transition area are shown below in longitudinal section [22, 23].

Even though, the gold standard in high productive manufacturing of textile reinforcement mats is currently set by the warp-knit technology, the production of hierarchically structured and branched

textile reinforcement topologies, which are strongly needed, can only be achieved by the unsurpassed flexibility of the robot-supported direct yarn placement technology and an appropriate, intelligent 3D-roving placement rack.

In order to match the demands of providing a load adapted fiber reinforcement structure by means of a CAE-supported designing with the requirements of a robot-supported fiber placement technology, the generic process chain, including designing and manufacturing, must be coordinated such that the fiber can be precisely placed and safely taken by the 3D-RPR according the structural reinforcement design. Figure 6 presents the computer-aided engineering process, which realize the design by several engineering tools, such as ANSYS Workbench and Matlab.

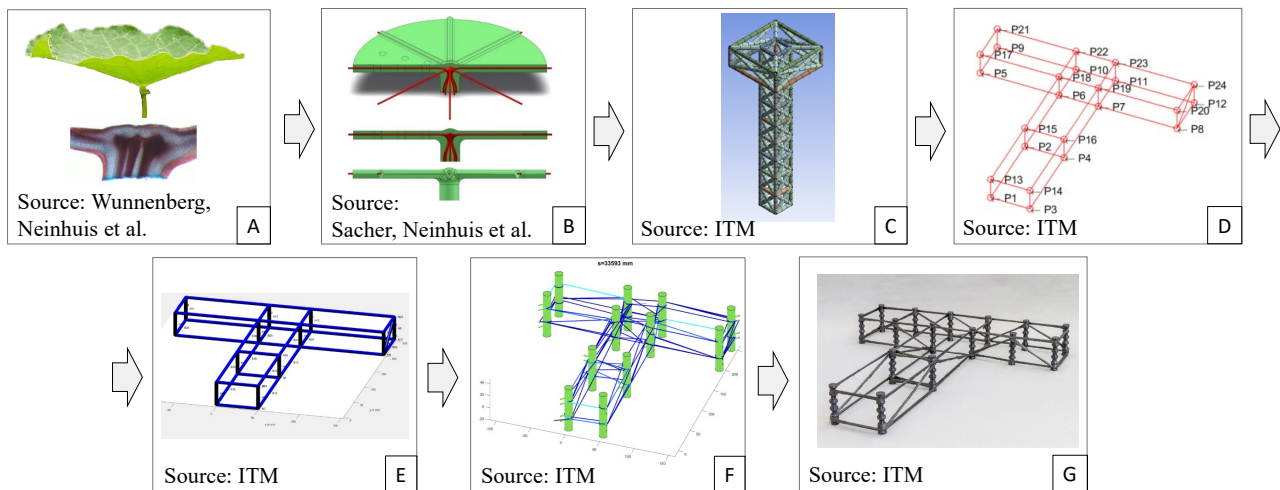


Figure 6: Computer-aided engineering process provides the structural design of the botanically inspired textile reinforcement topology.

As can be seen in illustration A, the biological role model is firstly considered with its individual strengthening tissue. By identifying of biological principles and abstracting the load transfer mechanisms, the findings are used to individually design the reinforcing textile topology (B). The FEM-supported consideration of the concrete components under a multitude of realistic load scenarios identifies the optimal fibre orientations for a comprehensive load collective (C). The most tensile stressed nodes are extracted and are used to automatically generate a new structural node model in MATLAB, which poses the basis for algorithm-based creation of the winding paths (D). The illustration E shows the setting of the boundary condition for the following calculation of the optimal winding paths. With the aid of a refined truss-like model with specific winding cores, which has to be considered during the robot travels, the winding path can be calculated. The calculated solution can be seen in graphic E. Subsequently, the robot-supported manufacturing technology can produce the 3D textile reinforcement structure (G) by means of generated machine control data.

Once the design process is almost ready-to-use, the robot-supported fiber placement technology and especially the 3D-roving placement rack needs to meet the requirements. Accordingly, the current robot-supported direct yarn placement technology must be empowered for manufacturing 3D textiles among the already realisable plain reinforcement mats. Hence, the development of a roving placement rack, which is able to take the rovings of 3D textile structures without restricting the windability, is essential in this research project.

In order to derive basic requirements for the novel roving placement rack for 3D structures, the current robotic driven fiber placement technology has been identified and preliminary investigations have been done, such as maximum yarn tension in order to get a minimum slack on the yarn of 1 mm. Another investigation dealt with the key problem of how the already placed yarn structure and the placement rack itself impedes the flexibility of manipulating the fiber placement tool. Therefore, a less complex reinforcement structure with branchings was manufactured in favor of pillar-like

concrete component (Figure 7). This preliminary test also poses an iteration for the development of the winding bodies, used to fix the textile structure as a part of the 3D-RPR.

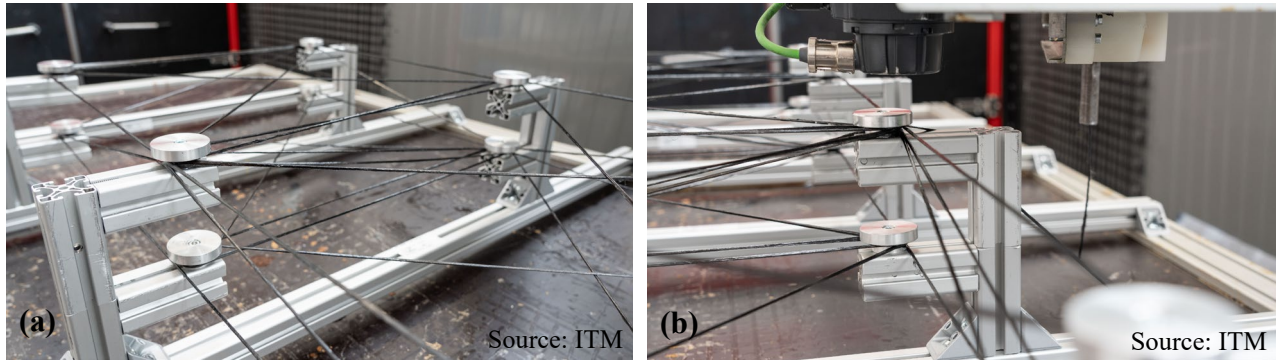


Figure 7: Manufacturing of a less complex branched reinforcement structure in the context of preliminary investigations.

The preliminary investigations helped to identify essential requirements among other specifications. Substantial requirements are for instance the geometry of the rack, the static-mechanical condition, the process temperature, the placement precision, the modularity of the rack system and the demoldability of the consolidated fiber reinforcement structure.

With reference to Figure 8, the intelligent roving placement rack must meet the bionic demands, by imaging the role model and thus the load transfer related fiber structure of the plant to the last detail. Basically, we need an intelligent roving placement rack with individually controllable placement points, which is engineered to model-faithfully take the rovings. Consequently, wherever the results of the computer-aided simulation reveals strongly stressed nodes, the 3D-RPR must be capable of drive out supporting bars with winding bodies to the needed winding points. As all tensile stressed nodes of the strained structure in addition to the nodes of the basic structure need a strengthening for tensile loads, the model-based design structure must resemble the structure to be produced. In order to implement this requirement the distance between the numerical nodes (finite element edge length) and the distance between the accessible winding/placement points in all directions is 150 mm. This condition enables model-faithfully production of the 3D textile reinforcement structure. The mentioned schematic illustration in Fig. 8 shows an unspecific course of load to clarify the compatibility between the design and the manufacturing process.

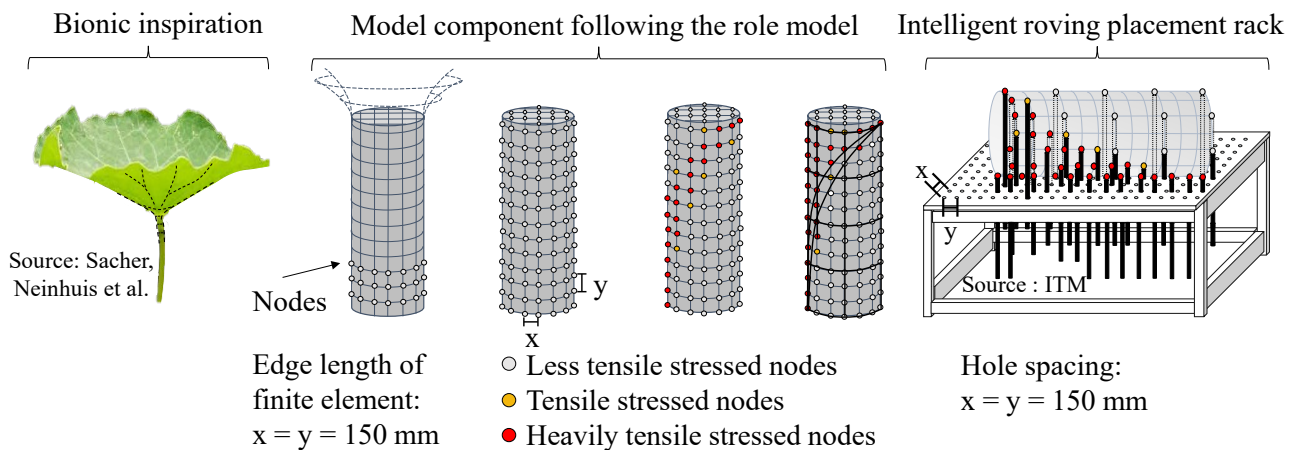


Figure 8: Schematic process flow to ensure compatibility by adjustment of the CAE-design method to the manufacturing by a model-faithful placement of rovings.

Results and Discussion

Following the development of the 3D-roving placement based on the already determined essential requirements is required in order to produce the textile reinforcement structure with high detailed quality. For this purpose, solution ideas for the different functionalities of the 3D-RPR have been evolved matching the given substantial criteria. Substantial categories of the 3D-RPR along with specific functionalities are the main basic rack, which provides the stability, the individually controllable supporting bars for the height adjustability, the winding bodies for fixation of the roving and the actuator technology for driving out the supporting bars. Finally, two efficient conceptual variants result from the morphological box with a little difference in the actuator technique (Figure 9). Variant A is shown on the left side and variant B on the right side. Linear actuators forming the x-y-z portal system drive variant A. Apart from the aluminium profiles based rack, the adjustable supporting bars, the panel with holes and the winding bodies, this concept contains linear brakes to fixate the supporting bars, once they are not control and so in an inactive condition. The variant B is powered by stepper motors, whereby each supporting bar has an own stepper motor for vertical movements. In contrast to and differing from the actuator technology of variant A, the concept shows a rotation lock as well as a spindle with a coupling. Afterwards the assessment of both technological variants happens with the help of the previously determined criteria from the list of requirements. Key criteria for my selection were the mentioned requirements weighted in accordance to its relevance. For instance, the demoldability of the final textile reinforcement has a higher rating than the current geometric dimension of the rack. In the end the preferred concept is the variant A with the linear actuators. This concept benefits from the property of decoupling by evolving two various construction – the positioning system and the deposition system. The upper deposition system can be decoupled and transferred into the furnace without harming the electric or producing increased installation efforts. The bottom positioning system remains fixed. The characteristic of only control and drive out required supporting bar without affecting the further roving placement process makes this technology intelligent.

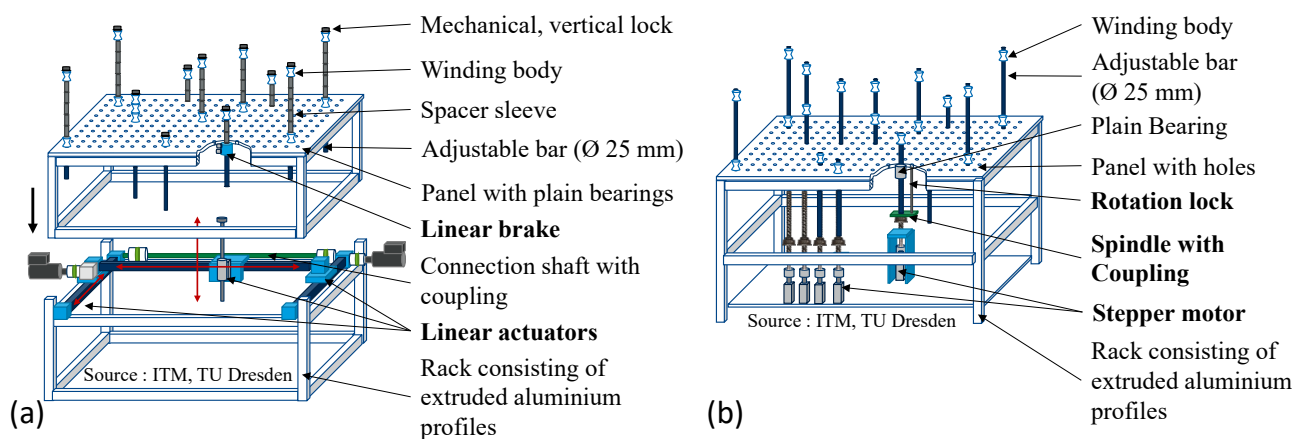


Figure 9: Concept variants derived by solutions from morphological box.

As a result, this elaborated intelligent and modular yarn placement system overcomes current challenges involved in the placing and stabilizing of spatial and highly branched reinforcement topologies during the manufacturing process. The Concept A as the preferred technology with the linear actuator to manipulate the supporting bars and so drive out the winding bodies shows high potential to diversely produce 3D textile reinforcement structures. We will be able to produce textile structures with a dimension of almost 3.0 m to 1.5 m to 0.8 m due to the feasible bar stroke of 800 mm. At the moment the dimension are mainly restricted by the consolidation technique and so by our convective furnace. In general this 3D-roving placement rack as a functional component of the robot-supported fiber placement technology is be upscaled easily. Figure 10 presents the final design of the concept variant A.

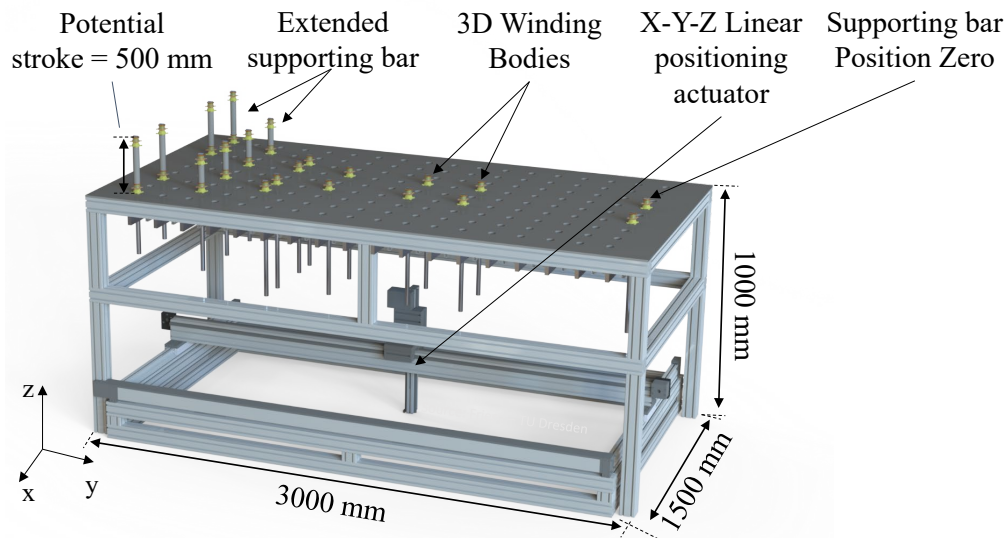


Figure 10: Preferred concept variant with individual linear actuators as drive technology for the different axis.

The preferred option of the 3D winding body can be seen in Figure 11. The focus of the development was on this crucial functional element, as it needs the ability to take yarns from different directions and thus various angles without causing a slipping off. Furthermore, the textile reinforcement structure has to non-destructively remove from the winding bodies after the consolidation step. Requirement criteria for the development have been the demoldability of textile structure, the reusability and the flexibility to take and fix fiber strands with a wide fiber angle spectrum. The dimension of the winding bodies of 50 mm in all direction facilitate the requirement of a model-faithful manufacturing with its nodes distance of 150 mm by stacking of the winding bodies or additional distance sleeves. The vertical wing technology for out-of-plane (3D) fiber orientations predestines this 3D winding body for complex structured textile topologies.

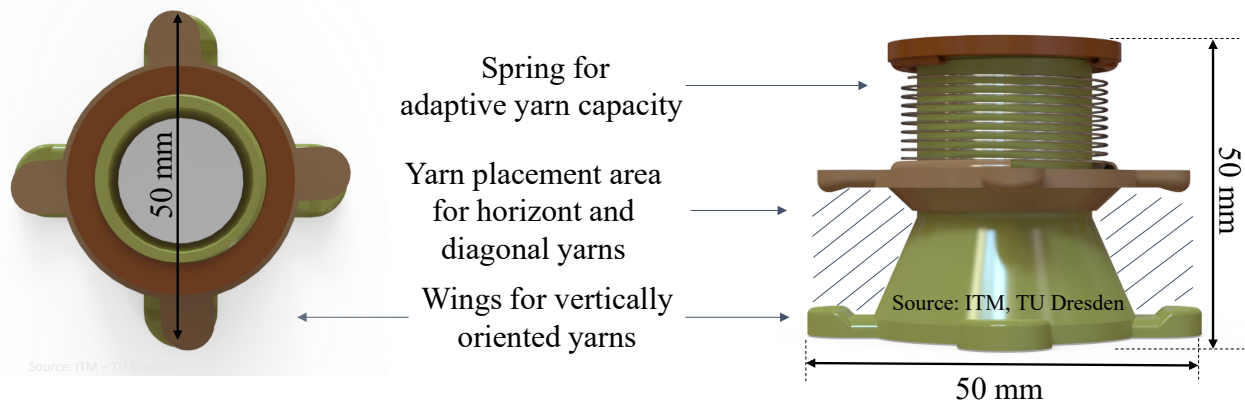


Figure 11: Developed 3D winding body with wings for vertical yarn orientation.

Building upon lessons learned from the development the final realization of the 3D-roving placement rack is still pending as well as the following fundamental validation and analyzation to optimize the roving positioning. Moreover it is necessary to optimize the yarn placement tool and develop the algorithms for the windability towards a fully 6-axis-flexibility.

Conclusion

The development approach considering novel methods and concepts for an intelligent modular yarn placement rack enables the manufacturing of complex and spatially branched three-dimensional textile reinforcement structures according to the principle of “form follows force”. These innovative 3D reinforcement topologies is the basis technology towards the realization of biologically inspired load adapted 3D-textile reinforcement structures. The developed 3D-RPR paves the way for novel concrete-based engineering principals with a material minimizing design ethos within the construction industry.

Acknowledgment

The project is funded by the Deutsche Forschungsgemeinschaft (DFG, German Research Foundation) – SFB/TRR280 (CRC/TRR280), Project-ID 417002380.



References

- [1] Beyond Zero Emissions, Rethinking cement : Zero carbon industry plan. Fitzroy, Victoria : Beyond Zero Emissions Inc, 2017
- [2] European Commission, Roadmap to a Resource Efficient Europe. COM(2011) 571 final. Brussels, 20.9.2011
- [3] European Commission, On Resource Efficiency Opportunities In The Building Sector. COM(2014) 445 final. URL <https://ec.europa.eu/environment/eussd/pdf/SustainableBuildingsCommunication.pdf>. – Last Update: 2014-07-01 – Inspection Date: 2021-03-11
- [4] A. Ruuska, T. Häkkinen, Material Efficiency of Building Construction, In: Buildings 4 (2014), No. 3, pp.266–294
- [5] Iurie Vakaliuk, C3 CUBE-House : Rendered Design Draft. URL <https://www.henn.com/en/projects/science-education/c3-cube-tu-dresden>
- [6] Bundesministerium für Umwelt, Naturschutz und nukleare Sicherheit, Klimaschutzplan 2050 : Klimaschutzpolitische Grundsätze und Ziele der Bundesregierung. 1. Auflage, Stand November 2016. Berlin : Bundesministerium für Umwelt, Naturschutz, Bau und Reaktorsicherheit, 2016
- [7] Umweltbundesamt, Dekarbonisierung der Zementindustrie. URL https://www.umweltbundesamt.de/sites/default/files/medien/376/dokumente/factsheet_zementindustrie.pdf. – Last Update: 2020-02-01
- [8] K. Minchenkov, A. Vedernikov, A. Safonov, I. Akhatov, Thermoplastic Pultrusion: A Review, In: Polymers 13 (2021), No. 2
- [9] A. Schumann, M. May, M. Curbach, Carbonstäbe im Bauwesen, In: Beton- und Stahlbetonbau 113 (2018), No. 12, pp.868–876. URL <https://onlinelibrary.wiley.com/doi/full/10.1002/best.201800077>
- [10] L. Hahn, S. Rittner, C. Cherif, Fertigungstechnologie zur Herstellung von vorgeformten textilen Bewehrungen. : Vortrag, Bd. 10. In: TUDALIT e. V.; C³ - Carbon Concrete Composite e.V. (Hrsg.): 10. Carbon- und Textilbetontage. Dresden, 2018
- [11] V. Sankaran, A. Younes, T. Engler, C. Cherif, A novel processing solution for the production of spatial three-dimensional stitch-bonded fabrics, In: Textile Research Journal 82 (2012), No. 15, pp.1531–1544

-
- [12] V. Sankaran: Development of a novel multiaxial warp knitting based technology for production of 3D near net shape preforms. München, Technische Universität Dresden; Verlag Dr. Hut. Dissertation
 - [13] V. Sankaran, S. Rittner, L. Hahn, C. Cherif, Development of multiaxial warp knitting technology for production of three-dimensional near net shape shell preforms, In: Textile Research Journal 87 (2017), No. 10, pp.1226–1241
 - [14] N. Minsch, M. Müller, T. Gereke, A. Nocke, C. Cherif, Novel fully automated 3D coreless filament winding technology, In: Journal of Composite Materials 52 (2018), No. 22, pp.3001–3013
 - [15] N. Minsch, Verfahrens- und Methodenentwicklung für die generative Fertigung von komplexen Leichtbaustrukturen in Hybridbauweise : Process- und method development for the generative manufacturing of complex lightweight structures in hybrid design. Dissertation. Dresden : epubli, 2018
 - [16] N. Minsch, M. Müller, T. Gereke, 3D truss structures with coreless 3D filament winding technology. London, England : SAGE Publications, 2019
 - [17] N. Minsch, F. H. Herrmann, T. Gereke, A. Nocke, C. Cherif, Analysis of Filament Winding Processes and Potential Equipment Technologies, In: Procedia CIRP 66 (2017), pp.125–130
 - [18] J. Knippers, V. Koslowski, J. Solly, T. Fildhuth, Modular Coreless Filament Winding For Lightweight Systems In Architecture. In: CICE (Hrsg.): CICE 2016 8th International Conference on Fibre-Reinforced Polymer (FRP) Composites in Civil Engineering. Hong Kong, 2016
 - [19] A. Michel, K. Zernsdorf, V. Mechtcherine, Mineral-bonded carbon fiber reinforcement for novel concrete construction technologies. In: Institute für Textilmaschinen und Textile Hochleistungswerkstofftechnik (Hrsg.): Proceedings: International Textile Conference 2019 : ADDITC 2019. Dresden, 2019, pp.84
 - [20] Allgemeine bauaufsichtliche Zulassung/ Allgemeine Bauartgenehmigung Z31.10-182. 2021-06-01. abZ+aBG: CARBOrefit - Verfahren zur Verstärkung von Stahlbeton mit Carbonbeton
 - [21] M. von Zuben, C. Cherif, Robot based Technology for the Production novel Resource-Saving and Cost-Efficient Textile Reinforcement Structures for Direct further Proceedings into Prefabricated Parts. In: AUTEX2019 (Hrsg.): 19th World Textile Conference on Textiles at the Crossroads, 2019
 - [22] M. Sacher, T. Lautenschläger, A. Kempe, C. Neinhuis, Umbrella leaves-Biomechanics of transition zone from lamina to petiole of peltate leaves, In: Bioinspiration & biomimetics 14 (2019), No. 4, pp.46011
 - [23] J. Wunnenberg, A. Rjosk, C. Neinhuis, T. Lautenschläger, Strengthening Structures in the Petiole-Lamina Junction of Peltate Leaves, In: Biomimetics (Basel, Switzerland) 6 (2021),No. 2

Textile-Based 3D Truss Reinforcement for Cement-Based Composites Subjected to Impact Loading – Part II: *In Situ* Stress Analysis under Quasistatic and Dynamic Tensile Loading

Hung Le Xuan^{1,a*}, Duy M.P. Vo^{1,b}, Andreas Nocke^{1,c}, Cornelia Sennewald^{1,d}
Gerald Hoffmann^{1,e} and Chokri Cherif^{1,f}

¹Faculty of Mechanical Science and Engineering, Institute of Textile Machinery and High Performance Material Technology (ITM) at Technische Universität Dresden (TUD), Germany

^ahung.le_xuan@tu-dresden.de, ^bduy.vo@tu-dresden.de, ^candreas.nocke@tu-dresden.de

^dcornelia.sennewald@tu-dresden.de, ^egerald.hoffmann@tu-dresden.de,

^fchokri.cherif@tu-dresden.de

Keywords: in-situ-sensors, piezoresistivity, structural health monitoring (SHM), textile reinforced concrete, SHCC, digital image correlation

Abstract. This research focuses on the electromechanical strain-sensing behaviour of steel wires on the fiber and composites scale. The electromechanical properties are investigated by using a uniaxial fiber tensile test with a simultaneous electrical resistance measurement. Further, this work conducts a comprehensive stress analysis of textile reinforced concrete (TRC) specimen in quasistatic and dynamic tensile tests by using integrated steel wires in a textile 3D-weaving reinforcement as piezoresistive in-situ-sensors. The results are compared to optical strain measurements using digital image correlation (DIC). The acquisition and analysis of the electrical resistance changes of the steel wire sensors enable an in-situ stress analysis as well as a better understanding of the mechanical response of the TRC specimen under different loading scenarios.

Introduction

Recently, the demand of smart composites [1] and the application of high-performance textile reinforcements in the construction industry is steadily increasing. Especially its high specific mechanical properties and chemical resistance allow new building approaches and designs while fulfilling highest requirements regarding safety, durability and sustainability [2]. To ensure the functionality and the resistance of TRC structures against short-term dynamic stress scenarios e.g. earthquake, natural disasters or a car crash, a deep understanding of the impact-induced stresses within the TRC is required.

One commonly used approach for the detection of structural damage are structural health monitoring (SHM) systems, which enable the in-situ acquisition of material and/or geometric property changes. The majority of conventional SHM systems are still too costly, time-consuming in their usage and often not structural compatible or integrated, which can lead to a degradation of the load-carrying capacity of the structure. To overcome these limitations the materials of the textile reinforcements are not only used because of their excellent structural properties and durability, but also because of additional functional properties (e.g. strain or damage sensing). Textile based sensors enable a simultaneous time- and costsaving implementation during the textile-technological manufacturing process. [3, 4]

Furthermore, they provide an in-situ measuring capability, which enable strain measurements within the composite itself. The results can be used for the analysis of the mechanical behaviour of the textile reinforcement. The strain sensing capability of a material is given due to the direct dependence of the electrical resistance (piezoresistivity) and its strain state. If a tensile stress is applied on the sensor material (Fig. 1a), the electrical resistance is increased caused by the change of geometrical and material properties. However, a compressive stress (Fig 1b), will cause a decrease. This behaviour is reversible in the elastic range of the material. Therefore, the electrical resistance will return to its original value after the load is removed [5] (Fig 1c).

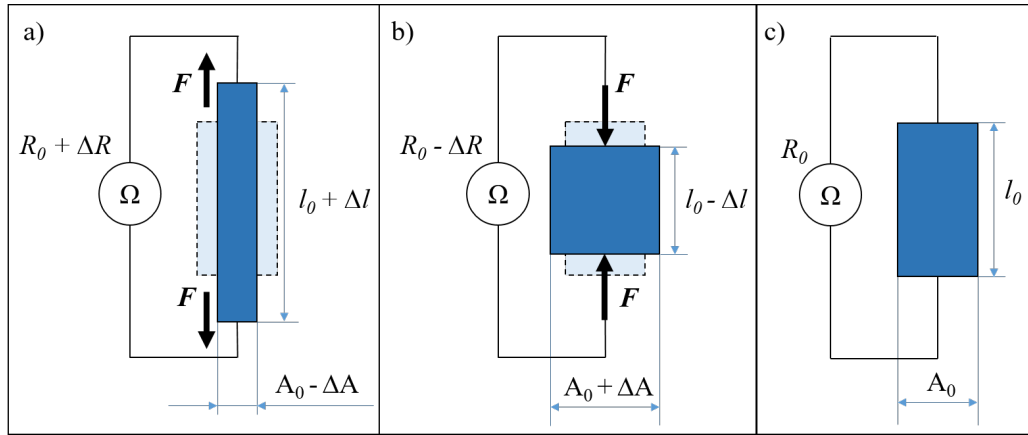


Fig. 1: Mechanism of piezoresistive sensors with ΔR as electrical resistance change, Δl as sensor length deformation, ΔA as cross-section change and R_0 , l_0 or A_0 as initial values respectively, (a) sensor under tension, (b) sensor under pressure, (c) initial state

The gauge factor (GF) is defined as the fractional change on the electrical resistance per unit strain and can be determined according to Eq. 1 [6]. Usually, it is referred to represent the sensitivity of the sensor under applied strain.

$$GF = \frac{\Delta R/R_0}{\Delta l/l_0} = \frac{\Delta R/R_0}{\varepsilon}, \quad (1)$$

where ΔR is the electrical resistance change, R_0 is the initial electrical resistance, Δl is the sensor length deformation, l_0 is the initial sensor length at zero strain and ε is the applied strain.

Materials and Methods

Materials. Two types of stainless steel wires (1.4301, Dahmen GmbH & Co. KG, Germany) with a diameter of 0.8 mm were used as in-situ-sensors as well as for the 3D-textile weaving reinforcement. The tensile strength and strain capacity of the high ductile (S-HD) and high strength steel (S-HS) wire were 796 MPa and 84 % or 1110 MPa and 5 %, respectively. Additionally, carbon rovings with 800 tex manufactured by Teijin Carbon Europe GmbH, Germany were coated with a low-viscosity styrene-butadiene rubber based coating (Lefasol VL 90/1, Lefatex Chemie GmbH, Germany) and textile technologically integrated in the weaving process. To ensure the electrical insulation of the steel wire sensors to the textile reinforcement itself, an epoxy resin coating (MGS® RIMR 135/RIMH 137, Hexion, USA) was selectively applied.

The fine-grained cementitious matrix for the tested TRC specimen was specifically designed for high-strength strain-hardening cement-based composite (SHCC), being made with short HDPE fibers (DSM, Netherlands) with a diameter of 0.02 mm and a fiber length of 6 mm. This SHCC matrix was previously investigated in [7, 8] under quasi-static and impact tensile loading. The mixture recipe is listed in Table 1 and contains a high content of cement as well as silica fume as additional binder.

Table 1: Mixture composition of the high strength, fine-grained cementitious matrix

Components	kg/m ³
CEM I 52.5R-SR3/NA	1460
Silica Fume	292
Quartz Sand (0.06-0.2 mm)	145
Super Plasticizer	45
Water	315
HDPE Fibres (Dyneema®)	10

Electromechanical characterization. The sensor behaviour was evaluated on the fiber level in electromechanical investigations by conducting uniaxial quasistatic and cyclic tensile tests (zwickiLine Z2.5, ZwickRoell GmbH & Co. KG, Germany) combined with a simultaneous resistance

measurement (Keithley DAQ6510, Keithley Instruments, USA) via four-point-probe method (Fig. 2). The testing parameters are summarized in Table 2. Using the cyclic testing procedure, the high strength steel wire was tested under strains of 0.5 %, 1 %, 1.5 % and 2 %, whereas the high ductile steel wire was tested using strain states of 2 %, 4 %, 6 %, 8 % and 10 %.

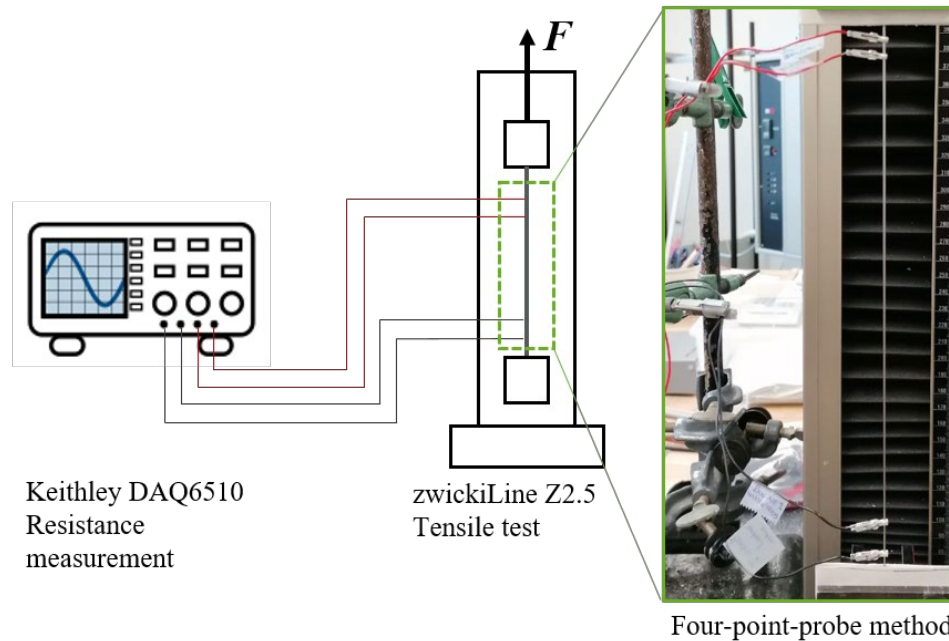


Fig. 2: Test-setup for the quasistatic and cyclic electromechanical investigation of the steel wire sensor using a tensile testing machine and resistance measurement via four-point probe method

Table 2: Testing parameters for the electromechanical characterization

Testing parameters	Value	Unit
Clamping length	250	mm
Preload force	5	N
Testing speed	1	mm/s
Sampling rate (for force and resistance measurement)	10	Hz

Textile reinforcement. The woven 3D-textile reinforcement was manufactured by using the above described materials on a modified rapier weaving machine (Lindauer DORNIER GmbH, Germany) with a linear take-off (Kieselstein GmbH, Germany). The steel wire sensors were bent into a U-shape, coated with epoxy resin and manually inserted into the 3D-textile reinforcement, so that each specimen was functionalized with two in-situ-sensors with an active sensor length of 10 mm.

TRC specimens – manufacturing and testing. The TRC specimen were produced by using a lamination technique. The first layer was realized by casting a SHCC layer into the mold. The 3D-textile reinforcement was then positioned and pressed into the SHCC matrix to ensure a central and complete embedment. Subsequently, a second layer of the matrix was cast on top followed by levelling and smoothing. After 24 hours, the specimens were demolded and sealed in plastic sheets. The final curing was carried out in a climatic chamber with a constant temperature of 20 °C and relative humidity of 65 %. The cured specimens were then cut to size with a final length, width and thickness of 100 mm, 40 mm and 25 mm, respectively and glued to adapters for the tensile test. The free deformation length is about 50 mm. Additionally, a speckle pattern was applied for an optical deformation measurement using DIC.

The parameters for both, quasistatic and dynamic tensile test are listed in Table 3. In the quasistatic regime, the acquisition of the electrical resistance change of the in-situ-steel wire sensors was realized using the same setup as depicted in Fig. 2. For the dynamic tensile test, an acquisition system with a higher sampling rate was required. The operating principle is shown in Fig. 3 and is based on a Wheatstone quarter-bridge. The measuring device provides two internal resistances R_1 , R_2 and a compensation of the lead resistances R_L . The Wheatstone bridge was completed by the strain

dependent steel wire resistance $R_0(\epsilon)$ and a potentiometer R_p , that was used for the bridge balancing. Whenever the electrical resistance of the steel wire changed caused by the applied strain, the bridge voltage V_B changed accordingly. The output was a ratio between V_B and the excitation voltage V_{EX} (2.5 V).

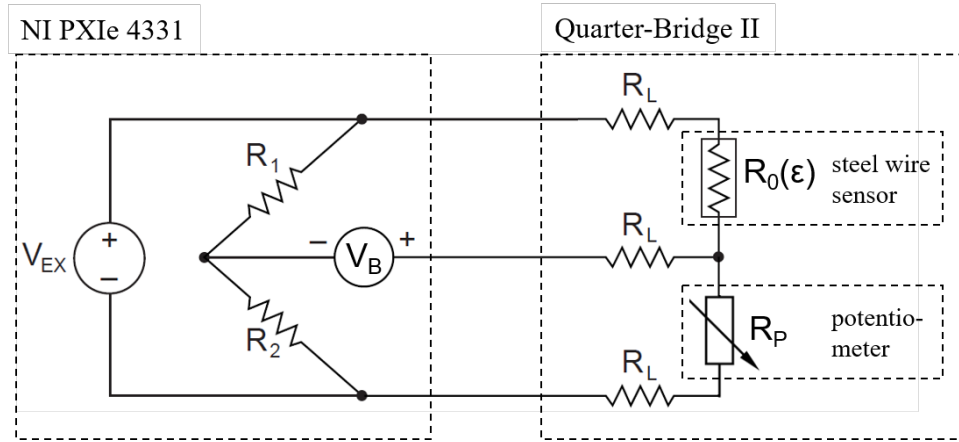


Fig. 3: Operating principle of the NI PXIe 4331 system; Wheatstone quarter-bridge II where R_1 , R_2 is the internal bridge resistors, R_L is the lead resistances, $R_0(\epsilon)$ is the initial resistance of the steel wire sensor, R_p is the potentiometer, V_{EX} is the excitation voltage and V_B is the bridge voltage [9]

Table 3: Parameters for the tensile test of the TRC specimens

	Quasistatic	Dynamic
Tensile testing machine	Instron 8501 (Instron Deutschland GmbH, Germany)	Zwick HTM5020 (ZwickRoell GmbH & Co. KG, Germany)
Testing speed	0.05 mm/s	10 m/s
Displacement measurement	Linear variable differential transformer (LVDT)	Movement of the transverse
Sensor signal acquisition system	Keithley DAQ6510 (Keithley Instruments, USA)	NI PXIe 4331 (National Instruments, USA)
- Sampling rate	10 Hz	102 000 Hz
Camera system	Nikon Z6 (Nikon Europe BV, Netherlands)	Photron SA-X2 (Photron Deutschland GmbH, Germany)
- Frame rate	0.5 FPS	67500 FPS

Results

Electromechanical characterization. The results of the quasistatic electromechanical investigation of both steel wire types are depicted in Fig. 4. It can be observed that the data points show a low scattering and follow a linear trend. With a linear regression analysis, a function for the regression line can be derived. The Eq. 1 can be used to determine a gauge factor of $GF_{S-HS} = 2.16$ and $GF_{S-HD} = 2.14$ for both the high strength (Fig. 4a) and high ductile (Fig. 4b) steel wire, respectively. For further electromechanical investigations, a cyclic testing procedure was conducted. Fig. 5a and b show the electrical resistance change and correlated strain during the cyclic tests for the high strength and high ductile steel wire.

A good sensing capability and correlation can be observed. During the loading process, an increase of the applied strain also results in an increase of the electrical resistance and vice versa. If the results are plotted in the same way as in Fig. 4, a nearly linear sensor behaviour can be observed for both steel wire types in a strain range of $0 \% \leq \epsilon \leq 2 \%$ (Fig. 5c and d). As expected the maximum strain sensing capacity of the high ductile steel wire is much higher because of its higher strain capacity. However, in cyclic loading scenarios above $\epsilon > 2 \%$ it can be observed, that the electrical resistance is not decreasing with decreasing strains, due to high plastic deformations. Therefore, the strain

sensing capability is limited to only increasing strains. These type of sensors can be used in areas, where a high deformation is expected, e.g. near the impact location.

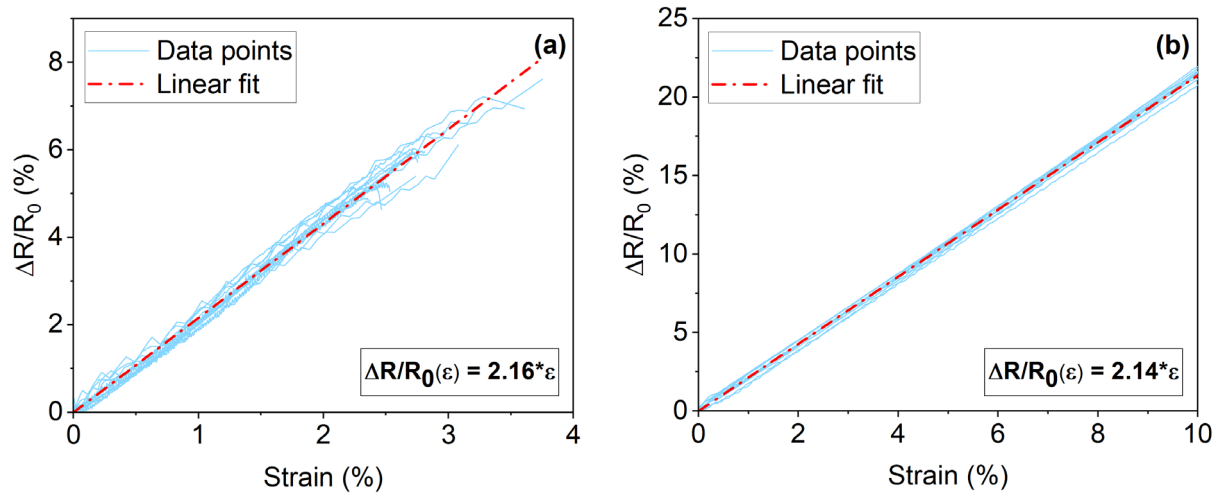


Fig. 4: Electrical resistance change of both steel wire types as a function of the applied strain for (a) high strength and (b) high ductile steel wire under quasistatic loading

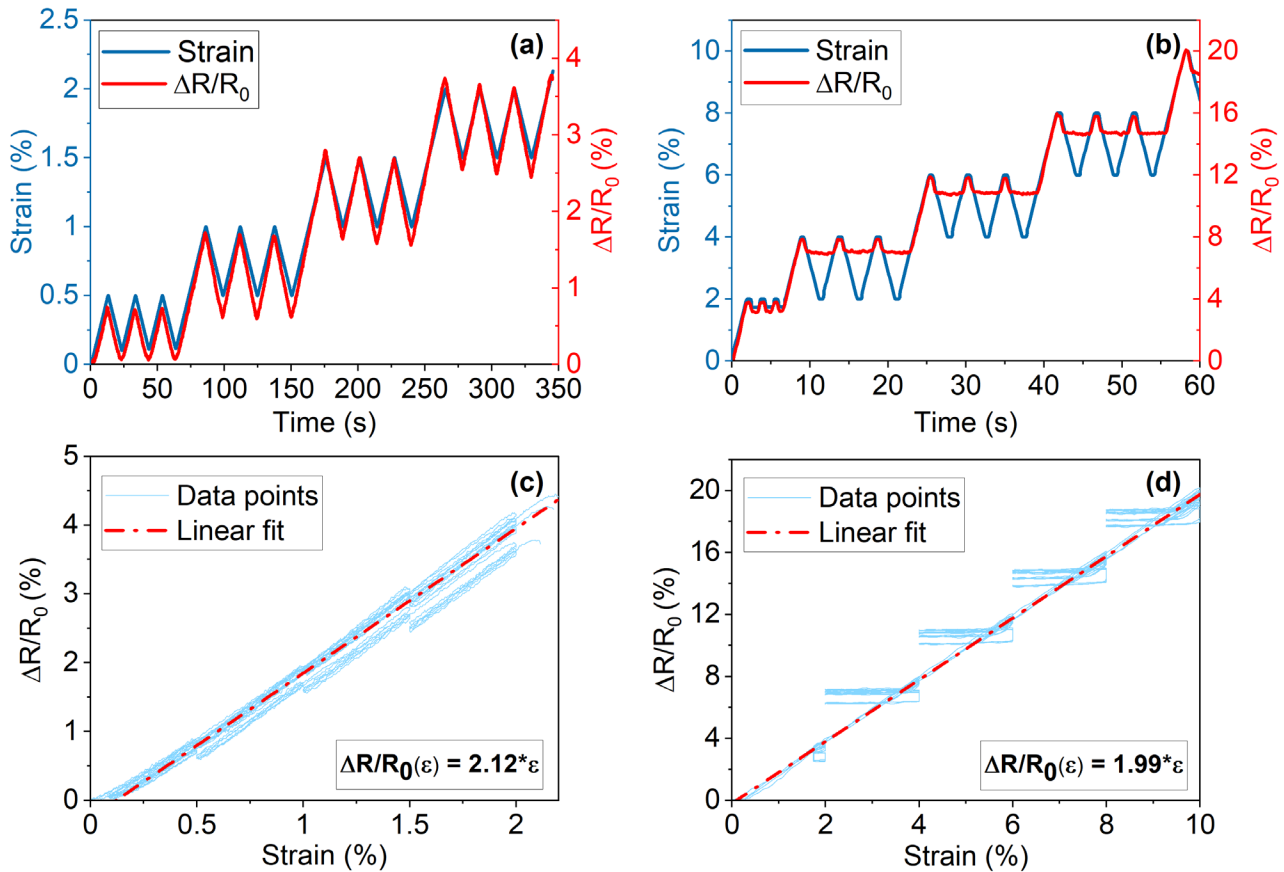


Fig. 5: Piezoresistive sensing behaviour of the (a) high strength and (b) high ductile steel wire under cyclic loading at different strains with three cycles at each strain state; electrical resistance change as a function of the applied strain for the (c) high strength and (d) high ductile steel wire under cyclic loading

A gauge factor of $GF_{S-HS} = 2.12$ and $GF_{S-HD} = 1.99$ can be calculated using Eq. 1. It can be seen, that the estimated gauge factor is approximately the same for both steel wire types and in both testing procedures. Only the gauge factor of the high ductile steel wire, which was calculated using only the increasing strain data points, is lower in the cyclic compared to the quasistatic loading. This is caused by the high plastic deformation and the resulting hysteresis.

Evaluation of the steel wires as strain sensor in TRC under quasistatic loading. An exemplary TRC specimen with a schematic drawing of the steel wire sensor positions is shown in Fig. 6a. The

front contained the speckle pattern for the DIC, whereas both the sensor ends and lead wires were on the back of the specimen. The Fig. 6b depicts the results of the quasistatic tensile test and the sensor measurements. In all experiments, it was observed, that the resistance of the upper sensor decreased slightly after the specimens were stressed. It is to be assumed, that this is because of the tensile loading starting at the upper adapter, causing minor movements in the lead wires.

In phase I (pre stress-strain peak), a linear increase of the stress-strain curve can be observed. At the marked point P1, a first smaller crack was formed, which also can be seen in the sudden decrease of the electrical resistance of the lower sensor. Consequently, both sensor signals are increasing steeply up until point P2, which is an indicator that the applied stress was now also carried by the whole 3D-textile reinforcement (Fig. 6c). At an approximate strain of 0.8 %, a major macro crack was observed at a stress of 6 MPa at the lower part of the specimen (Fig. 6d).

The phase II (post stress-strain peak) is characterized by multiple cracking of the SHCC-matrix (point P3 visualized in Fig. 6e) and pullout of the 3D-textile reinforcement, which can be identified by the constant stress level even after the matrix failed. This is realized by crack-bridging effects, caused by the short fibres and 3D-textile reinforcement.

Furthermore, it can be seen that the signal of the lower sensor is nearly constant after P3, which indicates a pullout behaviour and a structural deformation of the 3D-textile reinforcement. However, the upper sensor signal slightly increases, which shows a remaining stress loading capacity of the 3D-textile reinforcement near the upper sensor.

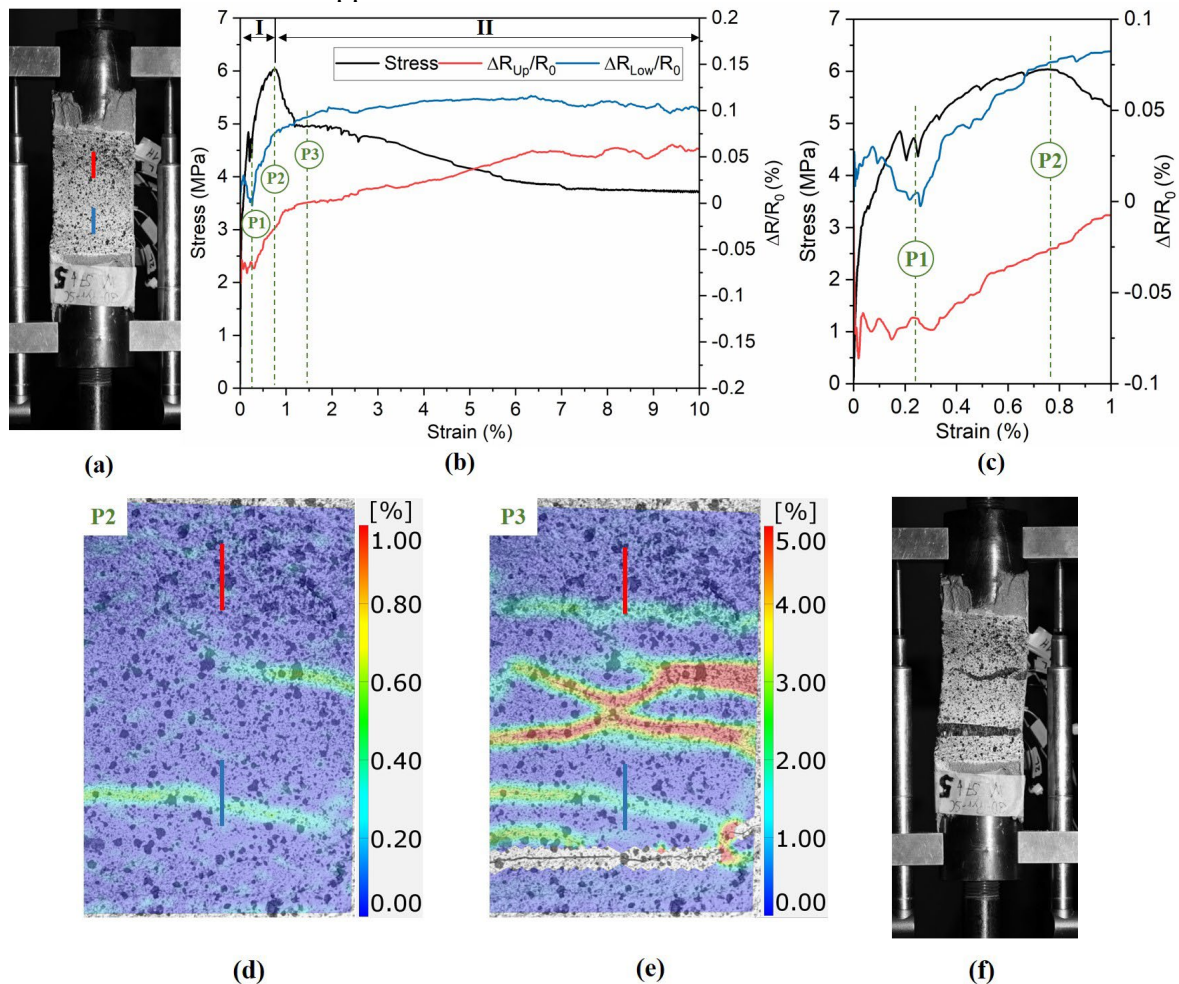


Fig. 6: (a) TRC specimen under quasistatic loading with a schematic drawing of the sensor positions, (b) stress-strain curve with the acquired electrical resistance change of the sensors, (c) enlarged phase I (pre stress-strain peak), optical crack analysis using DIC images at strain step (d) P2 and (e) P3, (f) final crack-pattern of tested TRC specimen

The final crack pattern of the TRC specimen is seen in Fig. 6f. By using the identified gauge factor from the electromechanical characterization and Eq. 1, the in-situ-sensors detected a maximum strain of 0.05 % for the upper and 0.07 % for the lower sensor, respectively. However, the DIC analysis

showed an integrative strain of 1.19 % and 1.83 % over the upper and lower sensor. These values were obtained by averaging the strain values over the sensor length of 10 mm.

Comparing the different strain measurements, it can be seen, that both results show the same trend of a higher deformation in the lower part of the specimen, but differentiate in their magnitude. The strain measured optically on the surface is not equal to the strain measured by the in-situ sensors within the textile. It can be concluded that the high potential of the load bearing capacity of the 3D-textile reinforcement is not exploited yet. However, the structural deformation capability that is given by the 3D-textile reinforcement has a significant impact on an improved ductile failing behaviour of the TRC specimen.

Evaluation of the steel wires as strain sensor in TRC under dynamic loading. Fig. 7a shows the results of an exemplary TRC specimen under dynamic loading. The testing environment, the specimen configuration and the sensor position were the same as in the quasistatic testing regime (Fig. 7b). In general, it can be observed, that the ultimate tensile strength is about 22.7 ± 6.6 MPa (12 specimen tested), which is approximately 2 to 4 times higher than the obtained results of quasistatic tensile loading. This phenomenon is caused by the strain rate dependency of the material properties [10–12].

Furthermore, the acquired and filtered sensor strain data are visualized. Over all experiments, both sensors (S_{Up} and S_{Low}) have shown a similar behaviour. In this testing series, the first macro crack is always located on the upper part of the specimen, near the stress-introducing adapter. Spatially, it can be derived, that there was a higher stress intensity on the upper part of the specimen and therefore 3D-textile reinforcement, which caused a higher sensor strain in the upper sensor. The maximum sensor strain of S_{Up} was 0.94 % compared to the slightly lower value of S_{Low} with 0.89 %. The obtained integrative strain values of the DIC analysis were 0.43 % and 0.40 % for the upper and lower sensor, respectively. It can be seen, that in the dynamic testing scenario, the different strain measurements show a similar order of magnitude in comparison to the quasistatic regime.

It can be concluded, that the mechanical response of both the composite and textile reinforcement were similar to the dynamic loading stresses. Due to the high strain rate, the mechanical properties of the materials are increasing, causing an overall improved composite behaviour e.g. by an increased mechanical anchorage of the 3D-textile reinforcement to the SHCC matrix. By evaluating the high-speed camera images, a wave propagation starting from the stress-inducing adapter was observed.

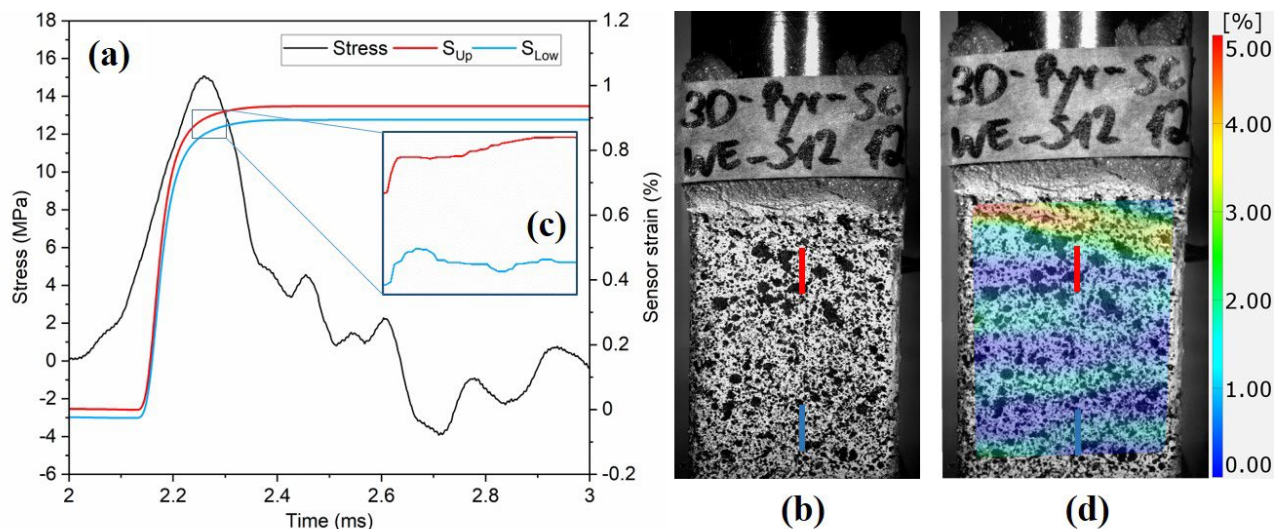


Fig. 7: (a) stress-time curve with sensor strain signals, (b) TRC specimen under dynamic loading with a schematic drawing of the sensor positions, (c) enlarged representation of the sensor behaviour after the stress-peak, (d) crack analysis using DIC to visualize the crack pattern

After the first macro crack, a “snap-back”-effect of the specimen was visible. The tensile stress transforms into a pressure wave. After reaching the lower end of the specimen, the wave transforms back to a tensile wave. Since the snap-back distance was negligibly small, the change in the sensor

strain was also marginal (Fig. 7c). The failing behaviour of the specimen is once again characterized by a multiple cracking pattern even after the first macro crack (Fig. 7d).

Summary

A comprehensive stress analysis of TRC specimen using in-situ steel wire sensors as well as optical measurements was presented. Fundamentally, an electromechanical characterization was conducted to examine the strain sensing capacity of both steel wire types in quasistatic and cyclic uniaxial tensile tests. A gauge factor in the range of $GF = 2.00 - 2.16$ was determined. Both steel wire types showed a near linear and similar sensing behaviour up until a strain of $\varepsilon \leq 2\%$. For higher strain states $\varepsilon > 2\%$, e.g. near the impact location, the high ductile steel wire can be used, but with the limitation to measure only increasing stresses (high hysteresis).

The integration of in-situ sensors in the 3D-textile reinforcement enabled a structural compatible, in-situ strain sensing capability within the TRC specimen. Quasistatic and dynamic tensile tests were conducted to investigate the functionality of the steel wires as in-situ-sensors in TRC under different loading scenarios. In the quasistatic regime, the sensor signals offered additional information about the behaviour of the 3D-textile reinforcement under loading. It was seen, that the short fibers were activated earlier than the 3D-textile reinforcement. By analysing the strain states up until $\varepsilon \leq 0.5\%$, a multiple cracking behaviour was observed, which is the result of the crack bridging of the short fibers. This state can be seen in the first part of both sensor signals, characterized by an fluctuating behaviour. The two different sensor positions also enabled spatial information such as either pullout or load carrying behaviour. It could be concluded that the high load bearing capacity of the 3D-textile reinforcement was not exploited yet.

The evaluation of the in-situ-sensors signals in the dynamic stressed TRC specimen showed, that the upper part of the specimen was stressed with a higher intensity, due to higher strain values measured by the upper sensor. In addition, the first macro crack was always observed at the upper part of the specimen. Furthermore, the stress-induced wave through the specimen was visible by analysing the high-speed camera images and was shown by small changes in the sensor strain signal.

The combined usage of in-situ-sensors and DIC enable a deeper understanding of the mechanical behaviour of the textile reinforcement and specimen itself. The comparison of both strain measurement approaches revealed that the acquired strains are more comparable to each other with increasing strain rates.

In future works, the acquired sensor information will be used to further develop the textile reinforcement, considering aspects of mechanical safety under different loading conditions as well as sustainability.

Acknowledgment

The authors express their gratitude to the Deutsche Forschungsgemeinschaft (DFG – German Research Foundation) for the financial support provided in the framework of the Research Training Group GRK 2250 “Mineral-bonded composites for enhanced structural impact safety”, project number 287321140.

References

- [1] M. Ashir, M. Vorhof, A. Nocke, Influence of thickness ratio and integrated weft yarn column numbers in shape memory alloys on the deformation behavior of adaptive fiber-reinforced plastics, *Composite Structures* 215 (2019) 493–501.
- [2] C³ - Carbon Concrete Composite e.V, TUDALIT e. V. (Eds.), 11. Carbon- und Textilbetontage, 2019.
- [3] E. Haentzsch, R. Mueller, M. Huebner, T. Ruder, R. Unger, A. Nocke, C. Cherif, Manufacturing technology of integrated textile-based sensor networks for in situ monitoring applications of composite wind turbine blades, *Smart Mater. Struct.* 25 (2016) 105012.

-
- [4] E. Häntzsche, A. Matthes, A. Nocke, C. Cherif, Characteristics of carbon fiber based strain sensors for structural-health monitoring of textile-reinforced thermoplastic composites depending on the textile technological integration process, *Sensors and Actuators A: Physical* 203 (2013) 189–203.
 - [5] O. Galao, F.J. Baeza, E. Zornoza, P. Garcés, Strain and damage sensing properties on multifunctional cement composites with CNF admixture, *Cement and Concrete Composites* 46 (2014) 90–98.
 - [6] D.D.L. Chung, Piezoresistive Cement-Based Materials for Strain Sensing, *Journal of Intelligent Material Systems and Structures* 13 (2002) 599–609.
 - [7] I. Curosu, V. Mechtcherine, O. Millon, Effect of fiber properties and matrix composition on the tensile behavior of strain-hardening cement-based composites (SHCCs) subject to impact loading, *Cement and Concrete Research* (2016) 23–35.
 - [8] T. Gong, A.A. Heravi, G. Alsous, I. Curosu, V. Mechtcherine, The Impact-Tensile Behavior of Cementitious Composites Reinforced with Carbon Textile and Short Polymer Fibers, *Applied Sciences* 9 (2019) 4048.
 - [9] National Instruments, Strain Gauge Measurement (1998).
 - [10] M. Quast, Betondruckfestigkeit unter zweiaxialer dynamischer Belastung. Dissertation, TU Dresden, 2018.
 - [11] T. Kühn, Experimentelle Grundlagen für die meso- und makroskopische Modellierung von Beton bei hohen Belastungsgeschwindigkeiten. Dissertation, TU Dresden, 2020.
 - [12] R. Unger, A. Nocke, G. Gerlach, C. Cherif, Evaluation of a novel test method for the determination of strain rate-dependent material properties of high-performance fibers, *Procedia Structural Integrity* 17 (2019) 942–948.

Textile-Based 3D Truss Reinforcement for Cement-Based Composites Subjected to Impact Loading

Part I: Development of Reinforcing Structure and Composite Characterization

Duy M.P. Vo^{1,a}, Cornelia Sennewald^{1,b*}, Anke Golla^{1,c}, Michael Vorhof^{1,d}, Gerald Hoffmann^{1,e}, Hung Le Xuan^{1,f}, Andreas Nocke^{1,g}, Chokri Cherif^{1,h}

¹TU Dresden, Institute of Textile Machinery and High Performance Material Technology (ITM), Dresden, Germany

^aduy.vo@tu-dresden.de, ^bcornelia.sennewald@tu-dresden.de, ^canke.golla@tu-dresden.de, ^dmichael.vorhof@tu-dresden.de, ^egerald.hoffmann@tu-dresden.de, ^fhung.le_xuan@tu-dresden.de, ^gandreas.nocke@tu-dresden.de, ^hchokri.cherif@tu-dresden.de

Keywords: strain-hardening cement-based composites SHCCs, textile reinforcement, impact, energy absorption, ductile behavior, hybrid reinforcement, strengthening layers

Abstract. Concrete is extremely vulnerable against impact loading due to its low tensile strength and pronounced brittleness. The application of thin strengthening layers, containing Textile Reinforced Concrete (TRC) and Strain-Hardening Cement-based Composites (SHCCs) in a ductile cement-based composite, is a promising solution to enhance the impact resistance of existing concrete structures. Three-dimensional (3D) textile structures exhibit numerous advantages over two-dimensional (2D) ones, most importantly higher shear, bending and energy absorption capacity, hence, appear to be instrumental in providing sufficient reinforcement to the target strengthening layers. However, design variability and optimization possibility of available 3D textile reinforcement are restricted. This paper presents the development of novel textile-based 3D truss reinforcement that can overcome these limitations. On the basis of woven 3D cellular structures, innovative pyramidal 3D truss reinforcement with favorable load-bearing capacity as well as notable energy absorption capability is developed and successfully realized. To investigate the feasibility and efficacy, cement-based composite consisting SHCC and newly developed pyramidal 3D truss reinforcement is prepared and tested under high-speed tensile loading as well as transversal impact loading. The experimental results show that woven 3D truss reinforcement is highly compatible with SHCC, and significantly enhances its impact resistance. Furthermore, SHCC reinforced with novel pyramidal 3D truss structure remarkably outperforms that with 2D carbon reinforcing structure approved for commercial use.

Introduction

Concrete and steel reinforced concrete are the most important building materials due to good compressive strength, significant durability, great availability of components and easy shape forming [1]. Despite the beneficial properties, this material also has brittle nature and quiet low tensile strength that make it extremely vulnerable against impact loading. This feature can lead to catastrophic consequences, costing lives and resources such as in the case of natural disasters, accidents or terrorist attacks [2]. To enhance the impact resistance of existing structures, the Research Training Group GRK 2250 introduces novel mineral-bonded composites with the focus on new materials as well as design approaches for thin strengthening layers that will be applied on the surfaces of available concrete members. The strengthening layers should yield high tensile ductility, sufficient mechanical strength and durability in order to prevent excessive damage and collapse of the concrete core [3, 4]. Hybrid reinforced material comprised of Strain-Hardening Cement-based Composites (SHCCs) and textile-based reinforcement promises to be highly instrumental for this purpose [5]. The addition of short dispersed fibers to the matrix of SHCC allows for multiple micro-cracking under increasing loading, resulting in enhanced ductility and high energy dissipation capacity. Additionally,

continuous textile reinforcement is able to improve tensile strength significantly, distribute stresses uniformly over larger area and ensure a strong confinement in the strengthening layers. Recent achievements in the SHCC research are reported in [6, 7].

Textile products presently used to reinforce concrete can be categorized into two distinct groups: two-dimensional (2D) and three-dimensional (3D) structures. The main difference is the presence of out-of-plane elements in 3D structures, which bridge adjacent 2D layers, provide orthogonal support as well as determine the structure thickness. 3D reinforcing structures exhibit several advantages over 2D structures. 3D reinforced concrete yield better shear and bending capacity, and absorb more energy. Concrete containing multiple 2D reinforcing layers tends to fail due to premature delamination. Contrarily, the complex 3D configuration facilitates strong mechanical anchorages within the reinforcement as well as between the reinforcement and the cementitious matrix, leading to a greater reinforcing efficiency. It was observed that material, configuration and arrangement of out-of-plane elements strongly influence the performance of 3D reinforced concrete [8, 9, 10, 11, 12, 13]. Regarding concrete production, stable pre-engineered 3D reinforcement helps to simplify the construction effort and prevent placement inaccuracy, hence, significantly reduces the manufacturing cost while ensuring the quality of final products [14]. Textile-based reinforcing structures can be fabricated using different techniques, including weaving, stitch-bonding, tailored fiber placement, robotic arm and adhesive bonding [15, 16, 17, 18, 19, 20, 21, 22, 23]. The working principles of available technologies either restrict the design variability of 3D structures—in particular fineness, stiffness and arrangement of out-of-plane elements—, contain the risk of material damage or reveal low productivity. These challenge the fulfillment of anticipated functions of target strengthening layers.

This paper presents the novel textile-based 3D truss reinforcement that is especially developed for cement-based composites to enhance their impact resistance. The work is motivated by the concept of woven 3D cellular structures [24, 25]. Textile-based 3D truss reinforcement is developed in several steps: systematic consideration of possible topologies, selection of preferable topology, development and implementation of woven structure. The efficacy of resulting structure in cement-based composite is verified by means of high-speed tension tests and small-scale plate impact tests, and compared with that of 2D carbon reinforcing structure approved for commercial use [26].

Development of Novel Impact-Resistant 3D Truss Reinforcement

Topology development and selection. Concrete member experiencing a localized impact undergoes a complex of stresses, typically, shear and compression on the impacted front side, and tension and flexure on the impacted rear side. To provide sufficient resistance against impact, reinforcement must be appropriately designed in correspondence with anticipated loads. Long, slender reinforcing elements are anisotropic and can be most efficiently exploited when being oriented in the direction of load. In accordance with this mechanism, 3D truss structures suggest to be an ideal reinforcement type for cement-based composites subjected to impact loading, as in-plane load-oriented elements can carry tensile and bending forces, while out-of-plane elements are designated to resist shear and compression. To achieve uniform effect over a large concrete area, the 3D truss reinforcement is required to be a periodic structure comprised of geometrically symmetric unit cells. Taking into account that the reinforcing structure will be fabricated using weaving technique, the base of each truss unit cell must have either rectangular or square shape. Within the GRK 2250, high-strength SHCC containing 6 mm long fibers—developed by Curosu et al. [7]—are used as matrix for the target strengthening layers. To ensure a good matrix penetration with uniform fiber distribution, 7 mm is set as the minimum measurement of truss unit cell in each dimension. A 20 mm strengthening layer thickness is realistic, which is also the maximum dimensional value of truss unit cell, as 3D truss structure can mechanically well bond with the matrix without any surficial cover.

Possible 3D truss reinforcement topologies were investigated and presented in the previous work of the authors [27]. For a systematic overview, a strategy is developed in which bar elements are considered as constituting components of a single unit cell. Depending on the inputted bar count, a matrix of numbers is created to describe the coordinate of the bar ends. Possible combinations of bar

elements are scanned by systematically varying the matrix values; those satisfying the given boundary conditions are then displayed. Fig. 1 shows selected examples of a 12-bars-cell.

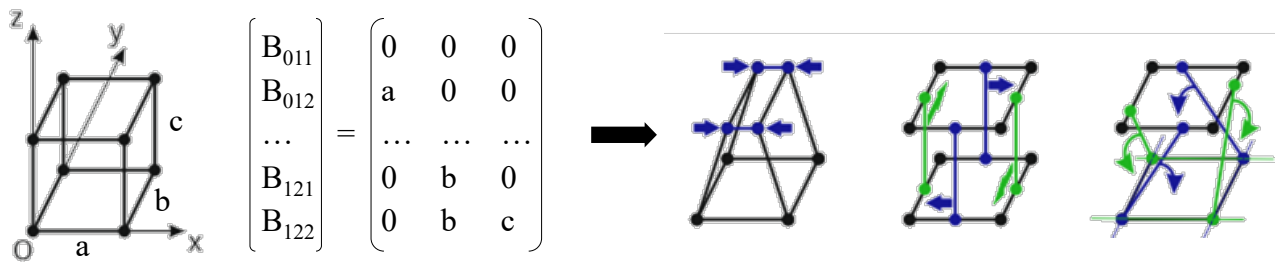


Fig. 1 Selected possible 12-bars-cell topologies

Criterion to determine suitable reinforcing topology include high energy absorption capacity contributed by good load-bearing capacity and sufficient deformability, good ability of stress propagation and wide distribution, and high weaving feasibility. Pyramidal truss structure has shown satisfactory performance in various theoretical and experimental investigations [28, 29, 30, 31], hence, is chosen as preferable 3D reinforcement for impact resistant cement-based composite.

Weave development and implementation. To realize 3D truss reinforcement using weaving technique, the structure must be analyzed into suitable weave elements in the first step. For this purpose, it is important to understand the formation principle and manufacturing method of woven 3D cellular structure [24]. A woven 3D cellular structure is constituted of warp and weft elements that can be distinguished as 1D, 2D, 2.5D and 3D depending on the geometry and arrangement. 1D and 2D elements lie in or parallel to the product surfaces and form the base construction of a unit cell. On the contrary, out-of-plane 2.5D and 3D elements serve as spacers that define the cell spatial property. Fig. 2 shows the principal elements of a woven 3D pyramidal unit cell. The cell base comprises of 1D warp and weft elements perpendicular to each other. Lateral edges are obtained using 2.5D zigzag elements, whose containing planes alternatively form angles α and $(180^\circ - \alpha)$ with the pyramid base. The principal elements are required to have certain rigidity to ensure satisfactory structural stability as well as high reinforcing efficacy, hence, preferably made of steel wires or polymeric bars (base material).

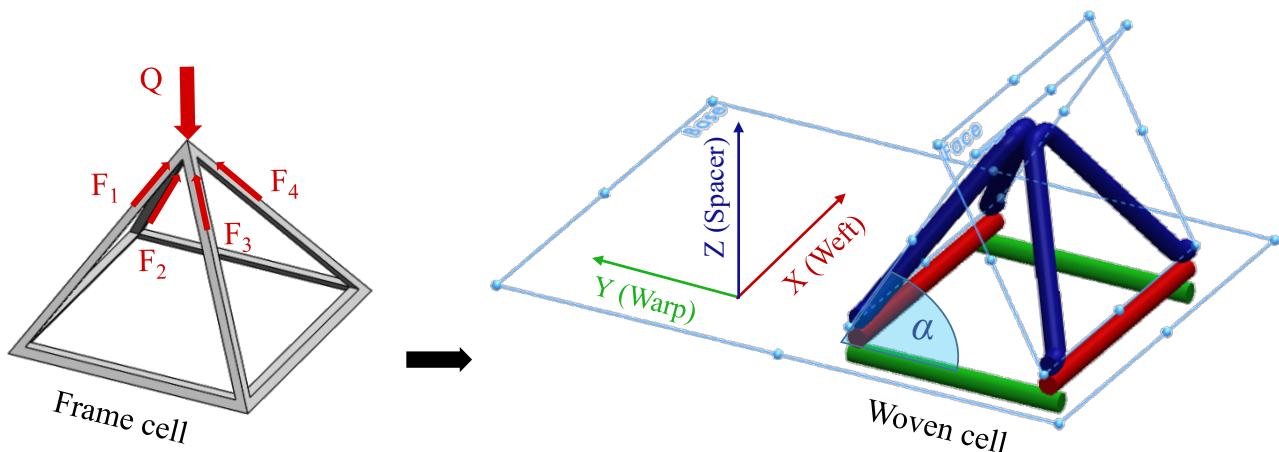


Fig. 2 Analyzing a pyramidal unit cell into principal weave elements

The second step involves developing appropriate weave program. On the one hand, a logical weft insertion sequence together with compatible take-up program must be determined to enable the formation of 3D truss construction in desired configuration and dimensions. On the other hand, weave pattern must be properly designed to ensure sufficient stability of the woven structure before as well as after removing from the loom. Particular challenges to overcome during the weave development of 3D pyramidal truss structure include:

- Out-of-plane diagonal arrangement of 2.5D zigzag elements ($0^\circ < \alpha < 90^\circ$),
- Variable inclination angles of 2.5D zigzag elements ($\alpha, 180^\circ - \alpha$),
- Tendency of weave elements to slide toward the open space in the cellular structure, and
- Capability of weaving machine to overcome bending limit of coarse rigid materials.

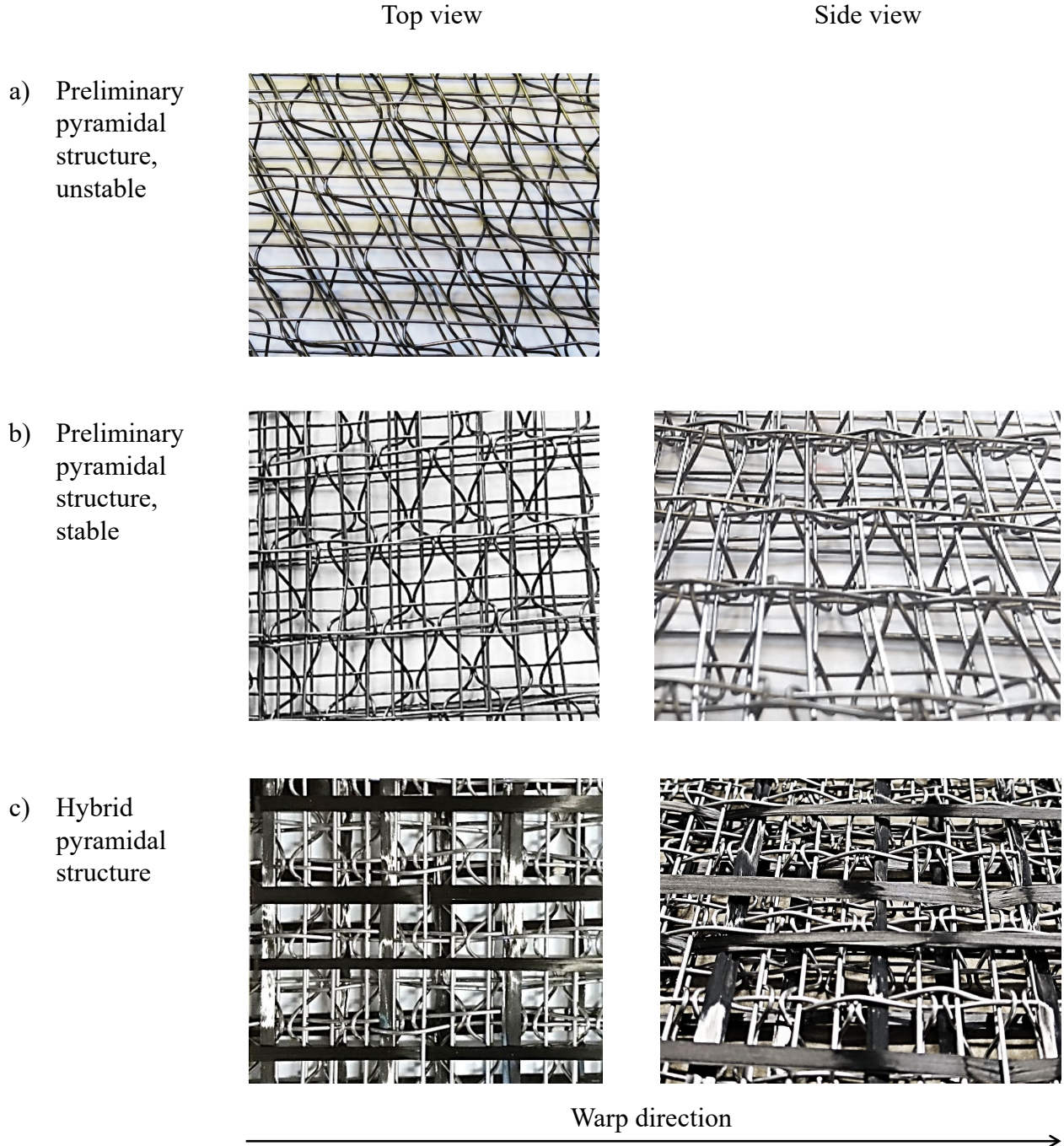


Fig. 3 Woven pyramidal 3D truss structures

Developed 3D truss reinforcing structures are fabricated on a DORNIER rapier weaving machine type HTVS4 with modifications made by researchers at ITM [24]. Different woven pyramidal truss structures are presented in Fig. 3. These are double-layered structures, in which 1D warp and weft elements in the top as well as bottom layers interlace with one another and with 2.5D zigzag spacers at the pyramid vertexes. Steel wire C50D with a diameter of 0.6 mm is chosen as base material for preliminary structures. For a reliable processing of rigid, coarse material and for a design flexibility, non-linear elements are pre-shaped separately before weaving and then inserted into the loom along

weft direction. In the structure shown in Fig. 3a, 1D and 2.5D weft elements are alternatively inserted and bound with warp elements in plain weave pattern. This interlacement design generates unsatisfactory structural stability: after removing from the loom, the structure skews, causing disordering of the out-of-plane diagonal arrangement of zigzag elements. In contrast, the double weft sequence (two times 1D and two times 2.5D) in accompany with modified weave pattern generates a self-supporting structure as can be seen in Fig. 3b. The geometrical parameters of obtained structure are highly consistent with those designed.

Improvement of energy absorption capability. Following the successful manufacture of woven pyramidal truss structure, further improvements are carried out with the aim of optimizing the energy absorption capability. Bistable structure exploits elements in different geometries and ductility levels to generate a tailored progressive failure behavior, leading to significant increase in strain energy without loss of load-bearing capacity [32, 33, 34]. Applying this concept, hybrid 3D truss reinforcement is developed, see Fig. 3c. Carbon rovings (CF-Rovings) and high-ductility steel wires (Steel-HD) are used as 1D elements in both warp and weft directions. Carbon rovings are pre-coated with the watery styrene-butadiene based dispersion SBR Lefasol VL90/2 for better bonding and performance in cementitious matrix. In the woven structure, the rovings are maximally straightened (minimal interlacing points) so that they can fully engage in the composite response from the beginning of load application. After cracks have formed, ductile steel wires start to yield and can significantly improve the composite deformability while strength continues to increase. 2.5D zigzag elements are made of high-strength steel wires (Steel-HS) to sufficiently sustain lateral loads such as shear and compression. The propensity to straighten of non-linear reinforcing elements when subjected to longitudinal loads is a further benefit for increasing strain energy of cement-based composite. The material characteristics and unit cell features of the developed hybrid 3D pyramidal truss reinforcing structure are given in Table 1 and Table 2, respectively.

Table 1 Material characteristics of woven 3D hybrid pyramidal truss reinforcing structure

	CF-Roving	Steel-HD	Steel-HS
Producer	Teijin	Dahmen	Dahmen
Type	Tenax ^R -E HTS40 F13	1.4301	
Fineness/ Diameter	800 [tex]	0.8 [mm]	0.8 [mm]
Tensile strength		600-800 [MPa]	1200 [MPa]
Elongation at break		30-55 [%]	

Table 2 Features of a hybrid pyramidal unit cell

Direction	Cell dimension	Element		
		Material	Geometry	Elements/cell
X (Weft)	12 [mm]	CF-Roving	1D	1
		Steel-HD	1D	2
		Steel-HS	1D	2
Y (Warp)	15 [mm]	CF-Roving	1D	2
		Steel-HD	1D	4
Z (Spacer)	8 [mm]	Steel-HS	2.5D zigzag	2

Impact behavior of cement-based composite reinforced with woven 3D truss structure

Specimen preparation. For a research consistency within the GRK 2250, specimens under investigation in this paper are prepared using high-strength SHCC as matrix and lamination technique as casting method, identical to those described in [35]. The SHCC matrix contains ultra-high molecular weight polyethylene (UHMWPE) fibers by 1% volume fraction. Investigated composites include:

- SHCC without continuous reinforcement (SHCC),
- SHCC with developed 3D hybrid pyramidal truss reinforcing structure (SHCC_3D-Hybrid), and
- SHCC with approved 2D carbon reinforcing structure (SHCC_2×2D-CF). To approximate the configuration of 3D reinforcement, two layers of 2D carbon structure are introduced. Due to a great difference between warp and weft elements in terms of cross-sectional area and density, the layers are rotated 90° to each other, resulting in an equal effect in both directions.

Fig. 4 shows a SHCC_3D-Hybrid specimen for plate impact test halfway through the casting process. It can be observed that the cementitious matrix fully penetrates through the open cells, indicating a high compatibility of woven 3D truss reinforcement with cement-based composites. After casting, specimens of tension tests are kept in a controlled climate (20°C and 65% relative humidity) while those of impact tests are simply stored in open air to imitate the actual condition of concrete structures in service. Before testing, black-white speckled pattern is sprayed on the specimen surface in preparation for digital image correlation (DIC). All specimens of a common series have the same age at testing.



Fig. 4 Placing woven 3D hybrid pyramidal truss reinforcement in SHCC matrix during casting

High-speed tension tests. High-speed tension tests are conducted in a ZwickRoell HTM 5020 high-speed testing machine at ITM. The specimen has a gauge length of 50 mm, is 20 mm thick and 40 mm wide. During testing, the specimen is fixed to the lower stationary grip head with built-in piezoelectric load cell and pulled upward at a speed of 10 m/s, equivalent to 200 s^{-1} strain rate. Note that additional components are constructed and installed to enable the attachment of specimen in the testing machine, as the available grip head is designed for specimen thickness up to 4 mm only. SHCC_3D-Hybrid is tested along both warp and weft directions of the reinforcement.

The representative stress-global strain curves of different composites under uniaxial high-speed tensile loading are plotted in Fig. 5. The tensile stress is obtained by dividing force values by cross-sectional area of the specimen. Theoretically, global strain refers to deformation over gauge length of the specimen and is accounted for by both SHCC matrix and the 3D truss structure. During the investigation presented in this paper, deformation values are taken from displacement data of the testing machine, hence, influence of the additional components cannot be excluded from the results. However, the uniformity in apparatus set up, testing configuration and parameters does allow for an equal effect of the influencing factors across all specimens. The authors recommend not to observe the presented results as pure material behavior, but rather for comparison between the investigated composites.

It is obvious that the introduction of continuous reinforcement leads to significant increase in load-bearing capacity of SHCC. The stress at which SHCC_3D-Hybrid and SHCC_2×2D-CF fail is 3 to 4 times higher than that observed with SHCC. Consequently, specimens with continuous reinforcement dissipate pronouncedly greater amount of energy than those without, as seen by the area beneath the corresponding stress-global strain curves. 3D-Hybrid yields approximately equivalent reinforcing effect in SHCC in both warp and weft directions and brings about a tensile strength increase by circa 125% compared to 2×2D-CF. Specimen tested in weft direction exhibits a larger plateau at peak

stress, indicating the important contribution of 2.5D zigzag reinforcing elements to the enhancement of deformability and energy absorption capacity of cement-based composite. The DIC analysis, performed using the GOM Correlate software, gives evidence that continuous reinforcement promotes the capability of SHCC to develop multiple cracks and exhibit strain-hardening behavior. SHCC_3D-Hybrid shows a better crack control as well as global stress distribution than SHCC_2×2D-CF, revealed by a higher number of cracks, smaller crack width and denser crack spacing. Multiple fine cracks are beneficial for overall dynamic response in association with increased strain capacity and energy. Along with the formation of multi-cracks, more fibers in the matrix are activated, leading to a higher load-bearing capacity. Overall, developed woven 3D hybrid pyramidal truss reinforcing structure presents numerous advantageous features for enhancing the impact resistance of cement-based composites. The high-speed tension test results demonstrates the outperformance of 3D truss reinforcing structure over the approved 2D carbon reinforcing structure.

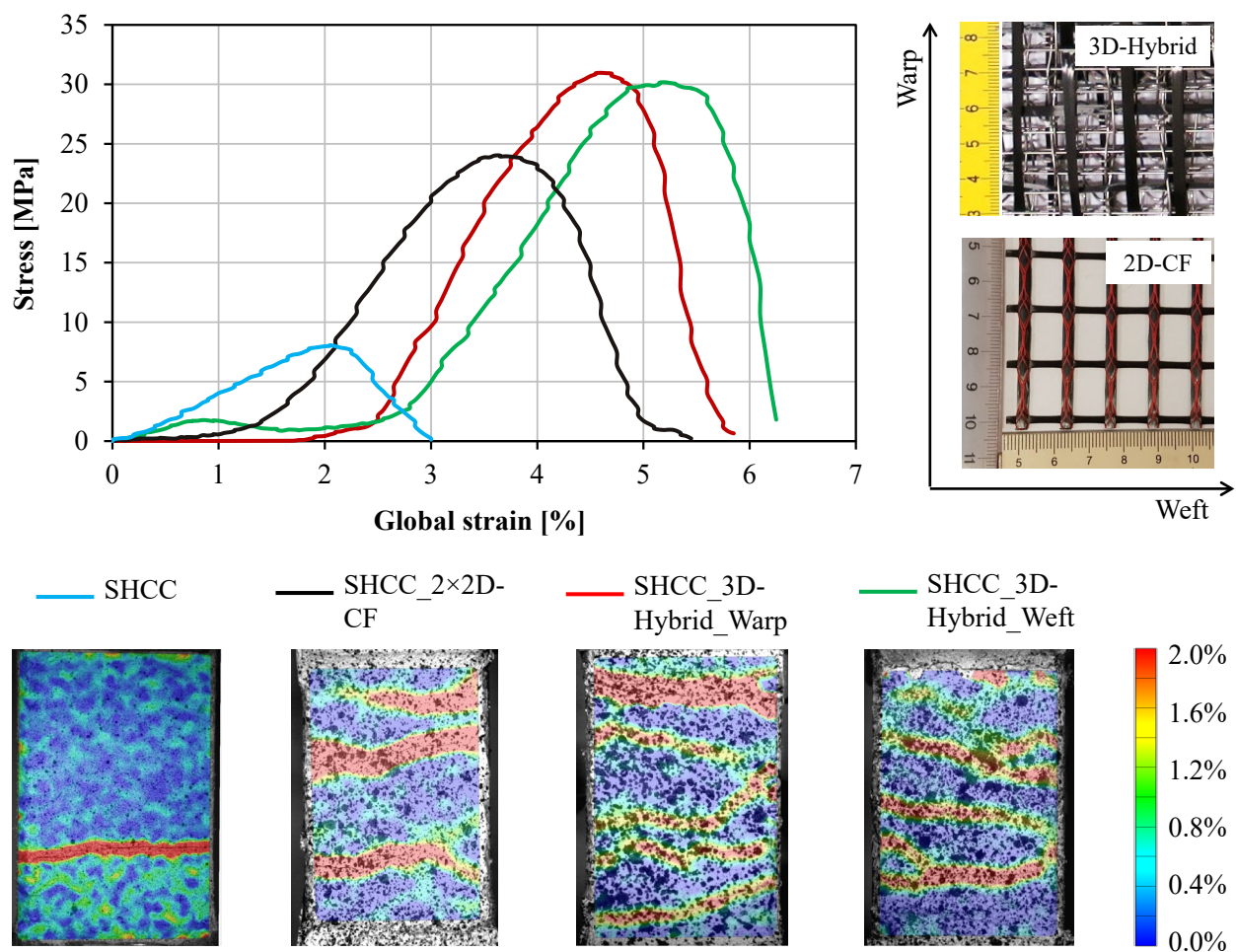


Fig. 5 Representative stress-global strain curves of investigated composites with corresponding crack patterns under uniaxial high-speed tensile loading

Small-scale plate impact tests. Small-scale plate impact tests were developed by researchers at the Institute of Concrete Structures (IMB), TU Dresden, which is also a member of the GRK 2250. The testing method has been proven to be suitable for evaluating and comparing the effect of different textile-based reinforcements in cement-based composites against impact loading [36, 37]. Impact experiments reported in this paper were performed in close collaboration with IMB. Square concrete plate with the dimensions of 610 mm × 610 mm × 30 mm is fixed to a horizontal support frame and struck by a falling steel impactor. The impactor has a cylindrical shape (100 mm diameter, 150 mm length), a weight m_{Imp} of 8.4 kg, and flat nose with slight curvature around the edge. A range of initial velocities can be realized by applying different accelerating pressure to the impactor. The

experiment is assisted with a stereo high-speed camera system for subsequent photogrammetric evaluation.

Energy absorption capacity presents an important parameter for evaluating the impact resistance of cement-based composites. Within the small-scale plate impact experiment, the amount of energy that a concrete plate absorbs can be substantially determined by the reduction of kinetic energy of the impactor immediately before and after contacting with the plate, suppose that other portions of energy (such as thermal energy) is neglected [38]. Note that impactor temporary kinetic energy is calculated based on the detected velocity v_{Imp} using Eq. 1. The differential energy $\Delta E_{kin,Imp}$ is plotted over corresponding striking kinetic energy $E_{kin,Imp,1}$ in Fig. 6.

$$E_{kin,Imp} = \frac{1}{2} \times v_{Imp}^2 \times m_{Imp}. \quad (1)$$

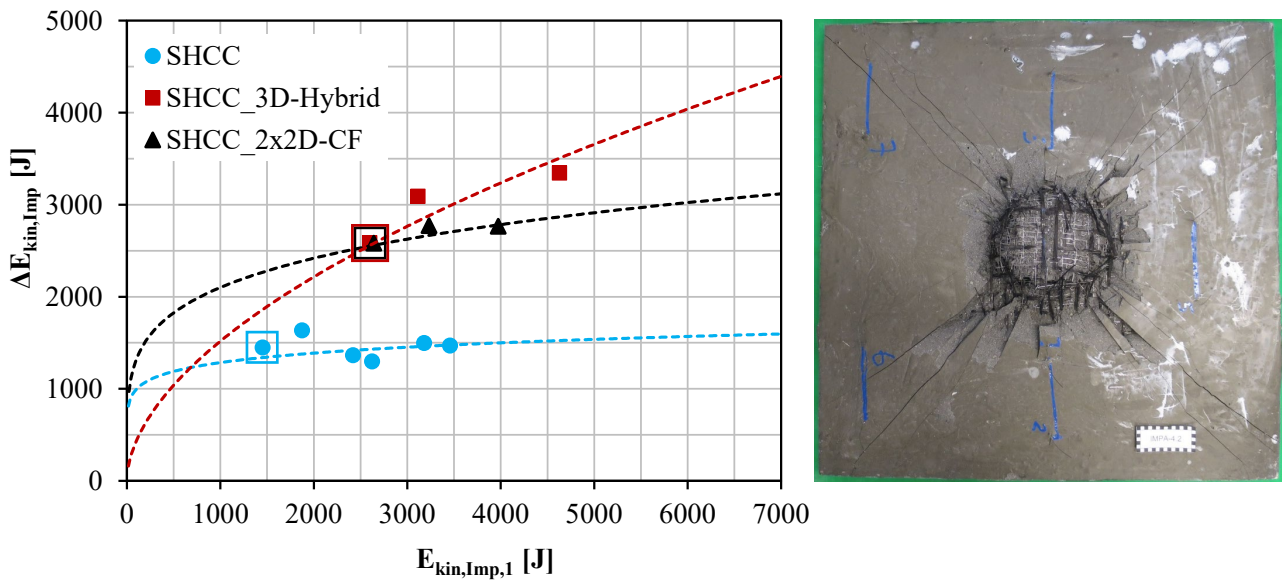


Fig. 6 Differential kinetic energy in relation to striking kinetic energy and back side of a SHCC_3D-Hybrid specimen without perforation

One essential criterion to compare the capability of resisting impact is the striking kinetic energy, from which the impactor completely perforates the concrete plate. This is hereinafter called perforation energy limit $E_{perf,Lim}$. Each test series contains one perforated specimen that is marked (square). One can suppose that $E_{perf,Lim}$ of the corresponding cement-based composite ranges between the marked value and the next adjacent result. The non-linear relation of obtained test results as well as the development trend can be visualized using power function shown in Eq. 2

$$\Delta E_{kin,Imp} = \alpha (E_{kin,Imp,1})^r. \quad (2)$$

Note that the authors are working on further experimental and numerical investigation to validate the prediction. It is evident that the introduction of continuous reinforcement substantially enhances the impact resistance of SHCC, its perforation energy limit approximately doubles when combined with both types of embedment. Even though both composites SHCC_3D-Hybrid and SHCC_2x2D-CF exhibit similar perforation energy limit and upward trend in energy absorption, the 3D-Hybrid structure yields considerably higher reinforcing efficiency and becomes advantageous over the other as the impact velocity as well as kinetic energy increases. This is significantly contributed by the complex woven 3D truss architecture. On one hand, the multi-directional reinforcement improves the mechanical strength of the composite. On the other hand, the strong matrix-reinforcement bond prevents premature yarn pull-out as well as concrete fragmentation, allowing for optimally exploiting

the positive synergy between discontinuous and continuous reinforcement within the composite. Overall, woven 3D truss reinforcement is capable of providing a secure confinement and activating a global response within the strengthening composite layer, which in turn can enhance the impact safety of the concrete core. The performance of woven 3D truss reinforcement can be further customized in many respects, including material combination, structure and parameter design, additional treatments.

Conclusion

The development of novel textile-based 3D truss reinforcement for cement-based composites with enhanced impact resistance is presented in this paper. Based on the consideration of loading scenarios and boundary conditions of the target composite, crucial requirements on 3D reinforcement are specified. The topology development provides a systematic overview of possible structures and serves as a basis for the selection of preferable design. Pyramidal truss structure is chosen because of a high energy absorption capability, good load-bearing capacity and sufficient global deformability. Textile-based pyramidal truss reinforcement is successfully realized using 3D cellular weaving technology in association with appropriate developed weave program. Applying the concept of bistable structure, obtained product is further developed into woven hybrid 3D pyramidal truss reinforcing structure that is comprised of multiple materials with different grades of strength, ductility and undulation. The hybrid 3D truss reinforcement facilitates a progressive failure behavior that leads to a significant increase in energy absorption capability, which the experimental results validate.

Cement-based composites made of SHCC matrix (SHCC, SHCC_3D-Hybrid and SHCC_2×2D-CF) are investigated in uniaxial high-speed tension tests and small-scale plate impact tests. The strength, strain capacity and energy absorption capacity of SHCC is considerably improved with the introduction of continuous reinforcement. SHCC_3D-Hybrid outperforms SHCC_2×2D-CF in all aspects. This can be traced back to the ability of complex woven 3D truss architecture to provide additional strength in multiple directions, to activate global dynamic response and to promote the positive synergy between short fibers and textile-based reinforcing structure within the composite.

The results presented in this paper demonstrate the technological feasibility of woven 3D truss structure as reinforcement for cement-based composites and its significance in enhancing the impact resistance. Further research is necessary to understand and optimally exploit the effect of material properties and parameters, structure design as well as pre- and post-treatment. To assist the development of appropriate 3D truss reinforcing structure, suitable numerical investigation method should be worked out. Additionally, more experiments would be useful for validation purpose.

Funding. This research is funded by the Deutsche Forschungsgemeinschaft (DFG – German Research Foundation) in the framework of the Research Training Group GRK 2250/1 “Mineral-bonded composites for enhanced structural impact safety”, project number 287321140.

Acknowledgements

The authors express their gratitude to the Deutsche Forschungsgemeinschaft (DFG – German Research Foundation) for the financial support provided in the framework of the Research Training Group GRK 2250 “Mineral-bonded composites for enhanced structural impact safety”, project number 287321140. Sincere words of appreciation are addressed to colleagues at ITM and within the GRK 2250 for their support in preparing and performing the experiments.

References

- [1] MEHTA, P. K.; MONTEIRO, P. J. M.: *Concrete: Microstructure, properties, and materials*. 4th Edition. New York: McGraw-Hill Education, 2014. – ISBN 9780071797870
- [2] BANGASH, M. Y. H.: *Shock, impact and explosion: Structural analysis and design*. Berlin, London: Springer, 2009. – ISBN 9783540770671
- [3] GRK 2250. <https://www.grk2250.de/>
- [4] CUROSU, I.: Mineral-bonded composites for enhanced structural impact safety - Overview of the format, goals and achievements of the research group GRK 2250. In: *Proceedings of the 10th International Conference on Fracture Mechanics of Concrete and Concrete Structures IA-FraMCoS*, Bayonne (France), 23-26 June 2019
- [5] GONG, T.: *Tensile behavior of high-performance cement-based composites with hybrid reinforcement subjected to quasi-static and impact loading*. Germany, Technische Universität Dresden, Dissertation, 2020
- [6] MECHTCHERINE, V.; MILLON, O.; BUTLER, M.; THOMA, K.: Mechanical behaviour of strain hardening cement-based composites under impact loading. In: *Cement and Concrete Composites* 33 (2011) 1, pp. 1–11. – DOI. 10.1016/j.cemconcomp.2010.09.018
- [7] CUROSU, I.; LIEBSCHER, M.; MECHTCHERINE, V.; BELLMANN, C.; MICHEL, S.: Tensile behavior of high-strength strain-hardening cement-based composites (HS-SHCC) made with high-performance polyethylene, aramid and PBO fibers. In: *Cement and Concrete Research* 98 (2017), pp. 71–81. – DOI. 10.1016/j.cemconres.2017.04.004
- [8] HAUSER, S.; WÖRNER, J. D.: DUCON, ein innovativer Hochleistungsbeton. In: *Beton- und Stahlbetonbau* 94 (1999) 2, pp. 66–75. – DOI. 10.1002/best.199900190
- [9] AMZALEG, E.; PELED, A.; JANETZKO, S.; GRIES, T.: Flexural behavior of cement based element reinforced with 3D fabric. In: *Proceedings of the 8th International Conference on Fracture Mechanics of Concrete and Concrete Structures*, Toledo (Spain), 10-14 March 2013, pp. 1–9
- [10] PELED, A.; ZHU, D.; MOBASHER, B.: Impact Behavior of 3D Fabric Reinforced Cementitious Composites, Bd. 2. In: PARRA-MONTESINOS, G.; REINHARDT, H. W.; NAAMAN, A. E. (Eds.): *High performance fiber reinforced cement composites 6*. Dordrecht: Springer, 2012 (2). – ISBN 978-94-007-2435-8, pp. 543–550
- [11] ZHU, D.; MOBASHER, B.; PELED, A.: Experimental study of dynamic behavior of cement-based composites. In: *Journal of Sustainable Cement-Based Materials* 2 (2013) 1, pp. 1–12. – DOI. 10.1080/21650373.2012.757831
- [12] SASI, E. A.; PELED, A.: Three dimensional (3D) fabrics as reinforcements for cement-based composites. In: *Composites Part A: Applied Science and Manufacturing* 74 (2015), pp. 153–165. – DOI. 10.1016/j.compositesa.2015.04.008
- [13] HAIK, R.; ADIEL SASI, E.; PELED, A.: Influence of three-dimensional (3D) fabric orientation on flexural properties of cement-based composites. In: *Cement and Concrete Composites* 80 (2017), pp. 1–9. – DOI. 10.1016/j.cemconcomp.2017.02.007
- [14] NAAMAN, A. E.: Thin TRC products. In: TRIANTAFILLOU, T. (Ed.): *Textile fibre composites in civil engineering*. Oxford: Woodhead Publishing, 2016. – ISBN 9781782424468, pp. 413–439
- [15] WEISE, D.; VORHOF, M.; BRÜNLER, R.; SENNEWALD, C.; HOFFMANN, G.; CHERIF, C.: Reduction of weaving process-induced warp yarn damage and crimp of leno scrims based on coarse high-performance fibers. In: *Textile Research Journal* 89 (2019) 16, pp. 3326–3341. – DOI. 10.1177/0040517518809049

- [16] FRANZ, C.; HÄNTZSCHE, E.; CHERIF, C.: Die Integration von lichtleitenden Fasern und die sensitive Aktivierung des Carbonbetons. In: *TUDALIT Magazin 15 Proceedings of the 8. Anwendertagung Textilbeton*, pp. 23
- [17] YOUNES, A.; SEIDEL, A.; RITTNER, S.; CHERIF, C.; THYROFF, R.: Innovative textile Bewehrungen für hochbelastbare Betonbauteile. In: *Beton- und Stahlbetonbau* 110 (2015) S1, pp. 16–21. – DOI. 10.1002/best.201400101
- [18] SANKARAN, V.; RITTNER, S.; HAHN, L.; CHERIF, C.: Development of multiaxial warp knitting technology for production of three-dimensional near net shape shell preforms. In: *Textile Research Journal* 87 (2017) 10, pp. 1226–1241. – DOI. 10.1177/0040517516651102
- [19] FEIX, J.: Beanspruchungsorientierte Textilbewehrungen. In: *Proceedings of the 10. Carbon- und Textilbetontage*, Dresden, 25-26 September 2018, pp. 20–21
- [20] HACK, N.; LAUER, W. V.: Mesh-Mould: Robotically Fabricated Spatial Meshes as Reinforced Concrete Formwork. In: *Architectural Design* 84 (2014) 3, pp. 44–53. – DOI. 10.1002/ad.1753
- [21] SCHNEIDER, J.; REYMENDT, J.: Properties and applications of DUCON® A micro-reinforced ultra-high-performance concrete. In: WALRAVEN, J. C.; STOELHORST, D. (Eds.): *Tailor made concrete structures — New solutions for our society / edited by Joost C. Walraven, Dick Stoelhorst*. Boca Raton, FL: CRC Press, 2008. – ISBN 978-0-415-47535-8, pp. 105
- [22] HAHN, L.; RITTNER, S.; BAUER, C.; CHERIF, C.: Development of alternative bondings for the production of stitch-free non-crimp fabrics made of multiple carbon fiber heavy tows for construction industry. In: *Journal of Industrial Textiles* 48 (2018) 3, pp. 660–681. – DOI. 10.1177/1528083717736100
- [23] ROYE, A.; GRIES, T.: 3-D Textiles for Advanced Cement Based Matrix Reinforcement. In: *Journal of Industrial Textiles* 37 (2007) 2, pp. 163–173. – DOI. 10.1177/1528083707078136
- [24] SENNEWALD, C.: *Generative Struktur-, Technologie- und Webmaschinenentwicklung für unikale zelluläre 3D Strukturen in Leichtbauweise*. Germany, Technische Universität Dresden, Dissertation, 2016
- [25] SENNEWALD, C.; KAINA, S.; WECK, D.; GRUHL, A.; THIEME, M.; HOFFMANN, G.; STEPHANI, G.; BÖHM, R.; CHERIF, C.; ANDERSEN, O.; KIEBACK, B.; HUFENBACH, W. A.: Metal Sandwiches and Metal-Matrix-Composites Based on 3D Woven Wire Structures for Hybrid Lightweight Construction. In: *Advanced Engineering Materials* 16 (2014) 10, pp. 1234–1242. – DOI. 10.1002/adem.201400180
- [26] DIBT: Allgemeine bauaufsichtliche Zulassung: Verfahren zur Verstärkung von Stahlbeton mit TUDALIT (Textilbewehrter Beton), Zulassungsnummer Z-31.10-182. Berlin: Deutsches Institut für Bautechnik, 2016
- [27] VO, D. M. P.; SENNEWALD, C.; HOFFMANN, G.; CHERIF, C.: Fiber-Based 3D Cellular Reinforcing Structures For Mineral-Bonded Composites With Enhanced Structural Impact Tolerance (2018). – DOI. 10.5281/ZENODO.1340575
- [28] VO, M. P. D.; SENNEWALD, C.; GONG, T.; HOFFMANN, G.; CUROSU, I.; MECHTERINE, V.; CHERIF, C.: 3D woven cellular structures as continuous reinforcement in cement-based composites subjected to impact loading. In: *Proceedings of 19th AUTEX World Textile Conference*, Ghent (Belgium), 11-15 June 2019
- [29] YUNGWIRTH, C. J.; WADLEY, H. N.; O'CONNOR, J. H.; ZAKRAYSEK, A. J.; DESHPANDE, V. S.: Impact response of sandwich plates with a pyramidal lattice core. In: *International Journal of Impact Engineering* 35 (2008) 8, pp. 920–936. – DOI. 10.1016/j.ijimpeng.2007.07.001

-
- [30] LEE, M.-G.; KO, G.-D.; SONG, J.; KANG, K.-J.: Compressive characteristics of a wire-woven cellular metal. In: *Materials Science and Engineering: A* 539 (2012), pp. 185–193. – DOI. 10.1016/j.msea.2012.01.079
- [31] HAMMETTER, C. I.; RINALDI, R. G.; ZOK, F. W.: Pyramidal Lattice Structures for High Strength and Energy Absorption. In: *Journal of Applied Mechanics* 80 (2013) 4. – DOI. 10.1115/1.4007865
- [32] CHERKAEV, A.; SLEPYAN, L.: Waiting Element Structures and Stability under Extension. In: *International Journal of Damage Mechanics* 4 (1995) 1, pp. 58–82. – DOI. 10.1177/105678959500400104
- [33] WHITMAN, Z.; LA SAPONARA, V.: Bistable structures for energy absorption, I: Metallic structures. In: *Journal of Mechanics of Materials and Structures* 2 (2007) 2, pp. 347–358. – DOI. 10.2140/jomms.2007.2.347
- [34] WHITMAN, Z.; LA SAPONARA, V.: Bistable structures for energy absorption, II: Composite structures under tension. In: *Journal of Mechanics of Materials and Structures* 2 (2007) 2, pp. 359–375. – DOI. 10.2140/jomms.2007.2.359
- [35] GONG, T.; HERAVI, A. A.; ALSOUS, G.; CUROSU, I.; MECHTCHERINE, V.: The Impact-Tensile Behavior of Cementitious Composites Reinforced with Carbon Textile and Short Polymer Fibers. In: *Applied Sciences* 9 (2019) 19, pp. 4048. – DOI. 10.3390/app9194048
- [36] HERING, M.; CURBACH, M.: A new testing method for textile reinforced concrete under impact load. In: *MATEC Web of Conferences* 199 (2018), pp. 11010. – DOI. 10.1051/mateconf/201819911010
- [37] HERING, M.; KÜHN, T.; CURBACH, M.: Small-scale plate tests with fine concrete in experiment and first simplified simulation. In: *Structural Concrete* 22 (2021) 2, pp. 637–649. – DOI. 10.1002/suco.201900333
- [38] HERING, M.: *Untersuchung von mineralisch gebundenen Verstärkungsschichten für Stahlbetonplatten gegen Impaktbeanspruchungen*. Dresden/Germany, Technische Universität Dresden, Fakultät Bauingenieurwesen, Dissertation, 2020

Uni-Directional Tape Structures Consisting of Recycled Carbon Fibres and Polyamide 6 Fibers for High-Performance Thermoplastic Composites

Muhammad Furqan Khurshid^{1,a*}, Mir Mohammad Badrul Hasan^{1,b},
Simon Hoebel^{1,c}, Anwar Abdkader^{1,d} and Chokri Cherif^{1,e}

¹Faculty of Mechanical Science and Engineering, Institute of Textile Machinery and High Performance Material Technology (ITM), Technische Universität Dresden, Germany

^{a*}muhammad_furqan.khurshid@tu-dresden.de, ^bmir_mohammad_badrul.hasan@tu-dresden.de,

^csimon.hoebel@tu-dresden.de, ^danwar.abdkader@tu-dresden.de, ^echokri.cherif@tu-dresden.de

Keywords: Uni directional tape, Recycled carbon fiber, Polyamide fibers, High performance composites, Thermoplastic composites

Abstract. Carbon fibers (CF) are indispensable for lightweight applications in the automotive, aircraft, construction, and wind energy sectors. In this paper, the focus is on the development of flexible, highly customizable Uni-directional tape structures (UD-tape) from recycled carbon fibers (rCF) and thermoplastic polyamide 6 (PA 6) fibers for thermoplastic composites with outstanding mechanical properties. For the development of UD-tapes, further developments of the carding and drawing processes for the production of rCF and PA6 slivers and the development of a prototype tape production are necessary. The production of the UD-tape takes place on a modified and constructively adapted set-up, consisting of a drafting unit, thermo-fixation unit, compacting unit, followed by the wind-up unit. The composite manufactured from the UD-tapes shows a very high tensile strength of 1339 ± 28 MPa and an E-module of 84.7 ± 2.3 GPa. The processing of rCF into UD-tapes shows high ecological and economic sustainability and, thus, the efficient usage of fossil resources to protect the environment.

Introduction

Carbon fibers reinforced plastics are intensively used as lightweight materials in the automotive, aircraft, construction, and wind energy sectors. Consequently, the consumption of carbon fiber reinforced plastics has been continuously rising for the last two decades [1]. The future market of carbon fiber reinforced plastics are automotive and wind energy sectors. It is anticipated that the automotive sector will become one of the leading consumers of carbon fiber reinforced plastics in the near future [2]. The global emission of greenhouse gases introduces light-weighting and electromobility strategies in the automotive industry. Therefore, utilization of carbon fiber reinforced plastics as lightweight material is trending and has become a focus of all future structural applications in automotive [3-5].

The problem associated with carbon fiber manufacturing and its composites is energy-intensive process and manufacturing cost. In addition, sustainability issues associated with the waste of carbon fiber reinforced plastics spotlight recycling and re-processing technologies. The purpose is to close the loop of carbon fiber reinforced plastics by reutilizing them for automotive applications. Therefore, plenty of work has been performed to develop recycling and re-processing technologies. Consequently, recycling of carbon fiber reinforced plastics becomes a reality, and cost-effective recycle carbon fibers are commercially available from mechanical, thermal, and chemical processes for further applications [6-9].

Recycle carbon fibers can be integrated into high-performance thermoplastic composites through re-processing technologies, including direct and indirect techniques. Direct techniques include injection molding and additive manufacturing technologies where recycle carbon fibers and polymer converted into high-performance composites in one step. While indirect technique, the first step is to fabricate fibrous structure and then develop high-performance composite through further

consolidation, e.g., compression molding. The fibrous structures include paper, nonwovens, and hybrid yarn that can be developed from wet-laid, dry-laid, and spinning technologies [10-13]. Structure analysis of high-performance thermoplastic composites developed from recycled carbon fibers highlights that the mechanical properties of high-performance composites are significantly affected by the degree of fiber orientation [13, 14]. Unfortunately, existing processing technologies cannot deliver unidirectional orientation in composites. Therefore, developing a fibrous structure with unidirectional fiber orientation can significantly maximize the resource efficiency of recycled carbon fibers in high-performance composites.

Therefore, this research's prime objective is to develop flexible, highly customizable unidirectional tape structures from recycled carbon fibers (rCF) and thermoplastic polyamide 6 fibers for high-performance thermoplastic composites with the highest resource efficiency. For this purpose, carding process was employed to produce partially oriented card slivers from rCF and PA6 fibers, which are then processed into drawn slivers by drawing process to enhance unidirectional orientation in drawn slivers. Furthermore, a constructively adapted set-up consisting of drafting, thermo-fixation, compacting, and winding units converts highly oriented drawn slivers into unidirectional tapes. In the last stage, unidirectional tape structures were utilized to develop high-performance composites. This study revealed that innovative tape structure possesses unidirectional fiber orientation that ensures thermoplastic composites with outstanding mechanical properties.

Material and Methods

Material

Recycle carbon and polyamide 6 fibers employed in this research were purchased from TEIJIN Carbon, Europe, and EMS Grilltech, Germany. The specifications of both staple fibers are given in Table 1

Table 1. Specifications of raw materials

Parameter	Unit	Raw materials	
		rCF	Polyamide 6
Fiber length	mm	40-60	40-60
Fiber linear density	dtex	0.5 ± 0.06	1.5 ± 0.15
Single fiber strength	MPa	3499 ± 250	440 ± 7.5
E- Modulus	GPa	240 ± 37	1.48 ± 0.45
Elongation	percent	1.79 ± 0.15	74.9 ± 15
Sizing	percent	1.3 ± 0.1	--

Development of rCF/PA6 sliver

In order to develop a sliver with unidirectional fiber orientation, recycle carbon and polyamide 6 fibers were blended and subjected to a special carding machine. The special carding machine was specifically optimized for processing recycled carbon fiber. In this optimization, technological and kinematical carding parameters were screened using Response Surface Methodology. This optimization provides a breakthrough towards the production of oriented card sliver with minimum fiber damage [15]. Subsequently, this card sliver is subjected to a drawing process to improve fiber orientation, uniformity, and homogeneity. In order to achieve unidirectional fiber orientation, three drawing passages were performed to develop a drawn sliver consisting of recycled carbon and polyamide fibers. The detail of technological parameters employed to produce 3-6 ktex drawn sliver reported in [16].

Development of rCF/PA6 Uni-directional tape structure

An innovative setup consisting of drafting, thermo-fixation, compacting, and winding units were designed and developed to transform highly oriented drawn sliver into unidirectional tape structure, as shown in Fig. 2. The purpose of using a thermo-fixation unit is to maintain unidirectional orientation in the tape structure and provide sufficient strength to the fibrous structure by introducing

partial consolidation. In addition to this, thermo-fixation also improves handling properties. As a result, a partially consolidated unidirectional tape structure can be used as prepreg for thermoplastic composites. In this research, unidirectional tapes structure is produced using different setup technological parameters as summarized in Table 2.

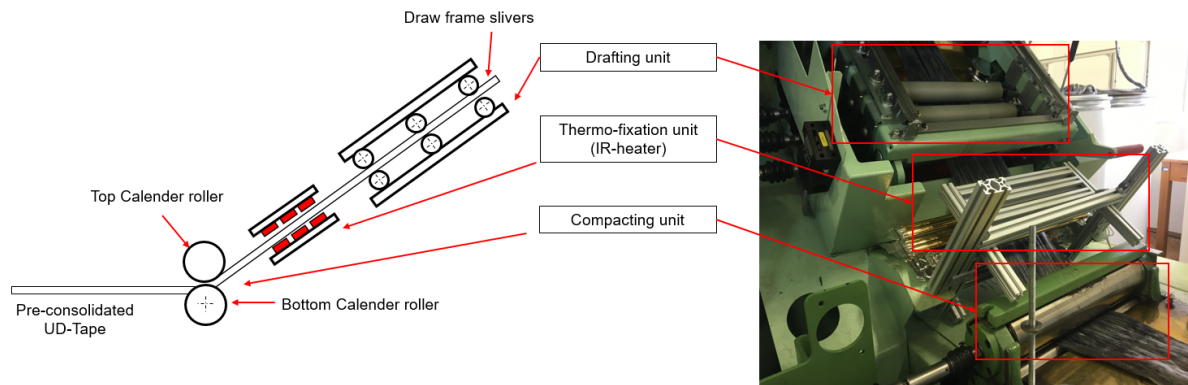


Fig. 1. Process chain for the development of UD-tape

Table 2. Technological parameters for the production of UD-tapes

Parameter	Unit	Tape Identification		
		V.1	V.2	V.3
Draft	--	1.4	1.7	2.1
Areal weight of Tape	g/m ²	166	133	119
Break draft	--		1.06	
Fiber volume content	percent		45	
Back / Front gauge	mm		65/60	
Thermo-fixation Intensity	percent		15	

Development of high performance thermoplastic composites

Unidirectional tape structures were cut and stacked [0]_s to develop unidirectional thermoplastic composites. The consolidation was performed using a laboratory press machine P 300 PV from Dr. Collin GmbH, Germany. Fig. 2 presents the unidirectional tapes, tape stacking, consolidation cycle, and high-performance composites.

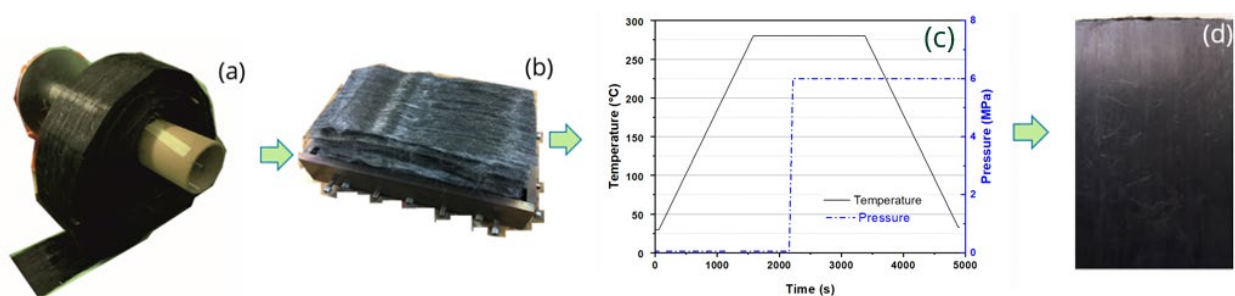


Fig. 2. (a) UD-tape, (b) tool for composite manufacturing, (c) the curves of temperature and pressure during composite manufacturing and (d) composite plate

Characterization techniques

The fiber orientation in fibrous structure (card-, drawn sliver, and unidirectional tapes) was measured by the Lindsey method [15, 17]. Composite plates with dimensions 260 mm × 150 mm × 2 mm were produced using the UD-tapes as detailed in Table 2 on the Laboratory press machine P 300 PV (Dr. Collin GmbH, Germany). The testing of UD thermoplastics composite was performed on the testing device Zwick type Z 100 (Zwick GmbH and Co., Germany) by DIN EN ISO 527-5 standard test method.

Results and Discussion

Fiber orientation in rCF/PA6 fibrous structure

Fig 3(a) presents fiber orientation results in rCF/PA6 card sliver, drawn sliver, and unidirectional tapes. The results show that discontinuous rCF/PA6 fibers, which are randomly oriented in mixing, become oriented after carding process. The degree of orientation reached up to 83 percent. It can be associated with the point-to-point action between the main cylinder and the worker. The carding action aligns, straightens, and orient the carbon fibers in the machine directions [15].

Furthermore, multiple passage drawing improves the orientation in rCF/PA6 drawn sliver [18, 19], and the values of the orientation index reached up to 93 percent. The results also show that the new setup equipped with drafting, thermo-fixation, and compression units successfully maintains the orientation in unidirectional tape structures without any disturbance. Based on orientation results, it can be concluded that unidirectional orientation in tape structure is achieved through innovative process chain development and systematic optimizations.

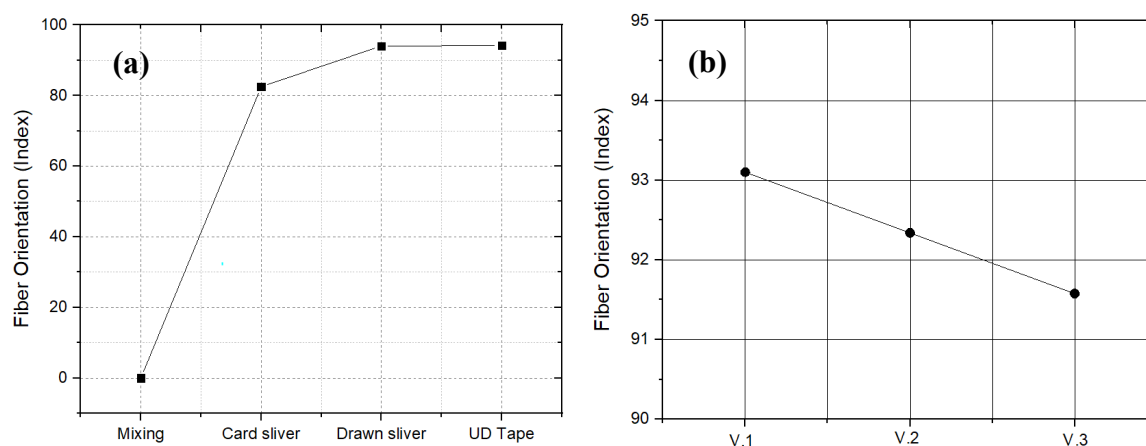


Fig. 3. Fiber orientation index vs. (a) process chain (b) different tape structure

Fig 3(b) presents fiber orientation results in different unidirectional tapes prepared by altering the draft. The results show that lower draft positively affects the fiber orientation of the unidirectional tape structure. In addition, the trend of fiber orientation in unidirectional tape shows that the fiber orientation index decreases with increasing the draft in the drafting system. It can be correlated with the non-uniform movement of the carbon fibers in drafting operations. It is well established that carbon fiber possess lower fiber-to-fiber cohesion due to its smooth and crimp-free surface. Therefore, a higher draft provokes non-uniform fiber movement that disturbs fiber orientation in the tape structure and leads to irregular tape structure.

Tensile properties of high performance thermoplastic composites

High-performance composites composed of different unidirectional tape structures were developed through constant thermo-fixation and consolidation parameters. The results of high-performance composites based on rCF/PA6 unidirectional tapes are given in Fig 4. The results show tensile strength of high-performance composites developed with 1.4 drafts is 1350 ± 28 MPa. In addition to this, the tensile strength of high-performance composites decreases with increasing the draft. It can be associated with decreasing trend of fiber orientation in tape structure, as reported earlier.

Furthermore, the areal density of the unidirectional tapes decreases with an increasing draft. The draft controls the thickness of the unidirectional tape structure by attenuating the fibers. Therefore, unidirectional tape with lower aerial density is intensively consolidated under constant thermo-fixation parameters. Additionally, the unidirectional tape was fabricated with 2.1 drafts deliver tape with 119 g/m^2 . Therefore, more layers of unidirectional tapes are required to develop a high-performance composite with the same thickness that enhances the chances of delamination in composite structure.

Consequently, lack of fiber orientation, intense degree of thermo-fixation, and proximity of delamination cause a decline in the composite strength. In contrast, the tensile modulus of the high-performance composites is unchanged in the composites. It can be attributed to the fiber volume fraction that remains in a range in the high-performance composites.

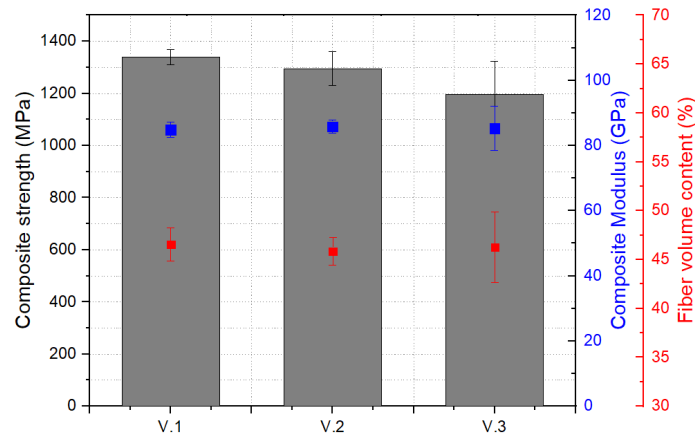


Fig. 4. Tensile properties of composites developed from UD-tapes

Summary

This paper introduces an innovative structure with unidirectional fiber orientation termed as unidirectional tape structure for high-performance recycled carbon fiber reinforced thermoplastic. Investigations results revealed that orientation index in tape structure reached up to 93 percent by utilizing optimum technological parameters of carding, drawing, and tape processes. Furthermore, this study also reveals that draft significantly contributes to the orientation of recycled carbon fibers in tapes and composites. Therefore, the right combinations of material, process, and consolidation parameters deliver composite with outstanding tensile properties. This study provides an opportunity to convert cost-effective recycled carbon fibers into high-performance composites through the unidirectional tape that can be used for load-bearing structural applications in the automotive and aerospace industries.

Acknowledgment

The authors would like to express appreciation for the support of the research projects [AZ-33809/01] and [IGF- 20515 BR] at the Technische Universität Dresden.

References

- [1] M. Sauer, "Composites Market Report 2019 - The global CF- and CC-Market 2019 - Market Developments, Trends, Outlook and Challenges," Composites United e.V., Germany 2020.
- [2] M. S. Schade W., Lembke M, "Analysis of the light weight fiber reinforced plastics value chain with regard to the German industry in its global context," M-Five working paper on behalf of the ECF and Cambridge Econometrics. Karlsruhe, 2017.
- [3] F. Meng, J. McKechnie, and S. J. Pickering, "An assessment of financial viability of recycled carbon fibre in automotive applications," Composites Part A: Applied Science and Manufacturing, vol. 109, pp. 207-220, 2018.
- [4] H. Mainka et al., "Lignin – an alternative precursor for sustainable and cost-effective automotive carbon fiber," Journal of Materials Research and Technology, vol. 4, no. 3, pp. 283-296, 2015.

-
- [5] K. Friedrich and A. A. Almajid, "Manufacturing aspects of advanced polymer composites for automotive applications," *Applied Composite Material*, vol. 20, pp. 107-128, 2013.
 - [6] S.R. Naqvi, H. Mysore Prabhakar, E.A. Bramer, W. Dierkesa, R. Akkerman, G. Brem, "A critical review on recycling of end-of-life carbon fibre/glass fibre reinforced composites waste using pyrolysis towards a circular economy," *Resources, Conservation & Recycling*, vol. 36, pp. 118–129, 2018
 - [7] S. Karuppannan Gopalraj and T. Kärki, "A review on the recycling of waste carbon fibre/glass fibre-reinforced composites: fibre recovery, properties and life-cycle analysis," *SN Applied Sciences*, vol. 2, no. 3, 2020.
 - [8] Y. F. Khalil, "Comparative environmental and human health evaluations of thermolysis and solvolysis recycling technologies of carbon fiber reinforced polymer waste," *Waste Management*, vol. March 2018, no. xxx, p. xxx, 2018.
 - [9] G. Oliveux, L. O. Dandy, and G. A. Leeke, "Current status of recycling of fibre reinforced polymers: Review of technologies, reuse and resulting properties," *Progress in Materials Science*, vol. 72, pp. 61-99, 2015.
 - [10] E. Pakdel, S. Kashi, R. Varley, and X. Wang, "Recent progress in recycling carbon fibre reinforced composites and dry carbon fibre wastes," *Resources, Conservation and Recycling*, vol. 166, 2021.
 - [11] J. Zhang, V. S. Chevali, H. Wang, and C.-H. Wang, "Current status of carbon fibre and carbon fibre composites recycling," *Composites Part B: Engineering*, vol. 193, 2020.
 - [12] A. Jacob. (2019) Building confidence in recycled carbon fibre. *Composites World*. 26-33.
 - [13] M. F. Khurshid, M. Hengstermann, Mir Mohammad Badrul Hasan, A. Abdkader, and C. Cherif, "Recent developments in the processing of waste carbon fibre for thermoplastic composites – A review," *Journal of Composite Materials*, vol. 54, no. 14, pp. 1925-1944, 2020.
 - [14] L. P. Kollar and G. S. Springer, *Mechanics of Composite Structures*. Cambridge, New York, Melbourne, Madrid, Cape Town, Singapore, São Paulo: Cambridge university press, 2003.
 - [15] Muhammad Furqan Khurshid, A. Abdkader, and C. Cherif, "Processing of waste carbon and polyamide fibres for high performance thermoplastic composites: Influence of carding parameters on fibre orientation, fibre length and sliver cohesion force " *Journal of the Textile Institute*, vol. 111, no. 9, pp. 1277–1287, 2020.
 - [16] M. F. Khurshid, M. Hillerbrand, A. Abdkader, and C. Cherif, "Processing of waste carbon and polyamide fibers for high-performance thermoplastic composites: Modifications to the auto-leveling system to enhance the quality of hybrid drawn sliver," *Journal of Industrial Textiles*, 2020.
 - [17] C. H. Lindsley, "Measurement of Fiber Orientation," *Textile Research Journal*, vol. January, pp. 39-46, 1951.
 - [18] C. A. Lawrence, *Fundamentals of spun yarn technology*. Boca Raton London New York Washington, D.C.: CRC PRESS, 2003.
 - [19] D. Das, S. M. Ishtiaque, and P. Dixit, "Influence of carding and drawing processes on orientation of fibers in slivers," *Journal of the Textile Institute*, vol. 103, no. 6, pp. 676-686, 2012.

From Grave to Cradle - Development of Weft Knitted Fabrics Based on Hybrid Yarns from Recycled Carbon Fibre Reclaimed by Solvolytic Process from of EOL-Components

David Rabe^{1,a*}, Mir Mohammad Badrul Hasan^{1,b}, Eric Häntzsche^{1,c},
Chokri Cherif^{1,d}, Yasushi Murakami^{2,e}, Limin Bao^{2,f}, Kanji Kajiwara^{2,g}

¹Institute of Textile Machinery and High Performance Material Technology (ITM),
Helmholtzstr. 5, Dresden, Germany

²Faculty of Textile Science and Technology, Shinshu University,
Tokita 3-15-1, Ueda, 386-8567 Japan

^{a*}david.rabe@tu-dresden.de, ^bmir_mohammad_badrul.hasan@tu-dresden.de,
^ceric.haentzsche@tu-dresden.de, ^dchokri.cherif@tu-dresden.de, ^eyasmura@shinshu-u.ac.jp,
^fbaolimin@shinshu-u.ac.jp, ^gkajiwara@shinshu-u.ac.jp,

Keywords: Recycling, carbon fibre, solvolysis, resizing, hybridization, hybrid yarn, spun fibre yarn, weft knitting, thermoplastic composite

Abstract. Carbon fibre (CF) is widely used in CF reinforced plastic (CFRP) components. However, waste CF, CFRP and the end-of-life (EOL) CFRP structures will cause an even bigger problem in the next years because of strict environmental regulations. Currently, recycling is carried out almost entirely by the use of pyrolysis to regain CF as a valuable resource. This high temperature process is very energy consuming and the resulting fibres are brittle. Hence, not suitable for textile processing into yarns or fabrics. To enable a grave to cradle circle, a new approach based on a solvolytic recovery of CF and the subsequent spinning process to obtain a hybrid yarn suitable for weft knitting processing is the focus of the international research project IGF/CORNET 256EBR “3D-r-CFRP”.

Introduction

CF is one of the most widely employed high-performance fibres for advanced light-weight structural composites. However, the huge amount of waste CF, which originates during the production of CFRP impacts global environment. Furthermore, the end-of-life CFRP will cause more serious socio-economic problems in near future [1]. For this reason, recovering of CF from CFRP is an urgent task considering environment pollution and CO₂ discharge [2]. Reclaiming of CF from CFRP is nowadays carried out almost entirely by the use of pyrolysis technique by exposing CFRP to high temperature (450 to 600 °C) [1, 3]. Compared to virgin CF, the strength of recycled CF (rCF) obtained from end of life (EOL) composites by pyrolysis is low. Furthermore, the brittle state of the pyrolysis fibres is not well suited for the textile processing (e. g. carding, spinning, knitting) and restricts their application range to the downcycling [4, 5]. As a result, rCF composites are currently classified as low performance products [1]. A new approach is required to satisfy all the requirements to obtain rCF that can be used for the textile processing into hybrid yarns for the production of high performance CFRP components.

At Shinshu University, several developments have been carried out to design a continuous process for CFRP recycling by use of overheated steam (< 300°C) with a suitable catalyst. Thereby epoxy matrix is decomposed to yield oily substances and CF can be recovered quickly and gently with 100 mm fibre length for novel loadbearing CFRP components. To meet the increasing demand for thermoplastic composites, the aim of the project is set to develop highly oriented rCF hybrid yarns suitable for the production of CFRP with high mechanical properties. Available yarn manufacturing technologies are not suitable for processing rCF due to its brittleness, lack of sizing, smooth surface and electrical conductivity. Within the project, new hybrid yarn structures with scalable mechanical properties were developed at ITM of TU Dresden by modifying DREF-friction spinning process. Furthermore, the hybrid yarns were processed into a new kind of easy formable textile reinforcing

structures by means of weft knitting techniques. Therefore, the weft knitting process with weft and warp yarns was adapted to rCF hybrid yarn processing properties.

Materials and Methods

In this work, Toray T700SC 50 C, 12k, 800 tex was used as the “reference” virgin filament yarn. The fibre “rCF-Type 1” means cut virgin fibres of 100 mm length from virgin filament yarn. The fibre type “rCF-Type 3” means fibres obtained from industrial wastes of uncured or partly cured CFRP unidirectional (UD) tape prepregs made from virgin filament yarn, which were cut into 100 mm x 100 mm pieces and subjected to solvolysis by overheated steam. The fibre recovery process by solvolysis consists of two steps. The first step, a carbonisation process in an inert gas atmosphere at 400 °C, which removes the epoxy resin up to a certain degree by the decomposition of epoxy. A water trap recovers decomposed epoxy resin for recycling purposes. In the second step, a removal reaction of the carbonized epoxy resin at 400 °C under controlled atmospheric conditions (overheated vapour) decomposes the remaining epoxy residues on the CF surface using a milder conditioned heat steam. In this two-step process, CF is preserved against a loss of mechanical properties. The third and last step of fibre recycling is a batch washing process with acetone to remove all reaction residuals. The resulting mechanical properties of the obtained rCF was determined by single fibre tensile tests and the surface was observed by scanning electron microscope (SEM) to optimize decomposition conditions. The gained fibres were resized in a fourth step in a batch process with two different sizing agents. To assure a good fibre-matrix interaction, new sizing agents based on titanium oxide were developed and investigated (cf. Fig. 1).

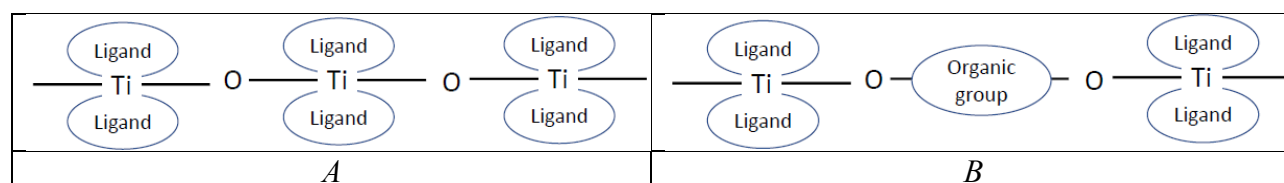


Fig. 1: Graphic formula of the developed and applied sizing type A and B containing oxygen and titanium for increasing fibre-matrix adhesion

For the spinning of rCF into hybrid yarn structures, the rCF Type 1 and Type3 (100 mm fibre length) reclaimed through the solvolysis process and finished with sizing A and polyamide 6 (PA6) staple fibre (80 mm fibre length) were used. At the first stage, rCF and PA6 fibre were processed on the carding and the draw frame machine to produce drawn slivers with a defined ratio of 72 and 18 weight percentage of rCF and PA6, respectively. The development of hybrid yarns was carried out on a DREF-3000 friction-spinning machine. The hybrid yarn consists of a core and sheath structure (cf. Fig. 2). As the core 1, the produced drawn sliver and as the core 2, a PA6-filament yarn of 30 tex was used. The sheath was made from PA6 staple fibres. The core to sheath weight ratio of the hybrid yarn is 90:10. The resulted rCF content in the hybrid yarn is 62 weight percentage (equivalent to 54 volume percentage in subsequent composite). The resulting count of the yarn is 600 tex.

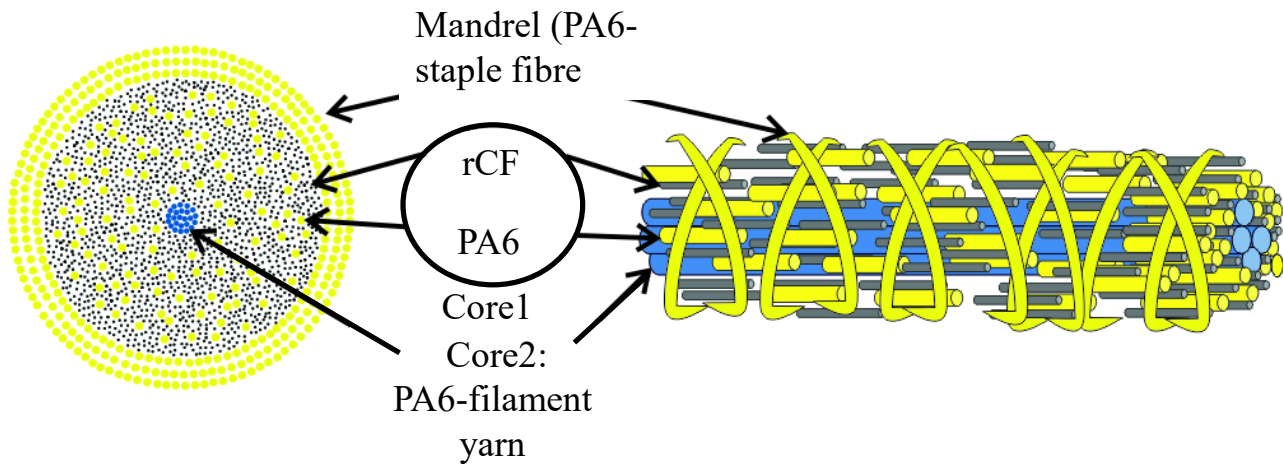


Fig. 2: Schematic picture of the structure of the rCF-hybrid yarn

The range of production parameters and necessary modifications at the carding, the draw frame, DREF 3000 friction spinning machine was investigated taking the weft knitting processability of the developed rCF-hybrid yarns into account. The composite properties achievable with different yarn constructions were examined by tensile testing based on unidirectional (UD) composites. Therefore, rCF-hybrid yarns were wound around a frame and pressed at 295°C and 4.2 MPa in a 75 min cycle including heating, pressing and cooling (cf. Fig. 3).

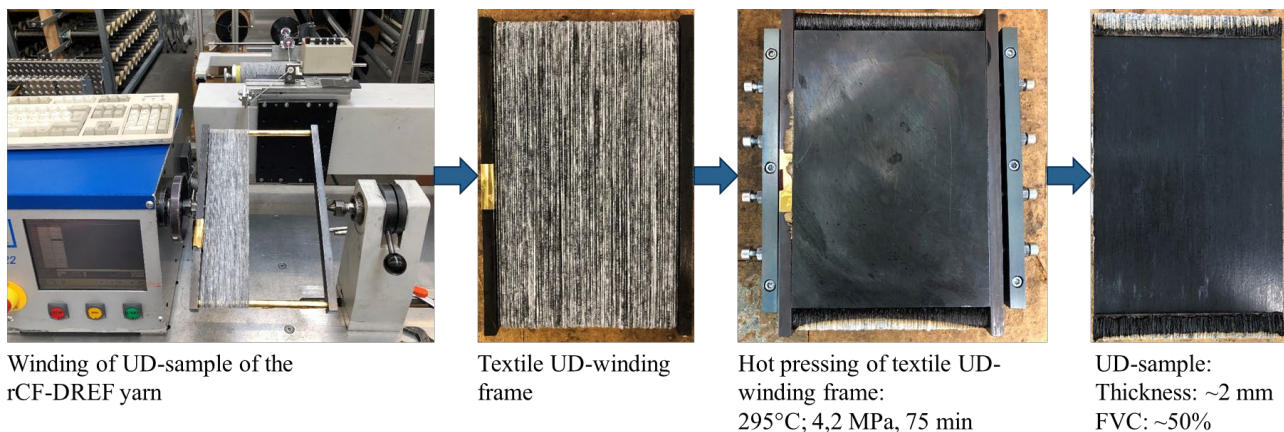


Fig. 3: Preparation and pressing procedure for the production of UD-composite plates from hybrid yarns

The UD composite plates were cut into 250 x 25 mm² specimen for tensile testing, according to the testing standard DIN EN ISO 527. For a comparison with the reference CF filament yarn, same procedure was done to make a UD composite plate from CF filament yarn and PA6 fibres. In this way two hybrid yarns from rCF-Type 1 and rCF-Type 3: sizing A were compared regarding the tensile strength with the reference made from CF filament yarn.

These hybrid yarns were processed subsequently on a modified biaxial weft knitting machine to a 900 mm wide multilayer flat knitted fabrics with two reinforcing layers (consisting of a 90° weft and 0° warp yarn layer) for extensive evaluation of the processing properties.

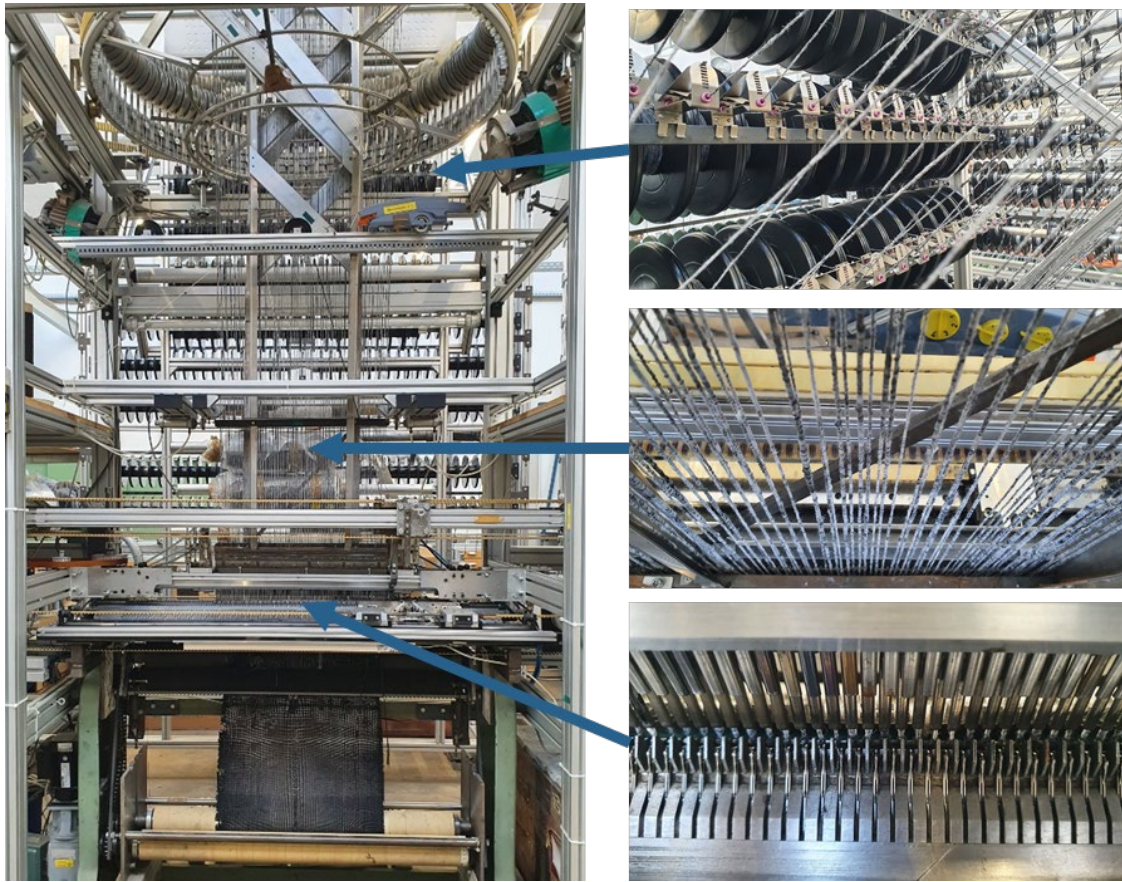
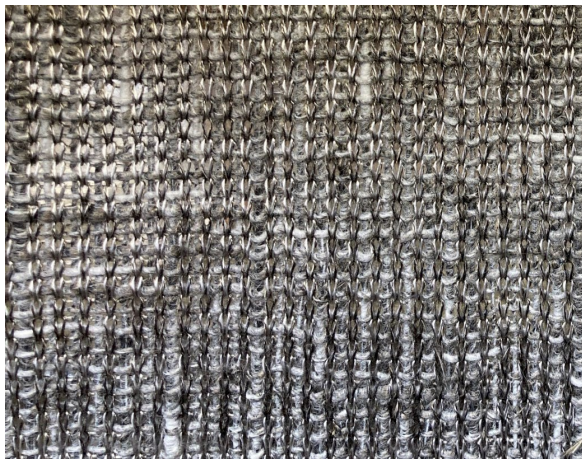
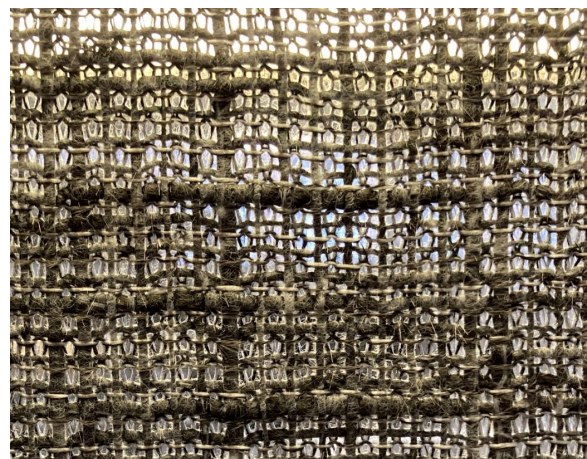


Fig. 4: Modified biaxial weft knitting machine (gauge E5, working width 500 mm)

The knitting machine (yarn delivery, yarn guides) and the knitting parameters (tension, speed, stitch length) were optimized to obtain demanded fabric quality. The weft knitting technology was used by considering its high production flexibility and its advantageous binding techniques to enable both a high drapable structure and a net shape geometry. The resulted weft knitted reinforcement structure contains the rCF-hybrid yarn (rCF-Type 3 sizing A) in weft and in warp direction. Both yarn systems were connected by a stitch thread. As the stitch thread, a hybrid yarn consisting of a stretch broken CF yarn (70 tex) and a PA6 filament yarn (94 tex) was used. The developed textile reinforcement structure possesses an aerial weight of approximately 590 g/m². The taper depth is the decisive machine parameter that has been changed to investigate its influence on the resulting structure and the mechanical behaviour (e. g. tensile and bending strength) as well as drapability.



a)



b)

Fig. 5: Weft knitted structure from the front (a) and the back (b) containing the rCF-hybrid yarn in weft (90°) and in warp (0°) direction

The weft knitted structures, as in the case of the yarns, were processed into composite plates using a hot press (cf. Fig. 6) for the characterisation of composite properties. Four layers of structure $[(0/90)_{2,s}]$ lead to a composite plate of 2 mm in thickness and a resulting fibre volume content of about 50 %. These plates were cut into specimen $250 \times 25 \text{ mm}^2$ and $80 \times 15 \text{ mm}^2$ for tensile tests (according to DIN EN ISO 527) and 4-point bending tests (according DIN EN ISO 14125), respectively.

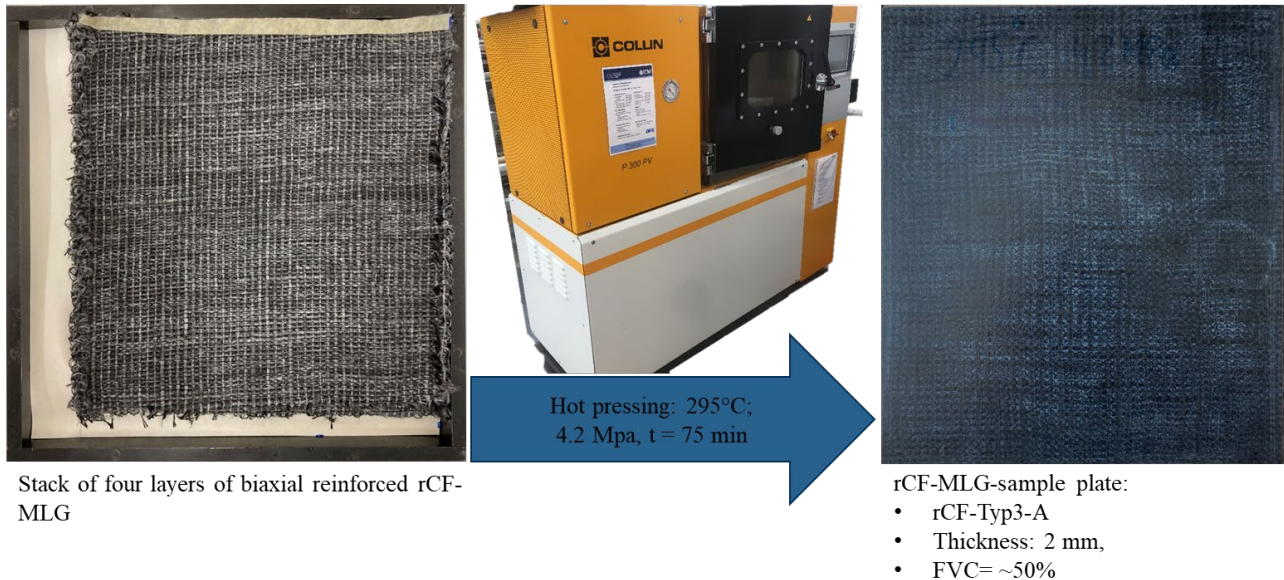


Fig. 6: Preparation and pressing procedure for producing of biaxial reinforced MLG-composite plates for mechanical characterisation

Results and Discussion

The recovered rCF with 100 mm in length possesses a tensile strength similar to that of a virgin CF (cf. Fig. 7). The slight loss in elasticity and tensile strength is within the standard deviation and can be regarded as insignificant (cf. Table 1).

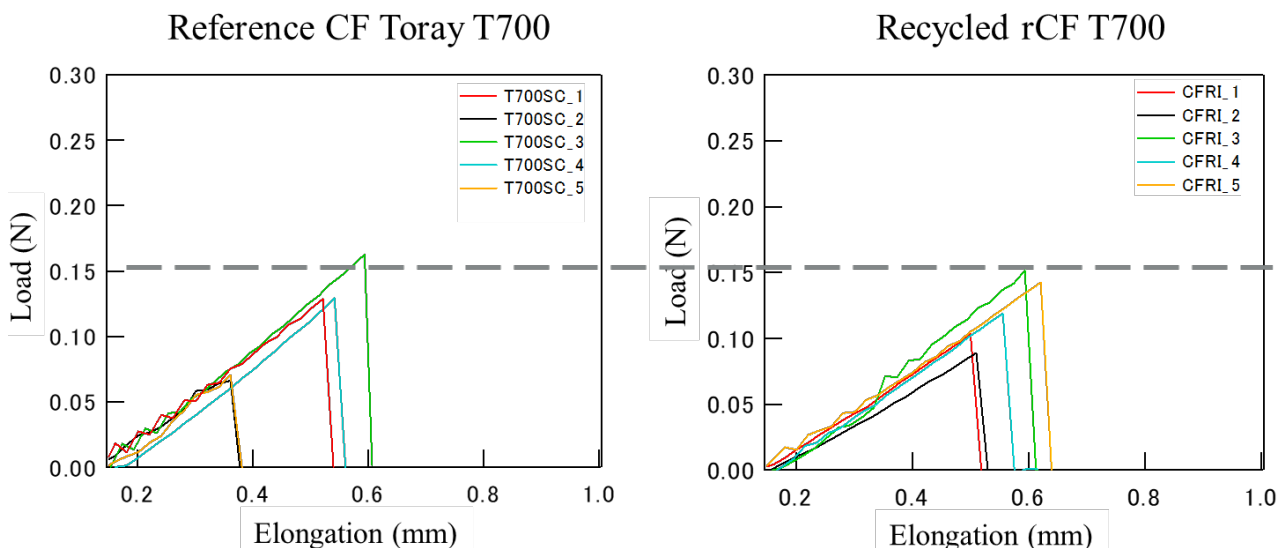


Fig. 7: Tensile behaviour of recycled carbon fibres (rCF) after solvolytic recycling process

Table 1: Tensile behaviour of the recycled CF

	Elastic modulus (GPa)	Average tensile strength (MPa)	
T700SC	238 ± 63	$3,768 \pm 464$	virgin fibre
rCF-Type 3	236 ± 17	$3,620 \pm 577$	recycled fibre

The SEM observation shows high similarity of fully recycled fibres (after third step: washing with acetone) with virgin fibres (Toray T700SC) (cf. Fig. 8). Matrix residual from the second step is completely removed after the final third step. On the fourth and last step (resizing), a new type of sizing agent (Type A and B, cf. Fig. 1) was developed based on a titanium complex suitable to PA6 matrix and applied on the rCF.

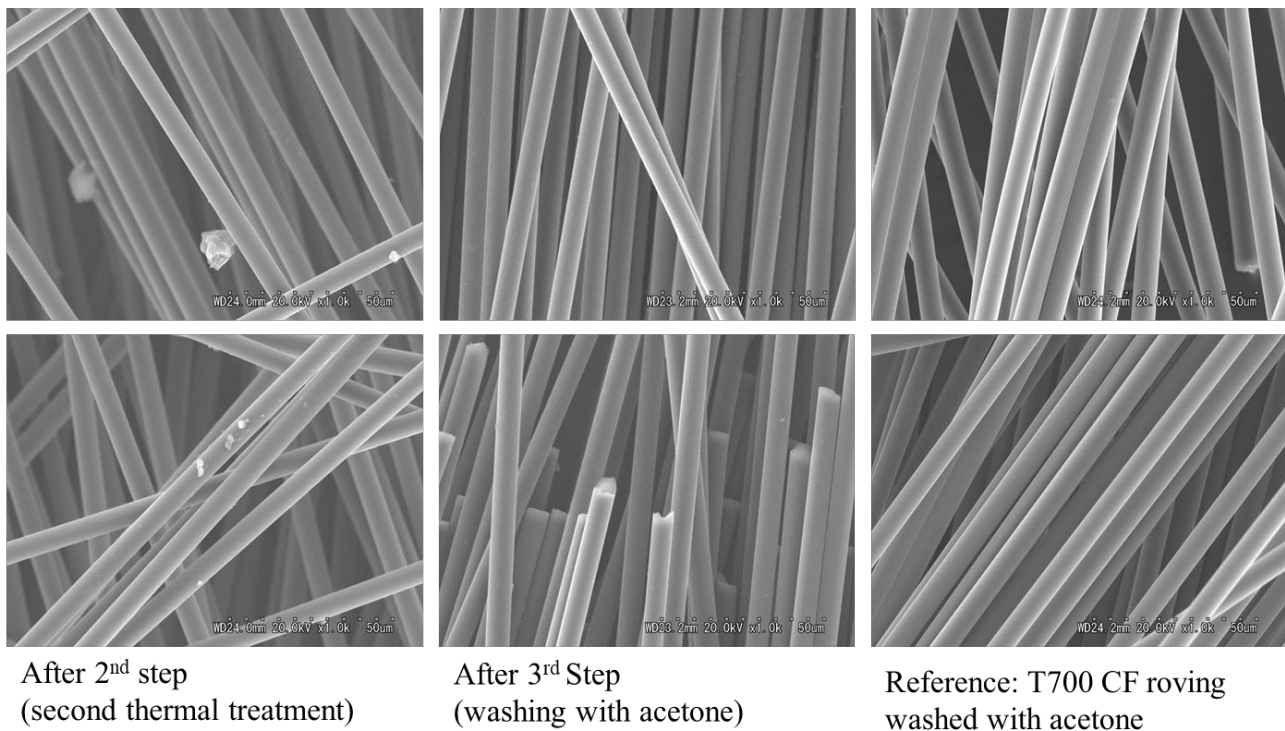


Fig. 8: SEM observation of recycled fibres (magnification: 1,000 x)

First investigations with rCF at the DREF-friction spinning technology shows a good processability of the rCF reclaimed through solvolysis. In Fig. 9, the comparison of the tensile strength of UD composites made from hybrid yarns consisting of rCF (Type 1 and 3) and virgin CF filament (as the reference) is shown. It can be revealed that there is a loss of about 35 % and 49% in the tensile strength of composite from hybrid yarns with rCF-Type 1 and rCF-Type3 fibres, respectively compared to the reference composite.

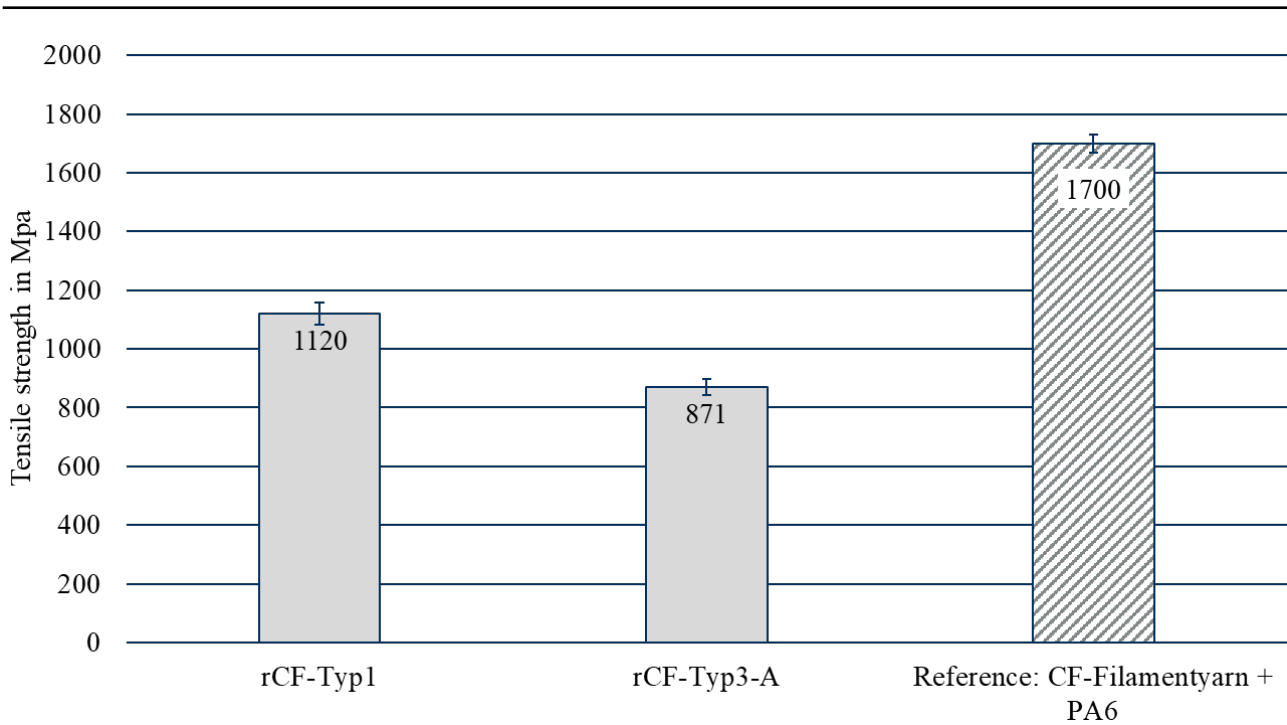


Fig. 9: Tensile strength of rCF UD-composites

The MLG flat knitting technology was optimized for the rCF hybrid yarns. Some modifications on the yarn guiding lead to a good processability. The taper depth was varied to get an insight of the influence of this machine parameter on the mechanical properties. The results show that the tensile and bending strength varies depending on the taper depth,. Although it must be stated that the difference is not significant. In comparison to the UD-material (rCF-Type3-A, cf. Fig. 9), the biaxial reinforced composite showed a significant lower tensile strength. Normally, a biaxial reinforcement material should show around 50 % of the strength of a UD-material made from the same fibres. Reason for these low specific values in the first characterisation are may be the stitch thread material or the new processing route. Further tests are being carried out to find out whether the strength can be improved by using different stitch thread material.

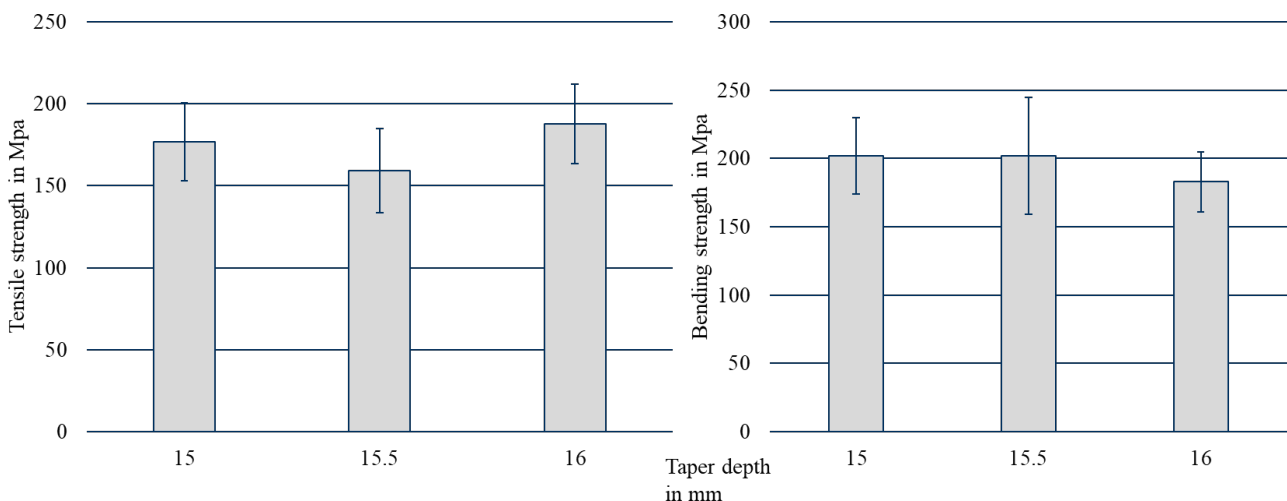


Fig. 10: Tensile and bending strength of rCF MLG composites

Summary

The developed process will enable for the first time a convenient and productive route for complete large scale CFRP recycling and transfer of high-level fibre properties into new composite products. In the same time, benefits of staple fibre yarns and textile structures will activate the production of

high-performance 3D composite parts from rCF for further applications, e.g., in automobiles or plant engineering. The proposed project will overcome most drawbacks of rCF, including high production costs, high environmental impact and disposal. The investigations showed good results from fibre recycling from EOL-components. The properties of the resulting rCF are well suited for textile processing. Two sizing systems were developed, and in next examinations the hybrid yarn made of rCF-Type 3 with sizing B will be studied. The hybrid yarn manufacturing process was modified for the processing of rCF reclaimed by solvolysis. The tensile strength of UD-composites from the developed hybrid yarns showed a slightly lower strength compared to UD-composites made from virgin CF. The hybrid yarns were processed further into biaxial reinforced weft knitted structures. Finally, a 3D-shell demonstrator part from the automotive industry is planned.

Acknowledgement

The IGF/CORNET project 265 EBR of the Forschungskuratorium Textil e.V. is funded through the AiF within the program for supporting the “Industrielle Gemeinschaftsforschung (IGF)” from funds of the Federal Ministry for Economic Affairs and Energy by a resolution of the German Bundestag. NEDO, Japan, supported CORNET project P14005 under the co-funding scheme in collaboration with AiF. The funding is gratefully acknowledged.

Supported by:



on the basis of a decision
by the German Bundestag

References

- [1] Bledzki, A. K.; Seidlitz, H.; Goracy, K.; Urbaniak, M.; Rösch, J. J.: Recycling of Carbon Fiber Reinforced Composite Polymers-Review-Part 1: Volume of Production, Recycling Technologies, Legislative Aspects. *Polymers* 13(2021)2, p. 300
- [2] Meng, F.; McKechnie, J.; Turner, T.; Wong, K. H.; Pickering, S. J.: Environmental Aspects of Use of Recycled Carbon Fiber Composites in Automotive Applications. *Environmental science & technology* 51(2017)21, pp. 12727-12736
- [3] Meyer, L. O.; Schulte, K.; Grove-Nielsen, E.: CFRP-Recycling Following a Pyrolysis Route: Process Optimization and Potentials. *Journal of Composite Materials* 43(2009)9, S. 1121-1132
- [4] Nahil, M. A.; Williams, P. T.: Recycling of carbon fibre reinforced polymeric waste for the production of activated carbon fibres. *Journal of Analytical and Applied Pyrolysis* 91(2011)1, S. 67-75
- [5] Greco, A.; Maffezzoli, A.; Buccoliero, G.; Caretto, F.; Cornacchia, G.: Thermal and chemical treatments of recycled carbon fibres for improved adhesion to polymeric matrix. *Journal of Composite Materials* 47(2013)3, S. 369-377

Low Twist Hybrid Yarns from Long Recycled Carbon Fibres for High Performance Thermoplastic Composites

Mir Mohammad Badrul Hasan^{1,a*}, Samuel Bachor^{2,b}, Anwar Abdkader^{1,c}
and Chokri Cherif^{1,d}

¹Institute of Textile Machinery and High Performance Material Technology (ITM), Technische Universität Dresden, Hohe Straße 6, Dresden, Germany

²Institute of Lightweight Engineering and Polymer Technology (ILK), Technische Universität Dresden, Holbeinstraße 3, 01307 Dresden, Germany

^{a*}mir_mohammad_badrul.hasan@tu-dresden.de, ^bsamuel.bachor@mailbox.tu-dresden.de,
^canwar.abdkader@tu-dresden.de, ^dchokri.cherif@tu-dresden.de

Keywords: Recycled carbon fibre; hybrid yarn; spun fibre yarn, thermoplastic composite tensile property

Abstract. With the increasing demand and use of carbon fibre reinforced composites (CFRP), the disposal of carbon fibres (CF) and end-of-life composite parts is gaining tremendous importance, particularly in terms of sustainability. The current focus of using recycled carbon fibre (rCF) is still on nonwovens or injection-moulded components, characterized by low performance. On the contrary, spinning rCF to yarn constructions offers good potential for improved CFRP material properties due to longer fiber length, high fibre orientation, compaction of rCF and even yarn structure. However, previous experiences reveal that the shortening of fibres increases with longer input rCF during carding. Therefore, the focus of this work is placed on broadening the knowledge concerning gentle processing of rCF, especially for fibres > 60 mm in combination with thermoplastic fibres. In this work, a new yarn construction is developed by significantly reducing the yarn twist to ensure a fibre orientation parallel to the yarn axis in order to increase mechanical properties of composites significantly. With the developed hybrid yarns, tensile strength and E-modulus of 1364 ± 49 MPa and 100 ± 15 GPa, respectively in composites could be achieved.

Introduction

Carbon fibre reinforced composites (CFRP) are widely used for load bearing structures because of their excellent strength, rigidity and damping properties as well as low weight. With an increased demand and usage of CFRPs, a high volume of CF waste is produced through a number of different processes, e. g. during the production of fabrics / pre-forming (cut edges) or rest yarn spool (bobbin waste). The manufacturing waste is approximately 40% of all the CFRP waste generated [1]. At this stage, there are a number of processes (e. g. pyrolysis, solvolysis etc.) available to obtain recycled CF (rCF) from end-of-life CFRP. Anyway, since waste CF or rCF products are not biodegradable, the disposal of these products assumes even greater significance. Due to European legislation, e. g. EU2000/53/EC, a recycling rate of disposed automotive vehicles of 85% is required. Therefore, environmental concerns both in terms of limiting the use of finite resources and the need to manage waste disposal have led to a focused attention on the need to find effective methods to re-use waste CF/rCF materials.

Intensive literature reviews show that the focus of manufacturing CFRP from rCF is on nonwovens (e.g. at STFI, ITA Augsberg, Tenowo) or on using chopped fibres, e.g. in injection moulding or Sheet Moulding Compounds. Tensile strength for such components is up to 500 MPa [2, 3], well below the unidirectional (UD) composites from virgin filament yarn that can achieve up to 1,800 MPa depending on the fibre volume content. In order to better utilize the potential of rCF, the development of hybrid yarn structures offers the possibility to achieve high fibre orientation, low fibre damage and high fibre volume content and thus higher mechanical properties on composite level.

At present, the machine technology developed can be used to achieve a gentle processing of rCF with a uniformly cut length of up to 60 mm, whereby a mean fibre length of 50 mm (in draw frame slivers) is obtained. The average fibre length decreases to 58 and 67 mm while processing rCF with length of 80 and 100 mm, respectively [4].

Another important aspect is the still relatively high process-driven twist of the hybrid yarns. Higher twists (> 80 T/m) are required in order to increase the yarn strength, so that further processing of hybrid yarns in subsequent process stages (e. g. weaving) is possible. However, composite strength decreases with an increase in yarn twist due to higher damage and disorientation of brittle rCF from the yarn axis as shown in Fig. 1a [5].

The effect of input rCF length at a constant yarn twist (102 T/m) on the tensile strength of UD composites manufactured from hybrid yarns consisting of rCF and polyamide 6 fibre (PA6) is shown in Fig. 1b [4]. It indicates that, although the average fibre length of slivers in the case of 80 and 100 mm input rCF is higher compared to that of 60 mm rCF, composite strength decreases using rCF > 60 mm. However, it is known that the composite strength should increase with the increase of reinforcing fibre length. The increased proportion of fibre shortening and lower fibre orientation at high fibre lengths resulting from non-adapted machine techniques are believed to be the cause of decreased composite strength.

Therefore, the novelty of this work are two folds: firstly to ensure the gentle processing of rCF especially for fibres > 60 mm in combination with thermoplastic fibres. Secondly, development of a new yarn construction with significantly low twist to ensure ideally the parallel orientation of fibres in the yarn axis in order to significantly increase the tensile strength of composites (Fig. 1b).

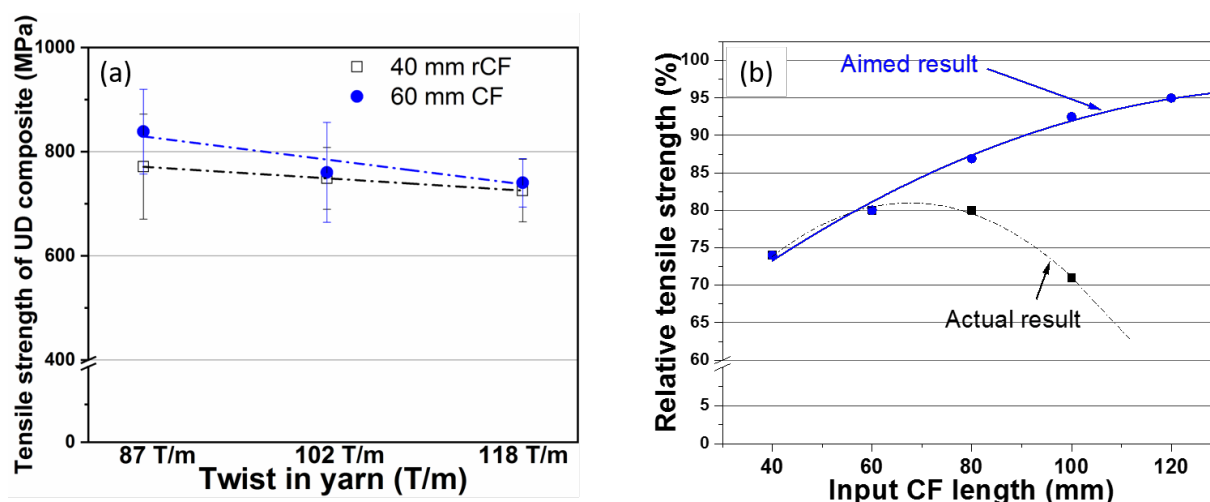


Fig. 1: Effect of yarn twist [4] (a) and input rCF length [5] (b) on average tensile strength of UD thermoplastic composites made from hybrid yarns on a roving frame

Development of Hybrid Yarns

Materials. The rCF used for the development of low twist hybrid yarns is obtained by cutting bobbin ends of continuous carbon filament tows (production waste) into defined length of 80 and 100 mm. As the matrix fibre, crimped PA 6 fibre of 80 mm is used. Tensile properties of the used fibres are summarized in Table 1.

Table 1: Tensile properties of the used fibre materials

Fibre Type	Fibre properties				
	Nominal Fibre length [mm]	Fineness [dtex]	Strength [GPa]	E-Modul [Gpa]	Elongation [%]
rCF	80 ± 2.0	0.45 ± 0.11	3.36 ± 0.63	227.50 ± 40.13	1.70 ± 0.26
	100 ± 2.0				
PA 6	80 ± 1.0	3.57 ± 0.12	0.54 ± 0.05	1.40 ± 0.03	59.70 ± 5.44

Carding process. One of the main objectives of this work is to explore the fibre dynamic and mechanism of fibre shortening, which occurs during carding processes. Thus, the damage in rCF can be systematically reduced to a great extent. For this purpose, following measurements are undertaken on the carding machine available at the ITM:

- Modification of the feeding unit to enable gentle opening of brittle rCF and pre-mixing with PA6 fibres.
- Systematic analysis of fibre damage occurring in different transfer zones on the carding machine especially, between taker-in and cylinder, cylinder and worker, cylinder and doffer regarding
- Design of experiments to find out the optimum gauges and speed of different rollers

Through different technological and constructive developments of the carding machine, fibre damage could be reduced significantly. With the best possible machine parameters, two different card slivers (Table 2) are produced for further use during the development of hybrid yarns. The rCF content of the card slivers is 60 weight-% (equivalent to 50 volume-% in subsequent composite).

Table 2: Overview of the produced card slivers

rCF fibre length (mm)	PA6 fibre length (mm)	Proportion of fibre in card sliver (weight%)		Fineness of card sliver (ktex)	Identification of card sliver
		rCF	PA 6		
80	80	60	40	2.8	CS_rCF_80mm
100	80	60	40	2.9	CS_rCF_100mm

Drawing process. Afterwards, drawing is carried out on the card slivers using a modified high performance draw frame machine at the ITM in order to improve sliver regularity and level of mixing between rCF and PA6. For this purpose, further modifications to reduce the scanning roller load of auto-leveling system is carried out by integrating a load adjustment device and replacing the existing spring with a new one. The results obtained suggest a recommended load of 70 N and enables a hybrid sliver with minimum fiber damage. Extensive analysis of different drawing parameters, e. g. delivery speed, draw ration and gauges is carried out to find the gentle processing parameters. With the best possible machine parameters, two different drawn slivers (Table 3) are produced for the development of hybrid yarns.

Table 3: Overview of the produced drawn slivers

Identification of card sliver	Fineness of draw frame sliver (ktex)	Identification of draw frame sliver
CS_rCF_80mm	1.7	DS_rCF_80mm
CS_rCF_100mm	1.9	DS_rCF_100mm

Spinning process. Furthermore, a new hybrid yarn construction is developed by significantly reducing the twisting (<60 T/m) to ensure ideally a parallel orientation of fibres in the yarn axis. The hybrid yarns are spun based on the flyer spinning principle using a special module developed at the ITM. With developed spinning module, it is possible to spin hybrid yarns with significantly low twists of upto 30 T/m. The hybrid yarns produced with three different twist levels and input rCF lengths can be seen in Table 4.

Table 4: Overview of the produced hybrid yarns

Identification of draw frame sliver	Yarn twist (T/m)	Fineness of hybrid yarn (tex)	Calculated angle of surface fibre of hybrid yarn ($^{\circ}$) [6]	Identification of draw frame sliver
DS_rCF_80mm	30	1000	6	Y_rCF_80mm_30T
	50		10	Y_rCF_80mm_50T
	75		14	Y_rCF_80mm_75T
DS_rCF_100mm	30	1000	6	Y_rCF_100mm_30T
	50		10	Y_rCF_100mm_50T
	75		14	Y_rCF_100mm_75T

Manufacturing of UD thermoplastic composites. In order to investigate the tensile properties of composites produced from the developed hybrid yarns, UD composite plates with dimensions $180\text{ mm} \times 260\text{ mm} \times 1\text{ mm}$ are produced. For this purpose, the wrapping of the hybrid yarn is performed on a wrapping frame (IWT Industrielle Wickeltechnik GmbH, Germany). The wrapping frames are consolidated by the Laboratory press machine P 300 PV (Dr. Collin GmbH, Germany). The consolidation is carried out at 295°C and with a pressure of 4.2 MPa. Test specimens with the dimension $250\text{ mm} \times 25\text{ mm} \times 2\text{ mm}$ are then cut out of the consolidated composite plates to carry out tensile tests in 0° direction according to DIN EN ISO 527-5.

Characterisations. In order to characterize and explore the influence of process parameters on the shortening of fibres, the characterization of rCF length distribution is carried out based on a new method. For the determination of rCF length, an alternative and promising image processing technique based on fibrograph method [7] introduced by Hengstermann et. al. in [8] is employed. This system is specifically selected for the measurement of rCF length since because of the limitations of conventional methods, e.g. Fibrograph and HVI, due to the electro-conductivity of rCF.

The tensile properties of the hybrid yarns are tested according to ISO 3341 by means of a tensile strength testing device Zwick type Z 2.5 (Zwick GmbH and Co., Germany) with special return clamps and external strain measuring. Samples of 250 mm yarn length are employed. The test velocity is set to 100 mm/min and the initial load is kept at 0.5 cN/tex.

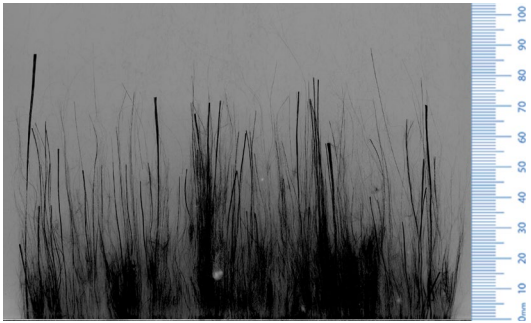

The testing of the tensile properties of the UD thermoplastics composite specimen is performed on the testing device Zwick type Z 100 (Zwick GmbH and Co., Germany) in accordance with the standard DIN EN ISO 527-5. The cross head speed of 2 mm/min and a test length of 150 mm are used for the tensile test. The elongation is measured using an optical sensor.

Results and Discussion

Fibre length. The fibre beard prepared from the draw frame slivers consisting of rCF and PA 6 fibre for the measurement of fibre length is displayed in Table 5. The mean and the upper half mean length (UHML, which is the mean length of the longer half of the fibre span length distribution determined from the fibrograph [9]) of rCF in the draw frame sliver produced from 80 mm rCF is 59.7 ± 1.8 and 76.7 ± 2.6 mm, respectively. Where as the mean and UHML of rCF in the draw frame

sliver produced from 100 mm rCF is 75.7 ± 4.7 and 98.0 ± 3.7 mm, respectively. This indicates a very low level of fibre shortening in waste CF and is the result of optimum machine set-up in carding and drawing process.

Table 5: Fibre beard and fibre length in draw frame slivers

Identification of card sliver	DS_rCF_80mm	DS_rCF_100mm
Fibre beard		
Mean length (mm)	59.7 ± 1.8	76.7 ± 2.6
Upper half mean length (UHML) (mm)	75.7 ± 4.7	98.0 ± 3.7

Influence of fibre length and yarn twist on yarn strength. The influence of yarn twist on hybrid yarn strength is shown in Fig 2a. The yarns strength increases linearly within the observed yarn twist level for both the rCF fibre lengths. On the other hand, the elongation of yarn decreases generally with the increase of yarn twists. This can be attributed to the increased yarn compactness and fibre to fibre cohesion of the hybrid yarns due to higher yarn twists.

The force elongation curves of the hybrid yarns with varying twists from 35 to 75 T/m are illustrated exemplarily for 100 mm rCF length in Fig. 2b. It shows that force elongation response varies from ductile to brittle nature with the increase of yarn twist. At 35 T/m, the hybrid yarns are also voluminous and hairy because of low lateral pressure. The tensile failure mechanism of the hybrid yarns is mainly dominated by fibre slippage. The constituent fibres are held with very low binding forces due to low fibre to fibre cohesion between brittle rCF and ductile PA 6 fibres. This can be recognized from the flat slope in the force elongation curves. As a result, the hybrid yarns show higher elongation and higher ductility. With the further increase of twist to 50 T/m, the hybrid yarns exhibit pseudo-ductile response. The initial stage of the force elongation curves is dominated by rCF of the hybrid yarn and is the result of higher frictional forces by the lateral pressures arising from the application of tensile stress along the yarn axis due to higher twists. As a result, the initial slope of the force elongation curves is steeper than that of hybrid yarns with 35 T/m and the elongation of hybrid yarns is lower than that of 35 T/m.

By further increasing the hybrid yarn twists to 75 T/m, the tensile strength increases also because of higher cohesive forces. The initial slope of the force elongation curves is the steepest and the elongation of the hybrid yarns is the lowest in the case of hybrid yarns with 75 T/m. The hybrid yarns show a more brittle behavior. This is the result of a lack of freedom to fibre slippage especially in the case of 75 T/m.

From the results, it can be revealed that through the variation of yarn twists, customized yarns from brittle up to ductile nature for different applications can be developed.

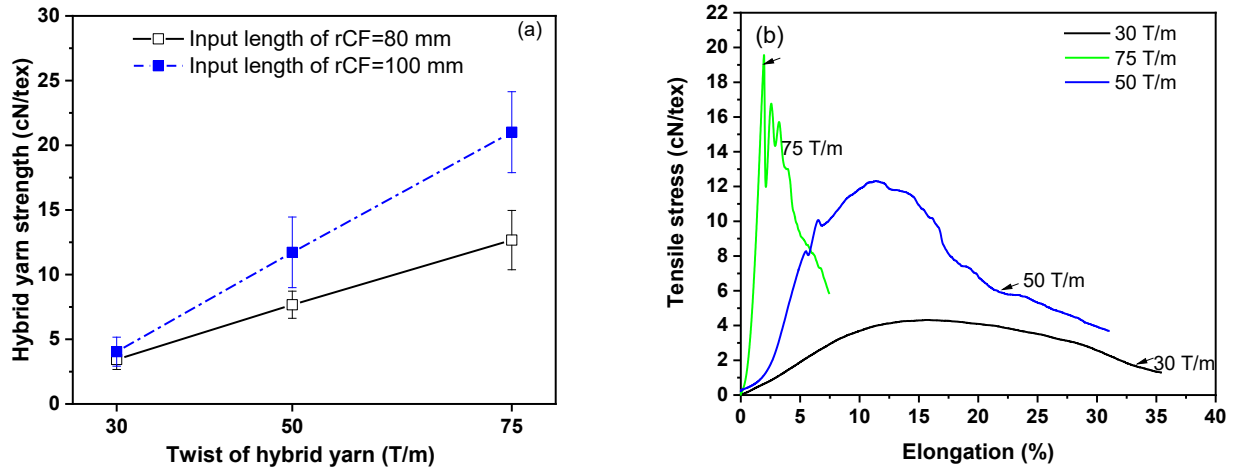


Figure 2: Effect of yarn twist on (a) tensile strength and (b) stress elongation behaviour of hybrid yarns from rCF and PA6 fibre

Influence of fibre length and yarn twist on composite tensile strength. The effect of hybrid yarn twist on the tensile properties of UD composites is illustrated in Fig. 3. It can be seen that composite strength (Fig. 3 (a)) and E-modulus (Fig. 3 (b)) gradually decrease with an increase of hybrid yarn twist. This can be attributed to the orientation of fibres (i.e. to the yarn axis) within the composite. As the load transfer mechanism in fibre reinforced composites is provided by interfacial bonding between fibre and polymer matrix in a non-slippage state [10], the higher surface angle of fibres on the yarn as a result of a greater twist level causes the strength of composites to decline. Similar phenomenon regarding the effect of yarn twist on composite strength and modulus is observed for natural fibre reinforced composites [6].

The maximum tensile strength and E-modulus of 1364 ± 49 MPa and 100 ± 15 GPa, respectively could be achieved in the case of a UD-composite manufactured from hybrid yarn with 35 T/m. Higher tensile strength can be achieved with 100 mm rCF length compared to 80 mm rCF. However, the effect of fibre length on the E-Modulus of composite is not statistically significant according to the analysis of variance (ANOVA) at 95% interval level. This high level of tensile strength and modulus can be attributed to the less shortening of length in rCF achieved by gentle processing. This indicates also optimum machine settings for the carding and drawing process. Additionally, very high level of mixing along with reduced fibre obliquity in the yarn structure as well as a stable spinning process contributed to obtain very good tensile properties in composites.

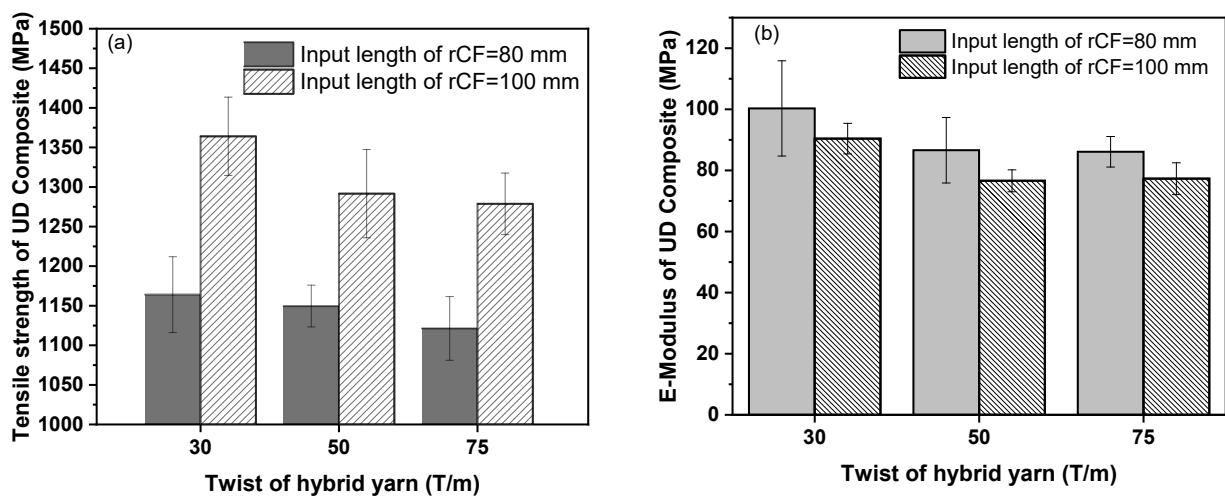


Figure 3: Influence of yarn twist on (a) tensile strength and (b) E-Modulus of UD composites from hybrid yarns

Summary

The results show that through different modifications in carding, drawing and spinning machines, the gentle processing of rCF by ensuring highly minimized fibre length degradation is possible. Furthermore, with the developed hybrid yarn with low twists, high tensile strength and E-modulus of 1364 ± 49 MPa and 100 ± 15 GPa, respectively in composites could be achieved. This will help to fully exhaust the potential of re-using rCF in high performance composites. Through the intensive investigations in this work, the hypothesis to achieve significantly high tensile strength in composite using developed hybrid yarns will be validated.

Acknowledgement

The Projekt CH 174/46-1 is funded by the Deutsche Forschungsgemeinschaft (DFG, German Research Foundation) – 407164652. The funding is gratefully acknowledged.

References

- [1] J. Zhang, V. S. Chevali, H. Wang, C.-H. Wang, Current status of carbon fibre and carbon fibre composites recycling, *Compos Part B-Eng.* 193(2020).
- [2] K. Heilos, H. Fischer, M. Hofmann, A. Miene, Nonwovens made of recycled carbon fibres (rCF) used for production of sophisticated carbon fibre-reinforced plastics. *Vlakna a Textil* 27(3) (2020) 65 – 75.
- [3] J. Wellekötter, J. Resch, S. Baz, G.T. Gresser, C. Bonten, Insights into the Processing of Recycled Carbon Fibers via Injection Molding Compounding. *J. Compos. Sci.* 161 (2020). doi:10.3390/jcs4040161
- [4] M. Hengstermann, M. M. B. Hasan, A. Abdkader, Ch. Cherif, Influence of fibre length and preparation on mechanical properties of CF/polyamide 6 hybrid yarns and composites. *Fibres and Textiles in Eastern Europe*, 119 (2016), 55-62.
- [5] M. Hengstermann, M. M. B. Hasan, A. Abdkader, Ch. Cherif, Development of a new hybrid yarn construction from recycled carbon fibers (rCF) for high-performance composites. Part-II: Influence of yarn parameters on tensile properties of composites. *Text. Res. J.* 87 (2017) 1655-1664.
- [6] D. U. Shah, Characterisation and optimisation of the mechanical performance of plant fibre composites for structural applications, PhD thesis, University of Nottingham, 2013. http://eprints.nottingham.ac.uk/13510/1/A4_Final_thesis_DSHAH.pdf.
- [7] K. L. Hertel, A Method of Fibre-Length Analysis Using the Fibrograph. *Tex. Res. J.* 10(1940). 510–520. DOI: 10.1177/004051754001001203
- [8] M. Hengstermann, G. Bardl, H. Rao, M. M. B. Hasan, A. Abdkader, Ch. Cherif, Development of a method for characterization of the fiber length of long staple carbon fibers based on image analysis. *Fibres and Textiles in Eastern Europe* 118 (2016) 39–44. DOI: 10.5604/12303666.1207845
- [9] C. A. Lawrence, *Fundamentals of spun yarn technology*, CRC Press LLC, New York, 2003.
- [10] N. Pan, Development of a constitutive theory for short fiber yarns: mechanics of staple yarn without slippage effect. *Text Res J* 62 (1992) 749–765. DOI: 10.1177/004051759306300902

CHAPTER 4:

Dyeing, Surface and Fibers Treatment

Thermochromic Properties of Textile Fabrics

Dimitroula Matsouka^{1,a*}, Savvas Vassiliadis^{1,b}, Sotiria Galata^{1,c},
Despoina Gkoutzeli^{1,d} and Ahmet Çay^{2,e}

¹University of West Attica, Department of Electrical and Electronics Engineering, Thivon 250,
Egaleo, 122 44 Athens, Greece

²Ege University, Department of Textile Engineering, Faculty of Engineering, 35100, Bornova, Izmir,
Turkey

^admats@uniwa.gr, ^bsvas@uniwa.gr, ^csgalata@uniwa.gr, ^ddespoina_89@live.com,
^eahmet.cay@ege.edu.tr

*corresponding author

Keywords: thermochromic dyes, colour measurement, leucodyes, textiles, hot plate

Abstract. The ability of certain dyestuffs to change colour in a predictable and reversible way with the change in temperature is a property that can be well utilized in smart textiles. Accurate and repeatable determination of the chromatic response of the dye stuff and as an extension, of the textile material dyed using these dyes, is a significant step towards developing such smart textiles. In this regard the current research project proposes a method for investigating the thermochromic properties of textiles using a custom made testing setup, that includes, digitally controlled heating and cooling equipment as well as a set up to obtain the chromatic response of the textiles every 0.5°C. Moreover, the proposed set up allows for the investigation of heating/ cooling cycling of the specimens, to confirm the repeatability of the chromatic response of the specimens.

Introduction

Thermochromism is the ability of various organic, inorganic compounds and liquid crystals to demonstrate a distinct colour change when their temperature is altered and to revert (with a varying amount of accuracy) to the original colour [1–3]. Thermochromic dyes have been widely used for a number of applications ranging from “novelty” applications (e.g. printed illustrations on drinking mugs that change based on the temperature of the liquid inside them or faux leather that changes colour when touched) to more practical applications such as smart packaging, security printing and textile colouring [4, 5].

The two most widely used thermochromic substances are liquid crystals and leuco dyes. Liquid crystals are based on organic materials that when passing from crystalline solid to isotropic liquid state can form stable intermediate phases (mesophases). Liquid crystals operate on direct colour change, i.e. molecular rearrangement and crystal changes that are sensitive to temperature. Liquid crystals need to be microencapsulated in order to retain their thermochromic properties when applied to textiles [6-8]

Leuco-dye pigments are composites formulated from three components, the colour former, a colour developer and a co-solvent. Colour formers are most commonly leuco-dyes, which change colour when the pH is altered [9-11]. Determination of the thermochromic response of the pigments would need to be two-fold, i.e., a system to accurately raise and maintain the temperature of the samples to a variety of temperatures (e.g., a hotplate) and a system that would measure the chromatic response of the pigment (e.g., a spectrophotometer) [12].

Literature review of research into measuring of the colour cycling of thermochromic textiles produced few examples of similar research and those papers described the use of conventional reflectance spectrophotometers [13-15].

For this research project a dedicated hotplate setup was built to achieve accurate temperature cycling of the specimens and the chromatic response was obtained by processing of photographs of the specimens taken during the temperature cycling.

Materials and Methods

Materials. In this research project, four fabrics samples (100% Cotton, 120.5g/m², plain weave) that had been dyed with thermochromic ink (Leuco dye-based thermochromic ink – Thermochromic TS Red 31) were investigated. The detailed list of materials and concentrations used can be seen in Table 1.

Table 1. Padding liquor recipe.

	Concentration [g/l]
Thermochromic dye	50/75/100/150
Binder (acrylic based, Tubiprint, CHT)	50
Fixating agent (Tubicoat fixierer HT, CHT)	20
Dispersing agent (SeraSpers, DyStar)	20
Surfactant (Tween 80)	10

Padding was carried out using a laboratory-scale padder (Ataç FT350), with a pickup ratio of 90%. After padding, the samples were dried at 80 °C for 3 minutes and cured for 5 minutes in a laboratory-scale dryer (Ataç, GK40) at 150°C. By varying the concentration of the thermochromic dye as shown in Table 1, four samples were obtained. The specimens were index from 1 to 4 in ascending dye concentration, i.e., Sample 1 corresponded to 50 g/l dye and Sample 4 to 150g/l dye.

Methods. The temperature of fabrics that had been dyed with different concentrations of thermochromic dyes was cycled (heated – cooled) in a controlled manner and from 25 °C to 43°C. To accomplish this, an experimental set-up was built. The set-up was based mainly on two units, an Arduino Uno micro-controller and an isothermal plate (Hotplate) (Fig. 1). To document the fabric colour changes, photographs were taken at approximately every 0.5°C with standard conditions. Graphs were produced regarding colour quantity (RGB) by analysing the photographs using MatLab.

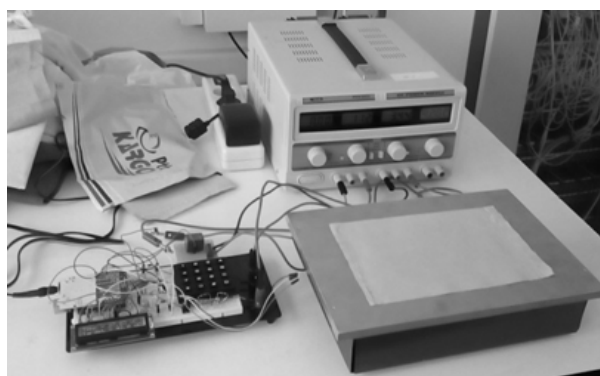


Fig. 1. Testing set-up

Results and Discussion

Based on the results of the research it was found that the chromatic response of the samples was quite similar when the blue (B) and green (G) values were plotted. Namely, for the first cycle of each sample, the colour response vs. dye concentration showed that the B and G component values started following an upwards gradient within the range of 28 to 32°C and then as the temperature was raised the gradient reached a plateau at 34 to 36°C (Fig.2 and Fig.3). Furthermore, the increased dye concentration seemed to displace the temperatures mentioned above towards the upper values of the range, but this effect was not seen with the maximum dye concentration of 150g/l.

Comparing the results of all the cycles (for the B and G components) for concentrations below 150g/l the successive cycles the colour response of the samples appeared to be grouped around the

first cycle. It should be noted that for all cycles after the first the temperatures at which the samples reached the gradient and plateau regions were lower than those seen for the first cycle. For the 150g/l concentration the response or B and G values for cycles 2, 3 & 4 was quite removed from the results for the first and fifth cycle.

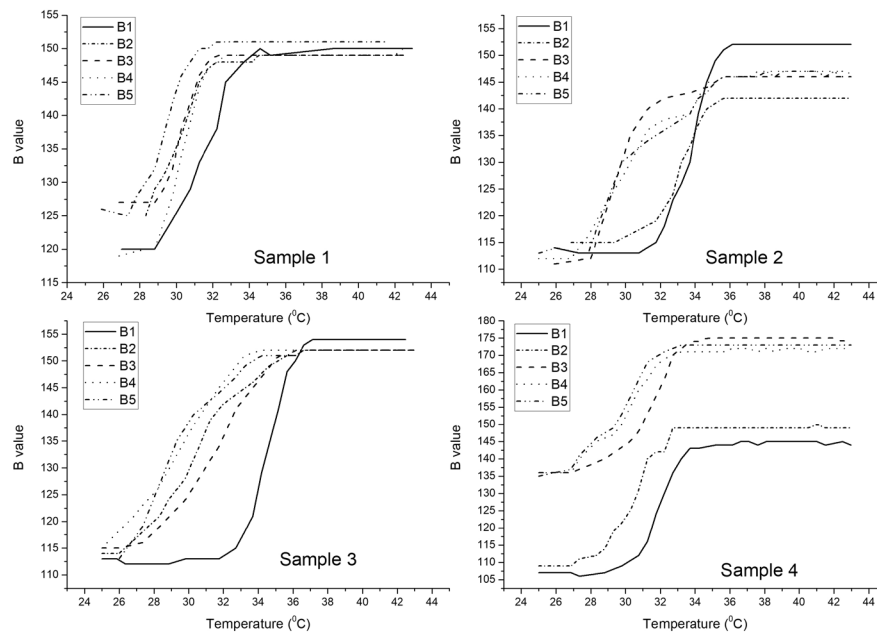


Fig. 2. Chromatic response of the B component for the 4 samples on the five temperature cycles

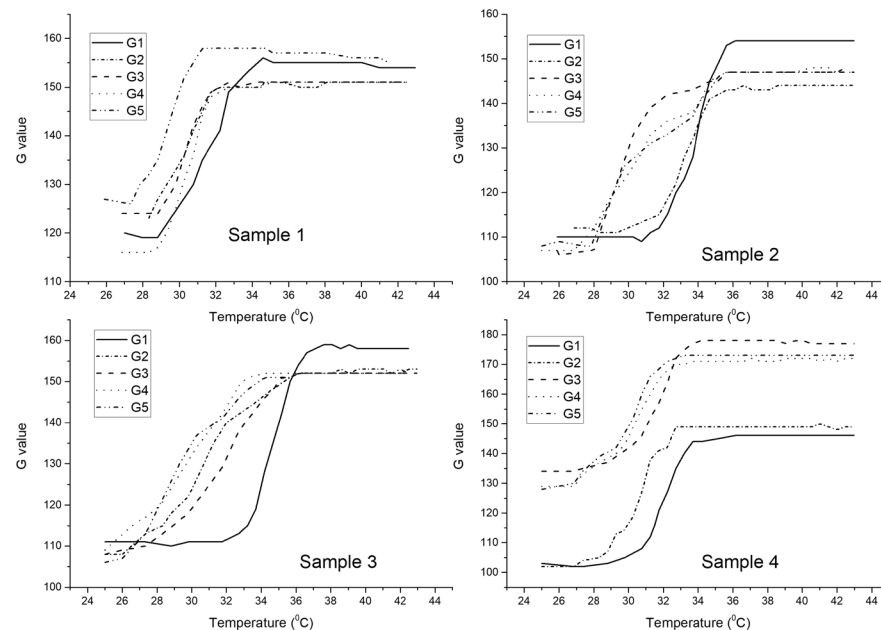


Fig. 3. Chromatic response of the G component for the 4 samples on the five temperature cycles

Concerning the results for the red (R) component (Fig. 4) the curve produced by the colour response was quite dissimilar to the B and G curves. The R component followed a downward gradient as the temperature increased, which corresponded with the visual assessment of the specimens during the testing procedure where the specimens turned from red to grey. Also the R values moved within a much tighter range than the B and G ones and the gradient were much shorter and less pronounced. The “drifting” of the characteristic temperatures at which colour change happened was again evident. Another characteristic that was not similar to the B and G curves was the dispersion of the results of the consecutive heating/ cooling cycles. While for samples 1-3 the B and G curves are more or less grouped together, for R component the results for the first cycle appear removed from the other cycles.

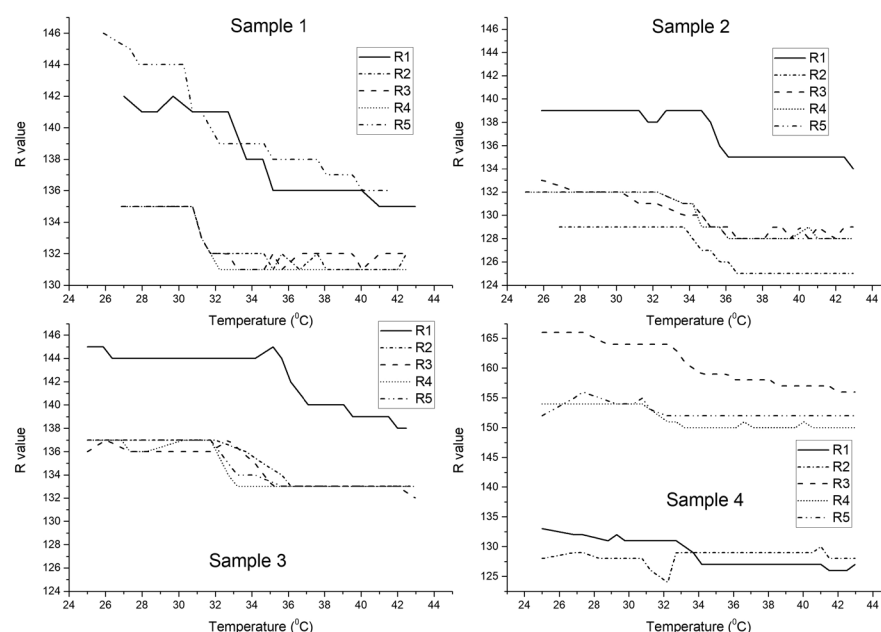


Fig. 4. Chromatic response of the R component for the 4 samples on the five temperature cycles

In Fig. 5 below the characteristic hysteresis curves produced for each cycle can be seen. Also these figures provide a much clearer picture of the behaviour of the RGB values for each specimen with the gradients clearly visible. An interesting observation is for the hysteresis curves (the cooling phase) the colour change of the samples happens at lower temperatures.

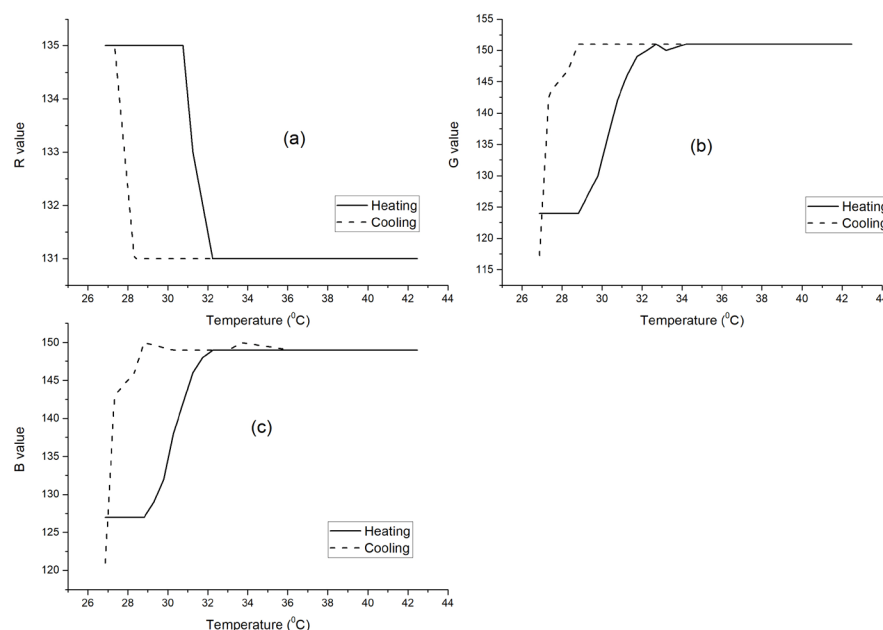


Fig. 5. Characteristic hysteresis curves (heating/cooling test cycle) of specimens

In Fig. 6 below the results for the R, G & B values for all the samples and the first heating cycle can be seen. These graphs highlight the effect of the increase in dye concentration, i.e. that a dramatic increase in dye concentration (50g/l vs. 150g/l) is required to show significant difference in the first cycle and then mainly in the R values. Also that a simple one off heating cycle of the samples is not enough to fully characterise the chromatic behaviour of the samples.

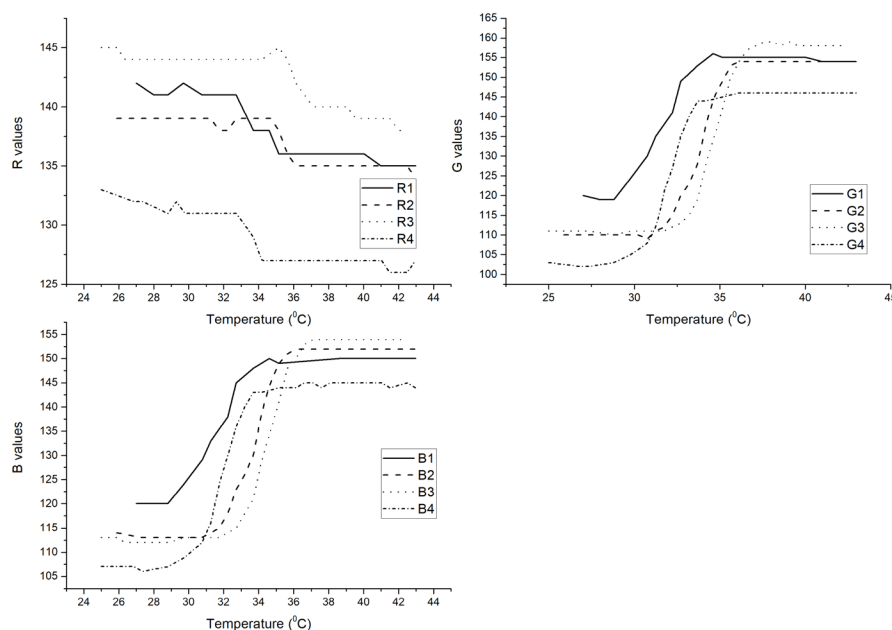


Fig. 6. R, G, and B values for all specimens for the first heating cycle

Conclusion

Thermochromic dyes are a very interesting option for obtaining visual feedback for the temperature change of materials. Significantly thermochromic dyes as applied to textiles provide solutions for among other areas, medical and safety applications. The lack of a dedicated method/equipment for the measurement of the colour response of the fabrics creates difficulties both for the development of smart thermochromic systems and for any fitness to purpose testing. The method proposed in this research paper aims to provide an easy to use and efficient system. The method offers the ability to carry out continuous real testing over multiple heating/ cooling cycles. Based on the results it is concluded that for the samples under investigation the effect of consecutive heating and cooling cycles on the chromatic response becomes more pronounced with a dramatic increase of the dye concentrations (50g/l vs. 150g/l). Furthermore, within the same specimen the first cycle has the most distinctive effect especially on the R component.

References

- [1] J. H. Day, Thermochromism, Chem. Rev. 63 (1963) 65-80.
- [2] S. Lee, J. Lee, M. Lee, Y. K. Cho, J. Baek, J. Kim, S. Park, M. Kim, R. Chang, and J. Yoon Thermochromic sensors: Construction and molecular understanding of an unprecedented, reversibly thermochromic bis-polydiacetylene, Adv. Funct. Mat., 24 (2014) 3699-3705.
- [3] M. Vik, A. P. Periyasamy Chromic materials: fundamentals, measurements, and applications, first ed., Apple Academic Press, New Jersey, 2018.
- [4] M.A. White, M. LeBlanc Thermochromism in commercial products, J. Chem. Educ. 76 (1999) 1201-1205.
- [5] GK. Phillips, Combining thermochromics and conventional inks to deter document fraud, in: Proc. SPIE 3973/optical security and counterfeit deterrence techniques III, 2000, pp. 99-104.
- [6] C. Moretti, X. Tao, L. Koehl, V. Koncar, Electrochromic textile displays for personal communication, in: V. Koncar (Ed.), Smart Textiles and Their Applications, Woodhead Publishing, Oxford, 2016, pp. 539-568.
- [7] P. Talvenmaa Introduction to chromic materials, in: H. Mattila (Ed.), Intelligent Textiles and Clothing, Woodhead Publishing Ltd, Cambridge, 2006, pp. 193-205.

-
- [8] M. A. Chowdhury, M. Joshi, B. S. Butola, Photochromic and Thermochromic Colourants, in Textile Applications, J. Eng. Fibers Fabr. 9 (2014) 107-123.
- [9] M. A. Chowdhury, B. S. Butola, M. Joshi Application of thermochromic colorants on textiles: temperature dependence of colorimetric properties, Color. Technol. 129 (2013) 232-237.
- [10] H. Oda New developments in the stabilization of leuco dyes: effect of UV absorbers containing an amphoteric counter-ion moiety on the light fastness of color formers, Dyes Pigm. 66 (2005) 103-108.
- [11] R. Kulčar, M. Friškovec, N. Hauptman, A. Vesel, M. K. Gunde Colorimetric properties of reversible thermochromic printing inks, Dyes Pigm. 86 (2010) 271-277.
- [12] O. Panák, M. Držková, M. Kaplanová, Insight into the evaluation of colour changes of leuco dye based thermochromic systems as a function of temperature, Dyes Pigm. 120 (2015) 279-287.
- [13] R. M. Christie, I. D. Bryant, An evaluation of thermochromic prints based on microencapsulated liquid crystals using variable temperature colour measurement, Color. Technol. 121 (2005) 187-192.
- [14] W. Ibrahim, An investigation into textile applications of thermochromic pigments: Doctoral dissertation. Heriot-Watt University, 2012, 103 pp
- [15] M. S. Tözüm, C. Alkan, S. Alay Aksoy, Preparation of poly(methyl methacrylate-co-ethylene glycol dimethacrylate-co-glycidyl methacrylate) walled thermochromic microcapsules and their application to cotton fabrics, J. Appl. Polym. Sci. 137 (2020) 48815.

New Method for Prediction of Photochromic Textiles Fatigue Behavior

Martina Viková^{1,a}, Utkarshsinh Solanki^{1,b*}, Michal Vik^{1,c}

¹Technical University of Liberec, Studentska 1402/2, Liberec, Czech Republic

^amartina.vikova@tul.cz, ^{b*}utkarshsinh.solanki@tul.cz, ^cmichal.vik@tul.cz

Keywords: Color intensity, Fatigue resistance, Photochromic phenomena, UV irradiance time

Abstract: The main objective of this work is to study the fatigue behavior of photochromic textiles under different UV irradiance times and develop a rapid testing method. When considering their possible applications, the fatigue resistance of photochromic materials has been considered. The photochromic woven fabric was prepared using the screen-printing method. Previous studies have demonstrated the sensitivity of photochromic pigments to UV radiation's intensity during the experiment. This work provides different thoughts in testing the fatigue resistance of spiro-indolines-based pigment applied on textile fabric. We found that color intensity performance and photodegradation of the photochromic pigment can be evaluated using a relatively small amount of necessary irradiation cycles and an advanced setup of time/intensity UV radiation exposure.

Introduction

Photochromic compounds undergo a light-induced reversible transition between two states with light absorption in a different spectral region (Fig. 1). The photochromic species can deliver unstable fatigue products in the isomeric form under external stimuli. Spirooxazine based chromic compounds have a high color-changing depth and a color bleaching rate. The compounds undergo reversible change into two states under the fluence of UV and visible light sources. The color change in the electromagnetic spectrum's visible spectra is observed visually with UV+ (under the fluence of UV light source). Upon removal of UV light source (under the fluence of the visible light source), i.e., UV-, the reversible relaxation of color change is observed as a change in wavelength in the visible range of the electromagnetic spectrum. Therefore, the photochromic reaction parameters – the rate, intensity, spectral distribution of the color change, and the unusual fatigue behavior with and without UV irradiation exposure for a particular time/intensity setup. The mentioned parameters are significant to harness as a UV sensor.

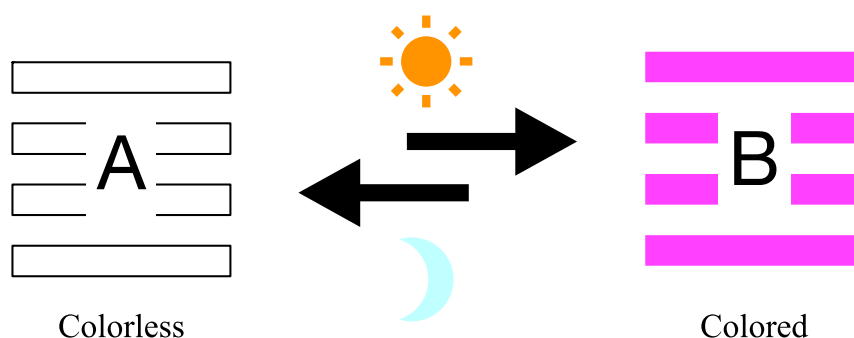


Fig. 1 General scheme of photochromism from A to B

Fatigue resistance of chromic compounds can be considered an increase in coloration of pigment under the UV influence and loss in decoloration of color in absence of a UV light source. i.e., UV+ and UV-. In contrast, while studying the fatigue resistance, irradiating the UV illumination dose opens the heterocyclic ring of spirooxazine compounds during the transit chromic phenomena. Therefore, the fatigue resistance of such compounds shows the dependency on the illuminated UV intensity of a specific wavelength used light source. i.e., UV LED light source of a specific wavelength and the absorption characteristics of the pigment molecules after activation in the visible

range of wavelength. UV irradiance opens the structure of the compound at a certain planar angle, and the change in color on the photochromic sample is observed. Upon removing the UV source and under the visible light source's fluency, it eventually comes back to its original form based on its decoloration rate. Therefore, the exposure time and the intensity of UV energy that is used for activation are mutually correlated to each other. Thus, it is significant to study the fatigue resistance of chromic compounds for their end-use as optical rewritable devices, optical switches, or a flexible UV sensor.

The photochromic system's pigment's fatigue resistance can be studied in cyclic, flash, and continuous modes. The chromic compound's fatigue resistance is affected by the linearity of photochromic response (color intensity), the chromic compound's concentration, temperature, and the filter used to remove the high energy level UVB and UVC from spectra. The photochromic response's linearity is related to the color intensity at its maximum wavelength at which the photo-induced reaction occurs under UVA irradiation.

The closed-form (CF) is colorless using spiro-indoline-based spirooxazine pigment, a heterocyclic ring in its chemical structure. Upon UV irradiation, the colored or faintly colored molecules are incorporated into the fabric structure using a screen-printing technique. Under continuous UV irradiance, a photo-stationary equilibrium is attained between the colored state and the uncolored state. The open-form (OF) or the colored state remains stable until the fabric sample is exposed to a UV light source. Upon removing the UV light source, the attain equilibrium shifts, and the photochromic system returns to the colorless state from the colored state, until the original state is achieved under the fluence of a visible light source. Thus, this reversible color change under the UV source's fluency and its original color upon its removal is a characteristic of the photochromic system. Under different UV irradiance times, coloring and fading kinetics of the photochromic system's fatigue behavior changes. Thus, a new approach to studying fatigue resistance has been analyzed based on UV irradiance time used for the exposure and decay phase of the photochromic system. The relation between the UV irradiance time and the dose of illumination is required to create a stable photochromic system until the equilibrium state has been achieved.

The chromic compound's fatigue behavior follows the photochromic cycle – the coloration and decoloration mode of conduct under the presence and absence of UV light source, respectively. The photochromic process generally includes thermal stabilization (UV-), growth phase (UV+), decay phase (UV-). The dynamics of photochromic material when exposed to external stimuli, i.e., UV source, the different stages of material – thermal stabilization, growth phase and decay phase as shown in Fig. 2, where, $t_{1/2E}$ = half-life measure during growth phase; $t_{1/2D}$ = half-life measure during decay phase; $(K/S)_0$ = color strength of inactivated sample (obviously at beginning and (K/S) value is mainly dependent on optical behavior of used substrate); $(K/S)_{1/2}$ = half of the total color strength before reaching the equilibrium state, $(K/S)_\infty$ = maximum color strength after reaching the equilibrium state.

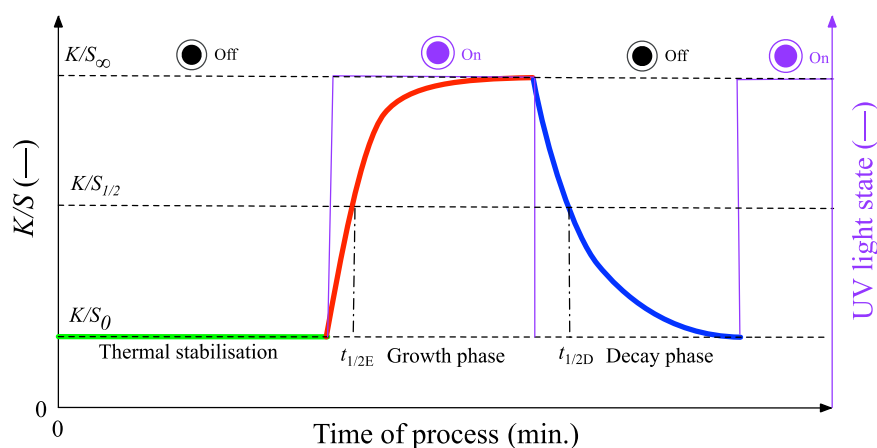


Fig. 2 Kinetic phases of the photochromic cycle

The various stages of a photochromic cycle have been illustrated by Fig. 2 [8]:

1. With a UV (-) - the thermal stabilization phase of the instrument starts where the sample is colorless at the initial step. Due to the device, which is an essential step, it is required to stabilize the instrument at a specific or used temperature to reach that state from the ambient temperature.
2. With UV (+) - the growth phase (coloration) starts at the time t_0 , the change in reaction gradually starts between the used UV light source and the photochromic sample. The change of coloration intensity is visualized at its dominant wavelength in the visible range as a measure of change in reflectance values of the electromagnetic spectrum. It achieves its maximum-colored intensity value until the exposure and remains in equilibrium under the light source till the time of exposure.
3. With UV (-) - the decay phase (decoloration) starts where the color intensity of the photochromic sample fades away with time and comes back to its original color. The color change can be observed in the decay phase from a colored to a colorless state. De-coloration rate or bleaching rate is measured in the fading phase of the sample.

The investigation of photochromic compounds can be carried out using colorimetric data. In photochromism, the photoinduced color change can be measured using a specifically designed spectrophotometer only, which provides us to measure the change in these colorations and decoloration modes of used pigment as a change in reflectance value in a visible range of the electromagnetic spectrum. However, the photochromic cycle consists of thermal stabilization, coloration mode utilizing the UV light source, and decoloration mode using a visible light source. For a certain amount of UV exposure time in seconds, the pigment behaves accordingly in its growth and decay phases. The color change is measure as a change in the reflectance, absorbance, or scattering of the light which can be visualized as chromogenic phenomena. The coloration of the pigment is a measurable property using the Kubelka-Munka function. As the Kubelka-Munk function, as well as Beer's law, is monochromatic. The color values (K/S) were calculated from the reflectance spectra using the Kubelka-Munk function [9].

The first-order kinetic model has been used for investigating the photochromic response of pigment under UV irradiance during its growth and decay phase. When a pigment undergoes a photochemical reaction under an external stimulus, UV radiance changes its form from colorless to a colored state. The changes in color appearance using external stimuli can be explained by studying its spectral characteristics and by calculating the Kubelka-Munk function (K/S) _{λ} [9].

The coloration intensity value (K/S) of the measured sample is obtained by the sum of (K/S) _{λ} from wavelength range from 380 nm to 780 nm, where the $\Delta\lambda$ - it depends on the bandpass of a spectrophotometer (usually 10 nm).

The kinetic parameters such as rate constant and half-life parameters can be obtained through fitting monochromatic data using K/S values at its dominant wavelength (λ_{max}). The model used for studying the fatigue behavior of pigment using a one-phase association and given by Eq. 1.

$$\left(\frac{K}{S}\right)_{\lambda,t} = \left[\left(\frac{K}{S}\right)_{\lambda,0} - \left(\frac{K}{S}\right)_{\lambda,\infty}\right] \times e^{-kt} + \left(\frac{K}{S}\right)_{\lambda,\infty} \quad \text{Eq. 1}$$

where, $\left(\frac{K}{S}\right)_{\lambda,0}$, $\left(\frac{K}{S}\right)_{\lambda,\infty}$ are the initial and final (equilibrium) color intensity values respectively attained upon exposure or relaxation of UV light at its dominant wavelength (λ), k is the rate constant, and t is the time of exposure. The subscripts define the time relationships: (0) = time in the beginning and (∞) = time at infinity.

The change in coloration and fading kinetics, determined from (K/S) _{λ} values which can be transformed spectroscopic reflectance data, measured using FOTOCHROM3 spectrophotometer in a

continuous irradiation mode. The photodegradation of photochromic pigment follows the one-phase association followed by plateau function, to study its fatigue behavior and compute the kinetic parameters. The kinetic parameters, the rate constant (k) and half-life ($t_{1/2}$) and span or the plateau were computed using a one-phase association model followed by plateau by writing the script code in MATLAB platform or can be fitted the transformed data using the PRISM software. From the obtained computed data, the kinetic parameters, the span value, or the plateau, which are obtained using the K/S values only, the change in coloration was measured as follows,

$$\Delta\left(\frac{K}{S}\right)_{\lambda,t} = \left(\frac{K}{S}\right)_{\lambda,UV\ ON} - \left(\frac{K}{S}\right)_{\lambda,UV\ OFF} \quad \text{Eq. 2}$$

Subsequently, the relative intensity ratio I_R , which is (I/I_0) which was measured as follows,

$$I_R = \Delta\left(\frac{K}{S}\right)_{\lambda,t,i} / \Delta\left(\frac{K}{S}\right)_{\lambda,t,i+1} \quad \text{Eq. 3}$$

where i = the irrespective number of cycles used for exposure and decay phase of the photochromic cycle

Even the photochromic behavior of the chromic pigment of specific amount concentration on fabric sample, as well the energy received by the photochromic sample can be measured, and the energy equation can be rewritten as also changes its energy and its kinetic parameters changes,

$$\frac{I}{I_0} = e^{-(Et)} \quad \text{Eq. 4}$$

where, E = light energy received from used UV light source, t = exposure time used for photochromic sample

The UV irradiance dose can be measured: UV dose (mW.s.cm^{-2}) = UV energy received (mW.cm^{-2}) of the used UV light source of specific wavelength multiplied by UV irradiance time (in seconds), which is used for excitation prolong to the exposure time used to measure the fatigue resistance of chromic compounds. This will give us the logarithmic relationship of the energy dose used to excite the photochromic species until the exposure time used for the growth phase. However, one can even measure for a larger number of UV irradiance cycles; the long-term fatigue behavior of chromic compounds can also be studied.

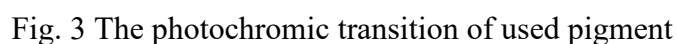
The coloration and decoloration of the fabric sample are observed during the exposure and the decay phase, respectively, under the continuous mode of UV irradiance. In this study, five irradiation cycles are used to study the fatigue resistance of used photochromic pigment in continuous mode. The obtained monochromatic spectroscopic data were fitted using the one-phase association function followed by a plateau at its dominant wavelength at which the equilibrium is attained.

The half-life values during the exposure phase represent the time required to develop pigment coloration or dye at excitement to the half value of maximum absorbance at a specific wavelength during the growth phase. The half-life time of reversion estimates the color fade rate during the decay phase to reach its original color state. The half-life time during the decay phase represents the time required for the decrease of the color from the absorbance at a specific wavelength in one cycle to attains its colorless form. Fatigue resistance describes the efficiency of chromic compounds through usage due to the degradation of pigment or dyes.

Three modes can be applied to characterize the photochromic species' fatigue resistance: cyclic, continuous, and flash degradation. The chromic fabric sample was exposed under UV and visible light sources in a cyclic degradation mode to study its fatigue resistance. The photochromic cyclic consists of UV+ and switch UV- as one cycle of the photochromic system. The repeating number of irradiating cycles used for the experiment to transform photochemically or thermally under

The colorimetric measurements were carried out using a specifically designed spectrophotometer for five consecutive cycles under the continuous mode of irradiance. The exposure time in (seconds, minutes, or hour) for one photochromic cycle (as UV+ and UV-) for growth and decay phase, irrespective of the number of irradiation cycles used, moreover, the time lapse between each measurement can be added manually using the user-friendly software which is interfaced with FOTOCHROM3 device. The stabilization of the device's temperature is of utmost priority before starting the measurement using a photochromic sample. The reflectance data can be acquired and stored and elaborately treated further to analyze the fatigue resistance.

Woven fabric, a blend of polyester and cotton 65:35, was printed with Photopia Purple Ink (Matsui) of a concentration of 100 g.kg⁻¹ using a screen printing technique. The chemical structure of this ink is as shown in the scheme in Fig. 3. The photochromic printed fabric was dried and cured at 120 °C and 150 °C for five and three minutes respectively.



FOTOCHROM3 device allows us to measure in continuous mode: UV+ and UV- mode for a given number of irradiance cycles, considering the UV irradiance time for one cycle. It consists of two light sources: excitation light source (360 nm UV light source) and visible light source, allowing to measure the used photochromic woven sample's reflectance data. The spectral power distribution (SPD) of used light sources was measured as shown in Fig. 5.

The obtained reflectance data were converted to color intensity values at its dominant wavelength and were treated further for evaluation. The dominant wavelength is 570 nm for the used pigment, which undergoes color change from colorless to purple. The color intensity values at its dominant wavelength were fitted to a one-phase association function followed by a plateau to compute its kinetic parameters and to evaluate further using the acquired reflectance data.

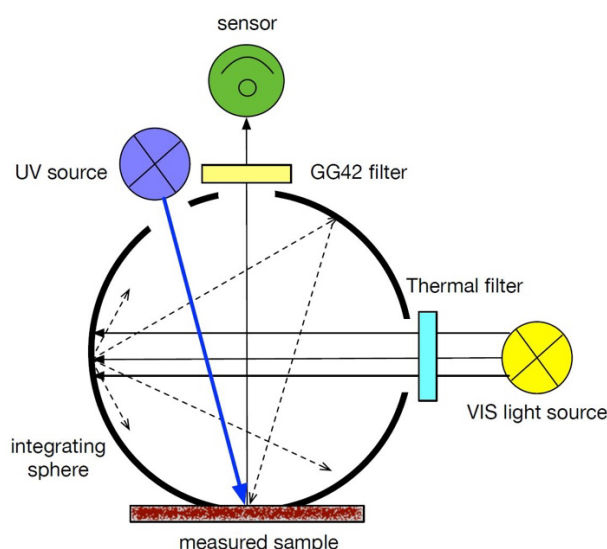


Fig. 4 General schematic diagram of FOTOCHROM 3 device [1]

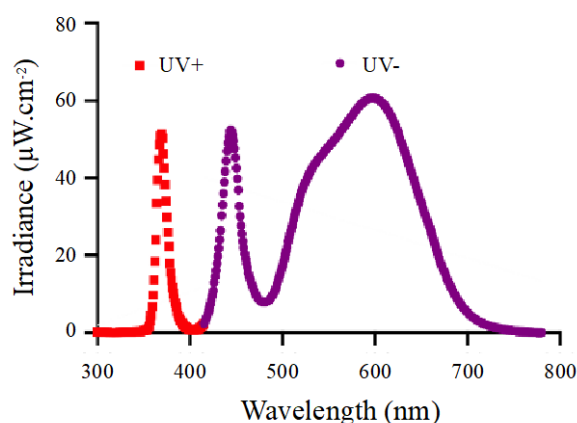


Fig. 5 Spectral power distribution of used light sources

Results and Discussions

A new insight for measuring the fatigue resistance of the photochromic system has been described. The degradation of used chromic pigment is related to the specific amount of UV light dose which is (the number of photons absorbed by the molecule to open the ring form) absorbed by the colorless state to attain the colored state. The UV illumination dose is measured for the used UV exposure time used for exposure to open up the hetero-cyclic ring of the pigment structure.

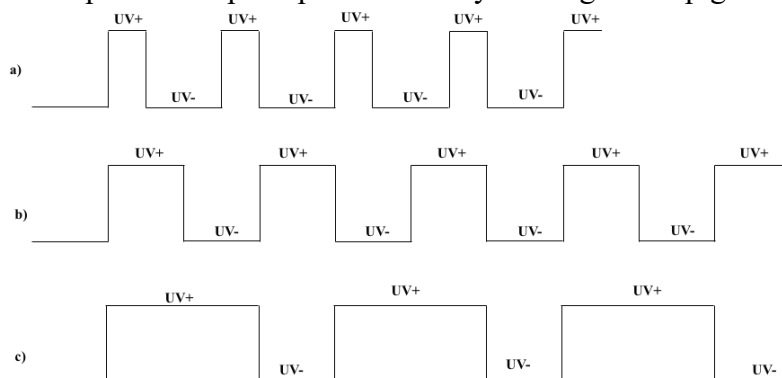


Fig. 6 Experimental set-up for studying fatigue behavior

The coloration and the decoloration of the used chromic pigment are related to the usage of a specific light dosage of UV illumination for a specific duration of time. Fig. 6 represents the experimental setup for studying the fatigue behavior under three exposure times, on the other hand keeping the same relaxation time, to observe the photodegradation rate of the pigment molecules over several consecutive cycles in a continuous mode.

Five photochromic cycles were used for the asymmetrical time used for the experiment, which is mentioned in the methodology section. Fig. 7 represents the relative intensity in corresponds to the used irradiance cycles used for the exposure phase. With the different amounts of exposure used for the photodegradation of the photochromic sample, the decrease in the degradation in the relative intensity can be seen in Fig. 7 over the number of exposure cycles used.

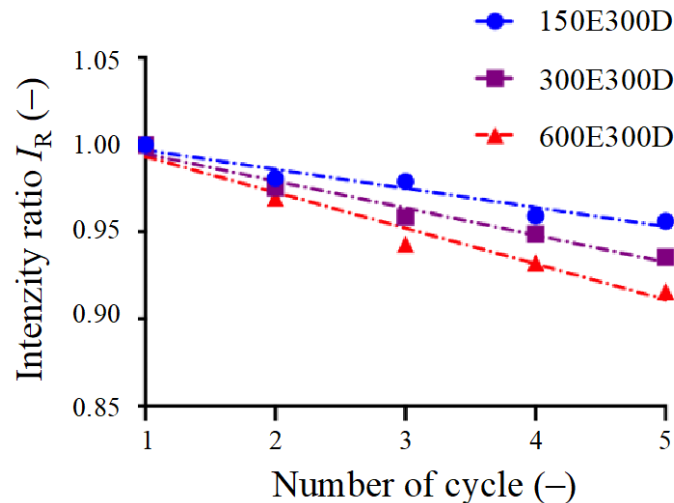


Fig. 7 Dependence of intensity ratio I_R exposure time t of individual cycle

The intensity decay (%) of the used photochromic pigment depends on the used exposure time and the amount of UV dose used for the activation of pigment molecules w.r.t exposure time used. Fig. 8 and Table 1 corresponds to each other to see how the UV dose behaves in corresponds to the photodegradation of the used pigment with a relaxation time of 300s. The data fit with exponential function with the coefficient of determination value 0.99. The fourth point in Fig.8 is the measurement, which was carried out for 50 cycles, as a long-term fatigue behavior of the used photochromic sample. If we want to have the degradation rate by 50% with the applied dose, we might need to increase the number of irradiance cycles.

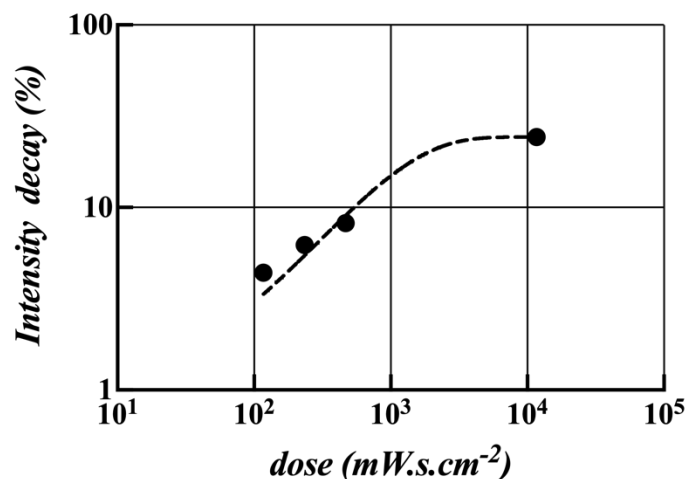


Fig. 8 Dependence of intensity decay on the used dose of UV radiation

Table 1 Dependence of photodegradation on the used UV dose corresponds to Fig. 8

Respective points in Fig. 8	UV irradiance time used in seconds	UV dose (mW.s.cm ⁻²)	Intensity decay (%)
		0	0
First point	150E300D	117	1.42
Second point	300E300D	234	5.48
Third point	600E300D	468	11.45
Fourth point	Decay at 50%	11700	24.35
	Fitted curve equation and coefficient of determination	$Y = 24.42 - 25 e^{-0.001x}$ $R^2 = 0.99$	

Tables 2 illustrate the computed kinetic parameters using the one-phase association followed by plateau function. It has been calculated irrespective of the five consecutive photochromic cycles of the growth phase. The pigment's half-life decreases over the consecutive number of irradiance cycles, as its degradation occurs with the same exposure time over the number of irradiance cycles used. The amount of UV energy at its dominant wavelength to activate such chromic compounds is related to the photodegradation rate of pigment as well as the fatigue behavior in a continuous mode.

Table 2: Kinetic parameters with 300s decoloration time

	0 th cycle		1 st cycle		2 nd cycle		3 rd cycle		4 th cycle	
Computed kinetic parameters	Half-life $\tau_{1/2}$ (s)	Rate constant k (s ⁻¹)	Half-life $\tau_{1/2}$ (s)	Rate constant k (s ⁻¹)	Half-life $\tau_{1/2}$ (s)	Rate constant k (s ⁻¹)	Half-life $\tau_{1/2}$ (s)	Rate constant k (s ⁻¹)	Half-life $\tau_{1/2}$ (s)	Rate constant k (s ⁻¹)
Time in (s) used for one cycle										
150E300D	8.93	0.07756	8.82	0.07854	8.35	0.08301	8.47	0.08189	8.57	0.08086
300E300D	8.78	0.07895	8.95	0.07744	8.38	0.08277	8.40	0.08253	8.76	0.07911
600E300D	8.96	0.07732	8.50	0.08157	8.92	0.07767	9.12	0.07597	8.57	0.08088

The forward reaction ($h\nu_1$) of the photochromic system is initiated using the UV light source, which activates the pigment molecules, which can be visualized through the change in color, in the visible range of the spectrum. However, the reverse reaction ($h\nu_2$) can be thermally or using a visible light source, where the molecules trying to close their heterocyclic ring and will achieve its original state gradually over time. The coloration with a certain amount of measured color intensity values is caused due to the amount of the irradiance UV dose and the time of exposure. Subsequently, the fading of the photochromic molecules needs relaxation time for its decoloration until it gains its original form. Moreover, there might be a probability that the intermediate by-products of the used pigment might form when the molecules are under UV influence, due to the changing of the state of molecules from the ground state to the excited state after receiving the energy as in UV form. In addition, the photochromic pigment is not in its pure form, and it is applied on the textile fabric using a screen-printing technique taking a certain amount of pigment concentration. The photochromic behavior might behave differently in solution form in some used solvents than applied on the surface of the textile substrate. We had studied the photodegradation behavior of used pigment under different exposure times over a small number of photochromic cycles.

A standard method of fatigue resistance test of photochromic materials is based on a relatively high number of necessary cycles that cause a 50% decrease of initial shade intensity/optical density. That means such kind of test takes a relatively long time. Above mentioned relation of fractional

survival/stability of the dye molecules exposed to UV gives us a tool allowing us to predict the number of necessary cycles to catch Z_{50} at different UV radiation intensities. In this experiment, from the measured UV irradiation relative intensity dependence graph, the Z_{50} cyclability can be predicted theoretically. The expected number of cycles for the used 150s, 300s, and 600s UV irradiation time comes out to be 42, 29, and 22 cycles (round digit), respectively, to reach Z_{50} . Here, the Z_{50} is the number of cycles required to decrease the initial absorbance at its specific wavelength by 50%. The number of cycles that undergo reversible transitions from the colorless state to the colored state depends on the used pigment or dye's degradation degree.

Conclusions

The main aim of this study is to give the insight to study and analyze the fatigue behavior of the photochromic system, considering a small number of photochromic cycles under the continuous mode of UV irradiance. The photodegradation property of the chromic pigment is dependent on the amount of exposure time and the amount of UV energy received by the photochromic molecules until that exposure time is used for the study. The intensity of the UV energy might be different from other UV light sources used of that specific wavelength. The degradation characteristic of the chromic pigment with the amount of time used for the exposure can be observed with a larger number of irradiance cycles. Fatigue resistance of photochromic dyes is measured by evaluation of time or cycles caused 50% of optical density decrease based on different method testing scenarios such as flash, continuous and cyclic modes. The photochromic behavior of such chromic compounds is studied as fatigue resistance as coloration and decoloration of pigment under different amounts of UV exposure in a continuous mode. With an increase in the UV exposure time with the same relaxation time to achieve its original state, we observe a decline in the photodegradation of the pigment molecules as a relative change in intensity decay during the photo coloration process over the used number of cycles. When the amount of spectral irradiance of the used light source is known, the system is more reliable to the relative decay intensity of photochromic color change to the dose of light used during the experiment. To achieve the 50% decay with the used experimental set-up, we might need to increase the number of irradiance cycles depending on the amount of UV dose used for the exposure phase.

Acknowledgments

I would like to thank Marcela Pechova for preparing the sample and her feedback while writing the manuscript.

This work was supported by the Student Grant Competition of the Technical University of Liberec within project no. SGS-2020-6038.

The authors have no conflicts of interest to declare.

References

- [1] Viková, M., Christie, R. M., Vik, M., A Unique Device for Measurement of Photochromic Textiles, *Research Journal Textile and Apparel*, 18 (2014) 6-14. <https://doi.org/10.1108/RJTA-18-01-2014-B002>
- [2] Viková, M., Vik, M., The determination of absorbance and scattering coefficients for photochromic composition with the application of the black and white background method, *Textile Research Journal*, 85(18) (2015) 1961-1971. <https://doi.org/10.1177%2F0040517515578332>
- [3] Viková, M., & Vik, M., Photochromic textiles and measurement of their temperature sensitivity, *Research Journal of Textile and Apparel*, 18(3) (2014) 15-21. <https://doi.org/10.1108/RJTA-18-03-2014-B002>

-
- [4] Dubest, R., Levoir, P., Meyer, J. J., Aubard, J., Baillet, G., Giusti, G., & Guglielmetti, R., Computer-controlled system designed to measure photodegradation of photochromic compounds, *Review of scientific instruments*, 64(7) (1993) 1803-1808. <https://doi.org/10.1063/1.1144014>
- [5] Pariani, G., Quintavalla, M., Colella, L., Oggioni, L., Castagna, R., Ortica, F., Bertarelli, C. & Bianco, A., New insight into the fatigue resistance of photochromic 1, 2-diarylethenes, *The Journal of Physical Chemistry C*, 121(42) (2017) 23592-23598. <https://doi.org/10.1021/acs.jpcc.7b04848>
- [6] Maafi, M., Useful spectrokinetic methods for the investigation of photochromic and thermo-photochromic spiropyrans, *Molecules*, 13(9) (2008) 2260-2302. <https://doi.org/10.3390/molecules13092260>
- [7] Christie, R. M., Agyako, C. K., & Mitchell, K., An investigation of the electronic spectral properties of the merocyanines derived from photochromic spiroindolinonaphth [2, 1-b][1, 4] oxazines, *Dyes and Pigments*, 29(3) (1995) 241-250. [https://doi.org/10.1016/0143-7208\(95\)00049-L](https://doi.org/10.1016/0143-7208(95)00049-L)
- [8] Periyasamy, A. P., Viková, M., & Vik, M., A review of photochromism in textiles and its measurement, *Textile Progress*, 49(2) (2017) 53-136. <https://doi.org/10.1080/00405167.2017.1305833>
- [9] Vikova, M., & Vik, M., Alternative UV sensors based on color-changeable pigments, *Advances in Chemical Engineering and Science*, 1 (04) (2011) 224. <http://dx.doi.org/10.4236/aces.2011.14032>
- [10] Vik, M., Periyasamy, A. P. & Viková, M. (Eds.), Chromic materials: fundamentals, measurements, and applications, *New York: Apple Academic Press., 2018, pp.283-314.* <https://doi.org/10.1201/9781351171007>

Polyester-Polyvinylalcohol Hydrophilization Strategies

TERESA Miranda^{1,a*}, CÁTIA Pinto^{1,b}, JORGE Santos^{1,c} and GRAÇA Soares^{1,d}

¹Minho University, Centre for Textile Science and Technology, Department of Textile Engineering
University of Minho, Campus de Azurém, 4800-058 Guimarães, Portugal

^atmiranda@det.uminho.pt, ^bpg32889@alunos.uminho.pt, ^cjsantos@det.uminho.pt,
^dgmbs@det.uminho.pt

Keywords: PET fabric, Poly (vinyl alcohol), Hydrophilicity, Soil-release

Abstract. Poly (ethylene terephthalate) (PET), also commonly called as polyester, is the most widely used polymer for the production of synthetic fibres over the past fifty years. The frequent use of this PET is due to its high mechanical strength combined with other properties such as the resistance to chemical products, stretching and abrasion. The fibre's hydrophobicity also impacts the difficulty of cleaning these materials [1, 2]. Previous works show that treatment with concentrated NaOH solutions can greatly improve hydrophilicity of PET fibre [1, 2, 3, 4]. However a significant decrease of mechanical properties takes place during this process. In this work, chemical strategies to counteract this negative effect and further increase the hydrophilicity of PET fibre's has been tested. In particular, the effect of polyvinyl alcohol (PVA) and N, N'-dimethylol-4, 5-dihydroxyethyleneurea (DMDHEU) chemically modified resin in the functionalization of saponified PET was carefully analysed. The treated fabrics were characterized by scanning electron microscopy (SEM), contact angle, ATR-FTIR spectroscopy and differential scanning calorimetry (DSC). When the best process conditions were considered for PVA-DMDHEU application, the modified PET presented a contact angle of 33.9°, stain release grade of 4 and a 45.6% increase in its mechanical properties when compared to saponified PET.

Introduction

Polyester is a textile fibre of huge commercial importance. It is a polymer formed by polycondensation of terephthalic acid with ethylene glycol diol. The frequent use of this textile substrate is due to the fact that it has excellent properties such as high uniformity, mechanical strength, abrasion and resistance to chemicals. However, polyester fibres are hydrophobic leading to poor performance regarding moisture management, anti-static and washability properties [3]. Improving the hydrophilicity of PET fibres allows its wide application in various fields, such as biomedical and textiles areas. The dyeing, soil-release and comfort properties are improved when the fabrics hydrophilicity is increased [4].

Several strategies can be used to improve the surface energy and consequently change the hydrophilicity of the polyester structure. Chemical finishing, grafting, surface chemical hydrolysis with sodium hydroxide, physical surface treatment using plasma, biochemical treatment with enzymes and cyclodextrins-based PET fabric finishes are some examples of tested procedures [2, 5].

The most common chemical process is the saponification using concentrated sodium hydroxide solutions. However, this process needs careful control in order to avoid excessive fibre degradation and loss of its mechanical properties, compromising its use.

Water-soluble polyols can be insolubilized in fibrous materials by reacting with the tetrafunctional resin DMDHEU. In this context, Vigo and Bruno studied the application of low molecular weight PEGs to cellulosic and synthetic fibres and they found that several properties of the materials change, namely with regard to their thermal comfort, hydrophilic character and water sorption properties [6]. In the case of PET, it was found that the beneficial effect on mechanical and cleaning properties also occurred due to the deposition of the hydrophilic polymer resulting from the reaction of PEG with resin but such treatment is not durable to laundering. The fewer OH groups on PET reduces the yield of the crosslinking reaction [6].

More recently, Miranda and other investigators found that the durability of the PEG-DMDHEU resin on PET surface can be improved by a previous saponification of the textile [2, 7]. This previous hydrolysis process creates hydroxyl and carboxylic acid groups on polymer, which will be responsible for binding the other polymers to the textile structure [2, 7].

Poly (vinyl alcohol) (PVA) is a polyol with unique properties, such as hydrophilicity, flexibility, nontoxicity, resistance against chemicals, easy preparation and biodegradability [1, 8]. It is obtained *via* hydrolysis of poly (vinyl acetate) in which acetate groups are replaced by hydroxyls [8].

The aim of the present work is to develop a chemical functionalization of PET saponified fabrics with PVA and DMDHEU chemically modified resin in order to improve its mechanical properties, hydrophilicity and soil-release properties.

Materials and Methods

Materials A 100% taffeta polyester fabric made from cut fibre was used. It was supplied by the company Lemar (Portugal), already bleached with a mass per unit area of the 102g/m², 7.5 tex (warp), 17.3 (weft) and a thickness of the 0.22 mm. PVA (average molecular weight 9000- 10000) with hydrolysis degree of 80% was purchased from MolecuAlchemy (Portugal). Adipret P-LF (modified DMDHEU resin with catalyst incorporated, from now on described as resin) was used as a crosslinking agent and kindly offered by ADI Group (Portugal).

Methods All samples (30x15 cm) were weighed after being stored in a conditioned atmosphere (30 ± 2 °C) for 24h.

The fabric PET samples were saponified in an Ahiba dyeing machine with NaOH aqueous solutions (3M), using a 1:20 liquor ratio, at 55 °C for 30 minutes [2, 7, 9, 10]. At the end, the samples were thoroughly washed in tap water to remove unreacted and soluble products, and dried.

The saponified PET samples were impregnated with the aqueous solution containing different concentrations of the modified resin (40 g/L and 60 g/L) and several concentrations of PVA (25, 50 and 70 g/L) with average molecular weight of 9000–10000 and an hydrolysis degree of 80%. After impregnation, the samples were first dried at room temperature, then cured 90 s at 180°C and finally washed and dried during 24h at 30°C.

The thermal properties of the fabrics were measured with a DSC – 822^e instrument (Mettler Toledo). The FTIR-ATR analyses were made on Fourier–transform infrared spectrophotometer SHIDMAZU IR Affinity S1. The FTIR spectra of treated and untreated PET fabric samples were recorded with 8 cm⁻¹ resolution and 45 scans, with a wavenumber range of 400-4000 cm⁻¹. The FTIR spectra were obtained by attenuated total reflectance technique (ATR), with the Diamond being the ATR crystal material used in this work. The ATR correction was made with the software LabSolutionsIR.

The contact angle was carried out on system OCA 15 Plus, DataPhysics Instruments GmbH.

Soil release tests were performed according to AATCC Standard Test Method 130-2018.

The surface morphology of all PET fabric samples were observed in SEM (NOVA 200 Nano SEM, FEI Company).

Mechanical properties of fabrics were evaluated according to ISO Standard Test Method 13934. These tensile strength tests were performed by Hounsfield Tester, model H1OKS.

Results and Discussion

Alkaline hydrolysis of polyester fibres is one of the most reported and widely used strategies to enhance PET reactivity, by increasing the number of reactive sites that can react during chemical functionalization. The nucleophilic attack of a base on the electron-deficient carbonyl carbon in polyester causes chain scissions at the ester linkages along the polyester chain, producing carboxylic acid and hydroxyl polar end groups [2, 6, 7, 10, 11]. Briefly, the functionalization process here described was carried out in two stages, one to hydrolyse the polyester in alkaline medium, through

the creation of hydroxyl and carboxylic acid groups on the surface and improve its hydrophilicity and the other to insolubilized the PVA-resin on PET.

The extent of the crosslinking reaction between polyols, namely the PVA and PEG and resin depends on many factors, such as the molecular weight and polymer solution concentration, the type and concentration of the crosslinking agent, catalyst and process conditions, such as, temperature and time [6]. In PVA's case, it should be noted that the reaction extent may also depend on the degree of hydrolysis. The range of average molecular weights that can be insolubilized is wide (M_n 600 – 20.000) as well as the curing conditions (0.25 – 10 minutes at 80 – 200°C) [6]. It is expected that the hydrophilicity and the soil-release properties of PET fabrics can be improved with the use of polyols, namely PEG and PVA, since these polymers are hydrophilic [2, 4]. In fact, PEG molecules have two terminal hydroxyl groups and ester groups along the chains favouring hydrogen bonds with water molecules. PVA molecules have hydroxyl groups along the chains, allowing the establishment of hydrogen bonds with the water molecules. However, PET does not have enough chemically active groups capable of reacting with the -OH groups of polyols, with the exception of a few acid end groups.

In the second stage of material functionalization, the PVA resin polymer is formed and insolubilized in the saponified PET fabric samples. [6].

Several treatments were developed to modified PET samples. The conditions are described in Table 1.

Table 1 Functionalization conditions of PET samples.

Treatments								
Untreated PET		X						
NaOH 3M			X	X	X	X	X	X
Resin	40 g/L			X		X	X	
	60 g/L				X			X
PVA	25 g/L					X		
	50 g/L						X	X
	70 g/L							X
Tests		Samples						
		A	B	C	D	E	F	G
Number of Tests			10	6	6	8	7	8
Weight gain average (%)			-5.31	0.96	1.38	3.32	4.97	5.92

The weight gain samples after each treatment is shown in the boxplot of Fig. 1a). The differences between the average weight gain of the samples obtained by the various treatments are graphically represented in Fig.1b) considering a confidence interval of 95%.

Analysing the results, a weight loss can be observed in the case of saponified PET. This result was expected, since there was a break in the PET chains according to the previous described. However, an increase in weight was observed in all treatments performed with the application of PVA and resin, and the differences between the average weight gains between all treatments were statistically significant as can be seen in Fig. 1b).

In the test corresponding to saponified PET, an average weight loss of 5.31% was obtained. This result was expected, since there was a break in the PET chains according to the previous described.

In the case of saponified PET treated with resin 40g/L (test C), a weight increase was observed. Hydrolysed PET fibres have functional groups available (such as -OH) that can bond by grafting and/or react directly with the resin [6]. With the increase of the resin concentration, from 40 to 60 g/L (test D), a weight increase was obtained (1.38%), which indicates that there was a greater extension of the reaction by grafting and/or react directly with the resin.

In turn, the saponified PET sample and treated with PVA (25 g/L) in the presence of resin (40 g/L) showed a weight gain of 3.32% when compared to the samples from tests C and D. By increasing the PVA concentration from 25 g/L to 50 g/L and maintaining the resin concentration, a higher weight gain of 4.97% was obtained. In the samples of tests E and F, keeping the PVA concentration and

increasing the resin amount from 40 to 60 g/L, a greater weight gain (5.92%) was obtained. Finally, keeping the resin concentration (60 g/L) and increasing the PVA concentration from 50 g/L to 70 g/L, an even greater weight gain (7.84%) was observed. These results indicate that the PVA and resin was insolubilized in saponified fabric samples and cross-linked in the PET. Similar effect was described by Vigo and collaborators regarding the binding of PEGs to PET through DMDHEU resin using a pad-dry-cure process [6, 12].

As shown in Fig.2a the increase in weight of samples treated with PVA and resin is accompanied by an increase in the mechanical strength of the fibre, which undergoes an increase of about 45.6% when compared to saponified PET treated with 60g/L of resin and 70 g/L of PVA (648 N after treatment against 445 N before treatment).

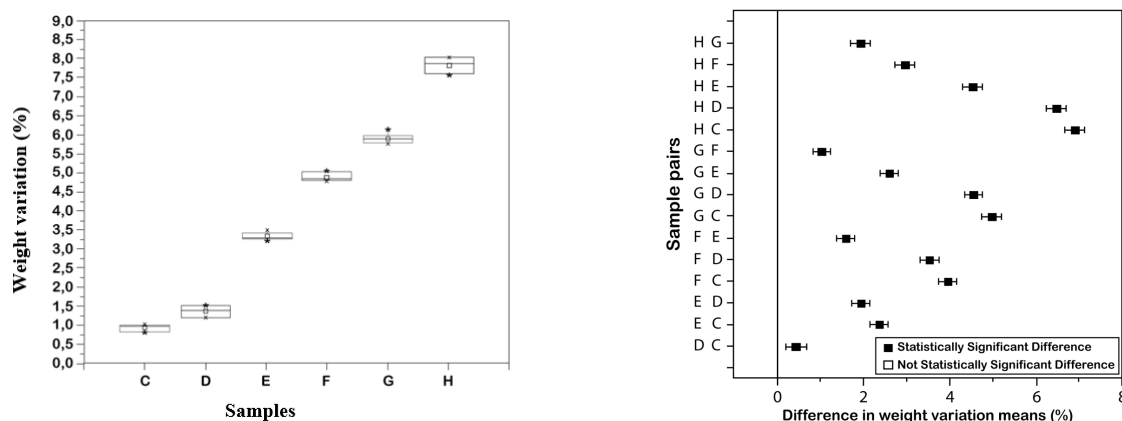


Fig. 1a) Weight gains of the treated samples. **Fig. 1b)** Weight gain mean values comparison (Tukey test).

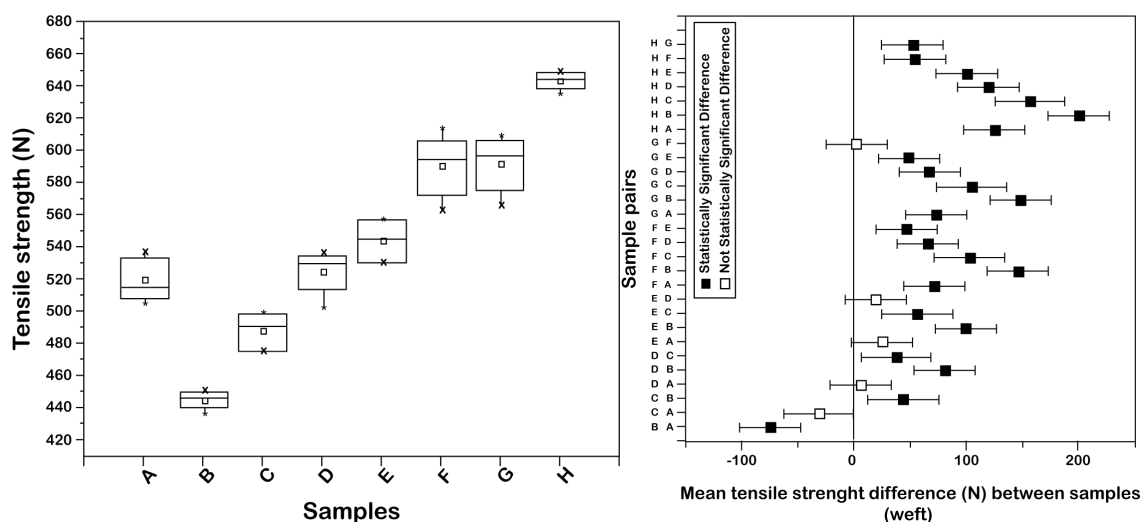


Fig. 2a) Tensile strength mean values of samples. **Fig. 2b)** Tensile strength means comparison (Tukey test).

It should be noted that the mechanical strength traction results presented and discussed above are statistically significant (Fig. 2b) proving that the incorporation of PVA crosslinked with resin and insolubilized in saponified PET produces an improvement in resistance to mechanical strength traction of textile material.

In order to characterize the PET samples, FTIR-ATR analysis were recorded. Fig. 3 shows the obtained FTIR-ATR spectrum of unmodified PET. It can be observed several PET characteristic absorption bands. The absorption peak around 1712 cm^{-1} is assigned to C=O stretching for the ester groups. The peaks at 1465 and 1403 cm^{-1} may correspond to the bending vibration in the plane of the C-H bond of the benzene ring. The absorption bands in the region of $1245\text{--}1000\text{ cm}^{-1}$ are assigned to stretching vibrations of the C-O bond. It should be noted that the original PET spectrum shows two

bands around 1506 cm^{-1} and 1408 cm^{-1} attributed to asymmetrical and symmetrical elongation vibrations of the COO^- anion respectively [13]. The appearance of these peaks indicates that the supplied PET had already been through a physical treatment that led to fibre degradation.

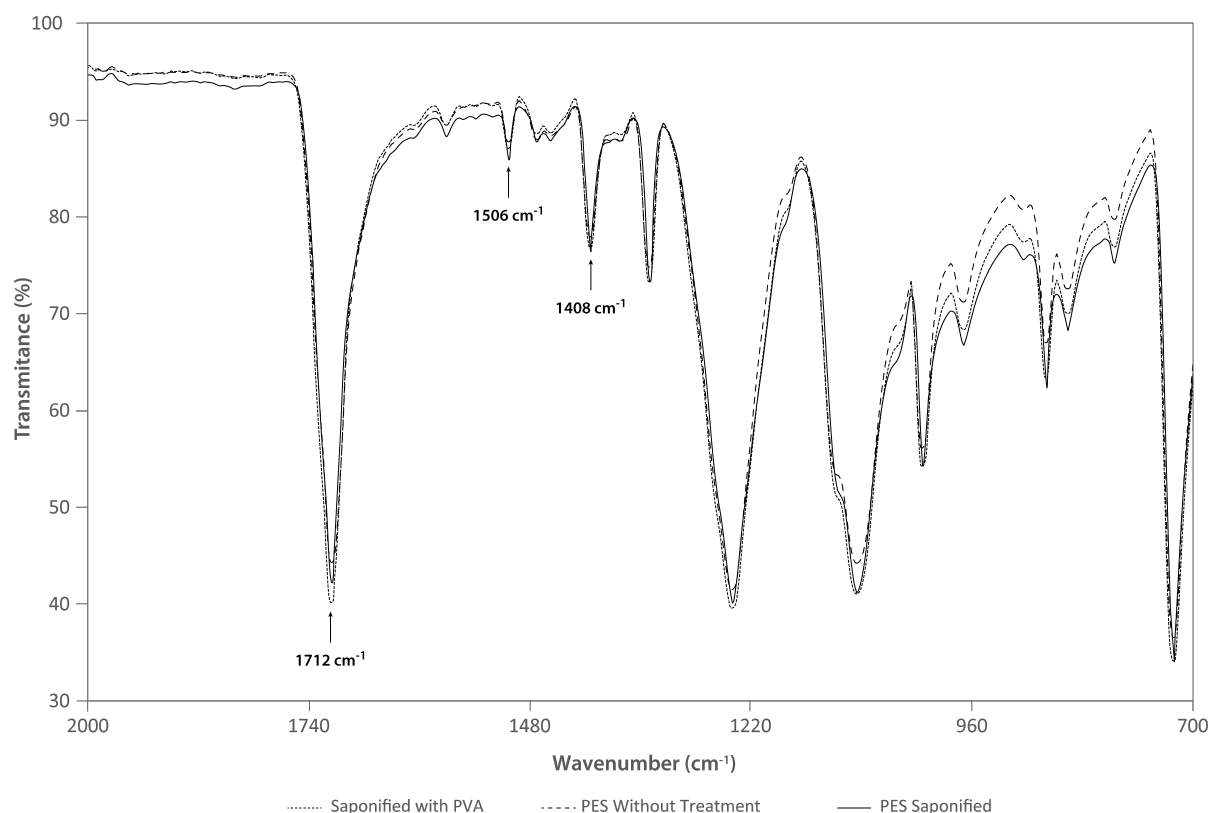


Fig. 3 ATR-FTIR spectrum of untreated PET fabric, ATR-FTIR spectrum of saponified PET fabric and ATR-FTIR spectrum of hydrolysed PET fabric treated with PVA (9000-10000), hydrolysis degree of 80% (50 g/L) and resin (60 g/L).

The FTIR-ATR spectrum of saponified PET fabric shows an additional peak at 2359 cm^{-1} (not considered in Fig.3). This is assigned to carboxylic group introduced on the PET surface due to hydrolysis of the ester linkage [14].

Comparing the spectra of saponified PET with PET treated with a combination of 50 g / L of PVA and 60 g / L of resin, it is possible to observe a slight increase in peak intensity at 1700 cm^{-1} which corresponds to the vibration of the carbonyl group of the tetrafunctional resin ring DMDHEU, which may result from the incorporation of the PVA-resin polymer in the PET fabric during the functionalization process [6].

The contact angle measurement is the main characterization method of hydrophobic and hydrophilic surfaces. The Fig. 4 shows respectively the static contact angles of the distilled water drops on the surfaces of untreated (a), hydrolysed (b) and treated with resin and PVA (c) PET samples. Fig. 5a) presents the contact angle mean values obtained for the different samples. The fibres become more hydrophilic (36.2°) by alkaline hydrolysis due to the break of the PET chains and the formation of acidic and hydroxyl groups. However, the slight increase in the mean hydrophilicity of saponified PET treated with PVA and resin (33.9°) is not statistically significant when compared to saponified sample (Fig. 5b)).

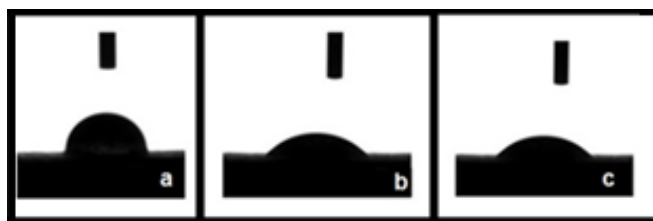


Fig. 4 Static contact angles of water drop on a) Untreated PET; b) Saponified PET c) Saponified PET treated with PVA (9000-10000) and DMDHEU (40 g/L).

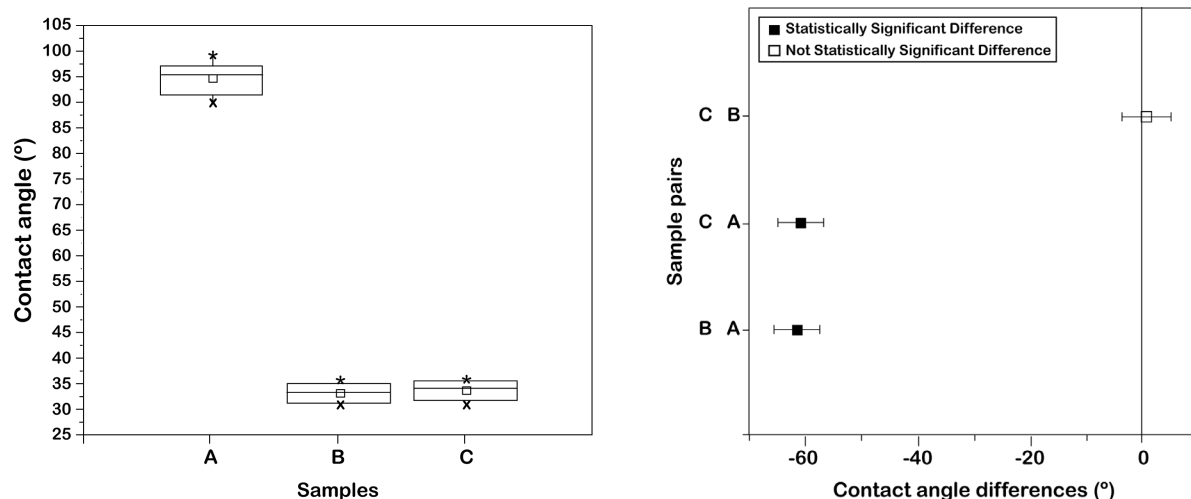


Fig. 5a) Contact angle mean values of samples. **Fig. 5b)** Contact angle means values comparison (Tukey test).

The thermal parameters of the treated and untreated PET fabrics are studied using differential scanning calorimeter (DSC). The melting temperature and fusion enthalpy of samples during the exothermic process were recorded (Fig. 6 and Fig. 7). DSC thermograms analysis show that there is a decrease in the enthalpy of fusion of treated PET when compared to the untreated one, obtaining 53.57 J/g and 66.35 J/g respectively. The enthalpy of fusion is the energy involved in the formation and melting of crystalline regions and it is proportional to the percentage of crystallinity of the sample. Fusion's enthalpy decreases in the case of PET samples treated with PVA and resin, indicating a loss in the degree of crystallinity of the fabric and, consequently, the loosening of compact structure [1]. It should be noted that there are no significant differences regarding the melting temperatures values of untreated and treated PET with PVA and resin.

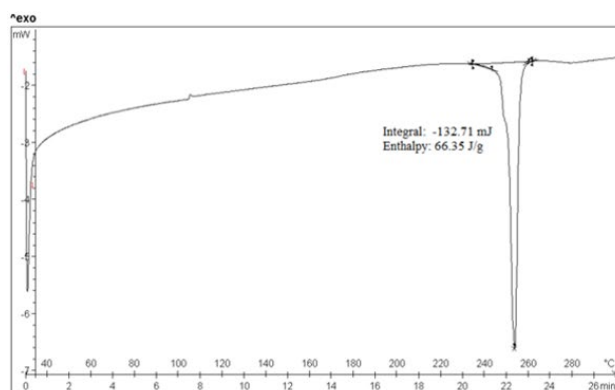


Fig. 6 DSC heating curve of original PET.

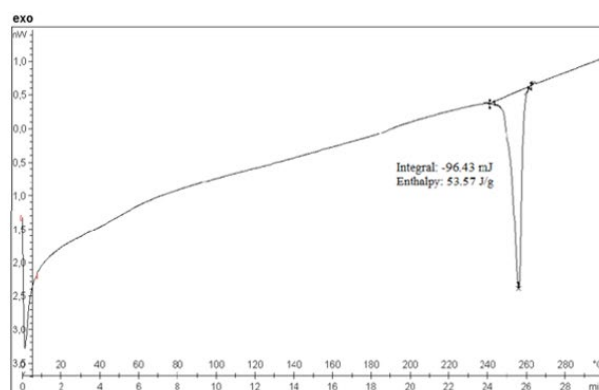


Fig. 7 DSC heating curve of PET treated with PVA (50 g/L) and resin solution (40 g/L).

The Scanning Electron Microscopy (SEM) technique has significantly contributed to the polymers characterization [14]. The surface morphology of original PET and the treated PET samples are shown in Fig. 8. It can be observed that untreated PET fibres are smooth. In SEM image that shows saponified PET with NaOH (3M) there are no fissures. These results are in line with those presented by Kish and other investigators [15].

The analysis of Fig. 8 allows us to observe a clear and accentuated change in the morphology of the hydrolysed PET fibres treated with PVA (50 g/L) and with resin (60 g/L). Regarding the image with a magnification of 10000x (f) it is possible to note the rough appearance and the deposition of the PVA- resin polymer on the fibres surface.

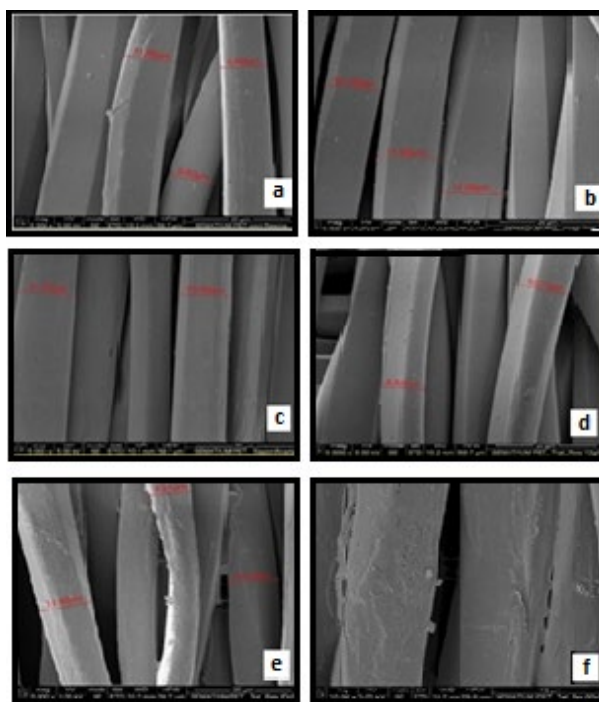


Fig. 8 SEM photographs with a magnification of 5000x (except f)): a) untreated PET; b) saponified PET c) saponified PET with resin (60 g/L); d) saponified PET with PVA (50 g/L) and resin (40 g/L); e) saponified PET with PVA (50 g/L) and resin (60 g/L) and f) PET treated with same conditions of e) but with a magnification of 10000x.

The soil-release properties of PET samples were determinate and a change from grade 2 of PET to 4 to PET after saponification was observed. The treatment of saponified PET with PVA 9000-10000 (50 g / L) and resin (40 g / L) did not change its soil-release behaviour.

Conclusions

This work allowed to conclude that the chemical modification of saponified PET with PVA and modified DMDHEU resin results in:

1. Better soil release properties than untreated polyester but similar to saponified PET.
2. Rough appearance of PET fibres by the deposition of the PVA-resin polymer, confirmed by SEM results.
3. PET materials less crystalline, but similar to saponified fibres.
4. PET with acceptable mechanical properties, analysed in terms of tensile strength.

Acknowledgment

Programme - COMPETE and by national funds through FCT – Foundation for Science and Technology within the scope of the project POCI-01-0145-FEDER-007136.

References

- [1] S. Natarajan, J.J. Moses, Surface modification of polyester fabric using polyvinyl alcohol in alkaline medium, *Indian Journal of Fibre & Textile Research*. 37 (2012) 287-291.
- [2] T.M.R., Miranda, J. Santos, G.M.B Soares, Soil-release behaviour of polyester fabrics after chemical modification with polyethylene glycol. *IOP Conference Series-Materials Science and Engineering*. (2017) 254 (3).
- [3] V. Takke, N. Behary, A. Perwuelz, C. Campagne, Surface and adhesion properties of poly(ethylene glycol) on polyester (polyethylene terephthalate) fabric surface: Effect of air-atmospheric plasma treatment. *Journal of Applied Polymer Science*. 122 (2011) 2621–2629.
- [4] B.S Butola, Polyesters and polyamides, in: B.L. Deopura, R. Alagirusamy, M. Joshi, B. Gupta Eds.), *Surface modification textiles*, Woodhead Publishing Limited Cambridge England, 2008, 272.
- [5] J. Wang, L.J. Zhejiang, *Surface modification of textiles*, Cambridge: Woodhead Publishing Limited, 2009.
- [6] T.L Vigo, J.S. Bruno. Textile Research Institute. Temperature - Adaptable Textiles Containing Durably Bound Polyethylene Glycols. *Textile Research Institute*. 57 (1986) 427-429.
- [7] R.F.M. Castro, Optimization of soil-release finishing processes for polyester fibers. Universidade do Minho, Guimarães 2017.
- [8] J-S. Park, J-W. Park, E. Ruckenstein. A Dynamic mechanical and thermal analysis of unplasticized and plasticized poly (vinyl alcohol)/methylcellulose blends. *Journal of Applied Polymer Science*. 80 (10) (2001) 1825-1834.
- [9] A.B.S. Barros, R.F. Farias, D.D. Siqueira, C. B. B. Luna, E.M. Araújo, M.S. Rabello, R. M. R. Wellen, The Effect of ZnO on the Failure of PET by Environmental Stress Cracking. *Materials*. 13 (2020) 2833-2844.
- [10] Q. Wey, *Surface modification of textiles*, Woodhead Publishing in Textiles: Number 97, New York 2009.
- [11] S.M. Burkinshaw, *Chemical Principles of Synthetic Fibre Dyeing*, First ed., published by Chapman Halli 1995.
- [12] X. Tao, *Handbook of Smart Textiles*, published by Springer Science+Business Media Singapore 2014.
- [13] X. Gu, D. Raghavan, T. Nguyen, M.R VanLandingham, D. Yebassaa, Characterization of polyester degradation using tapping mode atomic force microscopy: exposure to alkaline solution at room temperature. *Polymer degradation and stability*. 74 (2001) 139-149.
- [14] S. Pitchai, J. Moses, S. Natarajan. Study on the improvement of hydrophilic character on polyvinylalcohol treated polyester fabric. *Polish Journal of Chemical Technology* 16, (4)(2014)21-27.
- [15] M.H. Kish, M. Nouri. Effects of sodium hydroxide and calcium hydroxide on polyester fabrics. *Journal of Applied Polymer Science*, 72 (1999) 631-637.

Investigation of the Dyeability Behaviors of Cotton Surfaces with Natural Dyes Extracted from Rubia Tinctorum and Reseda Luteola L. Plants

Gizem CALISKAN^{1,a*}, Pinar SEZGIN^{2,b}, Emine Dilara KOCAK^{3,c},
Sevda ALTINDERE^{4,d} and Ozge KOSEMEK^{5,e}

¹Beymen Perakende ve Tekstil Yatırımları A.Ş, Sariyer, Istanbul, Turkey

²Beymen Perakende ve Tekstil Yatırımları A.Ş, Sariyer, Istanbul, Turkey

³Marmara Üniversitesi, Teknoloji Fakültesi, Kadıkoy, Istanbul, Turkey

⁴Beymen Perakende ve Tekstil Yatırımları A.Ş, Sariyer, Istanbul, Turkey

⁵Beymen Perakende ve Tekstil Yatırımları A.Ş, Sariyer, Istanbul, Turkey

^agizem.caliskan@beymen.com, ^bpinar.sezgin@beymen.com, ^cdkocak@marmara.edu.tr,
^dsevda.altindere@beymen.com, ^eozge.kosemek@beymen.com

Keywords: Natural Dye, Rubia Tinctorum, Reseda Luteola L, Cotton Knitted Fabric, Color Properties.

Abstract. In this study, the pigment obtained from Rubia Tinctorum plants growing around Central Anatolian Region (Konya) and the Reseda Luteola L plant extract collected from Black Sea Region, have been used as natural dye sources. The 100% cotton, single pique knitted surfaces with 190 g/m² weight are used as a material to be dyed. Prior to the dyeing process, the samples were mordanted with 1% potassium aluminum sulphate and copper sulphate in a laboratory dyeing machine (Thermal). Following the mordant process, the samples were dyed in the laboratory dyeing machine at boiling temperature for 60 minutes according to the exhaustion method. The samples were left to be cooled in the dyeing liquor and 12 hours later, cold overflow washing, hot washing, boiling soaping and cold rinsing were performed additionally. After the drying process, color measurements were carried out with a spectrophotometer (Machbeth 2 180 V) using Color office Textile program to create color coordinates according to the CIE Lab system under D65 illuminate and 10° standard observer. As a conclusion, the samples mordanted with potassium aluminum sulphate and then dyed with natural dye obtained from Rubia Tinctorum plant is considered the standard for color measurement, it has been determined that copper sulphate mordant is effective in the change of (ΔE^*) total color difference ($\Delta E^*=7.93$). The samples with Rubia Tinctorum have a lighter color than the standard, the green and blue nuance is more, and the color is more matte as well. The samples mordanted with potassium aluminum sulphate and then dyed with natural dye obtained from Reseda Luteola L plant is considered the standard for color measurement, it has been determined that copper sulphate mordant is effective in the change of (ΔE^*) total color difference ($\Delta E^*=24$). On the lightness axis (ΔL^*), the dyed sample is darker than the standard. The color of Reseda Luteola L. dyed the samples is darker than standard, more red and blue; the nuance is more, also the color is more matte. When the Color Strength (K / S) values of the samples dyed with the dyestuffs obtained from Rubia Tinctorum and Reseda Luteola L plants were compared; in both dyestuffs, the highest Color Strength Value (K / S) was obtained in samples dyed after mordant process with copper sulphate (Rubia Tinctorum: K / S= 3,336; Reseda Luteola L: K / S= 10,649). The washing fastness results are lower than the staining fastness for all performed dyeing process. Both the color change in washing and staining rates are between the values accepted by the industry. Likewise, the dry rubbing fastness and wet rub fastness of all dyeing are similar. Light fastness values of samples dyed with natural dye obtained from Rubia Tinctorum plant are higher than samples dyed with Reseda Luteola L.

Introduction

Dyeing of textile materials with natural root dyes started in India and Mesopotamia around 4000 BC. It has lost its importance with the production of synthetic dyestuffs in the 19th century. However, today, interest in natural dyes has increased due to the rapid implementation of sustainable strategies in the textile and fashion industry to minimize the damage caused by synthetic dyes to the environment that causing allergies [1]. The studies examining the color fastness and coloring properties of many plants used as natural dyes are available in the literature. [2-4].

Under the roots of the *Rubia Tinctorum* plant, the anthraquinone dye compounds are covered with a shell. 32 kinds of dark red colors are obtained from that plant, and it is widely used in the Mediterranean region and North Africa [5,6]. *Rubia Tinctorum* plant became widespread in the Ottoman Empire in the 16th century and entered the literature as a Turkish color in the 17th century [7]. The red color obtained from the *Rubia Tinctorum* plant has been used extensively in coloring silk, wool, and cotton fabrics [8].

Reseda Luteola L. is a plant that grows in Asia and the Mediterranean region [9]. It is the source of yellow color in textile dyeing and has been used a lot in silk and cotton dyeing since ancient times [10-12].

Materials and Methods

Materials

In this study, the 100% cotton, single pique knitted surfaces with 190 g / m² weight and mordant materials (99,9% purity Sigma-Aldrich, Germany) are used in this research was obtained from the Merit Textile Company (Turkey). *Tinctorum* is the pigment obtained from the *Rubia Tinctorum* plant grown in Konya region. *Reseda Luteola* L plant extract collected from the Black Sea Region is another natural pigment used in the study at Table 1.

Extraction

The 10 g/L solution of the dye obtained from *Rubia Tinctorum*, and *Reseda Luteola* L plants were first dissolved (distilled water) separately by boiling for 15 minutes, the plants were mixed with a magnet mixer. The temperature of the plant extracts was then reduced to 75 °C and the plant extracts were kept at that temperature for 1 h. The plant extracts were dried in an oven (40 °C ± 2 °C) for 8 hours after washing and were extracted by boiling in 750 mL of distilled water for 1 hour and made ready for dyeing by filtration. The filtered (Whatman, 595/1/2, 110 mm diameter) product then was dried in a laboratory oven at 60°C for at least 6 h, and weighted.

Mordanting and Dyeing

In this study, laboratory-type dyeing machine (Thermal) is used in dyeing and mordant processing. Metal mordant method was used for pre-mordant the samples. In both dyestuff applications, potassium aluminum sulphate and copper sulphate at 1% concentration were used as mordant substances. The mordant solution was prepared by use of 10 grams of in both dyestuff applications, potassium aluminum sulfate and copper sulfate in 1000 mL of distilled water. Then the fabrics were treated in a liquor ratio of 1:50 for one hour at the boiling temperature of about 98°C. The samples were mordanted at boiling temperature for 1 hour in flotte with a ratio of 1/40, and the dyeing process was applied without rinsing by removing the excess flotte.

Dyeing was done according to the exhaustion method and the dye extracts obtained were used without dilution. According to the temperature-time diagram given in Fig. 1, cotton containing pique knitted surface samples, were dyed in a float with a flotte ratio of 1/40. Then, cold overflow washing (250 mL), 60 °C hot washing (100 mL), boiling soaping (1g/L non-ionic detergent 100 mL) and cold rinsing (100 mL) were applied to the samples. At the end of the processes, cotton knitted surface samples were dried in an oven at 105 °C for 2 minutes.

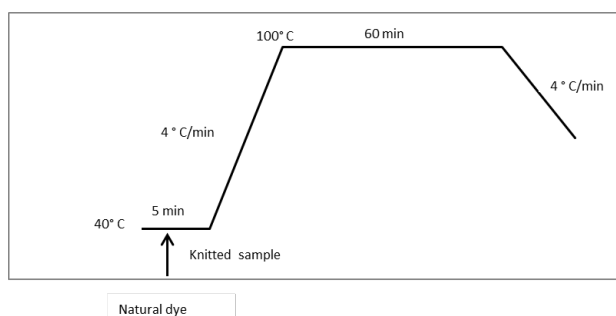


Figure 1. Dyeing Process

Color Measurements

Machbeth 2 180 V color measurement device and Color office Textile computer program was used for color measurements. According to the CIE Lab system, in the measurements made under D65 illuminant using a 10 ° standard observer, the samples were painted with two different natural dyes after blending with potassium aluminum sulphate and these samples were accepted as standard. The colors of dyed fabrics were calculated according to CIE Lab color coordinates (L^* , a^* , b^* , C^* and h) Eq. 1, and color strength values (K/S) were calculated using Eq. 2 from Kubelka-Munk equation [13].

$$\Delta E^* = [(\Delta L^*)^2 + (\Delta a^*)^2 + (\Delta b^*)^2]^{1/2} \quad (1)$$

Here; ΔL^* lightness - darkness, Δa^* redness - greenness, Δb^* yellowness - blueness, ΔE^* total color difference

$$K/S = (1-R)^2 / 2R \quad (2)$$

Here, K absorption coefficient, S scattering coefficient, R reflectance value of the fiber at wavelength at maximum absorption and K/S color strength

Color Fastness Measurements


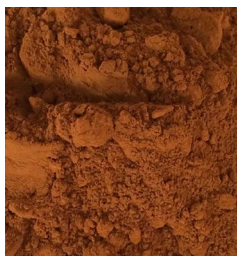
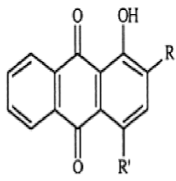
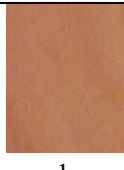
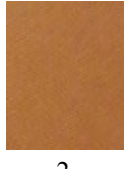

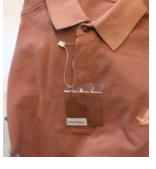


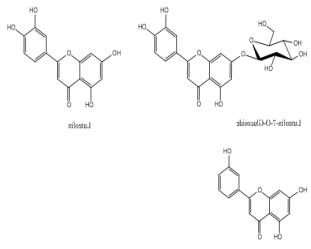
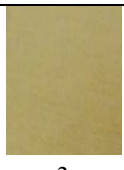


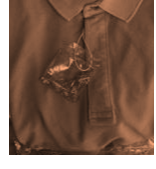
The washing fastness's of the dyed samples were made in the washing fastness tester (Gyrowash-James H. Heal) in accordance with ISO 105-C06 standards. The dyed samples were treated with a solution of 4 g / L ECE detergent at a ratio of 1/100 flote at 40 ° C for 30 minutes in Gyrowash Washer Tester and evaluated with grey scale.

The rubbing fastness tests of dyed cotton-containing pique knitted surfaces were tested in the Crockmeter Test device according to ISO 105-X12:2016, then the wet and dry staining fastness values were determined with grey scale. The light fastness of the dyeing was carried out in a light fastness tester (Atlas Alfa 150 S) according to the EN ISO 105-B02:1994 standard and the color change was evaluated with a blue scale [14-16].

Results

In this section, the results obtained from the research results are evaluated. Rubia Tinctorum and Reseda Luteola L plants, natural pigments obtained from these plants, chromophore structures and the color images of dyed samples are given in Table 1.

Table 1. Dye Plants, Pigments, Chromophore Structures and Resulting Colours

 <p>Rubia Tinctorum</p>	 <p>Rubia Tinctorum dye</p>	 <p>1 Alizarin $R=OH$ $R'=H$ 2 Rubberthric acid $R=O$ $R'=H$</p>	 <p>1</p>  <p>2</p>	 
 <p>Reseda Luteola L</p>	 <p>Reseda luteola L. natural dye</p>	 <p>Reseda Luteola L pigments</p>	 <p>3</p>  <p>4</p>	 

According to the CIE Lab system, in the measurements made under D65 illuminant using a 10° standard observer, the samples were painted with two different natural dyes after blending with potassium aluminium sulphate and these samples were accepted as standard and according to Eq. 1, ΔE^* , ΔL^* , Δa^* , Δb^* and ΔC^* values are calculated. Table 2 contains CIE Lab values of samples stained with natural dyes obtained from Rubia Tinctorum, Reseda Luteola L, and Table 3 includes ΔE^* , ΔL^* , Δa^* , Δb^* and ΔC^* values.

Table 2. CIE Lab Values

Source of light D65 - 10°	L*	a*	b*	C*	h°	X	Y	Z	x	Y
Rubia Tinctorum 1 (Potassium aluminium sulphate)	71,34	15,13	31,09	34,58	64,05	49,48	42,68	13,38	0,47	0,40
Rubia Tinctorum 2 (Copper sulphate)	66,89	19,39	36,09	40,97	61,75	44,03	36,48	9,56	0,49	0,41
Reseda Luteola L.1 (Potassium aluminium sulphate)	64,11	7,13	32,53	33,30	77,64	36,08	32,94	9,24	0,46	0,42
Reseda Luteola L.2 (Copper sulphate)	73,42	-1,13	53,60	53,61	91,20	46,77	45,81	7,98	0,47	0,46

Table 3. ΔE^* , ΔL^* , Δa^* , Δb^* and ΔC^* Values of Natural Dye Specimens Obtained from Rubia Tinctorum and Reseda Luteola L Plants

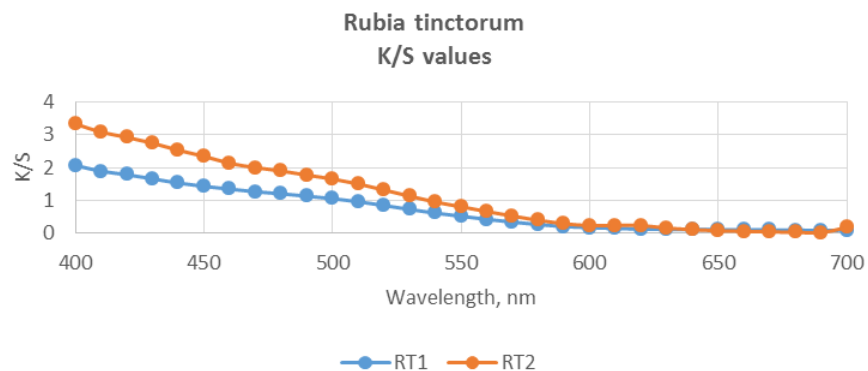
Natural Dye	ΔL^*	Δa^*	Δb^*	ΔC^*	ΔE^*
Rubia Tinctorum	4.45	-4.26	-5	-6.39	7.93
Reseda Luteola L.	-9.31	8.26	-21.07	-20.31	24

Standard: Samples dyed with two different natural dyes after being mordant with potassium aluminium sulphate

Since the sample dyed with natural dye obtained from Rubia Tinctorum plant and potassium aluminium sulphate mordant is considered the standard for colour measurement, it has been determined that copper sulphate mordant is effective in the change of total colour difference (ΔE^*) ($\Delta E^* = 7.93$). The colour of the cotton piqué knitted surface dyed with Rubia Tinctorum is lighter than the standard, the green and blue nuance is more, and the colour is more matte.

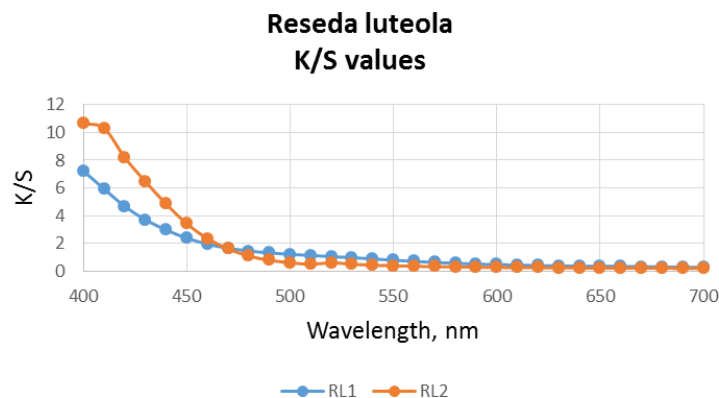
In the colour measurements of cotton piqué knitted surfaces dyed with natural dye obtained from *Reseda Luteola* L. plants, the sample dyed after being mordant with potassium aluminium sulphate was accepted as standard and it was determined that copper sulphate mordant was more effective in the change of total colour difference ($\Delta E^* = 24$). On the lightness-darkness axis (ΔL^*), sample dyeing is darker than standard. The colour of *Reseda Luteola* L. dyed cotton piqué knitted surface is darker than standard, more red and blue nuance, also the colour is more matte.

The reflectance values of the dyes measured at 400-700 nm wavelength, 10 nanometer intervals are determined and the curves created with the data calculated according to Eq. 2 with the help of these values are shown in Fig. 2 and Fig 3. (RT1: Rubia Tinctorum - Potassium Aluminium Sulphate; RT2: Rubia Tinctorum – Copper Sulphate; RL1: Reseda Luteola - Potassium Aluminium Sulphate; RL2: Reseda Luteola – Copper Sulphate)



RT1: Rubia Tinctorum - Potassium Aluminium Sulphate; RT2: Rubia Tinctorum – Copper Sulphate

Figure 2. K / S Curves of Rubia Tinctorum Dyed Samples in the 400-700 nm Wavelength Range



RL1: Reseda Luteola - Potassium Aluminium Sulphate; RL2: Reseda Luteola – Copper Sulphate

Figure 3. K / S Curves of Reseda Luteola Dyed Samples in the 400-700 nm Wavelength Range

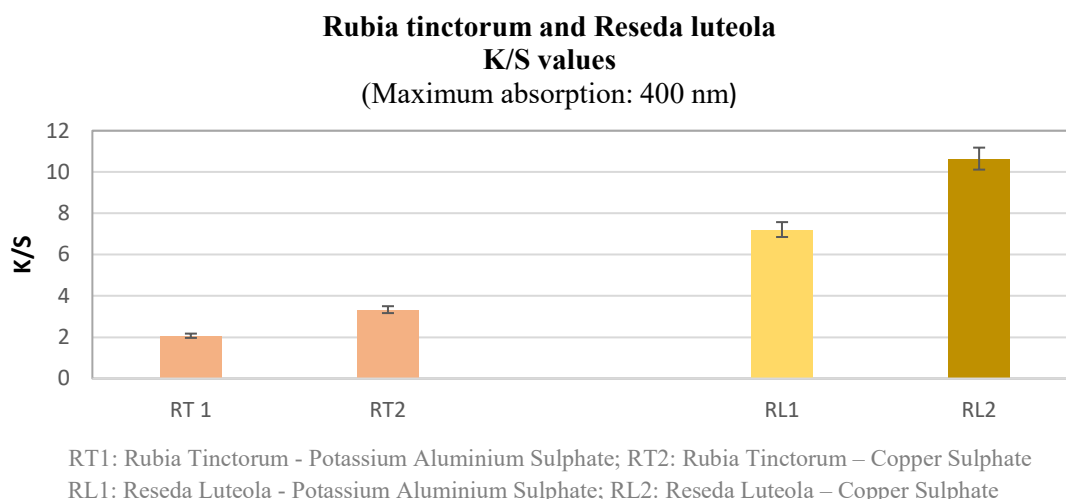


Figure 4. Dyed Samples at Maximum Absorption (400 nm)- K / S Color Strength

When the Colour Strength (K / S) values of the dyestuffs obtained from Rubia Tinctorum, and Reseda Luteola L plants were compared in Fig 4.; the highest Colour Strength Value (K / S) of both dyes was obtained in samples dyed after being mordant with copper sulphate (Rubia Tinctorum: K / S = 3,336; Reseda Luteola L: K / S = 10,649).

Table 4. Washing, Rubbing and Light Fastness of the natural dyed samples

Mordant	Washing							Rubbing Fastnesss		Light Fastness
	Color Change	Staining								
		CA	CO	PA	PET	PAN	WO	Dry	Wet	
RT1	3-4	5	5	5	5	5	5	4/5	4/5	4/5
RT2	4	5	5	5	5	5	5	4/5	4/5	4/5
RL1	3	4	4	3	3-4	4	2-3	4	4	4
RL2	3	4	4	3	3-4	4	2-3	4	4	4

RT1: Rubia Tinctorum - Potassium Aluminium Sulphate; RT2: Rubia Tinctorum – Copper Sulphate; RL1: Reseda Luteola - Potassium Aluminium Sulphate; RL2: Reseda Luteola – Copper Sulphate

The fastness values of the dyeing made with two different mordants, potassium aluminium sulphate, copper sulphate; It is higher in Rubia Tinctorum than samples stained with Reseda Luteola L. As is known, the fastness properties of natural dyes are low. Mordant process is applied to improve fastness properties [17]. When the fastness properties of the mordant matter were compared, it was seen that the type of mordant did not affect the fastness properties of the samples very much as seen at Table 4.

Conclusion

According to the results of this study, it was observed that copper sulphate mordant was effective in the color measurement results and K / S ratios of cotton pique knitted surfaces dyed with natural dye obtained from Rubia Tinctorum and Reseda Luteola L. Plants. However, when the fastness values of the mordant materials were compared with each other, it was observed that there was no change.

Acknowledgment

The author(s) disclosed receipt of the following financial support for research and authorship. This work was supported by Beymen Design Center (Project Number: T7000.0441-20CLU01)

References

- [1] Shahid M., Shahid-ul-Islam & Mohammad F., 2013, "Recent advancements in natural dye applications: a review", *Journal of Cleaner Production*, 53, 310-331
- [2] Mirjalili, M., Nazarpour, K., Karimi, L. 2011. Extraction and identification of dye from walnut green husks for silk dyeing. *Asian J. Chem.* 23, 1055–1059.
- [3] Lee, Y.H., Kim, H.D. 2004. Dyeing properties and colour fastness of cotton and silk fabrics dyed with *Cassia tora* L. extract. *Fiber. Polym.* 5, 303-308
- [4] Prabhu, K.H., Teli, M.D., Waghmare, N.G. 2011. Eco-friendly dyeing using natural mordant extracted from *Emblica officinalis* G. Fruit on cotton and silk fabrics with antibacterial activity. *Fiber. Polym.* 12, 753-759.
- [5] L. G. Angelini, L. Pistelli, P. B. A. Bertoli, S. Panconesi 1997, "Rubia tinctorum a source of natural dyes: agronomic evaluation, quantitative analysis of alizarin and industrial assays" *Industrial Crops and Products* 6 pp.303–311
- [6] De Santis, D., Moresi, M., 2007, Production of alizarin extracts from *Rubia tinctorum* and assessment of their dyeing properties *Industrial Crops and Products* Volume 26, Issue 2, Pages 151-162
- [7] Chenciner, R., Madder 2000, *Red: A history of luxury and trade*, Curzon Press.
- [8] Tutin, T.G., Heywood, V.H., Burges, N.A., Moore, D.M., Valentine, D.H., Walters, S.M., Webb, D.A., 1980. *Flora Europaea*, vol. 5. Cambridge University Press, Cambridge, p. 476.
- [9] L. Ford, C.M. Rayner, R.S. 2018, Blackburn Degradation of Lucidin: New insights into the fate of this natural pigment present in Dyer's madder (*Rubia tinctorum* L.) during the extraction of textile Artefacts Dyes& pigments., 154, pp. 290-295
- [10] G. Gedik, O. Avinc 2020, Hemp fiber as a sustainable raw material source for textile industry: can we use its potential for more eco-friendly production, *Sustainable Textiles: Production, Processing, Manufacturing & Chemistry* books Springerlink, pp 87-91
- [11] Goverdina C. H. Derksen, Frédérique L. van Holthoorn et al. Development of a process for obtaining non-mutagenic madder root (*Rubia tinctorum*) extract for textile dyeing
- [12] S.S. Muthu, M.A. Gardetti (Eds.), *Sustainability in the Textile and Apparel Industries: Sourcing Natural Raw Materials*, Springer International Publishing, Cham (2020), pp. 87-109
- [13] Fairchild, M.D., *Color Appearance Models*, 1997, ISBN 0-201-63464-3, Addison Westley Longman, Inc.
- [14] ISO 105-C06, Test for Colour Fastness of Textiles-Colour Fastness to Washing.
- [15] ISO 105-X12:2016, Tests for Colour Fastness -Part X12: Colour Fastness to Rubbing.
- [16] EN ISO 105-B02:1994 Colour fastness to artificial light: Xenon Arc Fading Lamp Test
- [17] Zuber, M., Adeel, S., Rehman, F., Anjum, F., Muneer, M., Abdullah, M., Zia, K.M. (2020). Influence of microwave radiation on dyeing of bio-mordanted silk fabric using neem bark (*azadirachta indica*)-based tannin natural dye, *Journal of Natural Fibers*, Volume 17, No 10, pp.1410–1422.

Pre, Post and Meta Mordanting Recycled Cotton with Chitosan

Serkan Uysal^{1,a}, Eva Bou-Belda^{1,b}, Marilés Bonet Aracil^{1,c},
Jaime Gisbert-Payá^{1,d*}

Departamento de Ingeniería Textil y Papelera, Universitat Politècnica de València, Plaza Ferrándiz y Carbonell s/n, Alcoi, (Alicante. Spain)

^aseruy@epsa.upv.es, ^bevbobel@upvnet.upv.es, ^cmaboar@txp.upv.es, ^{d*}jaigispa@txp.upv.es

Keywords: Chitosan Mordanting, Recycled cotton, Natural dyes, Ecological textile, antimicrobial finishes.

Abstract. The textile processing industry has been imposed strict ecological and economic restrictions on the chemicals used, including bans on certain consumer goods containing synthetic agents which are posing challenges to sustainability issues [1, 2]. The worldwide demand for the use of environmentally friendly products in the textile industry is nowadays of great interest, possibly because of the increasing concern about the environment, ecology, and pollution control [3, 4].

It is a fact that the textile industry has grown many times during the last decades to meet global and domestic demand. This tremendous growth has also led to a parallel growth in environmental problems, which remained unnoticed. Any industrial activity produces pollution in one form or the other, and the textile industry certainly released a wide spectrum of pollution into the environment. The textile manufacturing process is characterized by the high consumption of resources such as water, fuel and a variety of chemicals in a long process sequence which generates a significant amount of waste. The common practices of low process efficiency result in substantial wastage of resources and severe damage to the environment [5, 6].

Recycling implies the breakdown of a thing into its unrefined materials with the end goal that the rough material can be recuperated and used as a piece of new items. On the other hand, recycle insinuates a present thing being used again inside a comparable creation chain. Textile material recycling is the strategy by which old pieces of clothing and diverse materials are recovered for recycle or material recovery. It is the explanation behind the material recycling industry. Material recycling may incorporate recouping pre-consumer waste or post-consumer misuse. There are different ways to deal with perceive the sorts of recycling possible inside the material [7].

Pre-consumer waste is a material that was disposed of before it was prepared for customer utilize. Pre-consumer recycled materials can be separated and revamped into comparative or diverse materials or can be sold as such to outsider purchasers who at that point utilize those materials for buyer items. Pre-consumer material waste for the most part alludes to squander results from fibre, yarn, material, and clothing fabricating. It can be process closes, scraps, clippings, or merchandise harmed amid creation, and most is recovered and recycled as crude materials for the car, furniture, sleeping cushion, coarse yarn, home outfitting, paper, and different ventures. Pre-consumer squanders are produced all through the first phases of the inventory network. In the crude materials area (fibre and yarn creation), ginning squanders, opening squanders, checking squanders, comber noils, brushed waste yarns, meandering squanders, ring turning waste fibres, ring-spun squander yarns, open-end spinning waste fibres, and open-end spinning yarn squanders are usually gathered for recycling [8].

The ground root of the madder plant, *Rubia Tinctorum* L., formerly cultivated in many parts of Europe and North and South of America. Was largely used for dyeing Turkey Red on cotton mordant with alum in presence of lime. Applied to wool on an alum- or chrome-cream of tartar mordent [9].

Natural dyes with a few expectations are non-substantive and hence must be used in conjunction with mordants. Mordant is a chemical, which can fix itself on the fibre and combines with the dyestuff. The challenge before the natural dyers in application of natural colour is the necessity to use metallic mordants which themselves are pollutant and harmful. Due to the environmental hazard caused by metallic mordant while dyeing of textile fabric, dyers are always looking for safe natural mordant for natural dyes [10].

The applications of chitosan for different applications in textiles are reported [11–12], but the application of such functional biopolymer as a mordant in natural dyeing has been quite rare in the literature. In the current work, chitosan extracted from waste shrimp shells [12] was utilized as a mordant for simultaneous natural dye printing and antibacterial finishing of cotton in comparison with commonly used metal mordants. The efficacy of chitosan as eco-friendly mordant and antibacterial finish has been studied.

The paper discusses a comparison between different ways to mordant cotton with chitosan. This research as a first step of further experimental, provide us the optimum values and applications for the future research. As a result, we could conclude the mordanting process was more effective from the point of view of dyeing yield.

Materials and Methods

Recycled 100% cotton fibres raw white (which contains small part of other cellulosic fibres) were used in this study. These recycled cotton fibres were obtained by recycling pre-consumer textile clipping wastes.

Chitosan (low molecular weight, Sigma-Aldrich) in powder form was used. A solution with 10 g/L was prepared. Acetic acid solution 80% (Panreac): 6mL/L was used to obtain acid pH which allows to solve chitosan.

Rubia tinctorum was used as natural dye 10% spf: C.I. Natural Dye 8 (Lana y telar S.L.).

Dyeing was carried out by three different methods:

- PRE-mordanting; recycled cotton fibres were treated with chitosan by padding with chitosan solution at pH was 5,5. Then it was dried at 100° C and then a curing treatment (150° C, 3 minutes) was performed. Afterwards, dying bath was prepared with *rubia tinctorum* in a neutral pH. Bath exhaustion method was applied to the pre-mordanted fibres for 60 minutes at 60° C bath rate was 1:40.
- META-mordanting; recycled cotton fibres dyed and treated with chitosan in the same bath and at the same time in pH 5,5 during 60 minutes at 60° C with afore mentioned concentrations. Bath rate was 1:40
- POST-mordanting; recycled cotton fibres dyed with *rubia tinctorum* at first in neutral pH bath during 60 minutes at 60° C and then treated with chitosan in pH 5,5 during 60 minutes at 60° C. Bath rate was 1:40.

Dye concentration was calculated by means of a spectrophotometer and a calibration equation ($A = 0,3206 c - 0,0121$) was calculated according to Lamber Beer Law. Colour fastness to washing was also evaluated.



Figure 1. Recycled cotton fibres dyed with *Rubia Tinctorum*

Measurement of reflectance (%)

Reflectance (%) of the dyed fibre samples were measured by using Data colour 650 TM spectrophotometer [14].

Colour fastness to washing was conducted according to ISO 105 C06. Samples were switched to cotton and wool fabrics to determine the cross staining. Textiles were treated with the requested concentration of soap and 10 balls to simulate mechanical effect of washing machine. Temperature was 40° C and for 45 minutes.

Additionally, colour fastness to rubbing was performed according to ISO 105 X12. Rubbing method uses a Crockmeter to determine the level of colour resistance of the fabric sample to be absorbed into the white cotton cloth by rubbing a white cotton cloth against the fabric sample. The measurement scale in the rubbing method is staining scale. This rubbing method is divided into two types: dry rubbing test and wet rub test.

According to grey scale it is worthy to point out that, number 4 indicates the colour quality of the fabric is "good", while the number 5 shows the "excellent" quality [17].

Results and Discussion

A comparison between pre-mordanted, meta-mordanted and post-mordanted chitosan solution and the effects on absorbance of natural dyes was studied. As reference sample we used the same material without any chitosan treatment for mordanting. Table 1 show the % of dye on the fibre, according to eq 1. Consequently, it fits with % exhaustion. As it should be expected, the highest concentration of dye in wastewater (c), the less % Exhaustion. Results evidence the effectiveness of chitosan presence on the dyeing yield. However, the mordanting treatment shows an influence and it must be analysed. Meta-mordanting process seems to be more effective than the others showing post mordanting treatment the lowest values, barely post-mordanting % exhaustion is similar to the white sample.

$$\% E = (4 - c)/4 \cdot 100 \quad [16]$$

Table 1. Absorbance, concentration, exhaustion and colour results.

Ref.	Absorbance	Concentration (g/L)	% Exhaustion	ΔE_{ab}
W	0,908	2,8699	28,2517	--
META	0,678	2,1525	46,1868	16,090
PRE	0,796	2,5206	36,9853	15,403
POST	0,867	2,7420	31,4488	16,600

Regarding colour space, Table 2 shows the meaning of colour coordinates. When colour differences (ΔE_{ab}) are observed (Table 3), it can be clearly appreciated there are no significant differences between the mordanting processes studied, and apparently white sample without chitosan shows the lowest colour and mordanted samples show higher colour but similar between the three mordanted methods studied.

The sample without chitosan treatment shows slightly lower values for L^* which means chitosan treatment offers darker values. Post mordanting has the most intensive colours according to L^* but regarding to reddish tone, the one expected from *rubia tinctorum* dyeing process, meta-mordanting processed sample shows higher values for both red and yellow colour.

Table 2. Visual colour differences for respective differences in CIELAB colour-difference attributes. [13]

CIELAB Notation	Relevant perceptual differences	Visual perception for	
		Positive value (+)	Negative value (-)
ΔL^*	Lightness/darkness	Lighter	Darker
Δa^*	Redness/greenness	Redder	Greener
Δb^*	Yellowness/blueness	Yellower	Bluer
ΔC^*	Chroma	Brighter	Duller

Table 3. Colour coordinates of the treated fibre samples

Method	L^*	a^*	b^*	ΔE_{ab}
W	68,935	20,145	12,192	--
Pre	69,338	14,705	15,192	16,090
Meta	69,212	17,771	17,073	15,403
Post	70,066	14,647	14,641	16,600

The values of the colour coordinates of the samples were entered in the CIELab application and the result shown in the Figure 1. Result of the coordinates also shows visually, Meta-mordanting processed sample has more red colour, more yellow and more saturated colour on the right side of the Figure 1.

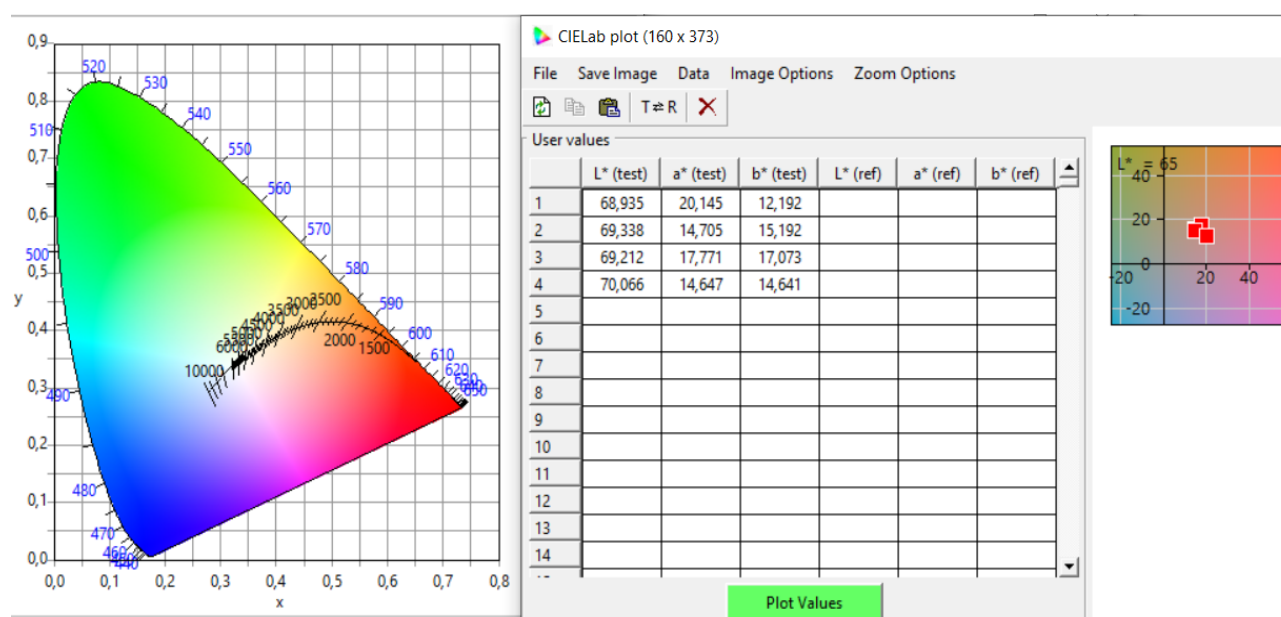


Figure 1. Spotted coordinates of the references on chromaticity diagram.

Colour fastness to washing results are shown in Table 4. The absence of mordanting can be directly related to the worst results, non-treated fibres show the highest degradation of colour once it has been washed. The mordanted samples show an improvement according to its degradation reaching 4/5. On

the other hand, when staining is evaluated, pre-mordanting treatment shows the highest results as there is no colour in none of the fabrics (neither cotton nor wool).

Table 4. Colour fastness to washing staining

Ref.	Degradation	Cotton	Wool
W	3	5	2
META	4/5	5	3/4
PRE	4/5	5	5
POST	4/5	5	3

Another test method made with Crockmeter was used to determine the effect of rubbing on the sample. Similar values were reached for degradation when the test was conducted in dry and wet samples. The staining was similar for every sample, slight colour for non-mordanted and no colour for mordanted samples. Only a difference can be observed for degradation on the non-mordanted sample, which is higher in the wet process in the non-treated sample. Degradation for every mordanted sample was the same (4/5) which implies the chitosan protection regardless the mordanting process applied. Tests made with dry and wet samples and the results compared with Grey Scale card.

Table 5. Colour fastness to Rubbing

Ref.	Degradation Dry	Degradation Wet	Staining Dry	Staining Wet
W	4	3	4/5	4/5
META	4/5	4/5	5	5
PRE	4/5	4/5	5	5
POST	4/5	4/5	5	5

While the samples without chitosan treatment show colour transfer to the cotton sampling fabric, chitosan treated fibre samples (Pre-Mordanting, Meta-Mordanting, Post-Mordanting) did not show and degradation.

Conclusion

Three different chitosan mordanting treatments analysed as Pre-Mordanting, Meta-Mordanting and Post-Mordanting. These different methods not only show us the colour absorbance and concentration variations by the process, also shows that the colour value coordinates changes by chosen mordanting process.

When dyeing recycled cotton with natural *Rubia tinctorum* dye (C.I. Natural 8), apparently it seems that chitosan offers an improvement in the colour shade after dyeing. However, it has been demonstrated that meta-mordanting process is not the most effective at all, as some reactions *Rubia tinctorum*-chitosan occur and a red precipitated is observed. The most effective process is selected according to the colour coordinates, colour fastness to washing and colour fastness to rubbing. Regarding this test it is the pre-mordanting process the one who shows the most promising results.

Pre-mordanting recycled cotton with chitosan will allow to obtain more sustainable cotton yarns obtained from recycled yarns, dyed with natural dyes

Samples treated with chitosan by Meta-mordanting process has more red colour, more yellow and more saturated colour but this does not means that the best results is obtained by Meta-Mordanting as some precipitated dye is observed and colour fastness are not the best ones.

As all natural fibres can have different molecular structures, detailed analyses on different colours are necessary to understand how effect chitosan treatments on recycled cotton fibres. While we obtained unstable results with our chosen natural dye 'Rubia Tinctoria' there would be more possibilities to find optimum processes and methods for the other natural dyes in next research.

References

- [1] Ahlström L-H, Sparr Eskilsson C, Björklund E (2005) Determination of banned azo dyes in consumer goods. *Trends Anal Chem* 24:49–56
- [2] Islam S, Shahid M, Mohammad F (2013) Perspectives for natural product based agents derived from industrial plants in textile applications—a review. *J Clean Prod* 57:2–18
- [3] Khan MI, Ahmad A, Khan SA, Yusuf M, Shahid M, Manzoor N, Mohammad F (2011) Assessment of antimicrobial activity of Catechu and its dyed substrate. *J Clean Prod* 19:1385–1394
- [4] Vankar PS, Shanker R, Verma A (2007) Enzymatic natural dyeing of cotton and silk fabrics without metal mordants. *J Clean Prod* 15:1441–1450
- [5] Karthik T, Gopalakrishnan D (2012) Eco-friendly fibres of the future. *Asian Text J* 21:67–71
- [6] Karthik T, Gopalakrishnan D (2012) Impact of textiles on environmental issues, Part-I, *Asian Dyer*, pp 52–58
- [7] Wang Y (2010) Fiber and textile waste utilization. *Waste Biomass Valor* 1:135–143
- [8] Roznev A, Puzakova E, Akpedeye F, Sillstén I, Dele O, Ilori O (2017) Recycling in textiles (19 April).
- [9] Colour Index, Third Edition, Volume 3 (1974). The Society of Dyes and Colourists, The Association of Textile Chemists and Colourists.
- [10] M. D. Teli, Javed Sheikh, and Pragati Shastrakar, Exploratory Investigation of Chitosan as Mordant for Eco-Friendly Antibacterial Printing of Cotton with Natural Dyes, Hindawi Publishing Corporation, Journal of Textiles, Volume 2013, Article ID 320510.
- [11] J.A. Rippon, "Improving the dye coverage of immature cotton fibres by treatment with chitosan," *Journal of the Society of Dyers and Colourists*, vol. 100, no. 10, pp. 298–303, 1984.
- [12] M.D. Teli and J. Sheikh, "Extraction of chitosan from shrimp shells waste and application in antibacterial finishing of bamboo rayon," *International Journal of Biological Macromolecules*, vol. 50, no. 5, pp. 1195–1200, 2012.
- [13] A.K. Roy Choudhury, in *Principles of Colour and Appearance Measurement*, 2015
- [14] Salima Sultana Shimo, Shamima Akter Smriti, Color co-ordinates and relative color strength of reactive dye influenced by fabric gsm and dye concentration, *International Journal of Research in Engineering and Technology*, eISSN: 2319-1163, pISSN: 2321-7308.
- [15] Angelini, L. G., Pistelli, L., Belloni, P., Bertoli, A. and Panconesi, S. (1997) *Rubia tinctorum* a source of natural dyes: agronomic evaluation quantitative analysis of alizarin and industrial assays, *Industrial Crops and Products*, 6, 303–311.
- [16] Gupta, D., & Haile, A. (2007). Multifunctional properties of cotton fabric treated with chitosan and carboxymethyl chitosan. *Carbohydrate Polymers*, 69(1), 164-171
- [17] Faisal RM and A Chafidz, Extraction of Natural Dye from Ketapang Leaf (*Terminalia catappa*) for Coloring Textile Materials, *IOP Conf. Series: Materials Science and Engineering* 543 (2019) 012074, doi:10.1088/1757-899X/543/1/012074

Substrate Color Prediction Through Active Monitoring of the Exhaustion Dyeing Process

BRUNO Alves^{1,a}, LUÍS Silva^{1,b}, GRAÇA Soares^{1,c} and JORGE Santos^{1,d,*}

¹Universidade do Minho, Campus de Azurém, Guimarães, Portugal

^abrunomiguelfernandesalves@gmail.com, ^bluispedrosilvaa@gmail.com, ^cgmbs@det.uminho.pt, ^djsantos@det.uminho.pt

Keywords: Exhaustion dyeing, Monitoring system, Color prediction.

Abstract. Nowadays, the monitoring and control of the exhaustion dyeing processes is still done in a reactive and indirect fashion. The monitoring focusses on variables that influence the output of the dyeing process, such as temperature, pH and electrolytes concentration. This approach is more reactive than preventive, since it does not proactively detect deviations in the dyed substrate color that are caused by other process variables.

The aim of this work is to develop a customized system that could actively monitor and predict the color of the dyed substrate after washing. This involves mathematical models and integration of a USB 4000 spectrophotometer and T300 dip probe made by Ocean Optics, which collects, analyzes and process the data from dyeing solutions. Validation tests performed with direct dyes and 100% cotton fabrics showed a good correlation with the real results, especially after 60 minutes of dyeing. For all the tested dyes, applied alone and combined, the color differences (ΔE_{94}) between the measured and the predicted color were equal or less than 0.70 and 1.52 respectively.

Introduction

The monitoring and control of production processes have evolved significantly in recent years. These systems are increasingly relying on the help of electronic equipment to perform tasks that were traditionally made by humans. The correct implementation of this type of systems contributes to increase production capacity and reduce the number of defects and the environmental impact of production processes. Thus, its use is increasingly common in all types of industry.

Dyeing is a critical step in the textile materials processing, since the results obtained strongly impact the customer assessment of the quality of the produced goods [1]. Therefore, systems responsible for the monitoring and control of dyeing processes have been implemented over the last few years, essentially focused on the evaluation of process parameters such as temperature, pH and electrolyte concentration. Despite its importance, this monitoring and control methodology does not evaluate the real output variable of the dyeing system, i.e. the color of the dyed substrate.

The color of substrate is only evaluated in the end of the dyeing cycle, through the collection and washing of a sample of the dyed fabric and subsequent comparison with a sample of the desired color. If it matches with the desired color, the process is finished. Otherwise, corrective measures are defined, prolonging the dyeing process, which affects the process in several ways; Quality: decrease in the quality of goods produced due to over-processing; Sustainability: increase in the consumption of raw materials, water and energy and Efficiency: increased processing and lead times.

Therefore, these deviations should be completely avoided both from an economic and sustainability perspectives. It is estimated that a single color correction could increase the processing cost between 24 and 36% [2].

These type of control methodologies usually used are more reactive than preventive, as they do not detect deviations in the output variables in relation to other unmonitored process variables, such as the presence of impurities in the fibres, dyes and auxiliaries, changes in the color strength of dyes, etc. This type of deviations produces color changes on substrate. These changes can result in slight modifications in the color strength of the substrate, but may also cause large changes in hue and color strength [3]. The reason to keep using this type of monitoring and control methodologies is related to

the impossibility of directly evaluate the color of the substrate during the exhaust dyeing processes, due to difficulties related to the conditions in which it is carried out and to limitations imposed by the equipment.

Nevertheless, to overcome the disadvantages associated to the described methodologies it is essential to monitor the real output variable of the system during dyeing. This approach would allow switching from a wrong-first-time dyeing philosophy, in which the substrate color is purposely below the desired intensity, in order to easily allow the necessary corrections for the right-first-time philosophy [2]. However, to achieve this goal, it is essential to find new monitoring techniques that can enable an indirect assessment of the substrate color at any time of the process. This will allow to develop a new control and monitoring methodology, enabling the implementation of corrective measures earlier [4, 5], and also to reduce the number of errors and non-conformities, promoting the sustainability of the dyeing process. The aim of the project is to develop a prototype that could actively monitor and predict the color of the dyed substrate throughout the dyeing process.

Materials and Methods

The prototype was composed by hardware and software elements that allow the collection and processing of the necessary information to infer the color of the dyed substrate. The color prediction of the dyed substrate was based on the evaluation of the dye concentration in the fiber at every moment and the amount of dye that will later be removed from the fibers in the final washes. The sequence of steps developed by the prototype to achieve the desired results is described in the flowchart of Fig. 1. Some of the process analysis steps used calibration models developed and implemented in the prototype software, which will be described below.

Type 1 calibration models are designed to calculate the dye concentration in solution knowing its absorbance. For this, two types of models were developed. The first was used in the evaluation of solutions with only one dye. It is based on the direct application of the Beer-Lambert law and establish a linear relationship between the concentration of dye in solution and its absorbance. This type of model was developed for each of the studied dyes. Principal component regression models (PCR) were also developed for the evaluation of solutions containing mixtures of the studied dyes.

Type 2 calibration models are intend to predict the concentration of dye in the fiber after final washings. In this case, linear regression models were developed for each dye that establish the relationship between the \log_{10} of the dye concentration in the fiber after dyeing and the \log_{10} of dye concentration in the fiber after final washings .

Type 3 calibration models establish, for each analyzed wavelength (400-700 nm), a linear relationship between the \log_{10} of dye concentration in the fiber after washing and the \log_{10} of the K/S of the dyed substrate.

Materials. The hardware of the prototype is composed by a USB 4000 spectrophotometer, T300 dip probe, DT-MINI-2GS light-source and fiber optic and patch cables from Ocean Optics and a laptop computer running the software developed in Labview[®] environment (National Instruments).

Sirius Scarlet K-CF, Sirius Yellow K-CF, Sirius Blue K-CFN, sodium chloride (99,2% purity) and plain weave 100% bleached cotton fabric with 125 g/m² were kindly provided by the University of Minho.

Methods

Development of the Calibration Models Type 1. To develop type 1 linear regression models, standard solutions of each of the three dyes studied were prepared, with concentrations of 0.005 gL⁻¹, 0.01 gL⁻¹, 0.02 gL⁻¹, 0.03 gL⁻¹, 0.04 gL⁻¹ and 0.05 gL⁻¹. The solutions were then analyzed by the prototype. The linear regression model that better defined the relationship between the absorbance of the solutions and their concentration was found and stored in the system.

To develop the PCR calibration model type 1, a calibration set of solutions was prepared using a three factors (3 dyes) and three levels (0, 0.015 and 0.03 gL⁻¹) factorial design. Each solution was

analyzed by the prototype and the data was stored in the database. Based on this data, a Principal Components Regression (PCR) calibration model was developed and then stored in the system.

To assess the accuracy of the developed model, the same set of calibration solutions was used, applying a Leave One Out (LOO) cross-validation methodology for this purpose [6, 7].

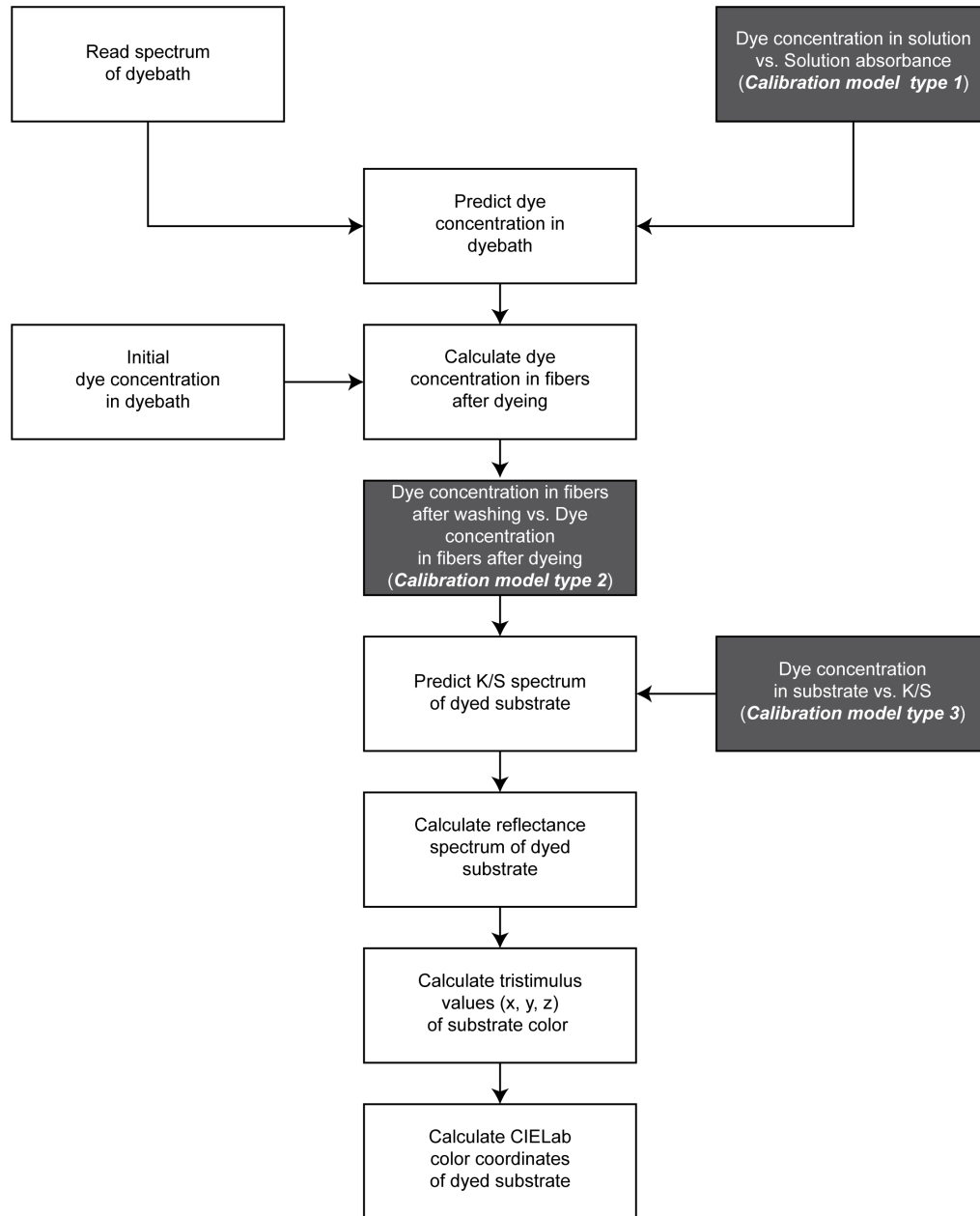


Fig. 1 - Operational flowchart

Development of the Calibration Models Type 2. To develop the calibration models type 2, 12 dyeings were carried out with each of the three dyes of the trichromy used in this work, in a AHIBA IR dyeing machine under the conditions specified in table 1, using a 1:10 liquor ratio. The dyeing process was carried out in an all-in process with the temperature-time profile represented in the scheme shown in Fig. 2. All tests were performed in triplicate.

Table 1 - Dyeing solutions used to develop Calibration Model type 2

Solution	Dye concentration [% owf]	NaCl Concentration [gL ⁻¹]
A _C	0.10	2.5
B _C	0.25	2.5
C _C	0.50	2.5
D _C	0.75	4.0
E _C	1.00	5.0
F _C	1.25	5.8
G _C	1.50	6.5
H _C	1.75	7.0
I _C	2.00	12.5
J _C	2.25	12.5
K _C	2.50	12.5
L _C	2.75	12.5
M _C	3.00	12.5

Table 2 - Dyeing solutions used to validate calibration Model type 2

Solution	Dye concentration [% owf]	NaCl Concentration [gL ⁻¹]
A _V	0,18	2,5
B _V	0,63	3,3
C _V	1,13	5,4
D _V	1,63	6,8
E _V	2,13	12,5
F _V	2,63	12,5
G _V	2,88	12,5

represented in Table 2, in order to assess the accuracy of the developed calibration models type 2. After each dyeing, the concentraion of dye in fiber after washing was determined and compared with the predicted value provided by the calibration model. All tests were performed in triplicate for all dyes.

Development of the Calibration Models Type3. The samples dyed under the conditions described in Table 1 were analyzed in a Datacolor Spectraflash 600 Plus-CT spectrophotometer to obtain reflectance and K/S spectra. From the collected data, calibration models that correlate the log₁₀ of the concentration of the dye on the fibers after washing with the log₁₀ of the respective K/S spectrum were developed.

To assess the precision of the developed models, the dyed samples obtained in the dyeings described in Table 2 were analyzed in the Datacolor Spectraflash 600 Plus-CT spectrophotometer, determining the respective K/S spectra, which were then compared with the K/S spectra predicted by the developed calibration models.

Dyeing Process Monitoring. The developed prototype was used to monitor the all-in dyeing processes carried out with the dyes alone and in trichromy, under the conditions described in Table 3, in a Mathis dyeing machine, with a 1:10 liquor ratio and the time-temperature profile described in Fig. 2.

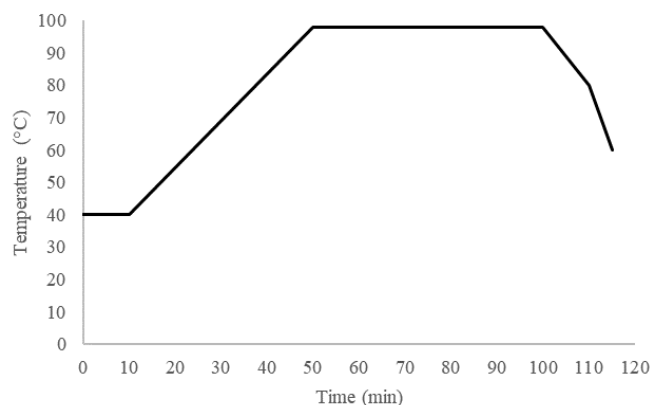


Fig. 2 – Profile time-temperature of the dyeing process

At the end of the process, the samples were squeezed into the respective dyeing vessels and the solutions were reserved and later analyzed, in order to evaluate the exhaustion of each dye. Based on these values, the concentration of each dye in fibre after dyeing was calculated. The dyed samples were then washed in water at room temperature. The concentration of each dye in the washing solution was determined, using the prototype. The calibration models that correlate the log₁₀ of the dye concentration in the fiber after the washing process with the log₁₀ of the dye concentration in the fiber immediately after the dyeing were developed.

The set of operations described above were repeated for each dye in a new set of dyeing solutions

Table 3 - Dyeing solutions monitored with the prototype

Solution	Dye	Dye concentration	NaCl Concentration
		[% owf]	[gL ⁻¹]
A _M	Sirius Scarlet K-CF	3.0	12.5
B _M	Sirius Yellow K-CF	3.0	12.5
C _M	Sirius Blue K-CFN	3.0	12.5
D _M	Sirius Scarlet K-CF	0.5	6.5
	Sirius Yellow K-CF	0.5	6.5
	Sirius Blue K-CFN	0.5	6.5

Solutions A_M, B_M and C_M were analyzed by the prototype every 10 minutes during the entire dyeing process, and after 50 minutes of dyeing in the case of solution D_M.

Results and Discussion

Calibration Models Type 1. The linear calibration models developed for each dye presented correlation coefficients (r^2) of 0.997 for the Sirius Scarlet K-CF, 0.993 for the Sirius Yellow K-CF and 0.999 for the Sirius Blue K-CFN dye.

The developed PCR calibration model type 1 revealed a very high accuracy having a global relative error of $1.71\% \pm 1.93\%$ with a maximum of 6.3% and a minimum of 0.0 %.

The multivariate PCR calibration models are expected to be more robust in the evaluation of solutions composed by mixtures of dyes than other techniques, such as classic least squares, when there are interactions between the species mixed in the solution and possible overlapping of their absorption spectra [7]. This type of occurrence causes serious problems in the development of these types of calibration models, drastically reducing their accuracy. In the present case, despite of the overlapping of the dyes absorption spectra of the trichromy, the results obtained are not significantly affected, allowing its use in monitoring the dyeing processes developed with it.

Calibration Models Type 2. The calibration models developed to calculate the concentration of dye in fiber after washings, presented correlation coefficients (r^2) of 0.999 for Sirius Scarlet K-CF, Sirius Yellow K-CF and Sirius Blue K-CFN.

To carry out its validation, the developed models were used to predict the dye concentration in the fiber after the final washes, in the dyeings performed with the solutions shown in Table 2. The predictions provided by the models showed a relative error of $1.59\% \pm 1.16\%$ for Sirius Scarlet K-CF, $2.07\% \pm 1.02\%$ for Sirius Yellow K-CF and $2.44\% \pm 2.07\%$ for Sirius Blue K-CFN. The global relative error was $2.03\% \pm 1.46\%$ with a maximum of 5.6% and a minimum of 0.0% (Table 4).

Table 4 - Relative error of the calibration model type 2

Dye	Solutions						
	A _V	B _V	C _V	D _V	E _V	F _V	G _V
Sirius Scarlet K-CF	2,80%	0,00%	0,60%	0,60%	2,00%	2,30%	2,80%
Sirius Yellow K-CF	1,60%	1,00%	1,10%	2,90%	2,40%	1,70%	3,80%
Sirius Blue K-CFN	2,20%	0,80%	0,50%	0,80%	2,20%	5,00%	5,60%

The reliability of the developed models can therefore be considered acceptable due to the reduced magnitude of the relative error associated with the prediction.

Calibration Models Type 3. The calibration models developed for each dye to predict the K/S value of dyed samples, in the 400-70 nm range, presented mean correlation coefficient values (r^2) of 0.997 ± 0.002 for Sirius Scarlet K-CF, 0.974 ± 0.037 for Sirius Yellow K-CF and 0.999 ± 0.001 for Sirius Blue K-CFN.

To carry out its validation, the models were used to predict the K/S spectra in the 400-70 nm range of the samples dyed with the solutions described in Table 2. When compared with the real K/S spectra

of the dyed samples, the results obtained showed mean relative errors of $6.48\% \pm 3.55\%$ for Sirius Scarlet K-CF, $7.14\% \pm 5.71\%$ for Sirius Yellow K-CF, and $3.13\% \pm 1.8\%$ for Sirius Blue K-CFN (Table 5).

Table 5- Mean relative errors of predictions provided by model type 3

Dye	Solutions						
	A _V	B _V	C _V	D _V	E _V	F _V	G _V
Sirius Scarlet K-CF	$8.50\% \pm 5.15\%$	$8.76\% \pm 2.91\%$	$5.93\% \pm 3.96\%$	$5.59\% \pm 3.65\%$	$4.30\% \pm 2.21\%$	$4.72\% \pm 3.90\%$	$7.56\% \pm 3.05\%$
Sirius Yellow K-CF	$7.51\% \pm 4.68\%$	$5.60\% \pm 4.52\%$	$4.31\% \pm 3.63\%$	$10.08\% \pm 12.44\%$	$4.23\% \pm 2.44\%$	$5.84\% \pm 3.12\%$	$12.45\% \pm 9.14\%$
Sirius Blue K-CFN	$2.69\% \pm 1.00\%$	$3.33\% \pm 1.97\%$	$2.94\% \pm 1.30\%$	$4.51\% \pm 2.50\%$	$2.31\% \pm 1.80\%$	$2.49\% \pm 1.49\%$	$3.69\% \pm 2.58\%$

As can be seen from the results presented in Table 5, the mean relative errors associated with samples dyed with Sirius Yellow K-CF, especially in the case of D_V and G_V solutions, are higher than those obtained with the other dyes and solutions. Despite this, the associated absolute error is relatively small as shown in the results presented in Table 6.

Table 6 – Maximum K/S absolute errors of predictions provided by model type 3

Dye	Solutions						
	A _V	B _V	C _V	D _V	E _V	F _V	G _V
Sirius Scarlet K-CF	0,261	0,366	0,360	0,432	0,510	0,396	1,070
Sirius Yellow K-CF	0,273	0,404	0,270	0,392	0,759	0,836	1,763
Sirius Blue K-CFN	0,086	0,207	0,432	0,865	0,573	0,637	1,220

The results presented show that, in general, the errors obtained by these models are higher than those obtained in the previous models. This situation is probably due to an accumulation of errors resulting from the successive application of models to predict the dye concentration in the solution and the dye concentration in the fibers after washing. These models also have associated errors that are carried over to the following models. Consequently, the global error progressively increases as each model is used in the process of predicting the final color of the substrate.

Dyeing Process Monitoring. The models developed to predict the evolution of the substrate color from the K/S spectrum, were used to monitor the dyeings performed under the conditions described in Table 3. In this analysis, the color difference (ΔE_{94}) between the dyed sample and the prediction provided by the calibration models implemented in the prototype was calculated.

The results presented in Table 7 show that in the dyeings carried out with only one dye (A_M, B_M and C_M), the color differences obtained gradually decrease as the process progresses, with values always less or equal to 0.70 for dyeing times longer than 60 minutes.

Table 7– Color differences (ΔE_{94}) between dyed samples and color predicted by the prototype

Solution	Time (min)													
	5	10	15	20	30	40	50	60	70	80	90	100	110	115
A _M (Sirius Scarlet K-CF)	1,69	1,71	1,48	1,41	1,05	0,77	0,99	0,70	0,17	0,07	0,18	0,23	0,24	0,09
B _M (Sirius Yellow K-CF)	1,06	0,95	0,73	0,69	0,42	0,34	0,65	0,54	0,53	0,51	0,55	0,53	0,60	0,38
C _M (Sirius Blue K-CFN)	2,35	2,16	1,89	1,87	1,21	1,05	0,64	0,35	0,37	0,13	0,44	0,80	0,53	0,48
D _M (Trichromy)	-	-	-	-	-	-	0,65	1,22	1,04	1,15	1,29	1,33	1,52	1,51

The higher ΔE_{94} values obtained in the early stage of dyeing are due to the fact that models for predicting the dye concentration in the fiber after washings have been developed from dyeing driven to equilibrium. As in the initial stage of dyeing the process is still far from the equilibrium stage, a significant part of the dye absorbed by the fibers is still on the fiber surface. Therefore, it is easily removed in the washes. This way, the constructed model predicts, at this stage of the process, a concentration of dye in the fiber after washing that is higher than what is actually found in the fiber.

The monitoring of the dyeing carried out with the D_M solution was only performed after 50 minutes of dyeing, for the reasons mentioned above. The dye solution used in this case is composed by a mixture of the three dyes of the studied trichromy. The results obtained show ΔE_{94} values ranging between 0.65 and 1.52 (Table 7). These values are higher than those obtained for the same period of analysis when monitoring the dyeings carried out with only one dye. One of the reasons that can explain this is the greater complexity of the PCR calibration models used in this case to predict the evolution of the dye concentration in the solution and their associated errors. Besides this, the existence of possible deviations in the application of the Kubelka-Munk law, regarding the principle of additivity of K/S values in the case of the use of dye mixtures, may have contributed to the greater intensity of the differences detected in this case.

Conclusions and Further Developments

The study proves that it is possible to develop a system that effectively evaluates the output of the exhaust dyeing process in real-time, allowing for a more in-depth analysis of the dyeing status. The collected data is converted into accurate and useful information that allow the user to indirectly evaluate the color of the substrate, without interrupting the dyeing cycle.

Both the data acquisition module and the developed mathematical models work together to provide good results regardless of whether it is a solution with only one dye or a trichromatic mixture of dyes. Even though the prototype was only tested in a laboratory environment the main goal would be to apply it on an industrial environment.

To get even better results, several developments can be introduced in the future to improve the accuracy of the collected data and to expand the prototype's monitoring capabilities. The most important progress would be the optimization and improvement of the developed mathematical models, which would also allow effectiveness improvements in the initial phase of dyeing.

The second step would be to expand the prototype's monitoring capacity in order to allow its use in other types of dye-fibre systems, making it more suitable for industrial applications.

In conclusion, this study proves that it is possible to develop new methods to monitor the dyeing process that provide accurate information about the color evolution of the substrate. This makes it possible to prematurely detect any color deviations and make corrections in useful time. This new approach will thus considerably reduce processing time and water consumption, chemicals and energy, contributing to the development of more sustainable processes.

References

- [1] Perkins, W. S. (1996) *Textile Coloration and Finishing*. Carolina Academic Press.
- [2] Park, J. and Shore, J. (2009) 'Evolution of right-first-time dyeing production', *Coloration Technology*, pp. 133–140
- [3] Shamey, R. and Zhao, X. (2014) *Modelling, Simulation and Control of the Dyeing Process*. Woodhead Publishing Limited in association with The Textile Institute.
- [4] Xin, J. H. (2006). *Total colour management in textiles*: Woodhead Publishing Limited in association with The Textile Institute, 25, 212.
- [5] Majumdar, A., Das, A., Alagirusamy, R., & Kothari, V. K. (2013). *Process control in textile manufacturing*. Woodhead Publishing Limited
- [6] Brereton, R. G., *Applied Chemometrics for Scientists*. Wiley: 2007.
- [7] Kramer, R., *Chemometric Techniques for Quantitative Analysis*. CRC Press: 1998.

Durable Moisture/Thermal Management Self-Adhesive Coating for Polyester Fabric

Gang Xia^{1,a}, John H. Xin^{2,b*}

^{1,2}Institute of Textiles and Clothing, The Hong Kong Polytechnic University, Hong Kong SAR 999077, China

^agang.xia@polyu.edu.hk, ^bjohn.xin@polyu.edu.hk

Keywords: polyester fibers, coating, self-adhesive, moisture/thermal management

Abstract. As global warming does not decay, functional textiles with moisture/thermal management performance are becoming more and more important. In this paper, a cationic hydrophilic polymer (CHIP) was developed, and combined with flexible and simple coating methods to achieve durable moisture/thermal management of polyester fabrics. The as-prepared fabrics exhibit excellent washing fastness, and the wettability of the coated fabrics can withstand 150 home laundry cycles. Owing to its firm fixation, the methods of single-side spraying and templated-spraying were adopted to achieve water/sweat unilateral penetration or directional transport through polyester fabrics, which realizes the timely and directionally transport of sweat as well as thermal in fabrics. This work is useful for the design of high-performance moisture/thermal management fabrics for various applications, e.g., quick-dry sportswear, outdoor uniforms, and other functional garments.

Introduction

With the gradual increase in the average temperature of the earth's atmosphere attributable to the greenhouse effect, more frequently the outdoor temperatures exceed the normal temperature of the human body, which causes many heat-related diseases and even deaths [1-2]. In intense sports activities, it is a common problem that the sweat cannot be dried quickly and sticks to the wearers' skin. This not only induces discomfort to wearers but also prevents heat dissipation and causes heat stress [3]. The problem is due to the poor moisture/thermal management performance of the textiles that are often associated with sportswear on the market [4].

Functional textiles with moisture/thermal management performance through controlling or transporting liquid water and sweat from the skin to environment in the hot and humid environments are of great interest for wearers [5-7]. There are plentiful methods that have been employed to improve the moisture/thermal management of textiles, such as Janus textiles with asymmetric modification by plasma technology [8], double-layer polyester/nitrocellulose textiles with conical micropores fabricated by laser perforation [9], tri-layered Murry membranes fulfilled by layer-by-layer deposition [10], and hurtling sweat transfer fabrics achieved through porous channels [11], etc. Although these approaches allow the creation of fast moisture management performance by structure and interfacial tension gradient, many limitations stem from the high-cost, complicated process, low durability, and restrictions of substrate materials [12-13]. Therefore, simple, low-cost, facile, large-scale, and durable methods for manufacturing moisture/thermal management fabrics have huge potential.

In this paper, a flexible and simple coating method was developed to achieve durable moisture/thermal management of polyester fabrics. This is done through the synthesis of a novel cationic hydrophilic polymer (CHIP) that has an excellent affinity for polyester fibers, which can be well aligned by self-adhesive on the surface of polyester fibers that rich in aromatic rings through

electrostatic attractions in water with the subsequent firm fixation on polyester fibers at an elevated temperature due to the melt co-crystallization[14-17]. Taking the advantage of its self-adhesive performance, we can apply this polymer on polyester fibers by single-side spraying or templated-spraying to achieve water or sweat unilateral penetration or directional transport through polyester fibers. Owing to its firm fixation, the adhesive hydrophilic polymer transforms hydrophobic polyester fiber to a superhydrophilic one, and its excellent wettability of the sprayed area can withstand 150 home laundry cycles, which gives it long-term performance. This way, we can manipulate the movement of water through customized spraying on clothing to realize the timely and directionally transport of sweat. In our experiment, a regional cooling effect of around 4.6 °C can be observed by Thermal Infrared Camera while a dry microclimate was created between the skin and clothes. This work is useful for the design of high-performance moisture/thermal management fabrics for various applications e.g., quick-dry sportswear, outdoor uniforms, and other functional garments.

Materials and Methods

Polyester knitted fabrics (PET, 160D/ 48F) were purchased from Dongguan Yunfan Textile Co. Ltd. The cationic hydrophilic polymer (CHIP) was synthesized by transesterification and polycondensation. Firstly, dimethyl terephthalate, bis(2-hydroxyethyl) dimethylammonium chloride, ethylene glycol, and catalyst zinc acetate were added into a flask under N₂ flow, and the mixture was gradually heated to 180 °C with stirring for 3 h until no solvent was released. After cooling to room temperature, polyethylene glycol (M_w = 1500), antioxidant 1010, and catalyst Sb₂O₃ were added to the mixture under a flow of N₂, and the system was then placed under vacuum (85–90 kPa) with the temperature was gradually increased from 200 to 240 °C. Finally, the cationic hydrophilic polymer (CHIP) was obtained upon cooling to room temperature.

The CHIP solutions with different mass concentrations were prepared by dissolving in deionized water. The fabrication of the CHIP-PET fabric was carried out via a simple spray-coating step on one side using a spray gun (HD-130, RUIYI, Taiwan) with or without a mask. After drying in the air, the fabric samples were cured at 170 °C for 60 s in an oven.

The microstructures of the fabric samples were analyzed using SEM equipment (TESCAN VEGA3, Czech Republic) operated at an accelerating voltage of 20.0 kV. The surface wettability of the PET fabric samples before and after finishing was studied using an OCA20 water contact angle meter (Data Physics, Germany). The hydrophilicity of fabric was evaluated by the standard method FZT/T 01071-2008: Textiles test method for capillary effect with modification (The ink was balanced and the ink height on fabric after 10 minutes was recorded). Each fabric sample was cut into 3×25 cm, and then was hung vertically on a vessel containing ink. When the bottom of the fabric touched the ink-water, the time and the ink height were recorded to show the hydrophilic effect owing to the capillary penetration of fabrics. The washing fastness of CHIP on fabrics was evaluated by AATCC-61 standard methods, in which one wash in the equipment is equivalent to five home washing cycles. In each washing cycle, the fabrics were washed in a capped steel can containing 150 mL standard detergent solution and 46 g steel ball at 49 °C for 45 min with intense stirring. After repeated washing cycles, the fabrics were rinsing for 30 min at 50 °C, and then dried to a constant weight. The water transport process was recorded by a camera and the blue ink was applied for the convenience of observation. IR thermal camera (Hti-18) was used to showcase the cooling effect, and a hotplate was set at ~35 °C to simulate human skin.

Results and Discussion

The durable CHIP is highly suitable for developing sweat transport fabrics of sportswear (Fig. 1a) that transports sweat from the inner to the outer side of fabrics and accelerates the evaporation of water. Fig. 1b shows the moisture/thermal management principles and fabrication procedure of CHIP on polyester (PET) fabrics. During the fabrication process, the CHIP (4 wt%) was dissolved in water. The spray coating process was conducted with or without a customized mask using a spray equipment (HD-130, RUIYI, Taiwan) under a fixed distance (5 cm) between the nozzle and fabrics. After drying in the air, the fabric samples were baked at 170 °C for 1 min to enhance the coating fastness.

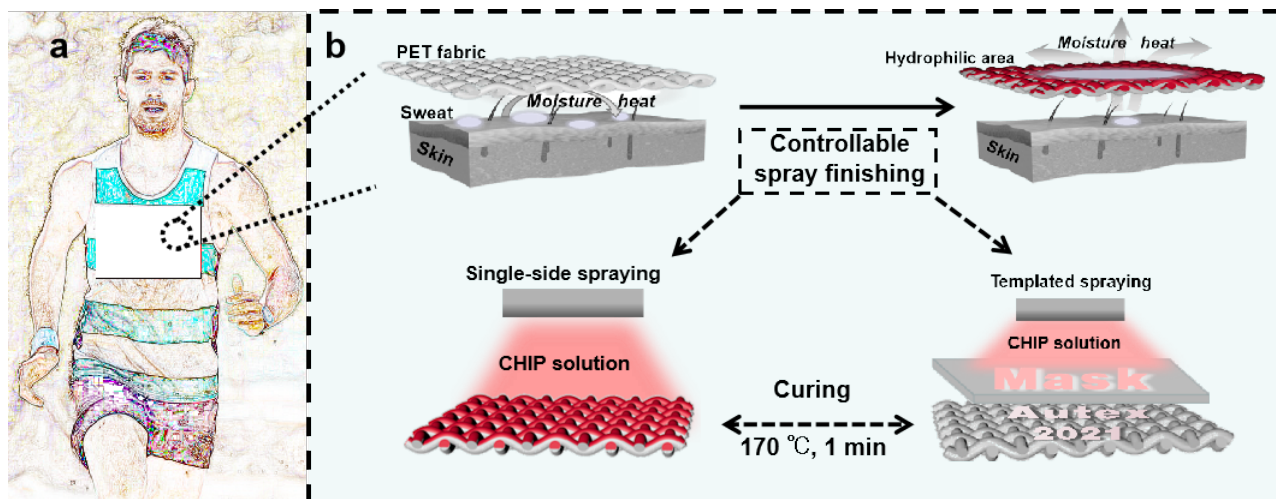


Fig 1. (a) Potential application of the durable coating in sportswear. (b) Illustration of moisture/thermal management principles and fabrication process for sweat transport fabrics.

The characterizations of the PET fabrics before and after the spraying-curing finishing process (4 wt%) using SEM equipment. The pristine PET sample displays a clean and smooth fiber surface (Fig. 2a-b). After finishing with CHIP, the surface of fiber was covered by a thin polymer coating (Fig. 2c-d), which indicates that the CHIP was coated on polyester fabric successfully. Because of CHIP its hydrophilic properties, it can efficiently transform the hydrophobic PET fabric to a superhydrophilic one. After coating with CHIP, the water contact angle of PET fabrics decrease from 140° to ~0°. This is due to the excellent hydrophilic properties of the CHIP, which changes the wettability of PET fabrics.

The washing fastness of CHIP on PET fabrics was evaluated by AATCC-61 standard method [18], in that method one accelerated wash cycle is equal to five household machine wash cycles. To evaluate the change of the hydrophilicity of PET fabrics before and after washing, the standard method (FZT/T 01071-2008) with embellishing was used by capillary penetration [19]. The water wicking height of pristine PET reached 0.8 cm after 10 mins, and then remained basically unchanged due to its hydrophobicity. During the washing test, every 5 cycles, the wicking height of the samples were measured. The average wicking height of 3 times was approximately 13.2 cm within 10 mins for the fabric samples before the washing test and it decreased slowly with increasing laundering tests (Fig. 2e). After 150 equivalent wash cycles, the wicking height of fabric samples was approximately 3.2 cm in 10 mins, which is still much higher than pristine PET fabric. These washing test results indicate that the CHIP has good durability.

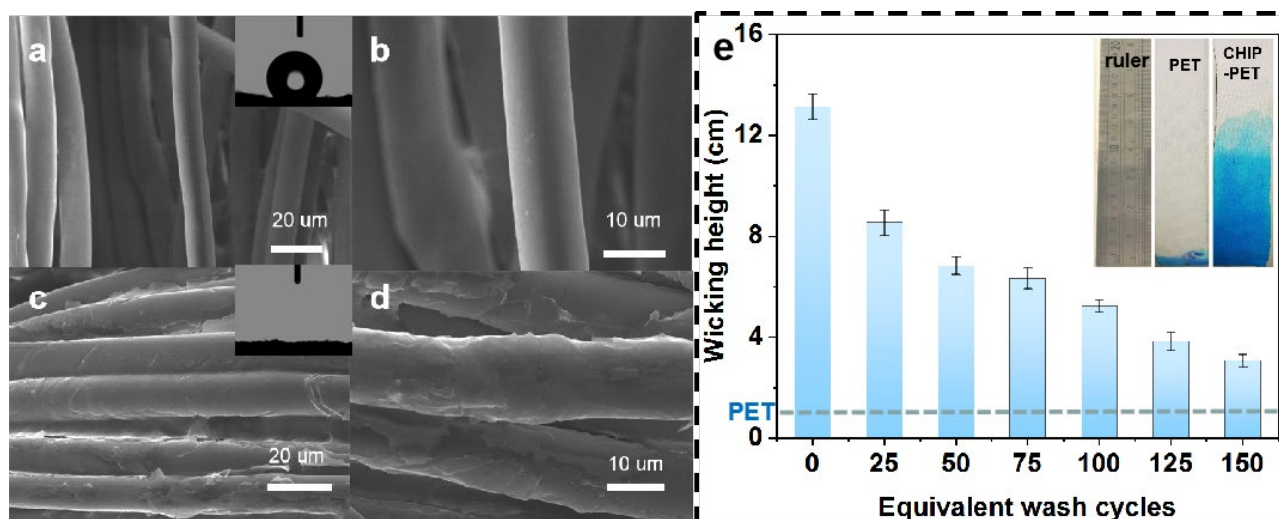


Fig 2. SEM images of (a-b) pristine PET and (c-d) coated PET fabric area; the insets of water contact angle show the change of wettability of PET fabric. (e) Changes in the wicking height of fabrics with different washing cycles, respectively.

To investigate the moisture management performance of CHIP-PET fabrics, the colored water droplet was dropped on both sides of the fabrics [20]. Fig. 3a shows that when ink-water was dropped onto the uncoated side of fabrics, it remained hemispherical shape at the beginning and then penetrated and dispersed on the CHIP coated side. On the contrary, the ink-water rapidly spread along when it was dropped onto the CHIP coated side (Fig. 3b). This indicates that the CHIP coated area of the PET fabric provides better wettability and can induce timely and directionally transport of sweat from the skin of wearers, which is important and could reduce the discomfort of fabrics sticking to the skin.

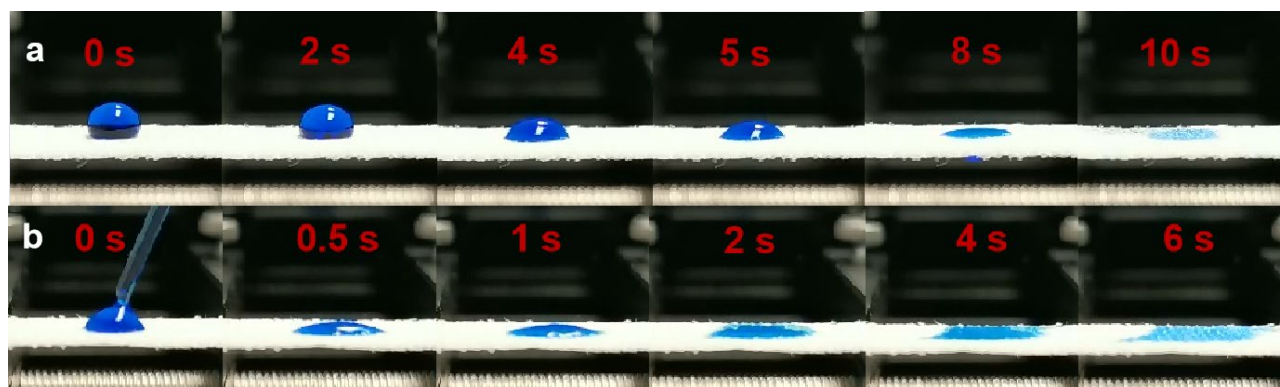


Fig 3. Moisture management performance. (a) Still frames taken from a video to show the dropping of ink-water onto the uncoated PET side; (b) Still frames taken from a video to show the dropping of ink-water onto the coated PET side.

Another advantage of CHIP coated PET fabric is that along with the transfer of sweat, it can take away heat from skin surface through the evaporation of water. Fig. 4(a-b) shows that when the PET and CHIP-PET fabric were placed on wet skin, the PET fabric did not allow water transfer, whereas the CHIP-PET fabric allowed water droplets to be transferred to the surface of the fabric, and a cooling effect of 4.6 °C was observed. Similarly, when the fabrics sprayed with CHIP to form different patterns were placed on a wet hotplate, the sprayed area attracted water droplets to form visible patterns (Fig. 4c-e). Further, the fabrics sprayed with patterns are capable of forming comfortable microclimates in areas for wearers by evaporating sweat and heat, providing a feeling

of comfort and coolness. From the point of practical application, it has great potential in functional garments and sportswear.

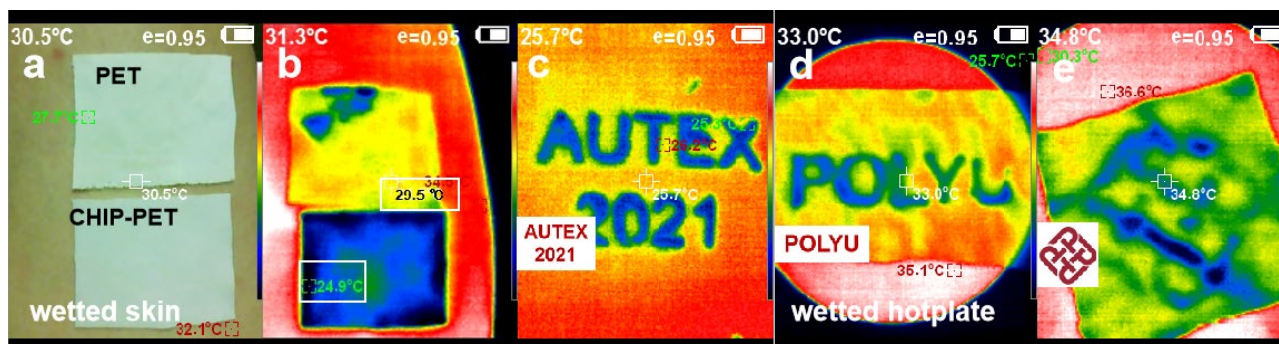


Fig 4. Thermal management performance. (a) Optical image and (b) infrared camera image of PET and one-side coated PET fabrics placed on wetted skin (a condensation effect of 4.6 °C was observed); Infrared camera images (c-e) of PET fabrics of templated spraying with different patterns placed on the wetted hotplate.

Summary

In summary, we have successfully developed a self-adhesive coating that possesses excellent washing fastness and hydrophilic properties when used to treat PET fabrics. Owing to its self-adhesive performance and firm fixation, the methods of single-side spraying and templated-spraying were adopted to achieve water or sweat unilateral penetration or directional transport through polyester fabrics, which realizes the timely and directionally transport of sweat as well as heat from wearers. This work is promising for the design of high-performance moisture/thermal management fabrics for various applications.

Acknowledgement

The authors would like to acknowledge the support of General Research Fund of the Research Grants Council of the Hong Kong SAR Government (Project no.: 15208420) for this research.

References

- [1] B. Grocholski, Cooling in a warming world, *Science*. 370 (2020) 776-777.
- [2] G.R. Walther, E. Post, P. Convey, A. Menzel, C. Parmesan, T.J.C. Beebee, J.M. Fromentin, O. Hoegh-Guldberg, and F. Bairlein, Ecological responses to recent climate change, *Nature*. 416 (2002) 389-395.
- [3] S.R. Notley, A.D. Flouris, G.P. Kenny, On the use of wearable physiological monitors to assess heat strain during occupational heat stress, *Applied Physiology, Nutrition, and Metabolism*. 43 (2018) 869-881.
- [4] M. Manshahia, A. Das, Moisture management of high active sportswear, *Fibers and Polymers*. 15 (2014) 1221-1229.
- [5] D. Miao, Z. Huang, X. Wang, J. Yu, B. Ding, Continuous, spontaneous, and directional water transport in the trilayered fibrous membranes for functional moisture wicking textiles, *Small*. 14 (2018) 1801527.
- [6] C. Zou, L. Lao, Q. Chen, et al. Nature-inspired moisture management fabric for unidirectional liquid transport and surface repellence and resistance, *Energy and Buildings*. 248 (2021) 111203.

-
- [7] Y. Wang, G. Xia, H. Yu H, B. Qian, Y.H. Cheung, L.H. Wong, J.H. Xin, Mussel - Inspired Design of a Self - Adhesive Agent for Durable Moisture Management and Bacterial Inhibition on PET Fabric, *Advanced Materials*. 33(2021) 2100140.
- [8] A. Airoudj, F.B. Gall, V. Roucoules, Textile with durable janus wetting properties produced by plasma polymerization, *The Journal of Physical Chemistry C*. 120(2016) 29162-29172.
- [9] B. Dai, K. Li, L. Shi, X. Wan, X. Liu, F. Zhang, L. Jiang, S. Wang. Bioinspired Janus Textile with Conical Micropores for Human Body Moisture and Thermal Management, *Advanced Materials*. 31(2019): 1904113.
- [10] X. Wang, Z. Huang, D. Miao, J. Zhao, J. Yu, B. Ding, Biomimetic fibrous murray membranes with ultrafast water transport and evaporation for smart moisture-wicking fabrics, *ACS nano*. 13(2019) 1060-1070.
- [11] L. Lao, D. Shou, Y.S. Wu, J.T. Fan, “Skin-like” fabric for personal moisture management, *Science advances*. 6 (2020) eaaz0013.
- [12] D. Feng, D. Weng, J. Wang, A facile interfacial self-assembly of crystalline colloidal monolayers by tension gradient, *Micromachines*. 9 (2018) 297.
- [13] Y. Zhao, H. Wang, H. Zhou, T. Lin, Directional fluid transport in thin porous materials and its functional applications, *Small*. 13 (2017) 1601070.
- [14] H. Fan, J. Wang, Z. Tao, J. Huang, P. Rao, T. Kurokawa and J.P. Gong, Adjacent cationic–aromatic sequences yield strong electrostatic adhesion of hydrogels in seawater, *Nature communications*. 10 (2019) 5127.
- [15] M.J. Perez-Roldan, D. Debarnot, F. Poncin-Epaillard. Surface chemistry of PET for enhancing its antifouling properties, *RSC Advances*. 4 (2014) 64006-64013.
- [16] S. Ploymalee. Charuchinda, K. Srikulkit. Hydrophilic property of polyester fabric coated with polyethylene glycolated bisphenol A, *Journal of applied polymer science*. 116 (2010) 473-478.
- [17] C. Yu, Y. Lu, F. Wu, Cationic organofluorosilicone as deepening agent in the application of dyed polyester fabric, *Journal of Applied Polymer Science*. 136(2019) 48208.
- [18] S. Natarajan, D. Gupta. Launderometer based test method for determining shrinkage of wool, *The Journal of The Textile Institute*. 109 (2018) 1224-1231.
- [19] S. Chen, S. Chen, S. Jiang, M. Xiong, J. Luo, J. Tang, and Z. Ge, Environmentally Friendly Antibacterial Cotton Textiles Finished with Siloxane Sulfopropylbetaine, *ACS applied materials & interfaces*. 3 (2011) 1154-1162.
- [20] L. Li, Y. Mai, Y. Wang, S. Chen. Stretchable Unidirectional Liquid-Transporting Membrane with Antibacterial and Biocompatible Features Based on Chitosan Derivative and Composite Nanofibers, *Carbohydrate Polymers*. 2021, 118703.

Extraction Optimization of *Sorghum vulgare* for Natural Wool Dyeing Applications

Nuno Belino^{1,a,*}, Estefânia Alves^{2,b}, Ema Almeida^{2,c}, Carina Gameiro^{2,d},
Tiago Rosado^{2,3,e}, Luís Passarinha^{2,3,4,5,f}, Eugenia Gallardo^{2,3,g}, Maria Pinto^{1,h},
Jesus Rodilla^{6,i}

¹Department of Textile Science and Technology, Faculty of Engineering,
University of Beira Interior, Covilhã, Portugal

²Centro de Investigação em Ciências da Saúde (CICS-UBI), University of Beira Interior,
Covilhã, Portugal

³Laboratório de Fármaco-Toxicologia, UBIMedical, University of Beira Interior, Covilhã, Portugal

⁴UCIBIO–Applied Molecular Biosciences Unit, Department of Chemistry, NOVA School of Science
and Technology, Universidade NOVA de Lisboa, Caparica 2829-516, Portugal

⁵Associate Laboratory i4HB - Institute for Health and Bioeconomy, NOVA School of Science
and Technology, Universidade NOVA, 2819-516 Caparica, Portugal

⁶Department of Chemistry, Faculty of Exact Science, University of Beira Interior, Covilhã, Portugal

^{a,*}belino@ubi.pt, ^bestefania.raquel5@gmail.com, ^cema.almeida97@gmail.com,
^dcarina.gameiro@hotmail.com, ^etiago.rosado@ubi.pt, ^flpassarinha@fcsaude.ubi.pt,
^gegallardo@fcsaude.ubi.pt, ^hmcpvmpinto14@gmail.com, ⁱrodilla@ubi.pt

Keywords: Natural dyeing; *Sorghum Vulgare*; kuromanin; apigeninidin Extraction optimization; Wool dyeing

Abstract. It is common knowledge that natural dyes are fit for textile dyeing since ancient times. Basically, natural dyes are elements derived from natural resources, and classified as plant, animal, mineral, and microbial dyes based upon their source of origin. Natural dyeing is a very important part of the old Portuguese tradition which is, currently, regaining awareness due to sustainability and health issues that has arisen from the massive application of synthetic dyes in textile coloration. In this study we sought to optimize the extraction of *Sorghum vulgare* (kuromanin and apigeninidin) through the use of a design of experiments (DOE) methodology and to develop an analytical method by high performance liquid chromatography-diode array detector (HPLC-DAD) for their quantification. Dyes extracted and isolated were then used to dye 100 % wool jersey knits by way of the exhaustion process. The color strength and fastness properties of the dyed samples against washing, and rubbing were evaluated. Our findings proved that meta-mordanted samples dyed at 80 °C for 4h obtained the best strength and color fastness results.

1. Introduction

Natural dyes have been known since ancient times, they are dyes derived and removed from plants, invertebrates, or minerals. Most of the natural colorants are vegetable colorants, extracted from different parts of plants: roots, fruits, bark of trees, leaves and wood; there are other biological sources that produce dyes such as fungi and lichens. Archaeologists have found evidence of fabric dyeing dating from the Neolithic period. In China, dyeing with plants, barks and insects has been traced to being more than 5,000 years old [1].

Throughout history, people have dyed their fabrics using common and locally available materials, but rare dyes that produced bright and permanent colors like natural dyes from invertebrates, tyrian purple and kermes carmine, have become luxury items in the ancient and medieval world. Herbal dyes such as pastel (*Isatis tinctoria*) and indigo were important commercial items in the economies of Asia and Europe. Throughout Asia and Africa, printed fabrics were produced using techniques to control color

absorption in part-dyed fabrics. Paints like cochineal and logwood (*Haematoxylum campechianum*) were brought to Europe by the Spanish, and European dyes were taken by the colonizers to America. The discovery of synthetic dyes in the middle of the 19th century triggered the decline of the large-scale market for natural dyes. Synthetic dyes, which could be produced in large quantities, and unlike natural dyes, could be used in the synthetic fibers created next. Artists from the Arts and Crafts Movement preferred pure hues and a subtle variety of natural dyes, which ripen over time but preserve their true colors, unlike the first synthetic paints, [1] and helped to ensure that ancient European techniques became dyeing and printing with natural inks were preserved. Natural dyeing techniques have also been preserved by artisans and traditional cultures around the world. At the beginning of the 21st century, the natural paint market is experiencing a resurgence in the fashion industry [2]. Western consumers have become more health-conscious about the environmental impact of synthetic dyes in the manufacturing process and there is an increasing demand for products that use natural dyes [3].

2. *Sorghum vulgare*

The *Sorgo* plant belongs to the Poaceae family with more than 30 species from tropical regions, from all continents. It is a plant grown in warm climates. On the European continent, the cultivation of *Sorghum* spp. remains limited mainly in the Mediterranean countries. It is not a demanding plant in soil, it grows in healthy and deep soils, growing well in alkaline soils and supports salinity. This plant is more resistant to drought and temperature than corn, soybeans, wheat, among others, has long and wide leaves and the height of the plant depends on all its cultivation, varying between 60 and 460 centimeters. The most significant of the *Sorghum* spp. dyes are kuromanin and apigeninidin [4] (Figure 1).

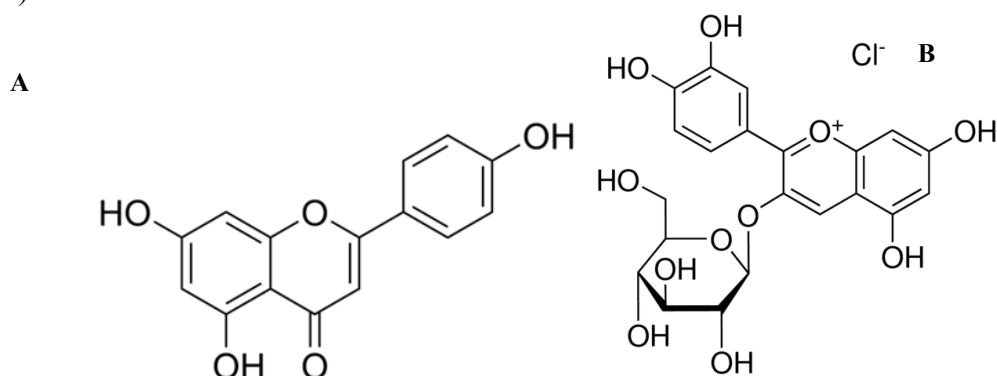


Figure 1 - Chemical structure of apigeninidin (A) and kuromanin (B).

2.1. Materials and Methods

2.1.1. Chemicals and Materials

S. vulgare was purchased from CRITT Horticole (France). Kuromanin and apigeninidin (also, apigenidin) analytical standards were obtained from José Manuel Gomes dos Santos, (Odivelas, Portugal). The working solutions of both compounds were pre-pared by proper dilution of stock solutions with methanol to the final concentrations of 1mg/mL. All stock and working solutions were stored at -20 °C and protected from light. Trifluoroacetic acid (Panreac Química SA, Barcelona, Spain) and ethanol (Fischer chemical, Loughborough, UK) were pro-analysis grade. Methanol (Merck Co, Darm-stadt, Germany), and acetonitrile (Prolabo, Lisbon, Portugal) were HPLC grade. De-ionised water was obtained from a Milli-Q System (Millipore, Billerica, MA, USA).

The analytical grade Copper (II) sulfate pentahydrate ($\text{CuSO}_4 \cdot 5\text{H}_2\text{O}$,) was used as a mordant and purchased from Merck company, Germany. A non-ionic wetting agent and detergent, Kieralon DS, was procured from BASF Portugal. All solutions were prepared with distilled water. The exhaustion dyeing process was carried in a laboratory machine Labomat BFA12 dyeing system from Mathis. A Jenway 6300 spectrophotometer model, from Keison, was used for the absorbance measurements

whereas a spectrophotometer Spectraflash SF300 model, from datacolor Int, (D65 illumination and 10° observer) was used for color strength measurements.

2.1.2. Instrumental and Chromatographic Conditions

The quantification of main compounds present in *S. vulgare* was performed on an high performance liquid chromatography system coupled to a diode array detector (HPLC-DAD) 1290 model (Agilent technologies Soquímica, Lisbon, Portugal) (Figure 2). The mobile phase was composed of acetonitrile: 0.1% trifluoroacetic acid (42:58, v / v). The elution was carried out in isocratic mode. The chromatographic time was 10 minutes. The flow rate was 1 mL/min, and the injection volume was 50 µL. The stationary phase consisted of an YMC-Triart PFP (5 µm, 4.6 i.d. × 150 mm) analytical column coupled to a Guard-c holder (4 × 10 mm) and a Triart PFP (5 µm, 3 × 10 mm) pre-column, all from YMC Europe GMBH (Solítica, Lisbon, Portugal), being maintained at 25 °C. Apigeninidin was detected at 480 nm and kuromanin at 520 nm. The temperature of the column and sampler were set at 30 °C and 4 °C, respectively.



Figure 2 - Chromatographic system.

2.1.3. Dyeing process

This investigation was focused on the ability of an aqueous and alcoholic extract of *S. vulgare*, acting as a natural dye, to carry out the dyeing of 100 % wool jersey knit samples under the influence of different conditions [5,6,7]. The color strength and washing fastness were then thoroughly investigated.

The jersey knit was produced in a rectilinear knit machine (model SVR123SP from Shima Seiki) and can be characterized as follows (Table 1):

Table 1 - Knit samples characterization.

Composition	100 % wool
Yarn linear density	115 Tex
Loop length (cm)	0.7
Wales per cm	4.7
Courses per cm	6.6
Stitch density per cm ²	29.04
Tightness factor (K)	15.3
GSM (g/m ²)	325
Knit structure	Jersey

Upon their production the knit fabric was scoured with a 3 g/L non-ionic detergent and 1 g/L sodium carbonate (Merck Company) at 70 °C for 30 min. Then, it was thoroughly rinsed and air dried at ambient temperature.

The mordanting, with a concentration of 1% ovm, and dyeing, took place in a simultaneous process (meta-mordanting). The samples were dyed at 80°C, with various concentrations of the *Sorghum spp.* extract: 10, 20, 30 and 40 g/L, and different durations: 1, 2, 3 and 4h. Dyeing was carried out in pH 4, adjusted with glacial acetic acid, purchased from sigma Aldrich, and with a liquor ratio of 50:1. Upon dyeing samples were thoroughly rinsed, washed, and dried at room temperature.

The color strength and color depth of mordanted and dyed samples were determined calorimetrically (colourspace: CIELab (1976)/D65) by light reflectance technique. The color strength (K/S) of all the samples was assessed by the Kubelka-Munk equation:

$$K/S = \frac{(1-R)^2}{2R}$$

With R being the observed reflectance at the wavelength of maximum absorption (λ_{\max} = 420 nm) of the dyed wool samples, K is the absorption coefficient and S the light scattering coefficient. The colors are given in CIELab coordinates (L^* , a^* , b^*), which refers to the three axes of the color space, in which L^* indicates the perceived brightness (the scale runs from 0 = black to 100 = white); whereas a^* denotes the red (+ a^*) and green (- a^*) value and b^* specifies the yellow (+ b^*) and (- b^*) coordinate. Other values normally measured are C^* which stands for the saturation value calculated from the reflectance data and h° which is the hue angle.

Washing fastness properties were evaluated in accordance with ISO 105 C06 standard method. The washing operation was carried out in the Linitest apparatus at 60°C for 30 minutes. Upon washing, samples were rinsed with tap water and air dried at room temperature. We repeated the procedure for 5, 10, 15, 20 and 25 cycles. Subsequently, and in order to find out the washing effect on dyed samples, we measured the color strength and CIELab coordinates for all the tested samples, for a more objective comparison.

2.1.4. Statistical Analysis

Statistical analyses used for optimization were carried out with Minitab Statistical Software version 17, and SPSS version 25.

2.1.5. Sample Preparation

From the dried plant, 25g of vegetable raw material were weighed and dissolved with 500 mL of ethanol in an erlenmeyer and then submitted to an extraction process on the stirring plate, for 24 hours at 30 °C. After that, the product resulting from the plant was filtered with the aid of the buchner funnel, for an erlenmeyer and paper filters. The solution was then placed in the rotary evaporator, in order to evaporate the solvent added to the plant and to obtain the precise amount of dye in a 100 mL flask. Upon the dye extraction, the weight of the extract obtained was approximately 200 mg. After the extraction procedure, a 20 mg extract was obtained, which was dissolved in 1 ml of ethanol and filtered using 0.20 μ m cellulose acetate filters before being transferred to the automatic sampler for injection in the HPLC-DAD system.

3. Results and Discussion

3.1. Identification and quantification of kuromanin and apigenidine

An analytical method was developed by HPLC-DAD. Initially, standard solutions were prepared using the pure compound at a concentration of 1 mg/mL in methanol. These solutions were stored in the absence of light at 4°C, until later use. With the conditions referer in (section 2.2) it was possible to identify kuromanin and apigeninidin having a retention time of 1.73 and 3.02 minutes, respectively (Figure3).

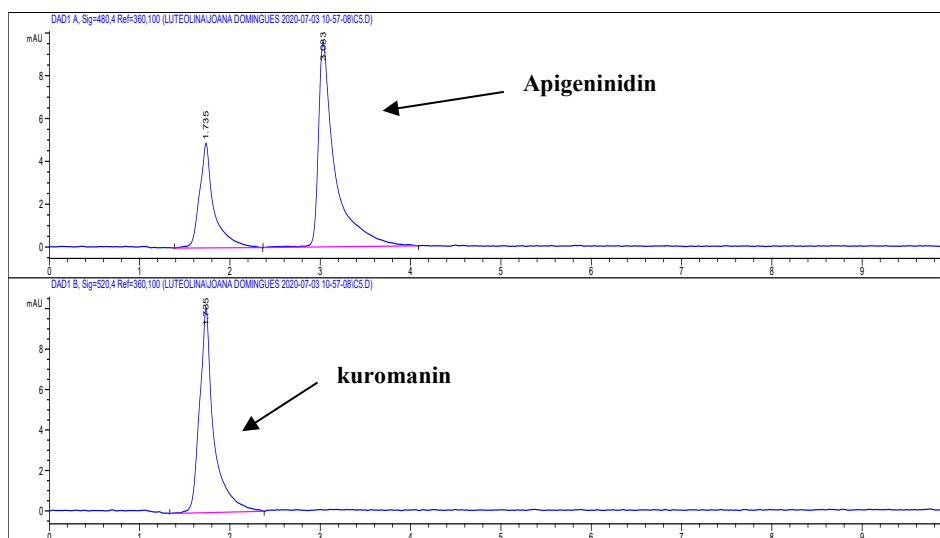


Figure 3 - Apigeninidin and kuromanin chromatograms at a concentration of 6.25 $\mu\text{g} / \text{mL}$.

This initial solution (1 mg/mL) of apigeninidin and kuromanin will allow the definition of calibration curves by successive dilutions. Once the compounds were identified, calibration curves were drawn up by successive dilutions of the initial standards. As the calibration curve is based on a wide range of concentrations and the variance between the different calibration points does not demonstrate homogeneity, the use of weighted linear regression was used so as to overcome the loss of accuracy that was observed, especially in the lowest concentration points. This model allows to harmonize the discrepancies between the variances in a simple and effective way, through the use of empirical weighting factors based on the dependent (y) or independent (x) variable: $1/x$; $1/\sqrt{x}$; $1/x^2$; $1/y$; $1/\sqrt{y}$ and $1/y^2$. Thus, in an attempt to reduce the influence of variance at each point of the calibration line for each analyte, the best weighting factor for the method under development based on the BIAS was tested, with $1/x$ being chosen. Using $1/x$ weighted linear regression, the developed method showed linearity between 0.78 and 100 $\mu\text{g/mL}$ for kuromanin and 0.39-100 $\mu\text{g/mL}$ for apigeninidin with determination coefficients (R^2) greater than 0.99 for each of the compounds and BIAS values for the calibrator less than $\pm 20\%$ and less than $\pm 15\%$ for the remaining points of the calibration line. Tables 2 summarizes the data related to linearity.

Table 2 - Linearity data.

Analyte	Weight	Linear range ($\mu\text{g/mL}$)	Linearity		R^2 *
			Slope*	Intercept*	
Apigeninidin	$1/x$	0.39-100	124.40 ± 3.11	-9.80 ± 5.54	0.9995 ± 0.0006
Kuromanin	$1/x$	0.78-100	38.21 ± 1.33	-8.54 ± 5.23	0.9992 ± 0.0004

* Mean values \pm standard deviation

3.2. Optimization of the extraction procedure

A DOE assay was developed in order to optimize the extraction process. For this, several procedures were analyzed using these dyes. These procedures were selected based on the scientific literature where conditions on temperature, agitation, solvents, volume of solvents and extraction time were sought. DOE is a statistical tool, which allows to identify and quantify the causes of an effect within an experimental study. DOE deliberately manipulates one or more variables, usually parameters associated with the experimental study, to measure the effect it has on other variables of interest. It also allows indicating the best procedure, main variables, the interaction between variables, how many times it is necessary to repeat the experience and the order to be able to confidently establish the relationship between the variables and the intended effect [8]. The parameters were evaluated in a multivariate manner and a fractional factorial design of 2^5 was used (since there were 5 factors under study). This approach allows us to simultaneously evaluate the effect of several variables from a small number of trials, and thus reduce the total number of experiments and obtain good results,

saving resources and time [8,9]. The treatment of results was subsequently carried out in the statistical program MINITAB®, version 17.

The parameters under study were extraction time (6-24h), percentage of water in the extraction (0-100%), agitation (yes / no), temperature (30-80° C) and addition of citric acid (yes / no). A central point (n=3) was added to the design matrix for precision evaluation. Table 3 resumes the experimental matrix.

Table 3 - Experimental matrix for *S. Vulgare*.

Percentage of water (%)	Percentage of ethanol (%)	Temperature (°C)	Agitation	Time (hour)	Addition of citric acid (1 %)
100	0	80	Yes	24	No
0	100	30	Yes	6	Yes
50	50	55	No	15	Yes
100	0	80	No	6	No
0	100	80	Yes	24	No
50	50	55	No	15	No
50	50	55	No	15	No
0	100	80	Yes	6	No
100	0	30	No	24	Yes
50	50	55	Yes	15	Yes
0	100	30	No	24	No
0	100	80	No	6	No
100	0	30	Yes	24	No
100	0	80	Yes	6	Yes
100	0	80	No	6	Yes
0	100	80	Yes	24	Yes
0	100	80	Yes	6	Yes
100	0	30	Yes	24	Yes
100	0	30	No	6	No
50	50	55	No	15	Yes
100	0	80	No	24	No
50	50	55	Yes	15	No
50	50	55	No	15	No
50	50	55	No	15	Yes
50	50	55	Yes	15	Yes
0	100	30	Sim	24	No
100	0	30	Não	24	No
0	100	30	No	24	Yes
100	0	80	No	24	Yes
50	50	55	Yes	15	No
100	0	30	Yes	6	No
0	100	80	No	24	Yes
0	100	30	No	6	Yes
0	100	80	No	6	Yes
0	100	30	Yes	24	Yes
50	50	55	Yes	15	No
100	0	80	Yes	6	No
0	100	80	No	24	No
100	0	80	Yes	24	Yes
100	0	30	Yes	6	Yes
0	100	30	No	6	No
50	50	55	Yes	15	Yes
0	100	30	Yes	6	No
100	0	30	No	6	Yes

From the dried *S. vulgare* plant, 25g of vegetable raw material (aerial parts) were weighed and dissolved with 500 mL of water and ethanol in an erlenmeyer and then submitted to an extraction process on the stirring plate, for several hours at different temperatures according the information present in Table 3.

After the process of concentrating the plant with the solvents, the product resulting from the plant was filtered with the aid of the buchner funnel, for an erlenmeyer and paper filters. It is worth notice that in some of the experiments, citric acid was added to improve the extraction. The solution was then placed in the rotary evaporator, in order to evaporate the solvent added to the plant and to obtain the precise amount of dye in a 100 mL flask. Upon the dye extraction, the weight of the weight of the extract obtained in the 44 experiments carried out, approximately 0.0200 - 0.0250 g was removed from each flask for 44 polytopes to perform the quantification analysis by HPLC/DAD.

In the case of kuromanin, the analysis of the pareto chart (Figure 4) clearly showed that s none of the factors significantly influence the extraction process (none of the factors / relationship between the factors significantly affect it, due to the fact that none exceeds the red dashed line).

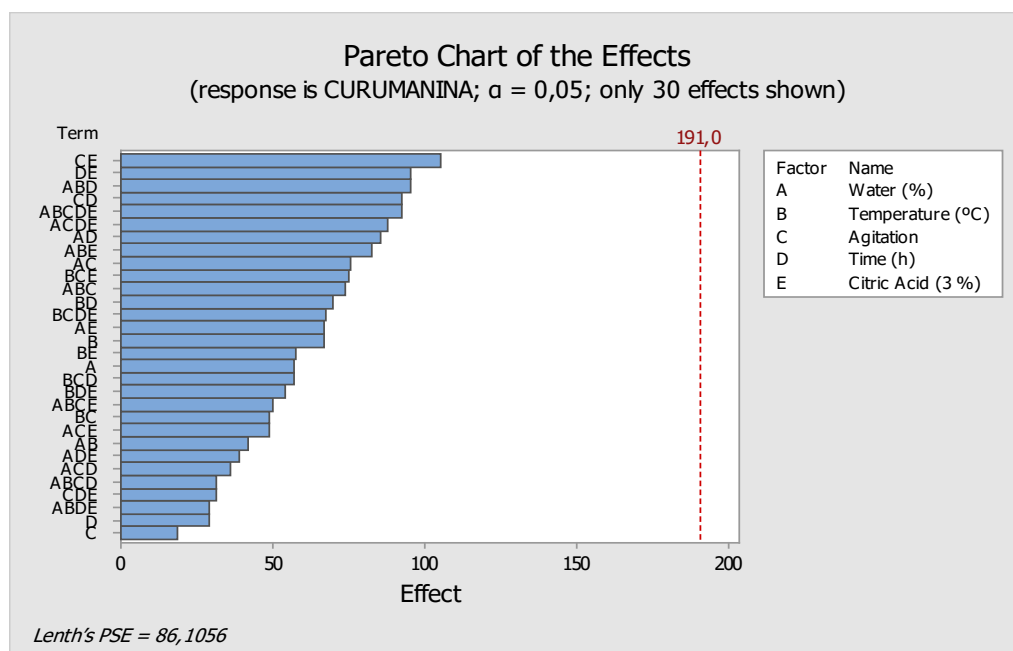


Figure 4 - DOE results of influential factors in the kuromanin extraction process.

From the analysis of the main effects plot (Figure 5) it is possible to verify that the best conditions for the extraction of the compound are: 100 % water, 30 °C, without agitation, 24 h of extraction and without acid citrus, although these results have no statistically significant difference. It should also be noted that for most experiments, no chromatographic signal was obtained.

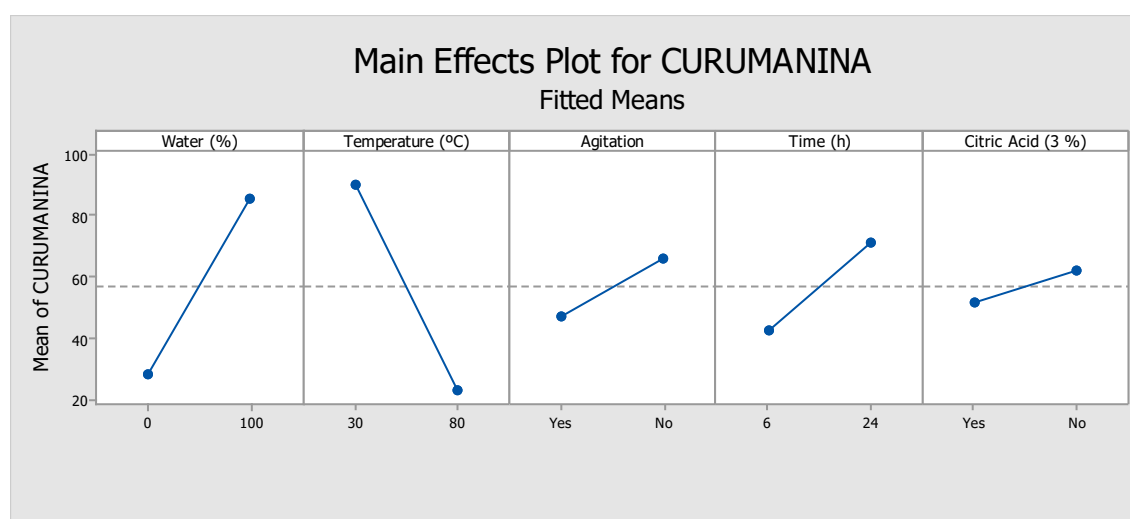


Figure 5 - DOE result of the main effects of factors on the extraction process of kuromanin.

With regard to apigeninidin, the assessment of the Pareto graph (Figure 6) showed that only the percentage of water influences the extraction process statistically significantly (exceeding the red dashed line).

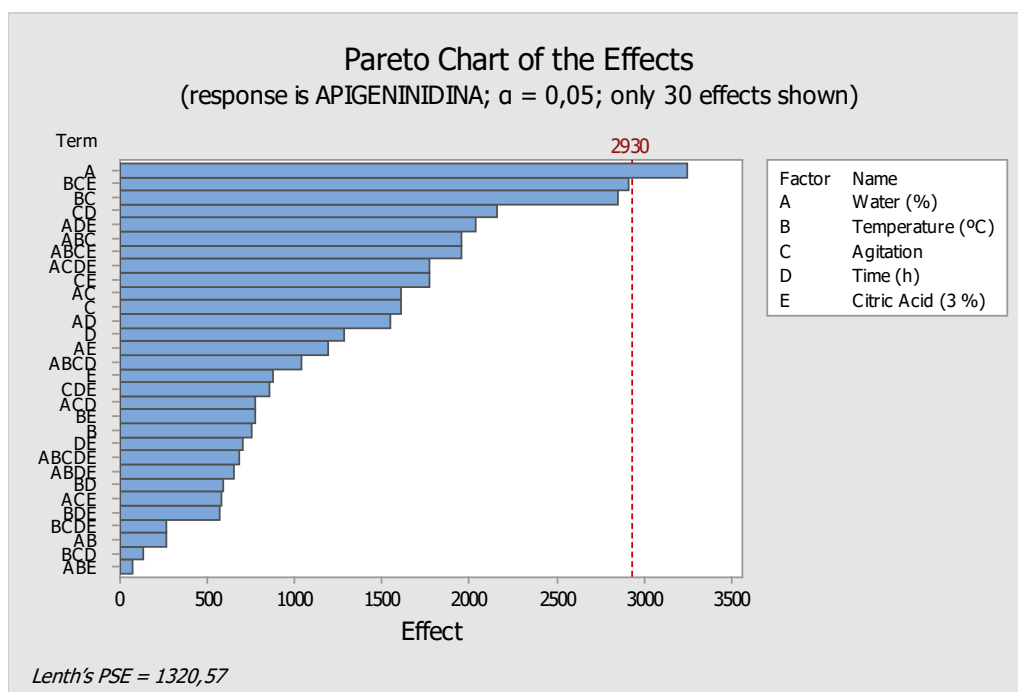


Figure 6 - DOE results of influential factors in the apigeninidin extraction process.

From the analysis of the main effects plot (Figure 7) it is possible to verify that the best conditions for the extraction of the compound are 0 % water, 30 °C, with stirring, 24 h and without citric acid. The water factor was statistically significant.

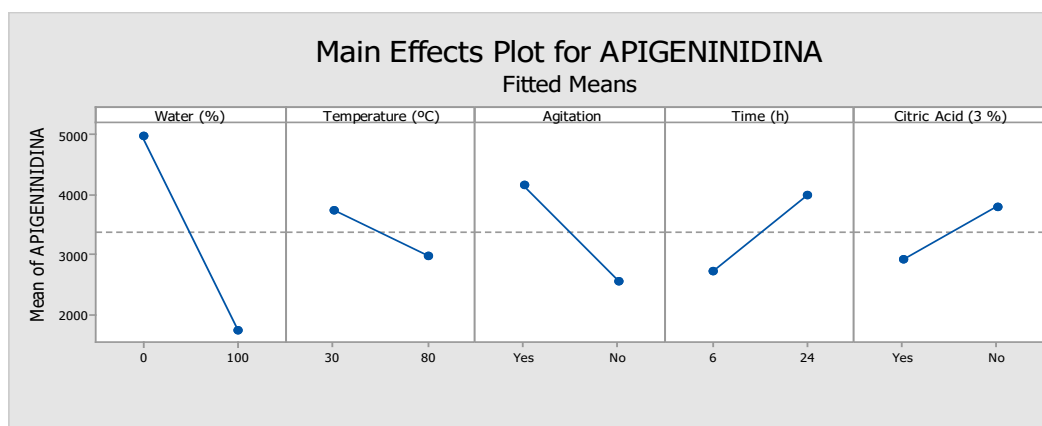


Figure 7 - DOE result of the main effects of factors on the extraction process of apigeninidin.

Based on this premise, it was possible to determine that the concentration of compound in the optimal conditions of extraction was 19.09 μg of kuromanin/20 mg of extract and 119.8 μg of apigeninidin/20 mg of extract, as it was the only sample that meets the ideal conditions. Finally, taking into account the final conditions previously described, a quadruplicate test was performed to verify these results. Table 4, summarizes the attained results.

To what concerns to kuromanin, it was not possible to verify these results since no chromatographic signal was observed in the retention time and wavelength of this compound. For this reason, we can conclude that the suggested extraction conditions may not be ideal.

Table 4 - Results related to the extraction process of the aerial parts of *S.vulgare* under optimal conditions of extraction.

Sample	Mass (g)	Concentration of kuromanin ($\mu\text{g}/\text{mL}$)	Concentration of kuromanin $\mu\text{g}/20\text{ mg}$ of extract	Concentration of apigeninidin ($\mu\text{g}/\text{mL}$)	Concentration of apigeninidin $\mu\text{g}/20\text{ mg}$ of extract
sampl1	0.023	22.70	19.57	141.06	118.54
sampl2	0.021	0	0	135.16	130.59
sampl3	0.026	0	0	128.81	112.01
sampl4	0.028	0	0	208.23	172.81
Average					133.48
Standard deviation					27.32
Coefficient of variation (%)					20.47%

3.3. Experimental Dyeings

3.3.1. Effect of the dyeing time

In the first set of experiments, we sought to ascertain the effect of the dyeing time onto meta-mordanted wool jersey samples. Four different dyeing times were considered, and their respective results are shown on Table 5 to 7.

Table 5 - Visual aspect of the unmordanted dyed samples.

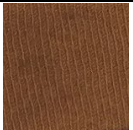
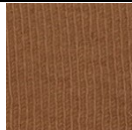
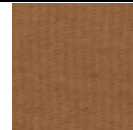
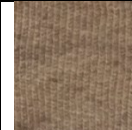

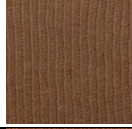
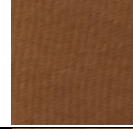
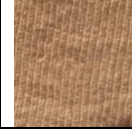
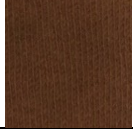

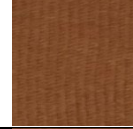
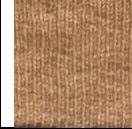
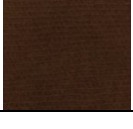
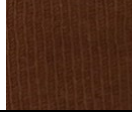
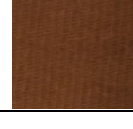

UNMORDANTED	Dyeing Time			
	4h	3h	2h	1h
Extract Concentration (g/L)	Dyed samples			
10				
20				
30				
40				

Table 6 - Visual aspect of the mordanted dyed samples.


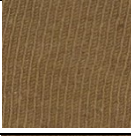
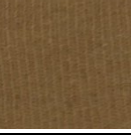
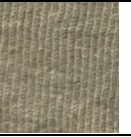

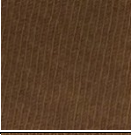

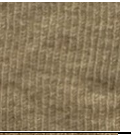

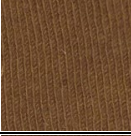
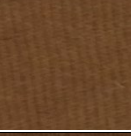
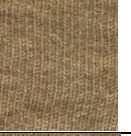

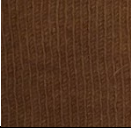
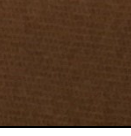
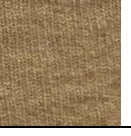
MORDANTED	Dyeing Time			
	4h	3h	2h	1h
Extract Concentration (g/L)	Dyed samples			
10				
20				
30				
40				

Table 7 - K / S and CIELab values for the dyed samples.

MORDANTED	80°C																
	Concentration (g/L)	4h				3h				2h				1h			
		K/S	L*	a*	b*	K/S	L*	a*	b*	K/S	L*	a*	b*	K/S	L*	a*	b*
	10	15.58	41.06	7.09	22.99	14.10	44.48	6.96	24.33	13.08	45.45	5.18	23.67	9.20	50.63	2.29	23.46
	20	19.71	37.58	8.24	23.10	18.65	39.80	8.19	23.19	15.76	42.79	7.43	24.00	11.91	50.63	11.02	28.74
	30	20.44	38.92	9.12	25.68	22.52	37.71	9.44	24.71	18.92	40.94	8.99	24.90	15.36	46.46	6.97	26.75
40	27.25	33.30	11.60	23.32	23.18	37.27	14.55	25.90	21.37	39.44	9.62	24.93	17.03	45.31	7.39	27.07	
UNMORDANTED	80°C																
	Concentration (g/L)	4h				3h				2h				1h			
		K/S	L*	a*	b*	K/S	L*	a*	b*	K/S	L*	a*	b*	K/S	L*	a*	b*
	10	12.25	44.58	9.56	23.55	11.47	47.99	11.69	25.39	10.10	50.22	10.52	25.52	7.43	54.92	8.72	25.65
	20	17.59	40.32	10.26	24.83	16.56	44.07	12.46	26.80	15.28	45.10	11.51	26.21	11.33	48.95	4.78	25.08
	30	19.06	41.84	11.96	28.45	17.02	41.60	12.47	25.78	16.21	44.54	12.35	26.76	14.68	48.72	11.48	29.18
40	22.53	29.29	18.48	18.81	22.61	39.14	12.82	25.99	20.68	30.59	19.19	19.12	16.64	46.42	11.94	29.00	

It can be perceived that all samples (mordanted and unmordanted) present an even and relatively well-fixed color with brown-redish shades.

As observed from the K/S values, all the dyed samples (with and without mordant) and for all the different dyeing times considered (4h, 3h, 2h and 1h), the value of color strength increases, consistently, with the increasing of dye bath concentration.

In all cases, the color strength is always higher - for any value of concentration and dyeing time - when the mordant agent is added to the dye bath. Thus, the absorption of dyestuff was enhanced by using a metal mordant - copper (II) sulphate pentahydrate - which is well known for their ability to form coordinate complexes and to chelate with the dye. Considering that the coordination number of copper is 4, some co-ordination sites are free to interact with the fiber. Functional groups such as amino and carboxylic groups on the fiber can occupy these sites. Hence, this metal can form a ternary complex, on one site with the fiber, and on the other site, with the dye [10, 11].

The dyed uptake was always greater for higher dyeing duration which means that time has a critical effect on the migration and fixation of the dye in the wool fiber.

The L* values tend to be lower with dyeing's performed with higher concentration values and higher when lower concentration values are used. This effect is particularly noticeable in unmordanted samples.

This behavior is in agreement with the respective color strength variation. Thus, for higher values of K/S we have a lower value of L* and vice versa.

From the results, is clear to verify that meta-mordanted wool jersey samples dyed for 4h with 40 g/L yielded the highest color strength.

3.3.2. Effect of the dyeing temperature

In this second set experiments, we sought to assess the effect of dyeing temperature in the final outcome. Thus, the dyeing time, 4h, remain constant, whereas the extract concentration: 10, 20, 30 and 40 g/L and temperature: 40, 60 and 80 °C, varied. The mordanting, dyeing and soaping conditions were conducted in the same manner as described above. The effect of dyeing temperature is shown in Tables 8 to 10.

Table 8 - Visual aspect of the unmordanted dyed samples.

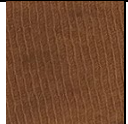

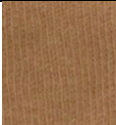

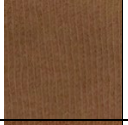
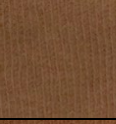



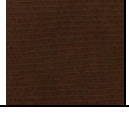
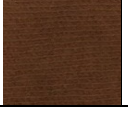
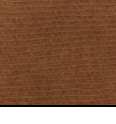
Extract Concentration (g/L)	UNMORDANTED		
	80 °C 4h	60 °C 4h	40 °C 4h
10			
20			
30			
40			

Table 9 - Visual aspect of the mordanted dyed samples.

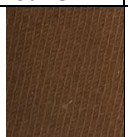











Extract Concentration (g/L)	MORDANTED		
	80 °C 4h	60 °C 4h	40 °C 4h
10			
20			
30			
40			

Table 10 - K / S and CIELab values for the dyed samples.

MORDANTED	4h												
	Concentration (g/L)	80 °C				60 °C				40 °C			
		K/S	L*	a*	b*	K/S	L*	a*	b*	K/S	L*	a*	b*
	10	15.58	41.06	7.09	22.99	7.79	52.98	2.21	23.28	6.35	57.72	1.75	24.85
	20	19.71	37.58	8.24	23.10	12.50	47.59	4.55	24.58	11.32	48.38	4.89	24.27
	30	20.44	38.92	9.12	25.68	16.19	45.61	6.54	26.04	15.07	45.21	6.79	25.39
40	27.25	33.30	11.60	23.32	16.90	46.08	7.47	27.48	16.48	45.99	7.41	27.13	
UNMORDANTED	4h												
	Concentration (g/L)	80 °C				60 °C				40 °C			
		K/S	L*	a*	b*	K/S	L*	a*	b*	K/S	L*	a*	b*
	10	12.25	44.58	9.56	23.55	6.80	54.17	8.19	23.45	4.26	59.14	7.20	21.47
	20	17.59	40.32	10.26	24.83	11.63	49.52	10.31	26.98	7.13	57.10	7.92	25.94
	30	19.06	41.84	11.96	28.45	14.78	48.18	11.52	28.59	7.40	57.90	8.76	29.16
40	22.53	29.29	18.48	18.81	15.06	48.31	11.22	28.87	12.05	52.49	12.20	29.74	

The color fastness to washing, for the wool jersey samples dyed at 80 °C for 4h, were assessed according to ISO 105-C06 standard method. The results are shown in tables 10 to 13. The color fastness to rubbing was conducted as defined in ISO 105-X12:2001, the fastness rating is showed is Table 14.

Table 11 - Visual aspect of unmordanted washed samples.





















80 °C - 4h					
UNMORDANTED					
Concentration (g/L)	N° Washing cycles				
	5	10	15	20	25
10					
20					
30					
40					

Table 12 - Visual aspect of mordanted washed samples.





















80 °C - 4h					
MORDANTED					
Concentration (g/L)	N° Washing Cycles				
	5	10	15	20	25
10					
20					
30					
40					

Table 13 - K / S and CIELab values for the washed samples 80 °C – 4h.

WASHING CYCLES		5				10				15				20				25			
UNMORDANTED	Concentration (g/L)	K/S	L*	a*	b*	K/S	L*	a*	b*	K/S	L*	a*	b*	K/S	L*	a*	b*	K/S	L*	a*	b*
	10	9.23	41.50	16.58	18.14	9.16	40.28	13.70	15.12	9.06	39.51	12.12	14.18	8.34	40.48	11.72	13.86	7.62	41.72	11.46	13.89
	20	12.01	36.87	16.60	17.08	1.99	35.13	12.78	13.59	1.08	34.41	11.69	12.97	11.88	36.35	14.02	14.73	10.96	35.75	11.82	12.86
	30	15.93	32.67	16.48	16.45	14.78	33.36	14.98	14.51	14.26	32.34	12.89	13.09	14.00	32.88	13.38	13.35	13.96	32.83	12.91	13.13
	40	17.42	33.04	18.72	18.43	16.70	30.70	14.19	13.59	16.66	32.56	16.22	15.60	16.40	31.02	14.43	13.54	16.28	31.32	14.83	14.01
MORDANTED	Concentration (g/L)	K/S	L*	a*	b*	K/S	L*	a*	b*	K/S	L*	a*	b*	K/S	L*	a*	b*	K/S	L*	a*	b*
	10	13.06	36.13	11.97	16.37	12.81	36.42	10.23	15.41	12.22	36.38	8.97	14.55	11.95	36.70	9.03	14.94	11.17	37.72	8.99	14.78
	20	14.83	35.20	13.80	17.25	14.69	35.19	11.31	16.29	14.57	34.57	10.10	15.85	14.00	34.80	10.02	15.53	12.37	36.89	9.83	15.91
	30	19.00	31.88	11.88	16.20	18.70	31.44	11.08	16.10	18.02	32.06	11.27	15.83	17.73	32.36	15.26	17.22	17.60	31.35	10.32	14.88
	40	21.28	30.64	12.97	16.87	20.19	30.19	11.39	15.83	19.67	30.15	11.82	15.19	19.36	30.37	11.47	15.58	18.76	31.39	15.91	17.15

Table 14 - Color fastness to washing (ISO 105-C06).

		Number of Washing Cycles				
UNMORDANTED	Concentration (g/L)	5	10	15	20	25
	10	4-5	4	4	4	4
	20	4-5	4	4	4	4
	30	4-5	4-5	4-5	4	4
	40	4-5	4-5	4-5	4	4
MORDANTED	Concentration (g/L)	5	10	15	20	25
	10	4-5	4-5	4-5	4-5	4
	20	4-5	4-5	4-5	4-5	4
	30	4-5	4-5	4-5	4-5	4-5
	40	5	5	4-5	4-5	4-5

Table 15 - Color fastness to rubbing (ISO 105-X12:2013).

UNMORDANTED						
Concentration (g/L)	80 °C - 4h		60 °C - 4h		40 °C - 4h	
	Dry	Wet	Dry	Wet	Dry	Wet
10	4	4	4	3-4	4	4
20	4	4	4	4	5	4-5
30	4-5	4	4-5	4	4	4
40	4-5	4	4-5	4	4	4
MORDANTED						
Concentration (g/L)	80 °C - 4h		60 °C - 4h		40 °C - 4h	
	Dry	Wet	Dry	Wet	Dry	Wet
10	4-5	4	5	4	5	4
20	5	4	4-5	4	4	4
30	4-5	4-5	4-5	4-5	4-5	4
40	4-5	4-5	4-5	4-5	4-5	4

A visual analysis of the dyed samples clearly shows that all samples (mordanted and unmordanted) denote an even and relatively well-fixed color with darker brown-redish shades in mordanted samples whereas unmordanted are brighter.

As derived from the K/S values, all the dyed samples, with and without mordant, and for all the different dyeing temperatures considered, 40, 60 and 80 °C, color strength value increases, consistently, with the increasing of dye bath concentration.

In all cases, the color strength is always higher - for any value of concentration and temperature – when the mordant agent is added to the dyebath.

The dyed uptake was always greater for higher temperatures which means that temperature plays a key role on the migration and fixation of the dye in the wool fiber.

The L* values tend to be lower with dyeing's performed with higher concentration values and higher when lower concentration values are used.

This behavior is in agreement with the respective color strength variation. Thus, for higher values of K/S we have a lower value of L* and vice versa.

Consistently, also the samples dyed at higher temperature have lower L* values for higher dye concentrations and also when the mordant added to the dyebath

From the results, is clear to realize that meta-mordanted wool jersey samples dyed at 80 °C with 40 g/L yielded the highest color strength and the best fastness properties.

The analysis of the washing fastness results showed that mordanted samples exhibit a better behavior when compared to unmordanted ones. This may be attributed to bonds formed between the fiber and the mordant, as explained above, which enhance the fastness of these samples. Nevertheless, ratings prove to be very good to excellent for both cases.

When comparing the rubbing fastness values on mordanted and unmordanted samples, it is possible to verify that results present little difference between them and nearly the same fastness properties. However, mordanted samples have slightly better results than unmordanted ones and, in all cases, dry friction results have always better or at least equal results than in wet friction.

4. Conclusion

The application of *S. vulgare* extract to act as natural dye onto wool jersey samples was carried under two different sets of experiments. In the first one we sought to assess the effect of the dyeing time whereas in the second one we evaluated the role of temperature. Additionally, both groups were tested in the presence and absence of a metal mordant, copper (II) sulphate pentahydrate, so as to ascertain his contribution for the dyeing outcome. From the results it can be postulated that wool jersey knits can be successively dyed with *S. vulgare* extract. This may attributed to fact that *S. vulgare* is rich in kuromanin and apigeninidin that can form hydrogen and ester bonds with the carboxyl groups in the protein fiber. In the overall, samples dyed with higher temperature – 80 °C – and long dyeing duration – 4h – yielded the best color strength and fastness properties.

Acknowledgment

The authors gratefully acknowledge the funding by Ministério da Agricultura, under grants ID Grupo Operacional 303, Operação N. ° PDR2020-101-031956. This work was partially supported by CICS-UBI, which is financed by National Funds from Fundação para a Ciência e a Tecnologia (FCT) and by Fundo Europeu de Desenvolvimento Re-gional (FEDER) under the scope of PORTUGAL 2020 and Programa Operacional do Centro (CENTRO 2020), with the project references UIDB/00709/2020 and UIDP/00709/2020.

References

- [1] Goodwin, Jill. A Dyer's Manual. (1982) ISBN 0-7207-1327-7.
- [2] Calderin, Jay (2009). Form, Fit, Fashion.: Rockport. p. 125. ISBN 978-1-59253-541-5.
- [3] Faizal, Elly Burhaini (2011). «Indonesia told to produce more 'green' products». The Jakarta Post.
- [4] Gilbert K.G., (2003), Secondary products: dyes. Encyclopedia of Applied Plant Sciences, p.1174-1179.
- [5] Virendra G., (2019), Fundamentals of Natural Dyes and Its Application on Textile Substrates, DOI: 10.5772/intechopen.89964.
- [6] Mathur P., Metha A., Kanwar R., Bhandari C.S. (2003), Use of neem bark as wool colourant—Optimum conditions of wool dyeing. Indian Journal of Fibre and Textile Research 2003; 28:95.
- [7] Hossein B., Shahdokht R. (2014), The dyeing procedures evaluation of wool fibers with prangos ferulacea and fastness characteristics. Advances in Materials Science and Engineering 2014: 1-6. DOI: 10.1155/2014/497278.
- [8] Costa S., Barroso M., Castañera A., Dias M. (2010), Design of experiments, a powerful tool for method development in forensic toxicology: application to the optimization of urinary morphine 3-glucuronide acid hydrolysis. Analytical and Bioanalytical Chemistry 396(7); 2533-42. DOI: 10.1007/s00216-009-3447-8.
- [9] Miller, J.N.; Miller J.C. Statistics and Chemometrics for Analytical Chemistry. 5th Ed. (2005) ISBN-13: 978-0131291928.
- [10] Rattanaphol M., Jiri K. Jakub W. and Jarmila S., (2011), Natural dye from eucalyptus leaves and application for wool fabric dyeing by using padding techniques. Natural Dyes, Ed. Emrye Kumbasar, Intech Open, ISBN 978-953-307-783-3.
- [11] Bhattacharya S. D., Shah A. K. (2000). Metal ion effect on dyeing of wool fabric with catechu, Coloration Technology, 116; 10-12. DOI: 10.1111/j.1478-4408.2000.tb00002. x.

CHAPTER 5:

Environmental Engineering in Textile Production

Secondary Raw Plastic Materials in Applied Design

Jaroslava Frajová^{1,a*}, Alena Opálková Šišková^{2,3,b*}

¹Faculty of Art and Architecture, Technical University of Liberec, Studentská 1402/2, 461 17 Liberec, Czechia;

²Polymer Institute of Slovak Academy of Sciences, Dúbravská cesta 9, 845 41 Bratislava, Slovakia

³Institute of Materials and Machine Mechanics, Slovak Academy of Sciences, Dúbravská cesta 9, 845 13 Bratislava, Slovakia

^ajaroslava.frajova@tul.cz, ^balena.siskova@savba.sk

Keywords: Plastic waste, poly(ethylene terephthalate), recycling, design, electrospinning.

Abstract. In modern society, it is impossible to imagine life without plastics. However, managing the waste composed of plastics is one of the most significant environmental issues confronting us today. *Recycling plastic waste* or recovering the secondary raw materials sources is the most crucial action available to reduce ecological impacts worldwide. With the need to recycle plastic waste, questions also arise about applying new products from recycled plastics and advanced processing technologies. *Advanced technologies* overlap actively with *applied design*, and their implementation enables them to move from extraordinary design ideas to the final object. Therefore, this contribution shows the possibility to prepare the unique textile pattern, interior accessories, and jewelry from the post-consumer use bottle poly(ethylene terephthalate) (PET) by *electrospinning*.

Introduction

Design involves combining creativity in the generation of insights and solutions, an empathetic understanding of the context of a challenge, and critical thinking for analyzing and fitting solutions to the context. To move from design to final product or service requires skills and technologies [1]. Some of these technologies have been known at the scientific level for decades, and they are stepwisely gaining use in industry as well.

Electrospinning belongs among the most attractive methods for fabricating fibrous membranes, which is a facile and effective approach for forming fine fibers [2]. Compared to the natural fibers such as sheep wool (Fig. 1A), cotton (Fig. 1B), or rabbit hair (Fig. 1C), the electrospun fibers can be produced from tens of nano- to a few micrometers under the application of electric field (Fig. 1D). Electrospun products have already been studied for many applications as in medicine [3], energy [4], sensing [5], filtration [6], protecting clothing [7], or environmental remediation [8]. Furthermore, this method offered the possibility to also prepare fibrous products from synthetic [9] or natural polymers [10] or virgin [11] and recycled polymers (plastic wastes) [12]. The use of secondary raw materials is usually driven by cost, to which transport is often a major contributor. Waste-derived raw materials may have sustainability benefits [13].

It is plastic waste that forms a huge storehouse of raw materials. Recycling plastic waste or recovering the secondary raw materials sources is the most crucial action available to reduce ecological impacts worldwide. In 2018, an estimated 359 million tons of plastic (synthetic polymers) were produced globally. Of these, 24.9% are landfilled, 42.6% are incinerated, and only 32.5% are recycled. According to the latest statistics, poly(ethylene terephthalate) (PET) accounts for 5% of the total annual production of plastics, which makes almost 18.2 million tons. Only about 20% is used for recycling [14]. Poly(ethylene terephthalate) is the standard thermoplastic polyester, which has excellent mechanical, thermal, chemical properties and good dimensional stability. It is highly flexible, semi-crystalline, and shows excellent electrical insulating properties and high strength. Poly(ethylene terephthalate) is the most common polymer for food, beverage packaging, or automotive [2, 15]. The PET waste can be reprocessed into fine fibers and widely used for fleece garments such as sweaters and jackets [16].

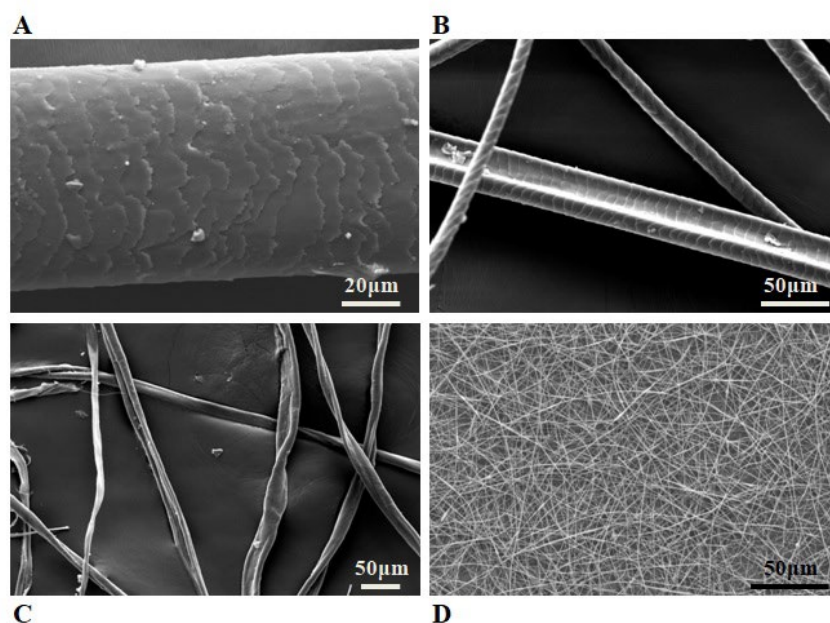


Figure 1. Comparison of natural fibers such as sheep wool (A), rabbit hair (B), cotton (C), and silk electrospun fibers (D). Photos from the archive of authors.

This contribution shows the possibility to prepare the unique textile pattern, interior accessories, and jewelry from the *beverage bottle poly(ethylene terephthalate) (PET) after customer use*. Electrospinning has been used as a fabrication technology.

Material and Methods

Poly(ethylene terephthalate) bottle has been used in this study. The PET bottle has been cut into pellets. The mixture of 1,1,1,3,3,3-hexafluoro-2-propanol/dichloromethane in a ratio of 20/80 v/v% was used as a solvent of PET. The PET solution was prepared in a concentration of 10 w/v%. For the color effect, rhodamine B and coumarin dyes have been added into the selected solutions in a concentration of 0.01 w/v%. The realization of objects includes the hand-crafting of the conductive collector into planar (A), or 3D (B) objects from the metal wire (aluminum), as shown in Fig. 2.

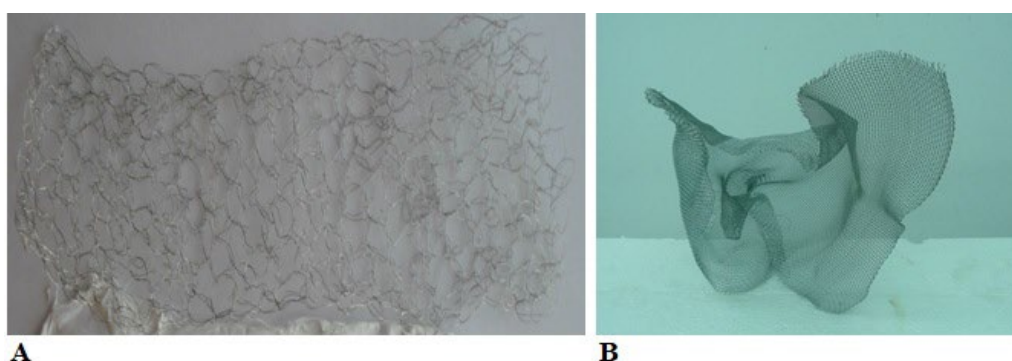


Figure 2. The hand-crafted conductive planar collector (A) and 3D collector (B) from the metal wire. Photos from the archive of authors.

Then the production is finished by coating the hand-crafted collector with nanofibers employing electrospinning customer-built apparatus in a horizontal spinning configuration.

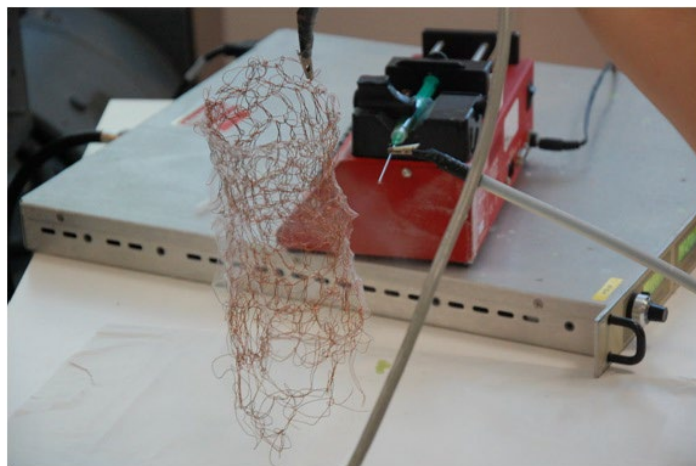


Figure 3. The coating process of the hand-crafted collector by electrospinning. Photo from the archive of authors.

The polymer solution was added into the plastic syringe with a flat-end needle with a 0.8 mm (21G) inner diameter. Applied voltage has been driven by a high voltage power supplier with positive polarity. The voltage of 13 – 16 kV and the working distance between the collector and top of the needle of 12 cm has been applied. A one-syringe pump has ensured the solution's feeding, and the flow rate of PET solution of 0.5 mL.h⁻¹ has been used.

The apparatus is shown in Fig. 3. The micrographs have been taken by scanning electron microscopy (SEM, JSM Jeol 6610 microscope). The images have been taken by professional photographers Michal Jakubec from the BASE factory and by MFA Peter Ivančic.

Results and Discussion

It has already been shown that the PET waste could be recycled by electrospinning into the air and water vapor permeable membrane with acceptable mechanical properties and excellent filtration effectivity [2, 12]. The PET waste has been used in applied design to realize planar and 3D interior accessories and jewelry. As shown in Fig. 4A, the electrospun membrane has taken the surface pattern from the hand-crafted collector. The thickness of such membrane is 0.18 mm. The colorful membrane was produced using fluorescent dyes as rhodamine B or coumarin (Fig.4B), and the selected membrane was observed by scanning electron microscopy. The SEM micrograph is shown in Fig. 4C. Micrograph has revealed the uniform fibers with an average fiber diameter of 240±120 nm.

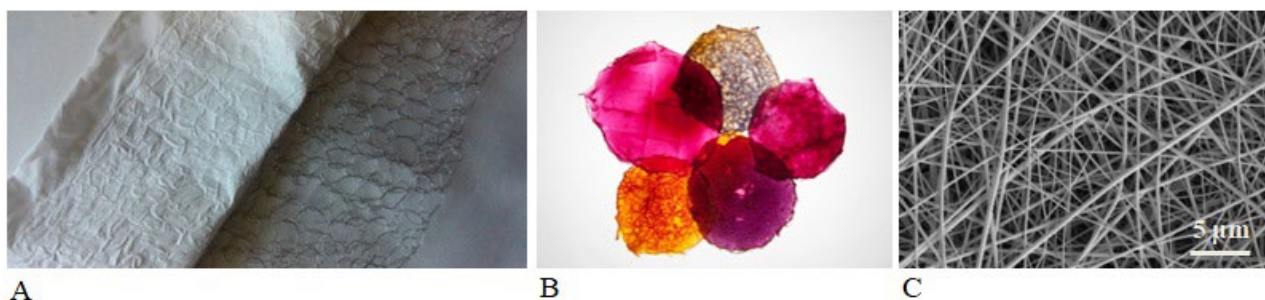


Figure 4. The pattern of the electrospun membrane (A), colorful membranes prepared by using rhodamine B and coumarin (B), the SEM micrograph of the electrospun membrane from rPET (C). Photos are from the archive of authors.

Although the membranes are applied to a metal support collector, their mechanical properties are good enough to be self-supporting [12]. It is proved on Fig. 4.

As shown in Fig.5, interior accessories such as lampshades (Fig. 5A, B) or jewelry (Fig. C, D, E) in different shapes could also be realized by coating the objects with fibers employing electrospinning. The spatial conductive collectors prepared from the metallic wires in the desired

shape have been covered by the nanofibrous mat. The coating has been realized by manually rotating the collector in the space using a ground cable. In such a way, the safety of the operator has been ensured. According to the operator's decision, the nanofibers have been randomly deposited on the surface of the collector and in thickness at discretion. Multi-colored accessories were obtained by mixing rhodamine B and coumarin, respectively, by depositing several layers of fibers with different colors (Fig. 5A). Therefore, each spatial accessory is unique and unrepeatable. It is impossible to produce two identical or only similar objects.



Figure 5. Final products are prepared by a combination of hand-crafting and electrospinning technology. Lampshade (A), spatial interior accessory (B), necklace (C), earring (D), a combination of colorful necklace and earring (E). Photos are from the archive of authors, and more could be seen in [17].

The nanofibrous mats perfectly copy the surface of the collector. The thickness of the nanofibrous mats varies according to the decision of the operator and designer. In the case of Fig. 5 B, the thickness was about $1 \pm 0.2 \mu\text{m}$. Contrary, in the case of Fig. 5E, the thickness was about $15 \pm 3 \mu\text{m}$. The micrographs of a cross-section of fibrous mats are shown in Fig. 6.

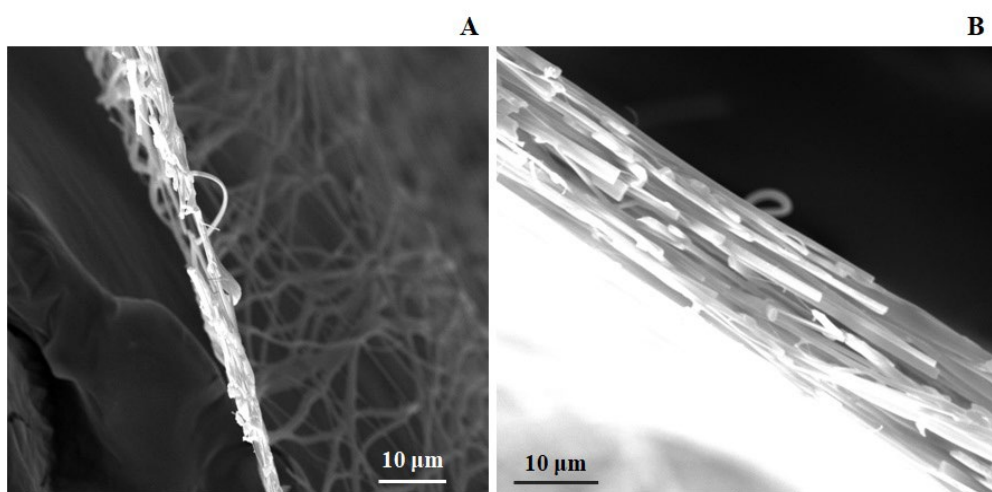


Figure 6. SEM micrograph of electrospun mats; (A) $1 \pm 0.2 \mu\text{m}$ and (B) $15 \pm 3 \mu\text{m}$. Photos are from the archive of authors.

With the addition of dyes into the polymer solution, the diameters of the fibers in the electrospun mat have been affected. The fiber's diameters increased up to $520 \pm 213 \text{ nm}$ (Fig. 5E). The additives' effects have been observed and discussed in many scientific articles [18, 19].

Electrospinning gives new possibilities and opportunities for plastic waste-based secondary raw materials applications. Such unique materials and structures have been in place since 2015 but have

not yet been published outside of art exhibitions. In this case, a combination of technology, materials recycling, and applied design is beneficial.

Conclusion

Recycling plastic waste is the most crucial action available to reduce the ecological impacts of wastes worldwide. When recycling and reducing the environmental impact of plastic waste, every possible technology and application of the new products need to be considered. This paper shows the possibility of producing effective material for applied design to realize unique interior accessories and jewelry.

Acknowledgment

The authors would like to thank to photographers Michal Jakubec BASE factory and MFA Peter Ivančic, to model Dominika Čáčana and Barbora Korinkova from Mix model management modeling agency and for providing make up to StayUnique.sk

References

- [1] Information on <https://curriculum.gov.bc.ca/content/applied-design-skills-and-technologies-introduction>
- [2] A. Opálková Šišková, K. Mosnáčková, J. Hruža, J. Frajová, A. Opálek, M. Bučková, K. Kozics, P. Peer, A. Eckstein Andicsová, Electrospun poly(ethylene terephthalate)/silk fibroin composite for filtration applications, *Polymers*. 13 (2021) 2499.
- [3] D.A. Lociendo, L.A. Mercante, R.S. Andre, L.H.C. Mattosi, G.L.F. Luna, P. Brassolatti, F.d.F. Anibal. D.S. Correa, Biocompatible and biodegradable electrospun nanofibrous membranes loaded with grape seed extract for wound dressing application, *J. Nanomater.* (2019) 2472964.
- [4] W.U. Arifeen, M. Kim, D. Ting, R. Kurniawan, J. Choi, Y. Kisoo, T.J. Ko, Hybrid thermal resistant electrospun polymer membrane as the separator of lithium ion batteries, *Mater. Chem. Phys.* 245 (2020) 122780.
- [5] N. Aliheidari, N. Aliahmad, M. Agarwal, H. Dalir, Electrospun nanofibers for label-free sensor application, *Sensor* 19 (2019) 3587.
- [6] F. Topuz, M.A. Abdulhamid, S.P. Nunes, G. Szekely, Hierarchically porous electrospun nanofibrous mats produced from intrinsically microporous fluorinated polyimide for the removal of oils and non-polar solvents, *Environ. Sci. Nano*. 7 (2020) 1365-1372.
- [7] X. Yu, X. Wu, Y. Si, X. Wang, J. Yu, B. Ding, Waterproof and breathable electrospun nanofibrous membranes, *Macromol. Rapid. Commun.* 40 (2019) e1800931.
- [8] F. Topuz, T. Holtzl, G. Szekely, Scavenging organic micropollutants from water with nanofibrous hypercrosslinked cyclodextrin membranes derived from green resources, *Chem. Eng. J.* 419 (2021) 129443.
- [9] S.H. Chen, P.Y. Chou, Z.Y. Chen, F.H. Lin, Electrospun water-borne polyurethane nanofibrous membrane as a barrier for preventing postoperative peritendinous adhesion, *Int. J. Mol. Sci.* 20 (2019) 1625.
- [10] C. Belbéoch, J. Lejeune, P. Vroman, F. Salaün, Silkworm and spider silk electrospinning: a review, *Environ. Chem. Letters* 19 (2021) 1737 – 1763.

-
- [11] S. Stojanov, A. Bercel, Electrospun nanofibers as carriers of microorganisms, stem cells, proteins, and nucleic acids in therapeutic and other applications, *Front. Bioeng. Biotechnol.* 8 (2020) 130.
- [12] A. Opálková Šišková, J. Frajová, M. Nosko, Recycling of poly(ethylene terephthalate) by electrospinning to enhance the filtration efficiency, *Mater. Letter* 278 (2020) 128426.
- [13] P. del Strother, Manufacture of Portland cement, in: P.C. Hewlett, M. Liska (Eds.), *Lea's chemistry of cement and concrete*, Elsevier, Amsterdam, 2021, pp. 31-56.
- [14] A. Opálková Šišková, P. Peer, A. Ecksten Andicsová, I. Jordanov, P. Rychter, Circulatory management of polymer waste: recycling into fine fibers and their applications, *Materials*. 14 (2021) 4694
- [15] S.A. Begum, A.V. Rane, K. Kanny, Application of compatibilized polymer blends in automobile industry, in: A.R. Ajitha, S. Thomas (Eds.), *Compatibilization of polymer blends, Micro and nano scale phase morphologies, interphase characterization, and properties*, Elsevier, Amsterdam, 2020, pp. 563-593.
- [16] Information on: <https://www.nationalgeographic.com/science/article/partner-content-evolution-of-recycled-fabrics>
- [17] Information on: <https://polymer.sav.sk/NANO-Art/>
- [18] X. Yan, M.H. You, T. Lou, M. Yu, J.Ch. Zhang, M.G. Gong, F.Y. Lv, Y.Y. Huang, Y.Z. Long, Colorful hydrophobic poly(vinyl butyral)/cationic dye fibrous membranes via a colored solution electrospinning process, *Nanoscale Res. Letter*. 11 (2016) 540.
- [19] L.A. Dobrzanski, M. Adamiak, M. Karon, B. Nieradka, Influence of inorganic additives on morphology of electrospun fibres, *J. Achiev. Mater. Manuf.* 68 (2015) 64-71.

Direct and Reactive Dyes Recovery in Textile Wastewater Using Calcinated Hydrotalcite

Eva Bou-Belda^{1,a}, Daniel López-Rodríguez^{1,b*}, Bàrbara Micó-Vicent^{2,c},
Marilés Bonet-Aracil^{1,d}

¹Departamento de Ingeniería Textil y Papelera, Universitat Politècnica de València, Plaza Ferrándiz y Carbonell s/n, Alcoy, Spain

²Departamento de Ingeniería Gráfica, Universitat Politècnica de València, Plaza Ferrándiz y Carbonell s/n, Alcoy, Spain

^aevbobel@upvnet.upv.es, ^bdalorod@upv.es, ^cbarmivi@upv.es, ^dmaboar@txp.upv.es

Keywords: nanoclay, dye recovery, clay pigment, direct dye recovery, reactive dye recovery, hydrotalcite.

Abstract: Growing environmental conservation concerns have led researchers to seek the means to treat and recover wastewater. The textile industry dumps vast quantities of wastewater from textile dyes. By means of clays, dye waste can be separated and reused for other industrial processes. Clay absorption varies depending on the type of dye employed because factors like the reactivity of the dye molecule and its size are very important during the absorption process. The absorption capacity of calcined hydrotalcite at several concentrations was compared in a 0.05 g·L⁻¹ solution of four distinct dyes: Direct Blue 199, Direct Red 23, Direct Blue 71 and Reactive Yellow. Dyes have different molecular weights because the weight of reactive dyes is considerably lighter than that of direct dyes, which is why the Lambert-Beer lines of each dye are previously considered. We worked with a 5 g·L⁻¹ clay concentration to introduce the dye into the clay by stirring for 24 h in 100 ml of each dye solution before filtering it and leaving it to dry. In all cases, the dye absorption by nanoclay was nearly absolute and the initial solution was very clean, which are excellent results from the wastewater treatment point of view. Color measurement was performed by a Jasco V-670, double-beam spectrophotometre between 190-2700 nm. Differences in color were calculated and represented in CIE-Lab* color space diagrams. Finally, thermogravimetric (TGA) and X-ray diffraction (XRD) analyses were carried out to ensure both nanoclay-dye interactions and hydrotalcite structure recovery. No large differences were observed under these conditions, which reinforces the idea of using low nanoclay concentrations.

Introduction

Nanoclays have entered the textile-chemistry industry world as an element with extremely efficient absorbing characteristics that allow them to be used for treating and recovering wastewater from the textile and other industries. Thanks to their specific characteristics, nanoclays are capable of absorbing and retaining dyes from the textile industry that are not absorbed during the dyeing process. Thus their final destination is being dumped in textile effluents, which has an environmental impact.

The textile chemical industry is that which most strongly affects wastewater and is the industry that undertakes the most chemical activity in the world. [1]. Recycling industrial wastewater has become an increasingly well-known need. The concentration at which dyes are found in effluents lies around 50-1000 ppm, but can be lower at 10-50 ppm. [2]. The nanoclays surface is very large, about 750 m² / g. The outcome of introducing small quantities of these materials into polymeric matrices is called a nanocomposite [3].

Some compounds or materials are known, such as cyclodextrins [4], agricultural waste [5], nanocomposites [6] or physical means like membrane filtration [7], and many other methods aim to treat wastewater. However, most of them have not reused dyes or the treatment element, which does not promote circular economy. What is more, their complexity is much greater compared to the treatment method here discussed.

Previous works have demonstrated the efficiency of such elements and the success of corresponding trials [8-15]. Thanks to these new applications, the quantity of dyes dumped in wastewater can significantly lower, or new research lines can open up that propose how to use these dyes which, to date, have been wasted, and all this could promote the much-acclaimed circular economy. Finally, apart from cleaning textile wastewater with low clay concentrations, the created dye-clay hybrid can be employed as a pigment [8, 11, 12, 16-20], which offers a great advantage over the aforementioned methods.

Materials and Methods

This study used different colors. The employed direct dyes were Direct Blue 199 CI 74.180, Direct Red 23 CI 29160 and Direct Blue 71 CI 34140. Reactive Drimaren Yellow HF-3GL was utilized as the reactive dye. These dyes were chosen for their trichrome color and because they come as different types with several molecular weights.

Hydrotalcite (HC) was employed as clay and was prepared in accordance with Dos Santos R.M.M. [21]. It was calcined at 600 °C for 3 h. Figure 1 shows the HC characterization, for which a microscope (Hitachi model S3000N) with an X-ray detector (Bruker XFlash 3001 model) was used for SEM, while the JEOL JEM-2010 model and a GATAN acquisition camera (ORIUS SC600 model) were employed for TEM imaging purposes. The SEM image shows how clay particle aggregates look like sheets owing to the structure of nanoclays, which break up after calcination. Thanks to their shape memory however, they recover after the absorption process. The TEM imaging can display amorphous areas and areas with stripes where clay sheets are seen with many small basal spaces.

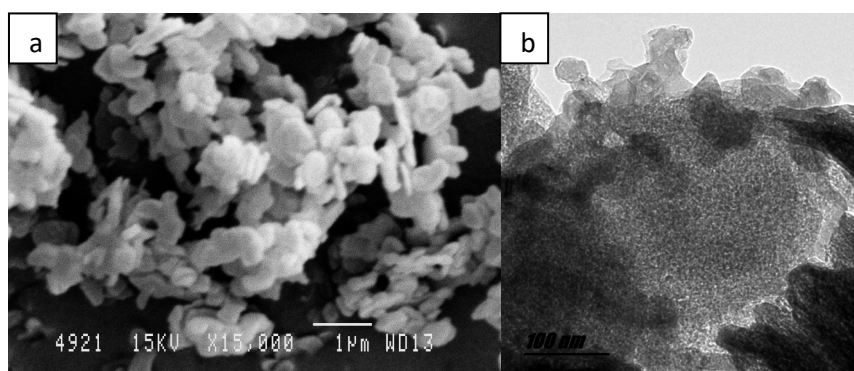


Figure 1. a) HC SEM b) HC TEM

Dilutions of all the dyes were prepared to obtain the Lambert-Beer line [22]. These lines allow the dye concentration remaining in wastewater to be known after applying clay. Table 1 shows line equations and determination coefficient R^2 .

Table 1. Lambert-Beer line equations and R^2

Dye	Equation	R^2
Direct Blue 199	$y = 21.784 x - 0.015$	0.9982
Reactive Yellow	$y = 14.943 x - 0.0021$	0.9993
Direct Red 23	$y = 34.357 x - 0.0148$	0.9991
Direct Blue 71	$y = 17.09 x - 0.0233$	0.9987

For each dye, 100 mL of the 0.05 g·L⁻¹ concentration solution were taken. Next 20 g·L⁻¹ of clay were used and the mixture was placed in a magnetic stirrer [23], which was run at maximum speed for the first 2 h and then at 600 r.p.m. until the 24 h. The solution was filtered with clay for 48 h and was spectrophotometrically measured in a Zuzi spectrophotometer (model 4251/50) to calculate the dye concentration that had not been absorbed by clay [24, 25]. The nanoclays with the absorbed dye were lyophilized [26, 27] to completely extract water in order to be measured in a Jasco V-670 double-beam spectrophotometer between 190 and 2700 nm. Differences in color and total solar reflectance

(TSR) were calculated [28]. A thermogravimetric analysis (TGA) was carried out to compare any possible variation in the degradation peaks of dyes, clays and the final hybrid [29-31]. An X-ray diffraction analysis (XRD) [32, 33] was performed to check that clay recovered its original shape before being calcined. To do so, Bruker D8-Advance XRD equipment was used (Bruker, Billerica, MA, USA) with a Göebel mirror (power: 3000W, voltage: 20-60 kV; current: 5-80 mA). Finally, measures were taken in an oxidant atmosphere at an angular rate of $1^\circ/\text{min}$. PASO 0.05° and with 2.7° - 70° angular scanning.

Results and Discussion

UV absorption

Our results showed that after clay had absorbed the dye, the dye concentration went from $5 \cdot 10^{-2} \text{ g} \cdot \text{L}^{-1}$ to about $4.08 \cdot 10^{-4}$ and $2.3 \cdot 10^{-3} \text{ g} \cdot \text{L}^{-1}$ (see Table 2).

Table 2. Difference in concentration after HC absorption

	Sample ref.	Initial conc. $\text{g} \cdot \text{L}^{-1}$	Final conc. $\text{g} \cdot \text{L}^{-1}$	% Absorption
Direct Blue 71	1	0.05	$2.30 \cdot 10^{-3}$	95.40%
Reactive Yellow	2	0.05	$4.08 \cdot 10^{-4}$	99.18%
Direct Red 23	3	0.05	$9.55 \cdot 10^{-4}$	98.09%
Direct Blue 199	4	0.05	$1.56 \cdot 10^{-3}$	96.88%

Color measurements

The color measurement of the dye-clay hybrid represented in the CIE-L* color space diagrams are found in Figure 2. The four samples have different hues close to the red, yellow and pure blue axes. A significant difference was observed between the two employed direct blue dyes. The tone in Sample 1 is more reddish than that of Sample 4, which is more greenish than the first one. Differences in colour saturation can also be seen. Sample 1 is less chromatic and darker than the other samples (except for the red one, which is slightly darker). As expected, the lightest and most chromatic sample is yellow (Sample 2).

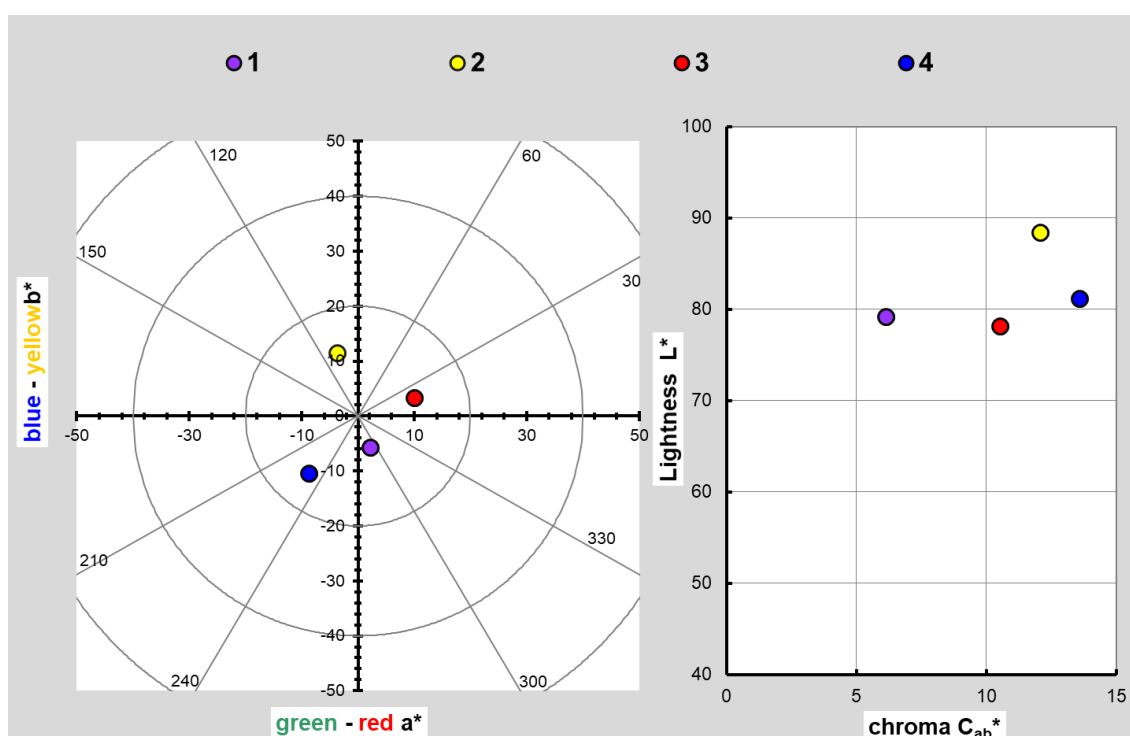


Figure 2. CIE-L*a*b* color space diagrams of the (1-4) samples

Total solar reflectance (TSR)

The total solar reflectance (TSR) absorbed by the top layer determines the heat build-up on a covered surface. The surface temperature very much depends on exposure length. To achieve cold surfaces, pigments in coatings must reflect the largest possible amount of energy. This reflection capacity is expressed as the TSR value, with 100% total reflection and zero total absorption.

Pigments with high TSR values present high reflection and low heat build-up. Conventional white coverings exhibit 75%TSR or higher which, by definition, would absorb 25% incident energy. A carbon black-based black covering might have a TSR as low as 4% and would, therefore, absorb 96% of incident solar energy.

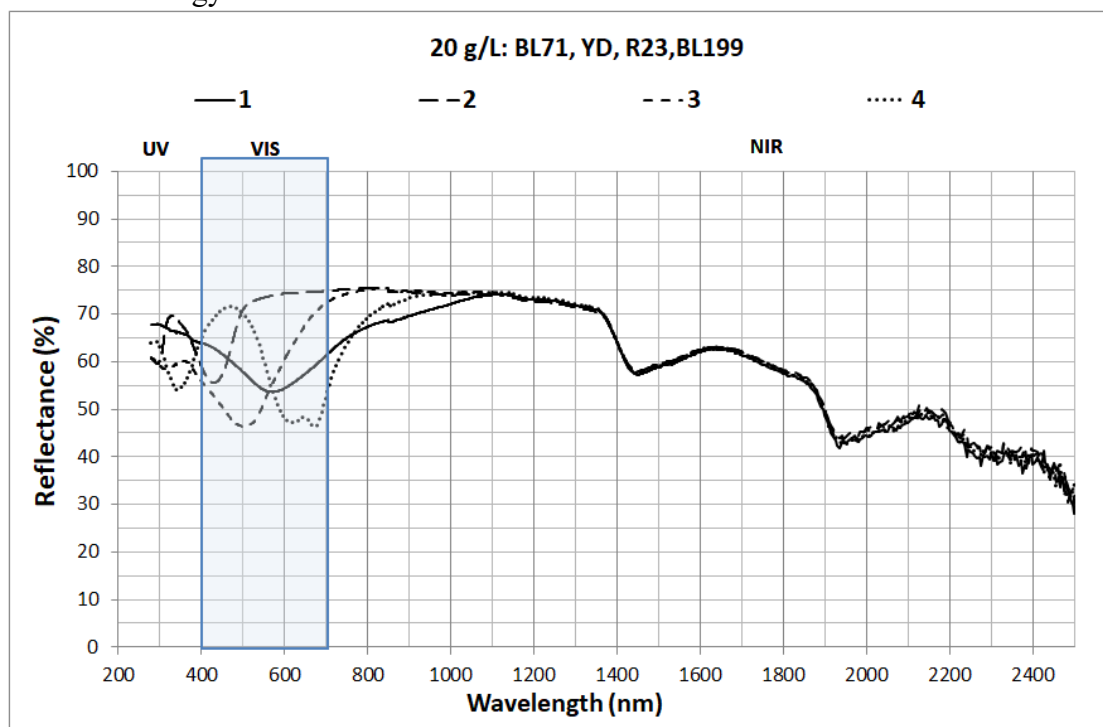


Figure 3. Reflectance (%) for the (1-4) samples; 190-2500 nm.

After performing the calculations to obtain the TSR percentages of each dye-clay hybrid, the results in Table 3 and Figure 3 were obtained. The main spectral differences fell within the visible range, which was expected owing to the dyes' characteristics. Spectral differences may also fall within the UV range, where Samples 2 and 4 obtained the highest reflectance value. Differences also appeared within the near NIR range (700-1000 nm), where Sample 4 (Direct Blue 199) had the lowest reflectance value. Within the 1000-2500 nm range, reflectance values were almost the same for all the samples owing to the nanoclay effect. These differences could explain the TSR% values and the gap in the analysed samples. As expected, the highest TSR% value was found in the yellow hybrid pigment (Sample 2) owing to the intrinsic color characteristic (light). Some interesting differences were found between the blue samples. The TSR% value of Sample 1 was 62.72%, and it was 63.45% for Sample 4. The four samples obtained high TSR% values due to the HC interaction. These hybrid pigments could be used as solar protection in various applications.

Table 3. TSR Values

	Sample ref.	TSR %
Direct Blue 71	1	62.72%
Reactive Yellow	2	69.97%
Direct Red 23	3	63.85%
Direct Blue 199	4	63.45%

Thermogravimetry

According to the TGA, the dye degradation results were independently compared as were those of clay alone. The results and degradation peaks are found in Figure 4. The bottom of this figure shows curves d(YD), d(A71), d(R23), d(A199) and d(H), which derived from the first curves indicating specific degradation peaks. In view of these results, we see that Direct Blue 71 is the lowest and its degradation is the slowest, and Blue 199 strongly peaks at 367-482 °C. Red 23 and Reactive Yellow start to degrade earlier, but their drop is gradual and less marked within a range of approximately 217-556 °C.

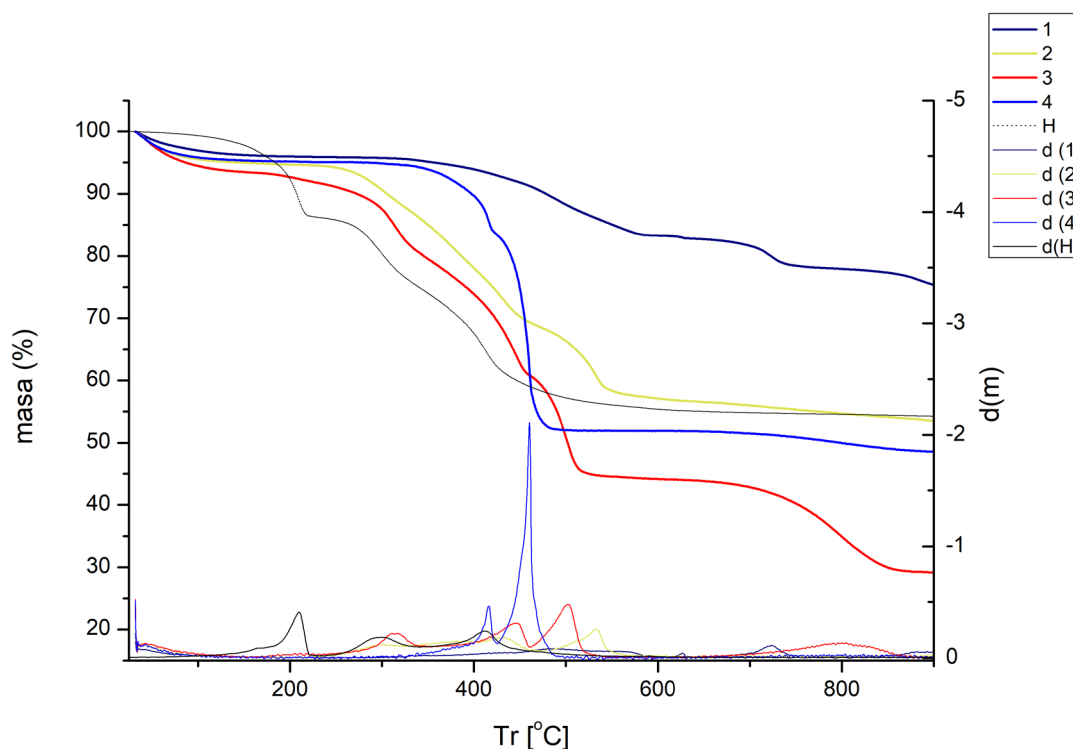


Figure 4. TGA for the original dyes and hydrotalcite

Next hybrid pigments were analyzed to see the effect of nanoclay as a host of the original dyes (Figure 5). We can see how the dye-clay interaction affected the original dye properties and how its degradation changed by temperature (Figure 5). We can observe how the first degradation peak lies at around 200°C.

Gravimetric performance was the same for the four hybrid samples because the four lines practically overlapped (Figure 5). By representing HC and only one of the HC + Dye hybrids (Figure 6), thermal performance was virtually the same as it was for HC alone. It was not easy to see the thermal degradation of the original dyes because all the hybrid pigments had a low dye content.

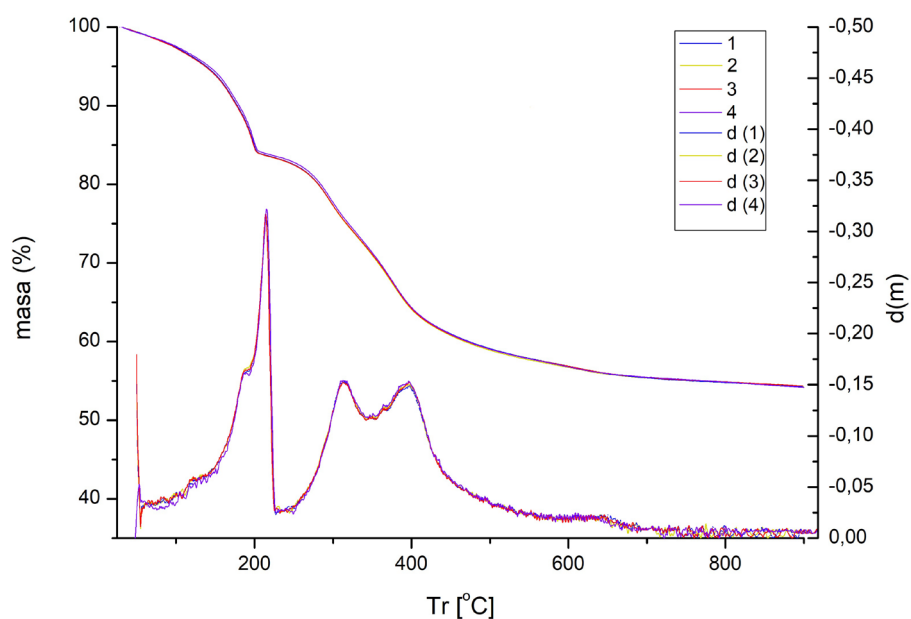


Figure 5. TGA for each hybrid sample

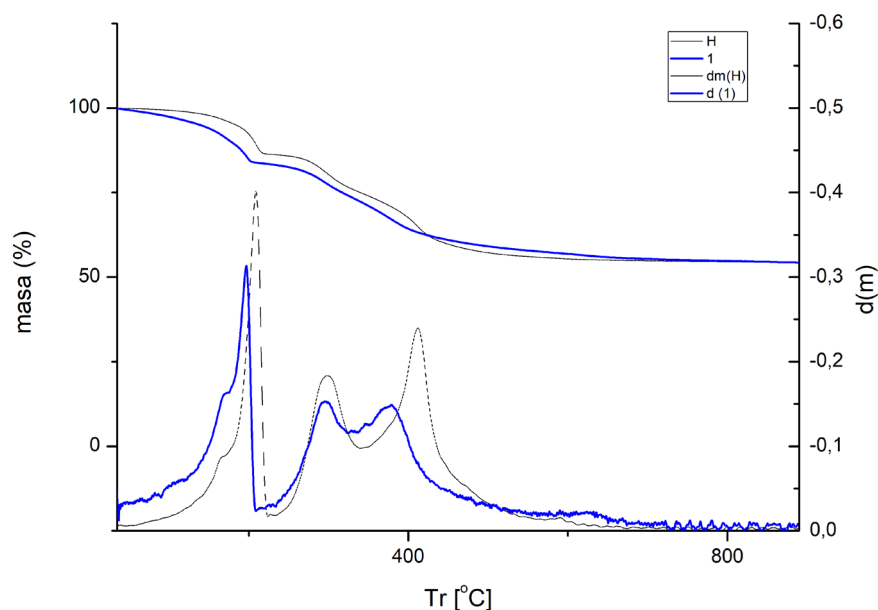


Figure 6. TGA for hydrotalcite and Sample 1

X-ray diffraction (XRD)

Thanks to X-ray diffraction, an intralaminar space opened up after clay calcination that facilitated dye penetration. The original structure became partially recomposed after the absorption process due to HC's shape memory. A peak showing the described characteristic between 11 and 12 degrees took place. As with the calcined HC, this peak disappeared because these layers opened (Figure 7). This peak slightly shifted owing to dye penetration. It can be assumed that this shift would be more marked at higher dye concentrations.

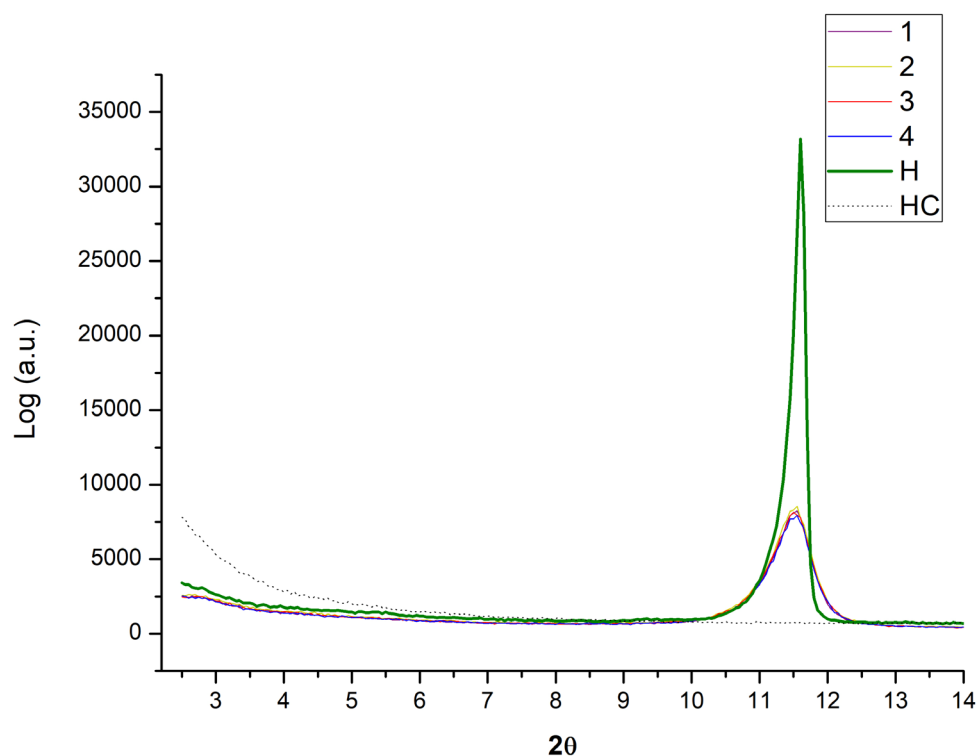


Figure 7. XRD for Hydrotalcite, Hydrotalcite calcined and hybrid pigments (Samples 1-4)

Conclusions

In view of our results, HC clay efficacy in absorbing reactive and direct dyes for wastewater treatment in textile dye processes was proven. The absorption percentages were considerably high because they exceeded 95% absorption in all cases. Good color fixation to clay was observed as far as its homogeneity and degree of stability are concerned. The color intensity that resulted from the clay-dye hybrid was very low, which was not surprising because clay concentration was $20 \text{ g}\cdot\text{L}^{-1}$, while that of dyes was only $0.05 \text{ g}\cdot\text{L}^{-1}$. For future work, it is planned to calculate the adsorption kinetics of the clay to reduce the 24-hour stirring time of the solution with the dye in order to thus improve the process.

The TSR of the four hybrids was between 60% and 70%. As the TSR of the conventional targets was 75%, the studied samples came very close to these percentages. This reinforces the previous discussion about very low color intensity, which was very white for the white clay color.

The TGA results fell in line with this. Hybrids performed almost identically to HC alone, which means that dyes barely influenced the sample's final TGA. The hybrid's degradation peaks were the same as those of clay without having absorbed dyes. Finally thanks to the XDA, HC partially recovered its intralaminar space due to its shape memory. This should help to fix dye in clay and, therefore, the resulting hybrid stability.

References

- [1] M. Wakkal, B. Khiari, F. Zagrouba, Textile Wastewater Treatment by Agro-Industrial Waste: Equilibrium Modelling, Thermodynamics and Mass Transfer Mechanisms of Cationic Dyes Adsorption onto Low-Cost Lignocellulosic Adsorbent. *J. Taiwan Inst. Chem. Eng.* **2019**, *96*, 439–452. <https://doi.org/10.1016/J.JTICE.2018.12.014>.
- [2] M. L. Mathew, A. Gopalakrishnan, C. T. Aravindakumar, Aravind, U. K. Low – Cost Multilayered Green Fiber for the Treatment of Textile Industry Waste Water. *J. Hazard. Mater.* **2019**, *365*, 297–305. <https://doi.org/10.1016/J.JHAZMAT.2018.11.014>.
- [3] B. Micó Vicent, F.M. Martinez Verdu, J.E. Gilabert Perez, Optimización de La Síntesis de Nanopigmentos de Origen Natural Para Biopolímeros Mediante El Uso Del Diseño de Experimentos. Doctoral Thesis. Universitat Politècnica de València 2015. <http://hdl.handle.net/10251/59449> (22/11/2021).
- [4] P. Semeraro, V. Rizzi, P. Fini, S. Matera, P. Cosma, E. Franco, R. García, M. Ferrándiz, E. Núñez, J. A. Gabaldón, I. Fortea, E. Pérez, M. Ferrándiz, Interaction between Industrial Textile Dyes and Cyclodextrins. *Dye. Pigment.* **2015**, *119*, 84–94. <https://doi.org/10.1016/J.DYEPIG.2015.03.012>.
- [5] D. Sana, S. Jalila, A Comparative Study of Adsorption and Regeneration with Different Agricultural Wastes as Adsorbents for the Removal of Methylene Blue from Aqueous Solution. *Chinese J. Chem. Eng.* **2017**, *25* (9), 1282–1287. <https://doi.org/10.1016/J.CJCHE.2017.01.012>.
- [6] L. Sanchez, M. Ollier, R. P. Gonzalez, J. S. Alvarez, V. A. Nanocomposite Materials for Dyes Removal. *Handb. Nanomater. Ind. Appl.* **2018**, 922–951. <https://doi.org/10.1016/B978-0-12-813351-4.00053-5>.
- [7] M. Erkanlı, L. Yilmaz, P. Z. Çulfaz-Emecen, U. Yetis, Brackish Water Recovery from Reactive Dyeing Wastewater via Ultrafiltration. *J. Clean. Prod.* **2017**, *165*, 1204–1214. <https://doi.org/10.1016/J.JCLEPRO.2017.07.195>.
- [8] M. Ogawa, R. Takee, Y. Okabe, Y. Seki, Bio-Geo Hybrid Pigment Clay-Anthocyanin Complex Which Changes Color Depending on the Atmosphere. *Dye. Pigment.* **2017**, *139*, 561–565. <https://doi.org/10.1016/J.DYEPIG.2016.12.054>.
- [9] F. López Arbeloa, V. Martínez Martínez, J. Bañuelos Prieto, I. López Arbeloa, Adsorption of Rhodamine 3B Dye on Saponite Colloidal Particles in Aqueous Suspensions. *Langmuir* **2002**, *18* (7), 2658–2664. <https://doi.org/10.1021/la0113163>.
- [10] M. I. Carretero, M. Pozo, C. Sánchez, F. J. García, J. A. Medina, J. M. Bernabé, Comparison of Saponite and Montmorillonite Behaviour during Static and Stirring Maturation with Seawater for Pelotherapy. *Appl. Clay Sci.* **2007**, *36* (1–3), 161–173. <https://doi.org/10.1016/J.CLAY.2006.05.010>.
- [11] D. Guillermin, T. Debroise, P. Trigueiro, L. de Viguerie, Rigaud, B. Morlet-Savary, F. Balme, S. Janot, J.-M. Tielens, F. Michot, L. Lalevee, J. Walter, P. Jaber, M. New Pigments Based on Carminic Acid and Smectites: A Molecular Investigation. *Dye. Pigment.* **2019**, *160*, 971–982. <https://doi.org/10.1016/J.DYEPIG.2018.07.021>.
- [12] E. M. Moujahid, R. Lahkale, H. Ouassif, F. Z. Bouragba, W. Elhatimi, New Organic Dye/Anionic Clay Hybrid Pigments: Preparation, Optical Properties and Structural Stability. *Dye. Pigment.* **2019**, *162*, 998–1004. <https://doi.org/10.1016/J.DYEPIG.2018.11.021>.
- [13] J.-Z. Yi, L.-M. Zhang, Removal of Methylene Blue Dye from Aqueous Solution by Adsorption onto Sodium Humate/Polyacrylamide/Clay Hybrid Hydrogels. *Bioresour. Technol.* **2008**, *99* (7), 2182–2186. <https://doi.org/10.1016/J.BIORTECH.2007.05.028>.

-
- [14] R.A. Schoonheydt, L. Heughebaert, Clay Adsorbed Dyes: Methylene Blue on Laponite. *Clay Miner.* **1992**, 27, 91–100, doi:10.1180/claymin.1992.027.1.09.
- [15] H. Mittal, R. Babu, A. A. Dabbawala, S. Stephen, S. Alhassan, M. Zeolite-Y Incorporated Karaya Gum Hydrogel Composites for Highly Effective Removal of Cationic Dyes. *Colloids Surfaces A Physicochem. Eng. Asp.* **2020**, 586, 124161. <https://doi.org/10.1016/J.COLSURFA.2019.124161>.
- [16] L. N. F. de Queiroga, D. B. França, F. Rodrigues, I. M. G. Santos, M. G. Fonseca, M. Jaber, Functionalized Bentonites for Dye Adsorption: Depollution and Production of New Pigments. *J. Environ. Chem. Eng.* **2019**, 7 (5), 103333. <https://doi.org/10.1016/J.JECE.2019.103333>.
- [17] H. Laguna, S. Loera, I. A. Ibarra, E. Lima, M. A. Vera, V. Lara, Azoic Dyes Hosted on Hydrotalcite-like Compounds: Non-Toxic Hybrid Pigments. *Microporous Mesoporous Mater.* **2007**, 98 (1–3), 234–241. <https://doi.org/10.1016/j.micromeso.2006.09.009>.
- [18] V. Rives, M. E. Pérez-Bernal, R. J. Ruano-Casero, I. Nebot-Díaz, Development of a Black Ceramic Pigment from Non Stoichiometric Hydrotalcites. *J. Eur. Ceram. Soc.* **2012**, 32 (5), 975–987. <https://doi.org/10.1016/j.jeurceramsoc.2011.11.033>.
- [19] X. Yu, J. Wang, M. Zhang, L. Yang, J. Li, P. Yang, D. Cao, Synthesis, Characterization and Anticorrosion Performance of Molybdate Pillared Hydrotalcite/in Situ Created ZnO Composite as Pigment for Mg-Li Alloy Protection. *Surf. Coatings Technol.* **2008**, 203 (3–4), 250–255. <https://doi.org/10.1016/j.surfcoat.2008.08.074>.
- [20] H. Chen, Z. Zhang, G. Zhuang, R. Jiang, A New Method to Prepare ‘Maya Red’ Pigment from Sepiolite and Basic Red 46. *Appl. Clay Sci.* **2019**, 174, 38–46. <https://doi.org/10.1016/J.CLAY.2019.03.023>.
- [21] R. M. M. dos Santos, R. G. L. Gonçalves, V. R. L. Constantino, L. M. da Costa, L. H. M. da Silva, Tronto, J. Pinto, F. G. Removal of Acid Green 68:1 from Aqueous Solutions by Calcined and Uncalcined Layered Double Hydroxides. *Appl. Clay Sci.* **2013**, 80–81, 189–195. <https://doi.org/10.1016/j.clay.2013.04.006>.
- [22] J. L. Bigman, Monitoring of Chemicals and Water. *Handb. Silicon Wafer Clean. Technol.* **2018**, 619–657. <https://doi.org/10.1016/B978-0-323-51084-4.00011-3>.
- [23] M. M. F. Silva, M. M. Oliveira, M. C. Avelino, M. G. Fonseca, R. K. S. Almeida, E. C. Silva Filho, Adsorption of an Industrial Anionic Dye by Modified-KSF-Montmorillonite: Evaluation of the Kinetic, Thermodynamic and Equilibrium Data. *Chem. Eng. J.* **2012**, 203, 259–268. <https://doi.org/10.1016/j.cej.2012.07.009>.
- [24] Huang, G.; He, J.; Zhang, X.; Feng, M.; Tan, Y.; Lv, C.; Huang, H.; Jin, Z. Applications of Lambert-Beer Law in the Preparation and Performance Evaluation of Graphene Modified Asphalt. *Constr. Build. Mater.* **2021**, 273, 121582, doi:10.1016/j.conbuildmat.2020.121582.
- [25] J. L. Bigman, K. A. Reinhardt, *Monitoring of Chemicals and Water* Elsevier Inc., 2018. <https://doi.org/10.1016/B978-0-323-51084-4.00011-3>.
- [26] C. Mensch, R. Chintala, D. Nawrocki, J. T. Blue, A. Bhambhani, Enabling Lyophilized Pneumococcal Conjugate Vaccines Through Formulation Design and Excipient Selection Suitable for A Multivalent Adjuvanted Vaccine. *J. Pharm. Sci.* **2020**, 1–11. <https://doi.org/10.1016/j.xphs.2020.10.038>.
- [27] L. S. Castillo-Peinado, M. Calderón-Santiago, F. Priego-Capote, Lyophilization as Pre-Processing for Sample Storage in the Determination of Vitamin D3 and Metabolites in Serum and Plasma. *Talanta* **2021**, 222 (September 2020). <https://doi.org/10.1016/j.talanta.2020.121692>.

-
- [28] S. Maharjan, K. S. Liao, A. J. Wang, S. A. Curran, Highly Effective Hydrophobic Solar Reflective Coating for Building Materials: Increasing Total Solar Reflectance via Functionalized Anatase Immobilization in an Organosiloxane Matrix. *Constr. Build. Mater.* **2020**, *243*, 118189. <https://doi.org/10.1016/j.conbuildmat.2020.118189>.
- [29] Y. Liu, R. Li, J. Yu, F. Ni, Y. Sheng, A. Scircle, J. V. Cizdziel, Y. Zhou, Separation and Identification of Microplastics in Marine Organisms by TGA-FTIR-GC/MS: A Case Study of Mussels from Coastal China. *Environ. Pollut.* **2020**, No. xxxx, 115946. <https://doi.org/10.1016/j.envpol.2020.115946>.
- [30] M. Umar, M. I. Ofem, A. S. Anwar, A. G. Salisu, Thermo Gravimetric Analysis (TGA) of PA6/G and PA6/GNP Composites Using Two Processing Streams. *J. King Saud Univ. - Eng. Sci.* **2020**, No. xxxx. <https://doi.org/10.1016/j.jksues.2020.09.003>.
- [31] I. Corazzari, F. Turci, R. Nisticò, TGA Coupled with FTIR Gas Analysis to Quantify the Vinyl Alcohol Unit Content in Ethylene-Vinyl Alcohol Copolymer. *Mater. Lett.* **2021**, *284*, 129030. <https://doi.org/10.1016/j.matlet.2020.129030>.
- [32] H. Pálková, J. Madejová, M. Zimowska, E. Bielańska, Z. Olejniczak, L. Lityńska-Dobrzyńska, E. M. Serwicka, Laponite-Derived Porous Clay Heterostructures: I. Synthesis and Physicochemical Characterization. *Microporous Mesoporous Mater.* **2010**, *127* (3), 228–236. <https://doi.org/10.1016/j.micromeso.2009.07.019>.
- [33] W. Zhuo, Y. Xie, M. T. Benson, J. Ge, R. D. Mariani, J. Zhang, XRD and SEM/EDS Characterization of Two Quaternary Fuel Alloys (U-2.5Mo-2.5Ti-5.0Zr and U-1.5Mo-1.5Ti-7.0Zr in Wt. %) for Fast Reactors. *Mater. Charact.* **2020**, *170* (September), 110696. <https://doi.org/10.1016/j.matchar.2020.110696>.

Polyamide 6.6 Degradation through Photo-Fenton Process

MARCELINO-PEREZ Edgar^{1,a*}, BONET-ARACIL Marilés^{2,b},
BOU-BELDA Eva^{2,c}, AMAT PAYÁ Ana^{1,d}, ARQUES SANZ Antonio^{1,e}
and VICENTE Rafael^{1,f}

¹Grupo de Procesos de Oxidación Avanzada, Departamento de Ingeniería Textil y Papelera,
Universitat Politècnica de València, Campus d'Alcoi, Spain.

²Grupo de Gestión Integral de la Industria Textil, Departamento de Ingeniería Textil y Papelera,
Universitat Politècnica de València, Campus d'Alcoi, Spain

^aedmarpe2@doctor.upv.es, ^bmaboar@txp.upv.es, ^cevbobel@upv.es, ^daamat@txp.upv.es,
^eaarques@txp.upv.es, ^frvicente@txp.upv.es

Keywords: Polyamide, microplastic, photo-Fenton, degradation.

Abstract. Synthetic polymers have become essential in our life, nevertheless, the high production and the low recycling around the world have caused serious problems of contamination in soil and water. In addition, its fragmentation into microplastics in environmental conditions has exacerbated the ecological problems due to its possible ingestion by organisms and its high capacity to transport and release a wide variety of organic pollutants. Photo-Fenton process was used to evaluate its capacity to degrade PA6.6 microplastic under simulated solar irradiation and natural solar irradiation plus LED visible light in order to get a best knowledge about its behavior in environmental conditions. PA6.6 was degraded for 7 h through photo-Fenton process under simulated solar irradiation. Superficial defects were observed along the PA6.6 microplastic after degradation experiments. However, FT-IR analysis did not show the formation of additional bands which indicated the formation of new products. DSC analysis showed changes in the melting point of the PA6.6 after the photo-Fenton treatment at different times. The assays carried out under natural solar irradiation showed lower degradation of the PA6.6 under the same experimental conditions, nevertheless, it was observed an increase of the specific surface area 90 times higher in the PA6.6 treated for 10 h.

Introduction

Since its synthesis, synthetic polymers have become one of the most used materials in the whole world. It has been reported that the global production of synthetic polymers reach 368 million tons in 2019 [1] and, as a consequence of the global population growth the demand of polymers increase every year. Some properties like durability, good stability to degradation, lightweight, and low cost make them an idoneous material. Since the fabrication of personal care products to clothing and parts in automotive and electronic devices the polymers become indispensable in our life. Besides the importance and benefits of this kind of materials to the society, in recent years its importance has focused on its potential as a pollutant in several environments. In this sense, the high stability and resistance to degradation of the synthetic polymers under environmental conditions and in conjunction with the low recycling capacity and the lack of waste management the problem has been exacerbated. It is reported that more than a half of plastics waste ends up on the environment and thus, making the soil and water two of the most affected environments by these pollutants [2]. In particular, in marine environments the entrance of plastics has several pathways which begins with the dumping of plastics products to the environment and later its incorporation and transport via wastewater outflows, rivers, as well as, by wind or tides [3,4]. Once in the water bodies, plastics are exposed to several environmental conditions like photoaging, chemical and physical forces, as well as, biological interaction [5,6,7] which depending of the polymer nature could cause its fragmentation into small particles with sizes less than 5 mm known as microplastics (MPs) [8]. Investigations focused on the dispersion of MPs have shown that this kind of pollutants can be found in almost every place of the world, since urban center to places where the human activity is limited like polar sea,

deep sea sediments and remote alpine regions [8,9]. In a short period, research about microplastics has been increasing notoriously as a consequence of its potential as a pollutant (Figure 1). The constant increase of MPs concentration in water environments brings with them serious ecological problems due to its interaction and ingestion by marine organism from lower to higher trophic levels [10,11]. Intake of MPs by organisms trigger a cascade of effects like accumulation in the digestive gland, false satiety, reduction in energy budgets, oxidative stress, immune reaction, cellular and DNA damage [8,12,13,14]. Further, due to its physical and chemical characteristics MPs has the capacity to adsorb and concentrated a wide variety of persistent organic pollutants (POPs) and heavy metals which have been widely described due to its high potential damage to the organisms. Bakir [14] studied the salinity effect of three different water systems (freshwater, estuarine and marine water) in the transport of phenanthrene and 4'4-DDT onto PVC and PE, results showed that the sorption is dependent to the POPs concentration while the salinity has no significant effect.

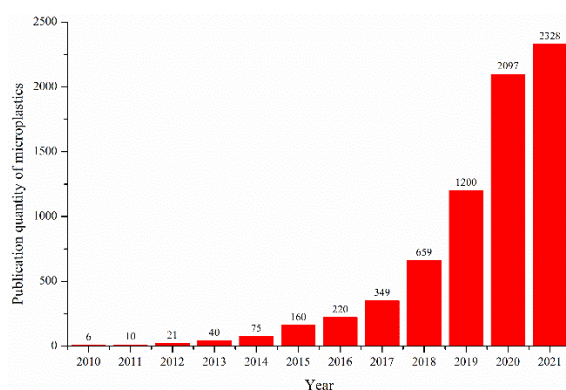


Figure 1. Statics of paper publications about microplastics from 2010 to 2021 by searching in Web of Science (accessed 24th September 2021).

Among the main detected MPs in soil and water are polypropylene (PP), polyethene (PE), polyvinyl chloride (PVC), polystyrene (PS), polyvinyl terephthalate (PET), polyoxymethylene (POM), polylactic acid and Polyamide (PA). Currently, in the market are available different types of polyamides, until now the principals are polyamide 6 (PA6) and polyamide 66 (PA6.6) which are produced as a fiber, plastic, adhesives or rubbers [15]. These fibers showed good thermal stability, abrasion resistance, high tensile strength, resistance to microbial and enzymatic attack [16] which make it a problem in waste water treatment plants. Several works have been focused to degrade these polymers through the use of microorganisms, photodegradation and photocatalysis. [17] reported the biological PA6 degradation, nevertheless, among the 58 fungi tested only one showed the capacity to degrade with a significant reduction on the PA6 molecular weight in 60-day incubation. reported the PA4 degradation in seawater in laboratory and in the sea with a reduction of the films weight by 10-70% as a consequence of bacterial degradation. [18] found that the presence of PA6.6 microplastics damage the sludge structure and then, reduce the removal pollution efficiency during the early treatment stage until the last 10 days, where the COD and ammonia nitrogen efficiencies increase regardless the PA6.6 microplastics concentration. [19] evaluated the degradation of the PA6.6 fiber through photocatalysis treatment with the use of TiO_2 under UV light (254 and 365 nm). With a concentration of 100 mg/L of TiO_2 and under UVC light it was reach the 97% mass loss of the fiber in a period of 48 h. Despite the efforts made in the abatement of this kind of pollutants is important to highlight the high degradation periods required, energy and amount of catalyst to reach the polymer degradation.

In this context, due to the high oxidation capacity and efficiency of the photo-Fenton process in the degradation of a wide variety of pollutants, low subproducts and sludge production, the present work proposes the use of photo-Fenton process as alternative for PA6.6 microplastic degradation at laboratory and pilot plant scale, as well as, the use of the surface area analysis as a parameter to characterize the PA6.6 degradation.

Experimental

Chemicals and materials

The PA6.6 used in this study has been supplied by the Textile Department of the Polytechnic University of Valencia. The chemicals used are hexahydrate ferric chloride ($\text{FeCl}_3 \cdot 6\text{H}_2\text{O}$, 99%, Scharlau), hydrogen peroxide (H_2O_2 , 30% w/w, Pareac), 1,10-phenantroline ($\text{C}_{12}\text{H}_8\text{N}_2$, 99%) and ammonium metavanadate ($\text{H}_4\text{NO}_3\text{V}$, 99.9%, Sigma Aldrich), ammonium acetate ($\text{CH}_3\text{COONH}_4$, 99%) and acetic acid (CH_3COOH , 100%) were purchased from Merk. The chemicals were used without further purification. Sulfuric acid and sodium hydroxide 0.1 M were used for pH adjustment. Millipore system was employed to produce high purity water ($18 \text{ M}\Omega \cdot \text{cm}$) used throughout all the experiments.

Photocatalytic degradation experiment

Photo-Fenton degradation studies were tested on PA6.6 microplastics with a size between 0.02-0.2 mm under simulated solar irradiation. Open glass reactors of a total volume of 250 mL were employed for the degradation experiments. In 250 mL of MQ water was dispersed 20 mg/L of PA6.6, 5 mg/L of Fe (III) as an iron source and 10 mg/L of H_2O_2 . pH was adjusted to 2.8 by dropwise addition H_2SO_4 and NaOH 0.1 M. The degradation experiment was initiated with the irradiation of the dispersion. In order to evaluate the behavior of the PA6.6 in the environment and evaluate new methodologies for its characterization, experiments on pilot plant under natural solar irradiation plus LED visible light irradiation were carried out. Experiments were performed in a volume of 28 L under previous lab conditions. Due to the difference between the intensity irradiation of the solar simulator and the solar irradiation the PA6.6 was treated for 10 h in the pilot plant. Hydrogen peroxide concentration was kept constant through manual addition each hour. Aliquots at different times and at the end of the irradiation experiments in lab and pilot plant scale were filtered with $0.45 \mu\text{m}$ nitrocellulose membrane (Millipore) and rinsed with MQ water. The PA6.6 was dried at room temperature and keep until its analysis. Control experiments were performed in dark conditions, nevertheless, no changes were observed in H_2O_2 concentration and superficial damage on PA6.6.

PA6.6 microplastic characterization

Field Emission Scanning Electron Microscopy

Changes on PA6.6 surface before and after photo-Fenton treatment were observed through Field Emission Scanning Electron Microscopy (FESEM). Samples were deposited on a double-face carbon adhesive and glued to the sample holder. The sample was sputter coated with a gold/platinum mixture by a coater SCD 005 (BAL-TEC), and analyzed using a Field Emission Scanning Electron Microscope ULTRA 55 (ZEISS). An acceleration voltage of 2 kV was applied and magnification was adjusted depending of the sample characteristics.

Differential Scanning Calorimetry

Melting behavior of the PA6.6 was evaluated before and after photo-Fenton treatment by Differential Scanning Calorimetry (DSC) analysis using a DSC1 (Mettler Toledo). Samples were heated from 30 to 300 °C with a heat rate of 10 °C/min under nitrogen gas flow. Melting temperature were measured during the second heating scan to remove previous thermal history of the sample.

Infrared Spectroscopy

The functional group in PA6.6 with and without treatment was done by Infrared Spectroscopy (FTIR) using an IFS 66/S (Bruker). Spectra was recorded between 500 to 4000 cm^{-1} with a resolution of 4 cm^{-1} and 64 scans for each spectrum.

Surface area

Specific surface area of PA6.6 before and after photo-Fenton treatment was determined based on absorption data using the Brunauer-Emmett-Teller (BET) model while the volume and size distribution of the pore were determined through the desorption isotherms and using the Barret-Joyner-Halenda (BJH) model. Measures were carried out by ASAP 2420 Accelerated Surface Area and Porosimetry System (Micromeritics).

Results

FESEM analysis was used to observe the superficial changes of the PA6.6 before and after the degradation treatment. Figure 2a shows the PA6.6 before the Photo-Fenton treatment. PA6.6 microplastic shows a smooth surface without surface damage, however, it is observed the presence of small particles on the surface which are formed because of the unpolymersized monomers, as well as, due to the presence of residues of the additives used in the synthesis process. Figure 2b shows the PA6.6 after 7 h of photo-Fenton treatment. The image shows a clear evidence of surface damage of the microplastic with the formation of holes and detachment of surface layers along the structure which could be as a consequence of the radical attack and posterior breaking of the C-N bond of the amide group [20]. Due to the presence of crystalline and amorphous regions in polymers, the observed damage in non-point areas along the PA6.6 has been assigned principally to the attack to amorphous regions where the oxygen diffusivity and permeability is higher due the lower packaging that make it vulnerable to radical attack. Similar behavior has been reported by [20] for polyamide degradation under UV light irradiation where after 14 days of irradiation the polymer showed the formation of holes due to the braking of the polymer chains.

The diameter of the holes in PA6.6 after 7 h of photo-Fenton degradation was measured through imageJ software and giving an average size diameter of 481.5 ± 78 nm, nevertheless, FESEM analysis has not shown the presence of particles that may suggested the release of fragments <500 nm from the holes which could indicated the breaking of the polymer chains into low molecular weight polymers of the same chemical structure.

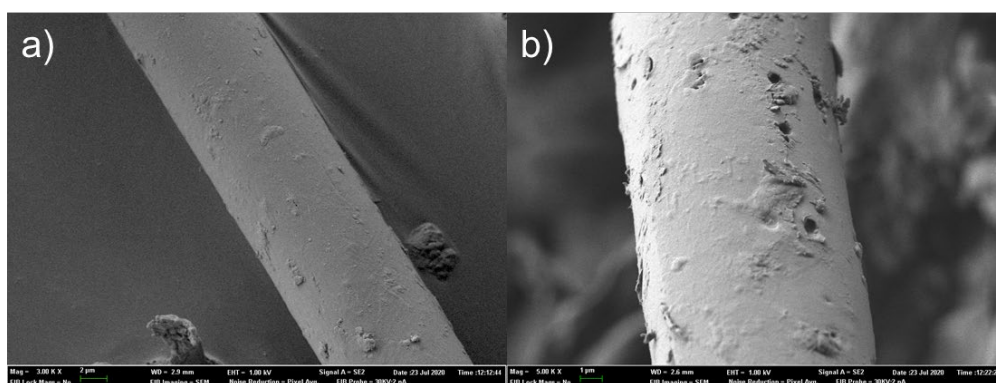


Figure 2. FESEM micrography of PA6.6 at a) 0h and b) 7 h of photo-Fenton treatment. PA6.6:20 mg/L, Fe: 5mg/L, H₂O₂: 10 mg/L and pH 2.8.

Functional group changes of PA6.6 with and without treatment were determined by FT-IR analysis. Figure 3 shows the FT-IR spectra of the PA6.6 at 0, 1 and 7 hours of photo-Fenton treatment, as well as table 1 shows the principal functional groups assignation. The peak at 3472 cm^{-1} assigned to hydroperoxides formation during PA6.6 oxidation shows a strong decrease since the 1 h until 7 h which could be due to the hydroperoxides decomposition by the breaking of the polymer chains. On another hand, the spectra shows a band at 1138 cm^{-1} attributed to the amorphous phase in PA6.6 [21], nevertheless, the second characteristic band of the amorphous region at 924 cm^{-1} was undetectable which may be due to its overlapping with the bands of the crystalline region that present a strong and broader intensity [3,4]. Despite the observed changes in the spectra, it was not detected the presence of additional bands that suggest the formation of new products which indicates the formation of molecules of the same unit of chemical structure.

Table 1. Functional groups and assignation of FT-IR bands.

Wavenumber [cm ⁻¹]	Functional group	Author
3472	Hydroperoxides	[22]
3294	NH stretching	[19]
3080	C-H/N-H band	[23]
2932	CH ₂ symmetric stretching	[24]
2858	CH ₂ symmetric stretching	[24]
1632	C=O stretching	[19]
1531	NH asymmetric stretching/CH ₂ asymmetric deformation	[3,4]
1462	C-H bond vibration	[3,6]
1416	CH ₂ scissoring vibration	[25]
1370	C-N bond/N-H/-CH ₃	[26]
1272	C-N stretching	[26]
1195	C-N stretching/CH ₂ vibration	[27,28]
1178	CH ₂ vibration	[28]
1138	CO-CH bond asymmetric vibration/ CH ₂ vibration	[21]
1039	C-C stretching	[23]
933	CO-NH vibration in plane/C-C stretching bond	[27,28]
857	C-C stretching	[29]
680	Amide mode IV/V	[19]
575	C-C vibration bond/C=O out plane bending	[23,26]

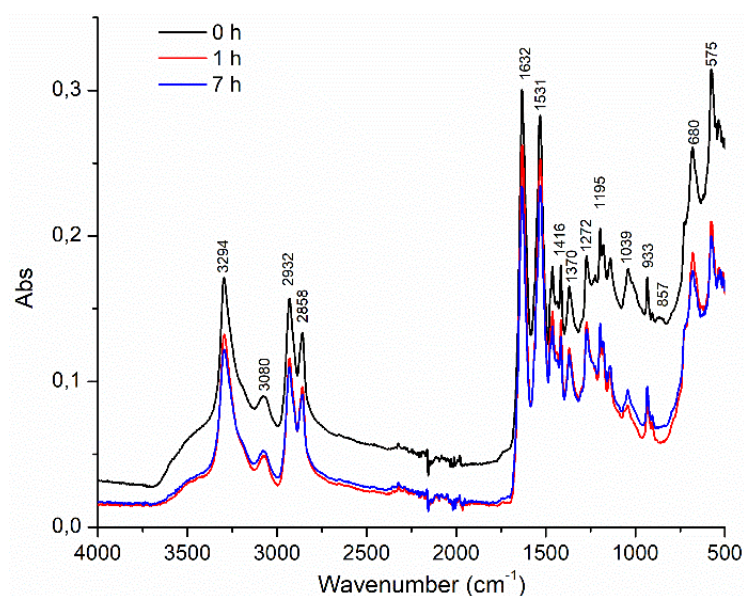
**Figure 3.** FT-IR spectra of PA6.6 at different times of degradation by photo-Fenton process.

Figure 4 shows the DSC analysis of the PA6.6 at 0, 4 and 7 h of photo-Fenton treatment. The PA6.6 at 0 h (without treatment) shows a melting point at 254°C which is in concordance with the reported in bibliography. After 4 h of treatment the melting point showed a decrement to 247°C which is attributed to the release of low molecular weight fragments due to cleavage of the C-N bond by the hydroxyl radical attack. The low molecular weight fragments releases present a lower melting point

than the PA6.6 and therefore this decrease could be an indicative sign of the degradation of the fiber [13,14,15]. On another hand, despite the superficial damage observed by FESEM in the PA6.6 after 7 h of degradation the melting point showed an increment to 256°C that could be due to the recrystallization of the low molecular weight fragments. In this sense, the aggregation of the release fragments from the PA6.6 and the increase of the heat in the analysis may cause the formation of large crystals with a better crystalline arrangement. [24] reported that morphological changes in the crystallite and the decreases in the size and stability of the crystalline unit may lead to the increase of the melting point in polymers like the observed in PA6.6.

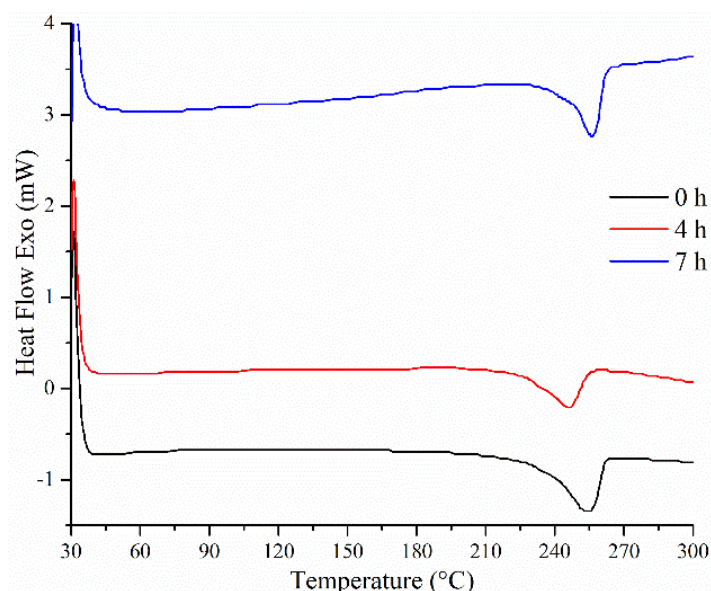


Figure 4. DSC thermogram of PA6.6 at different degradation times by Photo-Fenton process.

In order to have the knowledge about the possible behavior of the PA6.6 in the environmental conditions, experiments on pilot plant under natural solar irradiation plus LED visible was carried out as an environmental condition simulation, in the same way, due to the difference of the irradiation intensity between the solar simulator and the natural solar irradiation, the time exposure was extended to 10 h to ensure the maximum irradiation and therefore, degradation of the PA6.6. Figure 5 shows the FESEM image of the PA6.6 after 10 h of treatment in pilot plant. The fiber surface showed the presence of a large number of small particles of different sizes and shapes. These small particles on PA6.6 surface have been attributed to the iron deposition as a consequence of its aggregation after the irradiation process. Similar deposition behavior has been described with TiO_2 in the photocatalytic treatment of PA6.6 under UV light [19]. Furthermore, the figure evidence a lower presence of holes between 200-500 nm comparing with the observed in PA6.6 under laboratory degradation. As we described previously, the irradiation intensity plays an important role in the process, while in laboratory scale the irradiation is concentrated in a specific zone which allows to take the maximum advantage of the irradiation for the degradation of pollutants, in the case of the natural solar light the irradiation is not constant and present variations along the day for what it have to be concentrated as best as possible considering several factors in the experimental conditions and in the plant design, as well as, it is important to consider that the UV radiation is only the 5% of the terrestrial solar irradiation [30] which in this sense, the use of artificial sources of irradiation increase and keep constant the light intensity leading to a better radical hydroxyl production and thus, higher degradation can be reach [31] indicating that this is one of the most important factors to be considered. On another hand, the high complexity of polymers makes necessary the use of alternatives analysis for its characterization after degradation. The evident creation of defects on the PA6.6 surface could suggest and increment of its superficial area, for this reason, N_2 adsorption-desorption isotherms was done. Figure 6 shows the isotherms of the PA6.6 at with and without photo-Fenton treatment. According to the IUPAC classification the PA6.6 at 0 and 10 h presented an isotherm type III and II, respectively. Isotherm type III have been described for solids with low adsorption capacity as

polyethylene, while the isotherm II corresponds to nonporous or macroporous solids where at low relative pressures the available sites could be filled as monolayer and at high relative pressures the monolayer adsorbs more layers and, therefore increasing the adsorbate thickness continuously until reaches the condensation pressure [32]. As table 2 shows, according to BET model the PA6.6 without treatment has a specific surface area of $0.132 \text{ m}^2/\text{g}$ that is lower comparing with the surface area of the PA6.6 after 10 h of photo-Fenton treatment ($12.06 \text{ m}^2/\text{g}$) which represent an increment of 90 times the area of the PA6.6 at 0h. The increase of the specific surface area on the degraded PA6.6 is principally attributed to the defects formation on the PA6.6 surface which increase the available sites for N_2 adsorption and corroborating the results obtained by FESEM. Despite that the PA6.6 did not show the same behavior in pilot plant than in a laboratory scale, this kind of studies are important to get a better understatement about its degradation and possible enhances to be done in a future works.

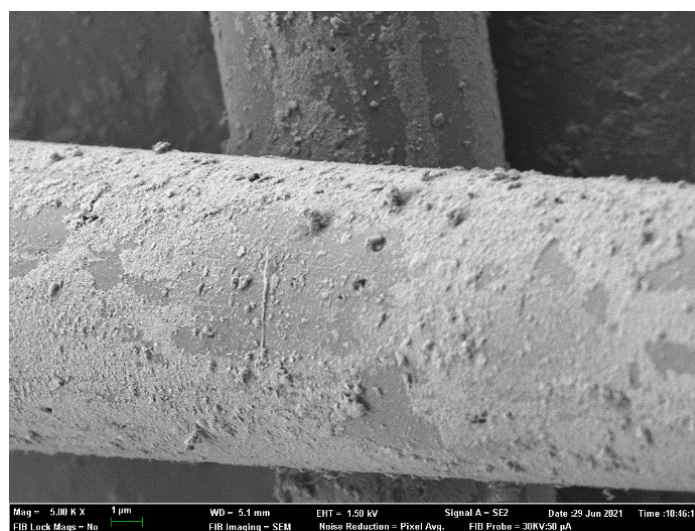


Figure 5. FESEM micrograph of PA6.6 after 10 h of treatment on pilot plant.

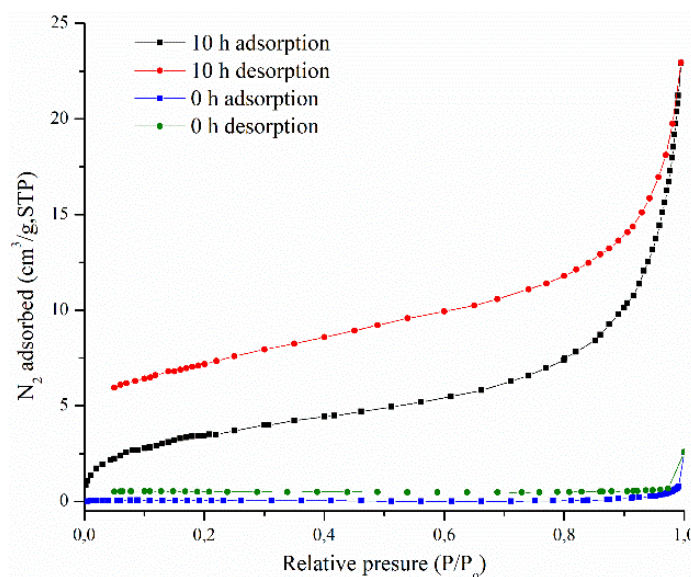


Figure 6. Nitrogen adsorption-desorption isotherms of PA6.6 at 0 h and 10 h of photo-Fenton treatment.

Table 2. Specific surface area and pore size of PA6.6 at 0 and 10 h of photo-Fenton treatment.

Sample	Specific Surface area [m ² /g]	Pore size [Å]
0 h	0.132	159.6
10 h	12.06	55.35

Conclusions

In this work, we demonstrated the capacity of degradation of the photo-Fenton process against the PA6.6 under solar simulator and terrestrial solar irradiation. The experiments showed that the photo-Fenton process degrade the PA6.6 through the formation of holes on its surface. As well as photo-Fenton degradation showed that the irradiation using a solar simulator promotes a better degradation of the PA6.6 microplastics than with the use of natural solar irradiation which become the irradiation intensity one of the principal factors that influence the process under the experimental conditions tested. The photocatalytic degradation of PA6.6 under natural solar irradiation increase the specific surface area of the PA6.6 which provide a new parameter to be considered in the characterization of the photodegraded polymers.

Acknowledgment

The authors wish to thank the Spanish Ministry of Science, Innovation and Universities (MCIU) for funding under the CalypSol Project (Reference: RTI2018-097997-B-C31-AR). PhD Scholarship from CONACYT for E. Marcelino-Perez (709357) is acknowledged.

References

- [1] Information on <https://www.plasticseurope.org/en/resources/publications/4312-plastics-facts-2020>
- [2] S. Chatterjee, S. Sharma, Microplastics in our oceans and marine health, *F. Actions Sci. Rep.* 19 (2019) 54–61.
- [3] B. Worm, H. K. Lotze, I. Jubinville, C. Wilcox, J. Jambeck, Plastic as a Persistent Marine Pollutant, *Annu. Rev. Environ. Resour.* 42 (2017) 1–26.
- [4] S. Wolff, J. Kerpen, J. Prediger, L. Barkmann, L. Müller, Determination of the microplastics emission in the effluent of a municipal waste water treatment plant using Raman microspectroscopy, *Water Res. X*, 2 (2019) 100014.
- [5] H. S. Auta, C. U. Emenike, S. H. Fauziah, Distribution and importance of microplastics in the marine environment: A review of the sources, fate, effects, and potential solutions, *Environ. Int.*, 102 (2017) 165–176.
- [6] H. S. Auta, C. U. Emenike, S. H. Fauziah, Screening of *Bacillus* strains isolated from mangrove ecosystems in Peninsular Malaysia for microplastic degradation, *Environ. Pollut.* 231 (2017) 1552–1559.
- [7] K. Zhang, A. H. Hamidian, A. Tubić, Y. Zhang, J. K. H. Fang, C. Wu, P. K. S. Lam, Understanding plastic degradation and microplastic formation in the environment: A review, *Environ. Pollut.* 274 (2021) 116554.

-
- [8] A. A. Horton, D. K. A. Barnes, Microplastic pollution in a rapidly changing world: Implications for remote and vulnerable marine ecosystems, *Sci. Total Environ.* 738 (2020) 140349.
- [9] H. Zang, J. Zhou, M. R. Marshall, D. R. Chadwick, Y. Wen, D. L. Jones, Microplastics in the agroecosystem: Are they an emerging threat to the plant-soil system?, *Soil Biol. Biochem.* 148 (2020) 107926.
- [10] M. Lehtiniemi, S. Hartikainen, P. NÄkki, J. Engström-Öst, A. Koistinen, O. Setälä, Size matters more than shape: Ingestion of primary and secondary microplastics by small predators, *Food Webs.* 17 (2018) e00097.
- [11] C. Wang, J. Zhao, B. Xing, Environmental source, fate, and toxicity of microplastics, *J. Hazard. Mater.* 407 (2020) 124357.
- [12] Y. Xiang, L. Jiang, Y. Zhou, Z. Lou, D. Zhi, J. Yang, S. S. Lam, Microplastics and environmental pollutants: Key interaction and toxicology in aquatic and soil environments, *J. Hazard. Mater.* 422 (2021) 126843.
- [13] Y. Deng, R. Zhao, Advanced Oxidation Processes (AOPs) in Wastewater Treatment, *Curr. Pollut. Reports.* 1 (2015) 167–176.
- [14] A. Bakir, S. J. Rowland, R. C. Thompson, Transport of persistent organic pollutants by microplastics in estuarine conditions, *Estuar. Coast. Shelf Sci.* 140 (2014) 14–21.
- [15] D. Feldman, Polyamide nanocomposites, *J. Macromol. Sci. Part A Pure Appl. Chem.* 54 (2017) 255–262.
- [16] J. Friedrich, P. Zalar, M. Mohorčič, U. Klun, A. Kržan, Ability of fungi to degrade synthetic polymer nylon-6, *Chemosphere.* 67 (2007) 2089–2095.
- [17] N. Yamano, N. Kawasaki, S. Ida, A. Nakayama, Biodegradation of polyamide 4 in seawater, *Polym. Degrad. Stab.* 166 (2019) 230–236.
- [18] L. Zhao, C. Su, W. Liu, R. Qin, L. Tang, X. Deng, S. Wu, M. Chen, Exposure to polyamide 66 microplastic leads to effects performance and microbial community structure of aerobic granular sludge, *Ecotoxicol. Environ. Saf.* 190 (2019) 110070.
- [19] J. M. Lee, R. Busquets, I. C. Choi, S. H. Lee, J. K. Kim, L. C. Campos, Photocatalytic degradation of polyamide 66: Evaluating the feasibility of photocatalysis as a microfibre-targeting technology, *Water (Switzerland).* 12 (2020) 1–20.
- [20] L. Sørensen, A. S. Groven, I. A. Hovsbakken, O. Del Puerto, D. F. Krause, A. Sarno, A. N. Booth, UV degradation of natural and synthetic microfibers causes fragmentation and release of polymer degradation products and chemical additives, *Sci. Total Environ.* 755 (2021) 143170.
- [21] N. Vasanthan, D. R. Salem, Structure characterization of heat set and drawn polyamide 66 fibers by FTIR spectroscopy, *Mater. Res. Innov.* 4 (2001) 155–160.
- [22] P. N. Thanki, R. P. Singh, Photo-oxidative degradation of nylon 66 under accelerated weathering, *Polymer (Guildf).* 39 (1998) 6363–6367.
- [23] J. Charles, G. R. Ramkumaar, S. Azhagiri, S. Gunasekaran, FTIR and thermal studies on nylon-66 and 30% glass fibre reinforced nylon-66, *E-Journal Chem.* 6 (2009) 23–33.
- [24] F. Navarro-Pardo, G. Martínez-Barrera, A. L. Martínez-Hernández, V. M. Castaño, J. L. Rivere-Armenta, F. Medellín-Rodríguez, C. Velasco-Santos, Effects on the thermo-mechanical and crystallinity properties of nylon 6,6 electrospun fibres reinforced with one dimensional (1D) and two dimensional (2D) carbon, *Materials (Basel).* 6 (2013) 3494–3513.

-
- [25] A. M. Pannase, R. K. Singh, B. Ruj, P. Gupta, Decomposition of polyamide via slow pyrolysis: Effect of heating rate and operating temperature on product yield and composition, *J. Anal. Appl. Pyrolysis*. 151 (2020) 104886.
- [26] L. A. Díaz-Alejo, E. C. Menchaca-Campos, J. Uruchurtu Chavarín, R. Sosa-Fonseca, M. A. García-Sánchez, Effects of the addition of ortho - And para NH₂ substituted tetraphenylporphyrins on the structure of nylon 66, *Int. J. Polym. Sci.* 2013 (2013) 1-14.
- [27] N. Vasanthan, Crystallinity determination of nylon 66 by density measurement and fourier transform infrared (FTIR) spectroscopy, *J. Chem. Educ.* 89 (2012) 387–390.
- [28] G. Zhang, T. Watanabe, H. Yoshida, T. Kawai, Phase transition behavior of nylon-66, nylon-48, and blends, *Polym. J.* 35 (2003) 173–177.
- [29] A. Dawelbeit, M. Yu, Transient Confinement of the Quaternary Tetramethylammonium Tetrafluoroborate Salt in Nylon 6 , 6 Fibres : Structural Developments for High Performance Properties, *Materials*, 14 (2021) 2938.
- [30] Information on <https://www.ncbi.nlm.nih.gov/books/NBK304366/>
- [31] S. Dominguez, P. Ribao, M. J. Rivero, I. Ortiz, Influence of radiation and TiO₂ concentration on the hydroxyl radicals generation in a photocatalytic LED reactor. Application to dodecylbenzenesulfonate degradation, *Appl. Catal. B Environ.* 178 (2014) 165–169.
- [32] S. Yurdakal, C. Garlisi, L. Özcan, M. Bellardita, and G. Palmisano, (Photo)catalyst characterization techniques: Adsorption isotherms and BET, SEM, FTIR, UV-Vis, photoluminescence, and electrochemical characterizations, in: G. Marci, L. Palmisano (Eds.), *Heterogeneous Photocatalysis Relationships with Heterogeneous Catalysis and Perspectives*, Elsevier, 2019, pp. 87-152.

Keyword Index

3D Printing 25
3D-Roving Placement Rack 101

A

Adhesion 25
Antibacterial Activity 63
Antimicrobial Activity 57
Antimicrobial Finishes 189
Antimicrobial Textile 83, 91
Ascorbic Acid 83

B

Bio-Based Textiles 3
Blended Yarn 15

C

CAE-Supported Design 101
Carbon Fiber 101, 139
Cellulosic Acetate Fiber 15
Chitosan 83
Chitosan Mordanting 189
Clay Pigment 233
Clindamycin 71
Coating 203
Collagenase 43
Color Intensity 163
Color Prediction 195
Color Properties 181
Colour Measurement 157
Copper Nanoparticles 83
Cotton Knitted Fabric 181

D

Degradation 243
Denim Fabric Performance 15
Design 227
Dielectric Barrier Discharge 91
Digital Image Correlation 111
Direct Dye Recovery 233
Ductile Behavior 121
Dye Plants 209
Dye Recovery 233
Dye Wool 209
Dying 209

E

Ecological Textile 189
Electrospinning 71, 227
Electrospinning Process 57
Energy Absorption 121
Exhaustion Deposition 91
Exhaustion Dyeing 195

F

Fabric 35
Fashion Design 3
Fatigue Resistance 163

G

Gelatin 71

H

High Performance Composites 133
Hot Plate 157
Hybrid Reinforcement 121
Hybrid Research Method 3
Hybrid Yarn 139, 147
Hybridization 139
Hydrogels 43
Hydrophilicity 173
Hydrotalcite 233

I

Impact 121
In Situ Sensors 111

L

Leucodyes 157
Lyocell 15

M

Matlab 35
Microplastic 243
Moisture/Thermal Management 203
Monitoring System 195

N		Strengthening Layers	121
Nanoclay		Structural Health Monitoring (SHM)	111
Nanofibers		Subtractive Textures	3
Natural Dyes		Surgical Mask	63
Natural Dyeing		Sustainability	209
Nonwoven		Sustainable Regenerative Yarn	15
O		T	
Opacity		Textile	3
Orange Waste		Textile Reinforced Concrete	101, 111
P		Textile Reinforcement	121
PCL Nanofibers		Textile Reinforcement Structures	101
PET Fabric		Textiles	157
Photo-Fenton		Thermochromic Dyes	157
Photochromic Phenomena		Thermoplastic Composite	139
Piezoresistivity		Thermoplastic Composite Tensile Property	147
Plastic Waste		Thermoplastic Composites	133
Poly(Ethylene Terephthalate)		Thickness	35
Poly(Vinyl Alcohol)		U	
Polyamide		Ultrafine Friction Grinding	3
Polyamide Fibers		Uni Directional Tape	133
Polycaprolactone		UV Irradiance Time	163
Polyester		W	
Polyester Fibers		Weave	35
Propolis		Weft Knitting	139
Protective Textiles		Wool	209
R		Wound Dressing	43, 71
Reactive Dye Recovery		Woven Structure	25
Recycled Carbon Fiber		Y	
Recycled Cotton		Yarn	35
Recycling			
Reseda Luteola L			
Resizing			
Robot-Supported			
Rubia Tinctorum			
S			
Self-Adhesive			
SHCC			
Silver Nanoparticles			
Soil-Release			
Solvolysis			
Spun Fibre Yarn			
Strain-Hardening Cement-Based Composites SHCCs			

Author Index

A

Abdkader, A.	133, 147
Almeida, E.	209
Altindere, S.	181
Alves, B.	195
Alves, E.	209
Amat Payá, A.	243
Antunes, J.	43
Aral, N.	63
Arques Sanz, A.	243

B

Babaarslan, O.	15
Bachor, S.	147
Bahrami, H.	71
Bao, L.M.	139
Belino, N.	209
Bezerra, F.M.	57
Bizjak, M.	25
Bonet-Aracil, M.	189, 233, 243
Bou-Belda, E.	35, 189, 233, 243

C

Caliskan, G.	181
Carbonell, A.	35
Çay, A.	157
Cherif, C.	101, 111, 121, 133, 139, 147
Cochrane, C.	71
Čuk, M.	25
Cvelbar, U.	91

D

de Almeida, D.S.	57
Díaz-García, P.	35
Dilek, S.	15
Dumitrescu, D.	3

F

Fernandes, R.	91
Frajová, J.	227
Friese, D.	101

G

Galata, S.	157
Gallardo, E.	209
Gameiro, C.	209
Gisbert-Payá, J.	35, 189
Gkoutzeli, D.	157
Golla, A.	121
Gramc, K.	25

H

Hahn, L.	101
Häntzsche, E.	139
Hasan, M.M.B.	133, 139, 147
Hoebel, S.	133
Hoffmann, G.	111, 121

K

Kajiwara, K.	139
Khurshid, M.F.	133
Kocak, E.D.	181
Koncar, V.	71
Kooroshnia, M.	3
Kosemek, O.	181

L

Lemos, D.	43
Lopes Aguiar, M.	57
López-Rodríguez, D.	233

M

Magalhães, C.	91
Marcelino-Perez, E.	243
Martins, L.D.	57
Matsouka, D.	157
Mehravani, B.	83, 91
Melro, L.	91
Micó-Vicent, B.	233
Miranda, T.	43, 173
Mirmoeini, G.	71
Mohamadi, P.	71
Mohsenzadeh, E.	71
Montava, I.	35
Montazer, M.	83

Muck, D.	25		
Murakami, Y.	139	X	
		Xia, G.	203
N		Xin, J.H.	203
Nicolau, T.	91	Xuan, H.L.	111, 121
Nocke, A.	111, 121		
		Y	
O		Yigit, I.	63
Opálková Šišková, A.	227		
		Z	
P		Zamani, A.	3
Padrão, J.	91	Zille, A.	83, 91
Passarinha, L.	209		
Pinto, C.	173		
Pinto, M.	209		
R			
Rabe, D.	139		
Ribeiro, A.	43		
Ribeiro, A.I.	83, 91		
Rodilla, J.	209		
Rosado, T.	209		
S			
Santana, M.H.S.	57		
Santos, J.	43, 173, 195		
Santos, R.	57		
Scacchetti, F.A.P.	57		
Sennewald, C.	111, 121		
Sezgin, P.	181		
Shahid, A.	15		
Shvalya, V.	91		
Silva, L.	195		
Soares, G.	43, 173, 195		
Solanki, U.	163		
Syed, S.	3		
U			
Uysal, S.	189		
V			
Vassiliadis, S.	157		
Vicente, R.	243		
Vik, M.	163		
Viková, M.	163		
Vo, D.M.P.	111, 121		
Vorhof, M.	121		